RECENT ADVANCES IN VOLCANIC GAS SCIENCE

EDITED BY: Andrew McGonigle, Alessandro Aiuppa, Nicole Bobrowski,
Franco Tassi and Fátima Viveiros

PUBLISHED IN: Frontiers in Earth Science

frontiers Research Topics

ISSN 1664-8714
ISBN 978-2-88963-382-1
DOI 10.3389/978-2-88963-382-1

About Frontiers

Frontiers is more than just an open-access publisher of scholarly articles: it is a pioneering approach to the world of academia, radically improving the way scholarly research is managed. The grand vision of Frontiers is a world where all people have an equal opportunity to seek, share and generate knowledge. Frontiers provides immediate and permanent online open access to all its publications, but this alone is not enough to realize our grand goals.

Frontiers Journal Series

The Frontiers Journal Series is a multi-tier and interdisciplinary set of open-access, online journals, promising a paradigm shift from the current review, selection and dissemination processes in academic publishing. All Frontiers journals are driven by researchers for researchers; therefore, they constitute a service to the scholarly community. At the same time, the Frontiers Journal Series operates on a revolutionary invention, the tiered publishing system, initially addressing specific communities of scholars, and gradually climbing up to broader public understanding, thus serving the interests of the lay society, too.

Dedication to Quality

Each Frontiers article is a landmark of the highest quality, thanks to genuinely collaborative interactions between authors and review editors, who include some of the world's best academicians. Research must be certified by peers before entering a stream of knowledge that may eventually reach the public - and shape society; therefore, Frontiers only applies the most rigorous and unbiased reviews.
Frontiers revolutionizes research publishing by freely delivering the most outstanding research, evaluated with no bias from both the academic and social point of view. By applying the most advanced information technologies, Frontiers is catapulting scholarly publishing into a new generation.

What are Frontiers Research Topics?

Frontiers Research Topics are very popular trademarks of the Frontiers Journals Series: they are collections of at least ten articles, all centered on a particular subject. With their unique mix of varied contributions from Original Research to Review Articles, Frontiers Research Topics unify the most influential researchers, the latest key findings and historical advances in a hot research area! Find out more on how to host your own Frontiers Research Topic or contribute to one as an author by contacting the Frontiers Editorial Office: researchtopics@frontiersin.org

RECENT ADVANCES IN VOLCANIC GAS SCIENCE

Topic Editors:
Andrew McGonigle, University of Sheffield, United Kingdom
Alessandro Aiuppa, University of Palermo, Italy
Nicole Bobrowski, Heidelberg University, Germany
Franco Tassi, University of Florence, Italy
Fátima Viveiros, IVAR, University of the Azores, Portugal

Volcanoes release gases to the atmosphere both during and between eruptive phases. Primary and secondary processes occurring within the mantle and crust control the gases' chemical and isotopic compositions as well as their emission rates. Therefore by measuring these gases a wealth of scientific information concerning the source and fate of these fluids is provided. Fluid geochemistry has been highly useful in advancing both our fundamental scientific understanding and procedures for operational volcano monitoring and eruption forecasting.

Gases from low-to-high temperature fumaroles and those diffusively released through the soils of volcanic flanks are investigated using various sampling and measurement techniques. Furthermore, a variety of remote sensing methods are applied at relatively great distances from the source to gather major gas composition and flux data for volcanic plumes using ground based, airborne (including UAV) and space borne platforms. The acquired data have advanced science in a number of key ways:

- firstly, with parallel thermodynamical modelling to advance our capacity to interpret acquired degassing data;
- secondly, through improved constraints on budgets for volcanically mediated geochemical cycling, particularly via regional subduction processes;
- thirdly, through improved constraints on the effects of volcanic gases on atmospheric composition, chemistry and radiative transfer, particularly in terms of halogen chemistry, volcanogenic climate change and impacts on human health;
- fourthly, there has been a growing body of work focused on combining degassing data with contemporaneous geophysical data and studies on conduit fluid dynamics to advance our understanding of how subterranean gas flow mediates activity at the surface;
- and fifthly, there have been considerable advances in the methods themselves, used to make the gas measurements, in particular in terms of extractive sampling (e.g., using MultiGAS units, mass spectrometry, spectroscopic isotope measurement approaches and diffusive denuder sampling) and remote sensing approaches (e.g., DOAS, UV cameras and other imaging techniques, LIDAR and FT)

Citation: McGonigle, A., Aiuppa, A., Bobrowski, N., Tassi, F., Viveiros, F., eds. (2020). Recent Advances in Volcanic Gas Science. Lausanne: Frontiers Media SA.
doi: 10.3389/978-2-88963-382-1

Table of Contents

frontiers
in Earth Science

ORIGINAL RESEARCH
published: 05 June 2018
doi: 10.3389/feart.2018.00069

The Geothermal Resource in the Guanacaste Region (Costa Rica): New Hints From the Geochemistry of Naturally Discharging Fluids

Franco Tassi[1,2]*, *Orlando Vaselli*[1,2], *Giulio Bini*[1], *Francesco Capecchiacci*[1], *J. Maarten de Moor*[3], *Giovannella Pecoraino*[4] and *Stefania Venturi*[2]

[1] Department of Earth Sciences, University of Florence, Florence, Italy, [2] CNR-IGG Institute of Geosciences and Earth Resources, Florence, Italy, [3] Observatorio Vulcanológico y Sismológico de Costa Rica, OVSICORI-UNA, Heredia, Costa Rica, [4] Sezione di Palermo, Istituto Nazionale di Geofisica e Vulcanologia, Palermo, Italy

The Guanacaste Geothermal Province (GGP) encompasses the three major volcanoes of northern Costa Rica, namely from NW to SE: Rincón de la Vieja, Miravalles, and Tenorio. The dominant occurrence of (i) SO_4-rich acidic fluids at Rincón de la Vieja, (ii) Cl-rich mature fluids at Miravalles, and (iii) HCO_3^--rich and low-temperature fluids at Tenorio was previously interpreted as due to a north-to-south general flow of thermal waters and a magmatic gas upwelling mostly centered at Rincón de la Vieja, whereas Miravalles volcano was regarded as fed by a typical geothermal reservoir consisting of a highly saline Na-Cl aquifer. The uniformity in chemical and isotopic (R/Ra and $\delta^{34}S$) compositions of the neutral Cl-rich waters suggested to state that all the thermal discharges in the GGP are linked at depth to a single, regional geothermal system. In this scenario, the thermal manifestations related to Tenorio volcano were regarded as a distal and diluted fluid outflow. In this study, a new gas geochemical dataset, including both chemical and isotopic ($\delta^{13}C$-CO_2 and R/Ra) parameters of fluid discharges from the three volcanoes, is presented and discussed. Particular attention was devoted to the Tenorio thermal manifestations, since they were poorly studied in the past because this area has been considered of low geothermal potential. The aim is to provide insights into the magmatic-hydrothermal fluid circulation and to verify the spatial distribution of the heat fluid source feeding the fluid manifestations. According to this new dataset, CO_2, i.e., the most abundant dry gas in the fluid manifestations, is mostly produced by limestone, whereas the mantle CO_2 contribution is $\leq$3.3%. Strongly acidic gas compounds from magma degassing were absent in the discharged fluids, being scrubbed by secondary processes related to prolonged fluid-rock interactions and mixing with shallow aquifers. Our results only partially confirm the previously depicted model, because the geochemical and isotopic features (e.g., relatively high concentrations of temperature-dependent gases and high R/Ra values) shown by fluids seeping out from the southern sector of Tenorio volcano are more representative of medium-to-high enthalpy volcanic systems than those typically occurring in distal areas. This implies that the geothermal potential in the south of the GGP is higher than previously thought.

Keywords: geothermal prospection, gas geothermometry, fluid geochemistry, fluid reservoir, Guanacaste province

Edited by:
Jacob B. Lowenstern, Cascades Volcano Observatory (CVO), Volcano Disaster Assistance Program (USGS), United States

Reviewed by:
Loic Peiffer, Centro de Investigación Científica y de Educación Superior de Ensenada, Mexico
Hiroshi Shinohara, Geological Survey of Japan (AIST), Japan

***Correspondence:**
Franco Tassi
franco.tassi@unifi.it

Specialty section:
This article was submitted to Volcanology, a section of the journal Frontiers in Earth Science

Received: *21 March 2018*
Accepted: *17 May 2018*
Published: *05 June 2018*

Citation:
Tassi F, Vaselli O, Bini G, Capecchiacci F, de Moor JM, Pecoraino G and Venturi S (2018) The Geothermal Resource in the Guanacaste Region (Costa Rica): New Hints From the Geochemistry of Naturally Discharging Fluids. Front. Earth Sci. 6:69. doi: 10.3389/feart.2018.00069

INTRODUCTION

Actions aimed to the evaluation of the sustainable potential of geothermal fluid reservoirs can provide fundamental information for minimizing the financial risk related to the exploitation activity of such natural resources. Geochemical prospections, coupled with geophysical measurements, are considered useful tools to investigate the chemical-physical features of hot, deep aquifers at relatively low cost (e.g., Giggenbach, 1991), especially for developing countries poor in conventional energy sources, such as carbon, oil, and natural gases. The geothermal potential in the Guanacaste Geothermal Province (GGP), northern Costa Rica, has been investigated since the early 1970's (Fergurson and Alfonso, 1977; Gardner and Corrales, 1977). There are three stratovolcanoes in this region, namely from NW to SE: Rincón de la Vieja, Miravalles, and Tenorio. In the last centuries, phreatic and phreatomagmatic eruptions frequently occurred at Rincón de la Vieja (e.g., Barquero and Segura, 1983; Boudon et al., 1996; Kempter et al., 1996), whereas at Miravalles and Tenorio (**Figure 1**) no historical eruptions were recorded (Mainieri et al., 1985; Alvarado, 2000). GGP shows numerous thermal fluid discharges, e.g., fumaroles, steam-heated soils, low-to-high temperature SO_4- and Cl-rich springs, and CO_2-rich bubbling pools (Giggenbach and Corrales, 1992; Gherardi et al., 2002; Tassi et al., 2005), which, as commonly occurs in a volcanic environment, are related to a hydrothermal-magmatic source. The spatial distribution of neutral, geothermal-type Cl^--rich water discharges, locally known as *salitrales*, and acidic SO_4^{2-}-rich springs produced by interaction of meteoric water and hydrothermal gases, was interpreted as an evidence for the presence of a single contiguous geothermal reservoir beneath the GGP (Giggenbach and Corrales, 1992). The Cl^- concentration and temperature of this deep aquifer were estimated at ∼3,500 mg/L and ∼250°C, respectively (Giggenbach and Corrales, 1992; Gherardi et al., 2002). A similar temperature was also found in fluids from other exploited geothermal systems of Central America, such as those located in Salvador (Ahuachapan and Berlin), whose Cl^- concentrations at the beginning of the exploitation where up to 9,000 and 11,000 mg/L, respectively (D'Amore and Mejia, 1999). The temperature hypothesized for the GGP reservoir, supported by calculations based on water isotopes and the contents of the main anions (Cl^- and SO_4^{2-}), were consistent with those measured on the fluids discharged from the geothermal wells along the SW slope of the Miravalles volcano (Gherardi et al., 2002). According to this scenario, the area named Las Pailas (on the NW flank of Rincón de la Vieja volcano; #6 in **Figure 1**) and the inner zone of the Miravalles caldera were regarded as the areas most affected by deep fluid upwelling, whereas the thermal manifestations located within the SE portion of GGP, corresponding to Tenorio volcano, were considered as distal fluid outflow (**Figure 1**). These indications gave a pulse to the development of the geothermal fluid exploitation at Miravalles (Vallejos-Ruiz et al., 2005), as well as the prospection at Rincón de la Vieja (Molina and Martì, 2016, and references therein) where the geothermal fluid exploitation is still at the preliminary stage.

In the present study, the chemical and isotopic ($\delta^{13}C$-CO_2 and R/Ra) composition of the GGP fluid discharges, with a special

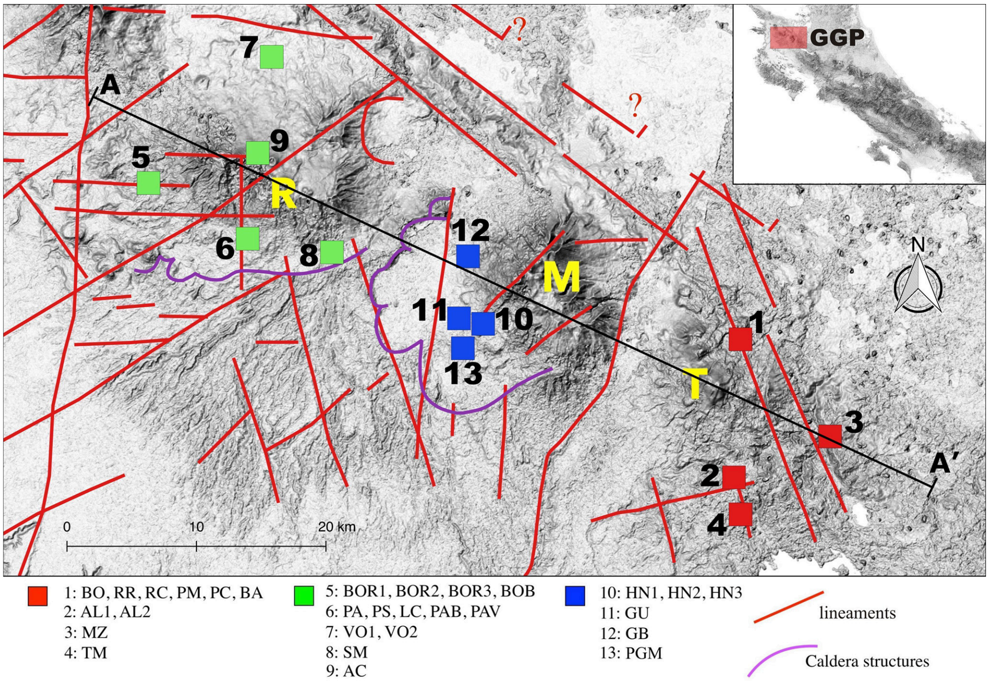

FIGURE 1 | Map of the Guanacaste region with the location of sampling sites. Green square: Rincón de la Vieja (R); blue square: Miravalles (M); red square: Tenorio (T).

focus on those related to Tenorio volcano, is reported. At the light of this robust geochemical database, integrated with data from literature, the primary sources and secondary chemical-physical processes controlling the fate of the hydrothermal fluids are investigated. A critical revision of the hydro-geochemical conceptual models proposed for GGP by the previous authors is carried out, providing new insight into the geothermal potential of this region.

REGIONAL SETTING AND VOLCANIC ACTIVITY

Costa Rica has a complex geology, related to the presence of three tectonic plates (Caribbean, Cocos and Nazca), the Panama microplate and an uncertain number of tectonic terranes (Alvarado and Cárdenes, 2016). These slabs are separated by a zone of diffusive deformation named Central Costa Rica Deformed Belt (CCRBD) and are bound to the southwest by the Middle America Trench (MAT; Montero et al., 2017). The magmatic arc, which is located ∼150 km northeast of MAT, consists of (i) two active volcanic ranges, namely Cordillera Central (CC) and Cordillera de Guanacaste (CG), and (ii) two extinct ranges, i.e., Cordillera de Tilarán-Aguacate (CAg) and Cordillera de Talamanca (CT) (Alvarado and Cárdenes, 2016).

The Cordillera de Guanacaste (NW Costa Rica) was formed about 0.6 Ma and comprises four stratovolcanic complexes (1,500–2,000 m high): Orosí-Cacao, Rincón de la Vieja-Santa María, Miravalles-Zapote, and Tenorio-Montezuma (Chiesa et al., 1994). A series of E-W-trending lineament were identified between Orosí-Cacao and Rincón de la Vieja volcanoes, whereas secondary lineaments showing a different trend (NNE-SSW, N-S-, and NNW-SSE) were recognized along the eastern flank of Miravalles volcano, as well as at Rincón de la Vieja and Tenorio volcanoes (Chavarría et al., 2010) (**Figure 1**).

Rincón de la Vieja is the largest volcano of the Cordillera de Guanacaste, with an estimated volume of 130 km^3 (Carr, 1984). It is a complex andesitic stratovolcano consisting of an elongated, arcuate NW-SE trending of nine coalescing pyroclastic cones, spreading over an 8-km long axis (Chiesa et al., 1994). The maximum elevation (Santa Maria cone) is 1916 m a.s.l. The last plinian eruption occurred 3.5 ka (Alvarado et al., 1992), whereas the historical activity was characterized by the occurrence of frequent phreatic and phreato-magmatic eruptions from the Active Crater (Tristan, 1921; Barquero and Segura, 1983). Since 1991, 20 phreatic eruptions, producing ash deposits and debris-flows, occurred (OVSICORI-UNA, 1998), while a transition to a phreato-magmatic activity took place in 1995 (OVSICORI-UNA, 1995). Intense phreatic activity was recorded in August-September 2011, February-April 2012, September 2014, February 2015, March 2016, February-October 2017 (OVSICORI-UNA, 2011, 2012, 2014, 2015, 2016, 2017).

Miravalles is the highest volcano of the Cordillera de Guanacaste (2028 m a.s.l.). This andesitic stratovolcano pertains to the Miravalles-Zapote complex, whose activity started with the edification of the Guayabo volcano (1.17–1.0 Ma; Alvarado and Gans, 2012). The latter was destroyed by the following explosive activity (1.5 and 0.6 Ma) giving rise to the formation of the 15 km wide Guayabo caldera (Chiesa et al., 1992). The latter hosts Cabro Muco volcano (0.57–0.28 Ma), in the eastern sector, and Zapote and Miravalles volcanoes (<0.28 Ma) in the northern sector (Chiesa et al., 1992; Alvarado and Gans, 2012). Tephrochronology data suggested that an important eruptive event occurred at about 5050 BC, whilst local witnesses reported a volcanic event on the 14th of September 1946 in the SW flank of Miravalles.

Tenorio-Montezuma, in the south-easternmost part of the Cordillera de Guanacaste, is a basaltic-andesitic volcanic complex, consisting of NNW-ESE-oriented volcanic structures, including pyroclastic cones and two twin-craters (Tenorio and Montezuma) (Alvarado, 1993). An andesitic dome field (Bijagua) grew over a relatively old volcanic center in the northern flank of Tenorio (Chiesa et al., 1994). Little is known about the geology of this intensely forested area. The andesitic and basaltic lavas of Monteverde (2.17–1.92 Ma) are the basement of the Tenorio edifice that developed during two main eruptive phases, dated 0.74–0.54 and 0.37–0.26 Ma, respectively (Alvarado and Gans, 2012). The occurrence of a caldera in the southern flank was hypothesized by ICE (Istituto Costaricence de Electricidad) and ENEL (Italian Board of Electricity) (ICE, 1990), although Alvarado and Gans (2012) suggested that the depression should be regarded as a northernmost branch of the Arenal graben. No historical volcanic activity has likely occurred at Tenorio-Montezuma. Notwithstanding, a legend, not supported by scientific investigation, speaks of an eruption that occurred in 1816 (Alvarado, 1993).

PREVIOUS GEOTHERMAL PROSPECTION AND EXPLOITATION

A pre-feasibility study carried out in 1976 in the Miravalles area suggested the presence of a geothermal reservoir with temperature ∼240°C (Gardner and Corrales, 1977). From 1977 to 1986, new exploratory activities, including the drilling of eight wells, provided the first insights into the geochemical features of the liquid-dominated system, i.e., neutral pH and a typical Na^+-Cl^- composition (Giggenbach and Corrales, 1992; Gherardi et al., 2002). The chemical and isotopic composition of fluid discharges from the GGP sampled between 1982 and 1988, allowed the construction of a hydro-geochemical model of the hydrothermal system (Giggenbach and Corrales, 1992). A geophysical prospection carried out by ICE and ELC (Electroconsult) between 1989 and 1991 (ICE, 1991), revealed areas of great interest for geothermal fluid exploitation along the slopes of Rincón de la Vieja, Miravalles, and Tenorio volcanoes. From 1994 to 2004, 5 geothermal power plants were installed in the Miravalles area, amounting for a maximum sustainable capacity of 163.5 MW (Sànchez-Rivera and Vallejos-Ruiz, 2015). Then, ICE focused its attention on the Rincón de la Vieja area, especially on the westernmost flank of this volcano (Las Pailas and Borinquen hydrothermal areas), where the occurrence of a number of fumaroles, silicified rocks, soils and thermal springs clearly indicated a significant thermal anomaly (Molina and

Martì, 2016). At Las Pailas, a first geothermal plant (Unit I; 41.5 MW) was installed in 2011, whereas a second unit (55 MW) is planned to be placed to the east of Unit I, in 2018. At Borinquen, the construction of two units (55 MW each) is planned for 2023-2024 (ICE, 2014; Sànchez-Rivera and Vallejos-Ruiz, 2015), following the indication of a recent study (Molina and Martì, 2016) suggesting the occurrence of an aquifer at a temperature ≥220°C located at <3 km depth.

In the Tenorio area, preliminary geothermal prospection, carried out by ICE in 1987-1991, recognized an area of geothermal interest on the southern flank of the volcano (Mayorga, 2009). According to this indication, in 1999, two exploratory wells, PGT-1 and PGT-2, were drilled down to 2,473 m and 1,345 m depth, respectively (Mayorga, 2009). Unfortunately, the low temperature of the discharged water (<160°C), the low permeability and the proximity of a protected area (Tenorio Volcano National Park) discouraged the development of geothermal exploitation (Mayorga, 2009). New preliminary geochemical prospecting activities, carried out since 2008 in a 198 km^2 wide area that includes the northern Tenorio Volcano National Park section and a zone located east of Bijagua (**Figure 1**), did not provide promising results (Sànchez-Rivera and Vallejos-Ruiz, 2015).

MATERIALS AND METHODS

Gases were collected during 4 campaigns (April 2000, March 2005, February 2009, and February 2017) from thermal manifestations located in the surroundings of Rincón de la Vieja, Miravalles, and Tenorio volcanoes (**Figure 1**).

Gases from fumaroles were collected using a sampling line consisting of a 1 m-long titanium tube (Ø = 2.5 cm) and pyrex glass dewared pipes connected to pre-weighted and pre-evacuated 50-mL glass Thorion®-tapped flasks filled with 20 mL of a 4N NaOH and 0.15M $Cd(OH)_2$ suspension (Montegrossi et al., 2001). Bubbling gases were sampled using a funnel up-side-down positioned above the bubbles and connected to the soda flasks using a silicon tube. Water vapor and CO_2, dissolved in the alkaline solution, whereas H_2S formed insoluble CdS. Low-solubility gas species (N_2, O_2, CO, H_2, He, Ar, CH_4, and light hydrocarbons) were trapped in the flask headspace. Dry gases (for the analysis of the $^{13}C/^{12}C$ ratios in CO_2 and He isotopes) were collected using a water-cooled condenser connected to the soda flask sampling line.

Inorganic (N_2, Ar, O_2, H_2, He, and CO) and organic (CH_4, C_2H_6, C_3H_8, and C_6H_6) gases were analyzed at the Laboratory of Fluid Geochemistry of the University of Florence (Italy) by gas chromatography (GC; Shimadzu 15A, Shimadzu 14, and Thermo Focus). The liquid and the solid phases of the suspension were separated by centrifuge, to analyze for CO_2 in the form of CO_3^{2-} by acidimetric titration (AT; Metrohm Basic Titrino). The CdS precipitate was dissolved by oxidation with H_2O_2 in order to analyze H_2S as SO_4^{2-} by ion chromatography (IC; Methrom 761). The analytical error for GC, AT and IC analyses was <5%.

The analysis of $^{13}C/^{12}C$ of CO_2 (expressed as $\delta^{13}C\text{-}CO_2$ ‰ vs. V-PDB) was carried out at the laboratory of Stable Isotopes of CNR-IGG (Pisa, Italy) using a Finningan MAT252 mass spectrometer after standard extraction and purification procedures of the gas mixtures (Evans et al., 1988) performed at the Department of Earth Sciences of Florence (Italy). Carrara and San Vincenzo marbles, as well as international NBS18 and NBS19 standards, were used to estimate the external precision. The analytical error and the reproducibility were ±0.05 and ±0.1‰, respectively.

The R/Ra (where R is the $^3He/^4He$ measured ratio and Ra is the $^3He/^4He$ ratio in the air: 1.39×10^{-6}; Mamyrin and Tolstikhin, 1984) and $^4He/^{20}Ne$ ratios were determined at the INGV laboratories in Palermo (Italy) by separately introducing He and Ne into a split-flight-tube mass spectrometer (GVI Helix SFT) after performing standard purification procedures (Rizzo et al., 2015). The analytical error was ±1%. The measured R/Ra values were corrected for air contamination using the $^4He/^{20}Ne$ ratios (Poreda and Craig, 1989), as follows:

$$Rc/Ra = [(R/Ra) - r)]/(1 - r) \qquad (1)$$

where $r = (^4He/^{20}Ne)_{air}/(^4He/^{20}Ne)_{meas}$, the $(^4He/^{20}Ne)_{air}$ ratio being that in the atmosphere (0.318; Ozima and Posodek, 1983) and the $(^4He/^{20}Ne)_{meas}$ ratio that measured in the gas sample.

RESULTS

Chemical Composition

The chemical compositions of gases collected in 2000, 2009, 2015, and 2017 from the GGP are reported in **Table 1**, whereas the location of the fluid discharges is shown in **Figure 1**. Data from literature of some of these thermal fluid discharges from Rincón de la Vieja and Miravalles that were sampled in 1984 and 1987 (BOR1 and PA; Giggenbach and Corrales, 1992), as well as in 1998, 1999, and 2001 (BOR1 and PA; Tassi et al., 2005), are also reported. The dataset also includes the chemical composition of gases collected from different sites within GGP in 1987 and 1990 (MZ, TM, and GB; Giggenbach and Corrales, 1992), 1998 (GB; Gherardi et al., 2002), 1999, 2001, and 2002 (BOR2, BOB, LC, PAB, PAV, VO2, SM, and AC; Tassi et al., 2005), as well as that of gases from exploitation wells of the Miravalles geothermal plant (PGM01, PGM05, PGM10, PGM11, PGM12, PGM17, PGM31, and PGM49; Gherardi et al., 2002).

The thermal manifestations consist of bubbling and boiling pools with temperatures ranging from 21 to 99°C. The chemical composition of the dry fraction of the fluids (the concentrations of steam were mostly controlled by the liquid phase at the surface) was dominated by CO_2 (up to 996 mmol/mol), followed by N_2 (from 2 to 53 and mmol/mol). The concentrations of H_2S and CH_4 ranged widely (from 0.075 to 17 and from 0.071 to 20, respectively), while those of H_2 were relatively high (up to 4.8 mmol/mol) with the exception of those (from 0.0013 to 0.0085 mmol/mol) measured in the gases from the NE flank of Tenorio volcano (BO, RR, RC, PM, PC and BA; **Figure 1**). Oxygen and Ar varied from 0.019 to 0.79 and from 0.015 to 0.44 mmol/mol, respectively, whereas CO and He were ≤0.054 and ≤0.0068 mmol/mol, respectively. The Miravalles thermal discharges were characterized by relatively high concentrations of ethane (C_2H_6;

TABLE 1 | Outlet temperature (°C), chemical and stable isotope (δ13C-CO_2, in ‰ vs. V-PDB; Rc/Ra; R/Ra) composition of fumaroles from GGP.

			Date	T °C	CO_2	H_2S	N_2	CH_4	Ar	O_2	H_2	He	CO	C_2H_6	C_3H_8	C_3H_6	C_6H_6	$d^{13}C$-CO_2	Rc/Ra	$^4He/^{20}Ne$	$CO_2/^3He \times 10^9$	L	S	M
1	Borbollones	BO	2017	96	993	3.5	2.5	9.6	0.620	0.31	0.0069	0.0012	0.00061	1.2	0.21	0.025	1.2	−3.44	6.21	21	96	87	11	1.5
	Borbollones	BO	2015	93	992	2.2	3.7	20	0.072	0.092	0.0052	0.0027	0.00065	8.2	1.3	0.0072	0.84	−3.41						
	Borbollones	BO	2000	94	993	3.1	2.3	10	0.052	0.49	0.0057	0.0010	0.00076	1.0	0.39	0.029	0.92	−4.29						
	Rio Roble	RR	2017	27	995	2.3	2.1	1.1	0.045	0.069	0.0019	0.0002	0.00028	0.29	0.038		0.39	−4.61						
	Rio Roble	RR	2000	21	993	2.9	2.8	1.2	0.069	0.80	0.0013	0.0003	0.00042	0.23	0.054		0.41	−2.80						
	Rio Celeste	RC	2017	61	995	1.1	3.6	0.45	0.051	0.095	0.0085	0.0013	0.00022	0.85	0.096		0.21	−4.30	4.44	16	124	85	14	1.2
	Rio Celeste	RC	2000	58	995	1.3	3.4	0.37	0.054	0.46	0.0078	0.0012	0.00020	0.21	0.031		0.28	−4.68						
	Pozo de la muerte	PM	2000	80	991	4.1	3.7	1.5	0.071	0.57	0.0017	0.0011	0.0044	0.75	0.090		0.18	−3.01						
	Poza Celeste	PC	2000	83	996	0.35	2.0	6.5	0.048	0.74	0.0024	0.0005	0.00019	0.55	0.29		0.040	−3.77						
	Bambù	BA	2000	36	995	1.3	3.4	1.6	0.081	0.12	0.0014	0.0012	0.00026	0.78	0.17		0.0066	−5.44						
2	Altomassis 1	AL1	2017	72	987	8.3	4.6	0.38	0.026	0.015	0.14	0.0022	0.0036	6.7	1.8	0.033	1.5	−2.11	7.11	31	45	90	6.5	3.3
	Altomassis 1	AL1	2015	81	988	6.9	4.2	0.23	0.039	0.037	0.10	0.0018	0.0031	5.1	2.0	0.029	1.8	−2.06	7.07	25	56	91	6.4	2.7
	Altomassis 2	AL2	2017	74	989	7.1	3.1	0.35	0.039	0.021	0.11	0.0021	0.0038	7.4	1.6	0.035	2.1	−2.22						
	Altomassis 2	AL2	2015	70	989	8.0	2.9	0.29	0.028	0.028	0.096	0.0023	0.0041	6.0	1.5	0.032	1.9	−2.22						
3	Montezuma*	MZ	1987	62	987	1.5	9.0	1.5	0.21	0.99		0.00040												
4	Tierra Morenas*	TM	1987	91	986	1.6	8.9	2.9	0.11		0.70	0.0026												
5	Borinquen1	BOR1	2017	83	980	9.1	6.5	0.075	0.18	0.15	3.9	0.0018	0.0015	2.9	0.56	0.091	1.3	−1.69	3.55	11	110	93	5.4	1.3
	Borinquen1	BOR1	2015	94	981	8.8	6.3	0.071	0.16	0.31	3.7	0.0021	0.0012	2.6	0.61	0.085	1.1	−1.88	4.12	12	82	92	6.0	1.8
	Borinquen1***	BOR1	2001	96	980	2.4	16	0.010	0.32	0.62	0.078	0.00050	0.0053	0.90	0.34		0.31	−1.11						
	Borinquen1***	BOR1	1999	96	987	0.45	8.7	0.028	0.16	0.0020	3.5	0.0014	0.0012	27	26	1.4	1.6	−0.89	3.78	8	134	96	2.8	1.1
	Borinquen1*	BOR1	1987	96	933	35	27	0.61	0.36		4.1	0.0030												
	Borinquen2***	BOR2	1999	75	986	0.28	12	0.038	0.26	0.0049	1.7	0.0028		11	1.6	0.22	5.0	−1.34						
	Borinquen3	BOR3	2017	97	972	9.5	13	0.10	0.25	0.11	4.8	0.0023	0.0026	2.3	0.76	0.11	2.1	−1.16						
	Borinquen Barro***	BOB	1999	95	951	23	19	0.16	0.34	0.014	7.3	0.0026	0.012	5.1	2.5	0.14								
	Borinquen Barro***	BOB	2001	96	976	3.1	16	0.012	0.30		4.7	0.00026	0.014	1.8	0.95	0.13	1.1							
6	Pailas de Agua	PA	2017	83	984	1.5	12	0.39	0.19	0.12	1.3	0.0018	0.00081	1.9	0.62	0.032	1.7	−2.44	4.66	18	84	90	7.8	1.8
	Pailas de Agua***	PA	1999	96	990	0.13	8.2	0.029	0.19	0.19	1.0	0.0022	0.0018	7.9	0.70	0.029	2.7							
	Pailas de Agua***	PA	1998	93	991	0.080	7.1	0.030	0.16		1.1	0.0015	0.00055	1.5	0.57	0.025	2.3		5.31	13	89			
	Pailas de Agua*	PA	1984	98	950	24	18	0.36	0.25	2.3	5.3	0.013												
	Pailas seca	PS	2017	83	990	1.1	6.2	0.41	0.11	0.14	1.5	0.0026	0.0028	6.5	0.66	0.031	2.4	−2.05						

(Continued)

TABLE 1 | Continued

			Date	T °C	CO_2	H_2S	N_2	CH_4	Ar	O_2	H_2	He	CO	C_2H_6	C_3H_8	C_3H_6	C_6H_6	$d^{13}C$-CO_2	Rc/Ra	$^4He/^{20}Ne$	$CO_2/^3He \times 10^9$	L	S	M
	Lago Caliente***	LC	1999	86	991	0.012	7.2	0.025	0.13	0.014	1.2	0.0023	0.00073	4.6	0.75	0.050	1.5	−0.68						
	Lago Caliente***	LC	1998	94	992	0.016	7.9	0.024	0.15		0.26	0.0018	0.00077	0.50	0.26	0.019	1.7							
	Pailas de Barro***	PAB	1999	89	905	11	70	0.37	1.3	1.8	11	0.0019	0.0047	35	8.2	0.85	37	−0.63	4.12	3	83	96	1.8	1.8
	Pailas de Volcancito***	PAV	1999	99	983	0.87	12	0.84	0.18	0.39	2.8	0.0018	0.0020	6.7	1.4	0.19	5.6	−0.64	4.00	12	99	97	1.9	1.5
7	Volcancito1	VO1	2017	53	977	0.075	22	0.51	0.44	0.18		0.0026		0.71				−3.78						
	Volcancito2***	VO2	1999	59	974	0.084	25	0.60	0.49	0.23		0.0037		0.83										
8	Santa Maria***	SM	1999	37	990	0.003	10	0.013	0.22	0.0030	0.0018	0.00039		9.9	0.91	0.13	0.86	−1.49	4.86	2	377	95	4.9	0.4
9	Active crater***	AC	2002	76	980	14	3.1	0.00006	0.019	0.38	0.21	0.0031	0.0033	0.0002	0.005		0.073							
10	Hornillas1	HN1	2017	82	985	11	1.8	1.9	0.036	0.059	0.61	0.00025	0.046	45	4.9	0.085	15	−2.02						
	Hornillas1	HN1	2015	97	982	15	1.6	1.2	0.035	0.028	0.54	0.00037	0.054	43	6.9	0.090	12	−2.71						
	Hornillas1	HN1	2009	58	980	12	4.7	1.7	0.11	0.019	1.5	0.0019	0.0021	58	11	0.21	75	−1.82	3.24	15	113	93	5.8	1.3
	Hornillas2	HN2	2017	83	980	16	2.2	1.6	0.036	0.062	0.27	0.00076	0.031	53	6.1	0.089	11	−2.68						
	Hornillas2	HN2	2009	71	960	17	21	1.5	0.33	0.62	0.097	0.00097	0.00077	19	4.4	0.069	6.0							
	Hornillas2	HN2	2015	71	963	16	19	1.4	0.31	0.57	0.091	0.00091	0.00075	67	11	0.11	18	−2.36						
	Hornillas3	HN3	2009	56	985	7.4	4.9	1.8	0.089	0.79	0.47	0.0026	0.00010	8.5	2.9	0.064	3.5							
11	Guayacan	GU	2015	97	986	2.6	9.4	1.5	0.11	0.19	0.20	0.00049	0.014	9.3	1.5	0.029	1.9	−1.43						
12	Guayabal*	GB	1990	70	982	0.50	15	1.1	0.30	1.4		0.0027							7.20	8	36			
	Guayabal**	GB	1998	64	995	0.04	4.3	1.1	0.11	0.37		0.0004												
13	Geothermal well**	PGM05	1998	n.d.	960	20	18	0.59	0.29	0.015	1.3	0.0028												
	Geothermal well**	PGM11	1998	n.d.	978	11	10	0.39	0.18	0.015	0.88	0.0021												
	Geothermal well**	PGM49	1998	n.d.	845	25	129	0.12	0.29	0.015	0.80	0.037												
	Geothermal well**	PGM01	1998	n.d.	970	14	14	0.19	0.16	0.11	1.6	0.0058												
	Geothermal well**	PGM17	1998	n.d.	947	16	34	1.6	0.11	0.29	1.2	0.0073												
	Geothermal well**	PGM12	1998	n.d.	948	16	34	0.79	0.11	0.010	0.65	0.0095												
	Geothermal well**	PGM31	1998	n.d.	969	18	12	0.30	0.085	0.12	0.25	0.0093												
	Geothermal well**	PGM10	1998	n.d.	932	8.5	58	0.58	0.32	0.015	1.0	0.0075												

*$^4He/^{20}Ne$ and $CO_2/^3He$ ratios, as well as %L, %S, and %M values are also reported. Concentrations are in mmol/mol, except for those of light hydrocarbons (C_2H_6, C_3H_8, C_3H_6, and C_6H_6) that are in µmol/mol. Data from *Giggenbach and Corrales (1992), **Gherardi et al. (2002), and ***Tassi et al. (2005) are also reported.*

up to 67 μmol/mol), propane (C_3H_8; up to 11 μmol/mol), and benzene (C_6H_6; up to 75 μmol/mol) with respect to those of the other thermal manifestations (≤8.2, ≤2.0, and ≤2.4 μmol/mol, respectively). Minor amounts (≤0.21 μmol/mol) of propene (C_3H_6) were also measured.

δ^{13}C-CO_2 and Rc/Ra Values

The δ^{13}C-CO_2 and Rc/Ra values of gases from the GGP are listed in **Table 1**. Data from literature (Tassi et al., 2005) of Rincón de la Vieja thermal manifestations are also reported. The δ^{13}C-CO_2 values of gases from the N flank of Tenorio (**Figure 1**) were significantly more negative (from −5.44 to −2.80‰ vs. V-PDB) with respect to those from the other thermal discharges (from −2.71 to −1.16‰ vs. V-PDB). The Rc/Ra values of gases from Rincón de la Vieja volcano ranged from 3.55 to 4.66, whereas that measured in HN1 gas (Miravalles volcano) was slightly lower (3.24). On the contrary, significantly higher Rc/Ra values were measured at Tenorio, especially in the AL1 gases (7.11 and 7.07, respectively).

DISCUSSION

Gas Sources and Secondary Chemical-Physical Processes

The isotopic ratios of He in hydrothermal gas discharges from different geodynamic settings are helpful to evaluate the contribution of mantle- and crust-related fluids (e.g., Polyak and Tolstikhin, 1985). The R/Ra values of gases released along convergent plate boundaries may vary between 3 and 8, depending on the degree of crustal contamination affecting the mantle source (Poreda and Craig, 1989; Hilton et al., 2002). The Rc/Ra values measured in the GGP gases (**Table 1**) fall within such range (**Table 1**). The highest mantle He contribution observed in the study area was found in GB (Miravalles), as already highlighted by previous data (Poreda and Craig, 1989), and, surprisingly, in AL (Tenorio) gases. It is worth noting that gas discharges from the same area, such as Borinquen and Las Pailas (**Figure 1**), i.e., located close to each other, were characterized by relatively strong differences in Rc/Ra values, suggesting that the hydrothermal fluids uprising from the deep reservoirs were affected by variable inputs of crustal gases at a local scale. The δ^{13}C-CO_2 values showed overlapping ranges between mantle and crustal CO_2 (Sherwood Lollar et al., 1997). Thus, this geochemical parameter cannot clearly distinguish gases from these two sources. The δ^{13}C-CO_2 values of most GGP gases, being higher than those that characterize mantle gases (from −7 to −3‰ vs. V-PDB) (Pineau and Javoy, 1983), may be interpreted as due to interactions of limestone with the hydrothermal/magmatic fluids, as also observed in other volcanic systems such as Vulcano Island (Tedesco and Nagao, 1996), Mt. Vesuvius (Chiodini et al., 2001), and Nysiros (Brombach et al., 2003). The δ^{13}C-CO_2 values of the gases from the NE sector of Tenorio volcano (**Figure 1**), which were slightly more negative, may imply (i) a pure mantle CO_2 source or (ii) a contribution of ^{12}C-enriched CO_2 (≤ -20‰ vs. V-PDB) from degradation of organic matter (O'Leary, 1988; Hoefs, 2009). These values may also be related to ^{13}C-^{12}C fractionation processes due to interactions with shallow aquifers and/or carbonate precipitation/dissolution (Venturi et al., 2017, and references therein). Useful insights into the origin of CO_2 of the GGP gases are provided by combining δ^{13}C-CO_2 values and $CO_2/^3He$ ratios (Marty and Jambon, 1987; O'Nions and Oxburgh, 1988). As shown in **Figure 2**, all the gases from the three volcanic systems of GGP displayed a strong CO_2-excess (1–2 orders of magnitude) with respect to mantle, mostly due to CO_2 production from limestone and/or marine carbonate. As suggested by Sano and Marty (1995), the relative contribution of carbon from mantle degassing (M), limestone (L), and/or organic-rich sediments (S) can be computed, as follows:

$$M + S + L = 1 \tag{2}$$

$$(\delta^{13}C - CO_2)_{meas} = M(\delta^{13}C - CO_2)_{MORB} + L(\delta^{13}C - CO_2)_{Lim} + S(\delta^{13}C - CO_2)_{Sed} \tag{3}$$

$$1/(CO_2/^3He)_{meas} = M/(CO_2/^3He)_{MORB} + L/(CO_2/^3He)_{Lim} + S/(CO_2/^3He)_{Sed} \tag{4}$$

Equations (3, 4) were solved considering the following data: $(\delta^{13}C\text{-}CO_2)_{MORB} = -6.5$‰, $(\delta^{13}C\text{-}CO_2)_{Sed} = -30$‰, $(\delta^{13}C\text{-}CO_2)_{Lim} = 0$‰, $(CO_2/^3He)_{MORB} = 1.5\times10^9$, $(CO_2/^3He)_{Sed} = 1\times10^{13}$ and $(CO_2/^3He)_{Lim} = 1\times10^{13}$. According to these calculations (**Table 1**), the highest mantle CO_2 fraction (3.3%) was measured at Altomassis (AL, Tenorio), whereas those of the other emissions ranged from 0.4 to 1.8%. As already shown in **Figure 2**, limestone was by far the most abundant crustal carbon source (from 85 to 87%), with variable contribution from organic-rich sediments (from 1.8 to 14%). As already reported by Shaw et al. (2003) on the basis of the CO_2-He systematics of various thermal fluid discharges from volcanoes and geothermal systems in the Costa Rica and Nicaragua regions including Rincón de la Vieja and Miravalles volcanoes, the fluids from the study area were characterized by a relatively high L/S average ratio (21.7), i.e., strongly higher than the worldwide arc L/S average value (6.0 ± 0.38; Sano and Williams, 1996), possibly due to the carbonate-rich composition of the Cocos Plate subducting sedimentary material (Patino et al., 2000; Saginor et al., 2013). Similar features were also observed in fluids from the Chilean Southern and Central Volcanic Zones (CVZ and SVZ) (Ray et al., 2009; Benavente et al., 2013, 2016).

The N_2/Ar ratios of most GGP gases were comprised between those of Air Saturated Water (ASW) and air (**Figure 3**), likely due to atmospheric gas contribution from shallow aquifers in contact with the uprising hydrothermal fluids. In contrast, gases from (i) the Miravalles geothermal gases (GW), (ii) the active crater (AC) of Rincón de la Vieja, and (iii) AL were marked by a significant N_2-excess (**Figure 3**). The GW gases were expected to show a limited interaction with the shallow environment, being preserved by the tubing of the wells, whereas the low air contamination of AC was likely related to a strong magmatic fluid inputs, considering that this gas collected from a high-flux emission at the border of the hyperacidic and extremely active carter lake of Rincón de la Vieja (Tassi et al., 2005). The high N_2/Ar ratios of the AL gases were surprising since these gas emissions were apparently similar to the other hydrothermal discharges, i.e., low flux bubbling pools with a relatively low (<100°C) outlet temperature (**Table 1**). Such a

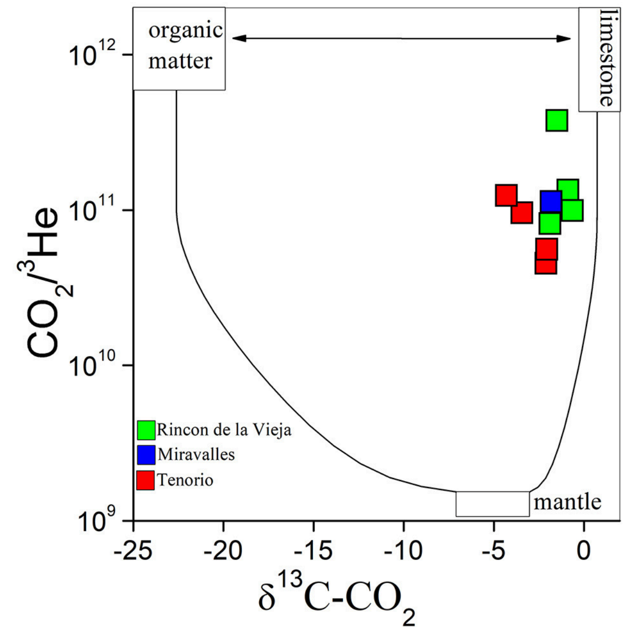

FIGURE 2 | $CO_2/^3He$ vs. $\delta^{13}C\text{-}CO_2$ binary diagram. End-member compositions of organic matter, limestone and mantle are from Sano and Marty (1995). Mixing curves between the three end-members are reported. Symbols as in **Figure 1**.

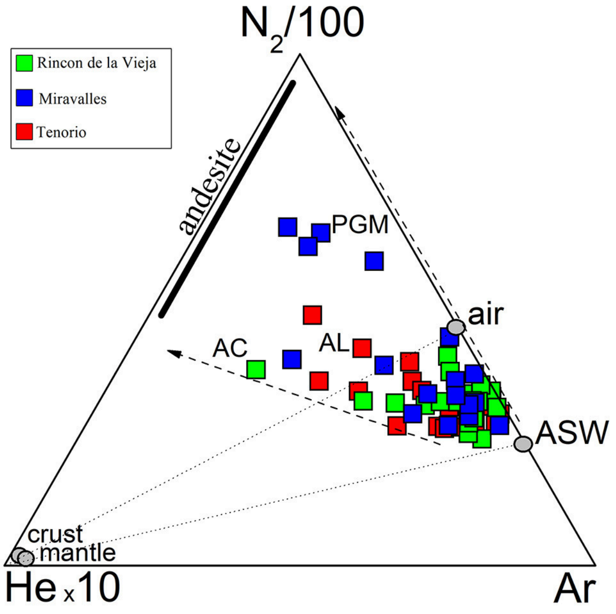

FIGURE 3 | $N_2/100$-He×10-Ar triangular diagram (Giggenbach, 1992). Symbols as in **Figure 1**.

N_2-excess, as well as the relatively high Rc/Ra values and H_2 and CO concentrations (**Table 1**), clearly distinguish the AL gases from those emitted on the northern flank of Tenorio volcano (**Figure 1**). A similar chemical composition was also shown by the TM boiling pools (**Table 1**; Giggenbach and Corrales, 1992), which are located relatively close to the AL discharges (**Figure 1**). These compositional features suggest that gases from this area were characterized by a relatively high contribution of a deep gas component, a peculiarity that may be related to the occurrence of tectonic structures able to favor the uprising of deep fluids. Unfortunately, the promising indications provided by gas geochemistry cannot be supported by the poorly developed studies on the local structural setting, since, to date, the intense vegetation and the relatively low temperatures of the fluids exploited during the preliminary geothermal prospection (Mayorga, 2009) discouraged appropriate investigations.

Gas Geothermometry

Temperature- and redox-sensitive compounds of waters and gases from volcanic systems are commonly used as geoindicators for fluid reservoirs (e.g., Giggenbach, 1991, and references therein). Geothermometers can provide reliable results when (i) the chemical reactions among the species considered for the geothermometric computations have attained equilibrium within the reservoirs, and (ii) no significant compositional changes have occurred during the uprising of fluids toward the surface. According to these assumptions, the composition of fluids exploited from geothermal wells, rapidly uprising through tubing that prevent the contact between the hydrothermal fluids and the external environment, tends to strictly reflect the chemical-physical conditions at the fluid source. On the contrary, secondary processes, such as cooling, steam condensation, mixing with shallow aquifers, and air contamination may affect fluids feeding the natural emissions, modifying the chemical features they have acquired at depth. For example, water vapor concentrations of deep-originated gases discharged from bubbling and boiling pools, such as those of the present study, are strongly depending on condensation processes occurring close to the surface, to shallow depth. Therefore, gas geothermometry was preferably carried out in the CO_2-CO-H_2-CH_4 system. Among these gas compounds, CO and H_2 have a similar rapid kinetics in response to changes of the chemical-physical conditions (Giggenbach, 1987, 1996; Chiodini et al., 1993), e.g., during the fluid uprising toward the surface. Thus, the following pressure-independent chemical reaction was considered:

$$CO_2 + H_2 \Leftrightarrow CO + H_2O \tag{5}$$

The dependence on temperature of reaction (5) in the vapor phase is given by:

$$\log(X_{CO}/X_{CO2})_V = 2.49 - 2248/T + R_H \tag{6}$$

whereas in the liquid phase is, as follows:

$$\log(X_{CO}/X_{CO2})_L = 2.49 - 2248/T + R_H + \log(B_{CO2}) - \log(B_{CO}) \tag{7}$$

where T is in K, X_{CO} and X_{CO2} are the molar fractions of CO_2 and CO, respectively, B_{CO2} and B_{CO} are the vapor/liquid distribution coefficients of CO_2 and CO, respectively, whereas

R_H is $\log(X_{H2}/X_{H2O})$ (Giggenbach, 1980, 1987). Assuming that Ar concentrations are fixed by the equilibrium between the atmosphere and air saturated water (ASW) (Giggenbach, 1991), the dependence of H_2 on R_H in the two phases can also be described by the following equations:

$$\log(X_{H2}/X_{Ar^*})_V = R_H + 6.52 - \log(B_{Ar}) \quad (8)$$

and

$$\log(X_{H2}/X_{Ar^*})_L = R_H + 6.52 - \log(B_{H2}) \quad (9)$$

where X_{H2}, X_{Ar^*}, B_{Ar^*}, and B_{H2} are the molar fractions and the vapor/liquid distribution coefficients of Ar* and H_2, respectively. The X_{Ar^*} values, computed by $Ar^* = X_{Ar} - (X_{O2}/22)$ considering that hydrothermal fluids are O_2-free, was used instead of the X_{Ar} to minimize the effects on hydrothermal fluids of air contamination at the surface. Assuming that the R_H values were controlled by the rock redox buffer system proposed by D'Amore and Panichi (1980) (DP), the combination of Equations (6–9) allowed to construct liquid-vapor equilibrium grid reported in **Figure 4**. Gases from Rincón de la Vieja and Miravalles plot within and out of the liquid-vapor grid, and their apparent equilibrium temperatures ranges from ∼180° to >300°C. Gases from the northern sector of Tenorio seem to indicate lower equilibrium temperatures (130–180°C). The strong scattering of these data suggests that secondary processes likely controlled H_2 and CO. Interactions with shallow aquifers, which are typically rich in free O_2, may have dramatically changed the redox conditions acting on the uprising fluid, severely affecting the behavior of these reduced gas species. Moreover, CO tends to dissolve in liquid water to form HCOOH (Shock, 1993).

On the contrary, the AL gases, which cluster close to the vapor equilibrium curve at 240–250°C (**Figure 4**), seem to have maintained the chemical composition attained at depth. This is consistent with the relatively high fraction of mantle He and CO_2 (**Table 1**) and the high N_2/Ar ratios (**Figure 3**) of these gases. The H_2/Ar values of the AL gases were similar to those measured by Giggenbach and Corrales (1992) in the TM gas emission (**Table 1**), located in the same area (**Figure 1**). However, those authors surprising interpreted these data as evidence of low-temperature conditions.

To complete the geothermometric estimations in the CO_2-CO-H_2-CH_4 system, we hypothesized that the CH_4 concentrations were controlled by the Sabatier reaction, as follows:

$$CH_4 + 2H_2O \Leftrightarrow CO_2 + 4H_2 \quad (10)$$

Considering that $\log(fH_2O) = 4.9 - 1820/T$ (Giggenbach, 1987), the dependence on temperature and R_H of the X_{CH4}/X_{CO2} log-ratios in the vapor and liquid phases can be expressed, as follows:

$$\log(X_{CH4}/X_{CO2})_V = 4R_H + 5181/T \quad (11)$$

and

$$\log(X_{CH4}/X_{CO2})_L = 4R_H + 5181/T + \log(B_{CO2}) - \log(B_{CH4}) \quad (12)$$

where B_{CH4} is the vapor/liquid distribution coefficient of CH_4.

The $\log(X_{H2}/X_{Ar*})$ vs. $\log(X_{CH4}/X_{CO2})$ diagram (**Figure 5**) was constructed on the basis of Equations (8–12) and assuming that the R_H values were regulated the DP redox buffer system. It confirms a strong chemical disequilibrium of the gases from

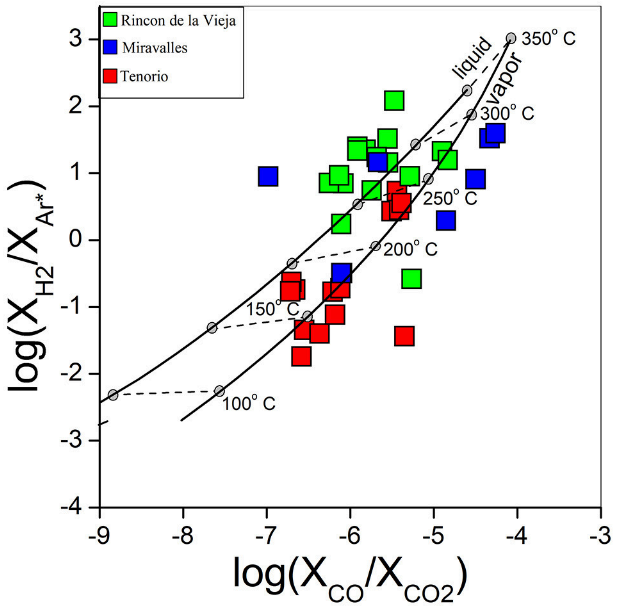

FIGURE 4 | $\log(X_{H2}/X_{Ar^*})$ vs. $\log(X_{CO}/X_{CO2})$ binary diagram. Symbols as in **Figure 1**.

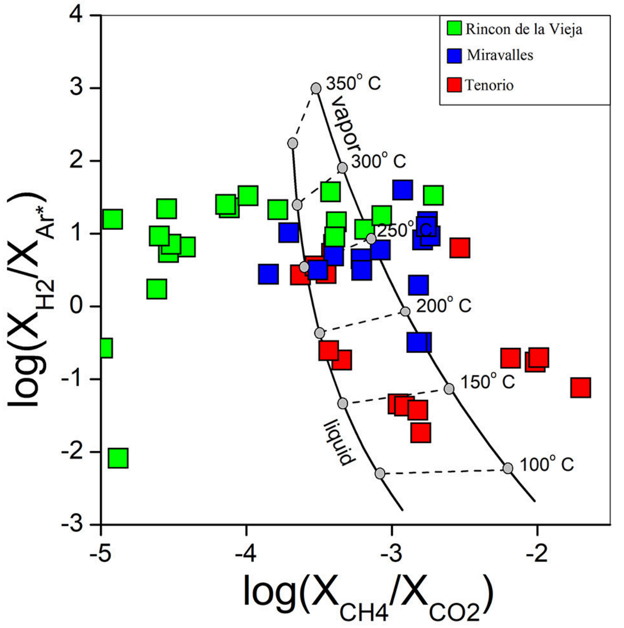

FIGURE 5 | $\log(X_{H2}/X_{Ar^*})$ vs. $\log(X_{CH4}/X_{CO2})$ binary diagram. Symbols as in **Figure 1**.

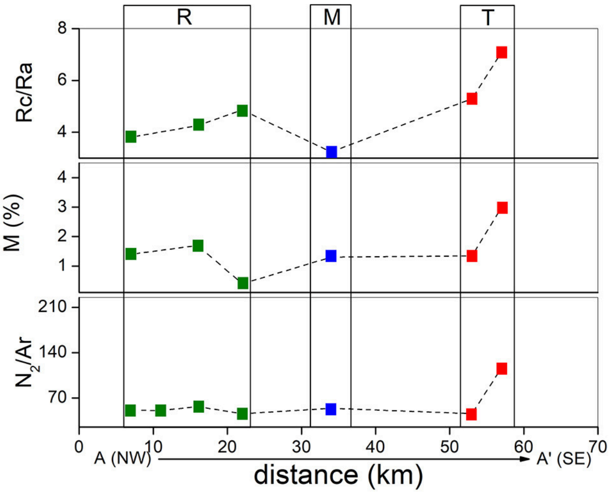

FIGURE 6 | Schematic draft of the spatial distribution of Rc/Ra and N_2/Ar ratios and mantle CO_2 fraction values (M in %) in hydrothermal fluid discharges from the studied volcanic systems of Guanacaste. Symbols as in **Figure 1**.

the three volcanoes, which is consistent with the large variations of the Rc/Ra values measured in gas emissions from the same volcanic system (i.e., Rincón de la Vieja, **Table 1**). AL gases are the only exception, their equilibrium temperatures were the same as those indicated by the H_2-CO pair. It is worth noting that the AL calculated temperatures were consistent with those hypothesized for the geothermal reservoir associated with the Miravalles volcano (Gardner and Corrales, 1977). It is worth noting that the CH_4-CO_2 ratios of the AL gases were one order of magnitude lower than those of the TM and MZ gases (Giggenbach and Corrales, 1992) (**Figure 1**), suggesting a large chemical heterogeneity even at a relatively small spatial scale. The X_{H2}/X_{Ar*} and X_{CH4}/X_{CO2} ratios of the Miravalles geothermal gases show strong variations (∼1 log-unit; **Figure 5**), although supposedly less affected by the influence of the shallow environment. Comparable results were also found by Gherardi et al. (2002), who suggested that the fluids from Miravalles suffered the influence of fluid reinjection.

CONCLUSIONS

The occurrence of a strong heat source, demonstrated by the numerous thermal manifestations of GGP, and the abundant meteoric water recharge characterizing the volcanic chain of Guanacaste explain the high geothermal potential of this region. The chemical and isotopic features of the discharged fluids are dictated by the interaction of the uprising hydrothermal fluids and shallow aquifers. At a first approximation, the highest deep-originated fluid contribution can be recognized at the active crater of the Rincón de la Vieja volcano, where phreatic and phreato-magmatic eruptions frequently occur, and progressively decreases with increasing distance from this site. Carbon dioxide production from limestone seems the main source for this gas, possibly related to carbonate assimilation at the magmatic source and/or due to interaction of carbonate-rich rocks and the hydrothermal fluids. The geochemical features of the fluids exploited from Miravalles correspond to those typically found in the surroundings of active volcanic systems, i.e., Na-Cl brines produced by prolonged fluid-rock interactions and dissolution of magmatic gases into a well-developed hydrothermal aquifer. The concentrations of minor reduced gases, such as CO, H_2, and CH_4 were likely controlled by chemical reactions occurring within the hydrothermal deep fluid source, although the chemical composition attained at depth was strongly modified by secondary processes resulting in a large scattering of the chemistry of the surficial manifestations. According to the scenario suggested by Giggenbach and Corrales (1992), the Tenorio thermal discharges would represent the distal fluid outflow of the regional geothermal reservoir. The new geochemical evidences reported in the present study significantly modify this schematic model. As shown in **Figure 6**, the relatively high contribution of CO_2 from the mantle (M in %), as well as the high Rc/Ra and N_2/Ar ratios shown by the fluid discharges located in the southern sector of Tenorio volcano with respect to those from Miravalles and Rincón de la Vieja, suggest a high-temperature source in this area. This implies that, although the preliminary geochemical prospections carried out in the 1990's produced discouraging results, an important geothermal resource is hosted in this peripheral zone of GGP, where local tectonics favor the uprising of hot fluids minimizing their cooling and mixing with crustal and atmospheric gases. In light of this hypothesis, which needs to be supported by geophysical prospection activities and accurate investigations of the geologic and tectonic settings, promising results are expected to be obtained by extending the exploitation activity to the south of the Miravalles geothermal plant. Accordingly, the geothermal potential of GGP should likely be regarded as higher than previously thought.

AUTHOR CONTRIBUTIONS

FT: field campaigns, gas analysis, manuscript preparation; OV, GB, FC, and JdM: field campaigns, manuscript preparation; GP: gas analysis, manuscript preparation; SV: manuscript preparation.

ACKNOWLEDGMENTS

This work was financially supported by the laboratories of Fluid and Rock Geochemistry and Stable Isotope Geochemistry of the Department of Earth Sciences and the Institute of Geosciences and Earth Resources of the National Research Council of Italy (IGG-CNR) of Florence.

REFERENCES

Alvarado, G. E. (2000). *Los Volcanes de Costa Rica: Geología, Historia y Riqueza Natural*. San José: Universidad Estatal a Distancia, UNED.

Alvarado, G. E. (1993). *Costa Rica: Land of Volcanoes*. Cartago: Gallo Pinto Press.

Alvarado, G. E., and Cárdenes, G. (2016). "Geology, tectonics, and geomorphology of costa rica: a natural history approach," in *Costa Rican Ecosystems*, ed M. Kappelle (Chicago, IL: The University of Chicago Press), 30–63.

Alvarado, G. E., and Gans, P. B. (2012). Síntesis geocronológica del magmatismo, metamorfismo y metalogenia de Costa Rica, América Central. *Rev. Geol. Am. Central* 46, 7–122. doi: 10.15517/rgac.v0i46.1836

Alvarado, G. E., Kussmaul, S., Chiesa, S., Gillot, P. Y., Appel, H., Worner, G., et al. (1992). Resumen cronoestratigrafico de las rocas igneas de Costa Rica basado en dataciones radiometricas. *J. South Am. Earth Sci.* 6, 151–168. doi: 10.1016/0895-9811(92)90005-J

Barquero, J. H., and Segura, J. (1983). La actividad del volcán Rincón de la Vieja. *Bol. Vulcanol.* 13, 5–10.

Benavente, O., Tassi, F., Gutiérrez, F., Vaselli, O., Aguilera, F., and Reich, M. (2013). Origin of fumarolic fluids from Tupungatito Volcano (Central Chile): interplay between magmatic, hydrothermal, and shallow meteoric sources. *Bull. Volcanol.* 75, 1–15. doi: 10.1007/s00445-013-0746-x

Benavente, O., Tassi, F., Reich, M., Aguilera, F., Capecchiacci, F., Gutiérrez, F., et al. (2016). Chemical and isotopic features of cold and thermal fluids discharged in the Southern Volcanic Zone between 32.5°S and 36°S: insights into the physical and chemical processes controlling fluid geochemistry in geothermal systems of Central Chile. *Chem. Geol.* 420, 97–113. doi: 10.1016/j.chemgeo.2015.11.010

Boudon, G., Rancon, J. P., Kieffer, G., Soto, G. J., Traineau, H., and Rossignol, J. C. (1996). Les eruptions de 1966-1970 et 1991-1992 du volcan Rincón de la Vieja, Costa Rica: exemple d'activité réecurrente d'un systéme hydromagmatique. *C. R. Acad. Sci.* 322, 101–108.

Brombach, T., Caliro, S., Chiodini, G., Fiebig, J., Hunziker, J., and Raco, B. (2003). Geochemical evidence for mixing of magmatic fluids with seawater, Nisyros hydrothermal system, Greece. *Bull. Volcanol.* 65, 505–516. doi: 10.1007/s00445-003-0278-x

Carr, M. J. (1984). Symmetrical and segmented variation of physical and geochemical characteristics of the Central America Volcanic front. *J. Volcanol. Geotherm. Res.* 20, 231–252. doi: 10.1016/0377-0273(84)90041-6

Chavarría, L., Mora, O., Hakanson, E., Galvez, M., Rojas, M., Molina, F., et al. (2010). "Geologic model of the pailas geothermal field, guanacaste, costa rica," in *Proceedings World Geothermal Congress* (Bali).

Chiesa, S., Alvarado, G. E., Pecchio, M., Corrella, M., and Zanchi, A. (1994). Contribution to petrological and stratigraphical understanding of the Cordillera de Guanacaste lava flows, Costa Rica. *Rev. Geol. Am. Central* 17, 19–43.

Chiesa, S., Civelli, G., Gillot, P. Y., Morz, O., and Alvarado, G. E. (1992). Rocas piroclásticas asociadas a la formación de la Caldera de Guayabo, Cordillera de Guanacaste, Costa Rica. *Rev. Geol. Am. Central* 14, 59–75.

Chiodini, G., Cioni, R., and Marini, L. (1993). Reactions governing the chemistry of crater fumaroles from Vulcano Island, Italy, and implications for volcanic surveillance. *Appl. Geochem*. 8, 357–371. doi: 10.1016/0883-2927(93)90004-Z

Chiodini, G., Marini, L., and Russo, M. (2001). Geochemical evidence for the existence of high-temperature hydrothermal brines at Vesuvio volcano, Italy. *Geochim. Cosmochim. Acta* 65, 2129–2147. doi: 10.1016/S0016-7037(01)00583-X

D'Amore, F., and Mejia, T. J. (1999). Chemical and physical reservoir parameters at initial conditions in Berlin geothermal field, El Salvador: a first assessment. *Geothermics* 28, 45–73.

D'Amore, F., and Panichi, C. (1980). Evaluation of deep temperatures of hydrothermal systems by a new gas geothermometer. *Geochim. Cosmochim. Acta* 44, 549–556. doi: 10.1016/0016-7037(80)90051-4

Evans, W., White, L., and Rapp, J. (1988). Geochemistry of some gases in hydrothermal fluids from the southern Juan de Fuca Ridge. *J. Geophys. Res.* 93, 15305–15313. doi: 10.1029/JB093iB12p15305

Fergurson, R. B., and Alfonso, P. S. (1977). Electrical investigations in the Guanacaste Geothermal Area (Costa Rica). *Geotherm. Resour. Counc. Trans.* 1, 99–100.

Gardner, M. C., and Corrales, R. (1977). Geochemical investigations of the Guanacaste Geothermal Project, Costa Rica. *Geotherm. Resour. Counc. Trans.* 1, 101–102.

Gherardi, F., Panichi, C., Yock, A., and Gerardo-Abaya, J. (2002). Geochemistry of the surface and deep fluids of the Miravalles volcano geothermal system (Costa Rica). *Geothermics* 31, 91–128. doi: 10.1016/S0375-6505(01)00030-X

Giggenbach, W. F. (1980). Geothermal gas equilibria. *Geochim. Cosmochim. Acta* 44, 2021–2032. doi: 10.1016/0016-7037(80)90200-8

Giggenbach, W. F. (1987). Redox processes governing the chemistry of fumarolic gas discharges from White Island, New Zealand. *Appl. Geochem*. 2, 143–161. doi: 10.1016/0883-2927(87)90030-8

Giggenbach, W. F. (1991). "Chemical techniques in geothermal exploration," in *Application of Geochemistry in Geothermal Reservoir Development*, ed F. D'Amore (New York, NY: UNITAR), 119–144.

Giggenbach, W. F. (1992). The composition of gases in geothermal and volcanic systems as a function of tectonic setting. *Proc. Int. Symp. Water Rock Inter*. 8, 873–878.

Giggenbach, W. F. (1996). "Chemical composition of volcanic gases," in *Monitoring and Mitigation of Volcano Hazards*, eds R. Scarpa and R. I. Tilling (Berlin: Springer), 222–256.

Giggenbach, W. F., and Corrales, R. S. (1992). Isotopic and chemical composition of water and steam discharges from volcanic-magmatic-hydrothermal systems of the Guanacaste Geothermal Province, Costa Rica. *Appl. Geochem*. 7, 309–332. doi: 10.1016/0883-2927(92)90022-U

Hilton, D. R., Fischer, T. P., and Marty, B. (2002). Noble gases and volatile recycling at subduction zones. *Rev. Miner. Geochem*. 47, 319–370. doi: 10.2138/rmg.2002.47.9

Hoefs, J. (2009). *Stable Isotope Geochemistry*. Berlin: Springer.

Instituto Costarricense de Electricidad (ICE) (1990). *Estudios de Reconocimiento y Prefactibilidad Geotérmica en la República de Costa Rica*. Fase II, Estudio de Prefactibilidad del área del Tenorio, Informe Geovulcanológico. Proyecto COS/83/T01 [Inf. Interno].

Instituto Costarricense de Electricidad (ICE) (1991). *Evaluación del Potencial Geotérmico de Costa Rica.* Internal Report, Instituto Costarricense de Electricidad San José, Costa Rica.

Instituto Costarricense de Electricidad (ICE) (2014). *Plan de Expansión de la Generación Eléctrica, Período 2014-2035*. Report, Centro Nacional de Planificación Eléctrica, Proceso de Expansión Integrada; Instituto Costarricense de Electricidad; San José, Costa Rica.

Kempter, K. A., Benner, S. G., and Williams, S. N. (1996). Rincón de la Vieja volcano, Guanacaste province, Costa Rica: geology of the south-western flank and hazard implication. *J. Volcanol. Geotherm. Res*. 71, 109–127. doi: 10.1016/0377-0273(95)00072-0

Mainieri, A., Granados, E., Corrales, R., and Vaca, L. (1985). Miravalles geothermal field, Costa Rica. Technical report. *Geotherm. Resour. Counc. Trans*. 9, 279–283.

Mamyrin, B. A., and Tolstikhin, I. N. (1984). *Helium Isotopes in Nature*, Vol. 3. Amsterdam: Elsevier.

Marty, B., and Jambon, A. (1987). C/^{3}He fluxes from the solid earth: implications for carbon geodynamics. *Earth Planet. Sci. Lett*. 83, 16–26. doi: 10.1016/0012-821X(87)90047-1

Mayorga (2009). Mayorga. Available online at: http://www.kinertech.com/yahoo_site_admin/assets/docs/Geotermia__Caso_de_Costa_Rica.27362721.pdf

Molina, F., and Martì, J. (2016). The Borinquen geothermal system (Canas Dulces caldera, Costa Rica). *Geothermics* 64, 410–425. doi: 10.1016/j.geothermics.2016.07.001

Montegrossi, G., Tassi, F., Vaselli, O., Buccianti, A., and Garofalo, K. (2001). Sulfur species in volcanic gases. *Anal. Chem*. 73, 3709–3715. doi: 10.1021/ac001429b

Montero, W., Lewis, J. C., and Araya, M. C. (2017). The Guanacaste volcanic arc sliver of northwestern costa rica. *Sci. Rep.* 7:1797. doi:10.1038/s41598-017-01593-8

O'Leary, M. H. (1988). Carbon isotopes in photosynthesis. *Bioscience* 38, 328–336.

O'Nions, R. K., and Oxburgh, E. R. (1988). Helium, volatile fluxes and the development of continental crust. *Earth Planet. Sci. Lett*. 90, 331–347.

Ozima, M., and Posodek, F. A. (1983). *Noble Gas Geochemistry*. Cambridge: Cambridge University Press.

OVSICORI-UNA (1995). *Actividad Eruptiva del Volcan Rincón de la Vieja Durante los Dias 6–13 de Noviembre, 1995*. Open Report, OVSICORI-UNA, 42.

OVSICORI-UNA (1998). *Report of the Rincón de la Vieja Volcanic Activity*. Smithsonian Institution, Global Volcanism Network Bulletin.

OVSICORI-UNA (2011). *Report of the Rincón de la Vieja Volcanic Activity*. Smithsonian Institution, Global Volcanism Network Bulletin.

OVSICORI-UNA (2012). *Report of the Rincón de la Vieja Volcanic Activity*. Smithsonian Institution, Global Volcanism Network Bulletin.

OVSICORI-UNA (2014). *Report of the Rincón de la Vieja Volcanic Activity*. Smithsonian Institution, Global Volcanism Network Bulletin.

OVSICORI-UNA (2015). *Report of the Rincón de la Vieja Volcanic Activity*. Smithsonian Institution, Global Volcanism Network Bulletin.

OVSICORI-UNA (2016). *Report of the Rincón de la Vieja Volcanic Activity*. Smithsonian Institution, Global Volcanism Network Bulletin.

OVSICORI-UNA (2017). *Report of the Rincón de la Vieja Volcanic Activity*. Smithsonian Institution, Global Volcanism Network Bulletin.

Patino, L. C., Carr, M. J., and Feigenson, M. D. (2000). Local and regional variations in Central American arc lavas controlled by variations in subducted sediment input. *Contrib. Miner. Petrol.* 138, 265–283. doi: 10.1007/s004100050562

Pineau, F., and Javoy, M. (1983). Carbon isotopes and concentration in mid-oceanic ridge basalts. *Earth Planet. Sci. Lett*. 62, 239–257. doi: 10.1016/0012-821X(83)90087-0

Polyak, B. G., and Tolstikhin, I. N. (1985). Isotopic composition of the Earth's helium and the problem of the motive forces of tectogenesis. *Chem. Geol*. 52, 9–33. doi: 10.1016/0168-9622(85)90005-3

Poreda, R. J., and Craig, H. (1989). Helium isotope ratios in circum-Pacific volcanic arcs. *Nature* 338, 473–478. doi: 10.1038/338473a0

Ray, M., Hilton, D., Muñoz, J., Fischer, T., and Shaw, A. (2009). The effects of volatile recycling, degassing and crustal contamination on the helium and carbon geochemistry of hydrothermal fluids from the southern volcanic zone of Chile. *Chem. Geol*. 266, 38–49. doi: 10.1016/j.chemgeo.2008.12.026

Rizzo, A., Barberi, F., Carapezza, M. L., Di Piazza, A., Francalanci, L., Sortino, F., et al. (2015). New mafic magma refilling a quiescent volcano: evidence from He-Ne-Ar isotopes during the 2011-2012 unrest at Santorini, Greece. *Geochem. Geophys. Geosyst*. 16, 798–814. doi: 10.1002/2014GC005653

Saginor, I., Gazel, E., Condie, C., and Carr, M. J. (2013). Evolution of geochemical variations along the Central American volcanic front. *Geochem. Geophys. Geosyst*. 14, 4504–4522. doi: 10.1002/ggge.20259

Sànchez-Rivera, E., and Vallejos-Ruiz, O. (2015). Costa Rica country update report," in *Proceedings World Geothermal Congress* (Melbourne, VIC), 1–12.

Sano, Y., and Marty, B. (1995). Origin of carbon in fumarolic gases from island arcs. *Chem. Geol*. 119, 265–274. doi: 10.1016/0009-2541(94)00097-R

Sano, Y., and Williams, S. N. (1996). Fluxes of mantle and subducted carbon along convergent plate boundaries. *Geophys. Res. Lett*. 23, 2749–2752. doi: 10.1029/96GL02260

Shaw, A. M., Hilton, D. R., Fischer, T. P., Walker, J. A., and Alvarado, G. E. (2003). Contrasting He-C relationships in Nicaragua and Costa Rica: insights into C cycling through subduction zones. *Earth Planet. Sci. Lett*. 214, 499–513. doi: 10.1016/S0012-821X(03)00401-1

Sherwood Lollar, B., Ballentine, C. J., and O'Nions, R. K. (1997). The fate of mantle-derived carbon in a continental sedimentary basin: integration of C/He relationships and stable isotope signatures. *Geochim. Cosmochim. Acta* 61, 2295–2307.

Shock, E. L. (1993). Hydrothermal dehydration of aqueous organic compounds. *Geochim. Cosmochim. Acta* 57, 3341–3349. doi: 10.1016/0016-7037(93)90542-5

Tassi, F., Vaselli, O., Capaccioni, B., Giolito, C., Duarte, E., Fernandez, et al. (2005). The hydrothermal-volcanic system of Rincón de la Vieja volcano (Costa Rica): a combined (inorganic and organic) geochemical approach to understanding the origin of the fluid discharges and its possible application to volcanic surveillance. *J. Volcanol. Geotherm. Res*. 148, 315–333. doi: 10.1016/j.jvolgeores.2005.05.001

Tedesco, D., and Nagao, K. (1996). Radiogenic ^{4}He, ^{21}Ne and ^{40}Ar in fumarolic gases at Vulcano island: implication for the subductuted African continental plate beneath Italy. *Earth Planet. Sci. Lett*. 144, 517–528. doi: 10.1016/S0012-821X(96)00196-3

Tristan, J. F. (1921). Apuntes sobre el volcano Rincón de la Vieja. *Rev. Costa Rica II* 6, 161–168.

Vallejos-Ruiz, O., Sànchez-Rivera, E., and Gonzàlez-Vargas, C. (2005). "Reservoir management at the Miravalles geothermal field, Costa Rica," in *Proceedings World Geothermal Congress* (Antalya), 1–8.

Venturi, S., Tassi, F., Bicocchi, G., Cabassi, J., Capecchiacci, F., Capasso, G., et al. (2017). Fractionation processes affecting the stable carbon isotope signature of thermal waters from hydrothermal/volcanic systems: the examples of Campi Flegrei and Vulcano Island (southern Italy). *J. Volcanol. Geotherm. Res*. 345, 46–57. doi: 10.1016/j.jvolgeores.2017.08.001

Conflict of Interest Statement: The authors declare that the research was conducted in the absence of any commercial or financial relationships that could be construed as a potential conflict of interest.

frontiers
in Earth Science

ORIGINAL RESEARCH
published: 15 October 2018
doi: 10.3389/feart.2018.00157

Coupling Between Magmatic Degassing and Volcanic Tremor in Basaltic Volcanism

Giuseppe G. Salerno[1]*, Mike Burton[2], Giuseppe Di Grazia[1], Tommaso Caltabiano[1] and Clive Oppenheimer[3]

[1] Istituto Nazionale di Geofisica e Vulcanologia, Osservatorio Etneo, Sezione di Catania, Catania, Italy, [2] School of Earth, Atmospheric and Environmental Sciences, University of Manchester, Manchester, United Kingdom, [3] Department of Geography, University of Cambridge, Cambridge, United Kingdom

Magmatic degassing, typically measured as SO_2 flux, plays a fundamental role in controlling volcanic eruption style and is one of the key parameters used by volcano observatories to assess volcanic unrest and detect eruption precursors. Volcanic tremor, the integrated amplitude of seismic energy release over a range of frequencies, is also a key parameter in volcano monitoring. A connection between volcanic degassing and tremor has been inferred through correlations between the signals which are often, but not always, observed during periods of unrest or eruption. However, data are often equivocal and our understanding of the physical processes, which couple degassing with tremor are still evolving. New insights into degassing-tremor coupling can be made by investigation of the long-term relationship between degassing and tremor, focusing on the frequency-dependence of tremor and passive degassing behavior. In this study, we examine how long-term SO_2 emission rates and volcanic tremor on Mt. Etna, track rapid variability in eruptive dynamics. Correlations between SO_2 flux and tremor are explored in both quiescent and eruptive periods, comparing the two parameters at both long and short time-scales ($< <$ 1 day) for $\sim$2 years. Our analysis reveals that over $\sim$month-long timescales passive degassing of SO_2 and tremor tend to be well-correlated, but these correlations are lost over shorter timescales. This reflects a coupling process between passive degassing and tremor, produced by a combination of gas flow through permeable magma and the convective flow of magma within the conduit. Short-term correlations are lost because variations in the continuous degassing process are relatively small compared with the overall degassing rate and fall below measurement noise. During eruptive periods strong correlations are observed between degassing and tremor, with a significant contribution of higher frequency signal in tremor, controlled by eruptive style. These observations suggest that in syn-eruptive periods the tremor source is dominated by the coupling between the eruption column and the ground through infrasonic waves, rather than conduit processes. Our results demonstrate the importance of high quality long-term observations and offer new insights into the physical mechanisms which couple degassing and volcanic tremor at active volcanoes.

Keywords: Mt. Etna, SO_2 flux, volcanic tremor, eruptive and quiescent degassing, volcano monitoring

Edited by:
Fátima Viveiros,
Instituto de Investigação em
Vulcanologia e Avaliação de Riscos
(IVAR), Portugal

Reviewed by:
Taryn Lopez,
University of Alaska Fairbanks,
United States
Oleg E. Melnik,
Lomonosov Moscow State University,
Russia

***Correspondence:**
Giuseppe G. Salerno
giuseppe.salerno@ingv.it

Specialty section:
This article was submitted to
Volcanology,
a section of the journal
Frontiers in Earth Science

Received: 29 June 2018
Accepted: 24 September 2018
Published: 15 October 2018

Citation:
Salerno GG, Burton M,
Di Grazia G, Caltabiano T and
Oppenheimer C (2018) Coupling
Between Magmatic Degassing
and Volcanic Tremor in Basaltic
Volcanism. Front. Earth Sci. 6:157.
doi: 10.3389/feart.2018.00157

INTRODUCTION

Over the last decades, technological advances have allowed volcanic activity to be monitored at ever-increasing spatial and temporal resolutions (e.g., Heliker et al., 2003; Calvari et al., 2008; Johnson and Poland, 2013). Particularly, in the case of volcanic ground-based gas measurements the development of automated networks of spectrometer gas sensors (e.g., Edmonds et al., 2003a; Salerno et al., 2009b), ultraviolet and thermal cameras (e.g., Mori and Burton, 2006; Burton et al., 2015a; Lopez et al., 2015), and FTIR and multigas sensors (e.g., Burton et al., 2003; Shinohara, 2005; Taquet et al., 2017), have improved the temporal resolution of magmatic gas composition and flux observations, e.g., SO_2 flux, from typically of order hours to ∼1 Hz. This has permitted comparison with geophysical measurements, thus allowing better integration of both geochemical and geophysical parameters for refining models and to identify eruptive anomalies and unrest (e.g., Aiuppa et al., 2010; Bonaccorso et al., 2011b; Poland et al., 2012; Patanè et al., 2013; Burton et al., 2015b; Hibert et al., 2015; Nadeau et al., 2015). In particular, volcanic SO_2 emissions are important indicators of subsurface processes, and the study of their temporal evolution provides inferences on processes occurring at shallow depth (∼4–5 km from crater top). Measurements of SO_2 emissions made over almost 40 years (e.g., Williams-Jones et al., 2008), have shown remarkable transitions from quiescence to unrest at both silicic magmatic systems (e.g., Fischer et al., 1994; Williams-Jones et al., 2001; Nadeau et al., 2011) and mafic volcanoes (e.g., Malinconico, 1979; Voight et al., 1999; Sutton et al., 2001; Caltabiano et al., 2004; Kazahaya et al., 2004). Measurement of SO_2 outgassing also provide constraints on magma-degassing budgets and mass balance (e.g., Wallace and Gerlach, 1994; Allard, 1997; Shinohara, 2008; Steffke et al., 2011).

Volcanic tremor is observed at volcanoes as background seismic radiation in quiescent stages and as peaks in amplitudes during eruptive episodes such as explosive eruptions (e.g., Alparone et al., 2003; Patanè et al., 2013). Dominant frequency ranges between 0.1 and 10 Hz and episodes of high amplitude tremor may persist for months (e.g., Kubotera, 1974; McNutt, 1992; Zobin, 2003). Physical processes generating volcanic tremor are thought to be associated with unsteady mass transport-flow of magma dynamically coupled with the surrounding rocks (Steinberg and Steinberg, 1975; Schick and Mugiono, 1991; Neuberg and Pointer, 2000; Battaglia et al., 2005). However, several other mechanisms (e.g., Gordeev, 1993; Benoit and McNutt, 1997) and models have been proposed as potential sources of tremor (e.g., Aki et al., 1977; Chouet et al., 1987) depending on individual volcanoes and eruption style (Konstantinou and Schlindwein, 2002; Matoza and Fee, 2014). In particular, a review of the engineering literature associated with studies of two phase fluid flow induced vibration in pipes was recently published (Miwa et al., 2015), focusing on the hydrodynamic force produced by flows that generate potentially destructive vibrations in industrial machines and infrastructure. The review highlighted the impact of different flow patterns, turbulence and pipe geometry, producing a fluctuation force magnitude spectrum with a frequency range similar to that observed for tremor in volcanic settings when velocities were in the range of magma flow during quiescent degassing ∼0.6 ms^{-1} (Burton et al., 2007).

Persistent degassing from active volcanoes is widely associated with volcanic tremor (e.g., Williams-Jones et al., 2001; Konstantinou and Schlindwein, 2002; McNutt, 2002). Evidence of coupling between the two parameters has been discussed at different volcanic systems (e.g., Mt. Etna: Gresta et al., 1991, Bruno et al., 1995; Patanè et al., 2013; Zuccarello et al., 2013; Soufrière Hills: Miller et al., 1998; Edmonds et al., 2003b; Piton de la Fournaise: Battaglia et al., 2005; Colima: Vargas-Bracamontes et al., 2009). Increases in tremor amplitude were observed prior to and during effusive eruptions and synchronous with explosive activity (e.g., Usu: Omori, 1911; Pavlof: McNutt, 1986; Hekla: Brandsdóttir and Einarsson, 1992; Galeras: Fischer et al., 1994; Mt. Etna: Cannata et al., 2008; Bonaccorso et al., 2011b; Kilauea: Nadeau et al., 2015). Changes in the dominant tremor frequency have been commonly associated with changes in the regime and style of eruptive activity (e.g., Ereditato and Luongo, 1994; Thompson et al., 2002; Alparone et al., 2003; Bryan and Sherburn, 2003; Cannata et al., 2018). At Mt. Etna, Leonardi et al. (2000a) studied the relationship between volcanic tremor and SO_2 flux in the period between 1987 and 1992 by cross-correlation analysis. Their results indicated that, in the case of eruptive activity, the two signals strongly correlated. The authors proposed that such as behavior might have resulted from common physical mechanisms related to magma dynamics. Similarly, at Soufrière Hills, Montserrat, Young et al. (2003) found systematic and direct correlation between SO_2 flux and tremor analyzing data between December 1999 and January 2000, with gas flux lagging behind the tremor signal. Similar correlations between SO_2 outgassing and seismic amplitude were observed also at Villarrica (Palma et al., 2008), Yasur (Bani and Lardy, 2007), Fuego (Nadeau et al., 2011), and Kilauea (Nadeau et al., 2015). Volcanic tremor has also shown good correlation with other geochemical parameters. For instance, Alparone et al. (2005) carried out a statistical analysis on radon emissions from the soil and reduced displacement of volcanic tremor both recorded during paroxysmal explosive phases of Mt. Etna's summit craters. Their studies revealed increase in radon concentrations ∼58 ± 12 h prior to changes in volcanic tremor. More recently, investigating the relationship between CO_2 flux and volcanic tremor at Mt. Etna, Cannata et al. (2009a) found that variations in the geochemical signal preceded those of volcanic tremor of ∼50 days. Nevertheless, in some cases contradictory or/and lack of relationship between eruptive activity and tremor amplitude has been observed. Doukas and Gerlach (1995), observed an episode of inverse correlation between SO_2 flux and volcanic tremor at Mount Spurr, Alaska during the 1991–1993 eruptive activity, interpreting the gas declined as a result of SO_2 absorption by the hydrothermal system. Similarly, inverse correlations between CO_2 flux and volcanic tremor were observed at Stromboli (Aiuppa et al., 2009). At Soufrière hills volcano, Watson et al. (2000) reported that high rates of SO_2 were associated with enhanced seismicity and ground deformation a month before the 1997 dome collapse. However, previous observations by Young et al. (1998) showed that the enhanced long-period seismicity at Soufrière Hills did not relate to increases in SO_2 flux. This indicates that, though tremor and degassing are somewhat coupled, the nature of their relationship, as well as the source mechanism for tremor, are still poorly understood. It is likely that several processes are involved in the generation of volcanic tremor from gas and magma flows, making the unraveling of the tremor and degassing relationship challenging.

Here, we focus on three mechanisms by which volcanic tremor may be coupled with degassing: (1) flow of gas through permeable magma (e.g., Burton et al., 2007; La Spina et al., 2017), (2) magma flow within a conduit (e.g., Kazahaya et al., 1994; Beckett et al., 2014), and (3) coupling of eruptive processes to ground seismicity through infrasound during explosive activity (Matoza and Fee, 2014). The links between these processes and magmatic degassing are explored on Mt. Etna by comparing seismic tremor measured with the INGV seismic network with SO_2 flux measurements collected with INGV FLAME network. Long- and short-timescale comparisons of the two parameters for six case studies selected between 2007 and 2008 were carried out by correlation analysis to investigate whether the correlation holds across different timescales.

ERUPTIVE ACTIVITY BETWEEN 2007 AND 2008

Mt. Etna is the most active volcano in Europe characterized by extensive quiescent and active degassing activity that occurs at the main craters (North-East Crater: NEC, South-East Crater: SEC, and central craters Voragine: VOR, and Bocca Nuova: BN, **Figure 1**; e.g., Allard, 1997; Aiuppa et al., 2008). Between 2007 and 2008, eruptive activity at Mt. Etna resumed after a quiescent period following the 2006 eruption (Bonaccorso et al., 2011a). Activity was vigorous and characterized by a series of relatively short explosive episodes and long-lasting lava effusion both occurring from the eastern flank of SEC. (Andronico et al., 2008; Corsaro and Miraglia, 2009; Bonaccorso et al., 2011a). This period is divided into two main phases, firstly the period January 2007 to early May 2008 characterized by intermittent lava fountains and the period May–December 2008, characterized by effusive activity (**Figure 2**). The first stage, from January 2007 to early May 2008, consisted of sporadic violent strombolian and lava fountaining episodes accompanied by short-lasting lava effusion (e.g., Andronico et al., 2008; Di Grazia et al., 2009; Bonaccorso et al., 2011a,b; Behncke et al., 2016). Paroxysms exhibited recurrent features consisting on increasing strombolian activity at first, lava flow output, and transition from strombolian to lava fountaining (Aloisi et al., 2009; Di Grazia et al., 2009; Langer et al., 2010). This activity was similar to the lava fountain sequences observed at SEC in 2000 (e.g., Alparone et al., 2003; Allard et al., 2005; La Spina et al., 2015), and between 2011 and 2015 (e.g., Calvari et al., 2011; Patanè et al., 2013; Corsaro et al., 2017). The effusion phase, between 13 May and December 2008, started 3 days after the 10 May paroxysm (Aloisi et al., 2009; James et al., 2011), and was dominated by lava effusion occasionally accompanied between May and early September 2008 with strombolian activity from the eruptive fissure (Cannata et al., 2009b; Bonaccorso et al., 2011a; Currenti et al., 2011).

DATA ACQUISITION AND ANALYSIS

All data presented here were acquired by the continuous geochemical and geophysical monitoring system of Istituto Nazionale di Geofisica e Vulcanologia, Osservatorio Etneo (INGV-OE).

SO_2 Flux

The bulk SO_2 flux from the summit craters and eruptive fissure of Mt. Etna was measured automatically by the FLAME scanning spectrometer network (Salerno et al., 2009b; Calvari et al., 2011). The network consists of ten ultraviolet scanning spectrometer stations spaced ∼7 km apart and installed at an altitude of ∼900 m above sea level (a.s.l.) on the flanks of Mt. Etna (Calvari et al., 2011). Recorded UV spectra were retrieved in SO_2 column amounts using the DOAS method (e.g., Platt and Stutz, 2008), and applying a modeled background reference spectrum (Burton et al., 2009; Salerno et al., 2009a). Retrieved SO_2 data were transmitted to INGV–OE where they were converted into mass flux rate. Each flux datum was time corrected to account for the travel time of the plume from the summit craters to the scanning plane of each scanner of the network (∼14 km). Uncertainty in computed SO_2 flux depends to an extent on plume velocity, because at very low velocities the absolute velocity error becomes a larger proportion of the relative error in calculated flux. Assumptions on plume height are made based on observations of the relationship between plume velocity and height, and light scattering effects also contribute to the flux error budget (e.g., Mori et al., 2006; Campion et al., 2015). Salerno et al. (2009b) estimates uncertainty in SO_2 flux by stationary automatic scanning array between $-22 + 36\%$, but error can vary to greater than 100% depending on conditions.

Seismic Data

The permanent seismic network of INGV comprises 45 three-component broadband (40 s) digital stations with continuous data acquisition and transmission at a sampling frequency of 100 Hz (**Figure 1**; e.g., Di Grazia et al., 2006; Patanè et al., 2008). In this work, we use data from the Etna Cratere del Piano (ECPN) station, which is set up on the southern flank of the volcano at an altitude of 2900 m a.s.l. and ∼1 km from the summit craters (**Figure 1**). The ECPN station was chosen as it offers the longest data continuity provided during the studied period, the best signal to noise ratio and its proximity to the summit craters makes it especially sensitive to eruptive activity. Volcanic tremor spectral amplitude was calculated using the root mean square (RMS expressed in arbitrary unit) of the seismic signal recorded on the vertical component. In this study, the daily RMS at overall spectral amplitude (OSA) was used for long-term characterization of volcanic tremor and to explore its relationship with daily SO_2 flux. In order to inspect the short-term relationship between SO_2 flux and tremor and identify if any and which frequency components correlated most strongly with

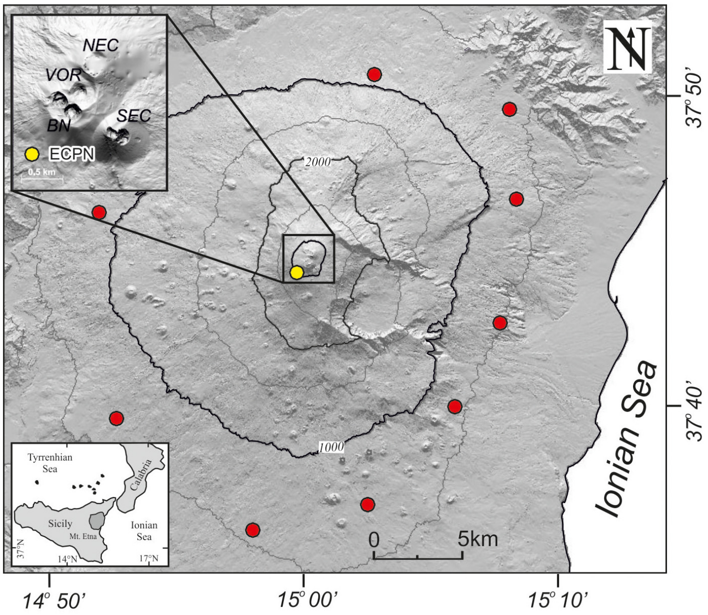

FIGURE 1 | Map of Mt. Etna with location of the FLAME scanning spectrometers network (red-solid circles) and the Etna Cratere del Piano (ECPN) seismic station used for this study (yellow-solid circle). The shaded relief on the upper left corner details the volcano four-summit craters (VOR, BN, SEC, and NEC) and the ECPN station. In the bottom left is showed the geographic location of Mt. Etna and Sicily.

degassing rates, seismic amplitude was decomposed into separate frequency bands (e.g., Gresta et al., 1987; Thompson et al., 2002; Di Grazia et al., 2009). RMS spectral amplitude was calculated for several frequency bands of 1 Hz width in the frequency range 0.025–10.5 Hz, and tremor amplitude was obtained by averaging the RMS values with a 5 min time window. This time window was chosen according Cannata et al. (2009a), who report that time windows of this length are a good compromise between the stability of the signal and the opportunity of observing details of the evolution of the parameter during eruptions. Uncertainties affecting RMS depends on the dispersion of the averaged RMS time window; it ranges between 10% for the short-5 min intraday study and up to mean 25%, enveloped between a minimum of 6% and maximum of 77%, for the long-temporal daily averaged RMS.

Data Analysis

To investigate the relationship between the SO_2 flux and volcanic tremor, we apply the correlation analysis, which expresses the strength of linkage or co-occurrence between two variables in a single value ranging from −1 to +1, i.e.,$-1 \leq r \leq +1$ (e.g., Davis, 1986; McKillup and Dyar, 2010). Usually for evaluating dependences between two parameters, the conventional Pearson's correlation analysis is used. However, this method requires normal distribution of the parameter samples. Since both SO_2 flux and volcanic tremor data were characterized by non-Gaussian distribution (mean skewness and kurtosis are 1.1 and 0.9, and 1.2 and 1.1, respectively; **Table 1** and **Supplementary Figure S1**) and the SO_2 flux sample sizes were small (maximum 120 daily-light observations), the non-parametric Spearman's Rank correlation analysis was applied (e.g., Zar, 1972; Davis, 1986; Swan and Sandilands, 1995). Compared to the Pearson's correlation analysis, the Spearman's correlation method does not require continuous-level data (interval or ratio), as it uses ranks instead of assumptions on the distributions of two variables. This allows analysis of the association between variables of ordinal measurement levels. Mathematically, Spearman's and Pearson's correlations are very similar in the way that they use different measurements to calculate the strength of association of two parameters. Pearson's correlation applies standard deviations, while Spearman's the difference in ranks (Davis, 1986; Swan and Sandilands, 1995).

RESULTS

Figure 2 reports the weekly averaged SO_2 flux and the daily OSA of the volcanic tremor RMS for long-term observation between 2007 and 2008. Over the investigated period, tremor and SO_2 flux show common changes at different temporal and magnitude scales associated in both stages of quiescent-passive degassing and eruptive activity (**Figure 2**). During the intermittent paroxysmal phase, preceding the opening of the eruptive fissure on May 13, 2008, the SO_2 rates and tremor behaved in a similar manner showing marked oscillations in correspondence to the explosive activity. These waxing-waning trends have higher amplitudes starting from the end of July 2007 until the opening of the 2008–2009 eruptive fissure (**Table 1**). Note that in **Figure 2**, volcanic tremor RMS is plotted in logarithmic scale to allow for better comparison with SO_2 flux, and values are expressed in arbitrary units. Short-term intraday comparison between SO_2 flux-volcanic tremor patterns were

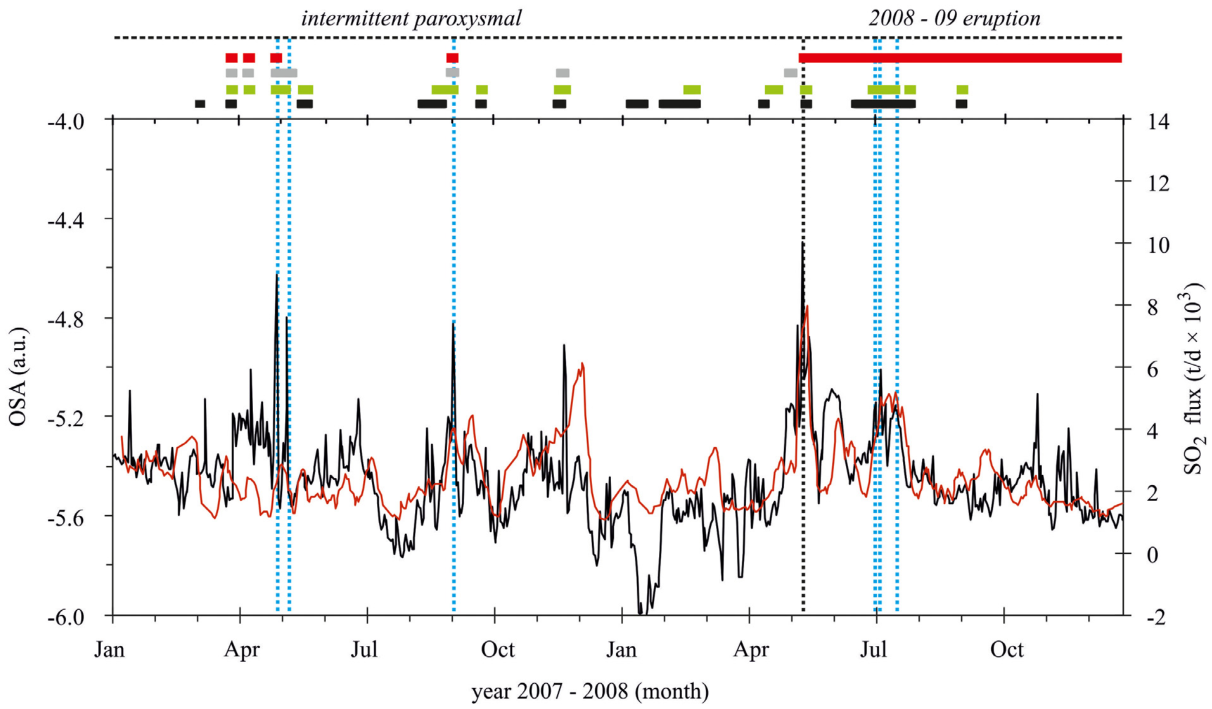

FIGURE 2 | Weekly averaged SO_2 flux (in red) and daily averaged overall spectral amplitude (OSA) of the volcanic tremor (in black) in 2007 and 2008; tremor is represented on a logarithmic. The black-dashed vertical line between April and July 2008 indicates the start of the 2008-09 eruptive activity on 13 May while the blue-dashed lines indicate the selected case studies explored at intraday scale. The upper graph shows the summary of the eruptive activity of Mt. Etna in the studied period. The 2-year long time window can be splitted into two phases according to the eruptive activity observed at the surface. The first phase relates to an intermittent paroxysmal phase consisting of ash emission (black square), strombolian activity (green-square), lava fountaining (gray-square), and lava emission (red-square), the second phase refer to a period characterized by persistent lava emission and irregular moderate strombolian explosions and ash emissions along the 2008-09 eruptive fissure. Uncertainty in SO_2 flux by stationary array arise from several sources, such as wind-plume transport speed, plume height and radiative transfer, these parameters maybe highly variable being the flux affected by and uncertainty that may ranges between –22 and 36, up to 100% in challenging condition. Uncertainty in daily RMS depends on the intraday variability of the seismic averaged signal and it ranges between 10% for the intraday study and mean of 25% for the daily long-term investigation.

carried out to explore potential correlation between the two signals on a scale of minutes (**Figure 3**). Of the seven lava fountain episodes of the intermittent paroxysmal phase and of the strombolian activity fed by the eruptive fissure on 14 May, only 6 days could be analyzed (**Table 1**). The other episodes had to be excluded due to eruptive events at night (when UV spectroscopy was not possible) or on days when the plume was blown to the northern and western flanks of the volcano beyond the coverage of the FLAME network. In addition, some of the eruptive episodes were also excluded from the analysis due to the limited number of SO_2 scans on the given days.

Figure 3 shows the intraday SO_2 flux and volcanic tremor data for the six case studies. In each of the six graphs, SO_2 flux is plotted together with RMS at a dominant frequency, i.e., that has shown the highest SO_2 flux-volcanic tremor correlation coefficient between 0.025 and 10.5 Hz; likewise correlation analysis was also performed considering the OSA (**Table 1**; **Figure 4**). Signals display simultaneous changes in both magnitude and temporal scale repeatedly over the course of the measurements and persist over time scales ranging from 6 to 12 h. This correlation occurs during both stage of onset and waning phase of strombolian activity (case 1 and 2) and transition from strombolian to lava fountaining (case 3), both eruptive styles superimposed on short-lived and persistent lava flow output (4–6; **Table 1**). SO_2 flux was strongly correlated with seismic tremor between 2.5 and 6.5 Hz during explosive eruptions and between 0.025 and 2.5 Hz (case studies 1–3, and in 4–6, respectively; **Table 1**), isolated anticorrelation were also observed for cases 1, 2, and 4, when SO_2 emission rates increased while RMS decreased.

DISCUSSION

From these observations, we see that in both the initial period between January 2007–May 2008 and the effusive eruption from May 2008 onwards, a strong correlation is observed between tremor and the weekly averaged SO_2 flux (**Figure 2**). We highlight in particular the quiet eruptive period between May and December 2007, when the relationship between tremor and SO_2 flux is marked, and a further period of close correlation is observed between May and December 2008, associated with the effusive eruption. We propose that this arises from a driving mechanism of magma flow, in which seismic energy is produced through friction between the flowing magma and conduit walls.

TABLE 1 | Details of the main features and parameters of the intermittent paroxysmal and eruptive 2008–2009 phases and of the six case studies investigated.

Phase	Parameter	Min	Max	Mean	δ	
Intermittent paroxysmal	$\Phi S0_2$	400	13,500	2400	1500	
	*V*t	−6.0	−4.6	−5.5	0.2	
Eruption 2008–2009	$\Phi S0_2$	450	20,000	2700	650	
	*V*t	−5.7	-4.5	-5.4	0.2	
Case study	1	2	3	4	5	6
Date	April 29, 2007	May 07, 2007	September 04, 2007	July 07, 2008	July 10, 2008	July 24, 2008
Eruptive style	explosive	explosive	explosive	effusive – explosive	effusive – mild explosive	effusive-mild explosive
Frequency band *V*t (Hz)	5.5–6.5	5.5–6.5	2.5–3.5	0.025–0.5	1.5–2.5	0.5–1.5
ρ	0.0.7	0.9	0.7	0.6	0.8	0.6
Min $\Phi S0_2$	700	1300	1300	2100	1100	750
Max $\Phi S0_2$	20,000	13,000	10,000	11,000	17,000	10,300
Mean $\Phi S0_2$	5600	6000	3500	5500	7500	2600
δ ΦSO_2	4500	3700	1500	2500	4100	1950
Min *V*t	4.0×10^{-7}	7.2×10^{-7}	4.2×10^{-6}	1.9×10^{-7}	1.4×10^{-6}	8.8×10^{-7}
Max *V*t	1.8×10^{-5}	2.8×10^{-5}	1.5×10^{-5}	3.3×10^{-7}	3.6×10^{-6}	1.9×10^{-6}
Mean *V*t	5.3×10^{-6}	9.2×10^{-6}	7.1×10^{-6}	2.4×10^{-7}	2.1×10^{-6}	1.1×10^{-6}
d *V*t	3.0×10^{-6}	1.1×10^{-5}	2.5×10^{-6}	2.6×10^{-8}	4.9×10^{-7}	1.8×10^{-7}

ΦSO_2 = SO_2 flux in t/d; *V*t = Volcanic tremor amplitude (arbitrary units); δ = Standard deviation; ρ = Coefficient of correlation

Results of the tremor frequency bands with maximum correlation used in this study together with statistical details on the SO_2 emission rate and volcanic tremor.

Analysis of the source depth of seismic tremor demonstrates that the entire shallow conduit is a tremor source (e.g., Patanè et al., 2008; Cannata et al., 2013), consistent with our frictional flow hypothesis, with a peak in energy at a depth of 2–3 km, perhaps due to the lower viscosity of magma at this depth permitting a maximum ascent rate (e.g., Burton et al., 2007). There are two main regimes of magma flow, firstly as a result of effusive eruption, in which magma degasses and crystallizes during ascent before erupting, and secondly due to the convective overturn of magma during quiescent degassing (Kazahaya et al., 1994; Beckett et al., 2014) which is required to sustain the persistent degassing flux of Mt. Etna (e.g., Allard, 1997). This flow transports magma from below 3 km depth (from the volcano summit) to near-surface, which is the principle pressure regime where sulfur and water exsolution takes place at Mt. Etna (Metrich et al., 2004; Spilliaert et al., 2006; Wallace and Edmonds, 2011). Convective overturn leads to permanent burial of degassed magma in the roots of the plumbing system, revealed as a voluminous plutonic body in seismic tomography observations (Patanè et al., 2006; Díaz-Moreno et al., 2018). We tentatively propose that periods of weak correlation between SO_2 flux and tremor, such as that observed in early 2007, are produced when magmatic overturn slows down, and degassing becomes dominated by permeable gas flow from depth. A further related process, which could play a key role, is the level and condition of magma in the conduit, as a lower magma level together with magma viscosity, gas and crystal content may attenuate the tremor amplitude (e.g., Collier et al., 2006). These processes will be investigated in future work through examination of CO_2/SO_2 and ground deformation time series. Short-term correlations on the scale of a day between gas flux and tremor during quiescent periods are not observed clearly, perhaps because variations in the continuous degassing process are relatively small compared with the overall degassing rate and fall below measurement noise. Future improvements in the precision and accuracy of SO_2 flux quantifications are required to reveal any short-term correlations during passive degassing.

In order to characterize the main oscillations of both intermittent paroxysmal and 2008–2009 eruptive phases, corresponding to the more intense explosive episodes of the study period, an inspection at daylight intraday scale was carried out. Tremor was decomposed to its spectral components between 0.025 and 10.5 Hz signal, and then each volcanic tremor frequency was compared with SO_2 flux using correlation analysis. This decomposition allowed statistical identification on the best correlation between SO_2 flux and volcanic tremor frequency, and highlights that in different eruptive contexts the geochemical signal correlated with tremor at different dominant frequencies (**Figure 4**). We found that SO_2 flux correlated strongly with volcanic tremor with high frequencies during the most explosive activity. This is consistent with the observation of coupling via infrasound between explosive volcanic activity and the ground, producing a high frequency tremor source (Matoza and Fee, 2014). In the six case studies investigated here, the first three of them, i.e., those falling within the intermittent paroxysmal phase (**Figure 2**) showed the highest SO_2 flux/tremor correlation coefficients at frequencies of 2.5–6.5 Hz (**Table 1**; **Figure 4**). Conversely, the case studies pertaining to the 2008–2009 eruptive fissure activity displayed the highest correlations at lower frequencies, i.e., from 0.025 to 2.5 Hz (**Table 1**; **Figure 4**). The fact that the two parameters correlated at different tremor frequencies, and that the frequency depended on the intensity of the associated eruptive phenomenon, suggests that on long time scales, some of the signal features could be masked or missed if the RMS is calculated for all frequencies. Falsaperla et al. (2005) analyzed amplitude and frequency content of the seismic

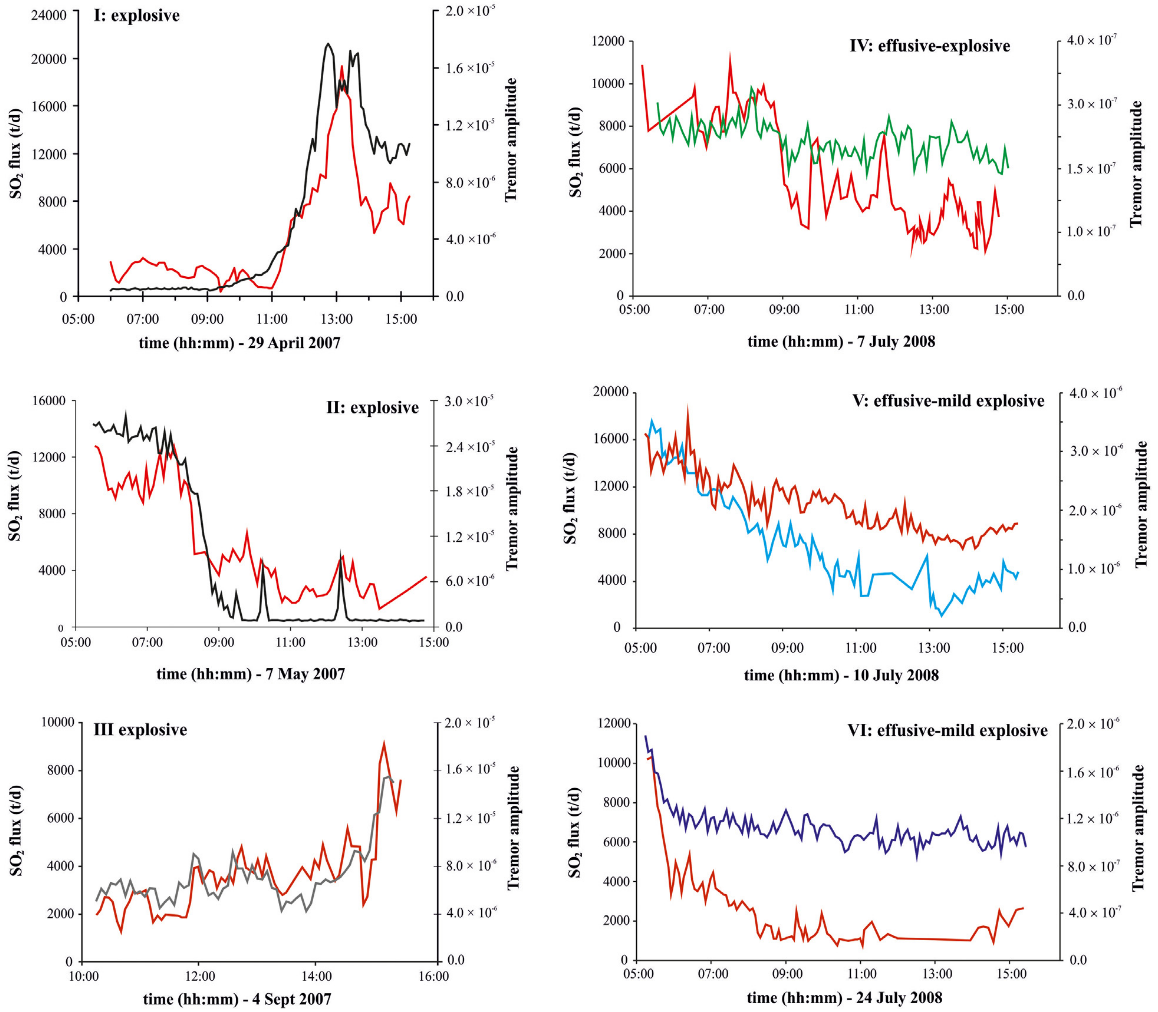

FIGURE 3 | Intraday SO$_2$ flux and volcanic tremor amplitude for the selected case studies (**Table 1**). In the six cases, tremor mirrored SO$_2$ outgassing in different eruptive style and transition. SO$_2$ flux (red line) was strongly correlated with volcanic tremor at frequency band with max correlation clustered in two groups of high (black line) and medium-low frequency (gray, green, cyan, and blue lines).

signal of the 2001 Mt. Etna's flank eruption finding considerable changes in the volcanic tremor associated with different styles of eruptive activity. In particular, they observed that the dominant frequency of the signal decreased from ∼5 Hz to 3 Hz during lava fountaining, and further decreased to ∼2 Hz during intense lava emissions, supporting the infrasound-coupling hypothesis as the source of seismic tremor during more explosive activity. There were also periods where SO$_2$ flux and tremor appear anticorrelated on short timescale, resulting from time shifts of the two parameters. Shifts were identified in cases 1, 2, and 4, with gas lagging behind seismic energy release. This behavior, which has also been observed on long-time scales by Leonardi et al., 2000b, has been interpreted as due to increasing pressurization of the volcano's shallow feeder system, which simultaneously increases tremor but with a lag time before gas release at the onset of eruptive activity (e.g., Young et al., 2003; Nadeau et al., 2011). A further process might rely on the turbulent magma-flow rate in the upper conduit triggered by gas-slug dynamics during ongoing eruptive events (e.g., Parfitt, 2004) coupled with instability of magma column (Bercovici et al., 2013).

These results underline that though the strong association between magmatic degassing and tremor, several process are involved in generating seismic energy. Their mutual behavior might change depending on the physical mechanism of magma flow regime and gas/melt separation in the conduit, revealing the gas-tremor study puzzling. Although further efforts are required to advance our understating in magmatic degassing – seismic tremor release relationship, the strong correlation observed in this study between the two parameters, indicates that degassing generates seismic tremor, and that gas flux might thereby provide a proxy for eruptive style and intensity and short-term warning for impeding eruptions.

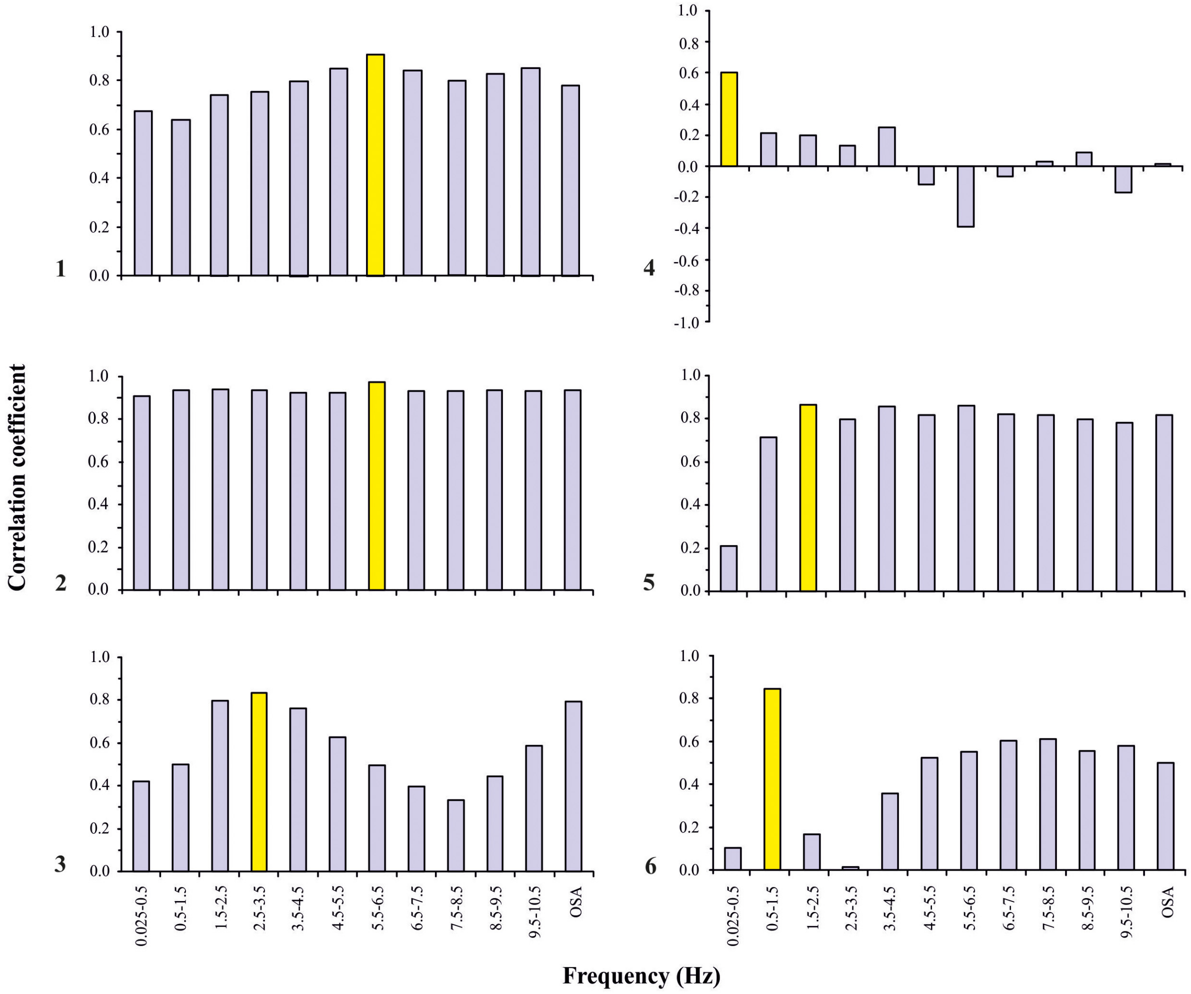

FIGURE 4 | Correlation coefficient of SO_2 flux vs. volcanic tremor in the six intraday case studies investigated at frequency bands between 0.025 and 10.5 Hz and OSA. Overall, the two parameters show reliable correlation between 0.6 and 0.9 Hz (Leonardi et al., 2000b). In each of the six histograms, the yellow bin represents the maximum correlation between the SO_2 flux and volcanic tremor. In detail, case studies 1, 2, and 5 (except for the frequency below 0.5 Hz) show good correlation at almost all frequencies. Case studies 3 and 6 display bimodal distribution of the correlation coefficients with dominant frequencies centered at 3 and 1 Hz in case study 3 and 6, respectively. Case study 4 is characterized by both positive and negative correlation coefficient values. The positive maximum value corresponds to below 0.5 Hz. The negative bars indicate the frequencies at which SO_2 flux and volcanic tremor anticorrelated

CONCLUSION

Both explosive and effusive eruptions are believed to be largely controlled by volatile content and magma flow rate (e.g., Woods and Cardoso, 1997), and by their mutual modulation within the shallow conduit (e.g., Jaupart and Vergniolle, 1988). Likewise, seismic tremor varies with volcanic activity and is considered originated by fluids dynamic process in volcanic conduit (e.g., Chouet, 1996). Results achieved in this study provide strong evidence that for extended periods the volcanic tremor and SO_2 flux signals on Mt. Etna are strongly correlated. The mutual relationship rely on a physical mechanism of magma flow, which through friction between magma and conduit walls produces a tremor signal with frequency dominated between 0.025 and 2.5 Hz. This magma flow provides the source of SO_2 emitted persistently at the summit craters during passive degassing and the eruptive vents during effusive activity, through exsolution and transport of SO_2 during magma ascent. We tentatively attribute periods of low correlation between tremor and SO_2 flux to a different degassing regime, dominated by fluxing of gas from depth, and this hypothesis will be tested in future work. Our examination of explosive activity demonstrates that the best correlation is achieved between high frequency tremor (2.5–6.5 Hz) and SO_2 flux, which we attribute to a process of coupling through infrasound between the explosive activity in the atmosphere and the surface, creating high frequency tremor. Our results underline the clear link between the geochemical and the geophysical signals. Their common behavior during both quiescent and eruptive stages, and during transitions between eruptive regimes, emphasizes that magmatic degassing produces volcanic tremor, and that both originate from a common physical mechanism of magma dynamics in the shallow conduit. This study provides a framework for the interpretation of tremor and SO_2 degassing to other persistently active basaltic systems worldwide, which will assist in the understanding of the processes and mechanisms controlling unrest and pre-eruptive activity.

AUTHOR CONTRIBUTIONS

GS and MB coordinated the research and mainly wrote the manuscript with the substantial, direct, and intellectual contribution to the work from all authors.

ACKNOWLEDGMENTS

We greatly acknowledge F. Murè and V. Longo for their technical assistance in the FLAME network. We thank Dr. L. Spampinato for useful discussions. We are also grateful to the two reviewers for helpful comments and suggestions.

SUPPLEMENTARY MATERIAL

The Supplementary Material for this article can be found online at: https://www.frontiersin.org/articles/10.3389/feart.2018.00157/full#supplementary-material

REFERENCES

Aiuppa, A., Burton, M., Caltabiano, T., and Ripepe, M. (2009). "Anti-correlation between gas flux and volcanic tremor on Stromboli volcano," in *Proceedings of the Geophysical Research Abstracts 11, EGU2009-13671, EGU General Assembly 2009*, Göttingen.

Aiuppa, A., Cannata, A., Cannavò, F., Di Grazia, G., Ferrari, F., Giudice, G., et al. (2010). Patterns in the recent 2007–2008 activity of Mount Etna volcano investigated by integrated geophysical and geochemical observations. *Geochem. Geophys. Geosyst.* 11:Q09008. doi: 10.1029/2010GC003168

Aiuppa, A., Giudice, G., Gurrieri, S., Liuzzo, M., Burton, M., Caltabiano, T., et al. (2008). Total volatile flux from Mount Etna. *Geophys. Res. Lett.* 35:L24302. doi: 10.1029/2008GL035871

Aki, K., Fehler, M., and Das, S. (1977). Source mechanism of volcanic tremor: fluid-driven crack models and their application to the 1963 Kilauea eruption. *J. Volcanol. Geotherm. Res.* 2, 259–287. doi: 10.1016/0377-0273(77)90003-8

Allard, P. (1997). Endogenous magma degassing and storage at Mount Etna. *Geophys. Res. Lett.* 24, 2219–2222. doi: 10.1029/97GL02101

Allard, P., Burton, M., and Murè, F. (2005). Spectroscopic evidence for a lava fountain driven by previously accumulated magmatic gas. *Nature* 433, 407–410. doi: 10.1038/nature03246

Aloisi, M., Bonaccorso, A., Cannavò, F., Gambino, S., Mattia, M., Puglisi, G., et al. (2009). A new dyke intrusion style for the Mount Etna May 2008 eruption modelled through continuous tilt and GPS data. *Terra Nova* 21, 316–321. doi: 10.1111/j.1365-3121.2009.00889.x

Alparone, S., Andronico, D., Lodato, L., and Sgroi, T. (2003). Relationship between tremor and volcanic activity during the Southeast Crater eruption on Mount Etna in early 2000. *J. Geophys. Res.* 108:2241. doi: 10.1029/2002JB001866

Alparone, S., Behncke, B., Giammanco, S., Neri, M., and Privitera, E. (2005). Paroxysmal summit activity at Mt. Etna (Italy) monitored through continuous soil radon measurements. *Geophys. Res. Lett.* 32:L16307. doi: 10.1029/2005GL023352

Andronico, D., Cristaldi, A., and Scollo, S. (2008). The 4–5 September 2007 lava fountain at South–East Crater of Mt. Etna, Italy. *J. Volcanol. Geotherm. Res.* 173, 325–328. doi: 10.1016/j.jvolgeores.2008.02.004

Bani, P., and Lardy, M. (2007). Sulphur dioxide emission rates from Yasur volcano, Vanuatu archipelago. *Geophys. Res. Lett.* 34:L20309. doi: 10.1029/2007GL030411

Battaglia, J., Aki, K., and Ferrazzini, V. (2005). Location of tremor sources and estimation of lava output using tremor source amplitude on the Piton de la Fournaise volcano: 2. Estimation of lava output. *J. Volcanol. Geotherm. Res.* 147, 291–308. doi: 10.1016/j.jvolgeores.2005.04.006

Beckett, F. M., Burton, M., Mader, H. M., Phillips, J. C., Polacci, M., Rust, A. C., et al. (2014). Conduit convection driving persistent degassing at basaltic volcanoes. *J. Volcanol. Geotherm. Res.* 283, 19–35. doi: 10.1016/j.jvolgeores.2014.06.006

Behncke, B., Fornaciai, A., Neri, M., Favalli, M., Ganci, G., and Mazzarini, F. (2016). Lidar surveys reveal eruptive volumes and rates at Etna, 2007–2010. *Geophys. Res. Lett.* 43, 4270–4278. doi: 10.1002/2016GL068495

Benoit, J. P., and McNutt, S. R. (1997). New constraints on source processes of volcanic tremor at Arenal Volcano, Costa Rica, using broadband seismic data. *Geophys. Res. Lett.* 24, 449–452. doi: 10.1029/97GL00179

Bercovici, D., Jellinek, A. M., Michaut, C., Roman, D. C., and Morse, R. (2013). Volcanic tremors and magma wagging: gas flux interactions and forcing mechanism. *Geophys. J. Int.* 195, 1001–1022. doi: 10.1093/gji/ggt277

Bonaccorso, A., Bonforte, A., Calvari, S., Del Negro, C., Di Grazia, G., Ganci, G., et al. (2011a). The initial phases of the 2008–2009 Mount Etna eruption: a multidisciplinary approach for hazard assessment. *J. Geophys. Res.* 116:B03203. doi: 10.1029/2010JB007906

Bonaccorso, A., Caltabiano, T., Currenti, G., Del Negro, C., Gambino, S., Ganci, G., et al. (2011b). Dynamics of a lava fountain revealed by geophysical, geochemical and thermal satellite measurements: the case of 10 April 2011 Mt. Etna eruption. *Geophys. Res. Lett.* 38:L24307. doi: 10.1029/2011GL049637

Brandsdóttir, B., and Einarsson, P. (1992). "Volcanic tremor and low frequency earthquakes in Iceland," in *Volcanic Seismology*, eds P. Gasparini, R. Scarpa, and K. Aki (Canberra: IAVCEI), 212–222.

Bruno, N., Caltabiano, T., Grasso, M. F., Porto, M., and Romano, R. (1995). "Studio dell 'emissione di anidride solforosa (SO2) all' Etna - 1993/1994," in *Progetto-Etna 1993-1995*, eds F. Ferrucci and F. Innocenti (Pisa: Giardini Editore), 29–33.

Bryan, C. J., and Sherburn, S. (2003). Eruption-induced modifications to volcanic seismicity at Ruapehu, New Zealand, and its implications for eruption forecasting. *Bull. Volcanol.* 65, 30–42. doi: 10.1007/s00445-002-0236-z

Burton, M., Allard, P., Murè, F., and Oppenheimer, C. (2003). "FTIR remote sensing of fractional magma degassing at Mount Etna, Sicily," in *Volcanic Degassing*, Vol. 213, eds C. Oppenheimer, D. M. Pyle, and J. Barclay (London: Geological Society Special Publication), 281–293. doi: 10.1144/GSL.SP.2003.213.01.17

Burton, M., Mader, H. M., and Polacci, M. (2007). The role of gas percolation in quiescent degassing o of persistently active basaltic volcanoes. *Earth Planet. Sci. Lett.* 264, 46–60. doi: 10.1016/j.epsl.2007.08.028

Burton, M. R., Caltabiano, T., Murè, F., Salerno, G., and Randazzo, D. (2009). SO2 flux from Stromboli during the 2007 eruption: results from the FLAME network and traverse measurements. *J. Volcanol. Geotherm. Res.* 182, 214–220. doi: 10.1016/j.jvolgeores.2008.11.025

Burton, M. R., Prata, F., and Platt, U. (2015a). Volcanological applications of SO2 cameras. *J. Volcanol. Geotherm. Res.* 300, 2–6. doi: 10.1016/j.jvolgeores.2014.09.008

Burton, M. R., Salerno, G. G., D'Auria, L., Caltabiano, T., Murè, F., and Maugeri, R. (2015b). SO2 flux monitoring at Stromboli with the new permanent INGV SO2 Camera system: a comparison with the FLAME network and seismological data. *J. Volcanol. Geotherm. Res.* 300, 95–102. doi: 10.1016/j.jvolgeores.2015.02.006

Caltabiano, T., Burton, M., Giammanco, S., Allard, P., Bruno, N., Murè, F., et al. (2004). "Volcanic gas emissions from the summit craters and flanks of Mt. Etna, 1987-2000," in *Mt. Etna: Volcano Laboratory*, Vol. 143, eds A. Bonaccorso, S. Calvari, M. Coltelli, C. Del Negro, and S. Falsaperla (Washington, DC: American Geophysical Union), 111–128. doi: 10.1029/143GM08

Calvari, S., Inguaggiato, S., Puglisi, G., Ripepe, M., and Rosi, M. (2008). *The Stromboli Volcano: An Integrated Study of the 2002-2003 Eruption. Geophysical Monograph Series* 182. Washington, DC: American Geophysical Union, doi: 10.1029/GM182

Calvari, S., Salerno, G. G., Spampinato, L., Gouhier, M., La Spina, A., Pecora, E., et al. (2011). An unloading foam model to constrain Etna's 11–13 January 2011 lava fountaining episode. *J. Geophys. Res.* 116:B11207. doi: 10.1029/2011JB008407

Campion, R., Delgado-Granados, H., and Mori, T. (2015). Image-based correction of the light dilution effect for SO2 camera measurements. *J. Volcanol. Geotherm. Res.* 300, 48–57. doi: 10.1016/j.jvolgeores.2015.01.004

Cannata, A., Catania, A., Alparone, S., and Gresta, S. (2008). Volcanic tremor at Mt. Etna: inferences on magma dynamics during effusive and explosive activity. *J. Volcanol. Geotherm. Res.* 178, 19–31. doi: 10.1016/j.jvolgeores.2007.11.027

Cannata, A., Di Grazia, G., Aliotta, M., Cassisi, C., Montalto, P., and Patanè, D. (2013). Monitoring Seismo-volcanic and infrasonic signals at volcanoes: Mt. Etna case study. *Pure Appl. Geophys.* 170, 1751–1771. doi: 10.1007/s00024-012-0634-x

Cannata, A., Di Grazia, G., Giuffrida, M., Gresta, S., Palano, M., Sciotto, M., et al. (2018). Space- time evolution of magma storage and transfer at Mt. Etna volcano (Italy): the 20152016 reawakening of Voragine crater. *Geochem. Geophys. Geosys.* 19, 471–495. doi: 10.1002/2017GC007296

Cannata, A., Giudice, G., Guerrieri, S., Montalto, P., Alparone, S., Di Grazia, G., et al. (2009a). Relationship between soil CO2 flux and volcanic tremor at Mt. Etna: implications for magma dynamics. *Environ. Earth Sci.* 61, 477–489. doi: 10.1007/s12665-009-0359-z

Cannata, A., Montalto, P., Privitera, E., Russo, G., and Gresta, S. (2009b). Tracking eruptive phenomena by infrasound: May 13, 2008 eruption at Mt. Etna. *Geophys. Res. Lett.* 36:L05304. doi: 10.1029/2008GL036738

Chouet, B. (1996). Long-Period volcano seismicity: its source and use in eruption forecasting. *Nature* 380, 309–316. doi: 10.1038/380309a0

Chouet, B., Koyanagi, R. Y., and Aki, K. (1987). "Origin of volcanic tremor in Hawaii, Part II: theory and discussion," in *Volcanism in Hawaii, U.S. Geological Survey Professional Paper*, Vol. 1350, eds R. W. Decker, T. L. Wright, and P. H. Stauffer (Washington, DC: US Government Publishing office), 1259–1280.

Collier, L., Neuberg, J., Lensky, N., and Lyakhovsky, V. (2006). Attenuation in gas-charged magma. *J. Volcanol. Geotherm. Res.* 153, 21–36. doi: 10.1016/j.jvolgeores.2005.08.009

Corsaro, R. A., Andronico, D., Behncke, B., Branca, S., Caltabiano, T., Ciancitto, F., et al. (2017). Monitoring the December 2015 summit eruptions of Mt. Etna (Italy): implications on eruptive dynamics. *J. Volcanol. Geotherm. Res.* 341, 53–69. doi: 10.1016/j.jvolgeores.2017.04.018

Corsaro, R. A., and Miraglia, L. (2009). Dynamics of magma in the plumbing system of Mt. Etna volcano, Sicily, Italy: a contribution from petrologic data of volcanic erupted from 2007 to 2009. *EOS Trans. AGU* 90:1690.

Currenti, G., Napoli, R., Di Stefano, A., Greco, F., and Del Negro, C. (2011). 3D integrated geophysical modeling for the 2008 magma intrusion at Etna: constraints on rheology and dike overpressure. *Phys. Earth Planet. Int.* 185, 44–52. doi: 10.1016/j.pepi.2011.01.002

Davis, J. C. (1986). *Statistics and Data analysis in Geology*, 2nd Edn. New York, NY: John Wiley & Sons.

Di Grazia, G., Cannata, A., Montalto, P., Patanè, D., Privitera, E., Zuccarello, L., et al. (2009). A multiparameter approach to volcano monitoring based on 4D analyses of seismo-volcanic and acoustic signals: the 2008 Mt. Etna eruption. *Geophys. Res. Lett.* 36:L18307. doi: 10.1029/2009GL039567

Di Grazia, G., Falsaperla, S., and Langer, H. (2006). Volcanic tremor location during the 2004 Mount Etna lava effusion. *Geophys. Res. Lett.* 33:L04304. doi: 10.1029/2005GL025177

Díaz-Moreno, A., Barberi, G., Cocina, O., Koulakov, I., Scarfì, L., Zuccarello, L., et al. (2018). New insights on Mt. Etna's crust and relationship with the regional tectonic framework from joint active and passive P-wave seismic tomography. *Surv. Geophys.* 39, 57–97. doi: 10.1007/s10712-017-9425-3

Doukas, M. P., and Gerlach, T. M. (1995). "Sulfur dioxide scrubbing during the 1992 eruptions of Crater Peak, Mount Spurr Volcano, Alaska," in *The 1992 Eruptions of Crater Peak Vent, Mount Spurr Volcano, Alaska*, Vol. 2139, ed. T. E. C. Keith (Reston, VA: U.S. Geological Survey), 47–57.

Edmonds, M., Herd, R. A., Galle, B., and Oppenheimer, C. M. (2003a). Automated, high time- resolution measurements of SO2 flux at Soufrière Hills Volcano, Montserrat. *Bull. Volcanol.* 65, 578–586. doi: 10.1007/s00445-003-0286-x

Edmonds, M., Oppenheimer, C., Pyle, D. M., Herd, R. A., and Thompson, G. (2003b). SO2 emissions from Soufrière Hills Volcano and their relationship to conduit permeability, hydrothermal interaction and degassing regime. *J. Volcanol. Geotherm. Res.* 124, 23–43. doi: 10.1016/S0377-0273(03)00041-6

Ereditato, D., and Luongo, G. (1994). Volcanic tremor wave field during quiescent and eruptive activity at Mt. Etna (Sicily). *J. Volcanol. Geotherm. Res.* 61, 239–251. doi: 10.1016/0377-0273(94)90006-X

Falsaperla, S., Alparone, S., D'Amico, S., Di Grazia, G., Ferrari, F., Langer, H., et al. (2005). Volcanic tremor at Mt. Etna, Italy, preceding and accompanying the eruption of July– August, 2001. *Pure Appl. Geophys.* 162, 1–22. doi: 10.1126/sciadv.1700219

Fischer, T. P., Morrissey, M. M., Calvache, M. L. V., Gòmez, D. M., Torres, R. C., Stix, J., et al. (1994). Correlations between SO2 flux and long-period seismicity at Galeras volcano. *Nature* 368, 135–137. doi: 10.1038/368135a0

Gordeev, E. (1993). Modeling of volcanic tremor as explosive point sources in a singled-layered, elastic half-space. *J. Geophys. Res.* 98, 19687–19703. doi: 10.1029/93JB00348

Gresta, S., Imposa, S., Patanè, D., and Patanè, G. (1987). Volcanic tremor at Mt. Etna: state-of- the-art and perspectives. *Pure Appl. Geophys.* 125, 1079–1095. doi: 10.1007/BF00879369

Gresta, S., Montalto, A., and Patanè, G. (1991). Volcanic tremor at Mount Etna (January 1984–March 1985): its relationship to the eruptive activity and modelling of the summit feeding system. *Bull. Volcanol.* 53, 309–320. doi: 10.1007/BF00414527

Heliker, C., Kauahikaua, J., Sherrod, D. R., Lisowski, M., and Cervelli, P. (2003). "The rise and fall of Pu'u 'Ô'ô cone, 1983–2002," in *The Pu'u 'Ô'ô -Kûpaianaha Eruption of Kîlauea Volcano, Hawai'i: The First 20 Years*, Vol. 1676, eds C. Heliker, D. A. Swanson, and T. J. Takahashi (Denver, CO: U.S. Geological Survey Professional Paper), 29–51.

Hibert, C., Mangeney, A., Polacci, M., Di Muro, A., Vergniolle, S., Ferrazzini, V., et al. (2015). Toward continuous quantification of lava extrusion rate: results from the multidisciplinary analysis of the 2 January 2010 eruption of Piton de la Fournaise volcano, La Réunion. *J. Geophys. Res. Solid Earth* 120, 3026–3047. doi: 10.1002/2014JB011769

James, M. R., Applegarth, L. J., and Pinkerton, H. (2011). Lava channel roofing, overflows, breaches and switching: insights from the 2008–2009 eruption of Mt. Etna. *Bull. Volcanol.* 74, 107–117. doi: 10.1007/s00445-011-0513-9

Jaupart, C., and Vergniolle, S. (1988). Laboratory models of Hawaiian and Strombolian eruptions. *Nature* 331, 58–60. doi: 10.1038/331058a0

Johnson, J. H., and Poland, M. P. (2013). Seismic detection of increased degassing before Kîlauea's 2008 summit explosion. *Nat. Commun.* 4:1668. doi: 10.1038/ncomms2703

Kazahaya, K., Shinohara, H., and Saito, G. (1994). Excessive degassing of Izu-Oshima volcano: magma convection in a conduit. *Bull. Volcanol.* 56, 207–216. doi: 10.1007/BF00279605

Kazahaya, K., Shinohara, H., Uto, K., Odai, M., Nalkahori, Y., Mori, H., et al. (2004). Gigantic SO2 emission from Miyakejima volcano, Japan, caused by caldera collapse. *Geology* 32, 425–428. doi: 10.1130/G20399.1

Konstantinou, K. I., and Schlindwein, V. (2002). Nature, wavefield properties and source mechanism of volcanic tremor: a review. *J. Volcanol. Geotherm. Res.* 119, 161–187. doi: 10.1016/S0377-0273(02)00311-6

Kubotera, A. (1974). "Volcanic tremors at Aso volcano," in *Physical Volcanology*, Vol. 6, eds L. Civetta, P. Gasparini, G. Luongo, and A. Rapolla (Amsterdam: Elsevier), 29–47. doi: 10.1016/B978-0-444-41141-9.50008-5

La Spina, A., Burton, M., Allard, P., Alparone, A., and Muré, F. (2015). Open-path FTIR spectroscopy of magma degassing processes during eight lava fountains on Mount Etna. *Earth Planet. Sci. Lett.* 413, 123–134. doi: 10.1016/j.epsl.2014.12.038

La Spina, G., Polacci, M., Burton, M., and de' Michieli Vitturi, M. (2017). Numerical investigation of permeability models for low viscosity magmas: application to the 2007 Stromboli effusive eruption. *Earth Planet. Sci. Lett.* 473, 279–290. doi: 10.1016/j.epsl.2017.06.013

Langer, H., Falsaperla, S., Messina, A., Spampinato, S., and Behncke, B. (2010). Detecting imminent eruptive activity at Mt. Etna, Italy, in 2007–2008 through pattern classification of volcanic tremor data. *J. Volcanol. Geotherm. Res.* 200, 1–17. doi: 10.1016/j.jvolgeores.2010.11.019

Leonardi, S., Gresta, S., and Mulargia, F. (2000a). Cross-correlation between tremor and SO2 flux data from Mount Etna volcano, 1987-1992. *Phys. Chem. Earth* 25, 737–740. doi: 10.1016/S1464-1895(00)00114-9

Leonardi, S., Gresta, S., and Mulargia, F. (2000b). Searching for a significant correlation between volcanic tremor amplitude and SO2 emissions at Mount Etna volcano, Sicily. *Geophys. J. Int.* 141, 832–834. doi: 10.1046/j.1365-246X.2000.00114.x

Lopez, T., Thomas, H. E., Prata, A. J., Amigo, A., Fee, D., and Moriano, D. (2015). Volcanic plume characteristics determined using an infrared imaging camera. *J. Volcanol. Geotherm. Res.* 300, 148–166. doi: 10.1016/j.jvolgeores.2014.12.009

Malinconico, L. L. (1979). Fluctuations in SO2 emission during recent eruptions of Etna. *Nature* 278, 43–45. doi: 10.1038/278043a0

Matoza, R. S., and Fee, D. (2014). Infrasonic component of volcano-seismic eruption tremor. *Geophys. Res. Lett.* 41, 1964–1970. doi: 10.1002/2014GL059301

McKillup, S., and Dyar, M. D. (2010). *Geostatistics Explained. An Introductory Guide for Earth Scientists*. Cambridge: Cambridge University Press, 396. doi: 10.1017/CBO9780511807558

McNutt, S. R. (1986). Observations and analysis of B-type earthquakes, explosions, and volcanic tremor at Pavlof Volcano, Alaska. *Bull. Seismol. Soc. Am.* 76, 153–175.

McNutt, S. R. (1992). "Volcanic tremor," in *Encyclopedia of Earth System Science*, Vol. 4, ed. W. A. Nierenberg (Cambridge, MA: Academic Press), 417–425.

McNutt, S. R. (2002). "Volcano seismology and monitoring for eruptions," in *International Geophysics, International Handbook of Earthquake & Engineering Seismology, Part B*, Vol. 81, eds W. Lee, H. Kanamori, P. Jennings, and C. Kisslinger (New York, NY: Elsevier), 383–406. doi: 10.1016/S0074-6142(02)80228-5

Metrich, N., Allard, P., Spilliaert, N., Andronico, D., and Burton, M. (2004). 2001 flank eruption of the alkali- and volatile-rich primitive basalt responsible for Mount Etna's evolution in the last three decades. *Earth Planet. Sci. Lett.* 228, 1–17. doi: 10.1016/j.epsl.2004.09.036

Miller, A. D., Stewart, R. C., White, R. A., Luckett, R., Baptie, B. J., Aspinall, W. P., et al. (1998). Seismicity associated with dome growth and collapse at the Soufriere Hills Volcano, Montserrat. *Geophys. Res. Lett.* 25, 3401–3404. doi: 10.1029/98GL01778

Miwa, S., Mori, M., and Hibiki, T. (2015). Two-phase flow induced vibration in piping systems. *Prog. Nucl. Energy* 78, 270–284. doi: 10.1016/j.pnucene.2014.10.003

Mori, T., and Burton, M. (2006). The SO2 camera: a simple, fast and cheap method for ground- based imaging of SO2 in volcanic plumes. *Geophys. Res. Lett.* 33:L24804. doi: 10.1029/2006GL027916

Mori, T., Mori, T., Kazahaya, K., Ohwada, M., Hirabayashi, J., and Yoshikawa, S. (2006). Effect of UV scattering on SO2 emission rate measurements. *Geophys. Res. Lett.* 33:L17315. doi: 10.1029/2006GL026285

Nadeau, P. A., Palma, J. L., and Waite, G. P. (2011). Linking volcanic tremor, degassing, and eruption dynamics via SO2 imaging. *Geophys. Res. Lett.* 38:L01304. doi: 10.1029/2010GL045820

Nadeau, P. A., Werner, C. A., Waite, G. P., Carn, S. A., Brewer, I. D., Elias, T., et al. (2015). Using SO2 camera imagery and seismicity to examine degassing and gas accumulation at Kîlauea Volcano, May 2010. *J. Volcanol. Geotherm. Res.* 300, 70–80. doi: 10.1016/j.jvolgeores.2014.12.005

Neuberg, J., and Pointer, T. (2000). Effects of volcano-topography on seismic broadband waveforms. *Geophys. J. Int.* 143, 239–248. doi: 10.1046/j.1365-246x.2000.00251.x

Omori, F. (1911). The Usu-san eruption and earthquake and elevation phenomena. *Bull. Imp. Earthq. Investig. Comm.* 5, 1–38.

Palma, J. L., Calder, E. S., Basualto, D., Blake, S., and Rothery, D. A. (2008). Correlations between SO2 flux, seismicity, and outgassing activity at the open vent of Villarrica volcano, Chile. *J. Geophys. Res.* 113:B10201. doi: 10.1029/2008JB005577

Parfitt, E. A. (2004). A discussion of the mechanisms of explosive basaltic eruptions. *J. Volcanol. Geotherm. Res.* 134, 77–107. doi: 10.1016/j.jvolgeores.2004.01.002

Patanè, D., Aiuppa, A., Aloisi, M., Behncke, B., Cannata, A., Coltelli, M., et al. (2013). Insights into magma and fluid transfer at Mount Etna by a multiparametric approach: a model of the events leading to the 2011 eruptive cycle. *J. Geophys. Res. Solid Earth* 118, 3519–3539. doi: 10.1002/jgrb.50248

Patanè, D., Barberi, G., Cocina, O., De Gori, P., and Chiarabba, C. (2006). Time-resolved seismic tomography detects magma intrusions at Mount Etna. *Science* 313, 821–823. doi: 10.1126/science.1127724

Patanè, D., Di Grazia, G., Cannata, A., Montalto, P., and Boschi, E. (2008). Shallow magma pathway geometry at Mt. Etna volcano. *Geochem. Geophys. Geosys.* 9:Q12021.

Platt, A., and Stutz, U. (2008). *Differential Optical Absorption Spectroscopy - Principles and Applications*. Heidelberg: Springer, doi: 10.1007/978-3-540-75776-4

Poland, M. P., Miklius, A., Sutton, J. A., and Thornber, C. R. (2012). A mantle-driven surge in magma supply to Kîlauea volcano during 2003–2007. *Nat. Geosci.* 5, 295–300. doi: 10.1038/NGEO1426

Salerno, G. G., Burton, M. R., Oppenheimer, C., Caltabiano, T., Randazzo, D., Bruno, N., et al. (2009a). Three-years of SO2 flux measurements of Mt. Etna using an automated UV scanner array: comparison with conventional traverses and uncertainties in flux retrieval. *J. Volcanol. Geotherm. Res.* 183, 76–83. doi: 10.1016/j.jvolgeores.2009.02.013

Salerno, G. G., Burton, M. R., Oppenheimer, C., Caltabiano, T., Tsanev, V., and Bruno, N. (2009b). Novel retrieval of volcanic SO2 abundance from ultraviolet spectra. *J. Volcanol. Geotherm. Res.* 181, 141–153. doi: 10.1016/j.jvolgeores.2009.01.009

Schick, R., and Mugiono, R. (1991). *Volcanic Tremor and Magma Flow*. Jülich: Forschungszentrum Jülich GmbH, 200.

Shinohara, H. (2005). New technique to estimate volcanic gas composition: plume measurements with a portable multi-sensor system. *J. Volcanol. Geotherm. Res.* 143, 319–333. doi: 10.1016/j.jvolgeores.2004.12.004

Shinohara, H. (2008). Excess degassing from volcanoes and its role on eruptive and intrusive activity. *Rev. Geophys.* 46:RG4005. doi: 10.1029/2007RG000244

Spilliaert, N., Allard, P., Mètrich, N., and Sobolev, A. V. (2006). Melt inclusion record of the conditions of ascent, degassing, and extrusion of volatile-rich alkali basalt during the powerful 2002 flank eruption of Mount Etna (Italy). *J. Geophys. Res.* 111:B04203. doi: 10.1029/2005JB003934

Steffke, A. M., Harris, A. J. L., Burton, M., Caltabiano, T., and Salerno, G. G. (2011). Coupled use of COSPEC and satellite measurements to define the volumetric balance during effusive eruptions at Mt. Etna, Italy. *J. Volcanol. Geotherm. Res.* 205, 47–53. doi: 10.1016/j.jvolgeores.2010.06.004

Steinberg, G. S., and Steinberg, A. S. (1975). On possible causes of volcanic tremor. *J. Geophys. Res.* 80, 1600–1604. doi: 10.1029/JB080i011p01600

Sutton, A. J., Elias, T., Gerlach, T. M., and Stokes, J. B. (2001). Implications for eruptive processes as indicated by sulfur dioxide emission from Kîlauea Volcano, Hawai'i, 1979-1997. *J. Volcanol. Geotherm. Res.* 108, 283–302. doi: 10.1016/S0377-0273(00)00291-2

Swan, A. R. H., and Sandilands, M. (1995). *Introduction to Geological Data analysis*. Hoboken, NJ: Blackwell Science.

Taquet, N., Meza Hernández, I., Stremme, W., Bezanilla, A., Grutter, M., Campion, R., et al. (2017). Continuous measurements of SiF4 and SO2 by thermal emission spectroscopy: insight from a 6-month survey at the Popocatépetl volcano. *J. Volcanol. Geotherm. Res.* 341, 255–268. doi: 10.1016/j.jvolgeores.2017.05.009

Thompson, G., McNutt, S. R., and Tytgat, G. (2002). Three distinct regimes of volcanic tremor associated with the eruption of Shishaldin Volcano, Alaska 1999. *Bull. Volcanol.* 64, 535–547. doi: 10.1007/s00445-002-0228-z

Vargas-Bracamontes, D. M., Nava, A. F., and Reyes-Dávila, G. A. (2009). Time-scale wavelet patterns related to the 1998–1999 eruptions of the Colima volcano, and their possible implications for eruption forecasting. *J. Volcanol. Geotherm. Res.* 184, 271–284. doi: 10.1016/j.jvolgeores.2009.01.025

Voight, B., Sparks, R. S. J., Miller, A. D., Stewart, R. C., Hoblitt, R. P., Clarke, A., et al. (1999). Magma flow instability and cyclic activity at Soufriere Hills volcano, Montserrat, British West Indies. *Science* 283, 1138–1142. doi: 10.1126/science.283.5405.1138

Wallace, P. J., and Edmonds, M. (2011). "The sulfur budget in magmas: evidence from melt inclusions, submarine glasses, and volcanic gas emissions," in *Reviews in Mineralogy and Geochemistry*, Vol. 73, eds H. Behrens and J. D. Webster (Chantilly, VA: Mineralogical Society of America), 215–246.

Wallace, P. J., and Gerlach, T. M. (1994). Magmatic vapor source for sulfur dioxide released during volcanic eruptions: evidence from Mount Pinatubo. *Science* 265, 497–499. doi: 10.1126/science.265.5171.497

Watson, I. M., Oppenheimer, C., Voight, B., Francis, P. W., Clarke, A., Stix, J., et al. (2000). The relationship between degassing and ground deformation at Soufriere Hills Volcano, Montserrat. *J. Volcanol. Geotherm. Res.* 98, 117–126. doi: 10.1016/S0377-0273(99)00187-0

Williams-Jones, G., Stix, J., Heiligmann, M., Barquero, J., Fernandez, E., and Gonzalez, E. D. (2001). A model of degassing and seismicity at Arenal volcano, Costa Rica. *J. Volcanol. Geotherm. Res.* 108, 121–139. doi: 10.1016/S0377-0273(00)00281-X

Williams-Jones, G., Stix, J., and Hickson, C. (2008). *The COSPEC Cookbook: Making SO2 Measurements at Active Volcanoes*. Rome: IAVCEI, 1. doi: 10.13140/RG.2.2.13728.99845

Woods, A. W., and Cardoso, S. S. S. (1997). Triggering basaltic volcanic eruptions by bubble-melt separation. *Nature* 385, 518–520. doi: 10.1038/385518a0

Young, S. R., Francis, P. W., Barclay, J., Casadevall, T. J., Gardner, C. A., Darroux, B., et al. (1998). Monitoring SO2 emissions at the Soufriere Hills Volcano: implications for changes in eruptive conditions. *Geophys. Res. Lett.* 25, 3681–3684. doi: 10.1029/98GL01406

Young, S. R., Voight, B., and Duffell, H. J. (2003). Magma extrusion dynamics revealed by high- frequency gas monitoring at Soufrière Hills volcano, Montserrat. *Geol. Soc. Spec. Publ.* 213, 219–230. doi: 10.1144/GSL.SP.2003.213.01.13

Zar, J. H. (1972). Significance testing of the spearman rank correlation coefficient. *J. Am. Stat. Assoc.* 67, 578–580. doi: 10.1080/01621459.1972.10481251

Zobin, V. M. (2003). *Introduction to Volcanic Seismology (Developments in Volcanology; 6)*. Amsterdam: Elsevier Science.

Zuccarello, L., Burton, M. R., Saccorotti, G., Bean, C. J., and Patanè, D. (2013). The coupling between very long period seismic events, volcanic tremor, and degassing rates at Mount Etna volcano. *J. Geophys. Res. Solid Earth* 118, 4910–4921. doi: 10.1002/jgrb.50363

Conflict of Interest Statement: The authors declare that the research was conducted in the absence of any commercial or financial relationships that could be construed as a potential conflict of interest.

frontiers
in Earth Science

ORIGINAL RESEARCH
published: 20 November 2018
doi: 10.3389/feart.2018.00208

Automatic Filtering of Soil CO_2 Flux Data; Different Statistical Approaches Applied to Long Time Series

Sérgio Oliveira[1], **Fátima Viveiros**[1]*, **Catarina Silva**[1,2] **and Joana E. Pacheco**[1,2]

[1] *Instituto de Investigação em Vulcanologia e Avaliação de Riscos (IVAR), Universidade dos Açores, Ponta Delgada, Portugal,*
[2] *Centro de Informação e Vigilância Sismovulcânica dos Açores, Ponta Delgada, Portugal*

OPEN ACCESS

Edited by:
Valerio Acocella,
Università degli Studi Roma Tre, Italy

Reviewed by:
Agnes Mazot,
GNS Science, New Zealand
Micol Todesco,
Istituto Nazionale di Geofisica e Vulcanologia, Italy

***Correspondence:**
Fátima Viveiros
maria.fb.viveiros@azores.gov.pt

Specialty section:
This article was submitted to Volcanology,
a section of the journal
Frontiers in Earth Science

Received: *30 July 2018*
Accepted: *31 October 2018*
Published: *20 November 2018*

Citation:
Oliveira S, Viveiros F, Silva C and Pacheco JE (2018) Automatic Filtering of Soil CO_2 Flux Data; Different Statistical Approaches Applied to Long Time Series.
Front. Earth Sci. 6:208.
doi: 10.3389/feart.2018.00208

Monitoring soil CO_2 diffuse degassing areas has become more relevant in the last decades to understand seismic and/or volcanic activity. These studies are specially valuable for volcanic areas without visible manifestations of volcanism, such as fumaroles or thermal springs. The development and installation of permanent soil CO_2 flux instruments has allowed to acquire long time series in different volcanic environments, and the results obtained highlight the influence of environmental variables on the gas flux variations. Filtering the influence of these external variables on the gas flux is crucial to understand deep processes on the volcanic system. This study focuses on the discussion of different statistical approaches applied to the long time series recorded in a diffuse degassing area of the Azores archipelago, mainly on the application of stepwise multivariate regression analysis, wavelets and Fast Fourier transforms to understand the CO_2 flux variations and to detect eventual anomalous periods that can represent deep changes in the volcano feeding reservoirs. A permanent soil CO_2 flux station is installed at Caldeiras da Ribeira Grande area since June 2010. This degassing site is located at Fogo Volcano, a polygenetic volcano at S. Miguel Island. The station performs measurements based on the accumulation chamber method and has coupled several environmental sensors. Average soil CO_2 flux and soil temperature values around 1,165 $gm^{-2}\ d^{-1}$ and 33°C, respectively, were measured in this site between June 2010 and June 2017. Multivariate regression analysis shows that about 47% of the soil CO_2 flux variations are explained by the effect of the soil and air temperature, wind speed, and soil water content. Spectral analysis highlights the existence of 24 h cycles in the soil CO_2 flux time series, mainly during the summer period. The filtered time series showed some anomalous periods and a correlation with the geophysical data recorded on the area was carried out. The models proposed have been applied on a near real-time automatic monitoring system and implementation of these approaches will be profitable in any volcano observatory of the world since it allows a fast understanding of the degassing processes and contribute to recognize unrest periods.

Keywords: soil CO_2 flux time series, stepwise multivariate regression analysis, Fast Fourier Transform, wavelets, seismo-volcanic monitoring

INTRODUCTION

Volcanic gas emissions may occur as visible manifestations, such as fumaroles, gas vents, and bubbling springs, or as invisible emissions through diffuse degassing (Fischer and Chiodini, 2015 and references therein). The degassing phenomena characterize the volcanic systems both during eruptive and quiescent periods of activity. Studies of these permanent and silent gas emissions started to be performed in the early nineties in Italian volcanoes (Baubron et al., 1990; Allard et al., 1991). The permanent soil CO_2 flux networks that have been set up in various volcanic areas of the world since then (Mori et al., 2002; Salazar et al., 2002; Granieri et al., 2003, 2010; Gurrieri et al., 2008; Padrón et al., 2008; Viveiros et al., 2008, 2015a; Hernández et al., 2012; Liuzzo et al., 2013; Laiolo et al., 2016) already contributed to identify geochemical signs that represent changes on the volcanic activity, namely by recognizing volcanic unrest episodes (Granieri et al., 2003, 2010; Salazar et al., 2004; Pérez et al., 2006) or as precursors of eruptive periods (Brusca et al., 2004; Carapezza et al., 2004; Aiuppa et al., 2010; Pérez et al., 2012; Liuzzo et al., 2013; Inguaggiato et al., 2017). Some gas flux anomalies were also associated with seismic activity (Salazar et al., 2002) and the stations installed have also been used as proxy for indoor environments and showed to be useful for risk assessment in diffuse degassing areas (Viveiros et al., 2009, 2015b).

Despite all the useful information obtained with these stations for the seismo-volcanic monitoring, the recorded soil CO_2 flux values have showed that gas fluxes are highly influenced by environmental factors, such as meteorological changes, which can be responsible for more than 50% of the gas flux variations (Granieri et al., 2003, 2010; Viveiros et al., 2009, 2015a). Different statistical methodologies have been applied to filter the recorded CO_2 time series in order to remove the external influences and produce a gas flux sign that may represent deep changes (e.g., Granieri et al., 2003; Viveiros et al., 2008, 2015a; Cannata et al., 2010; Liuzzo et al., 2013; Lelli and Raco, 2017). Several studies have also highlighted the existence of cyclic variations on the CO_2 flux time series with both daily and seasonal oscillations (Granieri et al., 2003; Padrón et al., 2008; Hernández et al., 2012; Rinaldi et al., 2012; Viveiros et al., 2014), even if only few of them attempt to model and explain the variations observed (Rinaldi et al., 2012; Viveiros et al., 2014). Even if most of the studies highlight the impact that meteorological changes may have on the soil gas fluxes, the use of raw data as routine in the volcano observatories is still common and may result in biased interpretations. The current study uses data from a permanent soil CO_2 flux station installed in 2010 in a geothermal area in the north flank of the active Fogo central volcano (São Miguel Island). This study will apply for the first time different statistical approaches to the data recorded by GFOG4 station, and will constitute an opportunity to discuss the results, highlight positive aspects and limitations, and to select an adequate methodology to filter the raw data. Despite the fact that several filtering techniques have been already applied to soil CO_2 flux time series, the present study focuses on an automatic filtering that may be used as routine in the volcano observatories to identify anomalous gas values and contribute to recognize unrest episodes.

CHARACTERIZATION OF THE STUDY AREA

Fogo is a polygenetic volcano located in the central part of São Miguel Island (Azores archipelago, Portugal) and has a summit caldera with maximum diameter of about 3.2 km (Wallenstein et al., 2015 and references therein). The volcanic edifice started to form more than 200 ka ago (Muecke et al., 1974) and the last intracaldera magmatic eruption occurred after the settlement of the island, in 1563, and was of sub-Plinian type. This explosive event was followed four days later by a basaltic eruption in the north flank of the volcano (Wallenstein et al., 2015). The main tectonic structures that cross this volcanic system show a dominant NW-SE trend, the same as the Ribeira Grande *graben* that dominates the north flank of the volcano (Carmo et al., 2015). Since 2003 several seismic swarms have affected the central area of São Miguel, namely Fogo and Congro volcanic systems (Silva et al., 2012). During the period under analysis in the current study a total of 4,479 seismic events were recorded by the CIVISA seismic network for the Fogo Volcano seismogenic area (Silva, 2011 and references therein). Maximum local magnitude (M_L) was 2.9 from an earthquake recorded on 29th April 2012 (CIVISA catalog: http://www.ivar.azores.gov.pt/civisa/Paginas/homeCIVISA.aspx).

Nowadays the volcanic activity in the area is characterized not only by seismic swarms (Silva et al., 2012), but also by episodes of ground deformation (Okada et al., 2015) and the presence of secondary manifestations of volcanism, such as three main hydrothermal fumarolic fields (Caldeira Velha, Caldeiras da Ribeira Grande and Pico Vermelho), thermal and cold CO_2-rich springs, as well as, several diffuse degassing areas (Ferreira et al., 2005; Caliro et al., 2015; Viveiros et al., 2015b). These manifestations are essentially found out in the north flank of the volcano, and seem to be tectonically controlled by the *graben* faults. Submarine gas emissions are also found out in the volcano area and are dominated by high CO_2 emissions.

A permanent soil CO_2 flux network started to be implemented in this volcanic system in February 2002 with the installation of the so-called GFOG1 station in the Pico Vermelho geothermal power plant area (Viveiros et al., 2008). The network expanded in May 2005 when a second soil CO_2 flux station was installed inside the Fogo caldera in an area with low CO_2 emissions, and the main goal was to evaluate changes that could be correlated with the unrest episode that was affecting Fogo-Congro volcanic systems (Viveiros et al., 2015a). During 2010 a new degassing anomaly developed in the area surrounding Caldeiras da Ribeira Grande fumarolic field, caused by the drilling of a geothermal well. A multidisciplinary monitoring programme was set up in the area aiming not only to evaluate the expansion of the anomaly zone but also to identify possible signs that could represent deep processes and changes on the gas pressure that could end up in hazardous situations. A permanent soil CO_2 flux station, named GFOG4, was installed in the area in June 2010 as part of the monitoring programme.

METHODOLOGY

Sampling and Data Acquisition

GFOG4 is a permanent automatic station that measures soil CO_2 flux and is part of the IVAR/CIVISA seismic-volcanic monitoring network. The station performs measurements based on the "time 0, depth 0" accumulation chamber method (Chiodini et al., 1998). The soil CO_2 flux measurement is made once every hour by lowering the chamber into the ground and by pumping the gases into an infrared gas analyzer (Dräeger detector, maximum scale 30 vol.%). The soil CO_2 flux is computed as the linear best fit of the flux curve over a predefined period of time. This method allows the measurement of the flux independently from the transport regime and the soil properties (Chiodini et al., 1998).

The station also has meteorological and soil sensors, which simultaneously acquire data related to atmospheric pressure, air, and soil temperatures, relative air humidity, wind speed and direction, rainfall, and soil water content. Thermo hygrometers and wind sensors are set about 1 m above the ground, whereas soil water content and soil temperature sensors give measurements at a depth of about 30 cm (Viveiros et al., 2015b). For additional details about the methodology and the characteristics of the equipment see Viveiros et al. (2015b).

The 2 years of data acquisition, between January 2013 and December 2014, was the period selected to apply the statistical methodologies and to understand the CO_2 flux variations for this monitoring site. This selected period was taken from the middle of the whole recorded period (June 2010–June 2017). The periods between June 2010 and December 2012, as well as, between January 2015 and June 2017 were used to check the adequacy of the models proposed.

Statistical Data Treatment

Stepwise Multiple Linear Regression

Previous studies (Granieri et al., 2003, 2010; Viveiros et al., 2008) applied multiple linear regression analysis (Draper and Smith, 1981) to the data in order to build a model that can explain the CO_2 flux variations. This regression is normally used when there is the need to explain the relationship between one dependent variable and two or more independent variables. In this case, the dependent variable is the CO_2 flux and the independent variables are chosen from the environmental factors measured by the station. The model follows Equation(1),

$$y = \beta_0 + \beta_1 x_1 + \beta_2 x_2 + \ldots + \beta_n x_n \tag{1}$$

Where β_0 is the intercept, β_n are the coefficients or the slope of the independent variables, x_n the measured environmental factors and y is the predicted CO_2 flux.

When building the model Neter et al. (1983) advice to choose independent variables in order that the regression model is as complete and realistic as possible, so the adequate prediction is reached. However, a balance is needed and the regression model must include only the relevant variables because the irrelevant ones decrease the precision of the predicted values, and increase the complexity of the model.

To determine, within a multiple regression model, if a particular factor (x_i) is making a contribution to the model, it is tested the hypothesis that the value of that coefficient is zero: H_0: $\beta_i = 0$; H_A: $\beta_i \neq 0$.

The null hypothesis says that a change in the value of x_i would neither linear increase or decrease y, meaning, y and x_i are not linearly related. To test these hypotheses the p-values for all coefficients in the model are determined and are based on a t-statistic, where the t score *(t^*)* is calculated (Neter et al., 1983) as:

$$t^* = (\textit{sample coefficient} - \textit{hypothesized value}) / \textit{standard error of coefficient}$$

If the p-value for a coefficient is higher than 0.05 the variable for that coefficient can be omitted, for a 95% confidence interval. The application of this parametric methodology requires that populations follow the normal distribution (Draper and Smith, 1981).

Because multiple linear regression involves multiple variables, omitting a variable can be challenging, Pardoe et al. (2018) warn us that this test only suggests that one variable is not needed in a model with all the other variables included. For example, if we have more than one variable with a p-value higher than 0.05, by omitting one of those variables, a new model without that variable must be considered because the other variables can now have significance.

An alternative method to identify a good subset of variables to include in the model, with considerably less computing than what is required for all possible regressions, is the Stepwise Multivariate Regression method. Rawlings et al. (1998) explain that these subset models are identified sequentially by adding or deleting the variable that has the greatest impact on the residual sum of squares. These stepwise methods are not guaranteed to find the "best" subset for each subset size, and the results produced by different methods may not agree with each other. This method consists of a forward stepwise selection, which chooses variables by adding one variable at a time to the previously chosen subset model. It starts by choosing the independent variable that accounts for the largest amount of variation in the dependent variable. At each successive step, it adds the variable that causes the largest decrease in the residual sum of squares. Forward selection continues until all variables are in the model. A backward elimination of variables, which starts with a full model and then eliminates, at each step, the variable whose deletion will cause the residual sum of squares to increase the least. Backward elimination continues until the subset model contains only one variable.

Neither forward selection nor backward elimination takes into account the effect that the addition or deletion of a variable can have on the contributions of the other variables to the model. A variable early added to the model can lose importance after other variables are added, or variables previously eliminated can become important after other variables are removed from the model. So, Stepwise Regression is a forward selection process that rechecks at each step the importance of all previously included variables and, if there is a variable that does not meet the minimum criterion, it changes the procedure to backward elimination and variables are dropped one at a time until all remaining variables meet the minimum criterion. Then, forward selection resumes. This process continues until the adding or the removing of variables does not meet the minimum criterion. Normally this criterion comes in form of a *F*-Test (Rawlings et al., 1998).

All the variables that increase more than 1% the explanatory power of the model are inserted in the model. Additional details about the methodological approach and criteria used to select the variables that fit in the model are found out in Viveiros et al. (2015a). Predicted and residuals values are calculated based on the proposed model. The Stepwise Multivariate Regression Analysis was applied using the MATLAB® software, version 2017b.

SPECTRAL ANALYSIS

Discrete Fast Fourier Transform

Previous soil CO_2 flux studies used the Fourier Transform as the method to identify potential periodicities on the analyzed datasets (Padrón et al., 2008; Hernández et al., 2012; Rinaldi et al., 2012; Viveiros et al., 2014). The Fourier Transform is a method to transform a time domain function into frequency domain. It decomposes any periodic function in a sum of cosines and sines of different frequencies making it a good tool to identify harmonic oscillations. It is a complex-valued function, whose absolute value represents the intensity of a frequency present in the function.

Because the data in this work is a finite time series of samples, i.e., discrete values, the Discrete Fourier Transform (DFT) is used. It will transform a finite sequence of equally spaced samples of a time domain function into a sequence of complex numbers on frequency domain. With *N* samples of input, we will have *N* independent values of output. Each output value corresponds to the intensity of a frequency.

To chose the adequate sampling rate, Press et al. (1992) explain that there is a special frequency, the Nyquist critical frequency, given by $f = 1/2\Delta$, where Δ is the sampling interval. This frequency corresponds to the value of *N/2* and it means that every frequency higher than *f* will be somewhat falsely translated into the frequencies lower than *f*. To overcome this problem, the sample rate must be, at least, the double of the maximum frequency to be measured, so that two points per cycle of that frequency are present. Also, the output of a DFT will repeat itself after *N/2*.

By definition the DFT (*H*) is given by Equation (2) and its inverse by Equation (3):

$$H_k = \sum_{n=0}^{N-1} h_n e^{-i2\pi kn/N}, k = 1, 2, 3, \ldots, N-1 \quad (2)$$

$$h_n = \frac{1}{N} \sum_{k=0}^{N-1} H_k e^{-i2\pi kn/N}, n = 1, 2, 3, \ldots, N-1 \quad (3)$$

where *N* is the number of samples, h_n a discrete time series and $e^{-i2\pi kn/N}$ is the Euler's formula, which states that $e^{i2\pi kn/N} = cos(2\pi kn/N) + i\ sin(2\pi kn/N)$.

Unfortunately DFT is a computational intensive algorithm and a powerful computer is not always available. So, a more efficient algorithm, the Fast Fourier Transform (FFT), will be used to simplify the calculation of the Discrete Fourier Transform and its inverse. The calculation of the DFT by definition and for a data sequence with *N* points has an order of N^2 arithmetic operations, but with the help of a FFT algorithm, it computes the same result having an order of *N.log(N)* operations as shown in Cooley and Tukey (1965). The difference in calculation time may be substantial, especially for a large set of data.

There are many different algorithms that can be called FFT, but the most widely used is the Radix-2 Decimation in Time algorithm by Cooley and Tukey (1965). This algorithm divides a *N* size transform into two *N/2* dimension intervals in each calculation step. It first calculates the transform of the even index elements and then the odd index elements, and then combines the two results to produce the Fourier transform of the sequence. This idea can be made recursively to reduce calculation time. This simplification assumes that *N* is a power of two (2^n), but since it is usually possible to choose the number of points to use or to pad the end of the time series with zeros, this restriction is not a major problem.

To decompose the local time-frequency of a waveform, a Windowed Fourier Transform is used. Because the transform is performed on a segment of constant time through a time series at a constant step, the transform will have a constant time frequency resolution and discontinuities will exist between the function at the start and finish of the window. Those discontinuities will cause the transform to develop non-zero values at frequencies that do not exist. This is commonly called spectral leakage (Mallat, 2009). In order to reduce this problem the waveform is multiplied by a windowing function that decreases smoothly from one at its center to zero at its ends. Also to change the resolution, the window size needs to be changed. The choice of a particular window size depends on the desired resolution trade-off between time and frequency (Mallat, 2009). There are many different choices of windowing functions and the one used in the present study was the Hanning, which was already applied previously by Viveiros et al. (2014) to similar datasets.

Wavelet Transform

Some studies performed on SO_2 and CO_2 flux time series recorded from different volcanoes plumes used wavelet analyses to identify potential cyclic variations (Boichu et al., 2010; Pering et al., 2014). Similarly to the Fourier analysis, wavelet analysis is also a method to decompose a time series into time-frequency, but instead of using a sum of cosines and sines, it uses special made functions to have specific properties, such as better frequency localization or better transient localization that make them useful for signal processing (Mallat, 2009).

Mallat (2009) highlights that wavelets request less coefficients to represent local transient structures, which leads to a fast computational algorithm comparing to the FFT. In addition, wavelets are less affected by the lack of data, which allows an easier analysis of long time series. Another drawback of FFT analysis is that the time information may be lost in the transform since, depending on the window's size, it may be difficult to tell when an event took place. Wavelet analysis is thus becoming a common tool for analyzing localized variations within a time series (Torrence and Compo, 1998). Wavelet transform also has continuous and discrete transforms, but, to analyze how the frequency content of a signal changes over time the continuous transform is the most used. Farge (1992) states that the continuous wavelet transform is better suited because its redundancy allows good legibility of the signal's information content.

The formulation of the continuous wavelet transform (CWT) (*Wx*) was developed by Grossmann and Morlet (1984) and for a function *x(t)* is expressed by Equation (4):

$$Wx(u,s) = \int_{-\infty}^{+\infty} x(t) \frac{1}{\sqrt{s}} \psi^{*} \left(\frac{t-u}{s}\right) dt \qquad (4)$$

where, s corresponds to the wavelet scale, u to the shift parameter and t is the time component.

Because this work uses discrete time series, Equation (5), defined by Torrence and Compo (1998), consists of the continuous wavelet transform of a discrete sequence x_n as the convolution of x_n with a scaled and translated version of a wavelet function ψ_0 *(η)*:

$$W_n(s) = \sum\nolimits_{n'=0}^{N-1} x_{n'} \psi^{*} \left[\frac{\left(n' - n\right)\delta t}{s}\right] \qquad (5)$$

where the (ψ^*) indicates the complex conjugate of the wavelet. By varying the wavelet scale s and translating along the localized time index n for a time step δt, it is possible to construct a graphic similar to a spectrogram, called scalogram, showing the amplitude power vs. the scale and how this amplitude varies with time. These calculations can be very computational intensive but they are considerably fast to do if they are done in the Fourier space (for additional details, see Torrence and Compo, 1998).

One of the criticism about using wavelet analyses is related with the randomness associated with the selection of the wavelet function, ψ. Choosing the wavelet function depends on the final objectives of the data analysis. In this work, the goal is to perform a time-frequency analysis. MATLAB® was used to perform the wavelet analysis and the wavelet function supported by MATLAB® that was used, was the bump wavelet because it provides good frequency localization. The Fourier transform of the bump wavelet with parameters σ and μ, is defined in Meignen et al. (2012) and is expressed by Equation (6):

$$\hat{\Psi}(\xi) = e^{1-\frac{1}{1-\left(\frac{\xi-\mu}{\sigma}\right)^{2}}} \chi_{[\mu-\sigma,\mu+\sigma]} \qquad (6)$$

Where ξ is a real value and χ is the indicator function for the interval $[\mu - \sigma, \mu + \sigma]$. In this last case, χ is 1 if inside the interval and 0 if lays outside. By default, the values of the parameters used by MATLAB are $\mu = 5$ and $\sigma = 0.6$. Another option could have been the Morlet wavelet, also available on the MATLAB's wavelet analysis toolbox, which exhibits poorer frequency localization than the bump wavelet, but superior time localization, making it a better choice for transient localization.

By using FFT, one can obtain the spectrum of the data; however, with wavelets, Shu and Qinyu (2005) demonstrated that the global wavelet spectrum on some occasions did not provide the correct results, especially when there are sharp peaks in the power spectrum. This happens because the global wavelet spectrum at small wavelets (high frequencies) will smooth the spectrum and at large wavelet scales (low frequencies) the peaks are sharper and have a higher amplitude. Shu and Qinyu (2005) state that because there is the need to know whether there are sharp peaks in the time series prior to this spectral analysis, the Fourier spectrum might be a better choice for this type of analysis.

Residuals Filtering

When cycles are identified in the time series, to remove unwanted cycles from the datasets (high frequencies) and reveal the constants components (low frequencies), a low pass filter may be used (Sedra and Smith, 2004). FFT was already applied in previous studies (Viveiros et al., 2014) and can be used for filtering since the signal may be converted between the time and the frequency domain. In order to apply a filter, one has to transform the signal into the frequency domain, apply the filter by zeroing the unwanted part of the spectrum, and transform it back into the time domain. But FFT filtering would imply high computational tasks and a high number of samples to be considered for filtering, increasing latency, and if the continuity of the waveform is no longer guaranteed artifacts will appear. For this reason, for time series with identified cyclic behavior, the application of other type of filtering, such as continuous-time filters, is suggested. Within this type of filters, one can choose from different families of filters, such as Chebyshev filter, which has the best approximation to the ideal response but with the cost of adding ripples, or the Butterworth filter that has a more flat frequency response. For this reason, this last type of filter is preferable to a Chebyshev filter (Jurišić et al., 2002).

RESULTS

The data analyzed in this work were collected from June 2010 to June 2017 (**Figure 1**). During this period the CO_2 flux varied between 0.37 and 6,606 g $m^{-2}d^{-1}$, with a mean of 1,165 gm^{-2} d^{-1} (**Table 1**). The permanent station is also installed in a thermal anomalous zone with soil temperature varying around 32.2°C and maximum recorded values for the whole period was 47.2°C (**Table 1**). Several spike-like variations are observed on the soil CO_2 flux time series and seasonal cycles with higher CO_2 emissions recorded during winter period are also observed. Higher scatter on the recorded data is also observed on the winter period when compared to the summer (**Figure 1**).

Building a Model

As mentioned above, the period selected for the construction of the explanatory model corresponded to 2 years of data, from January 2013 to December 2014. **Figure 2** shows the soil CO_2 flux and the various environmental time series recorded by the permanent station. Detailed analyses of the figure shows that some variables seem to correlate inversely with the soil CO_2 flux, namely the air (**Figure 2a**) and soil temperature (**Figure 2c**). On

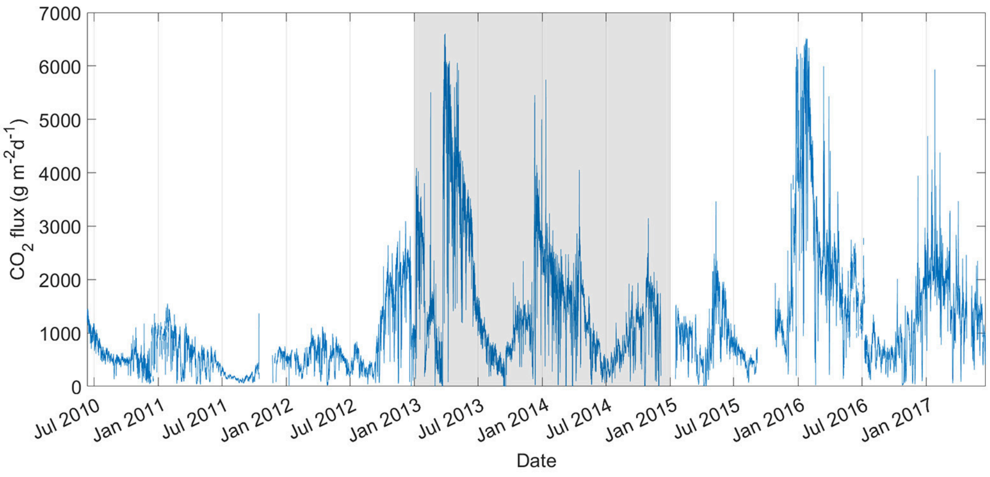

FIGURE 1 | Soil CO_2 flux data acquired in GFOG4 during the period June 2010–June 2017. The gray area represents the period used to produce the explanatory regression model.

TABLE 1 | Descriptive statistics of the data acquired in GFOG4.

	Average	SD	Median	Minimum	Maximum	Number of data
Soil CO_2 flux (g m^{-2} d^{-1})	1,165	1,034	819	0.37	6,606	55,726
Soil temperature (°C)	32.2	9.7	32.8	17.8	47.2	55,324
Soil water content (%)	25.6	3.2	25.8	14.0	48.1	57,786
Atmospheric pressure (hPa)	990	7	991	931	1010	57,874
Rainfall (mm)	0.2	1.0	0.0	0.0	64.2	57,678
Air relative humidity (%)	83.0	8.4	84.7	36.7	97.2	57,576
Air temperature (°C)	16.8	4.1	16.4	6.1	32.6	57,829
Wind speed (m/s)	1.02	0.89	0.75	0.0	10.81	57,829

the other hand, soil water content (**Figure 2b**) shows in general similar variations as the soil CO_2 fluxes. Pearson correlation coefficients confirm these observations (**Figure 3**), with soil temperature showing the highest inverse correlation (−0.63) with the soil CO_2 flux. For the other side, soil water content is the variable with highest direct correlation (0.56) with the gas flux. Rainfall is the least influential variable with a correlation of just 0.05.

The stepwise regression model selected is the number 4 (**Table 2**), which accounts with the air and soil temperature, wind speed, and soil water content as the explanatory variables to be included in the model. Before applying the stepwise model, several partial regression models were tested, but theoretically the same result can be obtained in a much faster way by using a stepwise regression. The rainfall variable showed always *p*-values higher than 0.05, and for this reason it was never selected as variable to include in the regression models (**Table 2**). By looking at the RMS (root mean square) error, it starts to stabilize at step 4. In fact, after that step, the gains in precision of the model by adding more variables are <1%, and for this reason the models are not considered. Similar criteria were used in previous studies (Viveiros et al., 2008, 2015a, 2016).

Equation (7) represents the proposed final regression model for the soil CO_2 flux (*y*), which is composed by the air temperature (*Air T.*), soil temperature (*Soil T.*), soil water content (*Soil W.*) and wind speed (*W. Speed*):

$$y = 1508.5 + 53.993 AirT. - 86.284 SoilT. + 85.877 SoilW. - 268.75 W.Speed \tag{7}$$

Soil temperature and wind speed have an inverse influence on the soil CO_2 flux, and for the other side air temperature and soil water content correlate positively.

According to the adjusted R^2, the model explains around 47% (0.4682) of the gas flux variations in this monitoring site, and soil temperature is the variable with higher explanatory power (about 30% of the CO_2 flux variation).

Based on the model, the predicted and residuals time series were calculated (**Figure 4**). The predicted values (*y*) correspond to the estimated values according to the proposed model and for the recent years there is a good agreement between the measured soil CO_2 fluxes and the predicted by the regression (Pearson correlation of 83%).

Based on Equation (7), predicted values were calculated and the difference between observed and predicted allows to calculate a third time series, the residuals (**Figure 4**), which correspond to the gas flux variations that cannot be explained by the proposed regression model.

Searching for Cycles

To evaluate the presence of harmonic oscillations a wavelet analysis and a spectral analysis were performed to the time series. The spectrogram was calculated using 512 samples of the time

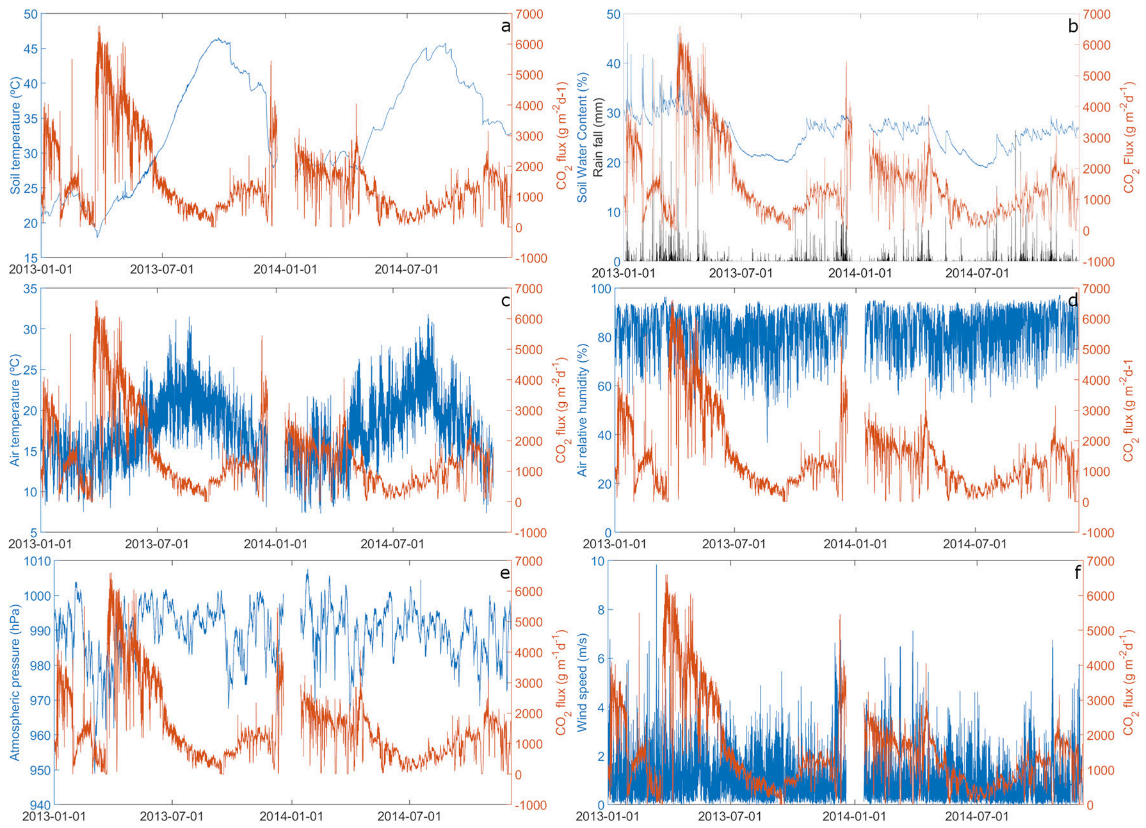

FIGURE 2 | Environmental and soil CO_2 flux time series for the period selected to build the regression model (2013–2014). Orange lines represent the soil CO_2 flux in all graphics, black line the rainfall **(b)**, and the blue lines the other monitored environmental variables, from **(a–f)** soil temperature, soil water content, air temperature, air relative humidity, atmospheric pressure and wind speed.

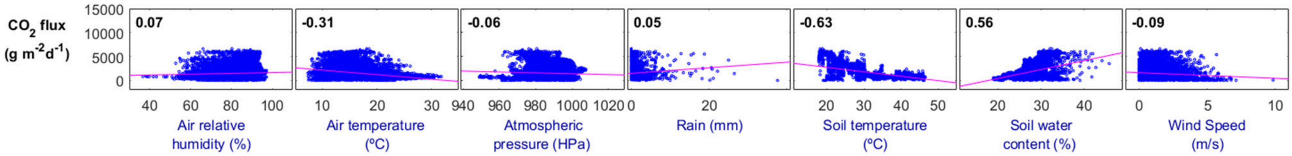

FIGURE 3 | Pearson correlation coefficients between soil CO_2 flux and the monitored environmental variables. Blue points correspond to the environmental variables vs. the soil CO_2 flux and the pink lines are the correlation trendlines.

series with a step of 24 samples and to minimize spectral leakage, a Hanning window was used, similarly to previous studies. Considering that the sample rate is 24 samples per day in the studied time series, the Nyquist critical frequency will be 12 cycles per day. Based on results obtained in previous works, more than 2 or 3 cycles per day should not be expected, which shows that this sample rate is adequate for this study.

Figure 5 shows the results of the FFT and wavelet analyses performed on the soil CO_2 fluxes and residuals for the period used to perform the models. One cycle per day (cpd), corresponding to the diurnal peak (S_1), may be observed on both the spectrogram (FFT analysis, **Figures 5A,C**) and on the scalogram (wavelet analysis, **Figure 5B**), even if 1 cpd signal is not constant along the time series and shows different intensities. The higher noise observed on the spectrogram close to the origin (**Figure 5A**) compared with the scalogram can be explained as the DFT normally represents the zero frequency as the offset from the time series to the origin.

The spectrum of the soil CO_2 fluxes shows however 1 and 2 cpd (**Figure 5C**); the weaker 2 cpd (12 h cycle) does not appear in the spectrogram or even in the scalogram. FFT and wavelet analyses were also applied to the environmental time series (**Supplementary Figure 1**) in order to identify the periodic behavior, as well as, to highlight eventual differences using both methodologies (**Table 3**). Higher number of cycles were identified based on the spectrograms when compared with the scalograms, namely for the atmospheric pressure, air and soil temperature.

FFT spectrum applied to the entire monitored period shows higher energy peaks at a periodicity of 358 day, which coincide in general with the annual cycle (**Figure 6**).

Spectral analysis was also applied to the residuals in order to check if the filtered time series still shows harmonic behavior. **Figures 5D–F** show that 1 cpd is also found out in this time series, even if the 2 cpd is practically absent on the spectrum. Considering that high frequency cycles are still observed on the residuals time series, a second order of filtering was applied to the residuals dataset, namely a Butterworth filter (**Figure 7**). The greenish band in **Figure 7** represents the mean plus-minus two times the standard deviation of the filtered residuals ($\bar{y} \pm 2\sigma$) estimated for the period 2013–2014.

DISCUSSION

GFOG4 station is installed in an anomalous soil CO_2 flux and temperature area, and is clearly located in a Diffuse Degassing Structure (DDS, Chiodini et al., 2001) in the north flank of Fogo Volcano (S. Miguel Island). This monitoring site corresponds to the one that shows the highest average soil CO_2 flux emissions (1,165 $gm^{-2}d^{-1}$) from all the permanent stations installed at S. Miguel Island (Viveiros et al., 2008, 2015a).

TABLE 2 | Stepwise regression model steps for GFOG4 data (period 2013–2014).

Step	Used variables	RMS error	Adj. R^2
1	Air T.	11,321.12	0.0990
2	Air T., Soil T.	923.58	0.4004
3	Air T., Soil T., W. Speed	892.43	0.4401
4	**Air T., Soil T., W. Speed, Soil W.**	**869.75**	**0.4682**
5	Air T., Soil T., W. Speed, Soil W., Atm. Press.	864.55	0.4747
6	Air T., Soil T., W. Speed, Soil W., Atm. Press., Air R.H.	862.34	0.4773

RMS, Root mean square; Adj. R-sq, Adjusted R^2; Air T, air temperature; Soil T, soil temperature; W. Speed, wind speed; Soil W, soil water content; Atm. Press, atmospheric pressure; Air R.H, air relative humidity. The bold values correspond to the model selected to explain the variations at GFOG4 station.

As previously mentioned, multivariate regression analysis has been commonly applied to gas geochemical time series in different degassing areas (e.g., Granieri et al., 2003, 2010; Padrón et al., 2008; Viveiros et al., 2008; Laiolo et al., 2012, 2016; Neri et al., 2016; Lelli and Raco, 2017) and showed to be adequate to highlight and filter the influences of the environmental parameters on the gas flux. The stepwise regression model here suggested as filtering methodology was already applied to other CO_2 and ^{222}Rn time series in the Azores archipelago (Silva et al., 2015; Viveiros et al., 2015a) and, despite all the advantages already mentioned for the linear regression analysis, the stepwise multivariate regression analysis also facilitates the selection of the independent variables to be included in the model, as well as, it is automatic and less user dependent. The model here proposed explains about 47% of the gas flux variations at GFOG4 site and the Pearson correlation coefficients between the observed and the predicted time series for the period between 2015 and 2017 is 0.83, which suggests a good agreement between both time series and the adequacy of the model to explain the observed CO_2 flux variations. The Pearson correlation coefficient for the period from 2010 to 2013 was significantly lower (0.46). This distinct behavior can be eventually justified by the initial period of instability of the expanded degassing area. In fact, previous studies (Viveiros et al., 2015a) already highlighted that the installation procedure of a permanent station can interfere with the initial acquired datasets, as it can cause higher variability on the gas flux data recorded.

The stepwise multivariate regression model proposed for the data between 2013 and 2014 shows that the soil temperature

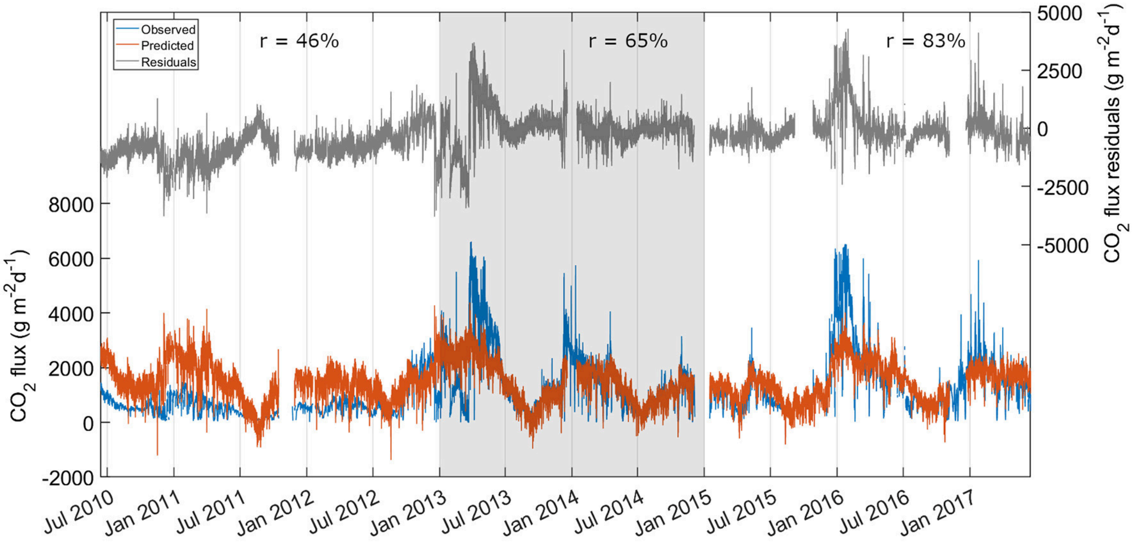

FIGURE 4 | Observed, predicted and residuals soil CO_2 flux time series for GFOG4 station. Pearson correlation coefficients (r) between predicted and observed values are displayed for the different periods. Gray area represents the period used to define the regression model.

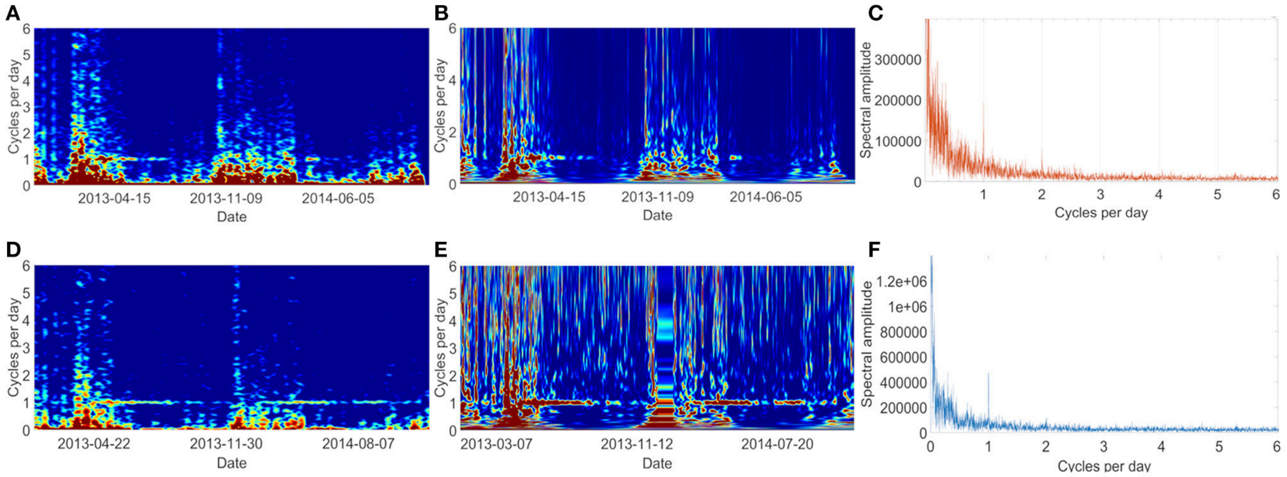

FIGURE 5 | Spectral results for the observed and residuals soil CO_2 fluxes for the period 2013–2014: **(A) s**pectrogram, **(B)** scalogram and **(C)** FFT spectrum of the observed values; **(D)** spectrogram, **(E)** scalogram **(F)** and FFT spectrum of the residuals.

TABLE 3 | Identified daily cycles for the different monitored variables based on the two spectral methodologies.

		1 cpd	2 cpd	3 cpd	4 cpd
Soil CO_2 flux	Scalogram	X	–	–	–
	Spectrogram	X	–	–	–
Atmospheric pressure	Scalogram	X	X	X	–
	Spectrogram	X	X	X	X
Air temperature	Scalogram	X	X	–	–
	Spectrogram	X	X	X	–
Air relative humidity	Scalogram	X	X	–	–
	Spectrogram	X	X	–	–
Soil temperature	Scalogram	X	–	–	–
	Spectrogram	X	X	–	–
Soil water content	Scalogram	–	–	–	–
	Spectrogram	–	–	–	–
Wind speed	Scalogram	X	–	–	–
	Spectrogram	X	–	–	–
Rainfall	Scalogram	–	–	–	–
	Spectrogram	–	–	–	–

cpd corresponds to cycles per day.

is the variable with greater influence on the soil CO_2 fluxes explaining about 30% of the gas variations (**Table 2**). Similar inverse correlation between soil CO_2 fluxes and soil temperature was already highlighted in other permanent soil CO_2 flux stations installed at Furnas and Fogo volcanoes (S. Miguel Island) (Viveiros et al., 2008, 2015a), or even in other degassing areas, such as Stromboli Volcano (Laiolo et al., 2016). Viveiros et al. (2008) suggested that these inverse correlations should result from the long-term seasonal effects, with the lower emissions occurring during summer time when compared with the winter period. Similar seasonal behavior is observed at GFOG4 site (**Figure 1**) and the seasonal cycle was identified (**Figure 6**).

Wind speed also correlates inversely with the soil CO_2 fluxes at GFOG4 station and this influence is in agreement with previous observations in other monitoring sites of S. Miguel Island (GFUR2, GFUR3, GFOG3, and GFOG3.1 stations). Intrusion of some air into the upper parts of the soil may dilute the soil gases and decrease the CO_2 fluxes during high wind speed periods. Air temperature and soil water content correlate positively with the soil gas flux according to the regression model proposed (Equation 7). The positive correlation between soil water content and gas fluxes was also previously identified in other monitoring sites and it was explained by the covering effect of the station shelter that maintains the soil dry during rainfall periods and allows the gas to escape. In the area surrounding the permanent stations the soil is wet and the pores are saturated, fact that hinders gas release. Several spike-like anomalies observed on the soil CO_2 fluxes time series are associated with the increases on the soil water content. This type of association was observed not only on the Azores monitoring sites (Viveiros et al., 2008, 2009, 2015a) but also on other sites with similar monitoring stations, such as at the summit area of Usu (Mori et al., 2002), Solfatara (Granieri et al., 2003, 2010) and Stromboli volcanoes (Carapezza et al., 2009). The positive correlation between air temperature and soil CO_2 flux is not widely observed and usually both variables correlate inversely as the CO_2 fluxes depend on the daily thermal cycles (Rinaldi et al., 2012; Viveiros et al., 2014). However, this positive correlation has been also identified at GFOG3.1 station and it was explained as resulting from an artifact, i.e., the superimposition of other monitored environmental variables. One additional explanation is that both monitoring sites are located in a thermally anomalous zone, that can eventually unbalance the expected pressure gradients on the soil-air interface due to the thermal cycles. In fact, and even if the models are specific for each monitoring site, considering that different characteristics (e.g., soil properties, drainage area, topography) can control the effect that environmental variables have on the soil CO_2 fluxes (Viveiros et al., 2008, 2014),

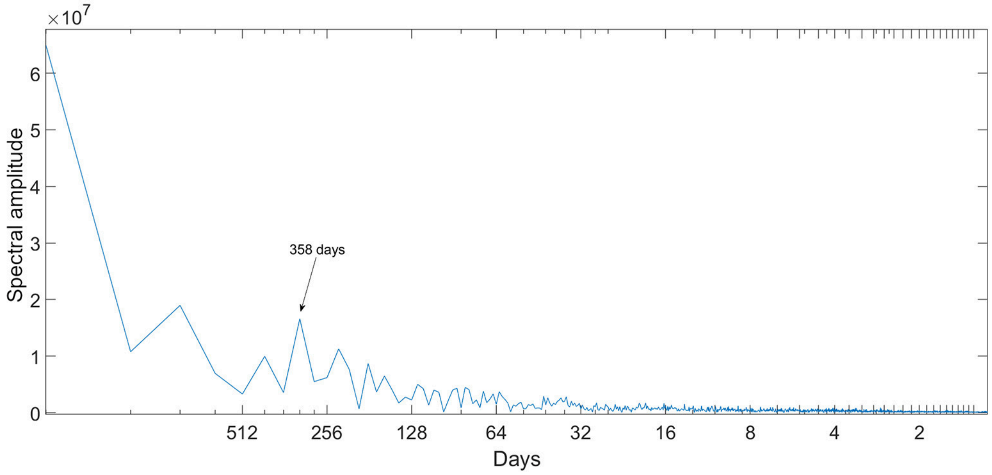

FIGURE 6 | Amplitude spectrum showing the low-frequency peaks for the entire monitored period of the observed soil CO_2 fluxes.

the model here proposed is quite similar to the regression defined to GFOG3.1 station. In this case, with exception to the atmospheric pressure, the same environmental variables correlate with the CO_2 fluxes and show similar type of influence (for more details on GFOG3.1 station see Viveiros et al., 2015a).

Considering that previous studies applied to volcanic gas emissions used both Fast Fourier Transform and wavelet analyses as the spectral techniques, we applied both techniques to the soil CO_2 flux time series in order to evaluate potential differences and discuss their adequacy to apply in a real-time monitoring system. Spectral analyses applied to the soil CO_2 flux time series identified the diurnal (S_1) peak (**Figure 5**), even if only the FFT spectra recognized a weaker semidiurnal cycle (12 h variation). Similar diurnal cycles were also recognized in the CO_2 flux time series not only in the Azores archipelago (Rinaldi et al., 2012; Viveiros et al., 2014), but also in other soil diffuse degassing areas (Granieri et al., 2003; Padrón et al., 2008; Hernández et al., 2012) and were mainly explained and modeled as consequence of the influence of the meteorological variables (Rinaldi et al., 2012; Viveiros et al., 2014). A low frequency signal (period of 358 days), which represents the annual period, was recognized on the spectrum soil CO_2 fluxes for the whole period. A cycle of about 340 days was previously identified at Furnas Volcano permanent stations (Viveiros et al., 2014) and it was interpreted as representing the annual period. The divergence to the 365 days was then interpreted as a FFT resolution problem caused by the length of the analyzed time series. In fact, in the current study with 7 years of data available, the identified annual cycle (358 days) approaches the annual band when compared with the results obtained by Viveiros et al. (2014).

This study used two different spectral approaches, which were previously applied to volcanic gas data, to the recorded time series in order to discriminate potential differences and evaluate which approach could be more adequate for a real-time monitoring environment. Even if both techniques identified the diurnal cycle on the soil CO_2 flux time series and showed quite similar behavior in the spectrogram and in the scalogram (**Figure 5**), by definition wavelet analysis should be more permissible to the lack of data, what can be advantageous to use for monitoring time series that frequently are affected by technical problems. Other positive aspect of the use of wavelets should be a better detection of the cycle (stability of the periodicities). These differences were not however particularly evident in the current study. In addition to the fact that it is easier to apply, FFT also allows to calculate the spectra and consequently allows to identify low frequencies. The soil CO_2 flux spectra (**Figure 5C**) also showed the semidiurnal cycle, which was not highlighted in the spectrogram or in the scalogram. One potential explanation may be that this weaker signal was hidden in the noise, especially in the winter periods, when the time series is more scattered. The existence of periodicities in the other monitored environmental variables was also evaluated (**Table 3**) and FFT again better discriminates high frequencies when compared with the wavelet analyses. Some of these high frequencies may eventually be due to harmonics of the diurnal signal, however looking at the other side one may suggest that wavelets hide some of the frequencies.

Considering the recognized periodicities in the environmental variables and the fact that the semidiurnal cycle is still detected in the residuals time series (**Figures 5D–F**), and even if there is a good agreement between the observed and predicted values, the regression model proposed does not seem to filter all the external influences on the soil CO_2 fluxes. Viveiros et al. (2014) also identified this problem in the time series recorded at Furnas Volcano (S. Miguel Island) and suggested a second filtering procedure using the FFT low-pass filter. In the current study we suggest the use of the Butterworth filter as it reduces the computational tasks and requires a lower number of samples to be considered for filtering, which is more appropriate for a real-time monitoring system.

The final calculated residuals dataset (**Figure 7**), resulting from two step filtering, should be the one used in any Volcano

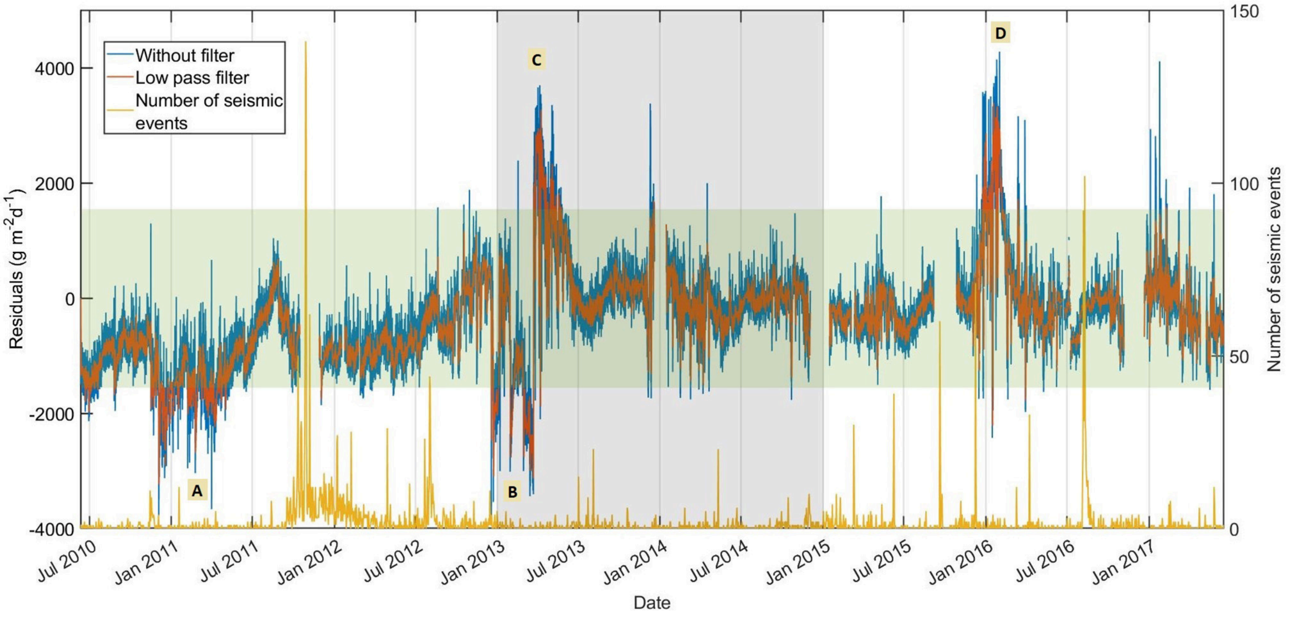

FIGURE 7 | Soil CO_2 flux residuals at GFOG4 station after applying the two step filtering (MRA and Butterworth filters). Orange line corresponds to the number of seismic events recorded at Fogo Volcano (CIVISA catalog). Gray vertical band represents the period used to produce the regression model and the green band corresponds to the interval ($\overline{y} \pm 2\sigma$).

Observatory as the best representative of the deep-source gas flux variations. Similarly to previous studies (Viveiros et al., 2014, 2015a), a band of variation was defined and any values that lay outside this band can represent anomalous periods of activity and need to be evaluated as a multidisciplinary approach since they may represent precursors of deep changes in the system. Four main periods in **Figures 7** (A, B, C and D) were highlighted and, even if the main scope of the current study was to apply different statistical methodologies to the soil gas flux time series and evaluate its adequacy for automation in a real-time monitoring basis, an attempt to correlate the gas flux residuals with the number of seismic events recorded at Fogo Volcano was done. No direct correlation was observed between the identified anomalous periods for the residuals and the number of seismic events. Periods identified as "B" and "C" are probably a local response of the system to some works carried out by the geothermal company in the area surrounding the station and that included injection of concrete at depth. These works were developed between July 2012 and March 2013, thus coincident with the above mentioned anomalous periods. As mentioned previously, the installation of a permanent station may also drive some period of instability in the gas release and this can potentially be the explanation to the lower than expected CO_2 fluxes at period "A". Even if anomalous period "D" (between end of December 2015 and early February 2016) occurs after a seismic swarm with 71 events, other similar seismic swarms did not cause significant changes on the CO_2 fluxes. A common observation for all the anomalous periods is that they occur during winter periods, when the gas flux data are more scattered and thus more challenging for the statistical approaches applied. GPS data are only available in the literature for the period from 2010 to May 2013 (Okada et al., 2015). Those authors highlighted deformation on the Fogo Volcano edifice for the period September 2011 to August 2012, associated with some of the recorded seismic swarms. The CO_2 flux residuals do not show any anomalous values for that period, but the anomalous vectors are mainly in the eastern part of the volcano edifice and not close to the GFOG4 monitoring site.

CONCLUSIONS

Environmental variables explain almost half of the variation observed on the soil CO_2 fluxes recorded in this monitoring site. This relevant correlation between gas fluxes and external factors was already shown in several degassing areas worldwide and, for this reason, it is fundamental to filter the data in order to highlight variations that may represent the deep volcanic/hydrothermal processes. In what concerns the statistical approaches applied, both spectral analyses seem adequate to apply to the soil CO_2 time series. However, considering that the wavelets are more complex to apply and may even hide eventual frequencies, we suggest the coupled use of stepwise multivariate regression analyses and FFT analyses as a good approach to filter external influences from the soil gas fluxes. The second order filtering, when high frequencies on the residuals are identified, may be carried out using the Butterworth filter since it is easy to apply in a routine time-real monitoring environment.

In the particular case of GFOG4 site, the final residuals do not show trends, nor any persistent increase that could eventually be correlated with some unrest, nor a decrease that could show a reduction of the anomaly in an area that expanded after a geothermal drilling. This observation seems to highlight that a constant and persistent deep flux of gas is being released in this degassing area. Nevertheless, analyses of the residuals show some periods laying outside the "normal" band and four anomalous periods were identified, but no direct correlation with the seismic and/or ground deformation observed at Fogo Volcano was established. We have to consider the low magnitude of the earthquakes and the fact that the ground deformation was identified in a different sector of the volcano edifice. Future studies should develop additional tools to join multidisciplinary time series recorded in the volcano observatories. A closer look to these variations shows that these periods occur essentially in the winter when the time series are more scattered and potentially represent periods of extreme weather conditions that the regression model does not manage to account.

The definition of intervals of variation considered "normal" are crucial to identify the anomalous periods especially in any Volcano Observatory, where recognizing precursors of volcanic activity is challenging and demanding. The application of automatic methods is a relevant approach that allows any user to identify potential anomalies. In addition to what mentioned above and considering the effect that environmental changes may have also on other gas species, such as radon (e.g., Perrier and Girault, 2013; Silva et al., 2015), the methodologies now proposed can be also tested and expanded to other degassing series and used as routine in any Volcano Observatory. Each Volcano Observatory should build specific models for the different monitoring sites. However, the use of the two steps filtering, coupling regression and spectral methodologies, will improve not only the knowledge about the gas flux behavior but also will allow to easily detect anomalous degassing periods.

AUTHOR CONTRIBUTIONS

SO and FV processed the data and mainly wrote the manuscript. CS and JP provided important suggestions during the processing and discussion of the data. All the authors have read and approved the final manuscript.

ACKNOWLEDGMENTS

The present study was developed with the support of VOLRISKMAC, INTERREG MAC 2014–2020 (MAC/3.5b/124). Authors would like to thank CIVISA to allow the use of the seismic data catalog. The first version of the manuscript was also improved with the contribution of the two reviewers and the editor.

SUPPLEMENTARY MATERIAL

The Supplementary Material for this article can be found online at: https://www.frontiersin.org/articles/10.3389/feart.2018.00208/full#supplementary-material

REFERENCES

Aiuppa, A., Burton, M., Caltabiano, T., Giudice, G., Gurrieri, S., Liuzzo, M., et al. (2010). Unusually large magmatic CO_2 gas emissions prior to a basaltic paroxysm. *Geophys. Res. Lett*. 37:L17303. doi: 10.1029/2010GL043837

Allard, P., Carbonnelle, J., Dajlevic, D., Le Bronec, J., Morel, P., Robe, M. C., et al. (1991). Eruptive and diffuse emissions of CO_2 from Mount Etna. *Nature* 351, 387–391.

Baubron, J. C., Allard, P., and Toutain, J. P. (1990). Diffuse volcanic emissions of carbon dioxide from Vulcano Island, Italy. *Nature* 344, 51–53.

Boichu, M., Oppenheimer, C., Tsanev, V., and Kyle, P. (2010). High temporal resolution SO_2 flux, measurements at Erebus volcano, Antarctica. *J. Volcanol. Geotherm. Res.* 190, 325–336. doi: 10.1016/j.jvolgeores.2009.11.020

Brusca, L., Inguaggiato, S., Longo, M., Madonia, P., and Maugeri, R. (2004). The 2002–2003 eruption of Stromboli (Italy): Evaluation of the volcanic activity by means of continuous monitoring of soil temperature, CO_2 flux, and meteorological parameters. *Geochem. Geophys. Geosyst*. 5:Q12001. doi: 10.1029/2004GC000732

Caliro, S., Viveiros, F., Chiodini, G., and Ferreira, T. (2015). Gas geochemistry of hydrothermal fluids of the S. Miguel and Terceira Islands, Azores. *Geochim. Cosmochim. Acta* 168, 43–57. doi: 10.1016/j.gca.2015.07.009

Cannata, A., Giudice, G., Gurrieri, S., Montalto, P., Alparone, S., Di Grazia, G., et al. (2010). Relationship between soil CO_2 flux and volcanic tremor at Mt. Etna: Implications for magma dynamics. *Environ. Earth. Sci.* 61, 477–489. doi: 10.1007/s12665-009-0359-z

Carapezza, M. L., Inguaggiato, S., Brusca, L., and Longo, M. (2004). Geochemical precursors of the activity of an open-conduit volcano: the Stromboli 2002–2003 eruptive events. *Geophys. Res. Lett*. 31:L07620. doi: 10.1029/2004GL019614

Carapezza, M. L., Ricci, T., Ranaldi, M., and Tarchini, L. (2009). Active degassing structures of Stromboli and variations in diffuse CO_2 output related to the volcanic activity. *J. Volcanol. Geotherm. Res.* 182, 231–245. doi: 10.1016/j.jvolgeores.2008.08.006

Carmo, R., Madeira, J., Ferreira, T., Queiroz, G., and Hipólito, A. (2015). "Volcano-tectonic structures of *S.* Miguel Island, Azores," in *Volcanic Geology of S. Miguel Island (Azores archipelago)*, eds J. L. Gaspar, J. E. Guest, A. M. Duncan, F. J. A. S. Barriga, and D. K. Chester (London: Geological Society, London, Memoirs), 65–86. doi: 10.1144/M44.6

Chiodini, G., Cioni, R., Guidi, M., Raco, B., and Marini, L. (1998). Soil CO_2 flux measurements in volcanic and geothermal areas. *Appl. Geochem*. 13, 543–552.

Chiodini, G., Frondini, F., Cardellini, C., Granieri, D., Marini, L., and Ventura, G. (2001). CO_2 degassing and energy release at Solfatara Volcano, Campi Flegrei, Italy. *J. Geophys. Res*. 106, 16213–16221. doi: 10.1029/2001JB000246

Cooley, W., and Tukey, J. W. (1965). An algorithm for the machine calculation of complex fourier series. *Math. Comput.* 19, 297–301.

Draper, N., and Smith, H. (1981). *Applied Regression Analysis, 2nd Edn*. New York, NY: John Wiley & Sons, Inc.

Farge, M. (1992). Wavelet transforms and their applications to turbulence. *Annu. Rev. Fluid Mech.* 24, 395–457.

Ferreira, T., Gaspar, J. L., Viveiros, F., Marcos, M., Faria, C., and Sousa, F. (2005). Monitoring of fumarole discharge and CO_2 soil degassing in the Azores: contribution to volcanic surveillance and public health risk assessment. *Ann. Geophys*. 48, 787–796. doi: 10.4401/ag-3234

Fischer, T. P., and Chiodini, G. (2015). "Volcanic, Magmatic and Hydrothermal Gases," in *The Encyclopedia of Volcanoes, 2nd Ed*., eds H. Sigurdsson, B. Houghton, S. R. McNutt, H. Rymer, and J. Stix (San Diego, CL: Elsevier Inc.), 779–797.

Granieri, D., Avino, R., and Chiodini, G. (2010). Carbon dioxide diffuse emission from the soil: ten years of observations at Vesuvio and Campi Flegrei (Pozzuoli), and linkages with volcanic activity. *Bull. Volcanol.* 72, 103–118. doi: 10.1007/s00445-009-0304-8

Granieri, D., Chiodini, G., Marzocchi, W., and Avino, R. (2003). Continuous monitoring of CO_2 soil diffuse degassing at Phlegraean Fields (Italy): influence of environmental and volcanic parameters. *Earth Planet. Sci. Lett.* 212, 167–179. doi: 10.1016/S0012-821X(03)00232-2

Grossmann, A., and Morlet, J. (1984). Decomposition of Hardy functions into square integrable wavelets of constant shape. *SIAM J. Math. Anal.* 15, 723–736. doi: 10.1137/0515056

Gurrieri, S., Liuzzo, M., and Giudice, G. (2008). Continuous monitoring of soil CO_2 flux on Mt. Etna: The 2004–2005 eruption and the role of regional tectonics and volcano tectonics, *J. Geophys. Res.* 113:B09206. doi: 10.1029/2007JB005003

Hernández, P. A., Padilla, G., Padrón, E., Pérez, N. M., Calvo, D., Nolasco, D., et al. (2012). Analysis of long- and short-term temporal variations of the diffuse CO_2 emission from Timanfaya volcano, Lanzarote, Canary Islands. *Appl. Geochem.* 27, 2486–2499. doi: 10.1016/j.apgeochem.2012.08.008

Inguaggiato, S., Vita, F., Cangemi, M., Mazot, A., Sollami, A., Calderone, L., et al. M. P. (2017). Stromboli volcanic activity variations inferred from observations of fluid geochemistry: 16 years of continuous monitoring of soil CO_2 fluxes (2000–2015). *Chem. Geol.* 469, 69–84. doi: 10.1016/j.chemgeo.2017.01.030

Jurišić, D., Moschytz, G. S., and Mijat, N. (2002). "Single Amplifier, Active-RC, Butterworth, and Chebyshev Filters Using Impedance Tapering," in *Proceedings of the IASTED International Conference: Signal Processing, Pattern Recognition & Applictions* (Creta).

Laiolo, M., Cigolini, C., Coppola, D., and Piscopo, D. (2012). Developments in real-time radon monitoring at Stromboli volcano. *J. Environ. Radioact.* 105, 21–29. doi: 10.1016/j.jenvrad.2011.10.006

Laiolo, M., Ranaldi, M., Tarchini, L., Carapezza, M. L., Coppola, D., Ricci, T., et al. (2016). The effects of environmental parameters on diffuse degassing at Stromboli volcano: Insights from joint monitoring of soil CO_2 flux and radon activity. *J. Volcanol. Geotherm. Res.* 315, 65–78. doi: 10.1016/j.jvolgeores.2016.02.004

Lelli, M., and Raco, B. (2017). A reliable and effective methodology to monitor CO_2 flux from soil: the case of Lipari Island (Sicily, Italy). *Appl. Geochem.* 85, 73–85. doi: 10.1016/j.apgeochem.2017.08.004

Liuzzo, M., Gurrieri, S., Giudice, G., and Giuffrida, G. (2013). Ten years of soil CO_2 continuous monitoring on Mt. Etna: exploring the relationship between processes of soil degassing and volcanic activity. *Geochem. Geophys. Geosyst.* 14, 2886–2899. doi: 10.1002/ggge.20196

Mallat, S. (2009). *A Wavelet Tour of Signal Processing, The Sparse Way.* Burlington, MA: Academic Press.

Meignen, S., Oberlin, T., and McLaughlin, S. (2012). A new algorithm for synchrosqueezing: with an application to multicomponent signals sampling and denoising. *IEEE Trans. Signal Proces.* 60, 5787–5798. doi: 10.1109/TSP.2012.2212891

Mori, T., Notsu, K., Hernández, P. A., Salazar, J. M. L., Pèrez, N., Virgili, G., et al. (2002). Continuous monitoring of soil CO_2 efflux from the summit region of Usu Volcano, Japan. *Bull. Volcanol. Soc. Japan* 47, 339–345.

Muecke, G. K., Ade-Hall, J. M., Aumento, F., Macdonald, A., Reynolds, P. H., Hyndman, R. D., et al. (1974). Deep drilling in an active geothermal area in the Azores. *Nature* 252, 281–285.

Neri, M., Ferrera, E., Giammanco, S., Currenti, G., Cirrincione, R., Patan,è, G., et al. (2016). Soil radon measurements as a potencial tracer of tectonic and volcanic activity. *Sci. Rep.* 6:24581. doi: 10.1038/srep24581

Neter, J., Wasserman, W., and Kunter, M. H. (1983). *Applied Linear Regression Models.* Homewood: Richard D. Irwin, Inc.

Okada, J., Sigmundsson, F., Ófeigsson, B., Ferreira, T., and Rodrigues, R. (2015). "Tectonic and volcanic deformation at São Miguel Island, Azores, observed by continuous GPS analysis 2008-13," in *Volcanic Geology of S. Miguel Island (Azores archipelago),* eds J. L. Gaspar, J. E. Guest, A. M. Duncan, F. J. A. S. Barriga, and D. K. Chester (London: Geological Society, London, Memoirs), 239–256.

Padrón, E., Melián, G., Marrero, R., Nolasco, D., Barrancos, J., Padilla, G., et al. (2008). Changes in the diffuse CO_2 emission and relation to seismic activity in and around El Hierro, Canary Islands. *Pure Appl. Geophys.* 165, 95–114. doi: 10.1007/s00024-007-0281-9

Pardoe, I., Simon, L., and Young, D. (2018). *Lesson 5: Multiple Linear Regression.* Available online at: https://onlinecourses.science.psu.edu/stat501/node/283

Pérez, N. M., Hernández, P. A., Padrón, E., Cartagena, R., Olmos, R., Barahona, F., et al. (2006). Anomalous diffuse CO_2 emission prior to the January 2002 short-term unrest at San Miguel Volcano, El Salvador, Central America. *Pure Appl. Geophys.* 163, 883–896. doi: 10.1007/s00024-006-0050-1

Pérez, N. M., Padilla, G. D., Padrón, E., Hernández, P. A., Melián, G. V., Barrancos, J., et al. (2012). Precursory diffuse CO_2 and H_2S emission signatures of the 2011–2012 El Hierro submarine eruption, Canary Islands. *Geophys. Res. Lett.* 39;L16311. doi: 10.1029/2012GL052410

Pering, T. D., Tamburello, G., McGonigle, A. J. S., Aiuppa, A., Cannata, A., Giudice, G., et al. (2014). High time resolution fluctuations in volcanic carbon dioxide degassing from Mount Etna. *J. Volcanol. Geotherm. Res.* 270, 115–121. doi: 10.1016/j.jvolgeores.2013.11.014

Perrier, F., and Girault, F. (2013). Harmonic response of soil radon-222 flux and concentration induced by barometric oscillations. *Geophys. J. Int.* 195, 945–971. doi: 10.1093/gji/ggt280

Press, W. H., Teukolsky, S. A., Vetterling, W. T., and Flannery, B. P. (1992). *Numerical Recipes in C: The Art of Scientific Computing.* New York, NY: Cambridge University Press.

Rawlings, J. O., Pantula, S. G., and Dickey, D. A. (1998). *Applied Regression Analysis: A Research Tool, 2nd Edn.* New York, NY: Springer-Verlag.

Rinaldi, A. P., Vandemeulebrouck, J., Todesco, M., and Viveiros, F. (2012). Effects of atmospheric conditions on surface diffuse degassing. *J. Geophys. Res.* 117:B11201. doi: 10. 1029/2012JB009490

Salazar, J. M. L., Hernández, P. A., Pérez, N. M., Olmos, R., Barahona, F., Cartagena, R., et al. (2004). Spatial and temporal variations of diffuse CO_2 degassing at the Santa Ana-Izalco-Coatepeque volcanic complex, El Salvador, Central America. *Geol. Soc. Am. Spec. Pap.* 375, 135–146. doi: 10.1130/0-8137-2375-2.135

Salazar, J. M. L., Pérez, N. M., Hernández, P. A., Soriano, T., Barahona, F., Olmos, R., et al. (2002). Precursory diffuse carbon dioxide degassing signature related to a 5.1 magnitude earthquake in El Salvador, Central America. *Earth Planet. Sci. Lett.* 205, 81–89. doi: 10.1016/S0012-821X(02)01014-2

Sedra, A., and Smith, K. (2004). *Microelectronic Circuits, 5th Edn.* Oxford, NY: Oxford University Press.

Shu, W., and Qinyu, L. (2005). Some Problems on the Global Wavelet Spectrum. *J. Ocean Univ. China* 4, 398–402. doi: 10.1007/s11802-005-0062-y

Silva, C., Viveiros, F., Ferreira, T., Gaspar, J. L., and Allard, P. (2015). "Diffuse soil emanations of radon and hazard implications at Furnas Volcano, São Miguel Island (Azores)," in *Volcanic Geology of S. Miguel Island (Azores archipelago),* eds J. L. Gaspar, J. E. Guest, A. M. Duncan, F. J. A. S. Barriga, and D. K. Chester (London: Geological Society, London, Memoirs), 197–211.

Silva, R. (2011). *Evaluation of Spatial and Temporal Seismicity Patterns in the Central Region of São Miguel (Azores): Implications for Whole-Island Seismic Hazard Assessment.* PhD Thesis, University of the Azores, 236.

Silva, R., Havskov, J., Bean, C., and Wallenstein, N. (2012). Seismic swarms, fault plane solutions and stress tensors for São Miguel Island central region (Azores). *J. Seismol.* 16, 389–407. doi: 10.1007/s10950-012-9275-x

Torrence, C., and Compo, G. (1998). A practical guide to wavelet analysis. *B. Am. Meteorol. Soc.* 79, 61–78.

Viveiros, F., Ferreira, T., Cabral Vieira, J., Silva, C., and Gaspar, J. L. (2008). Environmental influences on soil CO_2 degassing at Furnas and Fogo volcanoes (São Miguel Island, Azores archipelago). *J. Volcanol. Geotherm. Res.* 177, 883–893. doi: 10.1016/j.jvolgeores.2008.07.005

Viveiros, F., Ferreira, T., Silva, C., and Gaspar, J. L. (2009). Meteorological factors controlling soil gases and indoor CO_2 concentration: a permanent risk in degassing areas. *Sci. Tot. Environ.* 407, 1362–1372. doi: 10.1016/j.scitotenv.2008.10.009

Viveiros, F., Ferreira, T., Silva, C., Vieira, J. C., Gaspar, J. L., Virgili, G., et al. (2015a). "Permanent monitoring of soil CO_2 degassing at Furnas and Fogo volcanoes (São Miguel Island, Azores)," in *Volcanic Geology of S. Miguel Island (Azores archipelago)*, eds J. L. Gaspar, J. E. Guest, A. M. Duncan, F. J. A. S. Barriga, and D. K. Chester (London: Geological Society, London, Memoirs), 271–288.

Viveiros, F., Gaspar, J. L., Ferreira, T., and Silva, C. (2016). Hazardous indoor CO_2 concentrations in volcanic environments. *Environ. Pollut.* 214, 776–786. doi: 10.1016/j.envpol.2016.04.086

Viveiros, F., Gaspar, J. L., Ferreira, T., Silva, C., Marcos, M., and Hipólito, A. (2015b). "Mapping of soil CO_2 diffuse degassing at São Miguel Island and its public health implications," in *Volcanic Geology of S. Miguel Island (Azores archipelago)*, eds J. L. Gaspar, J. E. Guest, A. M. Duncan, F. J. A. S.

Barriga, and D. K. Chester (London: Geological Society, London, Memoirs), 185–195.

Viveiros, F., Vandemeulebrouck, J., Rinaldi, A. P., Ferreira, T., Silva, C., and Cruz, J. V. (2014). Periodic behavior of soil CO_2 emissions in diffuse degassing areas of the Azores archipelago: application to seismovolcanic monitoring. *J. Geophys. Res.* 119, 7578–7597. doi: 10.1002/2014JB011118

Wallenstein, N., Duncan, A. M., Guest, J. E., and Almeida, M. H. (2015). "Eruptive history of Fogo Volcano, São Miguel, Azores," in *Volcanic Geology of S. Miguel Island (Azores archipelago)*, eds J. L. Gaspar, J. E. Guest, A. M. Duncan, F. J. A. S. Barriga, and D. K. Chester (London: Geological Society, London, Memoirs), 105–123.

Conflict of Interest Statement: The authors declare that the research was conducted in the absence of any commercial or financial relationships that could be construed as a potential conflict of interest.

frontiers
in Earth Science

REVIEW
published: 30 November 2018
doi: 10.3389/feart.2018.00213

Advances in Bromine Speciation in Volcanic Plumes

Alexandra Gutmann[1]**, *Nicole Bobrowski*[2,3]**, *Tjarda Jane Roberts*[4], *Julian Rüdiger*[5] *and Thorsten Hoffmann*[1]

[1] Institute of Inorganic and Analytical Chemistry, Johannes Gutenberg-University Mainz, Mainz, Germany, [2] Institute of Environmental Physics, University of Heidelberg, Heidelberg, Germany, [3] Max Planck Institute for Chemistry, Mainz, Germany, [4] Laboratoire de Physique et de Chimie de l'Environnement et de l'Espace, Université d'Orléans, CNRS UMR7328, Orléans, France, [5] Atmospheric Chemistry, Bayreuth Center of Ecology and Environmental Research, University of Bayreuth, Bayreuth, Germany

Volcanoes are a significant halogen source to the atmosphere. After water, carbon dioxide and sulfur compounds, halogens are often the most abundant gases in volcanic plumes. In the past, less attention was given to the heavy halogens bromine and iodine. However, the discovery of bromine monoxide (BrO) in volcanic plumes led to new interest especially in volcanic bromine chemistry and its impact on atmospheric processes. The BrO detection came along with advances in volcanic remote sensing techniques, in particular, robust DOAS applications and the possibility of continuous measurements by automated instruments located at safe distances from the volcano. As one of the consequences, the volcanic community developed an increased interest to use BrO/SO_2 ratios as a potential tracer of volcanic activity. BrO is a secondary volcanic gas, but the only bromine species in volcanic plumes, which has been measured by remote sensing techniques today. For a better understanding on bromine chemistry in volcanic plumes and to gain information on the original amount of emitted bromine by only measuring BrO, additional techniques were developed (alkaline traps, diffusion denuders) and adapted for drone-based sampling to determine further gaseous bromine species (i.e. Br_2, HBr, HOBr, interhalogens) at various plume ages. Additionally models of plume-atmospheric chemistry were developed to help the interpretation of field-measurements. Model studies simulating plume conditions indicated that a complex atmospheric chemistry mechanism transforms emitted HBr into BrO and other reactive bromine species such as BrOH, Br_2, BrCl, $BrONO_2$ or $BrNO_2$. To reproduce the very rapid formation of BrO observed in volcanic plumes, the volcanic emission input to the (low-temperature) plume chemistry models also needs to consider the high-temperature near-vent plume conditions, as represented by thermodynamic models. The formation of BrO and other reactive bromine species depend not only on the amount of bromine emitted but also on plume mixing processes, relative humidity, and aerosol particle acidity. However, uncertainties remain in the validation of the plume chemistry models by a lack of field-measurements. This review provides a comprehensive summary on

OPEN ACCESS

Edited by:
Andrew McGonigle,
University of Sheffield,
United Kingdom

Reviewed by:
Eisuke Fujita,
National Research Institute for Earth Science and Disaster Prevention,
Japan
J. Eric Klobas,
Harvard University, United States

****Correspondence:***
Alexandra Gutmann
gutmann@uni-mainz.de
Nicole Bobrowski
nbobrows@iup.uni-heidelberg.de

Specialty section:
This article was submitted to Volcanology,
a section of the journal
Frontiers in Earth Science

Received: *30 June 2018*
Accepted: *05 November 2018*
Published: *30 November 2018*

Citation:
Gutmann A, Bobrowski N, Roberts TJ, Rüdiger J and Hoffmann T (2018)
Advances in Bromine Speciation in Volcanic Plumes.
Front. Earth Sci. 6:213.
doi: 10.3389/feart.2018.00213

volcanic bromine data of the last 15 years achieved from established and cutting edge measurement techniques as well as their treatment and interpretation in recent model experiments. It points out controversially discussed relation of bromine degassing to volcanic activity and puts a light on remaining uncertainties.

Keywords: volcanic halogen emissions, volcanic plumes, plume chemistry, bromine explosion, bromine speciation, gas monitoring, troposphere

INTRODUCTION

Volcanic activity is responsible for the formation of a permanent atmosphere on Earth, and volcanic emissions continue to influence atmospheric composition and thereby climate. Thus, even though volcanic activity has acted to promote the development of life it also induces risks and challenges for the terrestrial biosphere (Shaw, 2008). Measurements of volcanic emissions (gas flux, composition) made at the surface provide an indirect means to explore the inaccessible interior of volcanoes and their complex magmatic systems. They can thereby contribute to volcano hazard monitoring and eruption forecasting.

Knowledge about the chemistry occurring in the volcanic plume is required when making inferences about volcanic activity from volcanic gas measurements, particularly in the more chemically-aged downwind plume. Volcanic sulfur emissions become oxidized in the atmosphere to radiatively-active sulfate particles that can cause climate cooling in particular following large eruptions that injected gas into the stratosphere, e.g., Pinatubo 1991. Volcanic sulfate particles in the stratosphere also act as surfaces to activate halogens causing ozone layer depletion (Brasseur and Granier, 1992). More recently, the potentially chemistry-climate importance of volcanic halogen emissions has started to be of increased interest again (von Glasow et al., 2009; Kutterolf et al., 2013, 2015; Cadoux et al., 2015, 2018; Vidal et al., 2016; Klobas et al., 2017). Some eruptions to the stratosphere have been observed to co-inject halogens alongside sulfur (Theys et al., 2009; Hörmann et al., 2013; Carn et al., 2016), leading to volcanic halogen impact on stratospheric ozone and NO_X (Lurton et al., 2018). Besides remote sensing observations have been done via *in situ* sampling (Rose et al., 2006) and analysis of ice cores (Zdanowicz et al., 1999; De Angelis et al., 2003). Volcanic halogen emissions to the troposphere, particularly bromine (but also chlorine and iodine) can become activated through plume atmospheric chemistry that results in tropospheric ozone, NO_X, HO_X depletion and may convert mercury to a more easily deposited form (Bobrowski et al., 2007; Roberts et al., 2009; von Glasow, 2010; Jourdain et al., 2016). The plume chemical activation of volcanic halogen emissions, especially bromine, is the focus of this review.

In general, volcanic gas emissions consist of: 50–90% H_2O, 1–40% CO_2, 1–25% SO_2, and trace species such as ca. 0.5% H_2 and 0.03% CO (Gerlach, 2004; Textor et al., 2004). For arc volcanoes, halogen emissions are represented by about 0.84% HCl, 0.061% HF, 0.0025% HBr (Gerlach, 2004), with trace-level HI emissions. Global average bromine degassing fluxes from arc volcanoes are estimated to be 5 ± 15 Gg/year HBr (Pyle and Mather, 2009), based on collated data on Br/S ratios in volcanic emissions combined with assuming an annual arc-related SO_2 flux of 15 Tg/a. However, this may underestimate total volcanic bromine emissions, given the most recent estimate of the global SO_2 flux from passively degassing volcanoes is 23 ± 2 Tg/a (Carn et al., 2017), and the new identification of bromine-rich volcanic sources (e.g., Nyiragongo, Democratic Republic of the Congo, Bobrowski et al., 2015).

Previous reviews on volcanic halogens have focused on petrological approaches (e.g., Devine et al., 1984; Wallace, 2005) and volcanic degassing fluxes of halogens (Pyle and Mather, 2009) or their general cycling and distribution in the earth system (Webster et al., 2018). Platt and Bobrowski (2015) summarized observations of reactive bromine species mainly by spectroscopic technologies. Several reviews have also been published about the origin and impact of volcanic halocarbons as a minor halogen emission (Schwandner et al., 2004, 2013; Frische et al., 2006). Lately developments of new measurement techniques, collection and interpretation of data sets (by both, new and old techniques), and approach by model applications moved forward the knowledge related to bromine transformations in volcanic plumes. To our knowledge no comprehensive summary and overview of this still relatively new and fast advancing field has been done today. Here we conflate all recent approaches to draw an overall image about the state of the art by pointing out commonly confirmed statements, inconsistencies and general knowledge gaps suggesting further work. We focus on inorganic bromine compounds within passively degassing volcanic plumes entering the troposphere, for which the datasets and plume model studies are most comprehensive, but including a brief discussion of other halogens (Cl, I).

This review starts with an overview of existing measurement techniques for the determination of both speciated and total bromine in volcanic plumes. This is followed by a discussion of numerical modeling of plume bromine chemistry. Then a summary of volcanic bromine measurements is presented. An overview is given of the chemical reaction mechanisms that activate bromine (as well as chlorine and iodine) in volcanic plumes, detailing the roles of both low and high-temperature chemistry, photochemical and multi-phase reactions, aerosol/humidity, and impacts and feedbacks of ozone, NO_X, and mercury. This conceptual framework is then used to discuss reported field-studies and trends in the collated volcanic bromine datasets. The review concludes by describing the current knowledge gaps, particularly in relation to the use of bromine as monitoring parameter for forecasting eruptions, and highlights recent developments that provide new opportunities in this field.

METHODS USED TO INVESTIGATE BROMINE IN VOLCANIC PLUMES

Measurement Techniques

Volcanoes present a challenging context for both instruments and scientists seeking to measure volcanic plume gases in remote, inaccessible areas and during hazardous volcanic eruptions. For continuous and safe observations remote sensing techniques are often the instruments of choice. However, not all species can be measured by remote sensing. Also, *in situ* and direct sampling techniques can enable measurements closer to the emission source and thus capture degassed species at an earlier point of plume age. Making measurements very near-to-source is essential for the case of highly reactive species such as bromine: it allows to investigate as "pure" volcanic signal as possible, opening up the possibility to study the chemical transformation processes as a function of distance (and travel time) downwind, as the volcanic emissions progressively mix with the surrounding atmosphere.

In Situ – Application of Instruments in the Plume

Earlier determinations of volcanic halogens were realized by condensate sampling in volcanic fumaroles (Oana, 1962; Sugiura et al., 1963; Goff and McMurtry, 2000; Amachi et al., 2001) and by the use of passive alkaline traps (Noguchi and Kamiya, 1963; Goff et al., 1998; Witter et al., 2004). Today, actively pumped alkaline traps are typically applied. The main idea is to retain and enrich acid compounds within strong alkaline solutions (e.g., 1–4 M NaOH) when air is pumped through the substrate. Due to their light weight and easy handling, "filter-packs" (FP) are still the most commonly applied alkaline traps to sample volcanic plume gases. Different kinds of filters (cellulose, Nylon, Teflon) have been used with several mainly alkaline coatings (e.g., 1M $NaHCO_3$) and glycerol to improve the absorption efficiency. Nevertheless, saturation of filters or evaporation can readily occur. Limitations of the sampling efficiency were pointed out especially for saturated filter packs leading to elevated halogen/sulfur ratios due to distinct acidity (e.g., SO_2 and HF) and therefore different retention in the alkaline solution (Martin et al., 2010; Sawyer et al., 2011; Wittmer et al., 2014). To avoid or at least be aware of saturation effects, several filters are usually mounted in series. If the last filter of a pack yields <10% of the total amount of the species of interest, a quantitative trapping of the compounds is assumed (Lazrus et al., 1976; Sedlacek et al., 1984). If particle filters in front of filter packs are installed (i.e., to avoid uptake of aerosol and ash particles), possible interactions of gases with the particle-loaded filter have also to be considered. For volcanic bromine, HBr is assumed to be efficiently collected, but uncertainties remain whether species such as HOBr, Br_2, BrCl, $BrNO_2$, and $BrONO_2$ are trapped quantitatively by alkaline impregnated filters (Kitto et al., 1988).

Using these techniques extensive data sets of volcanic plume composition were established, however, in the case of halogens most of them focus on chlorine and fluorine and do not take bromine and iodine into account. One of the early plume studies on heavy halogens was carried out by Aiuppa et al. (2005) who assumed to determine the total molar amount of emitted bromine species (Br_{total}) on alkaline filters since bromine on particulate filters were negligible and no BrO was measurable with DOAS at the same location.

Uncoated filters can be used for the determination of particulate bromine, although few observations have been reported (Sturges and Shaw, 1993; Zelenski et al., 2013). Size-resolved analysis is enabled when cascade impactors are used. Here, the particles are deposited on several filter membranes according to their size. In comparison to alkaline filter sampling packs (sampling volume about 120 L; Aiuppa, 2009), particle analysis typically requires much higher sampling volumes ranging from 2,000 up to 10,000 L (Erebus, Antarctica: Ilyinskaya et al., 2010; about cascade impactors: Marple et al., 1991; Ma and Kim, 2008).

For avoiding saturation during sampling, active liquid alkaline traps were developed, which solve acid gas species in alkaline solutions by bubbling volcanic gases through the solution. To enhance the efficiency in Drechsel bottles (based on gas washing bottles named after Edmund Drechsel, DB) frits are used to decrease bubble size and therefore increase the relative surface of introduced gas samples to the alkaline solution (Liotta et al., 2012; Wittmer et al., 2014). The same aim of increasing the surface between the solution and introduced gas is used by filling a glass tube with glass rings (so-called Raschig rings; Raschig, 1914) and adding alkaline solution which is able to cover all the surface by rotating the tube (the so-called Raschig tube; RT, Levin et al., 1980). The enhanced efficiency allows a higher volume flow-rate that yields in increased sample concentrations and facilitates analyses close to detection limits for a specified sampling time or alternatively sampling time in the field can be reduced, in cases where a reduced detection limit is not necessary. Since it is assumed that the dominant fraction of bromine compounds are acidic and are therefore dissolved in the alkaline sampling solution the results are assumed to represent the Br_{total}. Today, all those alkaline trap samples are usually analyzed by IC and ICP-MS (see overview in Wittmer et al., 2014). An alternative are neutron activation analysis, but often much more expensive and comparison studies showed similar results between the methods (Strellis et al., 1996; Wittmer, 2012). Wittmer et al. (2014) characterized the sampling efficiency of various alkaline traps. In general, good agreements for filter packs, Drechsel bottles, and Raschig Tubes were found.

Alkaline sampling techniques do not allow speciation (i.e., the determination of individual halogen species). Moreover, alkaline traps cannot distinguish between gaseous and particulate phase. To provide a more in-depth halogen-speciation, gas diffusion denuders take advantage of the different diffusion coefficients of gaseous compounds and particles. The tube-shaped denuder systems are applied with a coated inner surface. Gas molecules diffuse to coated denuder walls, which represent an ideal sink for the gas molecules of interest and thus are retained and enriched in the coating. In contrast, due to the much smaller diffusion coefficient, the aerosol particles pass the denuder. Using various coatings, which undergo species specific derivatization of analytes, enables selective analysis of bromine species (Huang and Hoffmann, 2008, 2009; Rüdiger et al., 2017).

In situ techniques applicable for bromine determination are summarized in **Table 1**. Beside ground-based applications, drone–based sampling units proved to be a valuable tool for *in situ* volcanic gas measurements of difficult-to-access crater emissions as well as aged plumes downwind from the emission source that have become lofted away from the surface (e.g., McGonigle et al., 2008; Rüdiger et al., 2018b).

Remote Sensing

Especially during explosive episodes, remote sensing techniques become an indispensable tool for safe monitoring of volcanoes. Optical remote sensing techniques, using spectroscopic approaches from ultra-violet to thermal infrared, measure integrated gas concentrations through cross-sections of the plume. An overview of typical applied remote sensing techniques is given e.g., in McGonigle and Oppenheimer (2003) and Platt et al. (2018).

Restrictions for remote sensing techniques might occur due to high and/or variable atmospheric backgrounds for some gases (mainly for H_2O and CO_2) and since remote sensing techniques are sensitive for species with differential absorption structures, accessible compounds are limited to the wavelength range of the particular spectrometer and light source. Fourier transform infrared (FTIR) technique has been used for spectroscopic halogen observations of HCl and HF (e.g., Mori and Notsu, 1997; Oppenheimer et al., 1998). However, due to "small" absorption cross-sections, low abundances and limited spectral resolution, portable FTIR instruments have not been able to detect HBr.

In volcanic environments, BrO is the only bromine species that has been determined by remote sensing. Satellites, portable and continuously installed Differential Optical Absorption Spectroscopy (DOAS) instruments, are used to investigate BrO in volcanic plumes. DOAS instruments collect light (from scattered skylight, direct solar light or artificial lamps) that has passed through the volcanic plume. Light collected by a telescope is coupled into a spectrometer often by using an optical fiber and is then dispersed by a grating inside the spectrometer. Signal intensity is quantified via a CCD array or photomultiplier device. The most commonly used instrument are the so-called passive DOAS instruments, which use scattered skylight as a light source. The plume absorption spectrum is compared with an additional spectrum taken outside the plume under nearly identical conditions to correct influences of atmospheric background absorptions and the solar spectral structure (Fraunhofer lines). Today portable Multi-Axis-DOAS (MAX-DOAS) instruments are a widespread instrument in volcanic plume investigations yielding many observations of BrO alongside SO_2. Details are described in e.g., Hönninger et al. (2004), Bobrowski et al. (2007), Bobrowski and Platt (2007), and Gliß et al. (2015). Zenith-sky pointing DOAS instruments can be deployed whilst traversing underneath the plume to yield total column amounts across a transect, which in combination with wind-speed estimates provides total SO_2 and BrO fluxes. Traverses have been undertaken by foot, car, ship, and even by UAVs in inaccessible areas (e.g., McGonigle et al., 2002; Galle et al., 2003; López et al., 2013; Rüdiger et al., 2018b).

TABLE 1 | Overview *in situ* plume bromine sampling techniques.

Sampling technique		Species	Phase	References e.g.
Alkaline Traps	Drechsel bottle	Acidic species	Gas + particle	Wittmer et al., 2014
	Raschig Tube	Acidic species		Wittmer et al., 2014
	Coated Filter	Acidic species		Aiuppa et al., 2005
Denuder	Coating: 1,3,5-trimethoxybenzene	Halogen atom with the oxidations state +1 or 0 (e.g., Br_2 or BrCl)	Gas	Rüdiger et al., 2017
Particle	Filter	Particulate	Particle	Zelenski et al., 2013
	Cascade impactor	Particulate	Particle	Ilyinskaya et al., 2010

Imaging of plumes with SO_2-cameras (see e.g., Mori and Burton, 2006; Kern et al., 2015; McGonigle et al., 2017) enables to spatially map complex plumes at high time resolution (<1 s). Imaging of volcanic plume BrO has been achieved using Imaging DOAS (IDOAS). Spatial resolution is generated by spatial and spectrally resolved vertical columns applying a two dimensional detector and by horizontally scanning gaining the second spatial dimension (Lohberger et al., 2004; Louban et al., 2009). However, the temporal resolution to record a single image by this method is in the order of minutes, much slower than the fast (seconds) plume chemical and physical (dilution) processes. The BrO image obtained is only an average. Ongoing development of Fabry Perot Interferometers (FPI; Kern et al., 2010; Kuhn et al., 2018) may enable fast imaging of BrO in the future with a temporal resolution similar to SO_2 cameras (<1 s).

Beside portable instruments, instrument networks for permanent and automatic monitoring of several volcanoes by DOAS instruments have been created [NOVAC, (Galle et al., 2010); FLAME, (Burton et al., 2009), FLYSPEC, (Businger et al., 2015)]. Typically instruments are installed 5–10 km downwind of the crater observing plumes with an age of about 10–30 min (Galle et al., 2010). Further satellite ultraviolet instruments like GOME-2 (Global Ozone Monitoring Experiment), OMI (Ozone Monitoring Instrument) and the recently launched TROPOMI (Tropospheric Monitoring Instrument) enable BrO (and SO_2) monitoring in the troposphere and stratosphere on a global scale. Main differences between satellite instruments are spatial resolution and overpass time (for details see e.g., Theys et al., 2011; Carn et al., 2013; Hörmann et al., 2013). Systematic analysis of GOME-2 satellite observations of volcanic BrO are presented from volcanic eruptions entering the troposphere (Heue et al., 2011; Rix et al., 2012), and upper troposphere–lower stratosphere region (Theys et al., 2011; Hörmann et al., 2013). Due to the spatial resolution (100's km, reaching 10's km for the new TROPOMI instrument), observations are typically available for somewhat aged eruption plumes. Interpretation of such data is made more complicated because total bromine measurements are often not available and for commonly investigated plume ages >day, SO_2 might not be a reliable conservative plume tracer anymore. We focus our discussion of volcanic bromine speciation on ground based and airborne measurements made on the volcano flank (relatively close to the emission source) by remote sensing (DOAS), *in situ* methods, and associated numerical modeling studies.

Model Application

The volcanic plume is a diverse environment with dynamic variability in temperature, humidity, aerosol loading, and chemistry. Because of this, modelers typically employ separate techniques to describe phenomena at the vent (high-temperatures) and at ambient atmospheric conditions downwind (low temperatures). Numerical models of volcanic plume chemistry have been developed and applied at both high-temperature and low-temperatures. Comparison of model simulations to plume observations provides a wider context to improve our understanding of bromine evolution in the plume and to forecast impacts of bromine chemistry. Calculations identified that volcanic gases undergo high-temperature interactions followed by low-temperature reactions in the downwind plume that has been mixed with ambient air and cooled to ambient temperatures (Gerlach, 2004; Bobrowski et al., 2007; Roberts et al., 2009).

Model Initialization – High-Temperature Near-Vent Conditions, Dilution, and Aerosols

Following the discovery of BrO in a volcanic plume (Bobrowski et al., 2003) thermodynamic equilibrium models were applied at high-temperature to forecast bromine speciation. However, these were not able to simulate bromine monoxide to sulfur dioxide (BrO/SO_2) ratios (10^{-4} mol/mol) observed downwind from the crater (Gerlach, 2004). Rather, the predicted BrO/SO_2 ratios at the vent (10^{-8}) are consistent with the observation that BrO is often not detectable at the crater rim (see also section Dependence on Plume Age–Temporal Evolution).

Numerical models of atmospheric chemistry were then adapted to volcanic plume environments and/or newly developed and applied to forecast the plume halogen chemistry at ambient-temperatures. These model simulations were able to reproduce measurement results (e.g., BrO/SO_2 downwind from the crater). Three key aspects to the initialization of atmospheric chemistry models of volcanic plume halogen chemistry are: (1) the high-temperature near-vent conditions, (2) dilution (that controls entrainment of background air), and (3) volcanic aerosols.

For near vent conditions, it is assumed that near the emission source volcanic gases mix with atmospheric gases and undergo high-temperature chemistry. If reaction kinetics proceed faster than plume dilution a thermodynamic equilibrium may be assumed. This equilibrium systems depend on pressure, temperature (magmatic and ambient) and oxygen fugacity (P-T-fO_2) conditions and have been applied to calculate the composition of the "effective source region" (Gerlach and Nordlie, 1975; Gerlach, 2004; Martin et al., 2006; Bobrowski et al., 2007). One of the most common used thermodynamic equilibrium models is HSC Chemistry (Outokumpu Tech, Finland). A free-energy minimization algorithm is used to calculate molecular equilibrium compositions of gas mixtures. The estimated model input data are based on crater rim or fumarole measurements and include temperature and pressure as well as a starting elemental plume composition. This is based on mixing the observed composition of volcanic gases with air (N_2, O_2, Ar), for which the proportion of mixing between atmospheric and magmatic gases (V_A:V_M) must be assumed. Thermodynamic modeling of the hot plume-air mixing predicts that a V_A:V_M >0 ambient air oxidizes gases like H_2S and H_2 and produces small quantities of reactive halogen species such as Br, BrO, Cl and ClO, as well as relatively high quantities of HO_X (hydrogen oxide radicals) and NO_X (NO, NO_2 and combinations) (Gerlach, 2004; Martin et al., 2006). Thermodynamic modeling also predicts the high-temperature formation of SO_3 that is a precursor to sulfate aerosols (see also section Bromine Explosion). The output from the thermodynamic models is then used as input ("the effective source region") to atmospheric chemistry models that simulate halogen processes in the downwind plume at ambient temperatures. The high-temperature composition of the near vent plume is crucial for the initialization of low-temperature kinetic models: the radicals generated accelerating the onset ("kick-start") of halogen cycling at ambient temperatures, hence can affect plume evolution downwind from the crater.

However, the high-temperature near-vent conditions ("effective source region") remain a source of uncertainty in the initialization of low-temperature models of the plume halogen chemistry. The high-temperature modeling involves several unverified assumptions since high-temperature conditions are hard to constrain by direct measurements. For example, V_A:V_M in the near-vent plume exerts a strong influence on the predicted composition but is somewhat arbitrarily chosen: early studies used 40:60, and later on 15:85, 10:90 and 5:95. For some processes assumptions of the thermodynamic equilibrium seem to be inappropriate [e.g., re-equilibration of H_2S (Martin et al., 2009), H_2 (Aiuppa et al., 2011) or formation of NO_X from background N_2 that is likely kinetics limited due to the high bond strength for N_2 (Martin et al., 2012a)]. At V_A:V_M $= 40$:60, high levels of Cl radicals are predicted to form, that subsequently act to rapidly destroy H_2S in the atmospheric chemistry models. However, measurements by Aiuppa et al. (2007) did not show a decrease of H_2S as a function of distance to the emission source (0.1–1 km). Measurements of HO_2 and OH are very rare even though they play an important role in the atmospheric chemistry/halogen reaction cycles. OH radicals can be measured by very high-resolution active DOAS instruments (Platt et al., 1988) or by laser-induced fluorescence (LIF). Indirect detection of HO_2 is possible by titrating HO_2 with NO to form OH, which can be detected by LIF. Subtraction of the measured OH background then yields HO_2 (Hard et al., 1984; Brune et al., 1995). However, the power requirements and large size of such measurement techniques for OH and HO_2 generally limit their use on the volcano, restricting their potential applicability to aircraft measurements of the (typically more aged) plume. One of those examples is the airplane measurements of the eruptive plume of Mt Hekla, Iceland in 2000 (Hunton et al., 2005). No measurements are available, to the authors' knowledge, in the proximity of volcanic emission sources.

When the plume reaches the crater rim, more ambient air is entrained and the plume cools to ambient temperatures. The background air contains oxidants (HO_X, NO_X, O_3) whose entrainment into the plume affects the plume chemistry. Therefore, important controls on the halogen evolution in the downwind plume are the rate or extent of dilution and nature of the background atmosphere. Beside latitude, longitude and altitude dependent parameters (e.g., temperature, time of the day) more polluted and NO_X-rich atmosphere may need to be considered for some locations. In contrast to emissions entering cleaner free tropospheric conditions like for many high altitude volcanoes in the Andes, impacts of other environmental emissions on the plume chemistry have to be considered close to large cities or for instance, for volcanic emissions entering the planetary boundary layer like it is the case for Stromboli in the Mediterranean, or Masaya in Nicaragua. Dilution of the downwind plume can be represented by simple dispersion parameterizations such as Pasquill-Gifford or can be adapted to reproduce reported plume dilution rates.

Aerosol particles in volcanic plumes are highly acidic, often sulfate-rich, and include both primary aerosol (directly emitted) and secondary aerosols (e.g., formed from the atmospheric oxidation of volcanic SO_2). Volcanic aerosols can be measured by *in situ* offline time-averaged sampling using filter packs (Allen et al., 2002; Mather et al., 2003) or *in situ* real-time sampling by optical particle counters (Allen et al., 2006) and by remote sensing with sun-photometers (Watson and Oppenheimer, 2000; Roberts et al., 2018). The role of aerosol in partitioning between the gas phase and particles is considered by equilibrium models AIM (Aerosol Inorganic Model; Wexler and Clegg, 2002; Martin et al., 2012b) or MOCCA (Model of Chemistry in Clouds and Aerosols in MISTRA; Sander and Crutzen, 1996; Vogt et al., 1996; von Glasow, 2000). Aerosols catalyze heterogeneous reactions that have a crucial impact on plume halogen chemistry (see section Bromine Explosion). This is demonstrated by model simulations that can only reproduce downwind observations of BrO/SO_2 when volcanic aerosol is included. Reactions of halogens on volcanic aerosol are thus a key element in the atmospheric models of volcanic plume halogen chemistry outlined below.

Modeling Plume Chemistry – Low-Temperature Kinetic Models

In the downwind plume low-temperature kinetic models investigate plume chemistry. Mainly two low-temperature kinetic 0/1D models have been developed: MISTRA (simulates an advected column of air) and PlumeChem (in expanding box or multi-grid box modes). Recently also the regional 3D model CCAT-BRAMS was applied to study volcanic halogen chemistry. All these models take into account detailed atmospheric chemistry schemes including reactive halogens (bromine and chlorine) with gas-phase photolytic and gas-aerosol reactions. These kinetic models of volcanic plume chemistry at ambient temperatures used an "effective emissions source" (Bobrowski et al., 2007) in their inputs based on thermodynamic equilibrium models (HSC) representations of the near-vent high-temperature chemistry.

The numerical model MISTRA simulates a column of atmosphere that is divided into multiple layers. This column is moving over a volcano where the plume is emitted as a puff into few adjacent model layers at a given height. This column of air is then advected downwind according to an assumed wind speed (Bobrowski et al., 2007), whilst the plume puff disperses vertically in the column. Horizontal dilution is taken into account with a simple parameterization, assuming that the horizontal evolution of the plume corresponds to a Gaussian plume. MISTRA was originally developed for microphysics in the marine boundary layer including a hydrodynamic part, a radiation code and a parameterization of the turbulence by means of a first-order. The turbulence closure was based on the model of Mellor and Yamada (1982) and the meteorological core was developed by Bott et al. (1996). von Glasow (2000) extended MISTRA with a module that describes chemical reactions of the gas phase, aerosol particles and cloud droplets (this extension was based on MOCCA). So far, collision and coalescence of aerosol and new particle formation are not considered in the model. The one-dimensional MISTRA has been applied in volcanic plumes with focus on halogen mechanisms by Aiuppa et al. (2007), Bobrowski et al. (2007), von Glasow (2010), Bobrowski et al. (2015), and Surl et al. (2015).

PlumeChem is a 0D/1D box model that also uses a Lagrangian-type approach to follow a volcanic plume puff with time or distance downwind according to an assumed wind-speed (Roberts et al., 2009, 2014b, 2018; Kelly et al., 2013). The model simulates chemical reactions in the plume as it disperses and entrains background air. This approach is similar to that applied to modeling the chemistry of ship-plumes (Song, 2003). In the single grid box mode, plume dispersion is simulated by a single grid box (an ellipse) that expands as background atmospheric air is entrained into it. In the multiple grid box mode, the plume is described by a series of chemical boxes in a row, i.e., plume chemistry is spatially resolved horizontally. Plume dispersion is represented in the vertical direction by box-growth, whereas it is simulated in the horizontal direction by mixing between adjacent boxes. The plume dispersion is modeled assuming a Gaussian plume dispersion and parameters are given by Pasquill-Gifford parameterizations, or can be user-defined to approximate actual observed dispersion of plume tracers (Kelly et al., 2013). The PlumeChem model includes detailed volcanic plume halogen atmospheric chemistry similar to MISTRA, but the gas-aerosol reactions as treated using reactive uptake coefficients on an aerosol surface area rather than directly simulating the aqueous-phase chemistry. This reduces the computational requirements of the model, and is the approach also used in 3D models as discussed below. Considered model parameters are the chemical composition of model initialization, the aerosol loading and plume dispersion.

Recently a non-hydrostatic mesoscale atmospheric chemistry model, CCATT-BRAMS, was developed to simulate volcanic plume halogen chemistry and regional impacts in a Eulerian-type study (Jourdain et al., 2016). The BRAMS model has been used for studies of planetary boundary layer, operational weather forecasting and climate and includes parameterizations of physical processes such as surface–air exchanges, turbulence, convection, radiation and cloud microphysics that are particularly well adapted for tropics. Coupling to CCATT enables the transport, chemical evolution, emission and deposition of molecules and aerosol particles (Freitas et al., 2009; Longo et al., 2013). The CCATT preprocessor was adapted to include volcanic emissions, and the chemistry scheme developed to include volcanic halogens. Two-way nested grids are used to capture plume processes at the small-scale (<1 km) with larger grids simulating the tropospheric impacts of the dispersed plume at the regional scale (>1,000 km). A similar development has also been undertaken to include volcanic halogens in the WRFChem model (Surl et al., 2014).

First steps have also been made to introduce volcanic halogens and their tropospheric plume chemistry into global models. A major issue is the coarse resolution of global models (typically 100–200 km). This causes the volcanic emissions to be too rapidly diluted compared to reality. Global models, therefore, cannot resolve the volcanic plume halogen processes that occur at much smaller scales (km), particularly in young plumes/near-to-source. Grellier et al. (2014) proposed a sub-grid-scale parametrization approach to represent the near-source halogen chemistry plume processes in a global tropospheric model. Future work should further develop the volcanic plume halogen chemistry in such approaches.

The comparison of the currently available model results with one another and with measured observations is usually difficult because starting conditions vary between models due to consideration of different data arrays and volcanoes in model applications. In general, total emissions and their composition may vary immensely over just a few days or between different volcanoes. Furthermore, measurement data sets at different distances downwind are usually not taken simultaneously. The model parameter space is vast. Sensitivity studies show how variability in initial plume compositions (e.g., variable HBr emissions, plume composition, mixing or high-temperature interactions of the young plume in the source region) affect downwind BrO formation (e.g., Roberts et al., 2014b).

CURRENT UNDERSTANDING

Overview of BrO/SO_2 and Br/S Field-Measurements

Upon the discovery of BrO in the volcanic plume of Soufriere Hills, Montserrat (Bobrowski et al., 2003) detection of BrO in many volcanic plumes globally shows that BrO formation is a common process in volcanic plumes including different settings of arc, rift and hotspot volcanoes as shown below.

Nevertheless, data sets are still very limited regarding the geographical distribution and temporal variability of bromine emissions. **Figure 1** and the **Supplementary Table 1** summarize all available volcanic plume bromine data since 2003. Earlier results are already summarized elsewhere (e.g., Gerlach, 2004). **Figure 1** gives an overview on particulate and gaseous bromine to sulfur (Br/S) and BrO/SO_2 ratios, across different volcanological settings (arc, hotspot and rift).

Bromine species are typically reported relative to sulfur, to enable distinction between plume chemistry and dilution effects. Assuming slow in-plume oxidation, SO_2 will act as a plume tracer on the relatively short observation timescales (typically minutes to hours) of measurements on the volcano flank. Indeed, volcanic plume SO_2 can often be considered to be conserved over the short distance between "source" and "downwind" observation points on the volcano flank because the acidity of the volcanic aerosol in the plume, prevents the SO_2 uptake, and because SO_2 concentrations are in excess of most oxidants (McGonigle, 2004; von Glasow et al., 2009; Galeazzo et al., 2018). Variations in bromine/sulfur observed at just one fixed measurement point might be a result from changes in emission composition. But the assumption of SO_2 as a plume tracer may not always be valid for measurements of very dilute or aged plumes (in the order of days), e.g., as may be detected by satellites.

The Br/S emissions in alkaline-trap samples are assumed to represent total bromine, Br_{total}. **Figure 1** shows that Br/S values (displayed as blue circles) are generally higher than BrO/SO_2 ratios (red crosses) measured by DOAS instruments. This is consistent with the partial conversion of emitted bromine into BrO, Particulate measurements tend to report higher Br/S values (green dots) in comparison to gas ratios or gas-particle mixtures. Increased Br/S ratios in particles may demonstrate enhanced bromine partitioning into particles compared to sulfur, or unusually low sulfate for the few volcanoes studied e.g., Erebus, Antarctica (Ilyinskaya et al., 2010).

Several factors may explain the variability in **Figure 1**, including:

- Degassing derived from different magma types and volcanic (tectonic) environments e.g., deep or shallower sources associated with melt generation and degassing systems or crustal fluids (Pyle and Mather, 2009; Mather et al., 2012) as discussed below.
- Different states of volcanic activity such as eruptive or quiescent degassing (section Forecasting–Correlating Volcanic Plume Composition to Volcanic Activity).
- Different distances to the source and therefore different extents to which bromine has been chemically transformed into BrO as a function of plume age (section BrO Evolution in Volcanic Plumes).
- Also, processes such as scrubbing of water-soluble compounds may impact Br/S (Symonds et al., 2001; Textor, 2003).
- Uncertainties in individual measuring techniques (section Measurement Techniques), as discussed below.

Considering subaerial actively degassing volcanoes, arc volcanoes are the most abundant tectonic setting and therefore provide the majority of data. The volcanic Br/S shows a very large variation over five orders of magnitude. This is probably primarily due to variation in bromine abundance of the arc volcano plumes.

Hotspot volcanoes have typically been described as halogen-poor (e.g., Pyle and Mather, 2009). However, we find that the available hotspot volcanoes fall in the same range of the data available for arc zones (**Figure 1**). Note that the representation of the samples formerly and still up to now is not statistically relevant. Hawaii falls at the very low end (about 0.3×10^{-4})

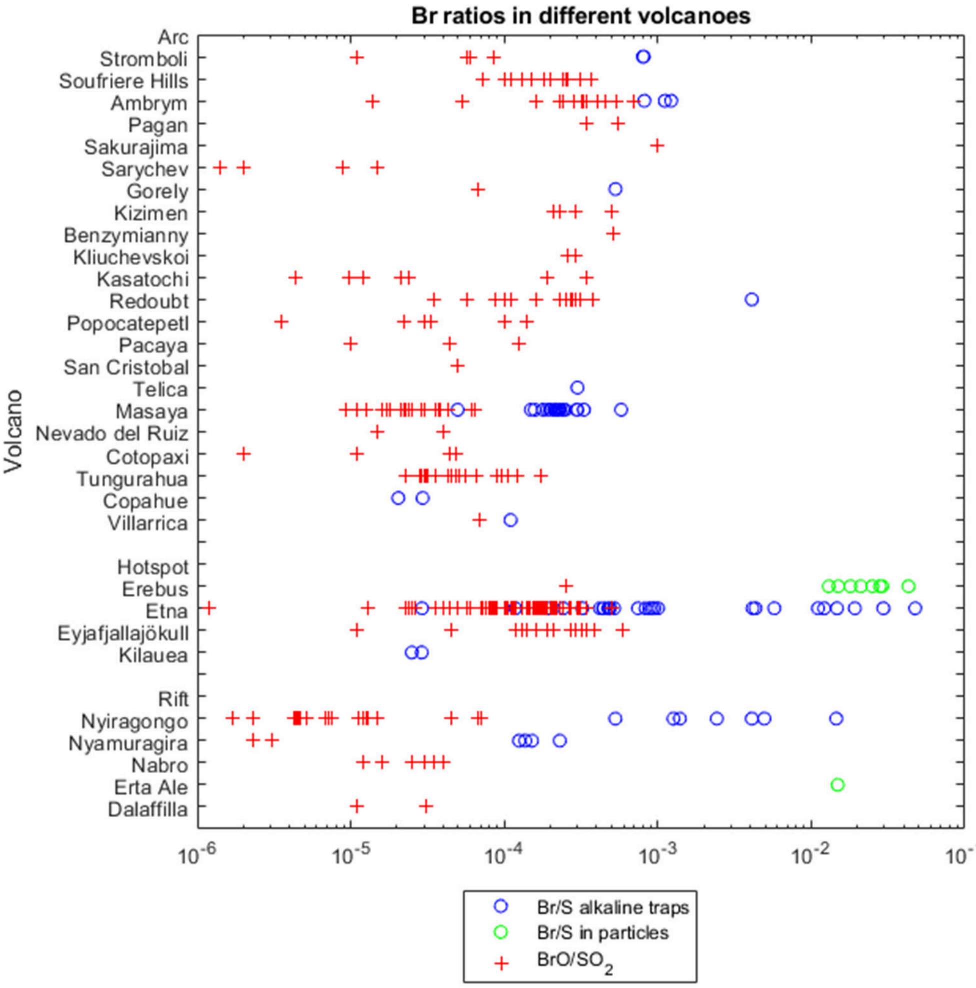

FIGURE 1 | Volcanoes and their bromine emissions. In blue circles Br/S ratios of total amounts measured by alkaline traps, in red crosses BrO/SO_2 ratios measured by DOAS instruments, in green circles Br/S ratios of total amounts in particles measured by particle filters. Data from **Supplementary Table 1**, x-axis follows a logarithmic scale. Variability may be due to magma types and volcanic (tectonic) environments, volcanic activity, distance to the source and chemical aging, or measurement uncertainties (see section Overview of BrO/SO_2 and Br/S Field-Measurements).

but Mt Etna, Sicily, Italy is at the high end of Br/S ratios (up to 0.05). There may be influence of recycled oceanic crust as a halogens source in some hotspot cases, e.g., Eyjafjallajökull, Iceland (Moune et al., 2012).

Intriguingly, the few samples taken from rift volcanoes tend to show lower BrO/SO_2 ratios, but no clear differences for Br/S ratios in comparison to arc and hotspot volcanoes.

Within the arc volcano category, the bromine abundances of southern American volcanoes seem to lay at the lower end of the Br/S range. Maximal BrO/SO_2 values for South American volcanoes are below the mean of other available arc volcanic values, with the exception of Tungurahua (max. 1.7×10^{-4}). Lowest global Br/S values since 2003 were found for Copahue's plume (0.20×10^{-4} and 0.29×10^{-4}). Although for Japanese arc volcanoes Gerlach (2004) cited also low Br/S ratios (Tokachi 0.25×10^{-4}, Kudryavy 7.8×10^{-4}), BrO/SO_2 obervations by Lee et al. (2005) at Sakurajima are a bit in contrast to those earlier determined values in Japan. However, some caution must be applied to the comparisons regarding the methods, because most of the observations of the South American volcanoes are ground-based, in contrast, many observations of the Kamchatka arc (Kizimen, Benzymianny, Kliuchevskoi) were gained by satellite measurements of potentially more aged plume.

Uncertainties in individual measuring techniques were discussed in section Measurement Techniques. Measurements of trace bromine emissions can be particularly challenging close to the detection limit. Also, high gas concentrations can limit the accuracy of the results e.g., due to saturation of alkaline filter packs (see section *In Situ*–Application of Instruments in the Plume). In **Figure 1** the high Br/S ratios of up to 475×10^{-4} measured on Etna, Sicily, Italy in 2005 (Martin et al., 2008) are significantly greater than Br/S observations from January to October 2004 where all data points are below 100×10^{-4} (Aiuppa et al., 2005), as well as Br/S on Etna reported by Oppenheimer et al. (2006) and Wittmer et al. (2014). Whilst change in volcanic activity could be one explanation, oversaturated filter samples might be a conceivable explanation of the exceptional high Br/S ratios by Martin et al. (2008).

Plume Chemistry and the Formation of Reactive Bromine

Bromine Explosion

Since observations show BrO is not directly emitted from the volcano (see section Dependence on Plume Age–Temporal Evolution), model studies were undertaken to explain the measured BrO content and its formation process.

Thermodynamic studies predict that halogens are mainly degassed as hydrogen halides, e.g., HBr (Symonds et al., 1994). Gerlach (2004) calculated that BrO in volcanic plumes must originate from the enhancement of reactive halogen species by oxidation of HBr and HCl through autocatalytic cycles involving heterogeneous chemistry. Numerical models of volcanic plume atmospheric chemistry were then developed to explain the measured BrO content and its formation process. Volcanic BrO formation is currently assumed to occur through a bromine reaction cycle, the so-called "bromine explosion," that has been previously identified in the polar and marine boundary layers and above salt plains (Barrie et al., 1988; von Glasow and Crutzen, 2003; Saiz-Lopez and von Glasow, 2012).

The most relevant gas phase reaction of HBr is the formation of Br radicals with OH radicals (R1; von Glasow, 2010).

$$\mathrm{HBr + OH \rightarrow Br + H_2O} \qquad \text{(R1)}$$

High-temperature chemistry is suggested to accelerate the start of low-temperature cycles by elevated concentrations of HO_X derived from high-temperature chemistry in the near-vent plume that enhance the initial formation of Br radicals via R1 (Oppenheimer et al., 2006; Martin et al., 2009; Roberts et al., 2009; von Glasow, 2010). Therefore, small amounts of BrO (R2) and subsequent formation of HOBr (R3) are already expected to be formed in the high temperature zone as calculated by thermodynamical equilibrium models.

$$\mathrm{Br + O_3 \rightarrow BrO + O_2} \qquad \text{(R2)}$$

$$\mathrm{BrO + HO_2 \rightarrow HOBr + O_2} \qquad \text{(R3)}$$

However, those gas phase reactions alone cannot explain the measured abundance of volcanic BrO. Calculations predict that heterogeneous reactions enhance BrO formation compared to gas phase oxidation. Indeed, plume model simulations that do not include volcanic aerosols cannot reproduce the downwind BrO. The key reaction is the reactive uptake of HOBr (reacting with aqueous HBr in the acidic aerosol) to form the reactive halogen Br_2 (R4).

$$\mathrm{HOBr + H^+_{(aq)} + Br^-_{(aq)} \xrightarrow{aerosol-surface} Br_2 + H_2O_{(aq)}} \qquad \text{(R4)}$$

Br_2 has low solubility in the aqueous acidic sulfate particles and thus partitions into the gas phase where it is photolyzed into Br radicals (R5).

$$\mathrm{Br_{2(g)} + h\nu \rightarrow 2Br} \qquad \text{(R5)}$$

Overall, this repeated sequence R2–R5 each time doubles BrO concentrations and is therefore known as the "bromine explosion" (**Figure 2**). Due to its autocatalytic nature, it can produce a very rapid increase in BrO concentrations.

The sequence can be terminated by the loss of Br due to its conversion back to HBr (R6–R7; von Glasow and Crutzen, 2003; Roberts et al., 2009).

$$\mathrm{Br + HCHO \rightarrow HBr + HCO} \qquad \text{(R6)}$$

$$\mathrm{Br + HO_2 \rightarrow HBr + O_2} \qquad \text{(R7)}$$

In the following, we discuss the importance of photochemistry, the role of aerosols, the production of HNO_2 (von Glasow, 2010) or HNO_3 (Roberts et al., 2009) predicted by models, the depletion of tropospheric ozone (section Causes and Effects of O_3 Depletion), interhalogen, chlorine and iodine plume chemistry (section Interhalogen, Chlorine, and Iodine Plume Chemistry), and conversion of mercury into a more toxic and easily deposited form (von Glasow, 2010; von Glasow et al., 2015) in relation to reactive bromine formation in volcanic plumes (section Mercury in Volcanic Plumes).

Importance of photochemistry

Photochemistry plays a key role for doubling Br radicals in the autocatalytic cycle of the bromine explosion (R5). BrO measurements made round–the–clock at Masaya volcano, Nicaragua, confirmed that photolytic reactions are necessary for the formation of BrO (Kern et al., 2009). Kern et al. (2009) observed significant BrO during daytime whereas BrO was below the detection limit during night. Other measurements were performed at Mt Etna, Sicily, Italy in the early morning during and shortly after sunrise (Gliß et al., 2015; Butz et al., 2017). The data shows an increase of the BrO/SO_2 ratio within the first hour of increasing sunlight and a constant ratio afterward.

Influence of aerosol or humidity

Regarding volcanic halogen emission estimates, the non-reactive uptake of HCl and HBr onto sulfate particles should be considered as it may overprint magmatic HX/SO_2 gas ratios. Significant uptake could lead to underestimation of volcanic halogen emissions if the particle phase is not taken into account alongside the gas phase (Pyle and Mather, 2009).

Aerosols provide surface area promoting heterogeneous reactions within or on the particles and therefore have a key role in volcanic BrO formation (R4), the cycling, and speciation of bromine in volcanic plumes. The volcanic plume environment is abundant in particles, including both primary and secondary aerosols (see also section Model Initialization–High-Temperature Near-Vent Conditions, Dilution, and Aerosols). Primary sulfate is emitted at up to about 1% (mol/mol) of the volcanic SO_2 emission. One mechanism for primary sulfate formation is the high-temperature formation of SO_3 radicals in the near-vent plume, that upon cooling are converted into H_2SO_4 in the presence of water vapor. Secondary sulfate aerosol particles are formed from the oxidation of SO_2 to H_2SO_4 as the plume disperses into the background

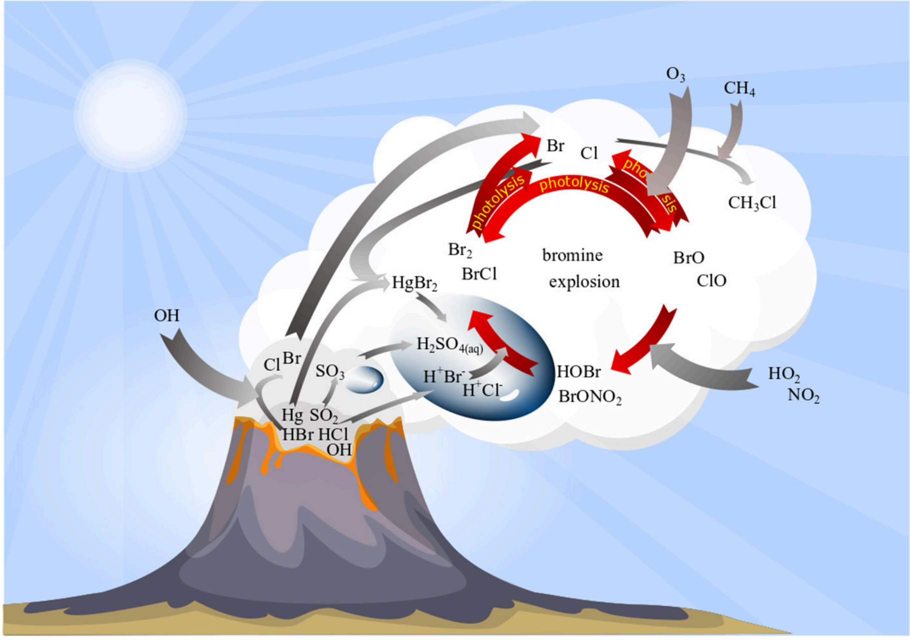

FIGURE 2 | Schematic overview on bromine plume chemistry. Volcanic emissions (dark gray cloud) are processed in high-temperature reactions forming minor amounts of halogen radicals (light gray cloud). Bromine radicals "kick-start" an autocatalytic cycle ("bromine explosion") that converts emitted HBr into BrO via multistep reactions including gas and particle phase and leads to O_3 depletion (for details see section bromine explosion).

atmosphere. Oxidation can occur by gas-phase reaction with OH, and aqueous-phase reaction with ozone, H_2O_2, and O_2 with transition metal ions. In volcanic plumes, catalysis by metallic ions might significantly enhance oxidation of SO_2 with O_2 (Galeazzo et al., 2018). H_2SO_4 is highly hygroscopic and can create aqueous $H_2SO_{4(aq)}$ droplets via homogeneous nucleation or condense onto existing accumulation mode particles (Seinfeld et al., 1998; Mather et al., 2006; Martin et al., 2012b; Galeazzo et al., 2018).

The surface area of hygroscopic sulfate-rich particles is a strong function of humidity and temperature conditions. However, as the abundant amounts of aerosol provide a substantial surface area for reactions, the formation of BrO may not be limited by aerosol availability, particularly near-downwind. Bobrowski and Giuffrida's studies (Bobrowski and Giuffrida, 2012) at 6 km downwind did not find influences on the BrO/SO_2 ratio due to seasons, relative humidity, and wind velocities. Although higher relative humidity and aerosol with high sulfuric acid concentrations are proposed to increase the probabilities and rates of halogen reactions, they seem not to be a real limiting factor in volcanic plumes. However, Dinger et al. (2018) identified correlations between observed BrO/SO_2 molar ratios and relative humidity (correlation coefficient 33%) by investigating periodic patterns in the BrO/SO_2 ratio of Cotopaxi's volcanic plume.

Nitrogen compounds

There is still a great deal of uncertainty as to whether nitrogen compounds NO_Y (NO_X and oxidation products including organic nitrogen compounds) are emitted or formed in volcanic emissions and which products are built by the interaction of bromine and nitrogen compounds in volcanic plumes. In polluted environments, NO_X might be present in the atmosphere and enter volcanic plumes upon dilution. Mather et al. (2004a) observed nitric acid at the volcano crater rim but proposed not a direct emission of nitric acid. Rather NO is predicted to be formed thermally by equilibrium models at near vent conditions from atmospheric N_2 and O_2 (Gerlach, 2004; Martin et al., 2006). It is assumed that in the volcanic plume at ambient temperature NO will be rapidly oxidized with O_3 to NO_2 (von Glasow, 2010). Further oxidation pathways (R10–R11 below), or reaction of NO_2 with OH may then produce HNO_3.

von Glasow (2000) suggested a reaction of Br radicals with volcanic NO_2 immediately after plume release of $BrNO_2$ (R8) and due to photolysis a lifetime of about 150 s (R9). Since large amounts of NO_2 are proposed in the plume the continuous reformation and accumulation of $BrNO_2$ is assumed. This reduces the amount of bromine available to form BrO.

$$\mathrm{Br} + \mathrm{NO_2}(+\mathrm{M}) \rightarrow \mathrm{BrNO_2}(+\mathrm{M}) \qquad \text{(R8)}$$

M is a chemically inert collisional partner.

$$\mathrm{BrNO_2} + h\nu \rightarrow \mathrm{Br} + \mathrm{NO_2} \qquad \text{(R9)}$$

In contrast, Roberts et al. (2014b) suggest the volcanic plume $BrNO_2$ lifetime will be short. Roberts et al. (2009) suggest rather a formation of $BrONO_2$ due to the reaction of BrO with NO_2 (R10). $BrONO_2$ rapidly reacts heterogeneous on volcanic aerosols producing HOBr that may immediately react via R4, forming Br_2 and nitric acid (R11). Under high aerosol conditions, $BrONO_2$ can thereby promote the "bromine explosion,"

$$BrO + NO_2(+M) \rightarrow BrONO_2(+M) \quad (R10)$$

$$BrONO_2 + H^+_{(aq)} + Br^-_{(aq)} \rightarrow Br_2 + HNO_{3(aq)} \quad (R11)$$

However, the importance of these chemical pathways depends on the abundance of NO_X in volcanic plumes. As mentioned above a key question is whether NO_X is generated from volcanoes or simply being entrained into the plume by dilution. Although the formation of NO_X is predicted by equilibrium models, a high-temperature kinetic model study found that the time-scale to produce significant quantities of thermal NO_X formation is too slow in the near-vent plumes (Martin et al., 2012a). However, several observations of elevated NO_X and NO_Y in volcanic plume have been reported: an overview is given in Martin et al. (2012a). For example, aircraft measurements were able to identify volcanogenic HNO_3 and HO_2NO_2 (Oppenheimer et al., 2010). However, this study did not observe any NO_X in the downwind plume. They assume that near-source NO_X was quickly oxidized to HNO_3 and HO_2NO_2. HNO_3 has been reported in several volcanic plumes (e.g., Mt Etna, Sicily, Italy; Voigt et al., 2014), Masaya, Nicaragua; Mather et al., 2004b). However, Martin et al. (2010) did not detect any HNO_3 at Masaya in 2009. For some eruptions (particularly explosive), volcanic-induced lightning could be a source of NO_X in parts of the plume. For volcanic plumes entering polluted background atmospheres, the entrained air can be a source of NO_X (and NO_Y) as the plume dilutes. Overall there remain uncertainties in the sources of volcanic plume NO_Y, and hence the role of coupled nitrogen-bromine chemistry in volcanic plumes and its importance for Br-speciation.

Mercury in volcanic plumes

Mercury is emitted from volcanoes, but is also present in the background atmosphere, predominantly in the inert form Hg(0). It is believed that reactive bromine (as well as chlorine, see section Interhalogen, Chlorine, and Iodine Plume Chemistry) species might promote conversion from relatively inert Hg(0) (emitted as well as atmospheric mercury) into more reactive and toxic oxidized mercury [Hg(II), R12–R13], although observations of volcanic mercury transformations are few and somewhat inconclusive to date. Oxidized mercury is soluble and partitions into aerosol particles so can be more easily deposited near the volcano (R14).

$$Hg^0 + Br\,(+M) \rightarrow HgBr\,(+M) \quad (R12)$$

$$HgBr + Br\,(+M) \rightarrow HgBr_2\,(+M) \quad (R13)$$

$$HgBr_{2(gas)} \leftrightarrow HgBr_{2(aq)} \quad (R14)$$

There are uncertainties in mercury chemistry in volcanic plume reactions, notably whether a back-reaction can reform inert Hg(0) from oxidized Hg(II), possibly involving photolysis, SO_2 and particles. Mercury concentrations are generally thought to be at sufficiently trace-levels that the mercury chemistry does not impact overall Br-speciation (Bagnato et al., 2007; von Glasow, 2010).

Causes and Effects of O_3 Depletion

Models predict the depletion of tropospheric ozone destroyed by the reaction sequence R2–R5 each cycle (e.g. Bobrowski et al., 2007; Roberts et al., 2009; von Glasow et al., 2009; Kelly et al., 2013; Surl et al., 2015). In addition, ozone loss occurs through a second cycle between the self-reactions of BrO (R15, R16). This rapid interconversion causes ozone loss in the plume at high halogen concentrations, and so can be particularly important in destroying ozone in the near-downwind (concentrated) volcanic plume.

$$BrO + BrO \rightarrow 2Br + O_2 \quad (R15)$$

$$BrO + BrO \rightarrow Br_2 + O_2 \quad (R16)$$

Note also that the reactions R15 and R16 will tend to reduce the abundance of BrO at high halogen concentrations and therefore can bring additional non-linearities to the chemistry of volcanic BrO formation. Determination of ozone in volcanic plumes by UV absorption is difficult due to high SO_2 concentrations (see **Table 2**). As both O_3 and SO_2 broadly absorb UV radiation, two or more simultaneous observations at different wavelengths are required to deconvolute SO_2 from O_3 by UV absorbance alone. Because many UV absorbance instruments employ a UV line source (frequently Hg vapor, 253.7 nm), additional treatments are needed to correct for SO_2 coabsorption. In those cases to avoid SO_2 interferences a CrO_3 scrubber is necessary to remove SO_2 from the inflow to the instrument (e.g., Schumann et al., 2011; Surl et al., 2015). Dual channel ozone instruments also yield accurate results in the presence of SO_2. These detect ozone by taking the difference between a "measurement" cell and "background" cell (with in-line ozone scrubber), therefore any SO_2 interference cancels out (Vance et al., 2010). In cases of large ozone depletion at low SO_2 the interference may be estimated using field-observations of SO_2 and subtracted in data post-processing (Kelly et al., 2013). Electrochemical concentration cells (ECCs) sense ozone as it reacts with a diluted solution of potassium iodide to produce a weak electrical current proportional to the ozone concentration of the sampled air. A negative cross-sensitivity (observed ozone destruction) on mole-per-mole-basis may be caused due to SO_2 (Vömel and Diaz, 2010). However, no interferences in volcanic applications are known with chemiluminescence-based techniques that measure O_3 by sensing light output from the reaction of O_3 with ethylene, although an overread of O_3 (few %) at high humidity may occur (Vance et al., 2010). Recently an Aeroqual instrument, WO_3 semiconductor, was used for ozone measurements, for which the most important cross-sensitivity in volcanic plumes is that of H_2S (Roberts, 2018). Time-averaged ozone measurements have also been made using diffusion tube passive sampling devices (Vance et al., 2010). These are filled with an adsorbing cartridge that has a highly specific irreversible chemical affinity to ozone (e.g., the "ozonolysis" of double bonds to form an aldehyde). In the lab, hydrazine is added to form an acid that can be detected via absorption.

Ozone loss due to heterogeneous reactions in the presence of halogens has already been observed in several tropospheric

TABLE 2 | Ozone measurement devices and their advantages and disadvantages for application in volcanic plumes.

instrumentation	Advantage	Disadvantage
UV absorption		High positive SO_2 cross-sensitivity
UV absorption + CrO_3 scrubber	No SO_2 cross-sensitivity	
Dual UV absorption + O_3 scrubber	No SO_2 cross-sensitivity	
Electrochemical concentration cell		Negative SO_2 cross-sensitivity
Chemiluminescence	No known interferences Response time <5s	High humidity causes O_3 overread
Diffusion Tubes	Highly specific	Poor time resolution (passive sampling)
WO_3 sensor	Small, low cost	H_2S cross-sensitivity

TABLE 3 | Overview of sampling campaigns on O_3 depletion in volcanic plumes.

Volcano	Instrumentation	% O_3 loss	Reference
Sakurajima	Dual UV absorption	n.a.	Lee et al., 2005; Surl et al., 2015
Augustine	Chemiluminescence	0–100, av 60	Vance et al., 2010
Etna	Diffusion Tubes	<70%	
	UV absorption + CrO_3	15–40	
Eyjafjallajökull	Dual UV absorption + O_3 scrubber	4–84, av 37	
Erebus	UV absorption	max 35	Oppenheimer et al., 2010
Redoubt	Dual UV absorption + O_3 scrubber	max 90	Kelly et al., 2013
Etna	UV + CrO_3 scrubber	15–45	Surl et al., 2015
Kilauea	WO_3 sensor	<5%	Roberts, 2018

n.a., not available.

volcanic plumes (see **Table 3**, for a discussion of halogen impacts on ozone in the stratosphere see section Introduction). Ozone in Kilauea's plumes was reported close to ambient levels in crater-rim emissions (Halema "uma"u) and only slightly depleted in the 10 km downwind plume (Pu‘u ‘Ō‘ō) (Roberts, 2018). This is consistent with Kilauea being a low halogen emitter. Large ozone depletions (several 10's%) were observed in the plumes of higher halogen emitters such as Mt Etna, Sicily, Italy and Mt Redoubt, Alaska (see **Table 3**). In general, the largest O_3 depletion was observed in the core of the plume and was correlated with volcanic gases (e.g. Kelly et al., 2013), with a maximum deficit of −30 ppbv and an average O_3 deficit reaching −12 ppbv at 20–40 min plume age. That is consistent with model simulations that reproduced ozone depletion in the core of the plume (Kelly et al., 2013). Observational and modeling results suggest that the conversion of volcanic Br emissions into reactive bromine are key controls in the depletion of tropospheric ozone downwind from the volcano. If ozone becomes entirely depleted in the plume this might in turn limit the partitioning of reactive bromine into BrO in the near-source (concentrated) plume, e.g., as suggested for conditions of extreme emissions and/or low background ozone concentrations (Jourdain et al., 2016). However, full depletion of ozone in a volcanic plume has only been observed in two measurements at Augustine in 1976 (Vance et al., 2010). Note that humidity might have an influence and is not considered here and that Hegg et al. (1976) reported a calibration accuracy of ±5% when the chemiluminscence technique was compared to ozone detection via potassium iodide. Reactive bromine is the principal cause of ozone depletion in volcanic plumes, but models predict that the interaction of BrO with reactive chlorine (or iodine) can augment the ozone loss.

Interhalogen, Chlorine, and Iodine Plume Chemistry

Chlorine

The bromine explosion can ultimately also lead to the production of reactive chlorine. First, studies of Roberts et al. (2009) using the AIM model (Wexler and Clegg, 2002) on gas-particle-partitioning for mean arc volcanic compositions (Gerlach, 2004) reported that Br_2 is the favored product in heterogeneous reactions (R4) for typical volcanic Br/Cl emission compositions, according to aqueous-phase equilibria (R18). However, depletion of plume HBr through the bromine explosion can significantly reduce HBr/HCl ratios (100–1,000 times lower than arc mean composition). Under these conditions, the reactive uptake of HOBr can lead to the formation of BrCl (R17) instead of Br_2 in R4.

$$\mathrm{HOBr} + \mathrm{H}^+_{(aq)} + \mathrm{Cl}^-_{(aq)} \xrightarrow{\text{aerosol}-\text{surface}} \mathrm{BrCl} + \mathrm{H_2O}_{(aq)} \tag{R17}$$

$$\mathrm{Br}^-_{(aq)} + \mathrm{BrCl}_{(aq)} \rightleftharpoons \mathrm{Br_2Cl}^-_{(aq)} \rightleftharpoons \mathrm{Br}_{2(aq)} + \mathrm{Cl}^-_{(aq)} \tag{R18}$$

Subsequent partitioning of BrCl (and Br_2) into the gas phase and photolysis produces Cl alongside Br radicals (R19) that can react with ozone (R20) and contribute to ozone loss (see also R5 and R2).

$$\mathrm{BrCl} + h\nu \rightarrow \mathrm{Br} + \mathrm{Cl} \tag{R19}$$

$$\mathrm{Cl} + \mathrm{O_3} \rightarrow \mathrm{ClO} + \mathrm{O_2} \tag{R20}$$

The reaction of ClO with BrO can lead to OClO (R21, Bobrowski and Platt, 2007; Gliß et al., 2015; Roberts et al., 2018).

$$\mathrm{BrO} + \mathrm{ClO} \rightarrow \mathrm{OClO} + \mathrm{Br} \tag{R21}$$

$OClO/SO_2$ has been reported to increase from below detection limit at the vent up to (3–6) × 10^{-5} at Mt. Etna, Sicily, Italy [BrO/SO_2: (1–5) × 10^{-4}; Bobrowski et al., 2007; General et al., 2015; Gliß et al., 2015] and (4–6) × 10^{-4} at Soufriere Hills, Montserrat [BrO/SO_2: (1–4) × 10^{-4}; Donovan et al., 2014]. Compared to bromine activation <1% HCl is converted into reactive chlorine, according to both models and observations (Gliß et al., 2015). The few field-data are too limited to determine further controls on OClO formation, although the increasing $OClO/SO_2$ is consistent with an in-plume formation pathway.

Recently, models have been able to reproduce volcanic OClO observations (Roberts et al., 2018), according to the HBr depletion and BrCl formation pathway. Models predict that bromine emissions and humidity can both impact OClO formation rates. For higher bromine emissions HBr may not become depleted immediately by the bromine explosion, leading to a later onset of BrCl formation and thus delayed rise in OClO/SO_2. Modeled OClO/SO_2 formation near downwind is enhanced at greater relative humidity because this enhances the aerosol surface that supports the heterogeneous reactions, leading to a more rapid bromine cycling and faster depletion of HBr and enabling BrCl formation (Roberts et al., 2018).

Kern and Lyons (2018) report observations of OClO (with BrO) at the plume edge, whilst only BrO is observed at the plume center. The measurements are very consistent with the horizontal spatial distribution of BrO-OClO predicted by Roberts et al. (2018). Kern and Lyons (2018) propose that measurements of OClO alongside BrO can help determine the degree of depletion of $Br_{(aq)}$ (and HBr) and therefore guide interpretation of BrO observations in terms of total bromine emission.

Importantly, the fact that Br_2 (or BrCl when HBr is depleted) are the preferential products released from the reactive uptake of HO_X (X = Br, Cl) and the fast reaction of Cl with methane (R22) prevents a self-amplifying cycle for chlorine oxides. Thus, HCl cannot become depleted by plume reactive halogen chemistry (unlike HBr).

$$CH_4 + Cl \rightarrow CH_3 + HCl \qquad (R22)$$

Iodine

Only a few studies are available that report about iodine in tropospheric volcanic plumes, although iodine chemistry is well-studied in marine environments (Saiz-Lopez and von Glasow, 2012 and references therein). Iodine is released as a trace emission in tropospheric volcanic plumes. For instance a total iodine to sulfur ratio (I/S) has been observed between (4–7) × 10^{-6} detected with filter packs at Etna, Sicily, Italy in 2004 (Aiuppa et al., 2005), (7–22) × 10^{-6} and (4–90) × 10^{-6} at Etna and Stromboli, Mediterranean with alkaline traps in 2010–2012 (Wittmer et al., 2014), (3–5) × 10^{-6} with the Raschig Tube at Nyamuragira, in the Virunga Mountains of the Democratic Republic of the Congo in 2015 (Bobrowski et al., 2017) and 2 × 10^{-5} and 5.8 × 10^{-6} at Masaya and Telica, both Nicaragua respectively with filter packs in 2006 (Witt et al., 2008). Bobrowski et al. (2017) reported that the total iodine already comprises 8–18% non-hydrogen iodide measured at the crater rim of the pit crater at Nyamuragira. A major eruption of Kasatochi, Aleutian Islands 2008 enabled rare detection of IO in the volcanic plume in the stratosphere by satellite (Schönhardt et al., 2017). We highlight that the ozone depletion potential of iodine may have significant ozone-depletion impacts even as a trace emission. Iodine has an alpha factor (chemical effectiveness relative to chlorine for global ozone destruction, globally and annually averaged) of 150–300. Compared to bromine (alpha factor ca. 60), iodine can affect ozone levels even more effectively (World Meteorological Organization, 2014 and references therein).

Like the other halogens volcanic iodine is thought to be emitted mainly as hydrogen iodide with subsequent radical formation near the vent in a similar manner to bromine (R1, see section Bromine Explosion). IO is formed out of iodine radicals reacting with ozone (R23).

$$I + O_3 \rightarrow IO + O_2 \qquad (R23)$$

The reaction of IO with another halogen oxide (XO, with X = Br, I) leads to OIO formation (R24). OIO can form higher iodine oxides which are precursors in particle formation and thus affect the atmospheric radiation balance (Hoffmann et al., 2001).

$$IO + XO \rightarrow OIO + X \qquad (R24)$$

Reactions with HOI (formed analogously to R3) form interhalogens (R25, XI with X = Br, Cl) that are released to the gas phase. Interhalogens can be photolyzed (analogous to R10) leading to halogen radicals that are involved in the catalytic cycles of halogens through plume chemistry as outlined above.

$$HOI + H^+_{(aq)} + X^-_{(aq)} \xrightarrow{\text{aerosol-surface}} XI + H_2O_{(aq)} \qquad (R25)$$

Further details are given in von Glasow and Crutzen (2003) and literature therein.

BrO Evolution in Volcanic Plumes

Dependence on Plume Age – Temporal Evolution

Observations of BrO/SO_2 ratios as a function of distance from the emission source allow to trace chemical transformations of volcanic bromine (under the condition that SO_2 is conserved). BrO was reported to be not detectable at crater rims but is formed inside the atmosphere-volcanic gas plume mixture over very short time-scales (minutes). The development of BrO/SO_2 with distance downwind is shown in **Figure 3**, based on results of Bobrowski and Giuffrida (2012) and Platt and Bobrowski (2015) complemented by further measurement series (derived from the **Supplementary Table 1**). Each data series is normalized to the maximum BrO/SO_2 observed, and averages were taken for measurements at the same distance within a given data series. All data arrays confirm a general rising trend. Close to the emission source BrO/SO_2-ratios are low. Excluding Ambrym, Vanuatu BrO/SO_2-ratios seem to reach a relatively stable level within 5–10 km from the source. The near-constant levels then appear to decrease in some cases, for example Etna, Sicily, Italy 2004, Nyiragongo, in the Virunga Mountains of the Democratic Republic of the Congo 2004 but not for other data series e.g., Etna 2005 and Ambrym 2007.

The development of BrO is a function of plume age (and therefore depends as well on the distance); however, the distance-time interconversion depends on wind-speeds that are specific to each data-series. This means BrO formation, even if taking place at the same plume age, might be measured at a different distance. Mixing between the plume and air is also a function of distance or time downwind, and is suggested by models to strongly influence halogen speciation, hence BrO/SO_2. Indeed, whilst all volcanic plume model studies predict the initial rise

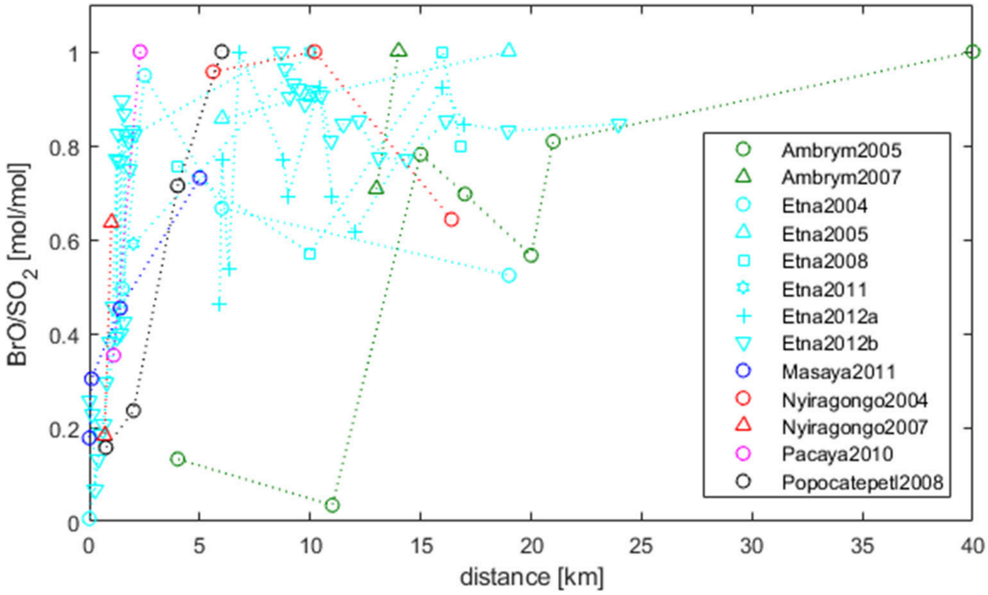

FIGURE 3 | Development of BrO/SO$_2$-ratios (normalized) in the plume as a function of distance from the emission source [extended from Bobrowski and Giuffrida (2012) and Platt and Bobrowski (2015), using datasets in **Supplementary Table 1** and references therein]. For data-series with the same distance averages are formed. BrO is not detectable at crater rims but typically rises to a near stable level within 5–10 km (for details see section Dependence on Plume Age–Temporal Evolution).

in BrO/SO$_2$, the occurrence of a subsequent plateau or decline depends strongly on the downwind plume-air mixing (Roberts et al., 2014b). For large gas emission fluxes like at Ambrym a lower proportion of air may initially mix into the plume. This could reduce BrO/SO$_2$ close to the source, as is found for both models and observations (Bani et al., 2009; Jourdain et al., 2016). However, this aspect still needs to be further investigated using measurement data.

Spatial Distribution in the Cross-Section of the Plume

Beside distribution of BrO along the plume-direction (as a function of plume age, dependent on distance from the emission source), measurement and model studies have also investigated the vertical or horizontal distribution of BrO and OClO in the cross-section of the plume.

Vertical profiles were calculated from two-dimensional BrO and SO$_2$ distributions measured by imaging DOAS instruments (Bobrowski et al., 2007; Louban et al., 2009; General et al., 2015). Glißet al. (2015) and recently Kern and Lyons (2018) investigated the vertical BrO/SO$_2$ distribution by using a 1 dimensional scanner unit. Bobrowski et al. (2007) found highest BrO/SO$_2$ values at the edges of the plume (3×10^{-4}) compared to lower values in the center (2×10^{-4}) and reproduced this trend with their model data.

Jourdain et al. (2016) discussed favored BrO formation for the edges of a volcanic plume more quantitatively, finding general agreement between model and measurement data in the trend in BrO/SO$_2$. While at the edges BrO reached up to 60% of the total bromine species, in the core BrO remains below 30%. Modeling predicts that Br radicals are the abundant species in the core. An explanation might be the entrainment of O$_3$-rich ambient air at the plume edges to promote BrO formation, but limited transport of tropospheric O$_3$ and HO$_X$ radicals toward the plume center (see section Causes and Effects of O$_3$ Depletion). However model studies show that plumes without ozone depletion in the core can also exhibit greater BrO/SO$_2$ (and OClO/SO$_2$) at the plume edge (Roberts et al., 2018). This is due to the interconversion reactions between reactive bromine species, in particular Br, BrO (section Causes and Effects of O$_3$ Depletion), that enhances BrO/Br in the more dilute edge compared to the core of the near-downwind plume.

BrO as a Fraction of Total Bromine Under Different Plume Conditions

The conversion of HBr and the formation of BrO compared with total SO$_2$ flux, as well as the depletion of ozone have been reported in few measurement observations (see section Causes and Effects of O$_3$ Depletion) and have been investigated with model studies. Roberts et al. (2014b) showed in studies of Etna's plume HBr fully converted within tens of minutes with HBr/SO$_2$ ratios of 7.4×10^{-4}. While HBr/SO$_2$ ratios of 24×10^{-4} a conversion of only about 50% was determined within an hour of simulation (both with 20 kg/s SO$_2$). Bani et al. (2009) observed an increased and faster BrO/SO$_2$ formation dependent on the distance by comparing data with SO$_2$ flux below 100 kg/s and above 100 kg/s at Ambrym, Vanuatu in 2005 and 2007. Although it has to be noted that no influence of bromine emissions can be investigated in this case due to the lack of simultaneous HBr measurements.

The impact of total (Br flux) and relative (Br/S) bromine emissions on BrO development can be investigated using simultaneous measurements of Br/S and BrO/SO$_2$, which enables the calculation of BrO as a fraction of total bromine (BrO%). Near-simultaneous Br/S and BrO/SO_2 data sets from **Supplementary Table 1** have been used to calculate the BrO% fraction as a function of the distance from the emission source in **Figure 4**. The dependence of BrO% with distance shows a positive dependency (similar as for **Figure 3**) further supporting the assumption that increased BrO/SO_2 is caused by the formation of BrO. The particularly low BrO% for Redoubt, Alaska might be explained by the fact that the measurements of Br/S and BrO/SO_2 were not quite simultaneous (which could introduce non-linearities if the bromine emission changed).

The highest BrO% between 40 and 65% was observed at Ambrym, Vanuatu in 2007 (SO_2 flux of 47 kg/s). These datasets were also obtained at the furthest distance downwind (12–14 km) i.e., greater time-evolution to form BrO. Note that BrO/SO_2 were measured in August 2007 (Bani et al., 2009) while Br/S results derive from October 2007 (Allard et al., 2016). Jourdain et al. (2016) performed model simulations of the Ambrym plume, comparing to BrO/SO_2 measurements in January 2005 (Bani et al., 2009). The SO_2 flux was significant higher in 2005 (average 218 kg/s) than in 2007. The model predicted up to 60% BrO% at 200 km distance to the emission source at the edge of the plume (HBr/SO_2 6.87×10^{-4}). In the core only below 30% BrO% is observed.

A high BrO fraction of about 40% was observed at Etna, Sicily, Italy in 2004 with Br/S 4.8×10^{-4} and an SO_2 flux of 11 kg/s (Oppenheimer et al., 2006). Note that measurements on Etna in 2012 (Wittmer et al., 2014) resulting in 3 and 6% at similar Br/S ratios of 8.8×10^{-4} and 4.2×10^{-4} respectively occurred at plume ages <1 min. While 40% were reached by observations of Oppenheimer et al. (2006) at 2–3 km (3–4 min estimated plume age), the model results by Roberts et al. (2014b) mentioned above with HBr/SO_2 7.4×10^{-4} (SO_2 20 kg/s) resulted in approximately 25% at 5 min plume age. This comparison lacks of the fact that we do not know if the model set-up would agree with Oppenheimer et al.'s plume measurement parameters. It is worth highlighting that the value of 40% BrO% found for the Etna 2004 measurements is rather high compared to other datasets around this distance downwind (**Figure 4**).

Model studies of Bobrowski et al. (2015) compared Etna's plume (bromine flux 22 g/s, maximum BrO/SO_2 2.1×10^{-4}) with slightly greater bromine flux of Nyiragongo's plume (in the Virunga Mountains of the Democratic Republic of the Congo, bromine flux 30 g/s, maximum BrO/SO_2 0.7×10^{-4}). Simulations predicted similar BrO columns in both cases but differ in relative BrO formation. Even though Nyiragongo has greater Br/S ratios in its volcanic plume than Etna, observations of the relative conversion to BrO downwind show smaller values (BrO%: 0–2%) in the aged plume. For Nyiragongo 2007 model predictions fit with measurements, if a plume age of 1–2 min is assumed.

Comparison of Nyiragongo with studies by Kelly et al. (2013) at Mt Redoubt results in a slightly higher conversion of HBr (although low compared to Etna) in Mt Redoubt's plume. Even though Br/S emissions of 41×10^{-4} are smaller than in some cases of Nyiragongo (note also the SO_2 flux of 4.3 kg/s is lower, resulting in also lower quantities of bromine compared to Nyiragongo as well as Etna). Model simulations that reproduced the observed ozone loss in the plume of Mt. Redoubt predicted only 30% of emitted HBr to be converted into reactive forms. This may be due to the rather dilute Redoubt plume because conversion of HBr into reactive bromine via the autocatalytic bromine explosion strongly depends on abundances of bromine and aerosols. BrO formation in this case seems to be rather low compared to other data sets mentioned above (see **Figure 4**). Note that model parameters and Br/S results are based on measurements at Mt Redoubt in June 2010 but BrO/SO_2 observations were made in August 2010. The observed BrO/SO_2 of 1×10^{-4} in August is rather low (BrO% of 2.4%) compared to the June model results (maximum BrO/SO_2: 6×10^{-4}, BrO%: 14%). For comparison, GOME-2 observations of Mt. Redoubt plume in the end of May found 2.5×10^{-4} BrO/SO_2 (Hörmann et al., 2013, see **Supplementary Table 1**). Also, the ozone depletion of August (up to 70% below ambient air at 19 min estimated plume age) is lower than observed in June (up to 90% below ambient air at 38 min estimated plume age). Since the rapid conversion of HBr to form BrO leads to ozone consumption (see section Causes and Effects of O_3 Depletion), the differences in observed ozone loss over June-August imply that BrO/SO_2 was likely higher in June 2010 than reported in August 2010. A possible explanation is that the bromine emission decreased over these months, or that changes in the plume chemistry led to a reduced conversion of emitted bromine into BrO. Unfortunately, this hypothesis cannot easily be tested as Br/S was not monitored throughout.

To study the relationship between emission fluxes and BrO fractions there are mainly three mandatory tasks: (1) Simultaneous measurements of Br/S and BrO/SO_2. (2) The determination of bromine fluxes or at least SO_2 fluxes so Br flux can be calculated from Br/S ratios. (3) Observations of BrO should be made at a certain distance/plume age from the emission source. As discussed before (section Dependence on Plume Age–Temporal Evolution) for comparison of BrO results in plumes measurements should be used, which reached the BrO/SO_2 "plateau" after ∼5–10 min (2,5–10 km, depending on wind speed and plume condition). All three tasks are more or less realized by only two data sets for Etna in 2004 (Oppenheimer et al., 2006) and Gorely in 2011 (Aiuppa et al., 2012; Bobrowski et al., 2012; Platt and Bobrowski, 2015). Remarkable is the fact that Etna's plume (Br/S: 4.8×10^{-4}, SO_2: 11 kg/s) results in a significant higher HBr to BrO conversion of ∼40% (BrO% 40%) than in Gorely's plume that had a slightly lower SO_2 flux (9.3 kg/s) and slightly higher Br/S ratio (5.3×10^{-4}, i.e., resulting in similar Br flux) resulting in ∼13% BrO%.

All low-temperature kinetic models pointed out that the absolute amount of total gas emission, the total emitted bromine (also chlorine) and the initial formation of HO_X or halogen radicals in the effective source region, and the role of plume-air mixing all seem to be exert strong controls on BrO formation. However, these parameters are not well constrained in the models, nor for the intercompared field-observations, due to lack of datasets. For the intercomparison of volcanoes, the overall atmospheric setting where volcanoes are located at

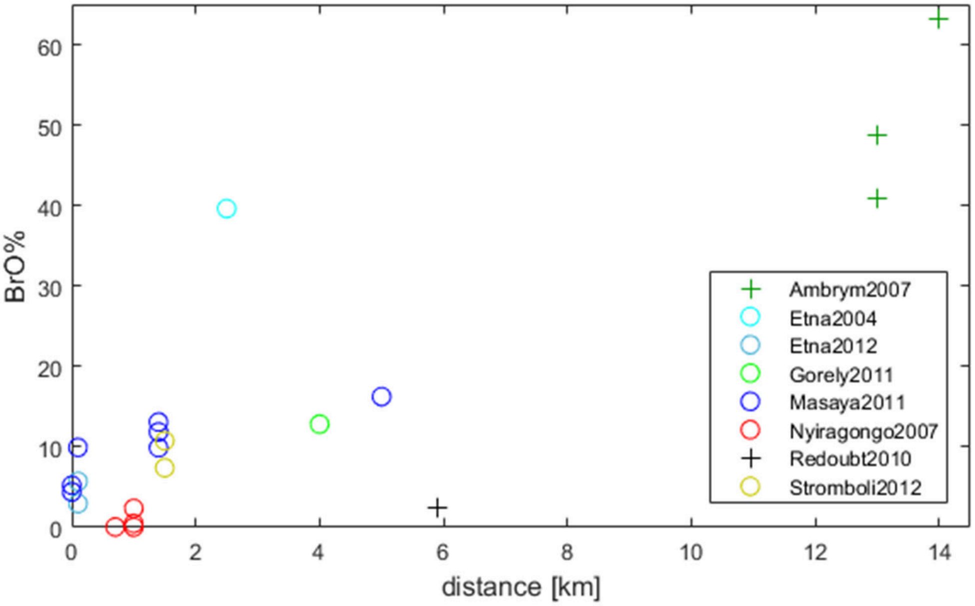

FIGURE 4 | The BrO% fraction is shown dependent on the distance to the emission source. BrO% describes (BrO/SO_2)/(Br/S). The trend (also observed in **Figure 3**) leads to the assumption that increased BrO/SO_2 is caused by the formation of BrO. Circles (o): simultaneous taken data-sets; Plus (+): non-simultaneous data sets but have been compared in other publications (Ambrym: Bani et al., 2009; Allard et al., 2016; Redoubt: Kelly et al., 2013). For further details see **Supplementary Table 1** and section BrO as a Fraction of Total Bromine Under Different Plume Conditions.

should also be noted. Etna is in a more polluted region, while Nyiragongo and Redoubt release plumes in more remote, clean atmospheres. Therefore, there might be a difference in the ambient ozone and NO_X levels. It is also possible that volcanic plume halogen chemistry might be influenced by marine sources of halogens and aerosols. Finally, temporal variations due to meteorological or/and volcanological conditions may introduce variability in the datasets used for intercomparisons (noting Br/S and BrO/SO_2 measurements are difficult to perform exactly simultaneously as they are made at different locations on the volcano).

The challenge to interpreting BrO observations is highlighted by Cadoux et al. (2018). GOME-2 observations of Merapi's eruption in Indonesia 2010 resulted in extremely low BrO/SO_2 ratios (maximum 8×10^{-6}; Hörmann et al., 2013), much lower than expected based on petrological estimates of the halogen/sulfur emission. Cadoux et al. (2018) discussed that BrO formation could be limited by the restriction of photochemical driven reactions caused by the ash-rich paroxysmal phase and the absence of UV light during the eruption in the night (the BrO was detected by GOME-2 in the following day). According to Cadoux et al. (2018) other possibilities include: (a) scavenging of bromine in the troposphere (e.g., adsorption of bromine on ash), (b) kinetic factors lead to favored S degassing from the magma, (c) brine saturation leading to Br uptake when magma rises, and (d) changes in Br partitioning caused by other volatile species in the magma. To this, we add the important role of plume chemistry in converting emitted HBr into BrO, as emphasized in this review.

Forecasting – Correlating Volcanic Plume Composition to Volcanic Activity

The characterization of volcanic gases can give insights about processes inside volcanoes. Volcanic gases are solved in magma at depth under high pressure. When magma is rising, decompression, diffusion, and coalescence lead to bubble formation and growth and therefore the release of gases. The depth at which gases start to escape can be different with different types of magma. The release of gases has an influence on the rising magma due to their influence on density, compressibility and flow properties. Therefore, magma degassing is a crucial control of eruption dynamics (Malinconico, 1979; Carroll and Holloway, 1994; Sparks, 2003; Moussallam et al., 2016). A strong influence is already known for the most abundant emitted gases like H_2O and CO_2. Nevertheless, even trace gases like fluorine are thought to control the viscosity of magmas with effects on crystallization-fractionation paths, controlling degassing paths and therefore the eruptive behavior (Giordano et al., 2004).

H_2O is the most abundant emitted species, but water vapor emissions are difficult to determine due to high and very variable atmospheric background. Further, emitted water vapor is difficult to interpret because it does not always purely originate from magma but might derive also from hydrothermal systems or in some cases even from incorporated local seawater. Nevertheless, recent studies show the potential to determine water vapor in volcanic plumes and renew the hope to use them as eruption precursors in the future (Moor et al., 2016a,b; Kern et al., 2017).

Monitoring of CO_2 by remote sensing instruments is difficult as well. Non-volcanic CO_2 sources and high and variable atmospheric background concentrations may lead to variability in volcanic CO_2/SO_2 measurements (Burton et al., 2000). Today, CO_2/SO_2 ratios need usually to be determined by *in situ* sampling, however these are spatially limited and sampling points are not always representative and are frequently destroyed during eruptive periods. CO_2 is exsolved at relatively large depth and SO_2 is released at much shallower levels. Degassing of the halogens Cl and F occurs often at even lower pressure, closer to the Earth's surface (**Figure 5**; Spilliaert et al., 2006; Burton et al., 2007; Aiuppa, 2009). Observations of decreasing CO_2/SO_2 ratios and increasing Cl/SO_2 ratios could therefore be interpreted as gases derived from magma moving to shallower depth or magma from already exhausted reservoirs.

Although bromine is not known to have a large influence on eruption dynamics, bromine degassing could be nevertheless a good indicator for rising magma. In contrast to CO_2 and H_2O, SO_2 and bromine species have negligible background concentrations and clearly derive from magma degassing. The fact that SO_2 and BrO are measurable simultaneously by remote sensing instruments facilitates its applicability for monitoring volcanic activity.

Aiuppa et al. (2005) correlated Br/S ratios from filter pack samples to Etna's activity in 2004 observing increasing Br/S as well as Cl(F)/S prior to an eruption, followed by a rapid decrease. In contrast to the Br/S observation of Aiuppa et al. (2005), several authors observed lower BrO/SO_2 ratios during or also prior to eruptive activities in comparison to observations made during quiescent degassing or after eruptive activity phases. For instance as reported by Bobrowski and Giuffrida (2012) during eruptive and non-eruptive periods of Etna, Sicily, Italy from 2006 to 2009, Lübcke et al. (2014) at Nevado del Ruiz, Colombia from 2009 to 2013, Dinger et al. (2018) and Hidalgo et al. (2018) at Cotopaxi, Ecuador 2008, Warnach et al. (in review) at Tungurahua, Ecuador 2008–2014. The time lag between gas composition change and start of eruptive activities differs between the various studies and volcanoes; however, the general trend seems to be similar. Conversely, the discussion of BrO-mediated ozone depletion at Mt Redoubt, Alaska (see section BrO as a Fraction of Total Bromine Under Different Plume Conditions) points toward a possible decrease in bromine emission with assured activity.

In contrast to most chlorine and fluorine studies, recent investigations observe a correlation between BrO/SO_2 ratios and CO_2/SO_2 ratios (Bobrowski et al., 2015, 2017) leading to the assumption that bromine exsolution might be deeper than sulfur. Only recently studies on partitioning and/or knowledge of the magma movement through other geophysical or geochemical data start to deliver a basis for the interpretation of available field data (Cadoux et al., 2018). With increased degassing a change of the gas composition from S-rich to Cl-Br-rich is predicted, favoring the hypothesis of a relatively shallow degassing of bromine in comparison to sulfur that goes along with measurement results of Aiuppa et al. (2005). However, both possibilities are discussed–shallow and deep degassing of bromine (**Figure 5**).

SUMMARY OF MAIN FINDINGS

For the interpretation of BrO data regarding volcanic activity, it is essential to have a detailed understanding of the ongoing chemistry, to be able to recalculate total bromine emissions. There is a temporal and spatial heterogeneous distribution of the BrO concentration in volcanic plumes (see sections Dependence on Plume Age–Temporal Evolution and Spatial Distribution in the Cross-Section of the Plume). Current model and field

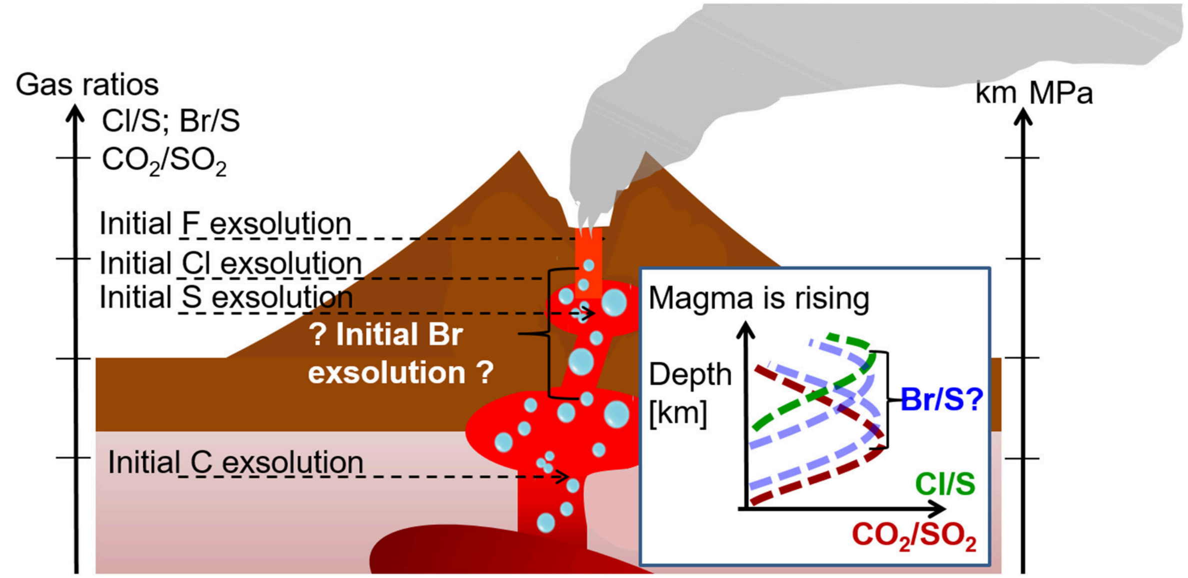

FIGURE 5 | Magma degassing model for volcanic gases. Carbon is held to exsolve at depth, S, Cl, F follow at lower pressures closer to the surface. Diagram illustrates changes of observed gas ratios if magma is rising. Whether bromine partitioning occurs at higher or lower pressure than sulfur is not clarified and part of current scientific discussions (for details see section Forecasting–Correlating Volcanic Plume Composition to Volcanic Activity).

studies demonstrate that most of the BrO is not directly emitted and describe its formation through low-temperature, kinetically controlled photochemical and multiphase reactions and mixing processes with the surrounding atmosphere in the downwind plume (see section Plume Chemistry and the Formation of Reactive Bromine, summary in **Figure 2**).

Common main findings are:

- BrO/Br_{total} rises rapidly within the first minutes of plume age but usually stabilizes and then decreases again further downwind (section Dependence on Plume Age–Temporal Evolution).
- Low-temperature "bromine explosion" chemistry mechanism is able to explain BrO abundances in the downwind plume. But elevated concentrations of radicals e.g., HO_X and/or NO_X derived from high-temperature near-vent chemistry in the initial plume seem necessary to accelerate the start to enhance low-temperature BrO formation downwind in order to reach observed magnitudes of BrO (section Plume Chemistry and the Formation of Reactive Bromine).
- The autocatalytic cycles forming BrO are driven by reaction cycles involving aerosol- and gas-phase and photolysis reactions and affected by O_3 entrainment, leading to spatial heterogeneity in plume BrO/SO_2 as seen in vertical plume profiles (sections Spatial Distribution in the Cross-Section of the Plume).
- The products from heterogeneous halogen reactions are controlled by aqueous-phase equilibria that produce Br_2 (hence BrO) in volcanic plume environment. Formation of BrCl (hence OClO) occurs upon very low levels of HBr as a consequence of the bromine explosion (section Interhalogen, Chlorine, and Iodine Plume Chemistry).
- Studies of the near-source plume chemistry point to non-linearities in HBr conversion into BrO depending on the bromine content of the emissions, plume-air mixing and other factors.

LIMITATIONS

Today, the knowledge on bromine plume chemistry is limited mainly by measurement restrictions. Model studies that have been performed in relation to particular data arrays can generally reproduce the available (limited) observations but operate in a vast parameter space that is currently not well constrained. Discrepancies exist in the predicted bromine speciation between the two available model (MISTRA and PlumeChem) probably as a result from differences in simulation algorithms, but also the wide volcanological and meteorological parameter space to which they have been applied. A general takeaway of obtained findings on one volcano cannot necessarily be applied to other volcanoes (e.g., comparison of Etna, Sicily, Italy and Nyiragongo, in the Virunga Mountains of the Democratic Republic of the Congo in Bobrowski et al., 2017). The high-temperature near-vent plume compositions are crucial for initializing low-temperature models that simulate the downwind plume chemistry. Near-source chemistry is usually investigated with high-temperature thermodynamic models. Since the hot near-vent plume cannot easily be observed by measurements, there are still uncertainties in parameterizations. The often assumed thermodynamically equilibrium conditions might not hold true (see section Model Initialization–High-Temperature Near-Vent Conditions, Dilution and Aerosols), therefore, a better characterization of the near-source volcanic plume chemistry is an essential step for understanding the evolution of volcanic plumes in the atmosphere. Even though the "bromine explosion" chemistry mechanism is relatively well-understood although still not fully characterized for volcanic plume environments there remain also some uncertainties in the low-temperature modeling for example in the parameterization of the gas-aerosol reactions (Roberts et al., 2014a), and the role of NO_X in volcanic plumes. A major issue, however, is that available datasets are typically too limited to fully constrain the model initialization such that some parameters have to be assumed, and only very limited data exist for model evaluation.

The growing amount of data sets and detailed model studies help to improve hypotheses. However, most collected data sets are incomplete toward bromine speciation and development in the plume. Future data sampling is recommended to be taken as comprehensive as possible. Therefore, three main points need to be considered: (1) Simultaneous measurements of the emissions-plume chemistry and physics are needed as both emissions and plume dynamics can vary rapidly with time. (2) Measurements of BrO for volcanic activity monitoring should be systematically undertaken at a certain plume age also because the influence of plume age on bromine chemistry needs to be taken into account to enable the interpretation of the data in the context of volcanic activity. (3) Additional parameters like ozone, aerosol particle composition, and size distribution as well as meteorological conditions, and constraints on gas flux and plume dilution/mixing into the background atmosphere are mandatory. Evidently, many restrictions reduce the availability of those data sets. For most of the bromine species as well as key chemical compounds such as OH and HO_2 no applicable methods are available for definite speciation. Recent developments have started to provide complement measurements for reactive bromine species, as outlined below. However, data sets are still rare. This activity demands a large pool of instruments, involved people, and logistical resources. Application of UAV systems is revealed as a useful tool for plume investigation but is still limited in its scope due to the often high altitude of volcanoes or other environmental effects.

Recent Developments – Opportunities and Challenges

Development of measuring techniques to add further knowledge on bromine speciation and quantification of other involved species such as OH and bromine speciation is needed to evaluate model predictions of plume chemistry. To pursue this target Rüdiger et al. (2017) presented a new *in situ* method for the determination of gaseous reactive bromine species in volcanic plumes (see section *In Situ*–Application of Instruments in the Plume). Applying active alkaline traps (Raschig Tubes) can simultaneously determine Br_{total}. So far, data sets are very rare. The method has been applied at Etna, Sicily, Italy 2015 (Rüdiger et al., 2017), Nyamuragira, in the Virunga Mountains of the Democratic Republic of the Congo 2015 (Bobrowski et al., 2017), Stromboli, Mediterranean 2016 (Rüdiger et al., 2018b) and Masaya, Nicaragua 2016 (Rüdiger et al., in preparation). The proof of principle of ground-based sampling sets in 2015's campaigns resulted in averaged reactive bromine to Br_{total} ratios of 29 ±17% at Etna (plume age <1 min) and 25% ±9% at Nyamuragira. In 2016 applicability of UAV-based sampling at Stromboli was undertaken and resulted in an average reactive bromine to SO_2 ratio of $(5.1 \pm 4.2) \times 10^{-4}$ for the very young plume. Measurement results regarding reactive bromine do not allow an ideal and entire description of bromine plume evolution yet, because spatial information in the plume is still very limited (distances mainly at 100–200 m from emission sources and at several craters in the case of Etna). Additional methods for determination of other bromine species such as HBr in the gas phase are under development (Gutmann et al., 2018) and may complement bromine speciation soon.

Development of Fabry Perot Interferometers (FPI, Kern et al., 2010; Kuhn et al., 2018) may allow faster imaging of BrO in the future, than current DOAS application. This can be particularly valuable to separate plume chemistry (as a function of dilution, plume age etc.) from temporal variability in bromine emissions. Permanently installed DOAS instruments (e.g., NOVAC network) now provide the potential for long-term BrO/SO_2 time series on a daily basis, at many volcanoes worldwide. Whilst these datasets are regularly being exploited for SO_2, so far only a few of these datasets have been analyzed for BrO, but the number is increasing. As our understanding of volcanic plume bromine chemistry improves, we may be able to better interpret these observations in terms of volcanological and meteorological conditions, to yield a valuable resource for daily bromine emissions monitoring. Recently, Kern and Lyons (2018) demonstrate the use of co-measured OClO to help better interpret volcanic BrO.

Atmospheric simulation chamber studies show promise to discover further details of volcanic plume chemistry by mimicking the plume gas and particle conditions in a controlled environment. In those experiments chemical reactions are continuously observed in real-time by a multi-instrument setup, measuring BrO, O_3, NO_X and further compounds as well as meteorological parameters to constrain their effect on the bromine activation (Rüdiger et al., 2018a).

To provide better constraints for the initial composition of the emissions-plume ("effective source region") there are efforts to improve the understanding of high-temperature chemistry in the transient near-vent plume. A major limitation to existing thermodynamic models is the assumption of chemical equilibrium. Development of new chemical-kinetics approaches is being undertaken to more accurately reproduce the transient (hot, rapidly diluting and cooling) near-vent plume (Roberts et al., in review). This effort will improve the representation of the high-temperature near-vent chemistry as needed for initialization of the low-temperature atmospheric models of volcanic BrO.

Recent advances introducing the mechanisms developed from 1D/box models into 3D models deliver a more comprehensive understanding of volcanic halogen chemistry as plumes disperse more widely into the atmosphere, enabling the quantification of impacts on tropospheric composition and the potential for halogens to be transported into the stratosphere. Mesoscale models with nested grids enable the simulation of plume processes and impacts from local up to regional scales (Surl et al., 2014; Jourdain et al., 2016). Advances have also been made toward developing parameterizations to include volcanic plume halogen processes in global models (Grellier et al., 2014). Whilst the box/1D models are an essential tool to probe the chemistry of volcanic plumes at the plume-scale and for comparison and to aid interpretation of near-downwind plume observations, regional and global models are needed to assess more fully impacts and to compare to satellite observations of BrO in more aged/evolved plumes. In particular, the recently launched TROPOMI satellite instrument will enable to measure BrO globally at higher spatial resolutions than previously possible.

Advances in *in situ* and remote sensing field-observations from the crater to flank, and by satellite, and development of a chain of numerical models from local (0D/1D) to regional and global (3D) scales, as well as laboratory experiments, will together address current knowledge gaps in volcanic plume bromine chemistry. Anticipated future benefits include the potential for widespread use of bromine monitoring as part of volcano hazard forecasting and a quantitative assessment of volcanic bromine impacts on the atmosphere over regional-global scales.

AUTHOR CONTRIBUTIONS

AG and NB collected research results. AG processed data collections. AG, NB, and TR wrote the paper with input from all authors. JR and TH contributed to the final version of the manuscript. All authors provided critical feedback and helped shape the research, analysis and manuscript.

ACKNOWLEDGMENTS

This work was supported by the Research Center VAMOS (Volcanoes and Atmosphere in Magmatic Open Systems) at the Johannes Gutenberg-Universität Mainz. NB and JR thank the Deutsche Forschungsgemeinschaft DFG for financial support in the frame of the the project BO 3611/2-1/HE5214/8-1. TR acknowledges the Orleans Labex VOLTAIRE (VOLatils-Terre Atmosphère Interactions–Ressources et Environnement, ANR-10-LABX-100-0) and ANR Projet de Recherche Collaborative VOLC-HALCLIM (Volcanic Halogens: from Deep Earth to Atmospheric Impacts, ANR-18-CE01-0018-01). We thank the reviewers for their detailed comments and constructive suggestions, which helped to significantly improve the manuscript.

SUPPLEMENTARY MATERIAL

The Supplementary Material for this article can be found online at: https://www.frontiersin.org/articles/10.3389/feart.2018.00213/full#supplementary-material

REFERENCES

Aiuppa, A. (2009). Degassing of halogens from basaltic volcanism: insights from volcanic gas observations. *Chem. Geol.* 263, 99–109. doi: 10.1016/j.chemgeo.2008.08.022

Aiuppa, A., Federico, C., Franco, A., Giudice, G., Gurrieri, S., Inguaggiato, S., et al. (2005). Emission of bromine and iodine from Mount Etna volcano. *Geochem. Geophys. Geosyst.* 6:Q08008. doi: 10.1029/2005GC000965

Aiuppa, A., Franco, A., von Glasow, R., Allen, A. G., D'Alessandro, W., Mather, T. A., et al. (2007). The tropospheric processing of acidic gases and hydrogen sulphide in volcanic gas plumes as inferred from field and model investigations. *Atmos. Chem. Phys.* 7, 1441–1450. doi: 10.5194/acp-7-1441-2007

Aiuppa, A., Giudice, G., Liuzzo, M., Tamburello, G., Allard, P., Calabrese, S., et al. (2012). First volatile inventory for Gorely volcano, Kamchatka. *Geophys. Res. Lett.* 39:L06307. doi: 10.1029/2012GL051177

Aiuppa, A., Shinohara, H., Tamburello, G., Giudice, G., Liuzzo, M., and Moretti, R. (2011). Hydrogen in the gas plume of an open-vent volcano, Mount Etna, Italy. *J. Geophys. Res. Solid Earth* 116:1861. doi: 10.1029/2011JB008461

Allard, P., Aiuppa, A., Bani, P., Métrich, N., Bertagnini, A., Gauthier, P.-J., et al. (2016). Prodigious emission rates and magma degassing budget of major, trace and radioactive volatile species from Ambrym basaltic volcano, Vanuatu island Arc. *J. Volcanol. Geotherm. Res.* 322, 119–143. doi: 10.1016/j.jvolgeores.2015.10.004

Allen, A. G., Mather, T. A., McGonigle, A. J. S., Aiuppa, A., Delmelle, P., Davison, B., et al. (2006). Sources, size distribution, and downwind grounding of aerosols from Mount Etna. *J. Geophys. Res. Atmos.* 111:D10302. doi: 10.1029/2005JD006015

Allen, A. G., Oppenheimer, C., Ferm, M., Baxter, P. J., Horrocks, L. A., Galle, B., et al. (2002). Primary sulfate aerosol and associated emissions from Masaya Volcano, Nicaragua. *J. Geophys. Res. Atmos.* 107, ACH 5-1-ACH 5-8. doi: 10.1029/2002JD002120

Amachi, S., Muramatsu, Y., and Kamagata, Y. (2001). Radioanalytical determination of biogenic volatile iodine emitted from aqueous environmental samples. *J. Radioanal. Nucl. Chem.* 246, 337–341. doi: 10.1023/A:1006786826998

Bagnato, E., Aiuppa, A., Parello, F., Calabrese, S., D'Alessandro, W., Mather, T. A., et al. (2007). Degassing of gaseous (elemental and reactive) and particulate mercury from Mount Etna volcano (Southern Italy). *Atmos. Environ.* 41, 7377–7388. doi: 10.1016/j.atmosenv.2007.05.060

Bani, P., Oppenheimer, C., Tsanev, V. I., Carn, S. A., Cronin, S. J., Crimp, R., et al. (2009). Surge in sulphur and halogen degassing from Ambrym volcano, Vanuatu. *Bull. Volcanol.* 71, 1159–1168. doi: 10.1007/s00445-009-0293-7

Barrie, L. A., Bottenheim, J. W., Schnell, R. C., Crutzen, P. J., and Rasmussen, R. A. (1988). Ozone destruction and photochemical reactions at polar sunrise in the lower Arctic atmosphere. *Nature* 334, 138–141. doi: 10.1038/334138a0

Bobrowski, N., and Giuffrida, G. (2012). Bromine monoxide/sulphur dioxide ratios in relation to volcanological observations at Mt. Etna. *Solid Earth* 3, 433–445. doi: 10.5194/se-3-433-2012

Bobrowski, N., Giuffrida, G. B., Arellano, S., Yalire, M., Liotta, M., Brusca, L., et al. (2017). Plume composition and volatile flux of Nyamulagira volcano, Democratic Republic of Congo, during birth and evolution of the lava lake, 2014–2015. *Bull. Volcanol.* 79:B09207. doi: 10.1007/s00445-017-1174-0

Bobrowski, N., Hönninger, G., Galle, B., and Platt, U. (2003). Detection of bromine monoxide in a volcanic plume. *Nature* 423, 273–276. doi: 10.1038/nature01625

Bobrowski, N., and Platt, U. (2007). SO2/BrO ratios studied in five volcanic plumes. *J. Volcanol. Geotherm. Res.* 166, 147–160. doi: 10.1016/j.jvolgeores.2007.07.003

Bobrowski, N., Vogel, L., Platt, U., Arellano, S., Galle, B., Hansteen, T., et al. (2012). "Bromine monoxide evolution in early plumes of Mutnovsky and Gorely (Kamchatka, Russia)," in *EGU General Assembly 2012, held 22-27 April, 2012 in* (Vienna), 6556.

Bobrowski, N., von Glasow, R., Aiuppa, A., Inguaggiato, S., Louban, I., Ibrahim, O. W., et al. (2007). Reactive halogen chemistry in volcanic plumes. *J. Geophys. Res.* 112:D06311. doi: 10.1029/2006JD007206

Bobrowski, N., von Glasow, R., Giuffrida, G. B., Tedesco, D., Aiuppa, A., Yalire, M., et al. (2015). Gas emission strength and evolution of the molar ratio of BrO/SO$_2$ in the plume of Nyiragongo in comparison to Etna. *J. Geophys. Res. Atmos.* 120, 277–291. doi: 10.1002/2013JD021069

Bott, A., Trautmann, T., and Zdunkowski, W. (1996). A numerical model of the cloud-topped planetary boundary-layer: radiation, turbulence and spectral microphysics in marine stratus. *Q. J. R. Meteorol. Soc.* 122, 635–667. doi: 10.1002/qj.49712253105

Brasseur, G., and Granier, C. (1992). Mount pinatubo aerosols, chlorofluorocarbons, and ozone depletion. *Science* 257, 1239–1242. doi: 10.1126/science.257.5074.1239

Brune, W. H., Stevens, P. S., and Mather, J. H. (1995). Measuring OH and HO$_2$ in the troposphere by laser-induced fluorescence at low pressure. *J. Atmos. Sci.* 52, 3328–3336. doi: 10.1175/1520-0469(1995)052<3328:MOAHIT>2.0.CO;2

Burton, M. R., Caltabiano, T., Murè, F., Salerno, G., and Randazzo, D. (2009). SO$_2$ flux from Stromboli during the 2007 eruption: results from the FLAME network and traverse measurements. *J. Volcanol. Geotherm. Res.* 182, 214–220. doi: 10.1016/j.jvolgeores.2008.11.025

Burton, M. R., Mader, H. M., and Polacci, M. (2007). The role of gas percolation in quiescent degassing of persistently active basaltic volcanoes. *Earth Planet. Sci. Lett.* 264, 46–60. doi: 10.1016/j.epsl.2007.08.028

Burton, M. R., Oppenheimer, C., Horrocks, L. A., and Francis, P. W. (2000). Remote sensing of CO$_2$ and H$_2$O emission rates from Masaya volcano, Nicaragua. *Geology* 28, 915. doi: 10.1130/0091-7613(2000)28<915:Rsocah>2.0.Co;2

Businger, S., Huff, R., Pattantyus, A., Horton, K., Sutton, A. J., Elias, T., et al. (2015). Observing and Forecasting Vog Dispersion from Kilauea Volcano, Hawaii. *Bull. Am. Meteorol. Soc.* 96, 1667–1686. doi: 10.1175/BAMS-D-14-00150.1

Butz, A., Dinger, A. S., Bobrowski, N., Kostinek, J., Fieber, L., Fischerkeller, C., et al. (2017). Remote sensing of volcanic CO$_2$, HF, HCl, SO$_2$, and BrO in the downwind plume of Mt. *Etna. Atmos. Meas. Tech.* 10, 1–14. doi: 10.5194/amt-10-1-2017

Cadoux, A., Iacono-Marziano, G., Scaillet, B., Aiuppa, A., Mather, T. A., Pyle, D. M., et al. (2018). The role of melt composition on aqueous fluid vs. silicate melt partitioning of bromine in magmas. *Earth Planet. Sci. Lett.* 498, 450–463. doi: 10.1016/j.epsl.2018.06.038

Cadoux, A., Scaillet, B., Bekki, S., Oppenheimer, C., and Druitt, T. H. (2015). Stratospheric Ozone destruction by the Bronze-Age Minoan eruption (Santorini Volcano, Greece). *Sci. Rep.* 5:12243. doi: 10.1038/srep12243

Carn, S. A., Clarisse, L., and Prata, A. J. (2016). Multi-decadal satellite measurements of global volcanic degassing. *J. Volcanol. Geotherm. Res.* 311, 99–134. doi: 10.1016/j.jvolgeores.2016.01.002

Carn, S. A., Fioletov, V. E., Mclinden, C. A., Li, C., and Krotkov, N. A. (2017). A decade of global volcanic SO$_2$ emissions measured from space. *Sci. Rep.* 7:44095. doi: 10.1038/srep44095

Carn, S. A., Krotkov, N. A., Yang, K., and Krueger, A. J. (2013). "Measuring global volcanic degassing with the Ozone Monitoring Instrument (OMI)," in *Remote Sensing of Volcanoes and Volcanic Processes: Integrating Observation and Modelling*, eds D. M. Pyle, T. A. Mather, and J. Biggs (McLean: Va. GeoScienceWorld), 229–257.

Carroll, M. R., and Holloway, J. R. (eds.). (1994). *Volatiles in Magmas*. Washington, DC: Mineralogical Society of America.

De Angelis, M., Simões, J., Bonnaveira, H., Taupin, J.-D., and Delmas, R. J. (2003). Volcanic eruptions recorded in the Illimani ice core (Bolivia): 1918–1998 and Tambora periods. *Atmos. Chem. Phys.* 3, 1725–1741. doi: 10.5194/acp-3-1725-2003

Devine, J. D., Sigurdsson, H., Davis, A. N., and Self, S. (1984). Estimates of sulfur and chlorine yield to the atmosphere from volcanic eruptions and potential climatic effects. *J. Geophys. Res. Solid Earth* 89, 6309–6325. doi: 10.1029/JB089iB07p06309

Dinger, F., Bobrowski, N., Warnach, S., Bredemeyer, S., Hidalgo, S., Arellano, S., et al. (2018). Periodicity in the BrO/SO$_2$; molar ratios in the volcanic gas plume of Cotopaxi and its correlation with the Earth tides during the eruption in 2015. *Solid Earth* 9, 247–266. doi: 10.5194/se-9-247-2018

Donovan, A., Tsanev, V., Oppenheimer, C., and Edmonds, M. (2014). Reactive halogens (BrO and OClO) detected in the plume of Soufrière Hills Volcano during an eruption hiatus. *Geochem. Geophys. Geosyst.* 15, 3346–3363. doi: 10.1002/2014GC005419

Freitas, S. R., Longo, K. M., Silva Dias, M. A. F., Chatfield, R., Silva Dias, P., Artaxo, P., et al. (2009). The Coupled Aerosol and Tracer Transport model to the Brazilian developments on the Regional Atmospheric Modeling System

(CATT-BRAMS)–Part 1: model description and evaluation. *Atmos. Chem. Phys.* 9, 2843–2861. doi: 10.5194/acp-9-2843-2009

Frische, M., Garofalo, K., Hansteen, T. H., Borchers, R., and Harnisch, J. (2006). The origin of stable halogenated compounds in volcanic gases. *Environ. Sci. Pollut. Res.* 13, 406–413. doi: 10.1065/espr2006.01.291

Galeazzo, T., Bekki, S., Martin, E., Savarino, J., and Arnold, S. R. (2018). Photochemical box-modelling of volcanic SO_2 oxidation: Isotopic constraints. *Atmos. Chem. Phys. Discuss.* 1–38. doi: 10.5194/acp-2018-381

Galle, B., Johansson, M., Rivera, C., Zhang, Y., Kihlman, M., Kern, C., et al. (2010). Network for observation of volcanic and atmospheric change (NOVAC)—A global network for volcanic gas monitoring: network layout and instrument description. *J. Geophys. Res.* 115:151. doi: 10.1029/2009JD011823

Galle, B., Oppenheimer, C., Geyer, A., McGonigle, A. J. S., Edmonds, M., and Horrocks, L. (2003). A miniaturised ultraviolet spectrometer for remote sensing of SO_2 fluxes: a new tool for volcano surveillance. *J. Volcanol. Geotherm. Res.* 119, 241–254. doi: 10.1016/S0377-0273(02)00356-6

General, S., Bobrowski, N., Pöhler, D., Weber, K., Fischer, C., and Platt, U. (2015). Airborne I-DOAS measurements at Mt. Etna: BrO and OClO evolution in the plume. *J. Volcanol. Geotherm. Res.* 300, 175–186. doi: 10.1016/j.jvolgeores.2014.05.012

Gerlach, T. M. (2004). Volcanic sources of tropospheric ozone-depleting trace gases. *Geochem. Geophys. Geosyst.* 5:Q09007. doi: 10.1029/2004GC000747

Gerlach, T. M., and Nordlie, B. E. (1975). The C-O-H-S gaseous system; Part II, Temperature, atomic composition, and molecular equilibria in volcanic gases. *Am. J. Sci.* 275, 377–394. doi: 10.2475/ajs.275.4.377

Giordano, D., Romano, C., Dingwell, D. B., Poe, B., and Behrens, H. (2004). The combined effects of water and fluorine on the viscosity of silicic magmas. *Geochim. Cosmochim. Acta* 68, 5159–5168. doi: 10.1016/j.gca.2004.08.012

Gliß, J., Bobrowski, N., Vogel, L., Pöhler, D., and Platt, U. (2015). OClO and BrO observations in the volcanic plume of Mt. Etna – implications on the chemistry of chlorine and bromine species in volcanic plumes. *Atmos. Chem. Phys.* 15, 5659–5681. doi: 10.5194/acp-15-5659-2015

Goff, F., Janik, C. J., Delgado, H., Werner, C., Counce, D., Stimac, J. A., et al. (1998). Geochemical surveillance of magmatic volatiles at Popocatèpetl volcano, Mexico. *Geol. Soc. Am. Bull.* 110, 695. doi: 10.1130/0016-7606(1998)110<0695:GSOMVA>2.3.CO;2

Goff, F., and McMurtry, G. M. (2000). Tritium and stable isotopes of magmatic waters. *J. Volcanol. Geotherm. Res.* 97, 347–396. doi: 10.1016/S0377-0273(99)00177-8

Grellier, L., Marécal, V., Josse, B., Hamer, P. D., Roberts, T. J., Aiuppa, A., et al. (2014). Towards a representation of halogen chemistry within volcanic plumes in a chemistry transport model. *Geosci. Model Dev. Discuss.* 7, 2581–2650. doi: 10.5194/gmdd-7-2581-2014

Gutmann, A., Bobrowski, N., Liotta, M., Rüdiger, J., and Hoffmann, T. (2018). "Bromine Chemistry in volcanic plumes – Development of in-situ denuder sampling techniques for hydrogen bromine," in *EGU General Assembly 2018, held 8-13 April, 2018* (Vienna), 17096.

Hard, T. M., O'Brien, R. J., Chan, C. Y., and Mehrabzadeh, A. A. (1984). Tropospheric free radical determination by fluorescence assay with gas expansion. *Environ. Sci. Technol.* 18, 768–777. doi: 10.1021/es00128a009

Hegg, D. A., Hobbs, P. V., and Radke, L. F. (1976). *Reactions of Nitrogen Oxides and Sulfur in Power Plant Plumes*. Techcnical Report, EPRI EA-270, Electric Power Research Institute, Palo Alto, CA. Available online at: http://carg.atmos.washington.edu/sys/research/archive/react_no_o_so2_power.pdf

Heue, K.-P., Brenninkmeijer, C. A. M., Baker, A. K., Rauthe-Schöch, A., Walter, D., Wagner, T., et al. (2011). SO_2 and BrO observation in the plume of the Eyjafjallajökull volcano 2010: CARIBIC and GOME-2 retrievals. *Atmos. Chem. Phys.* 11, 2973–2989. doi: 10.5194/acp-11-2973-2011

Hidalgo, S., Battaglia, J., Arellano, S., Sierra, D., Bernard, B., Parra, R., et al. (2018). Evolution of the 2015 cotopaxi eruption revealed by combined geochemical & seismic observations. *Geochem. Geophys. Geosyst.* 19, 2087–2108. doi: 10.1029/2018GC007514

Hoffmann, T., O'Dowd, C. D., and Seinfeld, J. H. (2001). Iodine oxide homogeneous nucleation: an explanation for coastal new particle production. *Geophys. Res. Lett.* 28, 1949–1952. doi: 10.1029/2000GL012399

Hönninger, G., von Friedeburg, C., and Platt, U. (2004). Multi axis differential optical absorption spectroscopy (MAX-DOAS). *Atmos. Chem. Phys.* 4, 231–254. doi: 10.5194/acp-4-231-2004

Hörmann, C., Sihler, H., Bobrowski, N., Beirle, S., Penning de Vries, M., Platt, U., et al. (2013). Systematic investigation of bromine monoxide in volcanic plumes from space by using the GOME-2 instrument. *Atmos. Chem. Phys.* 13, 4749–4781. doi: 10.5194/acp-13-4749-2013

Huang, R.-J., and Hoffmann, T. (2008). A denuder-impinger system with *in situ* derivatization followed by gas chromatography-mass spectrometry for the determination of gaseous iodine-containing halogen species. *J. Chromatogr. A* 1210, 135–141. doi: 10.1016/j.chroma.2008.08.003

Huang, R.-J., and Hoffmann, T. (2009). Development of a coupled diffusion denuder system combined with gas chromatography/mass spectrometry for the separation and quantification of molecular iodine and the activated iodine compounds iodine monochloride and hypoiodous acid in the marine atmosphere. *Anal. Chem.* 81, 1777–1783. doi: 10.1021/ac801839v

Hunton, D. E., Viggiano, A. A., Miller, T. M., Ballenthin, J. O., Reeves, J. M., Wilson, J. C., et al. (2005). *In-situ* aircraft observations of the 2000 Mt. Hekla volcanic cloud: Composition and chemical evolution in the Arctic lower stratosphere. *J. Volcanol. Geotherm. Res.* 145, 23–34. doi: 10.1016/j.jvolgeores.2005.01.005

Ilyinskaya, E., Oppenheimer, C., Mather, T. A., Martin, R. S., and Kyle, P. R. (2010). Size-resolved chemical composition of aerosol emitted by Erebus volcano, Antarctica. *Geochem. Geophys. Geosyst.* 11:Q03017. doi: 10.1029/2009GC002855

Jourdain, L., Roberts, T. J., Pirre, M., and Josse, B. (2016). Modeling the reactive halogen plume from Ambrym and its impact on the troposphere with the CCATT-BRAMS mesoscale model. *Atmos. Chem. Phys.* 16, 12099–12125. doi: 10.5194/acp-16-12099-2016

Kelly, P. J., Kern, C., Roberts, T. J., Lopez, T., Werner, C., and Aiuppa, A. (2013). Rapid chemical evolution of tropospheric volcanic emissions from Redoubt Volcano, Alaska, based on observations of ozone and halogen-containing gases. *J. Volcanol. Geotherm. Res.* 259, 317–333. doi: 10.1016/j.jvolgeores.2012.04.023

Kern, C., Kick, F., Lübcke, P., Vogel, L., Wöhrbach, M., and Platt, U. (2010). Theoretical description of functionality, applications, and limitations of SO_2 cameras for the remote sensing of volcanic plumes. *Atmos. Meas. Tech.* 3, 733–749. doi: 10.5194/amt-3-733-2010

Kern, C., Lübcke, P., Bobrowski, N., Campion, R., Mori, T., Smekens, J.-F., et al. (2015). Intercomparison of SO 2 camera systems for imaging volcanic gas plumes. *J. Volcanol. Geotherm. Res.* 300, 22–36. doi: 10.1016/j.jvolgeores.2014.08.026

Kern, C., and Lyons, J. J. (2018). Spatial distribution of halogen oxides in the plume of Mount Pagan volcano, Mariana Islands. *Geophys. Res. Lett.* 45, 9588–9596. doi: 10.1029/2018GL079245

Kern, C., Masias, P., Apaza, F., Reath, K. A., and Platt, U. (2017). Remote measurement of high preeruptive water vapor emissions at Sabancaya volcano by passive differential optical absorption spectroscopy. *J. Geophys. Res. Solid Earth* 122, 3540–3564. doi: 10.1002/2017JB014020

Kern, C., Sihler, H., Vogel, L., Rivera, C., Herrera, M., and Platt, U. (2009). Halogen oxide measurements at Masaya Volcano, Nicaragua using active long path differential optical absorption spectroscopy. *Bull. Volcanol.* 71, 659–670. doi: 10.1007/s00445-008-0252-8

Kitto, M. E., Anderson, D. L., and Zoller, W. H. (1988). Simultaneous collection of particles and gases followed by multielement analysis using nuclear techniques. *J. Atmos. Chem.* 7, 241–259. doi: 10.1007/BF00130932

Klobas, J. E., Wilmouth, D. M., Weisenstein, D. K., Anderson, J. G., and Salawitch, R. J. (2017). Ozone depletion following future volcanic eruptions. *Geophys. Res. Lett.* 44, 7490–7499. doi: 10.1002/2017GL073972

Kuhn, J., Platt, U., Bobrowski, N., and Wagner, T. (2018). Towards imaging of atmospheric trace gases using Fabry Perot Interferometer Correlation Spectroscopy in the UV and visible spectral range. *Atmos. Meas. Tech. Discuss.* 1–19. doi: 10.5194/amt-2018-350

Kutterolf, S., Hansteen, T. H., Appel, K., Freundt, A., Krüger, K., Pérez, W., et al. (2013). Combined bromine and chlorine release from large explosive volcanic eruptions: a threat to stratospheric ozone? *Geology* 41, 707–710. doi: 10.1130/G34044.1

Kutterolf, S., Hansteen, T. H., Freundt, A., Wehrmann, H., Appel, K., Krüger, K., et al. (2015). Bromine and chlorine emissions from Plinian eruptions along the Central American Volcanic Arc: from source to atmosphere. *Earth Planet. Sci. Lett.* 429, 234–246. doi: 10.1016/j.epsl.2015.07.064

Lazrus, A. L., Gandrud, B. W., Woodard, R. N., and Sedlacek, W. A. (1976). Direct measurements of stratospheric chlorine and bromine. *J. Geophys. Res.* 81, 1067–1070. doi: 10.1029/JC081i006p01067

Lee, C., Kim, Y. J., Tanimoto, H., Bobrowski, N., Platt, U., Mori, T., et al. (2005). High ClO and ozone depletion observed in the plume of Sakurajima volcano, Japan. *Geophys. Res. Lett.* 32:450. doi: 10.1029/2005GL023785

Levin, I., Münnich, K. O., and Weiss, W. (1980). The Effect of Anthropogenic CO_2 and 14C Sources on the Distribution of 14C in the Atmosphere. *Radiocarbon* 22, 379–391. doi: 10.1017/S003382220000967X

Liotta, M., Rizzo, A., Paonita, A., Caracausi, A., and Martelli, M. (2012). Sulfur isotopic compositions of fumarolic and plume gases at Mount Etna (Italy) and inferences on their magmatic source. *Geochem. Geophys. Geosyst.* 13:1861. doi: 10.1029/2012GC004118

Lohberger, F., Hönninger, G., and Platt, U. (2004). Ground-based imaging differential optical absorption spectroscopy of atmospheric gases. *Appl. Opt.* 43:4711. doi: 10.1364/AO.43.004711

Longo, K. M., Freitas, S. R., Pirre, M., Marécal, V., Rodrigues, L. F., Panetta, J., et al. (2013). The Chemistry CATT-BRAMS model (CCATT-BRAMS 4.5): a regional atmospheric model system for integrated air quality and weather forecasting and research. *Geosci. Model Dev.* 6, 1389–1405. doi: 10.5194/gmd-6-1389-2013

López, T., Ushakov, S., Izbekov, P., Tassi, F., Cahill, C., Neill, O., et al. (2013). Constraints on magma processes, subsurface conditions, and total volatile flux at Bezymianny Volcano in 2007–2010 from direct and remote volcanic gas measurements. *J. Volcanol. Geotherm. Res.* 263, 92–107. doi: 10.1016/j.jvolgeores.2012.10.015

Louban, I., Bobrowski, N., Rouwet, D., Inguaggiato, S., and Platt, U. (2009). Imaging DOAS for volcanological applications. *Bull. Volcanol.* 71, 753–765. doi: 10.1007/s00445-008-0262-6

Lübcke, P., Bobrowski, N., Arellano, S., Galle, B., Garzón, G., Vogel, L., et al. (2014). BrO/SO_2 molar ratios from scanning DOAS measurements in the NOVAC network. *Solid Earth* 5, 409–424. doi: 10.5194/se-5-409-2014

Lurton, T., Jégou, F., Berthet, G., Renard, J.-B., Clarisse, L., Schmidt, A., et al. (2018). Model simulations of the chemical and aerosol microphysical evolution of the Sarychev Peak 2009 eruption cloud compared to *in situ* and satellite observations. *Atmos. Chem. Phys.* 18, 3223–3247. doi: 10.5194/acp-18-3223-2018

Ma, C.-J., and Kim, K.-H. (2008). A combination of size-resolved particle samplers and XRF microprobe technique for single particle study. *Atmos. Environ.* 42, 7022–7026. doi: 10.1016/j.atmosenv.2008.04.045

Malinconico, L. L. (1979). Fluctuations in SO_2 emission during recent eruptions of Etna. *Nature* 278, 43–45. doi: 10.1038/278043a0

Marple, V. A., Rubow, K. L., and Behm, S. M. (1991). A microorifice uniform deposit impactor (MOUDI): description, calibration, and use. *Aerosol Sci. Technol.* 14, 434–446. doi: 10.1080/02786829108959504

Martin, R. S., Ilyinskaya, E., and Oppenheimer, C. (2012a). The enigma of reactive nitrogen in volcanic emissions. *Geochim. Cosmochim. Acta* 95, 93–105. doi: 10.1016/j.gca.2012.07.027

Martin, R. S., Mather, T. A., and Pyle, D. M. (2006). High-temperature mixtures of magmatic and atmospheric gases. *Geochem. Geophys. Geosyst.* 7:Q04006. doi: 10.1029/2005GC001186

Martin, R. S., Mather, T. A., Pyle, D. M., Power, M., Allen, A. G., Aiuppa, A., et al. (2008). Composition-resolved size distributions of volcanic aerosols in the Mt. Etna plumes. *J. Geophys. Res.* 113:D17211. doi: 10.1029/2007JD009648

Martin, R. S., Roberts, T. J., Mather, T. A., and Pyle, D. M. (2009). The implications of H_2S and H_2 kinetic stability in high-T mixtures of magmatic and atmospheric gases for the production of oxidized trace species (e.g., BrO and NOx). *Chem. Geol.* 263, 143–150. doi: 10.1016/j.chemgeo.2008.12.028

Martin, R. S., Sawyer, G. M., Spampinato, L., Salerno, G. G., Ramirez, C., Ilyinskaya, E., et al. (2010). A total volatile inventory for Masaya Volcano, Nicaragua. *J. Geophys. Res.* 115:L02610. doi: 10.1029/2010JB007480

Martin, R. S., Wheeler, J. C., Ilyinskaya, E., Braban, C. F., and Oppenheimer, C. (2012b). The uptake of halogen (HF, HCl, HBr and HI) and nitric (HNO_3) acids into acidic sulphate particles in quiescent volcanic plumes. *Chem. Geol.* 296-297, 19–25. doi: 10.1016/j.chemgeo.2011.12.013

Mather, T. A., Allen, A. G., Davison, B. M., Pyle, D. M., Oppenheimer, C., and McGonigle, A. J. S. (2004a). Nitric acid from volcanoes. *Earth Planet. Sci. Lett.* 218, 17–30. doi: 10.1016/S0012-821X(03)00640-X

Mather, T. A., Allen, A. G., Oppenheimer, C., Pyle, D. M., and McGonigle, A. J. S. (2003). Size-resolved characterisation of soluble ions in the particles in the tropospheric plume of masaya volcano, nicaragua: origins and plume processing. *J. Atmos. Chem.* 46, 207–237. doi: 10.1023/A:1026327502060

Mather, T. A., Pyle, D. M., and Allen, A. G. (2004b). Volcanic source for fixed nitrogen in the early Earth's atmosphere. *Geology* 32:905. doi: 10.1130/G20679.1

Mather, T. A., Pyle, D. M., Tsanev, V. I., McGonigle, A. J. S., Oppenheimer, C., and Allen, A. G. (2006). A reassessment of current volcanic emissions from the Central American arc with specific examples from Nicaragua. *J. Volcanol. Geotherm. Res.* 149, 297–311. doi: 10.1016/j.jvolgeores.2005.07.021

Mather, T. A., Witt, M. L. I., Pyle, D. M., Quayle, B. M., Aiuppa, A., Bagnato, E., et al. (2012). Halogens and trace metal emissions from the ongoing 2008 summit eruption of Kilauea volcano, Hawai'i. *Geochim. Cosmochim. Acta* 83, 292–323. doi: 10.1016/j.gca.2011.11.029

McGonigle, A. J. S. (2004). SO_2 depletion in tropospheric volcanic plumes. *Geophys. Res. Lett.* 31:L13201. doi: 10.1029/2004GL019990

McGonigle, A. J. S., Aiuppa, A., Giudice, G., Tamburello, G., Hodson, A. J., and Gurrieri, S. (2008). Unmanned aerial vehicle measurements of volcanic carbon dioxide fluxes. *Geophys. Res. Lett.* 35:L06303. doi: 10.1029/2007GL032508

McGonigle, A. J. S., and Oppenheimer, C. (2003). "Optical sensing of volcanic gas and aerosol emissions," in *Volcanic Degassing*, eds C. Oppenheimer, D. M. Pyle, and J. Barclay (London: Geological Society of London), 149–168.

McGonigle, A. J. S., Oppenheimer, C., Galle, B., Mather, T. A., and Pyle, D. M. (2002). Walking traverse and scanning DOAS measurements of volcanic gas emission rates. *Geophys. Res. Lett.* 29, 46-1-46-4. doi: 10.1029/2002GL015827

McGonigle, A. J. S., Pering, T. D., Wilkes, T. C., Tamburello, G., D'Aleo, R., Bitetto, M., et al. (2017). Ultraviolet imaging of volcanic plumes: a new paradigm in volcanology. *Geosciences* 7:68. doi: 10.20944/preprints201707.0076.v1

Mellor, G. L., and Yamada, T. (1982). Development of a turbulence closure model for geophysical fluid problems. *Rev. Geophys.* 20:851. doi: 10.1029/RG020i004p00851

Moor, J. M. d., Aiuppa, A., Avard, G., Wehrmann, H., Dunbar, N., Muller, C., et al. (2016a). Turmoil at Turrialba Volcano (Costa Rica): degassing and eruptive processes inferred from high-frequency gas monitoring. *J. Geophys. Res. Solid Earth* 121, 5761–5775. doi: 10.1002/2016JB013150

Moor, J. M. d., Aiuppa, A., Pacheco, J., Avard, G., Kern, C., Liuzzo, M., et al. (2016b). Short-period volcanic gas precursors to phreatic eruptions: insights from Poás Volcano, Costa Rica. *Earth Planet. Sci. Lett.* 442, 218–227. doi: 10.1016/j.epsl.2016.02.056

Mori, T., and Burton, M. (2006). The SO 2 camera: a simple, fast and cheap method for ground-based imaging of SO_2 in volcanic plumes. *Geophys. Res. Lett.* 33:329. doi: 10.1029/2006GL027916

Mori, T., and Notsu, K. (1997). Remote CO, COS, CO_2, SO_2, HCl detection and temperature estimation of volcanic gas. *Geophys. Res. Lett.* 24, 2047–2050. doi: 10.1029/97GL52058

Moune, S., Sigmarsson, O., Schiano, P., Thordarson, T., and Keiding, J. K. (2012). Melt inclusion constraints on the magma source of Eyjafjallajökull 2010 flank eruption. *J. Geophys. Res. Solid Earth* 117:1485. doi: 10.1029/2011JB008718

Moussallam, Y., Edmonds, M., Scaillet, B., Peters, N., Gennaro, E., Sides, I., et al. (2016). The impact of degassing on the oxidation state of basaltic magmas: a case study of Kilauea volcano. *Earth Planet. Sci. Lett.* 450, 317–325. doi: 10.1016/j.epsl.2016.06.031

Noguchi, K., and Kamiya, H. (1963). Prediction of volcanic eruption by measuring the chemical composition and amounts of gases. *Bull. Volcanol.* 26, 367–378. doi: 10.1007/BF02597298

Oana, S. (1962). Volcanic gases and sublimates from Showashinzan. *Bull. Volcanol.* 24, 49–57. doi: 10.1007/BF02599328

Oppenheimer, C., Francis, P., Burton, M., Maciejewski, A. J. H., and Boardman, L. (1998). Remote measurement of volcanic gases by Fourier transform infrared spectroscopy. *Appl. Phys. B Lasers Opt.* 67, 505–515. doi: 10.1007/s003400050536

Oppenheimer, C., Kyle, P., Eisele, F., Crawford, J., Huey, G., Tanner, D., et al. (2010). Atmospheric chemistry of an Antarctic volcanic plume. *J. Geophys. Res.* 115, 5473. doi: 10.1029/2009JD011910

Oppenheimer, C., Tsanev, V. I., Braban, C. F., Cox, R. A., Adams, J. W., Aiuppa, A., et al. (2006). BrO formation in volcanic plumes. *Geochim. Cosmochim. Acta* 70, 2935–2941. doi: 10.1016/j.gca.2006.04.001

Platt, U., and Bobrowski, N. (2015). "Quantification of volcanic reactive halogen emissions," in *Volcanism and Global Environmental Change*, eds A. Schmidt, K. E. Fristad, and L. T. Elkins-Tanton (Cambridge: Cambridge University Press), 115–132.

Platt, U., Bobrowski, N., and Butz, A. (2018). Ground-based remote sensing and imaging of volcanic gases and quantitative determination of multi-species emission fluxes. *Geosciences* 8:44. doi: 10.3390/geosciences8020044

Platt, U., Rateike, M., Junkermann, W., Rudolph, J., and Ehhalt, D. H. (1988). New tropospheric OH measurements. *J. Geophys. Res.* 93:5159. doi: 10.1029/JD093iD05p05159

Pyle, D. M., and Mather, T. A. (2009). Halogens in igneous processes and their fluxes to the atmosphere and oceans from volcanic activity: a review. *Chem. Geol.* 263, 110–121. doi: 10.1016/j.chemgeo.2008.11.013

Raschig, F. (1914). *Füllkörper*. DRP 286 122. Deutsches Reich.

Rix, M., Valks, P., Hao, N., Loyola, D., Schlager, H., Huntrieser, H., et al. (2012). Volcanic SO_2, BrO and plume height estimations using GOME-2 satellite measurements during the eruption of Eyjafjallajökull in May 2010. *J. Geophys. Res. Atmos.* 117, 147. doi: 10.1029/2011JD016718

Roberts, T. (2018). Ozone Depletion in Tropospheric Volcanic Plumes: From Halogen-Poor to Halogen-Rich Emissions. *Geosciences* 8, 68. doi: 10.3390/geosciences8020068

Roberts, T. J., Braban, C. F., Martin, R. S., Oppenheimer, C., Adams, J. W., Cox, R. A., et al. (2009). Modelling reactive halogen formation and ozone depletion in volcanic plumes. *Chem. Geol.* 263, 151–163. doi: 10.1016/j.chemgeo.2008.11.012

Roberts, T. J., Jourdain, L., Griffiths, P. T., and Pirre, M. (2014a). Re-evaluating the reactive uptake of HOBr in the troposphere with implications for the marine boundary layer and volcanic plumes. *Atmos. Chem. Phys.* 14, 11185–11199. doi: 10.5194/acp-14-11185-2014

Roberts, T. J., Martin, R. S., and Jourdain, L. (2014b). Reactive bromine chemistry in Mount Etna's volcanic plume: the influence of total Br, high-temperature processing, aerosol loading and plume–air mixing. *Atmos. Chem. Phys.* 14, 11201–11219. doi: 10.5194/acp-14-11201-2014

Roberts, T. J., Vignelles, D., Liuzzo, M., Giudice, G., Aiuppa, A., Coltelli, M., et al. (2018). The primary volcanic aerosol emission from Mt Etna: size-resolved particles with SO_2 and role in plume reactive halogen chemistry. *Geochim. Cosmochim. Acta* 222, 74–93. doi: 10.1016/j.gca.2017.09.040

Rose, W. I., Millard, G. A., Mather, T. A., Hunton, D. E., Anderson, B., Oppenheimer, C., et al. (2006). Atmospheric chemistry of a 33–34 hour old volcanic cloud from Hekla Volcano (Iceland): insights from direct sampling and the application of chemical box modeling. *J. Geophys. Res.* 111, Q08008. doi: 10.1029/2005JD006872

Rüdiger, J., Bobrowski, N., Liotta, M., and Hoffmann, T. (2017). Development and application of a sampling method for the determination of reactive halogen species in volcanic gas emissions. *Anal. Bioanal. Chem.* 409, 5975–5985. doi: 10.1007/s00216-017-0525-1

Rüdiger, J., Schmitt, S., Pitton, D., Tirpitz, J.-L., Gutmann, A., Gutierrez, X., et al. (2018a). "HALVIRE: HALogen activation in Volcanic plumes In Reaction chamber Experiments,"in *EGU General Assembly 2018, held 8-13 April, 2018* (Vienna), 14827.

Rüdiger, J., Tirpitz, J.-L., Moor, J. M., de, Bobrowski, N., Gutmann, A., Liuzzo, M., et al. (2018b). Implementation of electrochemical, optical and denuder-based sensors and sampling techniques on UAV for volcanic gas measurements: examples from Masaya, Turrialba and Stromboli volcanoes. *Atmos. Meas. Tech.* 11, 2441–2457. doi: 10.5194/amt-11-2441-2018

Saiz-Lopez, A., and von Glasow, R. (2012). Reactive halogen chemistry in the troposphere. *Chem. Soc. Rev.* 41, 6448–6472. doi: 10.1039/c2cs35208g

Sander, R., and Crutzen, P. J. (1996). Model study indicating halogen activation and ozone destruction in polluted air masses transported to the sea. *J. Geophys. Res. Atmos.* 101, 9121–9138. doi: 10.1029/95JD03793

Sawyer, G. M., Salerno, G. G., Le Blond, J. S., Martin, R. S., Spampinato, L., Roberts, T. J., et al. (2011). Gas and aerosol emissions from Villarrica volcano, Chile. *J. Volcanol. Geotherm. Res.* 203, 62–75. doi: 10.1016/j.jvolgeores.2011.04.003

Schönhardt, A., Richter, A., Theys, N., and Burrows, J. P. (2017). Space-based observation of volcanic iodine monoxide. *Atmos. Chem. Phys.* 17, 4857–4870. doi: 10.5194/acp-17-4857-2017

Schumann, U., Weinzierl, B., Reitebuch, O., Schlager, H., Minikin, A., Forster, C., et al. (2011). Airborne observations of the Eyjafjalla volcano ash cloud over Europe during air space closure in April and May 2010. *Atmos. Chem. Phys.* 11, 2245–2279. doi: 10.5194/acp-11-2245-2011

Schwandner, F. M., Seward, T. M., Gize, A. P., Hall, K., and Dietrich, V. J. (2013). Halocarbons and other trace heteroatomic organic compounds in volcanic gases from Vulcano (Aeolian Islands, Italy). *Geochim. Cosmochim. Acta* 101, 191–221. doi: 10.1016/j.gca.2012.10.004

Schwandner, F. M., Seward, T. M., Gize, A. P., Hall, P. A., and Dietrich, V. J. (2004). Diffuse emission of organic trace gases from the flank and crater of a quiescent active volcano (Vulcano, Aeolian Islands, Italy). *J. Geophys. Res. Atmos.* 109. doi: 10.1029/2003JD003890

Sedlacek, W. A., Lazrus, A. L., and Gandrud, B. W. (1984). Measurements of stratospheric bromine. *J. Geophys. Res.* 89, 4821. doi: 10.1029/JD089iD03p04821

Seinfeld, J. H., Pandis, S. N., and Noone, K. (1998). Atmospheric chemistry and physics: from air pollution to climate change. *Phys. Today* 51, 88–90. doi: 10.1063/1.882420

Shaw, G. H. (2008). Earth's atmosphere–Hadean to early Proterozoic. *Chem. Erde* 68, 235–264. doi: 10.1016/j.chemer.2008.05.001

Song, C. H. (2003). Dispersion and chemical evolution of ship plumes in the marine boundary layer: Investigation of O 3 /NO y /HO x chemistry. *J. Geophys. Res.* 108:215. doi: 10.1029/2002JD002216

Sparks, R. S. J. (2003). "Dynamics of magma degassing," in *Volcanic Degassing*, eds C. Oppenheimer, D. M. Pyle, and J. Barclay (London: Geological Society of London), 5–22.

Spilliaert, N., Metrich, N., and Allard, P. (2006). S–Cl–F degassing pattern of water-rich alkali basalt: modelling and relationship with eruption styles on Mount Etna volcano. *Earth Planet. Sci. Lett.* 248, 772–786. doi: 10.1016/j.epsl.2006.06.031

Strellis, D. A., Hwang, H. H., Anderson, T. F., and Landsberger, S. (1996). A comparative study of IC, ICP-AES, and NAA measurements on chlorine, bromine, and sodium in natural waters. *J. Radioanal. Nucl. Chem.* 211, 473–484. doi: 10.1007/BF02039713

Sturges, W. T., and Shaw, G. E. (1993). Halogens in aerosols in Central Alaska. *Atmos. Environ. A* 27, 2969–2977. doi: 10.1016/0960-1686(93)90329-W

Sugiura, T., Mizutani, Y., and Oana, S. (1963). Fluorine, chlorine, bromine and iodine in volcanic gases. *J. Earth Sci. Nagoya Univ.* 11, 272–278.

Surl, L., Donohoue, D., Aiuppa, A., Bobrowski, N., and von Glasow, R. (2015). Quantification of the depletion of ozone in the plume of Mount Etna. *Atmos. Chem. Phys.* 15, 2613–2628. doi: 10.5194/acp-15-2613-2015

Surl, L., Donohoue, D., and von Glasow, R. (2014). "Modelling the regional impact of volcanic bromine using WRF-Chem,"in *EGU General Assembly 2014, held 27 April-2 May, 2014* (Vienna), 1509.

Symonds, R. B., Gerlach, T. M., and Reed, M. H. (2001). Magmatic gas scrubbing: implications for volcano monitoring. *J. Volcanol. Geotherm. Res.* 108, 303–341. doi: 10.1016/S0377-0273(00)00292-4

Symonds, R. B., Rose, W. I., Bluth, G. J. S., and Gerlach, T. M. (1994). Volcanic-gas studies; methods, results, and applications. *Rev. Mineral. Geochem.* 30, 1–66.

Textor, C. (2003). Injection of gases into the stratosphere by explosive volcanic eruptions. *J. Geophys. Res.* 108:647. doi: 10.1029/2002JD 002987

Textor, C., Graf, H.-F., Timmreck, C., and Robock, A. (eds.). (2004). *Emissions from volcanoes: Emissions of Atmospheric Trace Compounds*. Dordrecht: Springer Netherlands.

Theys, N., van Roozendael, M., Dils, B., Hendrick, F., Hao, N., and de Mazière, M., (2009). First satellite detection of volcanic bromine monoxide emission after the Kasatochi eruption. *Geophys. Res. Lett.* 36:L03809. doi: 10.1029/2008GL036552

Theys, N., van Roozendael, M., Hendrick, F., Yang, X., Smedt, I., de, Richter, A., et al. (2011). Global observations of tropospheric BrO columns using GOME-2 satellite data. *Atmos. Chem. Phys.* 11, 1791–1811. doi: 10.5194/acp-11-1791-2011

Vance, A., McGonigle, A. J. S., Aiuppa, A., Stith, J. L., Turnbull, K., and von Glasow, R. (2010). Ozone depletion in tropospheric volcanic plumes. *Geophys. Res. Lett.* 37:L22802. doi: 10.1029/2010GL044997

Vidal, C. M., Métrich, N., Komorowski, J.-C., Pratomo, I., Michel, A., Kartadinata, N., et al. (2016). The 1257 Samalas eruption (Lombok, Indonesia): the single greatest stratospheric gas release of the Common Era. *Sci. Rep.* 6:34868. doi: 10.1038/srep34868

Vogt, R., Crutzen, P. J., and Sander, R. (1996). A mechanism for halogen release from sea-salt aerosol in the remote marine boundary layer. *Nature* 383, 327–330. doi: 10.1038/383327a0

Voigt, C., Jessberger, P., Jurkat, T., Kaufmann, S., Baumann, R., Schlager, H., et al. (2014). Evolution of CO_2, SO_2, HCl, and HNO_3 in the volcanic plumes from Etna. *Geophys. Res. Lett.* 41, 2196–2203. doi: 10.1002/2013GL058974

Vömel, H., and Diaz, K. (2010). Ozone sonde cell current measurements and implications for observations of near-zero ozone concentrations in the tropical upper troposphere. *Atmos. Meas. Tech.* 3, 495–505. doi: 10.5194/amt-3-495-2010

von Glasow, R. (2000). *Modeling the Gas and Aqueous Phase Chemistry of the Marine Boundary Layer*. Dissertation. Mainz: Johannes Gutenberg-Universität, Physik.

von Glasow, R. (2010). Atmospheric chemistry in volcanic plumes. *Proc. Natl. Acad. Sci. U.S.A.* 107, 6594–6599. doi: 10.1073/pnas.0913164107

von Glasow, R., Bobrowski, N., and Kern, C. (2009). The effects of volcanic eruptions on atmospheric chemistry. *Chem. Geol.* 263, 131–142. doi: 10.1016/j.chemgeo.2008.08.020

von Glasow, R., and Crutzen, P. J. (2003). "Tropospheric halogen chemistry," in *Treatise on Geochemistry*, eds H. D. Holland and K. K. Turekian (Oxford: Elsevier), 1–67.

von Glasow, R., Donohoue, D., Bobrowski, N., Witt, M., and Mather, T. (2015). "Reactive plume chemistry and links to mercury deposition at Masaya volcano, Nicaragua," in *EGU General Assembly 2015, held 12-17 April, 2015* (Vienna), 6134.

Wallace, P. J. (2005). Volatiles in subduction zone magmas: concentrations and fluxes based on melt inclusion and volcanic gas data. *J. Volcanol. Geotherm. Res.* 140, 217–240. doi: 10.1016/j.jvolgeores.2004.07.023

Watson, I. M., and Oppenheimer, C. (2000). Particle size distributions of Mount Etna's aerosol plume constrained by Sun photometry. *J. Geophys. Res. Atmos.* 105, 9823–9829. doi: 10.1029/2000JD900042

Webster, J. D., Baker, D. R., and Aiuppa, A. (2018). "Halogens in mafic and intermediate-silica content magmas," in *The Role of Halogens in Terrestrial and Extraterrestrial Geochemical Processes*, eds D. E. Harlov and L. Aranovich (Cham: Springer International Publishing), 307–430.

Wexler, A. S., and Clegg, S. L. (2002). Atmospheric aerosol models for systems including the ions H^+, NH_4^+, Na^+, SO_4^{2-}, NO_3^-, Cl^-, Br^-, and H_2O. *J. Geophys. Res.* 107:745. doi: 10.1029/2001JD000451

Witt, M. L. I., Mather, T. A., Pyle, D. M., Aiuppa, A., Bagnato, E., and Tsanev, V. I. (2008). Mercury and halogen emissions from Masaya and Telica volcanoes, Nicaragua. *J. Geophys. Res.* 113, Q08008. doi: 10.1029/2007JB005401

Witter, J. B., Kress, V. C., Delmelle, P., and Stix, J. (2004). Volatile degassing, petrology, and magma dynamics of the Villarrica Lava Lake, Southern Chile. *J. Volcanol. Geotherm. Res.* 134:303–337. doi: 10.1016/j.jvolgeores.2004.03.002

Wittmer, J. (2012). *Development of an Active Alkaline Trap to Determine Acidic Gas Ratios in Volcanic Plumes: Sampling Technique and Analytical Methods*. Diploma Thesis. Heidelberg University Library: University of Heidelberg.

Wittmer, J., Bobrowski, N., Liotta, M., Giuffrida, G., Calabrese, S., and Platt, U. (2014). Active alkaline traps to determine acidic-gas ratios in volcanic plumes: sampling techniques and analytical methods. *Geochem. Geophys. Geosyst.* 15, 2797–2820. doi: 10.1002/2013GC005133

World Meteorological Organization (2014). *Scientific Assessment of Ozone Depletion: 2014*, Global Ozone Research and Monitoring Project-Report No. 55, 1.50.

Zdanowicz, C. M., Zielinski, G. A., and Germani, M. S. (1999). Mount mazama eruption: calendrical age verified and atmospheric impact assessed. *Geology* 27:621. doi: 10.1130/0091-7613(1999)027<0621:MMECAV>2.3.CO;2

Zelenski, M. E., Fischer, T. P., Moor, J. M. d., Marty, B., Zimmermann, L., Ayalew, D., et al. (2013). Trace elements in the gas emissions from the Erta Ale volcano, Afar, Ethiopia. *Chem. Geol.* 357, 95–116. doi: 10.1016/j.chemgeo.2013.08.022

Conflict of Interest Statement: The authors declare that the research was conducted in the absence of any commercial or financial relationships that could be construed as a potential conflict of interest.

frontiers in Earth Science

ORIGINAL RESEARCH
published: 04 December 2018
doi: 10.3389/feart.2018.00215

Geochemistry of Noble Gases and CO_2 in Fluid Inclusions From Lithospheric Mantle Beneath Wilcza Góra (Lower Silesia, Southwest Poland)

Andrea Luca Rizzo[1,2]*, *Beatrice Pelorosso*[2], *Massimo Coltorti*[2], *Theodoros Ntaflos*[3], *Costanza Bonadiman*[2], *Magdalena Matusiak-Małek*[4], *Francesco Italiano*[1] and *Giovanni Bergonzoni*[2]

[1] Sezione di Palermo, Istituto Nazionale di Geofisica e Vulcanologia, Palermo, Italy, [2] Dipartimento di Fisica e Scienze della Terra, Università degli Studi di Ferrara, Ferrara, Italy, [3] Department of Lithospheric Research, University of Vienna, Vienna, Austria, [4] Institute of Geological Sciences, University of Wrocław, Wrocław, Poland

OPEN ACCESS

Edited by:
Alessandro Aiuppa,
Università degli Studi di Palermo, Italy

Reviewed by:
Orlando Vaselli,
Università degli Studi di Firenze, Italy
Franco Tassi,
Università degli Studi di Firenze, Italy
Veronique Gardien,
Claude Bernard University Lyon 1,
France

***Correspondence:**
Andrea Luca Rizzo
andrea.rizzo@ingv.it;
rzznrl@unife.it

Specialty section:
This article was submitted to
Petrology,
a section of the journal
Frontiers in Earth Science

Received: 15 May 2018
Accepted: 07 November 2018
Published: 04 December 2018

Citation:
Rizzo AL, Pelorosso B, Coltorti M,
Ntaflos T, Bonadiman C,
Matusiak-Małek M, Italiano F and
Bergonzoni G (2018) Geochemistry of
Noble Gases and CO_2 in Fluid
Inclusions From Lithospheric Mantle
Beneath Wilcza Góra (Lower Silesia,
Southwest Poland).
Front. Earth Sci. 6:215.
doi: 10.3389/feart.2018.00215

Knowledge of the products originating from the subcontinental lithospheric mantle (SCLM) is crucial for constraining the geochemical features and evolution of the mantle. This study investigated the chemistry and isotope composition (noble gases and CO_2) of fluid inclusions (FI) from selected mantle xenoliths originating from Wilcza Góra (Lower Silesia, southwest Poland), with the aim of integrating their petrography and mineral chemistry. Mantle xenoliths are mostly harzburgites and sometimes bear amphiboles, and are brought to the surface by intraplate alkaline basalts that erupted outside the north-easternmost part of the Eger (Ohře) Rift in Lower Silesia. Olivine (Ol) is classified into two groups based on its forsterite content: (1) $Fo_{88.9-91.5}$, which accounts for a fertile-to-residual mantle, and (2) $Fo_{85.5-88.1}$, which indicates large interactions with circulating (basic) melts. This dichotomy is also related to orthopyroxene (Opx) and clinopyroxene (Cpx), which show two ranges of Mg# values (87–90 and 91–93, respectively) and clear evidence of recrystallization. CO_2 predominates within FI, followed by N_2. The $\delta^{13}C$ of mantle CO_2 varies between −4.7‰ and −3.1‰, which mostly spans the MORB range ($-8‰ < \delta^{13}C < -4‰$). The $^3He/^4He$ ratio is 6.7–6.9 Ra in Cpx, 6.3–6.8 Ra in Opx, and 5.9–6.2 Ra in Ol. These values are within the range proposed for European SCLM (6.3±0.3 Ra). The decrease in $^3He/^4He$ from Cpx to Ol is decoupled from the He concentration, and excludes any diffusive fractionation from FI. The chemistry of FI entrapped in Ol indicates that the mantle is depleted by variable extents of partial melting, while that of Opx and Cpx suggests the overprinting of at least one metasomatic event. According to Matusiak-Małek et al. (2017), Cpx, Opx, and amphiboles were added to the original harzburgite by carbonated hydrous silicate melt related to Cenozoic volcanism. This process resulted in entrapment of CO_2-rich inclusions whose chemical and isotope composition resembles that of metasomatizing fluids. We argue that FI data reflect a mixing between two endmembers: (1) the residual mantle, resulting from partial melting of European SCLM, and (2) the metasomatic agent, which is strongly He-depleted and characterized by MORB-like features.

Keywords: noble gases, CO_2, fluid inclusions, mantle xenoliths, European mantle, SCLM, MORB, metasomatism

INTRODUCTION

During the last 60–70 Myr, Europe, and the circum-Mediterranean area have experienced extensive volcanic activity related to their complex geodynamic evolution. The erupted rocks have geochemical characteristics resembling two types of magmatism: (1) orogenic with calc-alkaline magmas, generated in subduction-related settings, and (2) anorogenic with alkaline magmas, generated in intraplate conditions (Lustrino and Wilson, 2007 and references therein). Most cases of anorogenic magmatism started up to 30 Myr later than orogenic magmatism, and brought mantle-derived ultramafic xenoliths to the surface. These xenoliths represent an essential source of information about (1) the nature and evolution of the European lithospheric mantle, (2) the genesis of basic magmas, and (3) magma–mantle geochemical interactions at mantle depth or at the Earth's surface (Downes et al., 2001; Gautheron and Moreira, 2002; Coltorti et al., 2009, 2010; Bonadiman and Coltorti, 2011; Day et al., 2015).

The easternmost major exposure of Cenozoic volcanic activity in Central Europe occurs in the Eger (Ohře) Rift (Bohemian Massif) and its surroundings. The northeastern prolongation of this rift is located in Lower Silesia (southwest Poland) at the margin of the Variscan orogenic belt, where some SiO_2-undersaturated basalts carry mantle xenoliths (Ćwiek et al., 2018 and references therein). Most of these xenoliths are anhydrous spinel-bearing harzburgites and dunites, but there are also some lherzolites. Studies of these xenoliths have shown that the subcontinental lithospheric mantle (SCLM) in this area is strongly depleted (up to 35%), and has been further affected by reactions with CO_2-bearing alkaline silicate metasomatic melt, possibly related to Cenozoic volcanism (e.g., Matusiak-Małek et al., 2014, 2017 and references therein). The amount of percolating metasomatic melt would decrease continuously during this reaction, thereby progressively modifying its chemical composition. Those two factors resulted in the formation of strong heterogeneities that are visible in the modal and chemical compositions of the mantle.

A considerable amount of information about features of the mantle beneath the north-easternmost part of the Eger (Ohře) Rift can be obtained by studying the geochemistry of fluid inclusions (FI) in ultramafic xenoliths. Several studies have already demonstrated that noble gases (He, Ne, and Ar) and CO_2 systematics in FI represent an useful tool for understanding the main processes that modify the original features of the mantle both temporally and spatially (Deines, 2002; Gautheron and Moreira, 2002; Gautheron et al., 2005; Martelli et al., 2011, 2014; Correale et al., 2012, 2016; Day et al., 2015; Gennaro et al., 2017). However, contemporaneous measurements of He, Ne, and Ar isotopes in European mantle xenoliths are limited to a few sample suites. Moreover, noble gases and C isotopes of CO_2 together have never been studied in mantle xenoliths from Europe and the circum-Mediterranean area, and hence the features of the mantle and its geodynamic implications remain unclear.

To the best of our knowledge, studies of noble gases from central European mantle xenoliths have only involved the volcanic provinces of the French Massif Central, Eifel, and Pannonian Basin (Dunai and Baur, 1995; Buikin et al., 2005; Gautheron et al., 2005). These studies suggest that the $^3He/^4He$ ratio normalized to the atmosphere is 6.32 ± 0.39 Ra (mean ± SD). This range of values is lower than that MORB mantle (8±1 Ra; Graham, 2002) or plume-related settings (e.g., up to 40 Ra in Hawaii and Iceland; Stuart et al., 2003), and the origin of this radiogenic isotope signature is still debated. It has been attributed to a mantle plume with a low $^3He/^4He$ ratio due to either the addition and recycling of crustal materials to a MORB-like source (Dunai and Baur, 1995), or being an original feature of the European SCLM (Gautheron et al., 2005). On the other hand, Ne and Ar isotopes from selected suites of ultramafic xenoliths from the Eifel and Pannonian Basin have been interpreted based on the presence of a mantle plume beneath these areas (Buikin et al., 2005). However, those authors used a multistep crushing method to extract gases from mineral-hosted FI, and this approach is notably less conservative than the single-step crushing applied by Gautheron et al. (2005) because it can result in the release of radiogenic and cosmogenic noble gases trapped within the crystal lattice. The consequences of this methodological difference need to be carefully evaluated and compared.

The present study is the first to investigate the chemistry and isotope composition of noble gases and CO_2 hosted in FI from mantle xenoliths found in basanite rocks from Wilcza Góra (WG) in Lower Silesia, southwest Poland. These data were integrated with the main information obtained in mineralogical and petrological studies to define the features of the mantle beneath this sector of the European SCLM and interpret the results in the context of other European mantle xenoliths. We also compare the isotope composition of FI with that of surface gases emitted along the Eger (Ohře) Rift.

GEODYNAMIC AND GEOLOGICAL SETTING

Anorogenic, mostly mafic volcanism has occurred in Central Europe (in the French Massif Central, Rhenish Massif, and Bohemian Massif) from the Cenozoic to the Pleistocene to form the Cenozoic central European Volcanic Province (Wilson and Downes, 2006; Lustrino and Wilson, 2007; CEVP). This volcanism occurred during the convergence between the African and European plates along with the progressive closure of oceanic basins in the Mediterranean region and the formation of the Alpine orogeny. Within this compressional regime, an extensional phase triggered the opening of the European Cenozoic Rift System (ECRS) (Dèzes et al., 2004), whose products occur typically in the proximity of graben systems. The north-easternmost part of the CEVP is related to the northeast–southwest trending Eger (Ohře) Rift in the western part of the Bohemian Massif in the Czech Republic (**Figure 1A**). Volcanic rocks occur both along the rift axis and in the off-rift environment in this area (Ulrych et al., 2011). Volcanic rocks located northeast of the rift in southwest Poland follow the northwest–southeast trending Odra fault zone (**Figure 1A**). Volcanism in southwest Poland has exhibited three main activity peaks: (1) Eocene-Oligocene (34–26 Ma), (2) Miocene

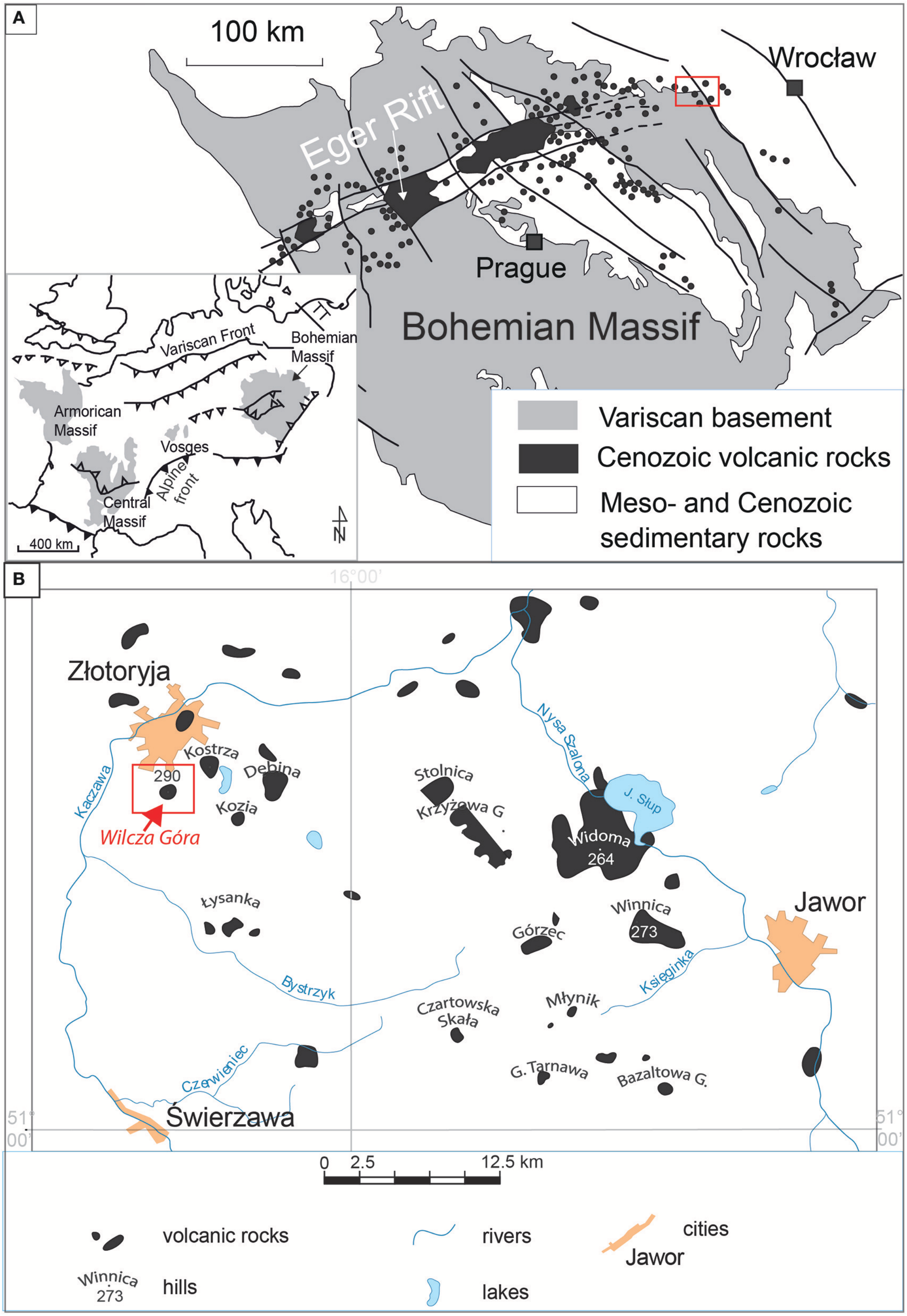

FIGURE 1 | (A) Location of Eger Rift in Bohemian Massif (based on Ulrych et al., 2011), inset shows European Variscan Basement and major fault zones (Mazur et al., 2006, modified); **(B)** Outcrops of Cenozoic volcanic rocks in the vicinity of Złotoryja city, location of Wilcza Góra indicated by arrow and red box (based on Sawicki, 1995).

(22–18 Ma), and (3) Pliocene-Pleistocene (5.5–1.0 Ma) (Pécskay and Birkenmajer, 2013). More than 300 outcrops of Cenozoic mafic volcanic rocks have been identified in southwest Poland, and around 3% of them contain xenoliths originating from the upper mantle and lower crust (Matusiak-Małek et al., 2017).

The present study investigated mantle xenoliths from WG basanite rocks (20.07 ± 0.90 Ma) (Birkenmajer et al., 2007) located in the Kaczawskie Mountains around 40 km east of the axis of the Eger Graben. These mountains constitute the western part of the Sudetes mountain range, which constitutes the northern part of the Bohemian Massif and was amalgamated during the Variscan closure of the Rheic Ocean ca. 370 Ma (Mazur et al., 2006 and references therein). The Kaczawskie Mountains comprise a metamorphosed volcano-sedimentary succession from Cambrian to late Devonian/early Carboniferous and Mesozoic clastic sediments (Mazur et al., 2006; Białek et al., 2007).

SAMPLES AND METHODS

Sample Preparation

Ultramafic mantle xenoliths were collected from an active quarry near Złotoryja city (**Figure 1B**). They were hosted in basanite lavas, and are relatively scarce and typically <5 cm in diameter, although occasionally up to 10 cm. The xenoliths were selected from among the largest unaltered specimens, and then cut, sliced, and polished into 80-μm-thick sections for defining the modal composition, petrography, and mineral chemistry. A suite of samples from the WG quarry was studied and well-characterized by Matusiak-Małek et al. (2017) for major and trace elements, and for Sr and Nd isotopes (see section Petrological Background for details). The present samples are appended with the subscript "II" (e.g., $WG1_{II}$) in order to avoid confusion with the nomenclature adopted by Matusiak-Małek et al. (2017).

Seventeen aliquots of pure and unaltered olivine (Ol), orthopyroxene (Opx), and clinopyroxene (Cpx) were separated for analyzing the noble gases and CO_2 in FI from nine mantle xenoliths. The only exception is for sample $WG5_{II}$ that due to the small dimension of the xenolith was only studied for the modal composition, petrography, and mineral chemistry. After grinding and sieving the rocks, crystals without impurities and larger than 0.5 mm were handpicked under a binocular microscope following the laboratory protocol developed at the Istituto Nazionale di Geofisica e Vulcanologia (INGV), Sezione di Palermo, Italy (e.g., Martelli et al., 2014; Rizzo et al., 2015; Gennaro et al., 2017, and references therein). Aliquots of the minerals were then cleaned ultrasonically in 6.5% HNO_3 before being rinsed with deionized water. The samples were then accurately weighed and loaded into an ultra-high-vacuum crusher for analyses. The amount of loaded sample varied from 0.02 to 1.0 g.

Analytical Procedure

The modal proportion of minerals was determined by point counting, averaging two runs with more than 2,000 points for each thin section (2.5 × 4.0 cm). The smallness of the xenolith samples (5–10 cm) prevented analyses of the bulk major and trace elements, and so the chemical characterization of this xenolith group was based on a detailed *in-situ* investigation.

The major-elements composition of mineral and glass chemistry was determined by a CAMECA SXFive FE electron microprobe equipped with five wavelength-dispersive spectrometers and one energy-dispersive spectrometer at the Department of Lithospheric Research, University of Vienna, Austria. The operating conditions were an accelerating voltage of 15 kV, a beam current of 20 nA, and a counting time 20 s at the peak position. Microscopic images allowed the description of fluid inclusions trapped within single minerals.

The element and isotope composition of noble gases (He, Ne, and Ar) and CO_2 in FI was determined at the laboratories of INGV-Palermo in Italy. The selected crystals were split into two aliquots: the first was loaded into a stainless-steel crusher capable of holding up to six samples simultaneously for noble-gas analysis, and the second was used for determining the concentration and isotope ratio of CO_2. FI were released by in-vacuo single-step crushing at about 200 bar. This conservative procedure was used to minimize the contribution of cosmogenic ^{3}He and radiogenic ^{4}He that could possibly have grown or been trapped in the crystal lattice (Kurz, 1986; Hilton et al., 1993, 2002; Rizzo et al., 2015). However, since our samples were collected in a quarry, there should have been no cosmogenic effect. The CO_2 measurement was first performed during noble-gas extraction at the time of crushing by quantifying the total gas pressure ($CO_2+N_2+O_2+$noble gases) and subtracting the residual pressure of N_2+O_2+noble gases after removing CO_2 using a "cold finger" immersed in liquid N_2 at −196°C. The noble gases were then cleaned in an ultra-high-vacuum (10^{-9}-10^{-10} mbar) purification line, and all species in the gas mixture except for noble gases were removed. He isotopes (^{3}He and ^{4}He) and Ne isotopes (^{20}Ne, ^{21}Ne, and ^{22}Ne) were measured separately using two different split-flight-tube mass spectrometers (Helix SFT, Thermo Scientific).

The values of the $^{3}He/^{4}He$ ratio are expressed in units of R/Ra, where Ra is the $^{3}He/^{4}He$ ratio of air, which is equal to 1.39×10^{-6}. The analytical uncertainty of the He-isotope ratio (1σ) was <3.7%, while this was <2.1 and <4.2% for $^{20}Ne/^{22}Ne$ and $^{21}Ne/^{22}Ne$, respectively. The reported values of both Ne-isotope ratios are corrected for isobaric interferences at m/z values of 20 ($^{40}Ar^{2+}$) and 22 ($^{44}CO_2^{2+}$). Corrections are generally performed by measuring ^{20}Ne, ^{21}Ne, ^{22}Ne, ^{40}Ar, and $^{44}CO_2$ during the same analysis, and considering the previously determined $^{40}Ar^{2+}/^{40}Ar^{+}$ and $^{44}CO_2^{2+}/CO_2^{+}$ ratios on the same Helix SFT that run FI samples. Ar isotopes (^{36}Ar, ^{38}Ar, and ^{40}Ar) were analyzed by a multicollector mass spectrometer (Argus, GVI) with an analytical uncertainty (1σ) of <1.5%. For each analytical session we analyzed at least one standard of each of He, Ne, and Ar that had previously been purified from air and stored in tanks. The analytical uncertainty (1σ) values for the $^{3}He/^{4}He$, $^{20}Ne/^{22}Ne$, $^{21}Ne/^{22}Ne$, $^{40}Ar/^{36}Ar$, and $^{38}Ar/^{36}Ar$ ratios were <0.94%, <0.07%, <0.3%, <0.05%, and <0.12%, respectively. The uncertainty in the determinations of the elemental He, Ne, and Ar contents was <5% after considering natural variability and the assumption of residual (not crushed) crystals for weight normalization of the number of moles of gas; typical blanks for He, Ne, and Ar were $<10^{-15}$, $<10^{-16}$, and $<10^{-14}$ mol, respectively. Further details about the sample preparation and analytical procedures are available in Martelli et al. (2014), Rizzo et al. (2015), and Robidoux et al. (2017).

Our protocol represents the first attempt to estimate the N_2 concentration corrected for atmospheric contamination during the simultaneous extraction of CO_2 and noble gases, which is hereafter reported as N_2^*. We did this by first quantifying ^{40}Ar corrected for air contamination ($^{40}Ar^*$) and then calculating the atmospheric ^{40}Ar present in our samples:

$$\begin{aligned} {}^{40}\mathrm{Ar}^* &= {}^{40}\mathrm{Ar}_{\mathrm{sample}} - [{}^{36}\mathrm{Ar}_{\mathrm{sample}} \cdot ({}^{40}\mathrm{Ar}/{}^{36}\mathrm{Ar})_{\mathrm{air}}] \\ {}^{40}\mathrm{Ar}_{\mathrm{air}} &= {}^{40}\mathrm{Ar}_{\mathrm{sample}} - {}^{40}\mathrm{Ar}^* \end{aligned}$$

Based on the $O_2/^{40}Ar$ and $N_2/^{40}Ar$ ratios in the atmosphere, we finally calculated the amounts of O_2 and N_2 pertaining to air and subtracted these values from the number of moles of N_2+O_2 measured during extraction. The only assumption was that mantle gases trapped in FI do not contain O_2.

Based on the $^{20}Ne/^{22}Ne$ and $^{21}Ne/^{22}Ne$ ratios (see section Isotope Compositions of He, Ne, Ar, and CO_2 in FI), we corrected ^{21}Ne as follows:

$$ {}^{21}\mathrm{Ne}^* = {}^{21}\mathrm{Ne}_{\mathrm{sample}} - [{}^{22}\mathrm{Ne}_{\mathrm{sample}} \cdot ({}^{21}\mathrm{Ne}/{}^{22}\mathrm{Ne})_{\mathrm{air}}] $$

Although most of the samples showed a low atmospheric contamination (air has $^4He/^{20}Ne = 0.318$, $^{20}Ne/^{22}Ne = 9.8$, $^{21}Ne/^{22}Ne = 0.029$, and $^{40}Ar/^{36}Ar = 295.5$; Ozima and Podosek, 1983), $^3He/^4He$ was corrected for contamination based on the measured $^4He/^{20}Ne$ ratio as follows:

$$ \mathrm{Rc/Ra} = ((\mathrm{R_M/Ra})(\mathrm{He/Ne})_M - (\mathrm{He/Ne})_A)/((\mathrm{He/Ne})_M - (\mathrm{He/Ne})_A) $$

where subscripts M and A refer to measured and atmospheric theoretical values, respectively. The corrected $^3He/^4He$ ratios are hereafter reported as Rc/Ra values. However, the correction was either small or negligible for most of the samples, with a maximum bias of ~0.06 Ra for Opx WG1$_{II}$ showing the lowest $^4He/^{20}Ne$ ratio. The CO_2 samples used in the analyses of C isotopes were extracted and quantified in a glass line, which avoids the adsorption and fractionation of CO_2 that can occur in powders and upon contact with stainless steel. We found a very good agreement between the number of moles of CO_2 extracted and quantified in the glass line and that measured during the extraction of noble gases (**Figure S1**). After purification, CO_2 was trapped in a glass sampler and moved to a stable-isotope laboratory for the isotope measurements. Further details about the extraction and analytical protocol can be found in Gennaro et al. (2017). The $^{13}C/^{12}C$ is expressed in delta notation ($\delta^{13}C$) as the difference in parts per mil relative to the V-PDB international standard. The analytical error estimated as 1σ was better than 0.3‰.

PETROLOGICAL BACKGROUND

Xenoliths from WG basanite have been studied by Smulikowski and Kozłowska-Koch (1984) and Matusiak-Małek et al. (2017). They are spinel-bearing peridotites, mostly harzburgites but also some dunites, wehrlites, and clinopyroxenites (**Figure S2**); approximately half of the studied xenoliths contained pargasitic amphibole, but their modal composition and dimensions prevented them from being separated for gas analyses. Xenoliths also contain numerous fine-grained intergranular glassy aggregates (so-called melt pockets). Matusiak-Małek et al. (2017) grouped WG xenoliths based on the chemical composition of Ol into (1) group A, characterized by Ol with $Fo_{89.1-92.5}$, (2) group B, characterized by Ol with $Fo_{85.5-88.1}$, and (3) group C (not described here), characterized by Ol with $Fo_{77.0-82.4}$. The forsterite content of Ol is positively correlated with the Mg# values of pyroxenes (Px) and amphiboles. The entire xenolith suite is interpreted as resulting from a metasomatic reaction between hydrous, CO_2-bearing alkaline silicate melt and a strongly depleted lithospheric mantle. From this viewpoint, group-C xenoliths represent products of reactions involving very high melt/rock ratios, close to that for an open conduit (hydraulic fracturing) system, while group-B and group-A xenoliths record decreasing amounts of melt percolating through and reacting with the refractory mantle. The metasomatic reaction initially enriched the peridotites located close to the source of the agent in Fe and Ti (group B), and the continuum metasomatic interaction introduced Cpx and amphiboles (and possibly also spinel).

TABLE 1 | Textural features and modal composition of Wilcza Góra xenoliths. Modal content of phases by volume percentages.

	Lithology	Texture	Olivine	Orthopyroxene	Clinopyroxene	Spinel	Amphibole
WG1$_{II}$	Harzburgite	protogranular	69.3	27.9	1.0	1.8	-
WG2$_{II}$	Harzburgite	equigranular	63.0	32.8	3.0	1.0	-
WG3$_{II}$	Harzburgite	equigranular	75.0	20.0	2.0	2.0	trace
WG4$_{II}$	Harzburgite	protogranular	60.6	34.1	3.1	2.2	trace
WG5$_{II}$	Harzburgite	porphyroclastic	84.7	13.0	1.7	0.5	trace
WG6$_{II}$	Lherzolite	porphyroclastic	67.1	27.1	5.7	trace	-
WG7$_{II}$	Harzburgite	protogranular	77.6	15.8	3.6	2.3	-
WG8$_{II}$	Harzburgite	porphyroclastic	71.9	25.8	trace	2.3	-
WG9$_{II}$	Lherzolite	protogranular	64.9	27.0	7.6	0.6	-
WG10$_{II}$	Dunite	protogranular	90.9	9.1	trace	trace	trace

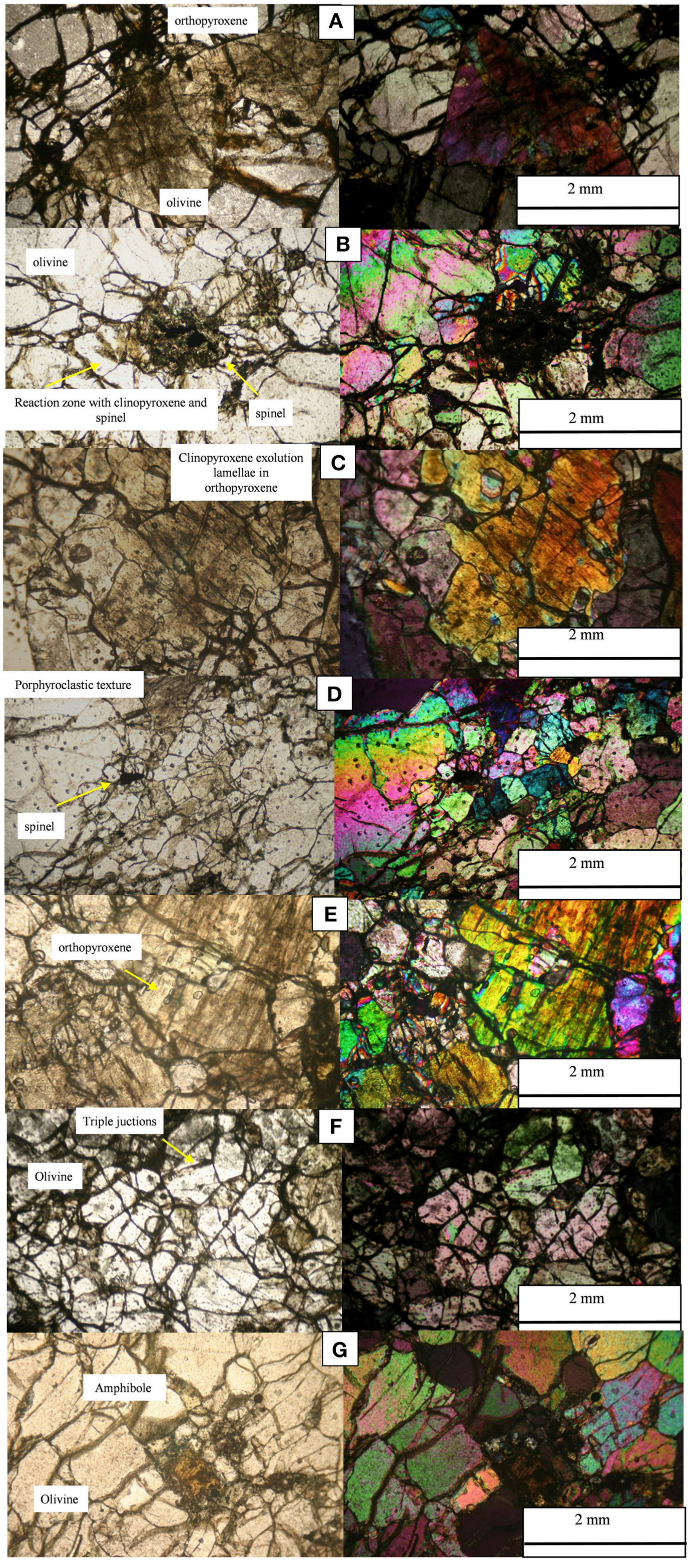

FIGURE 2 | (A–G) Photomicrographs of representative microstructures of WG xenoliths in transmitted plane-polarized light (left) and in cross-polarized light (right). In detail: **(A,B)** images showing protogranular textures with large Opx and Ol grains ($WG4_{II}$); **(B)** a reaction zone with the spongy rims of Cpx and spinel ($WG1_{II}$); **(C)** a protogranular texture with large Opx hosting Cpx exsolution lamellae ($WG9_{II}$); **(D)** examples of porphyroclastic textures with Ol neoblasts slightly oriented and with small Ol replacing large Opx; **(E)** Large opx and small equigranular ol in WGII8; **(F)** Equigranular texture with Ol converging at 120 degrees; **(G)** Small amphiboles associated with the spongy rim of Cpx. Bubbles are evident in Ol ($WG7_{II}$; d).

RESULTS

Petrography

The mantle peridotites are fresh and quite homogeneous. The modal proportion of minerals is presented in **Figure S2** and **Table 1**. The studied samples consist of seven harzburgites, two Cpx-poor lherzolites, and one dunite. The harzburgites contain 85–61 vol.% Ol, 34–13 vol.% Opx, <5 vol.% Cpx, and 1–2.3 vol.% spinel, while the two Cpx-poor lherzolites (Cpx <8 vol.%) contain 67–65 vol.% Ol, around 27 vol.% Opx, and <0.5 vol.% spinel. The dunite mainly consists of Ol (>90 vol.%), with a small amount of Opx (<10 vol.%). These rocks common exhibit a protogranular texture; that is, harzburgites $WG1_{II}$, $WG4_{II}$, and $WG7_{II}$, lherzolite $WG9_{II}$, and dunite $WG10_{II}$. They generally exhibit coarse-grained Opx and Ol (0.6–3 mm; **Figure 2A**); Cpx is smaller (typically 0.4–1 mm) than the other phases and it occurs primarily as a protogranular phase or as nearly formed crystals in the reaction zone (**Figure 2B**). In a few cases ($WG9_{II}$; **Figure 2C**) the Opx core is characterized by Cpx exsolution lamellae. Spinel appears as crystallites associated with a fine-grained reaction zone (**Figures 2B,D**).

Lherzolite $WG6_{II}$ and harzburgites $WG5_{II}$ and $WG8_{II}$ exhibit clearly phorphyroclastic (**Figure 2D**; $WG5_{II}$) textures and generally contain two generations of both Ol and Opx. The large Ol porphyroclasts were subjected to deformation and developed kink bands, whereas the small neoblasts commonly occur as an embayment and partly replace large Opx and Ol porphyroclasts (**Figures 2D,E**). Harzburgites $WG2_{II}$ and $WG3_{II}$ display a well-developed equigranular/granoblastic texture with Ol arranged with a 120° grain-boundary intersection (**Figure 2F**; $WG3_{II}$).

Disseminated amphiboles appear as small anhedral grains that are often associated with the spongy rim of Cpx (**Figure 2G**) or clearly enclose Cpx.

Mineral Chemistry

The mineral chemistry data are reported in **Table 2**. On the basis of Fo [calculated as $Mg/(Mg+Fe_{tot})$ in atoms per formula unit] vs. the distribution of NiO contents, Ol could be divided into two distinct groups: group A (Fo = 89.12–91.48 and NiO = 0.31–0.43 wt.%) and group B (Fo = 85.53–88.13 and NiO = 0.25–0.37 wt.%); this categorization is consistent with groups A and B reported by Matusiak-Małek et al. (2017) (**Figure 3A**).

The two geochemical groups observed in terms of Fo components in Ol are also observed in Px. Opx (En = 85.14–76.85, Fs = 10.07–21.09, and Wo = 1.77–2.04) exhibits a negative correlation between Al_2O_3 contents (1.27–3.31 wt.%) and Mg# values [$Mg/(Mg+Fe_{tot})$ = 86.65–92.05 mol.%; **Figure 3B**], without any significant variation in relation to petrographic features (i.e., Opx in the reaction zone or Opx with exsolution lamellae). Cpx (Wo = 38.52–55.47, En = 52.11–33.91, and Fs = 9.36–10.6) is characterized by a low TiO_2 content (0.02–0.27 wt.%; **Figure S3A**). Samples $WG7_{II}$ and $WG10_{II}$ have slightly elevated TiO_2 (0.66 wt.%), whereas a few of the secondary grains in samples $WG4_{II}$ and $WG6_{II}$ have TiO_2 contents ranging from 1 to 1.20 wt.%. In both Opx and Cpx the Al_2O_3 content (1.43–4.24 wt.%) is negatively correlated with Mg# (87.81–90.84) (**Figure S3B**). Irrespective of the lithology, spinel has Mg# values within the narrow range of 46.94–55.79, while Cr# [= Cr/(Cr+Al) mol.%] values span a larger range (38.88–69.46; **Figure S3C**). The only exception is for sample $WG5_{II}$ that plots out of the mentioned ranges (Mg#=71.63–71.78; Cr#=27.06–27.58; **Figure S3C**).

According to the classification of Leake et al. (1997), the amphiboles are pargasite (samples $WG3_{II}$ and $WG4_{II}$) and ferropargasite (samples $WG5_{II}$ and $WG10_{II}$), whose Mg# values span from 84.63 to 88.88 and their Al_2O_3 and TiO_2 contents are in the ranges of 12.23–13.74 and 0.81–2.85 wt.%, respectively (**Table 2**).

Chemistry of FI

The chemistry of FI hosted in WG xenoliths is reported in **Table 3** and shown in **Figure 4** and **Figure S4**. The gas mixture is dominated by CO_2, which ranges from 0.9×10^{-7} to 24×10^{-7} mol/g (**Figures 4A,B**). N_2 corrected for atmospheric contamination (N_2^*) represents the second major species, whose content varies from 0.86×10^{-9} to 42×10^{-9} mol/g (**Figure 4B**). The atmospheric component in FI, which here is considered to be N_2+O_2+Ar, varies within the same order of magnitude (1.2×10^{-10} to 1.1×10^{-9} mol/g) and with no systematic differences between mineral phases (**Table 3**), and represents <0.3% of the total gas mixture. $^{40}Ar^*$ is within the range of $0.53–7.2 \times 10^{-11}$ mol/g (**Figures 4C,D**), while ^4He ranges from 0.1×10^{11} to 1.4×10^{11} mol/g (**Figures 4A,C**). The ^{20}Ne concentration ranges from 0.47×10^{-14} to 7.3×10^{-14} mol/g (**Table 3**). Finally, $^{21}Ne^*$ varies from 9.3×10^{-19} to 1.1×10^{-17} mol/g (**Figure S4**).

The average numbers of moles of CO_2, N_2^*, $^{40}Ar^*$, and $^{21}Ne^*$ are higher in Opx than in Ol, which in turn shows a wider compositional range, while the values in Cpx are intermediate (**Figure 4** and **Figure S4**). The only exception is for He, whose content is comparable in Ol and Opx, while it is lowest in Cpx (**Figure 4A** and **Figure S4**). Among Ol, samples $WG4_{II}$, $WG7_{II}$, and $WG10_{II}$ (Fo<88) show the highest concentrations of He and CO_2, and among the largest amounts of N_2^*, $^{40}Ar^*$, and $^{21}Ne^*$. CO_2 is positively correlated with N_2^*, $^{40}Ar^*$, $^{21}Ne^*$, and ^4He (**Figures 4A,B,D** and **Figure S4C**), indicating that the CO_2-rich FI are also rich in the other gas species.

Isotope Compositions of He, Ne, Ar, and CO_2 in FI

The $^3He/^4He$ ratio not corrected for air contamination (R/Ra) is 5.9–6.2 Ra in Ol, 6.1–6.7 Ra in Opx, and 6.7–6.8 Ra in Cpx (**Table 3**). Ol from samples $WG4_{II}$, $WG7_{II}$, and $WG10_{II}$ (Fo < 88) does not show any significant difference in the $^3He/^4He$ ratio. The $^4He/^{20}Ne$ ratio is 163–2125 in Ol, 32–556 in Opx, and 41–176 in Cpx (**Table 3**). The $^{40}Ar/^{36}Ar$ ratio is 818–3,232 in Ol, 1,543–3,007 in Opx, and 1,217–1,270 in Cpx (**Table 2**). The $^{20}Ne/^{22}Ne$ and $^{21}Ne/^{22}Ne$ ratios are 9.9–10.5 and 0.0301–0.0354, respectively, in Ol, 10.0–10.5 and 0.0302–0.0387 in Opx, and 10.1–10.4 and 0.0308–0.0333 in Cpx (**Table 3** and **Figure 5**).

The $^3He/^4He$ ratio corrected for air contamination (Rc/Ra values) is 5.9–6.2 Ra in Ol, 6.1–6.8 Ra in Opx, and 6.7–6.9 Ra in Cpx (**Table 3** and **Figure 6**). It is worth noting that the $^3He/^4He$ ratio increases from Ol to Cpx, with Opx displaying intermediate values (**Figure 6**). This increase is decoupled from the He concentration, since Ol covers the entire range of He contents at almost constant $^3He/^4He$ ratios (6.0 ± 0.1 Ra;

TABLE 2 | Chemistry of minerals forming Wilcza Góra xenoliths.

OLIVINE										
	WG1$_{II}$	WG2$_{II}$	WG3$_{II}$	WG4$_{II}$	WG5$_{II}$	WG6$_{II}$	WG7$_{II}$	WG8$_{II}$	WG9$_{II}$	WG10$_{II}$
Group	A	A	A	B	B	A	B	A	A	B
n.of analyses	5	6	6	7	10	9	7	4	6	5
SiO_2	40.46	40.71	40.29	39.64	39.81	40.61	40.06	40.46	40.28	39.76
TiO_2	0.00	0.00	0.01	0.00	0.01	0.00	0.00	0.00	0.00	0.02
Al_2O_3	0.01	0.01	0.01	0.01	0.02	0.01	0.01	0.01	0.02	0.02
Fe_2O_3										
FeO	9.25	8.50	10.47	12.33	12.92	9.16	11.98	9.25	10.38	13.00
MnO	0.15	0.14	0.17	0.19	0.19	0.15	0.18	0.14	0.15	0.23
MgO	49.60	50.48	48.53	46.87	46.33	49.83	47.29	49.61	48.73	46.75
CaO	0.05	0.05	0.05	0.06	0.06	0.05	0.05	0.05	0.06	0.11
Na_2O										
K_2O										
Cr_2O3	0.02	0.02	0.02	0.01	0.01	0.02	0.01	0.02	0.02	0.02
NiO	0.41	0.40	0.38	0.35	0.32	0.38	0.35	0.40	0.39	0.32
Total	99.95	100.30	99.91	99.47	99.66	100.21	99.94	99.94	100.02	100.22
FeOtot										
Mg#	90.52	91.37	89.20	87.14	86.47	90.65	87.55	90.53	89.32	86.50
Cr#										
A.f.u.										
Si	0.992	0.991	0.994	0.991	0.995	0.993	0.995	0.992	0.992	0.990
Ti										
Al										0.001
FeIII										
FeII	0.190	0.173	0.216	0.258	0.270	0.187	0.249	0.190	0.214	0.271
Mn	0.003	0.003	0.004	0.004	0.004	0.003	0.004	0.003	0.003	0.005
Mg	1.813	1.832	1.784	1.747	1.726	1.815	1.750	1.813	1.789	1.734
Ca	0.001	0.001	0.001	0.002	0.002	0.001	0.001	0.001	0.002	0.003
Na										
K										
Cr										
Ni	0.008	0.008	0.007	0.007	0.006	0.008	0.007	0.008	0.008	0.006
ORTHOPYROXENE										
	WG1$_{II}$	WG2$_{II}$	WG3$_{II}$	WG4$_{II}$	WG5$_{II}$	WG6$_{II}$	WG7$_{II}$		WG9$_{II}$	WG10$_{II}$
	A	A	A	B	B	A	B		A	B
	4	7	3	3	8	4	6		11	3
	56.66	57.87	56.61	56.23	55.32	57.13	56.45		56.62	55.62
	0.02	0.02	0.05	0.15	0.22	0.03	0.08		0.07	0.27
	1.93	1.32	1.86	2.19	3.19	1.71	1.89		2.48	3.00
	0.12	0.02	0.00	0.00	0.02	0.05	0.02		0.01	0.10
	5.77	5.47	7.16	7.81	8.34	5.94	7.51		6.83	8.61
	0.15	0.14	0.18	0.20	0.19	0.15	0.19		0.16	0.23
	34.28	34.93	32.84	32.59	31.75	34.20	32.88		33.34	31.90
	0.67	0.73	0.73	0.77	0.77	0.74	0.79		0.73	0.84
	0.05	0.09	0.09	0.05	0.04	0.07	0.06		0.05	0.05
	0.00	0.00	0.00	0.00	0.00	0.00	0.00		0.00	0.00
	0.51	0.51	0.50	0.46	0.48	0.54	0.40		0.54	0.37
	100.17	101.03	99.39	100.31	100.17	100.34	100.19		100.59	100.96
	5.88	5.49	7.16	7.81	8.36	5.99	7.53		6.85	8.71
	91.22	91.89	89.07	88.15	87.13	91.05	88.62		89.66	86.72
	1.949	1.970	1.973	1.950	1.926	1.963	1.957		1.948	1.924

(Continued)

TABLE 2 | Continued

	0.000	0.001	0.001	0.004	0.006	0.001	0.002		0.002	0.007
	0.078	0.053	0.077	0.090	0.131	0.069	0.077		0.101	0.122
	0.003	0.000	0.000	0.000	0.000	0.001	0.000		0.000	0.003
	0.166	0.155	0.208	0.226	0.242	0.171	0.218		0.196	0.249
	0.005	0.004	0.005	0.006	0.006	0.004	0.006		0.005	0.007
	1.757	1.772	1.705	1.684	1.648	1.751	1.698		1.709	1.645
	0.025	0.027	0.028	0.029	0.029	0.028	0.030		0.027	0.031
	0.003	0.006	0.006	0.003	0.003	0.005	0.004		0.004	0.003
	0.014	0.014	0.014	0.013	0.013	0.014	0.011		0.015	0.010
CLINOPYROXENE										
	WG1$_{I}$	WG2$_{II}$	WG3$_{II}$	WG4$_{II}$	WG5$_{II}$	WG6$_{II}$	WG7$_{II}$	WG8$_{II}$	WG9$_{II}$	WG10II
	A	A	A	B	B	A	B	A	A	B
	3	6	3	1	4	11	6	8	5	4
	53.48	54.72	53.61	50.64	52.06	52.65	53.31	53.25	53.13	52.29
	0.01	0.11	0.13	1.21	0.69	0.36	0.07	0.22	0.21	0.69
	2.91	2.22	2.77	5.05	4.23	3.85	3.17	3.15	3.40	4.17
	0.29	0.14	0.27	0.21	0.20	0.22	0.33	0.17	0.09	0.25
	2.42	2.67	2.64	3.00	3.42	2.88	3.02	2.41	2.78	3.70
	0.08	0.10	0.11	0.10	0.11	0.10	0.11	0.09	0.10	0.15
	16.73	17.82	16.55	16.36	16.02	16.44	16.27	16.61	16.26	16.07
	21.47	19.96	21.45	20.92	21.90	20.78	21.17	21.75	21.67	21.42
	1.06	1.25	1.12	0.68	0.71	1.07	1.18	0.95	0.93	0.84
	1.28	1.74	1.43	1.45	0.87	1.92	1.51	1.50	1.42	1.05
	99.74	100.71	100.08	99.62	100.20	100.26	100.12	100.09	99.95	100.61
	2.68	2.79	2.88	3.19	3.60	3.07	3.31	2.57	2.86	3.92
	91.75	91.97	91.10	90.14	88.80	90.38	89.75	92.02	91.02	87.96
	1.940	1.962	1.942	1.850	1.892	1.906	1.932	1.929	1.930	1.893
	0.001	0.003	0.004	0.033	0.019	0.010	0.002	0.006	0.006	0.019
	0.125	0.094	0.118	0.217	0.181	0.165	0.136	0.135	0.146	0.178
	0.008	0.003	0.008	0.006	0.005	0.006	0.009	0.005	0.002	0.007
	0.073	0.080	0.080	0.092	0.104	0.087	0.091	0.073	0.084	0.112
	0.002	0.003	0.003	0.003	0.004	0.003	0.003	0.003	0.003	0.005
	0.905	0.952	0.893	0.890	0.868	0.886	0.879	0.897	0.880	0.867
	0.835	0.767	0.833	0.819	0.853	0.807	0.822	0.844	0.843	0.831
	0.075	0.087	0.079	0.048	0.050	0.075	0.083	0.067	0.065	0.059
	0.037	0.049	0.041	0.042	0.025	0.055	0.043	0.043	0.041	0.030
SPINEL										
	WG1$_{II}$	WG2$_{II}$	WG3$_{II}$	WG4$_{II}$	WG5$_{II}$		WG7$_{II}$	WG8$_{II}$	WG9$_{II}$	WG10$_{II}$
	A	A	A	B	B		B	A	A	B
	3	5	3	1	2		3	2	3	4
	0.11	0.02	0.02	0.06	0.05		0.04	0.04	0.03	0.10
	0.05	0.07	0.40	0.92	1.01		0.21	0.44	0.34	1.24
	22.08	15.40	18.83	25.12	40.89		21.87	23.62	27.78	30.68
	4.95	4.05	7.20	6.90	6.08		7.36	4.64	4.73	6.17
	12.97	13.79	13.84	15.80	8.38		15.10	12.95	13.69	15.77
	0.33	0.40	0.39	0.10	0.21		0.37	0.34	0.30	0.36
	13.80	12.76	13.32	12.85	19.70		12.49	14.41	14.23	13.57
	0.06	0.01	0.01	0.01	0.27		0.11	0.00	0.04	0.09
	0.00	0.00	0.00							
	0.00	0.00	0.00							
	42.33	51.28	44.17	34.26	22.92		39.82	41.33	36.32	29.17
	0.17	0.15	0.17	0.24	0.30		0.16	0.17	0.17	0.23

(Continued)

TABLE 2 | Continued

	96.85	97.92	98.35	96.26	99.78		97.53	97.92	97.64	97.36
	17.42	17.43	20.32	22.01	13.85		21.72	17.13	17.94	21.32
	58.53	56.61	53.87	51.00	71.71		50.62	59.98	58.57	53.14
	56.25	69.07	61.14	47.78	27.32		54.97	54.00	46.72	38.93
	0.004	0.001	0.001	0.002	0.002		0.001	0.001	0.001	0.003
	0.001	0.002	0.009	0.022	0.021		0.005	0.010	0.008	0.028
	0.820	0.587	0.702	0.934	1.329		0.816	0.861	0.998	1.097
	0.120	0.100	0.170	0.164	0.125		0.173	0.105	0.110	0.140
	0.343	0.372	0.367	0.417	0.195		0.397	0.335	0.350	0.400
	0.009	0.011	0.011	0.003	0.005		0.010	0.009	0.008	0.009
	0.648	0.615	0.628	0.604	0.810		0.589	0.664	0.647	0.614
	0.002	0.000	0.000		0.008		0.004	0.000	0.001	0.003
	0.000	0.000	0.000		0.000		0.000	0.000	0.000	0.000
	0.000	0.000	0.000		0.000		0.000	0.000	0.000	0.000
	1.054	1.310	1.106	0.855	0.500		0.996	1.010	0.875	0.700
	0.005	0.004	0.005		0.007		0.004	0.004	0.004	0.006
AMPHIBOLE										
			$WG3_{II}$	$WG4_{II}$	$WG5_{II}$					$WG10_{II}$
			A	B	B					B
			4	1	5					8
			44.28	43.13	42.56					42.67
			0.83	1.90	2.59					2.76
			12.25	12.84	13.51					13.19
			4.09	4.82	5.02					5.29
			0.08	0.08	0.09					0.10
			18.19	17.30	16.78					16.67
			10.97	11.27	11.50					11.24
			3.20	3.00	2.77					2.90
			0.83	0.89	0.96					0.98
			94.72	95.23	95.77					95.79
			88.79	86.47	85.64					84.89
			6.47	6.308	6.20					6.23
			0.09	0.209	0.28					0.30
			2.11	2.213	2.32					2.27
			0.00	0.000	0.00					0.00
			0.50	0.590	0.61					0.65
			0.01	0.010	0.01					0.01
			3.96	3.772	3.65					3.63
			1.72	1.766	1.80					1.76
			0.91	0.851	0.78					0.82
			0.15	0.167	0.18					0.18

Figure 6A). On the other hand, the $^3He/^4He$ ratios are highest in samples showing the lowest He contents and the largest amounts of CO_2 (**Figure 6B**), N_2^*, $^{40}Ar^*$, and $^{21}Ne^*$ (**Table 3**).

The $\delta^{13}C$ value of mantle CO_2 was determined in most of the mantle xenoliths according to the concentration of CO_2 and the availability of crystals (**Table 3**), with the exception of Cpx from $WG2_{II}$ and $WG8_{II}$, which were not sufficiently abundant to allow further measurements after the noble gases had been measured. $\delta^{13}C$ ranges between −4.2‰ and −3.1‰ in Ol and between −4.7‰ and −3.6‰ in Opx, without any evidence of a correlation with the CO_2 contents (**Figure 7A**). The ratio is slightly less negative for Ol (−3.8 ± 0.4‰) then for Opx (−4.1 ± 0.4‰). $\delta^{13}C$ in Ol was the most negative (−4.2‰) in sample $WG3_{II}$, which also showed the most-negative ratio for Opx (−4.7‰), whereas the least-negative $\delta^{13}C$ was measured in $WG10_{II}$, which did not contain enough Opx for the analysis (**Table 3**).

DISCUSSION

Description of FI

The thin section petrographic observations of the WG mantle xenoliths from which Ol, Opx, and Cpx were separated reveal

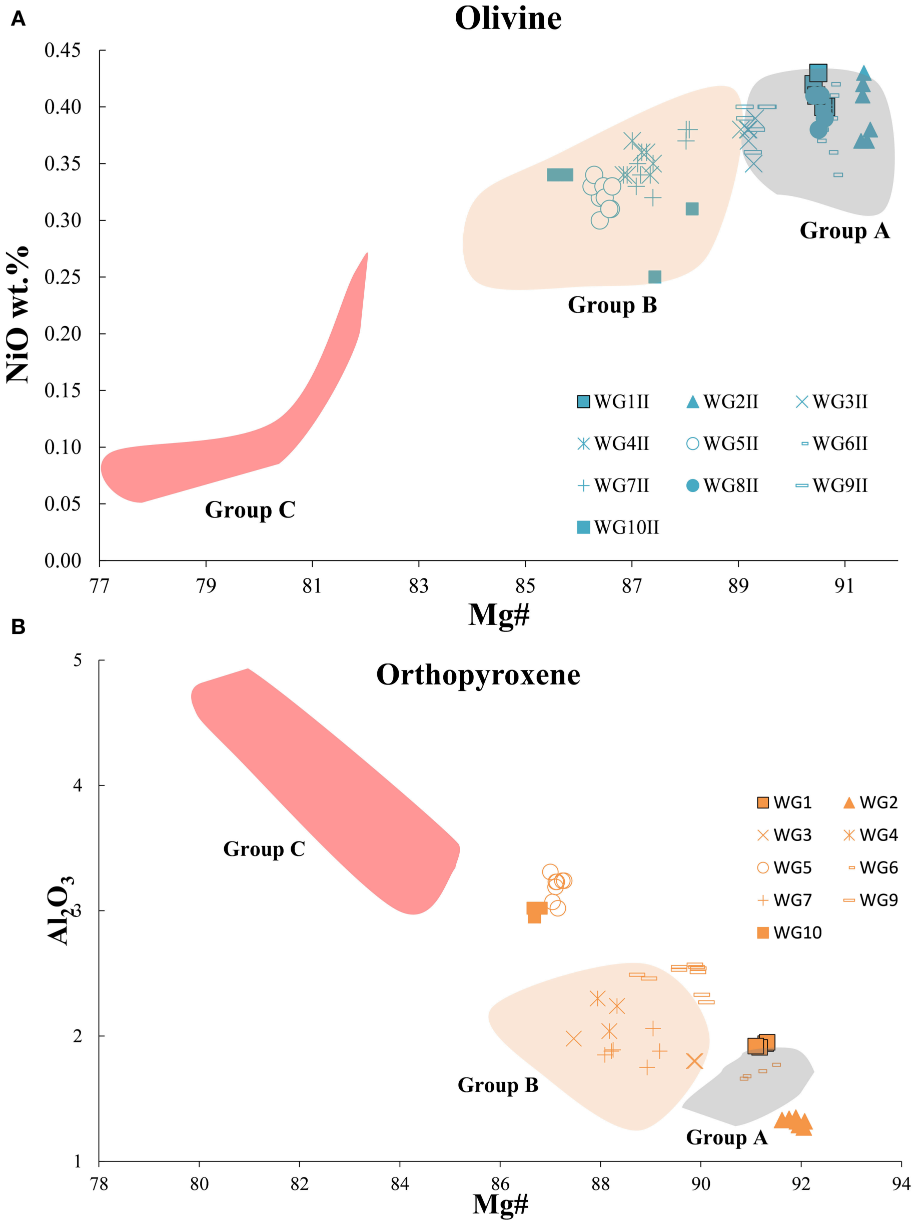

FIGURE 3 | (A) Mg# vs. NiO concentration in Ol. **(B)** Mg# vs. Al_2O_3 in Opx from WG xenoliths. The indicated areas are for the group data reported by Matusiak-Małek et al. (2017).

the clear presence of FI within single crystals (**Figures S5A–D**). These FI have variable dimensions, with the smallest ones being few µm in diameter and the biggest reaching some tens of µm (**Figures S5A–D**). We recognized two types of FI, in accordance with the classification made by Roedder (1984): (1) primary inclusions, present as single inclusions or clusters (**Figures S5A,B**) and/or trails (**Figure S5C**) sometimes developed along plans; (2) secondary inclusions that form clusters and/or trails (**Figure S5D**) mostly developed along plans. The primary inclusions (**Figures S5A–C**) were found always within single coarse grained olivine crystals without continuation to the neighbor grains, an indication that support their primary character (Roedder, 1984); (2) secondary inclusions (**Figure S5D**) form clusters or trails that propagate from clinopyroxene (right part of S5D) to the recrystallized fine grained olivine (left part of S5D). We did not observe FI located along healed fractures. We consider secondary inclusions also trails of FI developed within Cpx and Opx, present e.g., as exsolution lamellae (**Figure S5E**), because trapped after recrystallization due to metasomatic processes.

A detailed study of FI from WG mantle xenoliths was performed by Ladenberger et al. (2009) with similar findings. For this reason, we did not further investigate the morphology and structure of FI from our samples. Importantly, Ladenberger

TABLE 3 | Geochemistry of fluid inclusions hosted in minerals forming mantle xenoliths from Wilcza Góra.

Sample	Mineral	weight (g)	^{4}He mol/g	^{20}Ne mol/g	^{21}Ne mol/g	^{22}Ne mol/g	CO_2	N_2^*	Air mol/g	^{40}Ar mol/g	^{36}Ar mol/g
WG1$_{II}$	Ol	1.01	1.10E-12	5.27E-15	1.61E-17	5.26E-16	8.75E-08	8.62E-10	1.26E-10	6.48E-12	3.95E-15
WG1$_{II}$	Opx	0.30	1.35E-12	4.26E-14	1.28E-16	4.27E-15	5.69E-07	3.91E-09	3.36E-10	1.73E-11	1.06E-14
WG2$_{II}$	Ol	1.00	1.50E-12	9.20E-15	2.81E-17	9.35E-16	1.54E-07	9.38E-10	4.31E-10	1.11E-11	1.36E-14
WG2$_{II}$	Cpx	0.02	1.45E-12	3.54E-14	1.08E-16	3.57E-15	4.25E-07	1.52E-08	8.49E-10	3.40E-11	2.67E-14
WG2$_{II}$	Opx	0.20	2.96E-12	1.86E-14	5.94E-17	1.85E-15	1.25E-06	1.26E-08	7.83E-10	3.81E-11	2.47E-14
WG3$_{II}$	Ol	0.52	2.73E-12	7.05E-15	2.18E-17	6.97E-16	3.21E-07	3.63E-09	3.41E-10	1.38E-11	1.07E-14
WG3$_{II}$	Opx	0.22	5.15E-12	1.40E-14	4.69E-17	1.39E-15	1.75E-06	1.84E-08	5.47E-10	4.53E-11	1.72E-14
WG4$_{II}$	Ol	0.52	1.34E-11	6.29E-15	2.13E-17	6.04E-16	1.12E-06	n.a.	5.71E-10	3.40E-11	1.80E-14
WG4$_{II}$	Ol	0.12	2.56E-12	9.69E-15	3.09E-17	9.44E-16	1.36E-06	1.58E-08	3.85E-10	3.64E-11	1.21E-14
WG4$_{II}$	Opx	0.10	7.27E-12	7.33E-14	2.20E-16	7.27E-15	2.42E-06	1.75E-08	1.06E-09	8.14E-11	3.33E-14
WG6$_{II}$	Ol	1.06	4.89E-12	4.72E-15	1.53E-17	4.59E-16	3.41E-07	1.94E-09	3.54E-10	1.71E-11	1.11E-14
WG6$_{II}$	Opx	0.05	3.68E-12	9.28E-15	2.85E-17	9.22E-16	3.44E-07	n.a.	1.30E-10	1.32E-11	4.09E-15
WG7$_{II}$	Ol	1.02	6.24E-12	7.65E-15	2.35E-17	7.59E-16	3.60E-07	2.99E-09	3.41E-10	1.69E-11	1.07E-14
WG7$_{II}$	Opx	0.03	4.13E-12	3.54E-14	1.11E-16	3.48E-15	1.83E-06	1.19E-08	5.93E-10	4.67E-11	1.87E-14
WG8$_{II}$	Ol	0.51	1.43E-11	4.32E-14	1.30E-16	4.34E-15	1.91E-06	7.91E-09	4.66E-10	4.29E-11	1.47E-14
WG8$_{II}$	Cpx	0.04	8.60E-13	4.90E-15	1.56E-17	4.78E-16	4.50E-07	7.31E-09	5.61E-10	2.15E-11	1.77E-14
WG8$_{II}$	Opx	0.10	5.04E-12	3.96E-14	1.20E-16	3.91E-15	2.35E-06	4.24E-08	7.65E-10	5.67E-11	2.41E-14
WG9$_{II}$	Ol	1.02	2.65E-12	6.92E-15	2.16E-17	6.88E-16	3.01E-07	1.48E-09	1.98E-10	1.06E-11	6.25E-15
WG9$_{II}$	Opx	0.29	2.50E-12	7.03E-15	2.28E-17	6.62E-16	1.04E-06	6.99E-09	5.56E-10	3.79E-11	1.75E-14
WG10$_{II}$	Ol	0.90	8.58E-12	6.06E-15	1.86E-17	5.90E-16	7.73E-07	2.96E-09	9.48E-10	3.18E-11	2.99E-14
WG10$_{II}$	Opx	0.07	2.97E-12	5.35E-15	1.96E-17	5.12E-16	1.25E-06	1.07E-08	4.83E-10	3.44E-11	1.52E-14

^{40}Ar* mol/g	^{4}He/^{20}Ne	^{4}He/^{40}Ar*	^{4}He/N_2^*	^{4}He/CO_2	CO_2/N_2^*	CO_2/Ar*	Ar*/N_2^*	R/Ra	Rc/Ra	Err Rc/Ra +/ −	^{40}Ar/^{36}Ar
5.31E-12	209.1	0.21	1.28E-03	1.26E-05	101.58	1.65E+04	6.16E-03	5.92	5.93	0.07	1638.81
1.42E-11	31.7	0.10	3.45E-04	2.38E-06	145.34	4.00E+04	3.63E-03	6.71	6.77	0.08	1639.95
7.10E-12	163.4	0.21	1.60E-03	9.78E-06	163.82	2.16E+04	7.57E-03	5.90	5.91	0.06	818.33
2.61E-11	41.2	0.06	9.59E-05	3.42E-06	28.03	1.63E+04	1.72E-03	6.85	6.90	0.26	1270.54
3.08E-11	159.5	0.10	2.35E-04	2.37E-06	99.51	4.07E+04	2.45E-03	6.54	6.55	0.08	1543.41
1.06E-11	386.9	0.26	7.52E-04	8.51E-06	88.34	3.02E+04	2.93E-03	6.18	6.18	0.06	1283.53
4.02E-11	368.8	0.13	2.81E-04	2.94E-06	95.44	4.35E+04	2.19E-03	6.27	6.28	0.07	2631.27
2.87E-11	2125.5	0.47	n.a.	1.20E-05	n.a.	3.90E+04	n.a.	5.95	5.95	0.05	1890.39
3.29E-11	264.0	0.08	n.a.	1.89E-06	n.a.	4.13E+04	n.a.	6.11	6.12	0.07	3007.12
7.16E-11	99.2	0.10	4.15E-04	3.01E-06	138.19	3.38E+04	4.09E-03	6.30	6.32	0.09	2445.01
1.38E-11	1035.5	0.35	2.52E-03	1.43E-05	175.35	2.47E+04	7.09E-03	5.88	5.88	0.06	1532.60
1.20E-11	396.3	0.31	n.a.	1.07E-05	n.a.	2.86E+04	n.a.	5.90	5.91	0.06	3232.38
1.38E-11	815.4	0.45	2.09E-03	1.73E-05	120.29	2.61E+04	4.61E-03	5.93	5.93	0.05	1579.12
4.12E-11	116.7	0.10	3.47E-04	2.25E-06	153.90	4.45E+04	3.46E-03	6.60	6.61	0.09	2500.22
3.85E-11	331.5	0.37	1.81E-03	7.50E-06	241.46	4.95E+04	4.87E-03	6.07	6.07	0.06	2921.35
1.63E-11	175.6	0.05	1.18E-04	1.91E-06	61.51	2.76E+04	2.23E-03	6.66	6.67	0.20	1217.14
4.96E-11	127.3	0.10	1.19E-04	2.14E-06	55.43	4.74E+04	1.17E-03	6.06	6.08	0.08	2354.55
8.79E-12	383.6	0.30	1.79E-03	8.82E-06	203.16	3.42E+04	5.94E-03	5.94	5.94	0.09	1702.90
3.27E-11	355.2	0.08	3.57E-04	2.40E-06	149.10	3.18E+04	4.69E-03	6.26	6.26	0.12	2163.75
2.30E-11	1416.6	0.37	2.90E-03	1.11E-05	261.65	3.37E+04	7.77E-03	6.08	6.08	0.06	1064.79
2.99E-11	555.6	0.10	2.77E-04	2.38E-06	116.24	4.17E+04	2.79E-03	6.39	6.39	0.07	2260.23

(Continued)

TABLE 3 | Continued

Err (%)	$^{38}Ar/^{36}Ar$	Err (%)	$^{20}Ne/^{22}Ne$	Err 20/22 +/−	$^{21}Ne/^{22}Ne$	Err 21/22 +/−	^{3}He	$CO_2/^{3}He$	$^{\#}CO_2$	$\delta^{13}C$ ‰ VPDB
0.06	0.18630	0.19	10.07	0.02	0.0308	0.00032	9.08E-18	9.64E+09	n.a.	n.a.
0.07	0.18893	0.19	10.01	0.02	0.0302	0.00023	1.27E-17	4.48E+10	*3.66E-07*	−3.6
0.72	0.18708	0.19	9.87	0.02	0.0301	0.00022	1.24E-17	1.24E+10	1.58E-07	−3.8
0.33	0.18697	0.19	10.07	0.09	0.0308	0.00127	1.40E-17	3.05E+10	n.a.	n.a.
1.12	0.18940	0.19	10.15	0.02	0.0325	0.00053	2.70E-17	4.64E+10	*3.73E-07*	−4.1
0.05	0.18470	0.18	10.14	0.03	0.0315	0.00040	2.35E-17	1.37E+10	2.33E-07	−4.2
0.09	0.19146	0.19	10.15	0.03	0.0342	0.00042	4.50E-17	3.89E+10	1.41E-06	−4.7
0.94	0.18938	0.19	10.47	0.03	0.0354	0.00067	1.11E-16	1.01E+10	1.40E-06	−4.1
0.21	0.19221	0.19	10.23	0.07	0.0326	0.00140	2.18E-17	6.24E+10	n.a.	n.a.
0.13	0.18869	0.19	10.14	0.03	0.0305	0.00048	6.39E-17	3.79E+10	1.13E-06	−4.1
0.76	0.18676	0.19	10.30	0.02	0.0334	0.00053	3.99E-17	8.53E+09	5.55E-07	−3.9
0.08	0.18852	0.19	10.09	0.02	0.0310	0.00043	3.02E-17	1.14E+10	3.20E-07	−3.8
0.73	0.18825	0.19	10.12	0.02	0.0311	0.00041	5.14E-17	6.99E+09	4.34E-07	−4.0
0.09	0.19080	0.19	10.22	0.03	0.0322	0.00041	3.80E-17	4.82E+10	1.15E-06	−4.0
0.11	0.18788	0.19	10.05	0.02	0.0302	0.00036	1.21E-16	1.58E+10	n.a.	n.a.
0.24	0.18589	0.19	10.41	0.22	0.0333	0.00141	7.97E-18	5.64E+10	n.a.	n.a.
0.09	0.18628	0.19	10.10	0.02	0.0307	0.00052	4.25E-17	5.53E+10	n.a.	n.a.
1.32	0.18299	0.18	10.08	0.02	0.0315	0.00034	2.19E-17	1.37E+10	*4.17E-07*	−4.0
0.28	0.18860	0.19	10.58	0.17	0.0344	0.00271	2.17E-17	4.79E+10	n.a.	n.a.
0.38	0.18335	0.18	10.35	0.01	0.0319	0.00121	7.25E-17	1.07E+10	2.13E-07	−3.1
1.55	0.18960	0.19	10.52	0.06	0.0387	0.00074	2.64E-17	4.72E+10	n.a.	n.a.

Ol stands for olivine, cpx for clinopyroxene, and opx for orthopyroxene. $^{\#}$Indicates CO_2 measured from glass line. Among these measurements, those reported in italics and underlined are single analysis while the other represent average of two or more replicates.

et al. (2009) inferred that FI were formed under upper-mantle conditions, which supports the reliability of information on mantle features and processes obtained in the present work.

Petrological Evidence of the Type and Timing of Processes Modifying Local Mantle

The textural features and chemistry of major mineral phases of WG mantle xenoliths provide important evidence of the type and timing of processes that acted in modifying the local mantle before the mantle xenoliths were brought to the surface. In a hypothetical melting trend, fusible elements (Ti and Al) tend to decrease with increasing Mg# (Ionov and Hofmann, 2007; Bonadiman and Coltorti, 2011). We estimated the degree of melting of WG mantle based on the contents of Al_2O_3 vs. MgO in primary Opx (**Figure S6**) following the model of Upton et al. (2011). Comparing our results with those of Matusiak-Małek et al. (2017) confirms that WG xenoliths record a residual mantle that is strongly depleted after 25–30% of partial melting (**Figure S6**).

The textural characteristics (i.e., secondary Px and the presence of amphiboles; **Figure 3**) and geochemical characteristics (i.e., TiO_2 enrichment in Cpx; **Figure S3**) of the group-A and group-B xenoliths provide evidence of peridotite–melt interaction. This evidence is in accordance with the findings of Matusiak-Małek et al. (2017), who suggested that Ol from group-A xenoliths represent the residuum after partial melting. Instead, Cpx is clearly metasomatized, and consequently the FI entrapped by this mineral are secondary (**Figure S5D**) and inherited by the metasomatic agent (see section Mantle Metasomatism). Opx, which exhibits petrographic and mineral chemistry evidence of recrystallization, is at least partially modified by metasomatic interactions. Based on these evidence we argue that the residual mantle was subsequently modified by metasomatic processes.

Finally, the presence of amphiboles, sometimes enclosing Cpx, suggests the introduction of hydrous fluids that could originate from a previous (fossil) subduction, as proposed by the model of Faccenna et al. (2010).

Processes That Modify the Geochemistry of FI

Atmospheric Contamination

While the atmospheric concentration of He is relatively low, the heavy noble gases have accumulated during the evolution of the Earth and so are more prone to contamination. This process can partially or completely mask the original signature recorded by the minerals. The systematics of Ne and Ar isotopes (and complementarily the $^{4}He/^{20}Ne$ ratio) in WG xenoliths highlight the air contamination in FI, resulting in a mixing between mantle- and atmosphere-derived noble gases (**Table 3**). The plot of the three Ne isotopes in **Figure 5** shows that our data fall

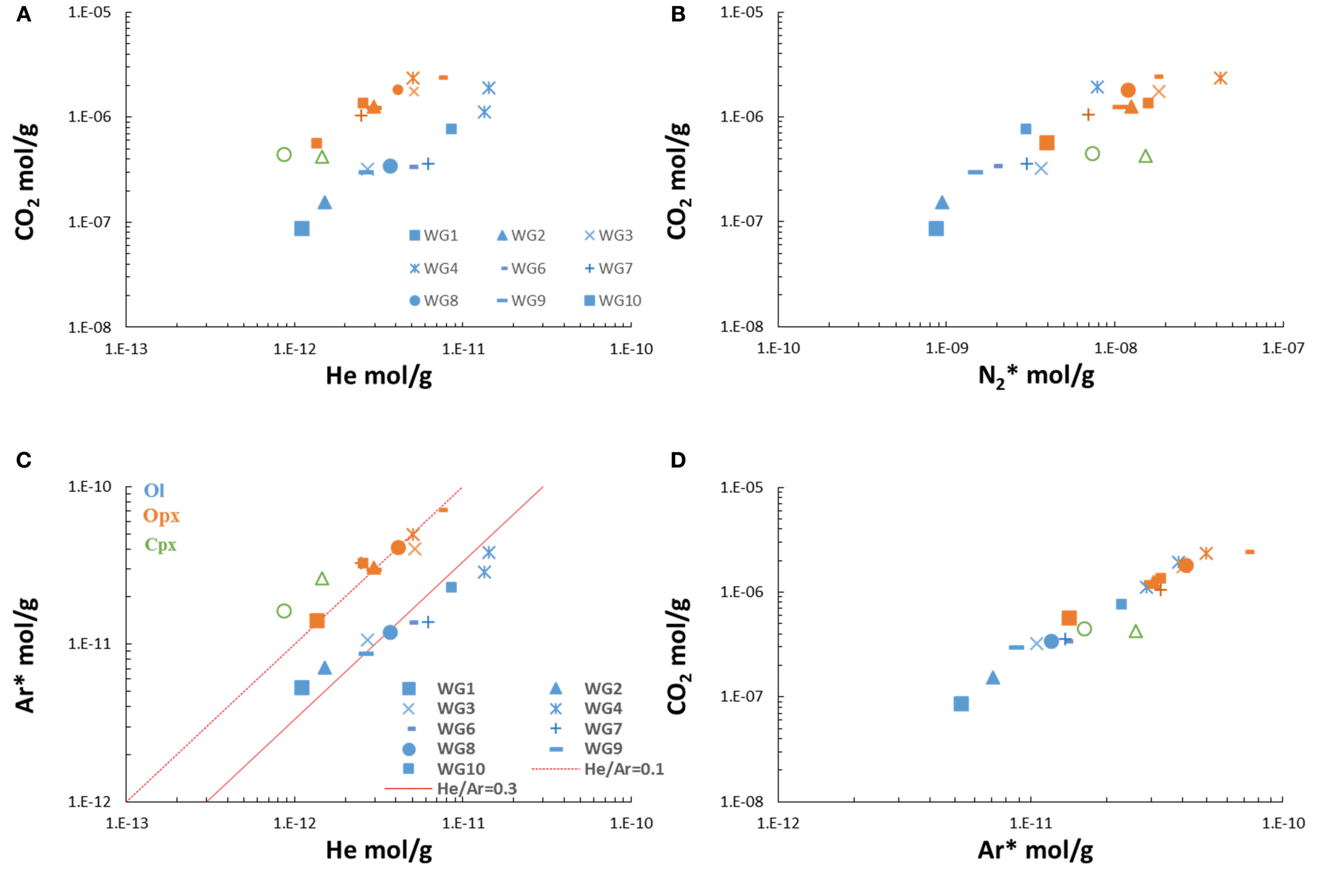

FIGURE 4 | Elemental concentrations measured in FI after single-step crushing of CO_2 vs. **(A)** He, **(B)** N_2^*; diagram of concentrations of Ar* vs. **(C)** He and **(D)** CO_2.

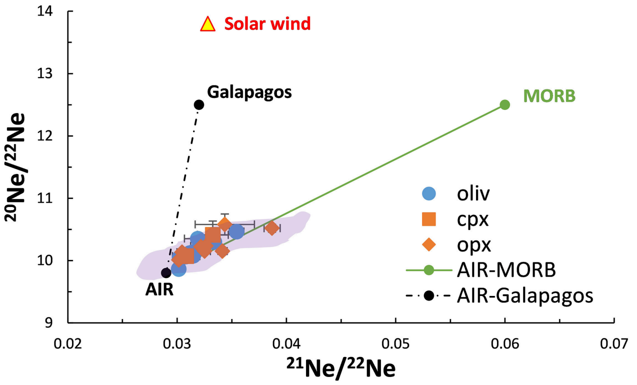

FIGURE 5 | Diagram of $^{21}Ne/^{22}Ne$ vs. $^{20}Ne/^{22}Ne$. The green line represents binary mixing between air and a MORB mantle as defined by Sarda et al. (1988) and Moreira et al. (1998) at $^{21}Ne/^{22}Ne = 0.06$ and $^{20}Ne/^{22}Ne = 12.5$. The black dotted line indicates binary mixing between air and the OIB domain of the Galapagos Islands as determined by Kurz et al. (2009) at $^{21}Ne/^{22}Ne = 0.032$ and $^{20}Ne/^{22}Ne = 12.5$. The primordial neon composition is also reported as Solar wind (e.g., Heber et al., 2009), with at $^{21}Ne/^{22}Ne = 0.0328$ and $^{20}Ne/^{22}Ne = 13.8$. The violet area indicates data from other European localities (French Massif Central, Eifel, and Pannonian Basin) measured by Gautheron et al. (2005).

along the theoretical mixing line between air and a MORB-like mantle, defined by Sarda et al. (1988) and Moreira et al. (1998) at $^{21}Ne/^{22}Ne = 0.06$ and $^{20}Ne/^{22}Ne = 12.5$. Similarly, $^{40}Ar/^{36}Ar$ values are well below the theoretical ratio in the mantle ($^{40}Ar/^{36}Ar$ up to 44,000; e.g., Burnard et al., 1997; Moreira et al., 1998) or typical mantle-derived samples (e.g., Kaneoka, 1983; Ozima and Podosek, 1983; Allègre et al., 1987), confirming the presence of a certain amount of contamination by atmosphere-derived fluids. Such evidence has also been found in other European as well as worldwide SCLM xenoliths (Valbracht et al., 1996; Matsumoto et al., 1998, 2000, 2001, 2002; Yamamoto et al., 2004; Gautheron et al., 2005; Martelli et al., 2011; Correale et al., 2012, 2016).

Several hypotheses were invoked to explain the presence of air in FI as indicated by the Ne- and Ar-isotope data from mantle xenoliths: (1) contamination of the xenoliths as they are brought from the mantle to the surface, caused by the percolation of melts or volatiles in the xenoliths (i.e., Buikin et al., 2005; Gautheron et al., 2005), (2) air entrapment in microcracks of the minerals during or after the eruptive activity (i.e., Martelli et al., 2011; Correale et al., 2012), and (3) mantle contamination at depth from the dehydration of atmospheric gases from subducting oceanic crust (i.e., Matsumoto et al., 1998, 2000, 2001; Yamamoto

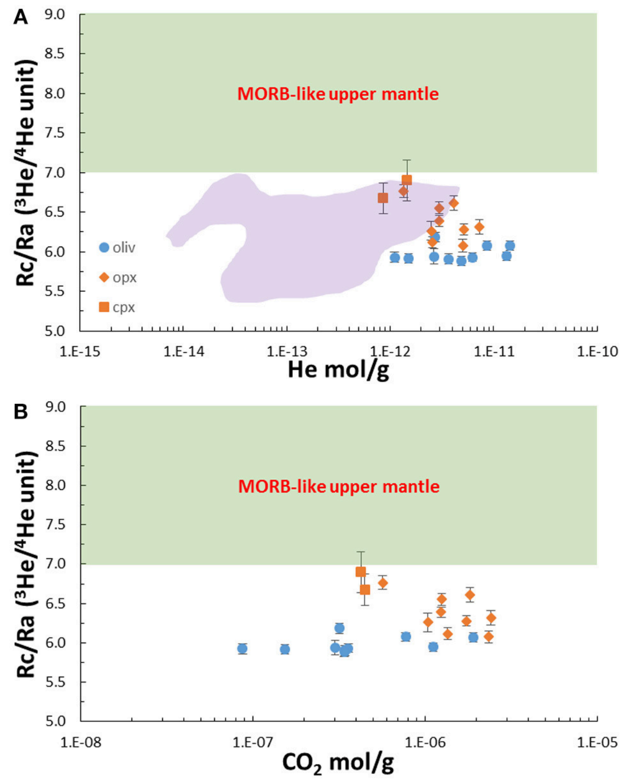

FIGURE 6 | Concentrations of He and CO_2 vs. $^3He/^4He$ corrected for air contamination (Rc/Ra values). The green bar indicates the range of $^3He/^4He$ ratios for a MORB-like mantle (8 ± 1 Ra; Graham, 2002).

et al., 2004; Gurenko et al., 2006). Our observations make the first two hypotheses unlikely because we found no difference between Ol and Px, with the latter having entrapped FI related to the metasomatic agent (see section Mantle Metasomatism). In addition, detailed observations of Ol and Px did not produce any evidence of microcracks, since their presence would have produced systematic differences between the analyzed minerals. We therefore consider the third hypothesis to be the most reasonable, although there is no evidence of a recent subduction in this part of Europe, with the last subduction event dated to the Ordovician-Devonian period (Kryza et al., 2011). More likely, the recent model proposed by Faccenna et al. (2010 and references therein) proposes that slab fragmentation within the upper mantle may influence outside-arc alkaline magmatism generated both ahead of the slab in the back-arc region and around the lateral edges of the slab. In fact, other geochemical tracers in erupted rocks (Sr, Nd, and Pb isotopes; Lustrino and Wilson, 2007) provide evidence for the recycling of subduction-related volatiles in the European mantle.

The most widely accepted model for explaining the noble-gas geochemistry of SCLM assumes a type of steady state resulting from the mixing between fluids infiltrating from the asthenosphere and those already present in the lithosphere and originating from the recycling of crustal- and atmosphere-derived noble gases introduced from past subduction events into the European mantle (Gautheron and Moreira, 2002; Gautheron et al., 2005). In the case of WG mantle xenoliths, the presence of amphiboles could indicate the presence of hydrous fluids originating from a previous (fossil) subduction event, in accordance with the model proposed by Faccenna et al. (2010).

As is the case in subduction-related settings (i.e., arc volcanoes), Ne- and Ar-isotope ratios are systematically lower and close to theoretical values in the atmosphere (Hilton et al., 2002; Martelli et al., 2014; Di Piazza et al., 2015; Rizzo et al., 2015; Robidoux et al., 2017; Battaglia et al., 2018), irrespective of whether Ol phenocrysts or mantle xenocrysts are analyzed.

Diffusive Fractionation of He

The clearest evidence from the chemistry of FI is that the He/CO_2, $He/^{40}Ar^*$, He/N_2^*, and $He/^{21}Ne^*$ (not shown) ratios are systematically lower in Cpx and Opx than in Ol (**Figures 8A,B**). This pattern is not observed for ratios that do not include He [i.e., $CO_2/^{40}Ar^*$, $^{40}Ar^*/N_2^*$, and $^{21}Ne^*/N_2^*$ (not shown); **Figure 8C**], which show at least a partial overlapping of data among Ol and Px. This difference might originate from the diffusive loss of He from mantle minerals (e.g., Burnard et al., 1998 and references therein), which increases from Ol to Cpx. This hypothesis is supported by the diffusion coefficient (D) being significantly higher for He than for the other noble gases (e.g., $D_{4He}/D_{40Ar} = 3.16$ in solid mantle; Burnard, 2004; Yamamoto et al., 2009), N_2^*, and CO_2.

Figure 9 plots $He/^{40}Ar^*$ and He/CO_2 vs. the He concentration to determine if the decreases in these ratios are associated with a clear decrease in the He concentration, as expected if partial loss occurs. Such a tendency is clearer for Ol than for Px, while it is less evident or absent for He/CO_2 vs. He (**Figure 9**). In the case of the diffusive loss of He, we should also expect an isotope fractionation of $^3He/^4He$ due to the appreciable difference in D_{3He} and D_{4He} among mantle minerals that is proportional to the atomic mass ($D_{3He}/D_{4He} = 1.15$; Trull and Kurz, 1993; Burnard, 2004; Yamamoto et al., 2009 and references therein.). However, plotting the He concentration vs. Rc/Ra (**Figure 6A**) for Ol reveals no obvious variations of the $^3He/^4He$ ratio for decreasing He, with the isotope ratio varying over a very narrow range (5.9–6.2 Ra). Moreover, Opx and Cpx display higher $^3He/^4He$ ratios (6.3–6.9 Ra) than Ol for comparable He contents. This behavior is the opposite of what would be expected in the presence of He diffusive loss (e.g., Burnard, 2004; Harrison et al., 2004; Nuccio et al., 2008), as also suggested by plots of $He/^{40}Ar^*$, $He/^{21}Ne^*$ (not shown), He/N_2^* (not shown), and He/CO_2 vs. Rc/Ra (**Figures 10A,B**).

Together these observations indicate that the observed data variability cannot be explained by a partial loss of He. A process of diffusive fractionation of noble gases within the mantle can also be excluded because this would lead to decreases in both $He/^{40}Ar^*$ and $^3He/^4He$ (Yamamoto et al., 2009). Finally, diffusive fractionation cannot explain our data irrespective of the assumed starting conditions. If this process had occurred in Ol and Px, it would be successively erased by the new injection of trapped fluids, especially within Px (see section Mantle Metasomatism).

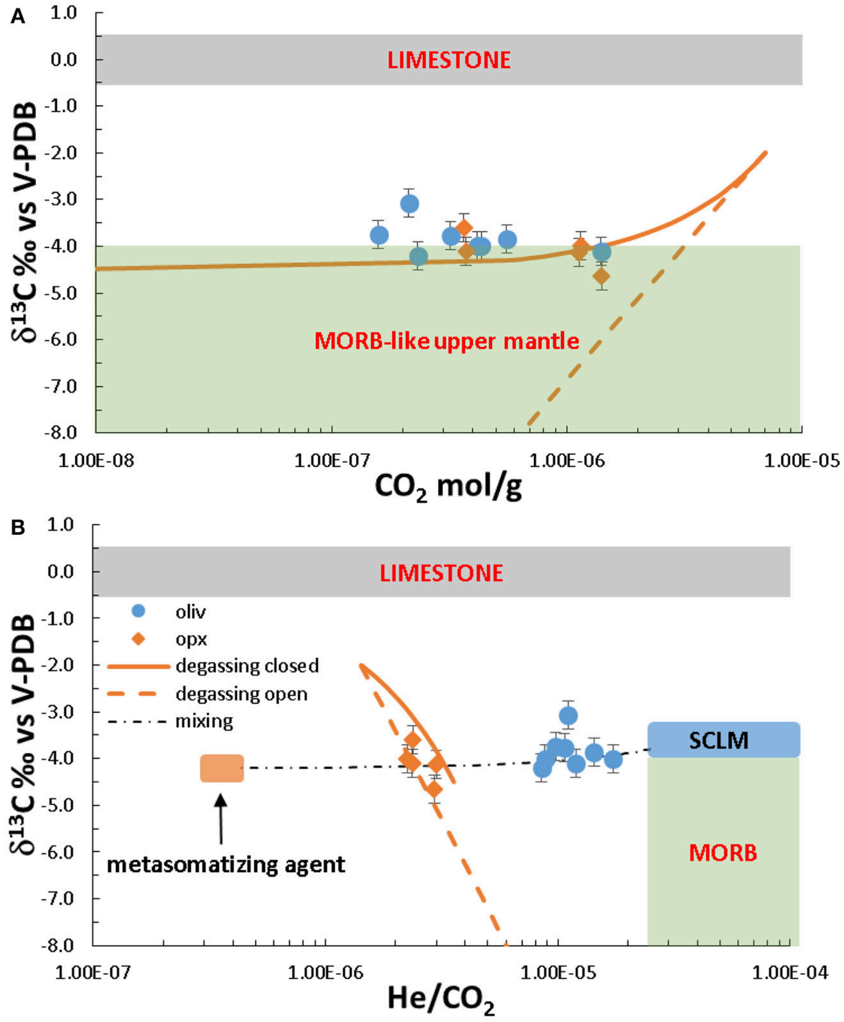

FIGURE 7 | (A) CO_2 concentration and **(B)** He/CO_2 vs. the C-isotope composition ($\delta^{13}C$ relative to V-PDB) in FI. The green bar [and rectangle in **(B)**] indicates the range of $\delta^{13}C$ values for a MORB-like mantle ($-8‰ < \delta^{13}C < -4‰$; Sano and Marty, 1995), while the gray bar is for limestone ($-1‰ < \delta^{13}C < +1‰$; Sano and Marty, 1995). The orange solid line indicates a closed-system equilibrium degassing path [equation from Jambon et al. (1986) and Macpherson and Mattey (1994)], while the orange dashed line indicates an open-system equilibrium degassing path (equation from Hoefs, 2015). The following starting conditions were assumed for degassing modeling: $CO_2 = 7 \times 10^{-6}$ mol/g, He $= 2.5 \times 10^{-11}$ mol/g, $\delta^{13}C = -4.5‰$, and $\varepsilon_{vap-melt} = 2.5‰$ (Mattey, 1991), solubility of $CO_2 = 7.6 \times 10^{-4}$ cc STP/g/bar (taken from Guillot and Sator, 2011) at 2 GPa and 1,673°K, and solubility of He $= 1.9 \times 10^{-3}$ cc STP/g/bar [assumed considering a He/CO_2 ($\alpha_{He,CO2}$) solubility ratio of 2.5 as indicated by Hilton et al. (1997), Barry et al. (2014), and Gennaro et al. (2017)]. The black dotted line in **(B)** represents binary mixing between two endmembers: (1) the residual mantle (blue rectangle) having $He/CO_2 = 2.5 \times 10^{-5}$ and $\delta^{13}C = -3.5‰$, and (2) the metasomatic agent (orange rectangle) having $He/CO_2 = 3.7 \times 10^{-7}$ and $\delta^{13}C = -4‰$.

Partial Melting of the Mantle

Plotting $He/^{40}Ar^*$ vs. the $^{40}Ar^*$ concentration (**Figure 11A**) and He/CO_2 vs. the CO_2 concentration (**Figure 11B**) reveals that the decreases in these ratios within Ol are accompanied by decreases in the absolute concentrations (although this is less clear for CO_2), as observed when plotting vs. the He concentration (see section Diffusive Fractionation of He and **Figures 9A,B**). This suggests that the process responsible for the variability within Ol modified the entire chemistry of FI. On the other hand, the decrease in these ratios from Ol to Cpx is associated with either no change or only a slight increase in the mean concentration of each species (**Figures 9**, **11**). We argue that the decreases in these ratios among Ol and Px are not caused by the same process underlying the variability in Ol, and also that the timing of the processes is probably different (see section Mantle Metasomatism). We therefore focus on the effect that partial melting has on the chemistry of FI within Ol resembling the residual mantle. This is supported by the evidence from petrography and mineral chemistry (see section Petrological Evidence of the Type and Timing of Processes Modifying Local Mantle) indicating that Ol with Fo>89 can be considered as a residuum from the partial melting of lithospheric

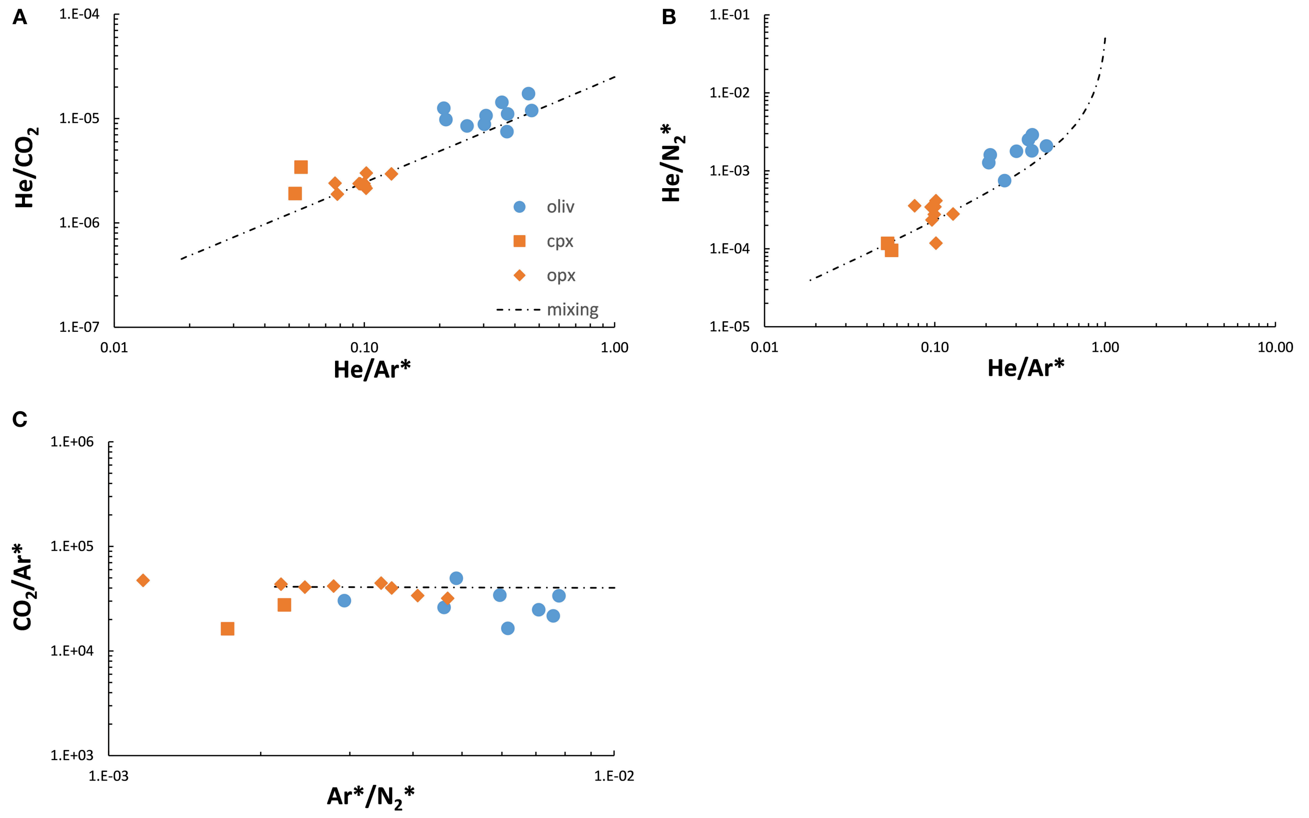

FIGURE 8 | He/Ar* vs. **(A)** He/CO_2 and **(B)** He/N_2^*, and **(C)** Ar*/N_2^* vs. CO_2/Ar* in FI. The black dotted line represents binary mixing between two endmembers: (1) the residual mantle having He/Ar* = 1, He/CO_2 = 2.5 × 10^{-5}, He/N_2^* = 5 × 10^{-2}, Ar*/N_2^* = 5 × 10^{-2}, and CO_2/Ar* = 4 × 10^4, and (2) the metasomatic agent having He/Ar* = 1.7 × 10^{-2}, He/CO_2 = 3.7 × 10^{-7}, He/N_2^* = 3.7 × 10^{-5}, Ar*/N_2^* = 2.1 × 10^{-3}, and CO_2/Ar* = 4.7 × 10^4. These two endmembers were assumed based on the minimum and maximum concentrations of single species in the three mineral phases and in order to fit the entire data set.

mantle (Matusiak-Małek et al., 2017; **Table 2**). Ol from samples $WG4_{II}$, $WG7_{II}$, and $WG10_{II}$ show Fo<89 and could have been partially influenced by metasomatic process leading to partial recrystallization and thus entrapment of new FI (see section Mantle Metasomatism). In this view the $^3He/^4He$ ratio does not show any relation with the forsterite content (**Figure S7**), while $He/^{40}Ar^*$ decreases slightly at Fo>89 and reflects increasing extents of partial melting.

Assuming the presence of crystal–melt partitioning of noble gases for Ol and Cpx (Heber et al., 2007), we modeled the trend of partial melting for batch and fractional melting of mantle in the spinel stability field. For the starting composition in the crystal, we assumed He = 5 × 10^{-11} mol/g, Ar* = 4 × 10^{-11} mol/g, and CO_2 = 1.5 × 10^{-6} mol/g. Briefly, we chose to use the highest Ar* and CO_2 concentrations measured in Ol, while the He content was chosen so that the $He/^{40}Ar^*$ ratio was within the reported range for mantle production ($He/^{40}Ar^*$ = 1–5; Marty, 2012). We considered the He and $^{40}Ar^*$ concentrations vs. $He/^{40}Ar^*$ (**Figures 9**, **11**), for which partitioning coefficients are known and more data are available in the literature for similar applications elsewhere (e.g., Burnard, 2004; Yamamoto et al., 2009). A particularly interesting observation was that the batch equilibrium melting trend fits most of the Ol data, especially those with Fo>89, whereas Px cannot be explained by this process. The chemical variation of FI within Ol traces the partial melting trend, and this is in accordance with the main lithophile-elements-based melting models (Matusiak-Małek et al., 2017; present study). However, estimations of the degree of melting based on noble-gas modeling yield much lower percentages (<1%) than the common petrological estimations (20–30% melt; **Figure S6**). This large discrepancy could be due to us measuring noble gases in the FI, while partitioning coefficients are given for a crystal–melt. In other words, we did not measure noble gases in the crystal lattice where we should expect that our estimations match those of lithophile-elements-based melting models. We argue that there is a general equilibrium between FI and the crystal lattice, and this explains why noble gases (and their relative ratios) follow the partial melting trend. In any case we use our tracers only as a proxy for the occurrence of partial melting, and not to speculate about the extent of this process.

Mantle Metasomatism

While the geochemistry of FI in Ol reflects variable extents of partial melting, that of Cpx and (at least partially) Opx cannot be explained by this process, and suggests a contribution

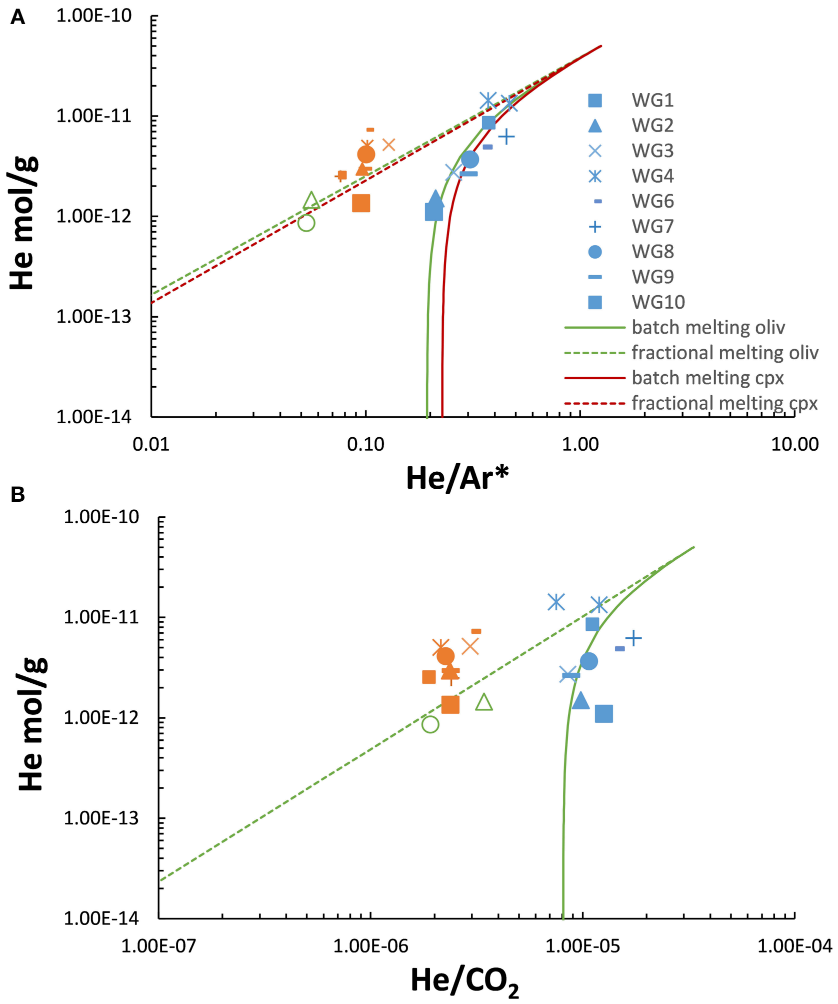

FIGURE 9 | (A) He/Ar* and **(B)** He/CO_2 vs. the He concentration. Modal batch and fractional equilibrium melting were modeled using the following equations:

$$C_i^m = \frac{C_i^s}{\left[F + D_i^{\frac{cryst}{melt}} \cdot (1-F)\right]} \text{ batch melting} \ldots\ldots C_i^m = \left[C_i^s \cdot \left(\frac{1}{D_i^{\frac{cryst}{melt}}}\right) \cdot (1-F)^{\left(\frac{1}{D_i^{\frac{cryst}{melt}}}-1\right)}\right] \text{ fractional melting}$$

where C_i^m and C_i^s are the concentrations of the *i*th species in the melt and solid source, respectively; *F* is the melting fraction, which varies from 0 to 1; and $D_i^{\frac{cryst}{melt}}$ is the crystal–melt partitioning coefficient of the *i*th species. The coefficients for the crystal–melt partitioning of He, Ar, and CO_2 for Ol and Cpx are as follows: ${}^{Ol/melt}D_{He} = 1.7 \times 10^{-4}$, ${}^{Ol/melt}D_{Ar} = 1.1 \times 10^{-3}$, ${}^{Ol/melt}D_{CO2} = 7 \times 10^{-4}$ (assumed in order to fit data), ${}^{Cpx/melt}D_{He} = 2 \times 10^{-4}$, and ${}^{Cpx/melt}D_{Ar} = 1.1 \times 10^{-3}$. The starting conditions for modeling are He $= 5 \times 10^{-11}$ mol/g, He/Ar* = 1.3, and He/$CO_2 = 3.3 \times 10^{-5}$.

from at least one additional process postdating the partial melting. Matusiak-Małek et al. (2017) argued that xenoliths from WG reflect a polyphase lithospheric mantle evolution, which started with up to 30% of melting from the protolith that left a harzburgitic residuum, with this residuum subsequently metasomatized by carbonated hydrous silicate melt related to Cenozoic volcanism (see section Petrological Background). This metasomatic event is responsible for the recrystallization of Cpx, Opx (at least partially), and amphiboles, resulting in the entrapment of secondary FI (e.g., **Figure S5D**) whose chemical and isotope composition resemble that of fluids dissolved in the metasomatizing agent. Matusiak-Małek et al. (2017) highlighted that the enrichment of LREE in Cpx relative to primitive mantle is a proxy of a metasomatic process, and that both Cpx itself as well as Opx (at least partially) have to be considered secondarily. Such a metasomatic history is typical for the lithospheric mantle located beneath the northern margin of the Bohemian Massif (e.g., Brandl et al., 2015), although WG is the only locality where hydrous minerals have been found.

Considering that we measured progressively lower He/^{40}Ar*, He/^{21}Ne* (not shown), He/N_2^*, and He/CO_2 ratios in Opx and

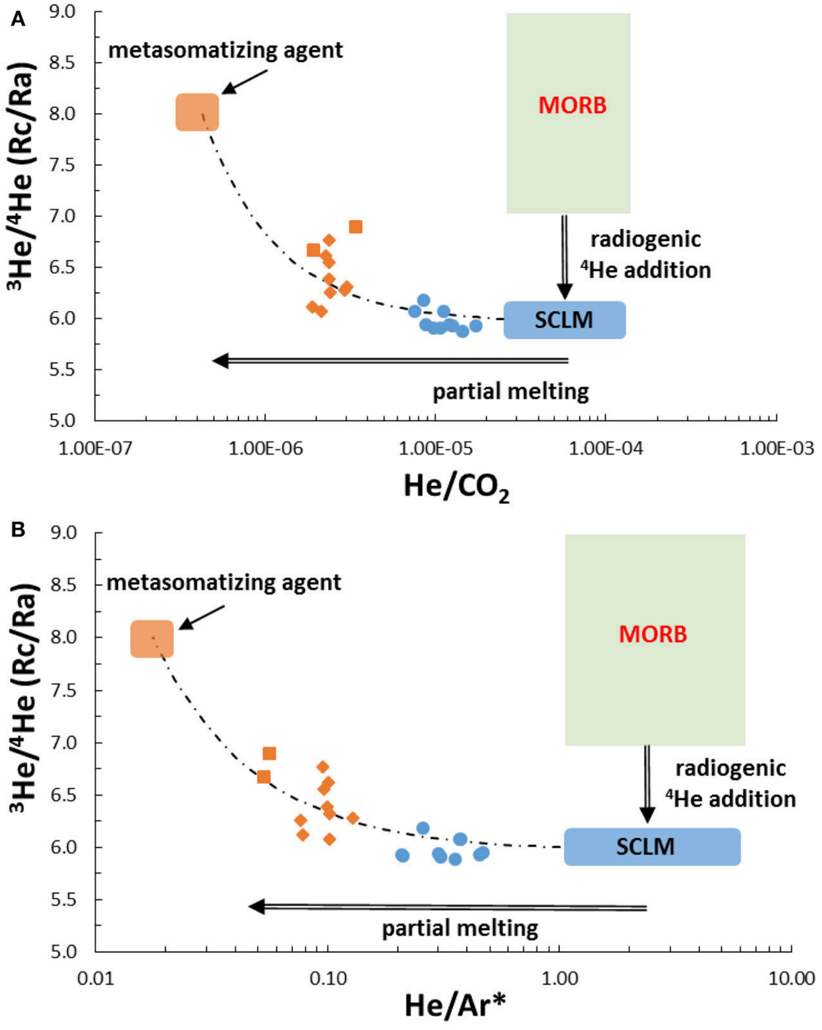

FIGURE 10 | He/CO_2 and He/Ar* vs. $^3He/^4He$ corrected for air contamination (Rc/Ra values). The green, blue, and orange rectangles are the same as in **Figure 7**. The black dotted line represents binary mixing between two endmembers: (1) the residual mantle (blue rectangle) having He/CO_2 $= 2.5 \times 10^{-5}$, He/Ar* = 1, and $^3He/^4He = 6$ Ra, and (2) the metasomatic agent (orange rectangle) having He/CO_2 $= 3.7 \times 10^{-7}$, He/Ar* $= 1.7 \times 10^{-2}$, and $^3He/^4He = 8$ Ra. The symbols are the same as in **Figure 5**.

Cpx than in Ol (**Table 3** and **Figures 8**, **9**, **11** and **Figure S6**), it is reasonable to suppose that the fluids entrapped during metasomatism were somehow depleted in He and rich in CO_2. Cpx shows the highest $^3He/^4He$ ratios close to the lower limit of MORB (**Figure 6**), indicating that fluids associated with the metasomatic agent originally had a MORB-like signature. This can also be observed in the C-isotope composition of CO_2, although it is less evident, which manifests in Opx as a mean $\delta^{13}C$ of −4.1‰ (**Figure 7**), which is very close to the upper limit of the MORB range (−8‰ < $\delta^{13}C$ < −4‰; Marty and Jambon, 1987; Javoy and Pineau, 1991; Macpherson and Mattey, 1994; Sano and Marty, 1995; Deines, 2002). Unfortunately, it was not possible to make any measurement(s) in Cpx, which we would have expected to show values well within the MORB range. On the other hand, Ol has a mean $\delta^{13}C$ of −3.8‰ (**Figure 7**), which could indicate a slight contamination of the residual mantle—possibly due to limestone originating from an old subduction component—as also shown by the lowest $^3He/^4He$ ratio of our data set (~6 Ra) (see section Inferences About the Mantle Features Beneath the North-Easternmost Part of the Eger (Ohře) Rift).

Considering that most of the studied Ol samples ($WG1_{II}$, $WG2_{II}$, $WG3_{II}$, $WG6_{II}$, $WG8_{II}$, and $WG9_{II}$) represent the residual mantle, while Cpx and some of the Opx (and Ol) samples ($WG4_{II}$, $WG7_{II}$, and $WG10_{II}$) are partially or completely modified by the metasomatic process, we argue that FI from Ol and Px represent a mixing of two endmembers: (1) a residuum after partial melting, characterized by narrow variability of $^3He/^4He$ (~6 Ra) and $\delta^{13}C$ (~ −3.8‰), and (2) a metasomatic agent, characterized by more-primitive and He-depleted fluids originating from an asthenosphere melt, originally with a

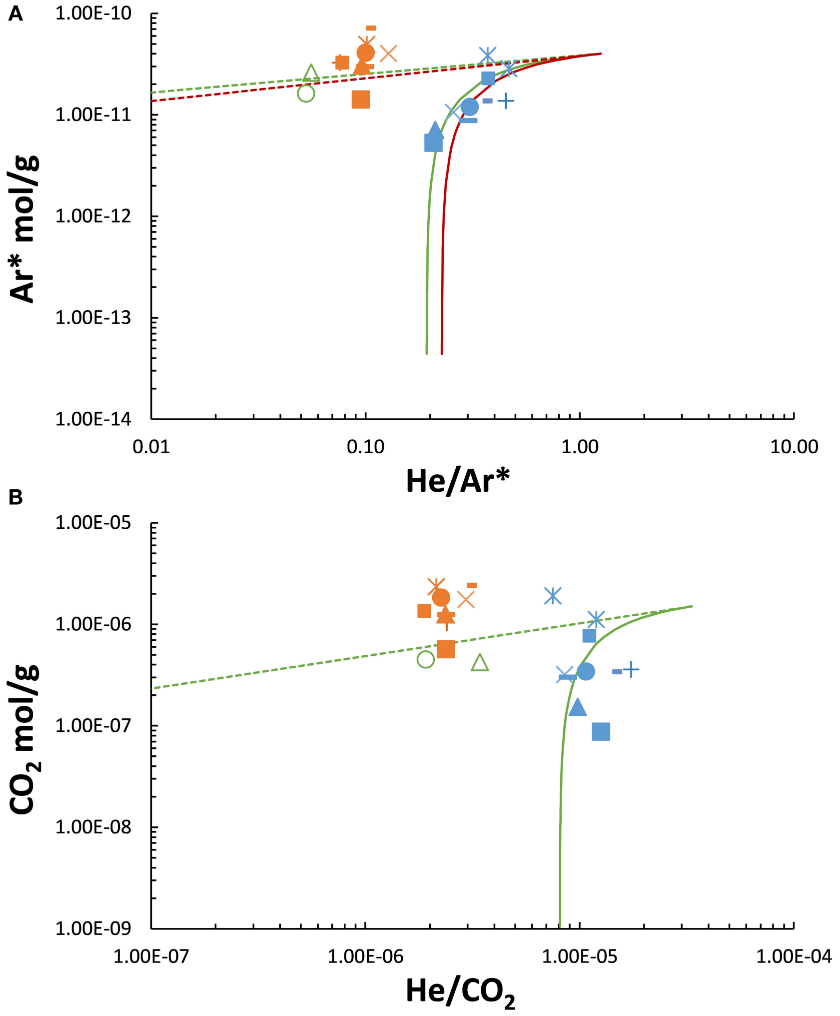

FIGURE 11 | (A) He/Ar* vs. Ar* concentration and **(B)** He/CO_2 vs. CO_2 concentration. The modeling of the modal batch and fractional equilibrium melting and starting conditions are the same as in **Figure 9**. The symbols are the same as in **Figure 9**.

MORB-like $^3He/^4He$ ratio (∼8 Ra) and $\delta^{13}C$ ∼ −4.2‰ (**Figures 7B**, **10**). This mixing hypothesis seems reasonable because our extraction procedure (single-step crushing) would result in the analysis of the total amount of FI released from crushing ∼0.02 to ∼1 g of crystals. We cannot exclude that these crystals contemporarily hosted primary and/or secondary FI (**Figures S5A–D**) belonging to the residual mantle and/or to the metasomatic agent. The boundary conditions of the mixing model were chosen as follows: for the residual mantle we assumed a mean $^3He/^4He$ ratio of 6 Ra, which is within the range of European SCLM (6.32 ± 0.39 Ra; Gautheron et al., 2005), while for the metasomatic agent we assumed the mean $^3He/^4He$ ratio of the MORB range (i.e., 8 Ra). Consequently, the He/CO_2 and He/$^{40}Ar^*$ ratios were chosen to fit our data. It should be noted that assuming lower $^3He/^4He$, He/CO_2, and He/$^{40}Ar^*$ ratios would not change the final interpretation, considering that the maximum $^3He/^4He$ ratio measured in Cpx is close to the lower limit of the MORB range (**Figure 10**).

Inferences About the Mantle Features Beneath the North-Easternmost Part of the Eger (Ohře) Rift

Origin of the $^3He/^4He$ Signature

The chemistry of FI coupled to the petrology of mantle xenoliths from WG provides evidence that a complex history of processes contributed to the local mantle composition at the time of the xenolith incorporation into the melts ascending in the volcanic system. The range of $^3He/^4He$ ratios measured in Ol and Px (5.9–6.9 Ra; **Figure 6**) suggests that the mantle beneath the north-easternmost part of the Eger (Ohře) Rift is slightly radiogenic relative to the typical MORB range (8 ± 1 Ra; e.g., Graham, 2002). This feature appears to be common to other central and western European magmatic provinces (i.e., Eifel, French Massif Central, Pannonian Basin, Calatrava, and Tallante; $^3He/^4He$ is 6.32 ± 0.39 Ra), whose noble gases in mantle xenoliths were analyzed using the same extraction method used in the present study (i.e., single-step crushing; Gautheron et al., 2005; Martelli et al., 2011). Gautheron et al. (2005) discussed three interpretative models for justifying this signature in the SCLM: (1) the addition of ^{4}He-rich fluids/melts due to dehydration of the subducting plate (e.g., Yamamoto et al., 2004), (2) the recent and localized infiltration of a MORB-like He composition from the asthenosphere mixing with a more-radiogenic isotope signature residing in the lithosphere (e.g., Dunai and Porcelli, 2002), and (3) continuous (and extensive) He enrichment of SCLM in the steady state (see section Atmospheric Contamination; Gautheron and Moreira, 2002). All of these three models are valid, and they can explain the features of the mantle beneath the north-easternmost part of the Eger (Ohře) Rift and its closest surroundings.

We have already inferred a direct mantle contamination of atmospheric gases from dehydration of subducting oceanic crust (see section Atmospheric Contamination). This process could also account for contamination of a MORB-like source by radiogenic ^{4}He, finally resulting in residual mantle with a ^{3}He/^{4}He ratio of ∼6 Ra. In this respect, the model proposed by Faccenna et al. (2010) would perfectly fit this scenario. The second model is essentially the same as what we argue in Section Mantle Metasomatism occurring in the mantle beneath the study area. In this respect the residual mantle represented by Ol with Fo>89 could result from model 1 or be due to the steady-state conditions of SCLM established by the continuous metasomatic flux of MORB-like He from the asthenosphere and the production of radiogenic ^{4}He from the decay of U and Th in crustal rocks recycled into the mantle by previous subduction events (model 3). Instead, metasomatic fluids ascending from the asthenosphere are preferentially trapped in Cpx and have a MORB-like signature, as reflected in hypotheses 2 and 3.

Implications for the Source of Magmatism

The origin of CEVP magmatism is vigorously debated and far from being fully understood. Seismic tomography studies have inferred the presence of mantle plumes beneath certain regions, such as the French Massif Central and Eifel, whereas geochemical and petrological studies of erupted products seem to exclude this hypothesis (Lustrino and Carminati, 2007; Lustrino and Wilson, 2007). In alternative to classical plumes, a more recent and intriguing model proposed by Faccenna et al. (2010) invokes a subduction-triggered decompression melting. This debate might be resolvable by considering He and Ne isotopes, which represent powerful tracers for assessing the origin of fluids, although the latter are sensitive to air contamination. The proportion of primordial nuclides (^{3}He, and also ^{20}Ne and ^{22}Ne) is higher in the lower mantle than in the degassed MORB, which exhibits relatively uniform ratios (Ozima and Podosek, 1983; Moreira, 2013 and references therein). The plume-related magmatism is expected to have a ^{3}He/^{4}He ratio above the MORB range (>9 Ra) and a lower ^{21}Ne/^{22}Ne ratio for a given ^{20}Ne/^{22}Ne (i.e., a lower ratio of nucleogenic Ne to primordial Ne) than MORB melts (e.g., Moreira, 2013 and references therein). This has already been observed in classical hotspot settings such as the Galapagos Islands (**Figure 5**; Kurz et al., 2009) and Iceland, Reunion, and Hawaii (e.g., Rison and Craig, 1983; Kurz et al., 2009; Füri et al., 2010, 2011).

The ^{3}He/^{4}He ratios observed beneath the north-easternmost part of the Eger (Ohře) Rift (5.9–6.9 Ra) are significantly lower not only than typical plume-related ratios but also MORB-like ratios (**Figure 6**). As stated in Section 6.4.1, this range is comparable to those for other European regions where no plume is present (Gautheron et al., 2005; Moreira et al., 2018). However, while the above reasoning suggests that there is no compelling evidence of plume signatures beneath the study area, other studies have inferred a plume contribution in European mantle based on Ne and Xe isotopes, although the ^{3}He/^{4}He ratios are lower than expected for a mantle influenced by a plume (Buikin et al., 2005; Caracausi et al., 2016). We did not analyze Xe isotopes in the present study, instead we only evaluated Ne isotopes that showed that the FI included in the WG xenoliths are consistent with mixing between air and a MORB-like mantle (**Figure 5**). Our data also overlap the range of values found by Gautheron et al. (2005) when applying the same method (single-step crushing) to mantle xenoliths from the French Massif Central, Pannonian Basin, and Eifel, and those authors interpreted their results in the same way. Since Buikin et al. (2005) extracted FI from minerals using a less-conservative method (in terms of releasing noble gases from the crystal lattice), it is difficult to compare their results with ours. We therefore argue that the magmatism in the north-easternmost part of the Eger (Ohře) Rift probably does not originate from the presence of a mantle plume, and instead suggest alternative explanations such as lithosphere extension (Plomerová et al., 2007; Ulrych et al., 2011) or decompression melting (Faccenna et al., 2010).

Origin of CO_2

As indicated in previous sections, FI of mantle xenoliths from WG are dominated by CO_2, as observed in many other mantle xenoliths worldwide (Deines, 2002 and references therein; Gautheron et al., 2005; Sapienza et al., 2005; Correale et al., 2015; Créon et al., 2017). This finding was confirmed by Ladenberger et al. (2009) using Raman spectroscopy in a different suite of xenoliths from the same locality. Those authors reported that these mantle xenoliths contain large amounts of FI, and infer that their minimum entrapment depth is 31–38 km, which is consistent with both seismic evidence (Babuska and Plomerova, 2001; Majdanski et al., 2006) and petrological evidence (Matusiak-Małek et al., 2017 and references therein) from various xenoliths in the region. The presence of CO_2-rich inclusions represents evidence of fluid circulation within the local mantle (see section Mantle Metasomatism). Matusiak-Małek et al. (2017) argued that metasomatism involves the percolation of an alkaline silicate melt containing a CO_2-rich vapor phase rather than a true carbonatite, which is supported by the large amount of CO_2 released from FI and by δ^{13}C varying between −4.7‰ and −3.1‰ and not being related to the CO_2 concentration (**Figure 7A**). Such a lack of a correlation between δ^{13}C and the CO_2 concentration excludes any influence of magmatic degassing. In support of this, we modeled the trends in the variation of δ^{13}C, the CO_2 concentration, and the He/CO_2 ratio due to this process in the melt in both open- and closed-system equilibrium conditions (**Figures 7A,B**).

The boundary conditions used are reported in the caption of **Figure 7**.

The range of isotope ratios reported above is mostly close to the upper limit of the MORB range ($-8‰ < \delta^{13}C < -4‰$; Marty and Jambon, 1987; Javoy and Pineau, 1991; Macpherson and Mattey, 1994; Sano and Marty, 1995; Deines, 2002). However, allowing for the stated uncertainty (±0.3‰), the measured $\delta^{13}C$ values overlap those of primary igneous carbonatites ($-8‰ < \delta^{13}C < -5‰$; Jones et al., 2013 and references therein). In addition, the most-^{13}C-enriched values found in Ol ($\delta^{13}C$ up to −3.1‰) could indicate slight contamination of the residual mantle—possibly by recycled limestone—beneath the study area, as inferred by the $^3He/^4He$ ratio being the lowest for our data set (~6 Ra). This supports the recycling of sediments with a small proportion (<0.1%) of carbonate in the SCLM.

We also considered the relationship between $\delta^{13}C$ and the $CO_2/^3He$ ratio. **Figure 12** plots the FI data together with the ranges suggested for a MORB-like mantle ($-8‰ < \delta^{13}C < -4‰$ and $CO_2/^3He \sim 1–2 \times 10^9$; Sano and Marty, 1995) and limestone ($-1‰ < \delta^{13}C < +1‰$ and $CO_2/^3He \sim 1 \times 10^{13}$; Sano and Marty, 1995), as well as their relative mixing trends. As argued for the differences in the He/CO_2 ratio between Ol and Px (see sections Partial Melting of the Mantle and Mantle Metasomatism), we infer that the differences in the $CO_2/^3He$ ratio among mineral phases probably reflects mixing between a residual mantle characterized by $\delta^{13}C = -3.8‰$ and $CO_2/^3He \sim 3.6 \times 10^9$ and a metasomatic agent having $\delta^{13}C = -4.2‰$ (at the upper limit of MORB range) and $CO_2/^3He \sim 1.3 \times 10^{11}$. In detail, the geochemistry of FI in Px would result from the modification of residual mantle due to partial melting and metasomatism (see sections Partial Melting of the Mantle and Mantle Metasomatism). The residual mantle (i.e., SCLM) would represent a MORB-like mantle modified by the addition of <0.1% limestone presumably inherited by a previous (fossil) subduction event (**Figure 12**). It is worth noting that Correale et al. (2015) used a similar analytical approach to invoke a similar process for explaining the $\delta^{13}C$ signature of the mantle source beneath the Hyblean Plateau in southeast Sicily, Italy. Importantly, the average $\delta^{13}C$ values and $CO_2/^3He$ ratios of FI from Hyblean mantle xenoliths ($\delta^{13}C \sim -3.1‰$ and $CO_2/^3He \sim 5.1 \times 10^9$) fall within the ideal ranges assumed for the pure (unmetasomatized) residual mantle beneath the north-easternmost part of the Eger (Ohře) Rift (**Figure 12**). These data are actually consistent with the trend for binary mixing between a MORB mantle and limestone. Greater recycling into the mantle of carbonates, as occurs in certain active subduction settings (Aiuppa et al., 2017), would increase the proportion of limestone involved in this mixing. This has already been observed by Gennaro et al. (2017) in FI from cumulates from Stromboli arc volcano (Italy); those authors inferred that the local mantle wedge is contaminated by CO_2 coming from the decarbonation of the sediments carried by the subducting Ionian slab (**Figure 12**).

Comparison With Gases Emitted Along the Eger (Ohře) Rift

The Eger (Ohře) Rift is part of the ECRS and has been characterized by the occurrence of intense intraplate magmatism (e.g., Prodehl et al., 1995; Ulrych et al., 2011, 2016; Andreani et al., 2014). Although there is currently no ongoing volcanic activity at the ECRS, the presence of strong CO_2 degassing and

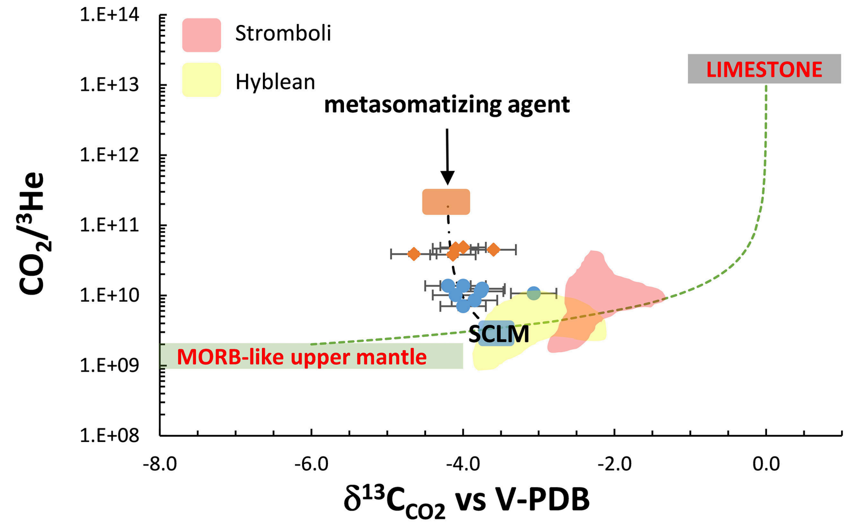

FIGURE 12 | C-isotope composition ($\delta^{13}C$) vs. $CO_2/^3He$. The green, blue, orange, and gray rectangles are the same as in **Figures 7**, **10**. Data from the Hyblean Plateau and Stromboli are from Correale et al. (2015) and Gennaro et al. (2017), respectively. The green dotted curve represents the binary mixing between a MORB-like upper mantle having $\delta^{13}C = -6‰$ and $CO_2/^3He = 2 \times 10^9$, and limestone having $\delta^{13}C = 0‰$ and $CO_2/^3He = 1 \times 10^{13}$ (Marty and Jambon, 1987; Javoy and Pineau, 1991; Sano and Marty, 1995). The black dotted line represents binary mixing between two endmembers: (1) the residual mantle (blue rectangle) having $CO_2/^3He = 4.8 \times 10^9$ and $\delta^{13}C = -3.5‰$, and (2) the metasomatic agent (orange rectangle) having $CO_2/^3He = 2.4 \times 10^{11}$ and $\delta^{13}C = -4‰$. The symbols are the same as in **Figure 5**.

persistent seismicity indicates that magmatism is still active at depth (Weinlich et al., 1999; Špaček et al., 2006; Hrubcová et al., 2017 and references therein). Most of the CO_2 degassing along the Eger (Ohře) Rift occurs in the central axis and shows a clear magmatic signature ($-4‰ < \delta^{13}C < -2‰$ and $^3He/^4He$ up to 6.3 Ra), while the magmatic component decreases with distance from the degassing locations, as indicated by decreasing $^3He/^4He$ ratios (Weinlich et al., 1999; Bräuer et al., 2004, 2008, 2011; Hrubcová et al., 2017 and references therein). As far as we are aware, the most-studied gas emissions are located in the western Eger (Ohře) Rift, at the boundary between Germany and the Czech Republic (i.e., Cheb Basin). The long-term monitoring of these emissions has revealed increasing $^3He/^4He$ ratios due to the link between ascending magmatic fluids and intracrustal seismicity (Bräuer et al., 2011). In contrast, the eastern Eger (Ohře) Rift has been subject to far less scrutiny, and to the best of our knowledge no He- and C-isotope data are available for surface gases. However, episodes of CO_2 emissions have been reported in the proximity of the main volcanic regions (e.g., Nízký Jeseník Mountains), and these might be related to the local magmatism (Špaček et al., 2006); however, this needs to be confirmed in a detailed study of the geochemistry of these fluids.

The lack of noble-gas measurements and CO_2-isotope data for gas emissions from the eastern Eger (Ohře) Rift makes it impossible to directly compare with our measurements in FI from WG mantle xenoliths. Nevertheless, considering that most of the magmatic gases emitted at or beneath the western Eger (Ohře) Rift (Bublák mofette, Cheb Basin) are interpreted as derived directly from the mantle beneath the region (Bräuer et al., 2004, 2008), we can make some comparative speculations. While the highest $^3He/^4He$ ratios measured for the Bublák mofette (up to 6.3 Ra; Bräuer et al., 2011) fall within the range of ratios measured in FI from WG (5.9–6.9 Ra), suggesting an homogeneous mantle source along the rift, $\delta^{13}C$ is significantly higher for the CO_2 emissions ($\delta^{13}C \sim -2‰$, Bräuer et al., 2008, 2011) than in FI ($-4.7‰ < \delta^{13}C < -3.1‰$). This discrepancy can be interpreted in two ways: (1) the mantle beneath the western Eger (Ohře) Rift has a slightly different isotope signature of CO_2, which is possibly related to interactions between carbonate-derived fluids and the residual mantle, or (2) $\delta^{13}C$ of mantle CO_2 is homogeneous along the Eger (Ohře) Rift, and the Bublák mofette emits gases that are slightly contaminated by intracrustal carbonate. The second hypothesis seems to be the most plausible given the homogeneous $^3He/^4He$ ratios along the Eger (Ohře) Rift and the presence of isolated carbonate deposits in the Cheb Basin (Buzek et al., 1996).

SUMMARY AND CONCLUSIONS

We have presented the first measurements of the concentration and isotope composition of noble gases and CO_2 in FI trapped in Ol and Px separated from ultramafic xenoliths hosted in WG basanite rocks that erupted a few tens of kilometers outside the north-easternmost part of the Eger (Ohře) Rift in Lower Silesia, southwest Poland. Data from FI were integrated with the evidence from petrography and geochemistry for minerals in order to define the mantle features beneath this sector of the European SCLM. This study highlights that Ol and Px (especially Cpx) may trap FI, recording different processes and timings that have occurred within the lithospheric mantle. The main results can be summarized as follows:

- Ultramafic xenoliths are mostly spinel-bearing harzburgites that sometimes contain amphiboles. Ol are classified into two groups based on forsterite contents: (1) $Fo_{88.9-91.5}$, which accounts for a fertile-to-residual mantle, and (2) $Fo_{85.5-88.1}$, which indicates large interactions with circulating (basic) melts. This dichotomy is also related to Opx and Cpx, which show two ranges of Mg# values (87–90 and 91–93, respectively) and clear evidence of recrystallization.
- The chemistry of FI is dominated by CO_2, with N_2 being the second-most-abundant species, and indicates that some Ol samples primarily represent a residual mantle depleted after various episodes of melt extractions, while the chemistry of Opx and Cpx suggests the overprinting of at least one metasomatic event postdating the partial melting. This event involved carbonated hydrous silicate melt related to Cenozoic volcanism that resulted in the entrapment of CO_2-rich inclusions. $\delta^{13}C$ relative to V-PDB is $-3.8\pm0.4‰$ in Ol and $-4.1\pm0.4‰$ in Opx, mostly falling at the upper limit of the MORB range ($-8‰ < \delta^{13}C < -4‰$), although a small percentage of carbonate recycling from a previous (fossil) subduction event cannot be excluded.
- The $^3He/^4He$ ratio corrected for air contamination (Rc/Ra values) is 6.7–6.9 Ra in Cpx, 6.3–6.8 Ra in Opx, and 5.9–6.2 Ra in Ol. The decrease in $^3He/^4He$ from Cpx to Ol is decoupled from the He concentration, thereby excluding any influence of diffusive fractionation from FI.
- The systematics of Ne and Ar isotopes indicate that most of the data are consistent with mixing between air and a MORB mantle. This evidence, together with that from the measured $^3He/^4He$ ratios, excludes the presence of a classical plume of the lower mantle beneath the study area. The geochemistry of FI results from a mixing of two endmembers: (1) the residual mantle, resulting from partial melting of European SCLM, and (2) the metasomatic agent, which is strongly He-depleted, CO_2-rich, and originally characterized by MORB-like $^3He/^4He$ ratios.

AUTHOR CONTRIBUTIONS

AR performed analyses of fluid inclusions, participated in mineral chemistry analyses, elaborated and interpreted data, conceptualized models, and drafted the manuscript and edited the final version. BP assisted in data elaboration and writing the final version of the manuscript. MC and CB collected samples. BP and GB prepared and interpreted thin sections, and handpicked minerals from mantle xenoliths. TN performed mineral chemistry analyses, and helped in petrography and mineral chemistry data interpretation. MC, TN, CB, MM-M,

and FI provided constructive comments on and edited the final version of the manuscript.

FUNDING

AR acknowledges financial support from Università degli Studi di Ferrara for the 2017 IUSS international mobility program during his PhD, as well as INGV-Palermo and the University of Vienna for providing analytical facilities.

ACKNOWLEDGMENTS

This work is part of the PhD (XXXII cycle) of ALR at the University of Ferrara. We thank Mariagrazia Misseri for helping in sample preparation, the isotope analysis of noble gases, and extracting CO_2 from fluid inclusions. We are grateful to Mariano Tantillo for his support in laboratory activities. We also thank Fausto Grassa, Giorgio Capasso, Ygor Oliveri, and Aldo Sollami for their efforts in the stable-isotopes laboratory. Michal Dajek is acknowledged for helping with map preparation. We thank the reviewers for useful suggestions that helped us to make the manuscript clearer and more complete. English language has been revised by English Science Editing (Paul Kolston).

SUPPLEMENTARY MATERIAL

The Supplementary Material for this article can be found online at: https://www.frontiersin.org/articles/10.3389/feart.2018.00215/full#supplementary-material

REFERENCES

Aiuppa, A., Fischer, T. P., Plank, T., Robidoux, P., and Di Napoli, R. (2017). Along-arc, inter-arc and arc-to-arc variations in volcanic gas CO_2/STratios reveal dual source of carbon in arc volcanism. *Earth-Science Rev.* 168, 24–47. doi: 10.1016/j.earscirev.2017.03.005

Allègre, J. C., Staudacher, T., and Sarda, P. (1987). Rare gas systematics: formation of the atmosphere, evolution and structure of the Earth's mantle. *Earth Planet. Sci. Lett.* 81, 127–150.

Andreani, L., Stanek, K. P., Gloaguen, R., Krentz, O., and Domínguez-González, L. (2014). DEM-based analysis of interactions between tectonics and landscapes in the Ore Mountains and Eger Rift (East Germany and NW Czech Republic). *Remote Sens.* 6, 7971–8001. doi: 10.3390/rs6097971

Babuska, V., and Plomerova, J. (2001). Subcrustal lithosphere around the Saxothuringian – Moldanubian Suture Zone – a model derived from anisotropy of seismic wave velocities. *Tectonophysics* 332, 185–199. doi: 10.1016/S0040-1951(00)00255-9

Barry, P. H., Hilton, D. R., Füri, E., Halldórsson, S. A., and Grönvold, K. (2014). Carbon isotope and abundance systematics of Icelandic geothermal gases, fluids and subglacial basalts with implications for mantle plume-related CO_2 fluxes. *Geochim. Cosmochim. Acta* 134, 74–99. doi: 10.1016/j.gca.2014.02.038

Battaglia, A., Bitetto, M., Aiuppa, A., Rizzo, A. L., Chigna, G., Watson, I. M., D'Aleo, R., Juárez Cacao, F. J., and de Moor, M. J. (2018). The Magmatic gas Signature of Pacaya Volcano, With Implications for the Volcanic CO_2 Flux From Guatemala. *Geochem. Geophys. Geosyst.* 19, 667–692. doi: 10.1002/2017GC007238

Białek, D., Raczyński, P., Sztajner, P., and Zawadzki, D. (2007). Archeocjaty wapieni wojcieszowskich. *Przegląd Geol.* 55, 1112–1116. Available online at: https://www.pgi.gov.pl/images/stories/przeglad/pg_2007_12_02_17.pdf

Birkenmajer, K., Pécskay, Z., Grabowski, J., and Lorenc,M. W., Zagożdżon, P. (2007). Radiometric dating of the Tertiary volcanics in Lower Silesia, Poland. V. K–Ar and palaeomagnetic data from late Oligocene to early Miocene basaltic rocks of theNorth-SudeticDepression. *Ann. Soc. Geol. Pol.* 77, 1–16.

Bonadiman, C., and Coltorti, M. (2011) Numerical modelling for peridotite phase melting trends in the SiO_2-Al_2O_3-FeO-MgO-CaO system at 2 GPa [abs.]. *Mineral. Magaz.* 75:548.

Brandl, P. A., Genske, F. S., Beier, C., Haase, K. M., Sprung, P., and Krumm, S. H. (2015). Magmatic evidence for carbonate metasomatism in the lithospheric mantle underneath the Ohře (Eger) Rift. *J. Petrol.* 56, 1743–1774. doi: 10.1093/petrology/egv052

Bräuer, K., Kämpf, H., Koch, U., and Strauch, G. (2011). Monthly monitoring of gas and isotope compositions in the free gas phase at degassing locations close to the Nový Kostel focal zone in the western Eger Rifţ Czech Republic. *Chem. Geol.* 290, 163–176. doi: 10.1016/j.chemgeo.2011.09.012

Bräuer, K., Kämpf, H., Niedermann, S., Strauch, G., and Tesař, J. (2008). Natural laboratory NW Bohemia: comprehensive fluid studies between 1992 and 2005 used to trace geodynamic processes. *Geochem. Geophys. Geosyst.* 9, 1–30. doi: 10.1029/2007GC001921

Bräuer, K., Kämpf, H., Niedermann, S., Strauch, G., and Weise, S. M. (2004). Evidence for a nitrogen flux directly derived from the European subcontinental mantle in the Western Eger Rift, Central Europe. *Geochim. Cosmochim. Acta* 68, 4935–4947. doi: 10.1016/j.gca.2004.05.032

Buikin, A., Trieloff, M., Hopp, J., Althaus, T., Korochantseva, E., Schwarz, W. H., and Altherr, R. (2005). Noble gas isotopes suggest deep mantle plume source of late Cenozoic mafic alkaline volcanism in Europe. *Earth Planet. Sci. Lett.* 230, 143–162. doi: 10.1016/j.epsl.2004.11.001

Burnard, P. (2004). Diffusive fractionation of noble gases and helium isotopes during mantle melting. *Earth Planet. Sci. Lett.* 220, 287–295. doi: 10.1016/S0012-821X(04)00060-3

Burnard, P., Graham, D., and Turner, G. (1997). Vesicle-specific noble gas analyses of "popping rock": Implications for primordial noble gases in earth. *Science* 276, 568–571.

Burnard, P. G., Farley, K., a., and Turner, G. (1998). Multiple fluid pulses in a Samoan harzburgite. *Chem. Geol.* 147, 99–114. doi: 10.1016/S0009-2541(97)00175-7

Buzek, C., Holy, F., and Kvacek, Z. (1996). Early Miocene flora of the Cypris shale (Western Bohemia). *Acta Musei Nat. Prague B Hist. Naturalis* 52, 1–72.

Caracausi, A., Avice, G., Burnard, P. G., Füri, E., and Marty, B. (2016). Chondritic xenon in the Earth's mantle. *Nature* 533, 82–85. doi: 10.1038/nature17434

Coltorti, M., Downes, H., Grégoire, M., and O'Reilly, S. Y. (2009). Petrological evolution of the European Lithospheric Mantle: from Archean to present day. *J.Petrol.* 50:223. doi: 10.1093/petrology/egp046

Coltorti, M., Downes, H., Gregoire, M., and O'Reilly, S. Y. (2010). Petrological evolution of the European Lithospheric Mantle. *J. Geol. Soc. Lond.* 377:246. doi: 10.1144/SP337.1

Correale, A., Martelli, M., Paonita, A., Rizzo, A., Brusca, L., and Scribano, V. (2012). New evidence of mantle heterogeneity beneath the Hyblean Plateau (southeast Sicily, Italy) as inferred from noble gases and geochemistry of ultramafic xenoliths. *Lithos* 132–133, 70–81. doi: 10.1016/j.lithos.2011.11.007

Correale, A., Paonita, A., Rizzo, A., Grassa, F., and Martelli, M. (2015). The carbon-isotope signature of ultramafic xenoliths from the Hyblean Plateau (southeast Sicily, Italy): evidence of mantle heterogeneity. *Geochem. Geophys. Geosyst.* 16, 600–611. doi: 10.1002/2014GC005656

Correale, A., Rizzo, A. L., Barry, P. H., Lu, J., and Zheng, J. (2016). Refertilization of lithospheric mantle beneath the Yangtze craton in south-east China: evidence from noble gases geochemistry. *Gondwana Res.* 38, 289–303. doi: 10.1016/j.gr.2016.01.003

Créon, L., Rouchon, V., Youssef, S., Rosenberg, E., Delpech, G., Szabó, C., et al. (2017). Highly CO_2-supersaturated melts in the Pannonian lithospheric mantle – A transient carbon reservoir? *Lithos* 286–287, 519–533. doi: 10.1016/j.lithos.2016.12.009

Ćwiek, M., Matusiak-Małek, M., Puziewicz, J., Ntaflos, T. (2018) Lithospheric mantle beneath NE part of Bohemian Massif and its rekation to overlying crust:

new insights from Pilchowice xenolith suite, Sudetes, SW Poland. *Int. J. Earth Sci.* 107,1731–1753 doi: 10.1007/s00531-017-1568-4

Day, J. M. D., Barry, P. H., Hilton, D. R., Burgess, R., Pearson, D. G., and Taylor, L. A. (2015). The helium flux from the continents and ubiquity of low-^{3}He/^{4}He recycled crust and lithosphere. *Geochim. Cosmochim. Acta* 153, 116–133. doi: 10.1016/j.gca.2015.01.008

Deines, P. (2002). The carbon isotope geochemistry of mantle xenoliths. *Earth Sci. Rev.* 58, 247–278. doi: 10.1016/S0012-8252(02)00064-8

Dèzes, P., Schmid, S. M., and Ziegler, P. A. (2004). Evolution of the European Cenozoic Rift System: Interaction of the Alpine and Pyrenean orogens with their foreland lithosphere. *Tectonophysics* 389, 1–33. doi: 10.1016/j.tecto.2004.06.011

Di Piazza, A., Rizzo, A. L., Barberi, F., Carapezza, M. L., De Astis, G., Romano, C., and Sortino, F. (2015). Geochemistry of the mantle source and magma feeding system beneath Turrialba volcano, Costa Rica. *Lithos* 232, 319–335. doi: 10.1016/j.lithos.2015.07.012

Downes, H., Thirlwall, M. F., and Trayhorn, S. C. (2001). Miocene subduction-related magmatism in southern Sardinia : Sr ± Nd- and oxygen isotopic evidence for mantle source enrichment. *J. Volcanol. Geotherm. Res.* 106. doi: 10.1016/S0377-0273(00)00269-9

Dunai, T. J., and Baur, H. (1995). Helium, neon, and argon systematics of the European subcontinental mantle: Implications for its geochemical evolution. *Geochim. Cosmochim. Acta* 59, 2767–2783. doi: 10.1016/0016-7037(95)00172-V

Dunai, T. J., and Porcelli, D. (2002). Storage and transport of noble gases in the subcontinental lithosphere. *Rev. Mineral. Geochem.* 47, 371–409. doi: 10.2138/rmg.2002.47.10

Faccenna, C., Becker, T. W., Lallemand, S., Lagabrielle, Y., Funiciello, F., and Piromallo, C. (2010). Subduction-triggered magmatic pulses: a new class of plumes? *Earth Planet. Sci. Lett.* 299, 54–68. doi: 10.1016/j.epsl.2010.08.012

Füri, E., Hilton, D. R., Halldórsson, S. A., Barry, P. H., Hahm, D., Fischer, T. P., and Grönvold, K. (2010). Apparent decoupling of the He and Ne isotope systematics of the Icelandic mantle: the role of He depletion, melt mixing, degassing fractionation and air interaction. *Geochim. Cosmochim. Acta* 74, 3307–3332. doi: 10.1016/j.gca.2010.03.023

Füri, E., Hilton, D. R., Murton, B. J., Hémond, C., Dyment, J., and Day, J. M. D. (2011). Helium isotope variations between Réunion Island and the Central Indian Ridge (17°-21°S): New evidence for ridge-hot spot interaction. *J. Geophys. Res. Solid Earth* 116, 1–17. doi: 10.1029/2010JB007609

Gautheron, C., and Moreira, M. (2002). Helium signature of the subcontinental lithospheric mantle. *Earth Planet. Sci. Lett.* 199, 39–47. doi: 10.1016/S0012-821X(02)00563-0

Gautheron, C., Moreira, M., and Allègre, C. (2005). He, Ne and Ar composition of the European lithospheric mantle. *Chem. Geol.* 217, 97–112. doi: 10.1016/j.chemgeo.2004.12.009

Gennaro, M. E., Grassa, F., Martelli, M., Renzulli, A., and Rizzo, A. L. (2017). Carbon isotope composition of CO_2-rich inclusions in cumulate-forming mantle minerals from Stromboli volcano (Italy). *J. Volcanol. Geotherm. Res.* 346, 95–103. doi: 10.1016/j.jvolgeores.2017.04.001

Graham (2002). Noble gas isotope geochemistry of mid-ocean ridge and ocean island basalts: characterization of mantle source reservoirs. *Rev. Mineral. Geochem.* 47, 247–317. doi: 10.2138/rmg.2002.47.8

Guillot, B., and Sator, N. (2011). Carbon dioxide in silicate melts: A molecular dynamics simulation study. *Geochim. Cosmochim. Acta* 75, 1829–1857. doi: 10.1016/j.gca.2011.01.004

Gurenko, A. A., Hoernle, K. A., Hauff, F., Schmincke, H. U., Han, D., Miura, Y. N., and Kaneoka, I. (2006). Major, trace element and Nd-Sr-Pb-O-He-Ar isotope signatures of shield stage lavas from the central and western Canary Islands: insights into mantle and crustal processes. *Chem. Geol.* 233, 75–112. doi: 10.1016/j.chemgeo.2006.02.016

Harrison, D., Barry, T., and Turner, G. (2004). Possible diffusive fractionation of helium isotopes in olivine and clinopyroxene phenocrysts. *Eur. J. Mineral.* 16, 213–220. doi: 10.1127/0935-1221/2004/0016-0213

Heber, V. S., Brooker, R. A., Kelley, S. P., and Wood, B. J. (2007). Crystal-melt partitioning of noble gases (helium, neon, argon, krypton, and xenon) for olivine and clinopyroxene. *Geochim. Cosmochim. Acta* 71, 1041–1061. doi: 10.1016/j.gca.2006.11.010

Heber, V. S., Wieler, R., Baur, H., Olinger, C., Friedmann, A., Burnett, D. S. (2009) Noble gas composition of the solar wind as collected by the Genesis mission. *Geochim. Cosmochim. Acta* 73, 7414–7432. doi: 10.1016/j.gca.2009.09.013

Hilton, D. R., Fischer, T. P., and Marty, B. (2002). Noble Gases and Volatile Recycling at Subduction Zones. *Rev. Mineral. Geochem.* 47, 319–370. doi: 10.2138/rmg.2002.47.9

Hilton, D. R., Hammerschmidt, K., Teufel, S., and Friedrichsen, H. (1993). Helium isotope characteristics of Andean geothermal fluids and lavas. *Earth Planet. Sci. Lett.* 120, 265–282. doi: 10.1016/0012-821X(93)90244-4

Hilton, D. R., McMurty, G. M., Kreulen, R. (1997). Evidence for extensive degassing of the Hawaiian mantle plume from helium-carbon relationship at Kilauea volcano. *Geophys. Res. Lett.* 24, 3065–3068. doi: 10.1029/97GL03046

Hoefs, J. (2015). *Stable Isotope Geochemistry*. Cham: Springer International Publishing AG. doi: 10.1007/978-3-319-19716-6

Hrubcová, P., Geissler, W. H., Bräuer, K., Vavryčuk, V., Tomek, Č., and Kämpf, H. (2017). Active Magmatic Underplating in Western Eger Rift, Central Europe. *Tectonics* 36, 2846–2862. doi: 10.1002/2017TC004710

Ionov, D. A., and Hofmann, A. W. (2007). Depth of formation of sub-continental off-craton peridotites. *Earth Planetary Sci. Lett.*261, 620–634. doi: 10.1016/j.epsl.2007.07.036

Jambon, A., Weber, H., Braun, O. (1986). Solubility of He, Ne, Ar, Kr and Xe in a basalt melt in the rauge 1250-1600°C. *Geochemical implicactions. Geochim. Cosmochim. Acta* 50, 401–408. doi: 10.1016/0016-7037(86)90193-6

Javoy, M., and Pineau, F. (1991). The volatiles record of a " popping " rock from the Mid-Atlantic Ridge at 14 ° N : chemical and isotopic composition of gas trapped in the *vesicles*. 107, 598–611. doi: 10.1016/0012-821X(91)90104-P

Jones, A. P., Genge, M., and Carmody, L. (2013). Carbonate melts and carbonatites. *Rev. Mineral. Geochem.* 75, 289–322. doi: 10.2138/rmg.2013.75.10

Kaneoka, I. (1983). Noble gas constraints on the layered structure of the mantle. *Nature* 302, 698–700. doi: 10.1038/302698a0

Kryza, R., Willner, A. P., Massonne, H. J., Muszyński, A., and Schertl, H. P. (2011). Blueschist-facies metamorphism in the Kaczawa Mountains (Sudetes, SW Poland) of the Central-European Variscides: P-T constraints from a jadeite-bearing metatrachyte. *Mineralog. Magaz.* 75, 241–263. doi: 10.1180/minmag.2011.075.1.241

Kurz, M. D., Curtice, J., Fornari, D., Geist, D., and Moreira, M. (2009). Primitive neon from the center of the Galápagos hotspot. *Earth Planet. Sci. Lett.* 286, 23–34. doi: 10.1016/j.epsl.2009.06.008

Kurz, M. K. (1986). Cosmogenic helium in a terrestrial igneous rock. *Nature* 320, 435–439. doi: 10.1038/320435a0

Ladenberger, A., Lazor, P., and Michalik, M. (2009). CO_2 fluid inclusions in mantle xenoliths from Lower Silesia (SW Poland): formation conditions and decompression history. *Eur. J. Mineral.* 21, 751–761. doi: 10.1127/0935-1221/2009/0021-1930

Leake, B., Woolley, A., Arps, C., Birch, W., Gilbert,M., Grice, J., et al. (1997). Nomenclature of amphiboles: report of the subcommittee on amphiboles of the International Mineralogical Association, Commission on New Minerals and Minerals Names. *Canad. Mineral.* (1997) 35, 219–246.

Lustrino, M., and Carminati, E. (2007). Phantom plumes in Europe and the circum-Mediterranean region. *Geol. Soc. Am. Spec. Pap.* 430, 723–745. doi: 10.1130/2007.2430(33)

Lustrino, M., and Wilson, M. (2007). The circum-Mediterranean anorogenic Cenozoic igneous province. *Earth-Science Rev.* 81, 1–65. doi: 10.1016/j.earscirev.2006.09.002

Macpherson, C., Mattey, D. (1994). Carbon isotope variations of CO_2 in Central Lau Basin basalats and ferrobasalts. *Earth Planet. Sci. Lett.* 121, 263–276. doi: 10.1016/0012-821X(94)90072-8

Majdanski, M., Grad, M., Guterch, A., SUDETES 2003 Working Group (2006). 2-D seismic tomographic and ray tracing modelling of the crustal structure across the Sudetes Mountains basing on SUDETES 2003 experiment data. *Tectonophysics* 413, 249–269. doi: 10.1016/j.tecto.2005.10.042

Martelli, M., Bianchini, G., Beccaluva, L., and Rizzo, A. (2011). Helium and argon isotopic compositions of mantle xenoliths from Tallante and Calatrava, Spain. *J. Volcanol. Geotherm. Res.* 200, 18–26. doi: 10.1016/j.jvolgeores.2010.11.015

Martelli, M., Rizzo, A. L., Renzulli, a., Ridolfi, F., Arienzo, I., and Rosciglione, a. (2014). Noble-gas signature of magmas from a heterogeneous mantle wedge: the case of Stromboli volcano (Aeolian Islands, Italy). *Chem. Geol.* 368, 39–53. doi: 10.1016/j.chemgeo.2014.01.003

Marty, B. (2012). The origins and concentrations of water, carbon, nitrogen and noble gases on Earth. *Earth Planet. Sci. Lett.* 313–314, 56–66. doi: 10.1016/j.epsl.2011.10.040

Marty, B., and Jambon, a. (1987). C3He in volatile fluxes from the solid Earth: implications for carbon geodynamics. *Earth Planet. Sci. Lett.* 83, 16–26. doi: 10.1016/0012-821X(87)90047-1

Matsumoto, T., Chen, Y., and Matsuda, J. (2001). Concomitant occurrence of primordial and recycled noble gases in the Earth's mantle. *Earth Planet. Sci. Lett.* 185, 35–47. doi: 10.1016/S0012-821X(00)00375-7

Matsumoto, T., Honda, M., McDougall, I., O'Really, S. Y., Norman, M., Yaxley, G. (2000). Noble gases in pyroxenites and metasomatised peridotites from the Newer Volcanics, southeastern Australia: implications for mantle metasomatism. *Chem. Geol.* 168, 49–73. doi: 10.1016/S0009-2541(00)00181-9

Matsumoto, T., Honda, M., McDougall, I., and O'Reilly, S. Y. (1998). Noble gases in anhydrous lherzolites from the Newer Volcanics, southeastern Australia: a MORB-like reservoir in the subcontinental mantle. *Geochim. Cosmochim. Acta* 62, 2521–2533.

Matsumoto, T., Pinti, D. I., Matsuda, J. I., and Umino, S. (2002). Recycled noble gas and nitrogen in the subcontinental lithospheric mantle: implications from N-He-Ar in fluid inclusions of SE Australian xenoliths. *Geochem. J.* 36, 209–217. doi: 10.2343/geochemj.36.209

Mattey, D. P. (1991). Carbon dioxide solubility and carbon isotope fractionation in basaltic melt. *Geochim. Cosmochim. Acta* 55, 3467–3473. doi: 10.1016/0016-7037(91)90508-3

Matusiak-Małek, M., Puziewicz, J., Ntaflos, T., GréGoire, M., Benoit, M., and KlüGel, A. (2014). Two contrasting lithologies in off-rift subcontinental lithospheric mantle beneath central Europec-the Krzeniów (SW Poland) case study. *J. Petrol.* 55, 1799–1828. doi: 10.1093/petrology/egu042

Matusiak-Małek, M., Puziewicz, J., Ntaflos, T., Grégoire, M., Kukuła, A., and Wojtulek, P. M. (2017). Origin and evolution of rare amphibole-bearing mantle peridotites from Wilcza Góra (SW Poland), Central Europe. *Lithos* 286–287, 302–323. doi: 10.1016/j.lithos.2017.06.017

Mazur, S., Aleksandrowski, P., Kryza, R., and Oberc-Dziedzic, T. (2006). The Variscan orogen in Poland. *Geol. Q.* 50, 89–118. Available online at: https://gq.pgi.gov.pl/article/view/7400/6050

Moreira, M. (2013). Noble gas constraints on the origin and evolution of earth's volatiles. *Geochem. Perspec.* 2, 229–230. doi: 10.7185/geochempersp.2.2

Moreira, M., Kunz, J., and Allegre, C. (1998). Rare gas systematics in popping rock: Isotopic and elemental compositions in the upper mantle. *Science (80-.).* 279, 1178–1181. doi: 10.1126/science.279.5354.1178

Moreira, M., Rouchon, V., Muller, E., and Noirez, S. (2018). The xenon isotopic signature of the mantle beneath Massif Central. *Geochemical Perspect. Lett.* 6, 28–32. doi: 10.7185/geochemlet.1805

Nuccio, P. M., Paonita, A., Rizzo, A., and Rosciglione, A. (2008). Elemental and isotope covariation of noble gases in mineral phases from Etnean volcanics erupted during 2001-2005, and genetic relation with peripheral gas discharges. *Earth Planet. Sci. Lett.* 272, 683–690. doi: 10.1016/j.epsl.2008.06.007

Ozima, M., Podosek, F. A. (1983). *Noble Gas Geochemistry*. New York, NY: Cambridge University Press.

Pécskay, Z., Birkenmajer, K. (2013). "Insight into the geochronology of Cenozoic alkaline basaltic volcanic activity in Lower Silesia (SW Poland) and adjacent areas," in *Basalt 2013 – Cenozoic Magmatism in Central Europe, Abstract and Excursion Guides*, eds J. Büchner, V. Rapprich, O. Tietz (Goerlitz: Czech Geological Survey; Prague and Seckneberg Museum of Natural History Görlitz), 66–67.

Plomerová, J., Achauer, U., Babuška, V., Vecsey, L., the BOHEMA working group (2007). Upper mantle beneath the Eger Rift (Central Europe): plume or asthenosphere upwelling? *Geophys. J. Int.* 169, 675–682. doi: 10.1111/j.1365-246X.2007.03361.x

Prodehl, C., Mueller, S., and Haak, V. (1995). "The European Cenozoic rift system," in *Continental rifts: Evolution, Structure, Tectonics. Developments in Geotectonics,* Vol. 25, eds K. H. Olsen (New York, NY: Elsevier). 133–212.

Rison, W., and Craig, H. (1983). Helium isotopes and mantle volatiles in Loihi Seamount and Hawaiian Island basalts and xenoliths. *Earth Planet. Sci. Lett.* 66, 407–426. doi: 10.1016/0012-821X(83)90155-3

Rizzo, A. L., Barberi, F., Carapezza, M. L., Di Piazza, A., Francalanci, L., Sortino, F., and D'Alessandro, W. (2015). New mafic magma refilling a quiescent volcano: evidence from He-Ne-Ar isotopes during the 2011-2012 unrest at Santorini, Greece. *Geochem. Geophys. Geosyst.* 16, 798–814. doi: 10.1002/2014GC005653

Robidoux, P., Aiuppa, A., Rotolo, S. G., Rizzo, A. L., Hauri, E. H., and Frezzotti, M. L. (2017). Volatile contents of mafic-to-intermediate magmas at San Cristóbal volcano in Nicaragua. *Lithos* 272–273. doi: 10.1016/j.lithos.2016.12.002

Roedder, E. (1984) Fluid inclusions reviews in mineralogy. *Mineral. Soc. Am.* 12, 644 doi: 10.1515/9781501508271

Sano, Y., Marty, B. (1995). Origin of carbon in fumarolic gas from island arcs. *Chem. Geol.* 119, 265–274. doi: 10.1016/0009-2541(94)00097-R

Sapienza, G., Hilton, D. R., and Scribano, V. (2005). Helium isotopes in peridotite mineral phases from Hyblean Plateau xenoliths (south-eastern Sicily, Italy). *Chem. Geol.* 219, 115–129. doi: 10.1016/j.chemgeo.2005.02.012

Sarda, P., Staudacher, T., and Allègre, C. J. (1988). Neon isotopes in submarine basalts. *Earth Planet. Sci. Lett.* 91, 73–88. doi: 10.1016/0012-821X(88)90152-5

Sawicki, L. (1995). *Geological Map of Lower Silesia With Adjacent Czech and German Territories (Without Quaternary Deposits)*. Warszawa: Polish Geological Institute.

Smulikowski, K., Kozłowska-Koch, M. (1984). Bazaltoidy Wilczej Góry koło Złotoryi (Dolny Śląsk) i ich enklawy. *Archiwum Mineralogiczne* 40, 53–104 (in Polish).

Špaček, P., Sýkorová, Z., Pazdírková, J., Švancara, J., and Havíř, J. (2006). Present-day seismicity of the south-eastern Elbe Fault System (NE Bohemian Massif). *Stud. Geophys. Geod.* 50, 233–258. doi: 10.1007/s11200-006-0014-z

Stuart, F. M., Lass-Evans, S., Fitton, J. G., and Ellam, R. M. (2003). High 3He/4He ratios in picritic basalts from Baffin Island and the role of a mixed reservoir in mantle plumes. *Nature* 424, 57–59. doi: 10.1038/nature01711

Trull, T. W., and Kurz, M. D. (1993). Experimental measurements of 3He and 4He mobility in olivine and clinopyroxene at magmatic temperatures. *Geochim. Cosmochim. Acta* 57, 1313–1324. doi: 10.1016/0016-7037(93)90068-8

Ulrych, J., Dostal, J., Adamović, J., Jelínek, E., Špaček, P., Hegner, E., et al. (2011). Recurrent Cenozoic volcanic activity in the Bohemian Massif (Czech Republic). *Lithos* 123, 133–144. doi: 10.1016/j.lithos.2010.12.008

Ulrych, J., Krmíček, L., Tomek, Č., Lloyd, F. E., Ladenberger, A., Ackerman, L., and Balogh, K. (2016). Petrogenesis of Miocene alkaline volcanic suites from western Bohemia: Whole rock geochemistry and Sr-Nd-Pb isotopic signatures. *Chemie der Erde Geochem.* 76, 77–93. doi: 10.1016/j.chemer.2015.11.003

Upton, B. G. J., Downes, H., Kirstein, L. A., Bonadiman, C., Hill, P. G., and Ntaflos, T. (2011) The lithospheric mantle and lower crust-mantle relationships under Scotland: a xenolithic perspective. *J. Geol. Soc.* 168, 873–886. doi: 10.1144/0016-76492009-172

Valbracht, P. J., Honda, M., Matsumoto, T., Mattielli, N., McDougall, I., Ragettli, R. et al. (1996). Helium, neon and argon isotope systematics in Kerguelen ultramafic xenoliths: implications for mantle source signatures. *Earth Planet. Sci. Lett.* 138, 29–38. doi: 10.1016/0012-821X(95)00226-3

Weinlich, F. H., Bräuer, K., Kämpf, H., Strauch, G., Tesař, J., and Weise, S. M. (1999). An active subcontinental mantle volatile system in the western Eger rift, Central Europe: Gas flux, isotopic (He, C, and N) and compositional fingerprints. *Geochim. Cosmochim. Acta* 63, 3653–3671. doi: 10.1016/S0016-7037(99)00187-8

Wilson, M., and Downes, H. (2006). Tertiary-Quaternary intra-plate magmatism and mantle dynamics in Europe. *Cent. Eur.* 32, 147–166. doi: 10.1144/GSL.MEM.2006.032.01.09

Yamamoto, J., Kaneoka, I., Nakai, S., Kagi, H., Prikhod'ko, V. S., and Arai, S. (2004). Evidence for subduction-related components in the subcontinental mantle from low 3He/4He and 40Ar/36Ar ratio in mantle xenoliths from Far Eastern Russia. *Chem. Geol.* 207, 237–259. doi: 10.1016/j.chemgeo.2004.03.007

Yamamoto, J., Nishimura, K., Sugimoto, T., Takemura, K., Takahata, N., and Sano, Y. (2009). Diffusive fractionation of noble gases in mantle with magma channels: origin of low He/Ar in mantle-derived rocks. *Earth Planet. Sci. Lett.* 280, 167–174. doi: 10.1016/j.epsl.2009.01.029

Conflict of Interest Statement: The authors declare that the research was conducted in the absence of any commercial or financial relationships that could be construed as a potential conflict of interest.

frontiers in Earth Science

METHODS
published: 17 December 2018
doi: 10.3389/feart.2018.00214

Measuring SO_2 Emission Rates at Kīlauea Volcano, Hawaii, Using an Array of Upward-Looking UV Spectrometers, 2014–2017

Tamar Elias[1]*, Christoph Kern[2], Keith A. Horton[3], Andrew J. Sutton[1] and Harold Garbeil[4]

[1] Hawaiian Volcano Observatory, U.S. Geological Survey, Hilo, HI, United States, [2] Cascades Volcano Observatory, U.S. Geological Survey, Vancouver, WA, United States, [3] FLYSPEC, Inc., Honolulu, HI, United States, [4] Hawai'i Institute of Geophysics and Planetology, University of Hawai'i at Mānoa, Honolulu, HI, United States

Edited by:
Alessandro Aiuppa,
Università degli Studi di Palermo, Italy

Reviewed by:
Dmitri Rouwet,
Istituto Nazionale di Geofisica e Vulcanologia, Italy
Marie Edmonds,
University of Cambridge, United Kingdom

***Correspondence:**
Tamar Elias
telias@usgs.gov

Specialty section:
This article was submitted to Volcanology, a section of the journal Frontiers in Earth Science

Received: *18 August 2018*
Accepted: *05 November 2018*
Published: *17 December 2018*

Citation:
Elias T, Kern C, Horton KA, Sutton AJ and Garbeil H (2018) Measuring SO_2 Emission Rates at Kīlauea Volcano, Hawaii, Using an Array of Upward-Looking UV Spectrometers, 2014–2017. Front. Earth Sci. 6:214. doi: 10.3389/feart.2018.00214

Retrieving accurate volcanic sulfur dioxide (SO_2) gas emission rates is important for a variety of purposes. It is an indicator of shallow subsurface magma, and thus may signal impending eruption or unrest. SO_2 emission rates are significant for accurately assessing climate impact, and providing context for assessing environmental, agricultural, and human health effects during volcanic eruptions. The U.S. Geological Survey Hawaiian Volcano Observatory uses an array of ten fixed, upward-looking ultraviolet spectrometer systems to measure SO_2 emission rates at 10-s sample intervals from the Kīlauea summit. We present Kīlauea SO_2 emission rates from the volcano's summit and middle East Rift Zone during 2014–2017 and discuss the major sources of error for these measurements. Due to the wide range of SO_2 emissions encountered at the summit vent, we used a variable wavelength spectral analysis range to accurately quantify both high and low SO_2 column densities. We compare measured emission rates from the fixed spectrometer array to independent road and helicopter-based traverse measurements and evaluate the magnitudes and sources of uncertainties for each method. To address the challenge of obtaining accurate plume speed measurements, we examine ground-based wind-speed, plume speed tracking via spectrometer, and SO_2 camera derived plume speeds. Our analysis shows that: (1) the summit array column densities calculated using a dual fit window, are within −6 to +22% of results obtained with a variety of other conventional and experimental retrieval methods; (2) emission rates calculated from the summit array located ∼3 km downwind provide the best, practical estimate of summit SO_2 release under normal trade wind conditions; (3) ground-based anemometer wind speeds are 22% less than plume speeds determined by cross-correlation of plume features; (4) our best estimate of average Kīlauea SO_2 release for 2014–2017 is 5100 t/d, which is comparable to the space-based OMI emissions of 5518 t/d; and (5) short-term variability of SO_2 emissions reflects Kīlauea lava lake dynamics.

Keywords: sulfur dioxide, Kīlauea, emission rate, DOAS, FLYSPEC

INTRODUCTION

Sulfur dioxide (SO_2) release is an important indicator of volcanic activity, and high quality SO_2 measurements inform interpretations of volcanic processes and may signal impending eruptions (e.g., Casadevall et al., 1987; Symonds et al., 1994; Sutton and Elias, 2014). SO_2 flux measurements are also significant for accurately assessing climate impact (e.g., Robock, 2000) and provide context for understanding local environmental, agricultural, and human-health effects. (Cronin and Sharp, 2002; Delmelle et al., 2002; Carlsen et al., 2012; van Manen, 2014; Tam et al., 2016). Emission rates for gasses such as CO_2, HCl, HF, and H_2S can be estimated by quantifying the volumetric concentration ratio of the species of interest to SO_2 and then scaling this value with the measured SO_2 emission rate (e.g., Gerlach et al., 1998; Halmer et al., 2002; Aiuppa et al., 2006; Mather et al., 2006). Thus, retrieving accurate volcanic SO_2 emission rates is significant for a variety of purposes.

Kīlauea Volcano, on the Island of Hawai‘i, has erupted nearly continuously since 1983. Changes in SO_2 release have heralded changes in vent location, eruptive character, and eruptive vigor (Elias and Sutton, 2002, 2007, 2012; Patrick et al., 2016a,b, 2018). Local SO_2 impacts over the last 10 years have been significant: farmers and ranchers have received Federal disaster assistance due to financial losses (Patrick et al., 2013; Elias and Sutton, 2017), the cost of medical care for respiratory outcomes has risen (Halliday et al., 2018), and public access to iconic areas has been restricted due to SO_2 hazards (Elias and Sutton, 2017). In addition, local and regional atmospheric studies show that Kīlauea's contemporary degassing regime, though non-explosive, has the potential to impact climate and weather (Eguchi et al., 2011; Uno et al., 2013; Beirle et al., 2014).

To quantify volcanic SO_2 release, ultra-violet (UV) Correlation Spectroscopy, and more recently, Differential Optical Absorption Spectroscopy (DOAS) have been used for many years (Moffat and Millan, 1971; Millán and Chung, 1977; Perner and Platt, 1979; Stoiber et al., 1983; Platt, 1994; Galle et al., 2003). Typically, instruments are either passed beneath the volcanic gas plume, or the instrument or an optical scanner is used to scan across the plume from horizon to horizon (Chartier et al., 1988; Andres et al., 1989; Sutton et al., 2001; Edmonds et al., 2003; Galle et al., 2003, 2010). In each case, the SO_2 load is determined in a cross-section of the volcanic plume, then multiplied by the plume speed (frequently approximated by wind speed) to obtain SO_2 emission rate.

Sulfur dioxide emission rate measurements at Kīlauea Volcano began in 1979, facilitated by convenient access and a good road located downwind of the summit and East Rift Zone (ERZ) degassing sources (**Figure 1**; Sutton et al., 2001; Elias and Sutton, 2002, 2007, 2012). Prior to 2008, regular road traverses quantified the generally low levels ($<$600 tons per day (t/d) and 1000 parts per million meters (ppmm)) of passively degassing SO_2 at the Kīlauea summit. However, in more recent years, standard methods for quantifying the summit SO_2 have been complicated by two issues: very high SO_2 column densities ($>$10,000 ppmm) and very low altitude and ground-hugging plumes.

Under prevailing northeasterly trade wind conditions, traverse measurements were most easily performed on Crater Rim Drive, which often intersected the plume less than 500 m from the gas emission source. Since the onset of the summit eruption in 2008 (Wilson et al., 2008) very high SO_2 emission rates have frequently been observed from the actively degassing lava lake within the Overlook crater. The proximity of the traverse to the emission source, combined with the high SO_2 emission rates, leads to frequent, very high SO_2 column densities overhead ($>$10,000 ppmm). When such high column densities are encountered, several assumptions commonly made when evaluating DOAS or correlation spectroscopy measurements of optically thin plumes become inaccurate, and specialized methods must be applied (Millan, 1980; Kern et al., 2012; Fickel and Delgado Granados, 2017). Traditional DOAS measurements assume that the optical depth of the measurement is relatively small, with only a fraction of the initial radiance absorbed, and that the measured radiation has taken a straight path through the volcanic plume (see section "Conventional DOAS Retrievals"). Optically thick plumes introduce complex light paths for ground-based radiance measurements, complicate radiative transfer, exacerbate wavelength-dependent attenuation of the UV signal, potentially lead to total absorption of incoming energy at certain wavelengths, and interfere with the fitting of calibration cell spectra to the collected atmospheric sample spectra.

Kīlauea's topography poses an additional challenge in quantifying summit emissions. Combined with the fact that the volcanic gasses were emitted from a vent within a ~100 m deep crater, the shield volcano's gentle slopes and strong trade winds often lead to very low altitude plumes. In fact, it is common for the gas plume to extend all the way to ground level. This makes application of scanning instruments for high-time resolution SO_2 emission rate monitoring difficult because instruments placed downwind are often surrounded by gas and therefore cannot properly determine the SO_2 load. Low angle scanning, as is required with a grounded or low altitude plume, yields measurements that are subject to atmospheric effects that plague low-angle viewing geometries (see Galle et al., 2003, for details). Challenges in accurately identifying the plume height, distance, geometry or speed for a low level dynamic plume contribute to widely varying results, with minimal constraint for realistically assessing results.

Difficulties in applying standard measurement techniques, combined with the desire for high resolution SO_2 emission rate measurements, lead the U.S. Geological Survey's Hawaiian Volcano Observatory (HVO) in 2012 to install an array of ten FLYSPEC spectrometer systems at the summit of the volcano (Horton et al., 2006). These instruments are permanently installed at a fixed distance of ~3 km from the Overlook Vent. They are in the predominant downwind direction and are separated laterally by 250–880 m (**Figure 2**). They each have a fixed, upward-looking view, with spatial information on the plume overhead derived from the array's layout rather than changes in the instruments' viewing geometry (as is the case for traverse or scanning measurements).

The advantage of the array-based data over scanning data is that the measurements are valid, even if the instruments are

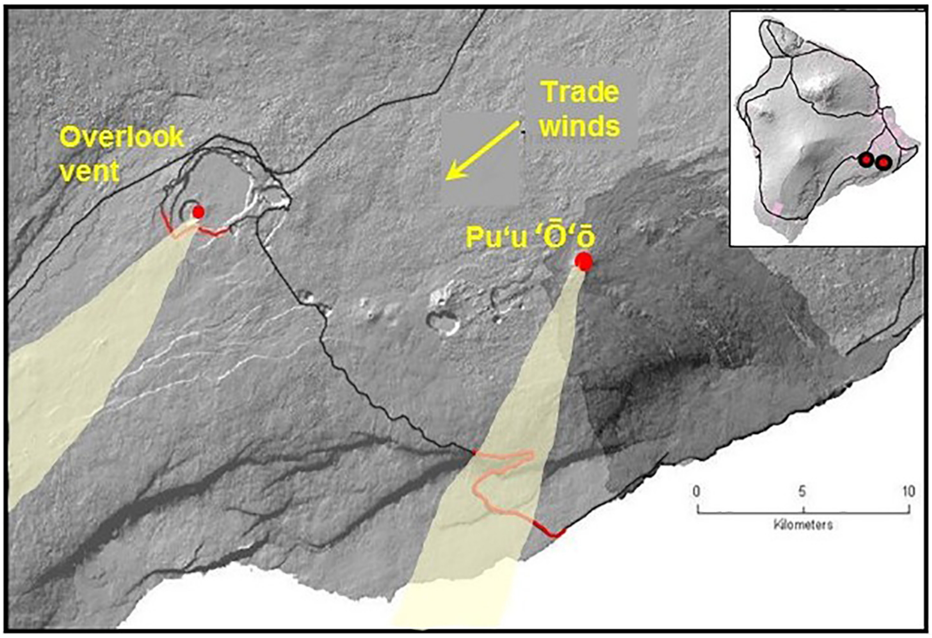

FIGURE 1 | Location of the main sources of SO_2 gas release at the summit and East Rift Zone of Kīlauea Volcano from 2014 to 2017, with inset of vent locations on the Island of Hawai‘i. The traditional road traverses (red lines) are located downwind of the outgassing sources during the dominant trade wind conditions (arrow).

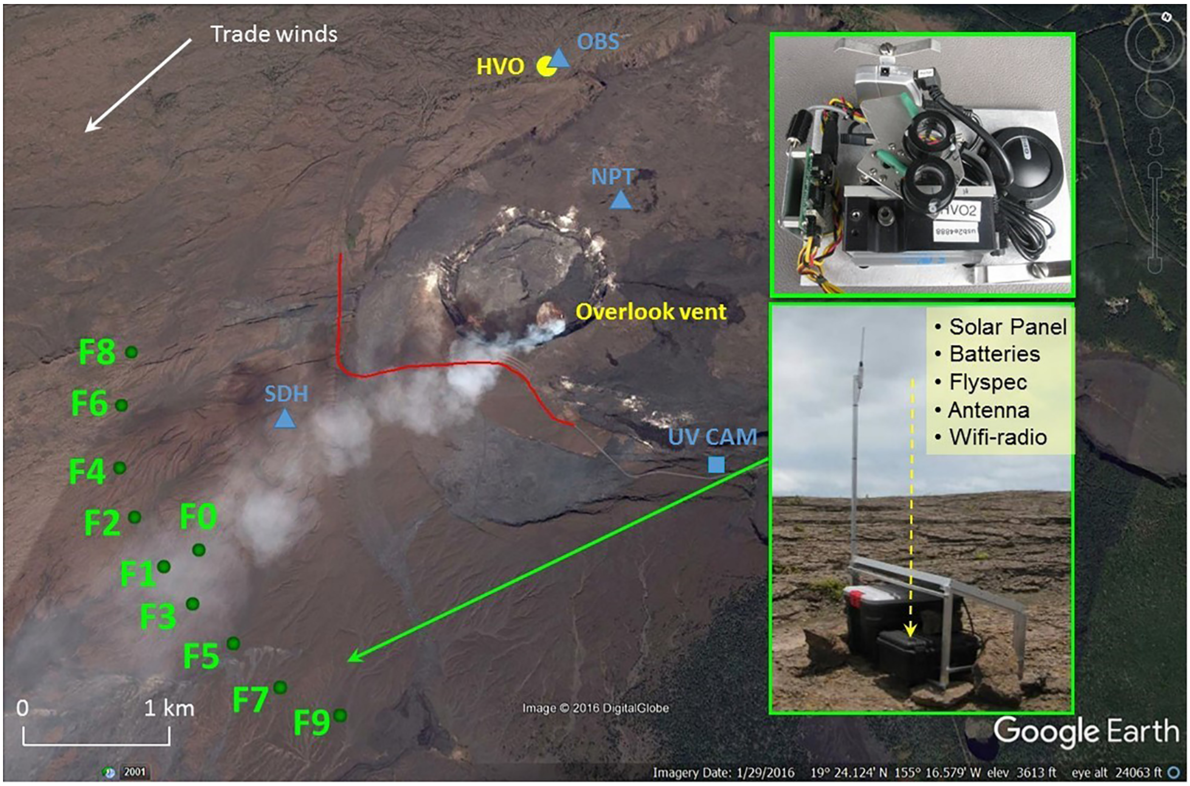

FIGURE 2 | Location of 10-spectrometer upward looking FLYSPEC array downwind of the summit of Kīlauea (F0–F9), with station and instrument inset, ground-based anemometers and UV camera used for approximating plume speed (blue), traverse route on Crater Rim Drive (red), 2014–2017 location of Hawaiian Volcano Observatory and Overlook vent (yellow). Dominant trade wind direction indicated by arrow in upper left.

surrounded by volcanic gas due to a grounded plume. Also, the array's 3 km distance from the vent makes for a more dilute plume than for road traverses on Crater Rim Drive thus allowing for quantification by DOAS or correlation methods. One disadvantage of the fixed array is degraded spatial resolution as compared to scanning or traverse techniques (see section "Errors Due to Location of Plume SO_2 Maximum Between Array Sensors"). SO_2 emission rates from Puʻu ʻŌʻo and other East Rift Zone (ERZ) degassing sources are still determined by vehicle traverses on Chain of Craters Road. As this road is 9 km from the gas source, plumes are generally quite dilute at the point of measurement and can therefore be accurately measured with standard DOAS or correlation analyses.

Focusing mainly on Kīlauea's summit area in this study, we examine the SO_2 emission rates determined by the FLYSPEC array from 2014 to 2017. First, we review the novel and conventional instruments and methods applied in this study and discuss the major sources of error and uncertainty. Next, we present our estimate of SO_2 emission rates from the Overlook vent, along with the uncertainty in these results. To address the total SO_2 degassing budget for Kīlauea Volcano, ERZ SO_2 traverse measurements are also presented for the studied time interval. Finally, we compare our summit results to independent measurements using mobile and space-based platforms.

INSTRUMENTATION AND METHODS

Spectrometer Array

The FLYSPEC array is located about 3 km southwest of the active summit vent, and it extends along an arc about 3 km wide (**Figure 2**). Each instrument incorporates an Ocean Optics USB 2000+ spectrometer fitted with a 74-DA collimating lens (providing a field of view of 2.5°), a low and high concentration SO_2 cell controlled by a servo motor, a GPS, and a netbook computer that controls the measurements (Businger et al., 2015). Column densities are retrieved on-site at each station. As is standard procedure for FLYSPEC instruments, the column amounts are retrieved by fitting the atmospheric sample spectrum to the gas cell calibration spectrum over the wavelength measurement window using the Levenberg-Marquardt least-squares fit. This compares the SO_2 optical depth of the overhead plume with that of a known column density in the reference cells (Moré, 1978; Elias et al., 2006; Horton et al., 2006).

The calculated column densities are telemetered to HVO at a data rate of 1 Hz; the raw spectra are also stored should they be needed for future analysis.

Each station calculates the overhead SO_2 column density at 1 s intervals between 0830 and 1700 Hawaii Standard Time when there is sufficient UV energy to obtain a reasonable signal-to-noise-ratio year-round in Hawaiʻi. The SO_2 load (X) in the plume cross section is then determined by summing the vertical column densities measured by the individual stations (i), according to equation 1:

$$X = \sum_i S_i \cdot \Delta x_{i,i+1} \tag{1}$$

where S_i is the SO_2 column density measured at station i and Δx_i is the average distance between station i and the two adjacent stations. Most stations are located ∼300–400 m apart to capture the main features of the plume, which is typically between 1200 and 2800 meters wide and detected by 3–10 stations at any one time. Emission rates are then calculated from the SO_2 load (X) in the plume cross section by multiplication with the wind speed (Horton et al., 2012; Businger et al., 2015).

The array's distance from the vent means that the plume is significantly more dilute than when measured by road traverse on Crater Rim Drive. This reduces the complexity of the DOAS retrieval since the plumes are less opaque when crossing the array than when passing over Crater Rim Drive. However, overhead column densities more than 5,000 ppmm are still common. Therefore, spectral analysis is performed using a dual fit window (DFW) approach (see section "The FLYSPEC Dual Fit Window" and Horton et al., 2012; Businger et al., 2015).

Under prevailing trade wind conditions, the array generally spans the width of the plume, however, the processed emission rates must meet specific criteria for a measurement to be reported as valid. To assure that the plume is predominantly inside the array arc, a minimum of seven spectrometers in the arc must report valid column amounts, and the spectrometer at either end of the arc must report < 350 ppmm. These conditions consider the spatial resolution of plume features, and the diurnal influence on signal-to-noise. If these conditions are met, the plume direction is reported as the azimuth from the Overlook vent to the FLYSPEC station reporting the maximum overhead SO_2 column density. A cosine correction is then applied to account for non-perpendicular plume direction over individual array segments.

Seasonal interruptions in the trade wind flow occur each winter and less valid data is available from the array.

Mobile UV Spectrometer Instruments

In this study, two types of mobile instruments were used to collect moderate resolution spectra of incident scattered solar UV radiation. For one, we used a mobile DOAS instrument consisting of an Ocean Optics spectrometer (either USB2000+ or SD2000) connected to an upward-looking telescope with a fused silica fiber optic cable. The spectrometers had an optical resolution of about 0.7 nm and recorded radiance in the 280–420 nm wavelength interval. For traverse measurements, the telescope was mounted on the outside of the vehicle (either car or helicopter), while the rest of the instrumentation was placed inside. A laptop computer acquired spectra with the Mobile DOAS software (e.g., Galle et al., 2003). The other instrument was the standard mobile version of the FLYSPEC described in section "Spectrometer Array" and by Horton et al. (2006).

Calculating SO_2 Column Densities From UV-Spectral Data

Conventional DOAS Retrievals

The DOAS technique measures absorption of scattered solar radiation as it passes through a volcanic plume. Different trace gasses within the plume, and particularly SO_2, have characteristic absorption cross-sections. This allows the selective detection of individual plume components. In conventional DOAS retrievals, quantitative measurements of column densities S are performed by comparing the spectrum of incident radiation obtained from the clear sky (I_0) to that obtained from the volcanic plume (I). The column density, or number of gas molecules per unit area (c) along the effective line of sight of the instrument (L), can then be obtained by inserting the measured spectra into the Beer-Lambert-Bouguer law of absorption.

$$S = \int_L c \cdot dl \tag{2}$$

$$\tau = ln\left(\frac{I_0}{I}\right) = \sum_i \sigma_i S_i \tag{3}$$

As the spectral optical depth τ and the absorption cross-sections σi are both vectors, the column density is obtained by fitting the absorption cross-sections of various trace gasses suspected in the plume to the measured optical depth. This approach has been shown to yield accurate trace gas column densities along the instrument line-of-sight if (1) the optical depth is relatively small so that only a fraction of the initial radiance is absorbed, and (2) the measured radiation has taken a straight path through the area of interest, in this case the volcanic plume (Perner and Platt, 1979; Platt, 1994; Platt and Stutz, 2008).

Complications arise if either of these two conditions are not met. If radiation is scattered within the volcanic plume, e.g., on aerosols or water droplets, then the effective light path along which the measurement is made may change. Though column densities S can still be retrieved in this situation, these can no longer be easily converted to average concentrations (Eq. 2) or cross-sectional plume loads if the effective path length L is unknown. Similarly, if a gas species in the plume absorbs more than a few percent of the incident solar radiation, the effective light path along which the measurement occurs begins to vary with wavelength, becoming shorter for wavelengths at which strong absorption occurs. This can lead to inaccurate column densities (several factors to orders of magnitude error) particularly when fitting uses the shorter wavelengths, where stronger absorption occurs (Mori et al., 2007; Kern et al., 2010, 2012; Fickel and Delgado Granados, 2017).

Several techniques have been suggested to avoid the problems associated with the complex radiative transfer effects (Mori et al., 2007; Kern et al., 2010, 2012; Fickel and Delgado Granados, 2017). The most straightforward method is to avoid measurements in conditions with very high SO_2 column densities or high plume opacities (e.g., condensed plumes). This consideration was fundamental in determining the optimum location of the spectrometer array (Businger et al., 2015), which is close enough to capture short time-variations in the outgassed plume but avoids very high SO_2 column densities.

When UV-spectroscopic measurements of optically dense plumes are evaluated with conventional DOAS approaches, the retrieved SO_2 column densities have been found to depend on the wavelength range in which the spectral fitting is performed (Mori et al., 2007; Kern et al., 2010, 2012; Fickel and Delgado Granados, 2017). This is problematic, as the actual amount of SO_2 in the instrument's viewing direction should not depend on the wavelength of light that is being measured. Instead, this is an indication that the conventional DOAS model does not adequately describe the physical processes governing the scattering and absorption of UV radiation between the sun and the instrument. A more sophisticated model is needed.

Variable Wavelength Fit Windows

Conventional DOAS retrievals assume a linear relationship between optical depth and column density. This relationship breaks down for high optical depths if the spectrometer does not fully resolve the spectral absorption features, as is typically the case for miniature DOAS spectrometers and most target gas species. Fortunately, in the case of SO_2, strong absorption can be avoided. Since the magnitude of the SO_2 absorption cross-section decreases rapidly toward wavelengths longer than 300 nm, moving the range in which the spectral analysis is performed (i.e., the 'fit window') toward longer wavelengths decreases the considered optical depth of SO_2 absorption.

Several algorithms have been suggested to take advantage of this circumstance. When analyzing data collected close to the fumaroles at Poas Volcano in Costa Rica, de Moor et al. (2016) dynamically adapted the lower end of their DOAS fit window to avoid SO_2 optical depths greater than 0.1. In this study, we considered this same approach, which we call 'Sliding Lower Fit Bound' (SLFB), in comparison to other retrieval methods. The SLFB algorithm first performs a conventional DOAS SO_2 retrieval in the 307 to 340 nm wavelength range. If the derived SO_2 optical depth exceeds 0.1 in this window, the lower bound of the fit range is increased by one tenth of the total width of the fit window (3.3 nm in this case), and the fit is performed again on this new window. This process is repeated until the fit returns an SO_2 optical depth below 0.1, at which point the retrieved column density is saved as the final fit result. To ensure that the number of pixels included in the fit always remained adequate to distinguish between the absorption features of SO_2 and ozone (O_3), the lower fit bound was not allowed to exceed 319 nm. The few spectra that did not return an optical depth below 0.1 with the 319 nm lower bound were omitted from the analysis. The algorithm aims to avoid high optical depths associated with SO_2 absorption while at the same time allowing for high sensitivity at times when low SO_2 loads are present in the instrument's field of view. Fickel and Delgado Granados (2017) used a similar approach and suggest using one of three partially overlapping fit windows, with the choice of window depending on the SO_2 column density derived in each.

The FLYSPEC Dual Fit Window

FLYSPEC instruments operate much the same as any other DOAS instrument but instead of fitting an SO_2 absorption cross-section taken from literature, each FLYSPEC records its own SO_2 absorption cross-section. This is achieved by inserting calibration gas cells of known SO_2 concentrations into the light path and recording the instrument response. To account for any first-order changes in instrument response while operating in a range of typical SO_2 column densities, two gas cells with different SO_2

concentrations are measured – one with about 400 ppmm (low cell) and one with around 1500 ppmm (high cell) (Horton et al., 2006).

The SO_2 retrieval used for operational analysis of FLYSPEC array data since 2014 at HVO is then very similar to the variable wavelength windows described above. The FLYSPEC 'Dual Fit Window' (DFW) approach selects the evaluation wavelength range based on how the encountered SO_2 optical depth compares to that obtained when measuring the FLYSPEC calibration cells. If the SO_2 optical depth is less than that of the low cell, then a fit window of 305 to 315 nm is used, and the low cell provides the absorption cross section for the fit. If the SO_2 optical depth is larger than that of the low cell ($cell_L$), but smaller than that of the high cell ($Cell_H$), then two fits are performed in the 305–315 nm window, one using each of the cells as absorption SO_2 cross section (S_{high} and S_{low}), and the weighted mean of the two results is calculated:

$$S(\lambda) = S_{low}(\lambda)^* \frac{Cell_H - S_{low}(\lambda)}{[Cell_H - S_{low}(\lambda)] + [S_{high}(\lambda) - cell_L]} +$$

$$S_{high}(\lambda)^* \frac{S_{high}(\lambda) - Cell_L}{[Cell_H - S_{low}(\lambda)] + [S_{high}(\lambda) - cell_L]} \tag{4}$$

Finally, if the SO_2 optical depth is greater than that of the high cell, then a second fit window is added. The SO_2 cross section from the high cell is now fit to the measured optical depth in both the 305–315 nm (short) fit window and in the 319.5–330 nm (long) fit window, resulting in two SO_2 column densities, S_{short} and S_{long}. If the long-fit window returns less than 1.5 times the SO_2 optical depth of the high cell, then a weighted average is calculated between the two different fit results according to:

$$S = (1 - w)^* S_{short} + w^* S_{long} \tag{5}$$

with

$$w = (S_{short}/Cell_H - 1)^* 2 \tag{6}$$

For SO_2 column densities larger than 1.5 times that of the high cell, the result from the long-fit window is used exclusively, with the high cell acting as the SO_2 reference cross section.

A logic diagram for selection of the FLYSPEC evaluation window is included in the **Supplementary Material**.

Simulated Radiative Transfer DOAS

To avoid strong SO_2 absorption, column densities can be measured at greater downwind distances and/or the fit wavelength range can be adjusted. However, these strategies do not account for signal dilution caused by radiation entering the field of view between the plume and the instrument or in-plume scattering on aerosols or condensed water droplets (Kern et al., 2010). At Kīlauea's summit, signal dilution is likely a minor concern since the plume is typically within 10's of meters of the ground, and all the measurements we are reporting were performed in a zenith-looking geometry. In-plume scattering, however, could cause inaccuracies in SO_2 retrievals, particularly when the measured plume is visibly opaque. An approach called Simulated Radiative Transfer DOAS (SRT-DOAS) was developed to deal with realistic radiative transfer in volcanic plumes (Kern et al., 2012) and applied to dense plumes detected at Kīlauea's summit in 2010–2011. This method uses a three-dimensional radiative transfer model to simulate the propagation of light in and around an idealized volcanic plume and compares the modeled spectra with measured ones. The best match between measurement and model yields the plume properties, such as the SO_2 column density.

Simulated Radiative Transfer DOAS can account for complex light paths in and around volcanic plumes, but also has drawbacks when compared to the previously mentioned methods. SRT-DOAS retrievals rely on the availability of a lookup table of modeled spectra, which are computed by considering all possible measurement conditions in a radiative transfer model. This is a computationally expensive and time-consuming task. Typically, the plume geometry and atmospheric conditions are kept constant, while the plume SO_2 loading and aerosol optical depth are varied to reflect all possible combinations of these parameters. The method is therefore limited to situations in which the plume geometry and atmospheric conditions are reasonably well constrained and constant during the measurement interval. Errors in the initialization of these parameters can cause systematic errors in the results. For these reasons, the method is currently not used for routine analysis of DOAS data, but rather only used in case studies where these external parameters can be adequately constrained.

Long UV Wavelength SO_2 Fit Window

Bobrowski et al. (2010) documented the use of a wavelength range at the long end of the UV spectrum (360–390 nm) specifically for examining plumes with high optical depths. We utilize this window for evaluating the very large column densities encountered during road traverses conducted along Crater Rim Drive (section "Spectrometer Array"). This wavelength window makes use of SO_2 absorption lines stemming from the spin-forbidden $a^3B_2 \leftarrow X^1A_1$ transition of the SO_2 molecule which are about two orders of magnitude weaker than the lines in the standard DOAS 310–325 nm wavelength region. Therefore, this retrieval window is insensitive to low SO_2 column densities but avoids strong SO_2 absorption and is therefore less affected by radiative transfer complexities in cases where extremely high SO_2 column densities (e.g., $>$10,000 ppmm) are encountered.

Determining Plume Speed

Regardless of the type of spectroscopic retrieval method, the plume speed is required to derive emission rates from cross-sectional SO_2 loads. In this study, three different methods were employed to determine plume speed based on the location of data collection.

Cross-Correlation Method

The spectrometer array was designed to allow continuous monitoring during daylight hours of SO_2 emission rates from the Overlook vent. To determine wind speed, a single spectrometer station was positioned 100 m closer to the vent than the rest of the array in the predominant trade wind direction (F0 in **Figure 2**). Overhead SO_2 column densities recorded every 10 s by this station are used to determine plume speed using a cross-correlation approach (Williams-Jones et al., 2006). A 10-min time series of SO_2 column density is generated every minute and is compared to the 10-min time series recorded by station F1, 100 m downwind. Examining the time lag between the two stations, the maximum cross-correlation between the time series is sought, which is representative of the time it takes for plume features to pass from station F0 to F1. The plume speed can therefore be determined by dividing the 100-m distance by the derived time lag.

Next, a quality filter is applied to the derived plume speeds to ensure that only valid data are reported. The plume speed is deemed valid if (1) the peak of the plume is recorded within the central part of the array (stations F1–F7), (2) stations F0 and F1 recorded column densities above the detection limit during at least 3 of the last 10 min and, (3) the calculated plume speed is less than twice that measured by a nearby anemometer (SDH Station, see next section). If any of these conditions are not met, the nearby anemometer wind speed is used to determine the emission rate.

Anemometers

When volcanic gas is passively released into the atmosphere, it quickly mixes with background air and travels together with surrounding air parcels. Therefore, wind speed can be an appropriate measure for plume speed in these situations. Although it is not usually possible to measure wind speed at the precise location of the plume using conventional methods, anemometers near ground level can provide useful information, particularly during times when other wind data are not available, or the plume is grounded. Gill 'Windsonic' ultrasonic anemometers are located 3 m above ground level (agl) ∼0.8 km north of the Overlook vent (station NPT) and the FLYSPEC array (station SDH). RM Young propeller and vane style anemometers are located 10 m agl on the north side of HVO on the rim of Kīlauea Caldera (station OBS, **Figure 2**). Measurements from these instruments are compared with other methods for determining the wind speed.

Plume Speed From SO_2 Camera Imagery

Time-resolved imagery of volcanic plumes can also be used to derive plume speeds. During the period of this study, HVO maintained an SO_2 camera on the southeast rim of Kīlauea Caldera (Kern et al., 2015). Aimed at the Overlook vent, this camera records UV images of the plume at two 10 nm-wide wavelength channels centered at 313 and 330 nm. Images are recorded every few seconds, with repeat intervals depending mostly on telemetry network latency. These images are used to derive SO_2 optical depths and, in combination with plume speeds measured by an optical flow algorithm, determine the SO_2 emission rate at high time resolution (e.g., Mori et al., 2006; Bluth et al., 2007).

Several studies have examined potential error sources in wind speed determination using optical flow models (Peters et al., 2015; Klein et al., 2017; Gliß et al., 2018). Thus, for the case studies presented here, plume features in the SO_2 camera imagery were manually tracked to calculate plume speed. A sequence of images was loaded for each period in question. In each sequence, prominent plume features were identified, and their movement was tracked through the sequence. The horizontal pixel displacement was calculated by simple differencing of subsequent feature pixel positions, and the pixel velocity was determined by dividing the displacement by the time difference of the respective images. The pixel velocity was then converted to an apparent plume speed (perpendicular to the camera's viewing angle) by multiplying the pixel velocity and pixel size at the distance to the plume (approximately 0.75 m, see Kern et al., 2015 for details).

In a final step, the derived plume speed was adjusted to account for potentially non-perpendicular viewing geometry. Each instance in which the SO_2 camera imagery was used to determined plume speed corresponds to a coincident vehicle traverse performed on Crater Rim Drive. The wind direction was determined by fitting a Gaussian curve to the progression of SO_2 column densities measured while traversing the plume, then calculating the direction from the vent to the peak of this curve. Multiplication of the camera-derived plume speed with the sine of the wind direction minus the camera viewing direction yielded the corrected plume speed.

Given that this is a direct observation of the plume propagation, this method is deemed to be accurate for determining plume speed above the Overlook vent. However, various parts of the plume move at slightly different speeds. Therefore, the procedure was repeated 4 times for every measurement period, and the mean and standard deviation of each value are reported below.

The SO_2 camera relies on imagery taken in only 2 wavelength channels (on SO_2 band at 313 nm and off SO_2 band at 330 nm) to derive the SO_2 column density of the plume. Recent findings suggest that this limited spectral information is not sufficient to obtain an unambiguous calibration in cases where plumes with high SO_2 loading and aerosol optical depth are encountered (Kern et al., 2013). In such situations, a collocated DOAS spectrometer can provide image calibration information, but this procedure relies on the same spectral retrieval methods used in our comparative study. Thus, a comparison of SO_2 camera and array derived emission rates is not presented in this study.

Uncertainty and Error Sources for Spectrometer Array Derived SO_2 Emission Rates

In the previous section, the methods used to evaluate data from the fixed spectrometer array were described. To quantify the uncertainty of our measurements, we now evaluate results using different fit-windows, plume speed data, and traverse measurement strategies.

The Impact of Fit Window

Several different spectral retrievals were introduced in section "Calculating SO_2 Column Densities From UV-Spectral Data," each representing a slightly different method for determining SO_2 column density along the instrument line of sight from the measured UV-spectral data. To test the sensitivity of the array measurements to different spectral retrieval methods, we performed a targeted experiment. On May 24, 2017, a mobile DOAS instrument was collocated with the F0 spectrometer array station. The DOAS telescope was mounted vertically on the FLYSPEC antennae mast, pointing toward zenith. Spectra were recorded from this stationary location at 1 s intervals between 12:49 and 14:46 local time.

The mobile DOAS data collection output format lends itself to performing a variety of spectral analyses using existing processing routines. Thus, we performed SO_2 column density retrievals on the collected (stationary) mobile DOAS data using four different analysis methods. The evaluation parameters for each method are summarized in **Table 1** (also see section "Calculating SO_2 Column Densities From UV-Spectral Data"). We ran conventional DOAS retrievals in two fixed-fit windows, as well as a very long wavelength range specific for high column densities (Bobrowski et al., 2010). Conventional DOAS retrievals used the 310–325 nm window, which is the standard range used for analyzing scanning DOAS data in the 'Network for Observation of Volcanic and Atmospheric Change' (NOVAC) network (Galle et al., 2010). For comparison, we added a 319–340 nm fixed window evaluation which is more suitable for the large SO_2 column densities encountered at Kīlauea's Overlook vent. This longer wavelength window has a lower sensitivity to SO_2, as it omits some of the strongest SO_2 absorption lines. Therefore, the retrieval will have a reduced signal-to-noise ratio for low SO_2 column densities. The use of a SLFB window mitigates this effect, and we ran an SLFB retrieval in which the lower fit bound varied between 307 and 319 nm (see section "Variable Wavelength Fit Windows"). An additional very long wavelength window (360–390 nm) was used for evaluating data collected during vehicle traverse measurements on Crater Rim Drive, where column amounts often exceeded 2,500 ppmm. A fourth and final analysis of the spectra was performed using an SRT-DOAS retrieval initialized with the approximate geometry of the measurements (see **Table 1**).

Figure 3 shows results of each spectral analysis method plotted against results obtained from a coincident measurement of FLYSPEC station F0 evaluated with the DFW technique. The main sources of scatter in the data are (1) lack of time synchronization between the upward-looking stationary mobile DOAS and array station F0 (the available FLYSPEC data were stored as 10 s averages, then interpolated to the 1 s measurement interval of the mobile DOAS) and (2) a slight mismatch between the viewing directions and viewing angles of the two instruments. The discrete steps in the SRT results are artifacts caused by the limited resolution of the lookup table.

Despite the scatter, linear regressions to each dataset reveal slight systematic differences between the analysis methods. Conventional DOAS retrieval in the 310–325 nm wavelength window systematically yields 6% lower SO_2 column densities than the DFW method. All other methods return values slightly higher than the DFW method, with the 319–340 nm DOAS retrieval giving 22% higher values, the SLFB retrieval giving 19% higher values, and the SRT-DOAS retrieval giving 21% higher values on average.

The systematic difference between the methods is not unexpected. The presence of aerosols in the plume overhead

TABLE 1 | Parameters defining SO_2 retrievals compared in this study.

DOAS retrieval parameter	Value
All evaluations	
Spectral corrections	Subtract dark current Subtract electronics offset
Calculation of optical depth	Divide by clear-sky or zenith spectrum Logarithm
Analysis method: Fixed fit window retrievals	
Fit wavelength ranges	
Conventional DOAS	310–325 nm (constant)
Extended range	319–340 nm (constant)
Very extended range	360–390 nm (constant)$^{1)}$
Fit references	SO_2 (Vandaele et al., 2009) O_3 (Bogumil et al., 2003) Ring correction (Grainger and Ring, 1962) Wavelength calibration correction (Beirle et al., 2013) Polynomial (3rd order)
Analysis method: Sliding lower fit bound (SLFB)	
Fit wavelength range	307$^{2)}$–340 nm
Fit references	Same as above
Analysis method: SRT-DOAS	
Fit wavelength range	307–338 nm
Lookup table measurement geometry	600 m plume diameter, circular cross-section with Gaussian concentration profile 300 m plume height (to plume center) Plume SO_2 column densities: 0 to 52,000 ppmm Plume aerosol optical depths: 0 to 20$^{3)}$ Plume aerosol single scattering albedo: 0.9 Zenith-looking instrument located under plume center Rayleigh atmosphere surrounding plume
Additional fit references	O_3 (Bogumil et al., 2003) Ring correction (Grainger and Ring, 1962)

All spectral analyses were performed using MATLAB. The literature absorption cross-sections were convolved with the mobile DOAS spectrometer instrument line shape prior to performing the fit. $^{1)}$*Analysis of SO_2 in the 360–390 nm wavelength range requires SO_2 column densities larger than about 2,500 ppmm and was therefore only performed on data collected during vehicle traverse measurements on Crater Rim Drive, where the frequency of large column densities is greater.* $^{2)}$*For each spectrum, the lower bound was increased until the optical depth in the entire fit region was < 0.1.* $^{3)}$*A range of 0 to 1 was used for analysis of measurements taken at the array, as this range was deemed representative of conditions in the more dilute plume.*

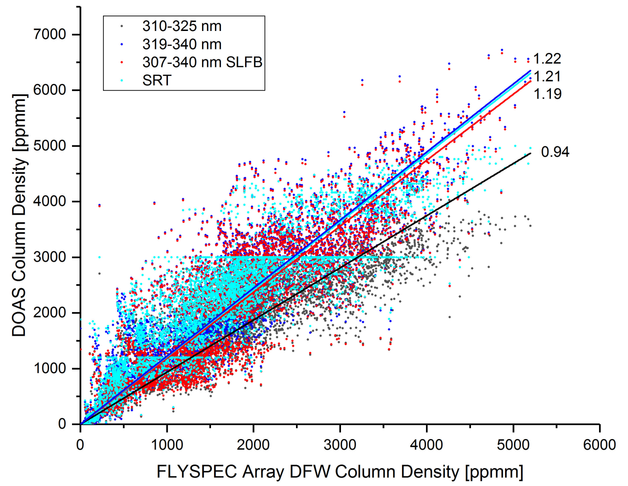

FIGURE 3 | Coincident measurements of FLYSPEC station F0 and co-located stationary upward looking DOAS instrument are analyzed to compare the FLYSPEC DFW spectral analysis method with four different DOAS retrievals. Linear regressions were fit to the results of each method and show systematic differences are relatively small. A conventional DOAS analysis in the 310–325 nm window yields 6% lower values than the FLYSPEC DFW, while the results of the other methods are between 19 and 22% higher than the DFW.

causes a non-negligible contribution of complex light paths to the radiance measured by the instruments on the ground. Since, in this situation, the path of light through the plume will depend to some degree on its wavelength, the various retrievals will give different results based on which wavelengths are used.

Retrievals using a broad fit window are dominated by the shorter, strong absorption wavelengths. Thus, the SLFB retrievals are nearly identical to the traditional DOAS fit window when measuring low column amounts, even though the SLFB includes wavelengths out to 340 nm. As column amounts increase, the sliding fit window and DFW do a better job quantifying column amounts than would a single broad fit window.

The SRT-DOAS method uses the wavelength-dependency of the fit results to derive information on the radiative transfer of the measurement, but it requires additional assumptions on the conditions within and around the plume. For example, we consider the plume to be 600 m wide with a circular cross-section and a Gaussian concentration profile. Clearly this is an idealized scenario, and actual conditions will vary, potentially skewing the results. Therefore, an agreement of all methods within 22% of the DFW method is considered a successful validation of this method, and we consider other sources of uncertainty in the emission rate calculation (e.g., wind speed) are likely of similar or larger magnitude.

Based on these results, we consider the 1-sigma uncertainty of the SO_2 column density DFW results to be about 22%.

The Impact of Plume Speed Source on Calculated Array Emission Rates

Obtaining an accurate plume speed is addressed by using several methods for the summit vehicle traverse and array-based emission rate measurements. When plume geometry does not allow array-based plume speed calculations using the cross-correlation technique, wind data collected 3 m agl, approximately 800 meters from the array mid-point (SDH station; **Figure 2**) are used to derive array emission rates.

A plot of ground-based (SDH anemometer) wind speed, and array-based (cross-correlation) plume speed for the time interval of June – September 2017 yields a linear regression with a 22% difference for the two methods during representative trade wind conditions (**Figure 4**). The error in the SDH ultrasonic anemometer wind speeds is reported by the manufacturer

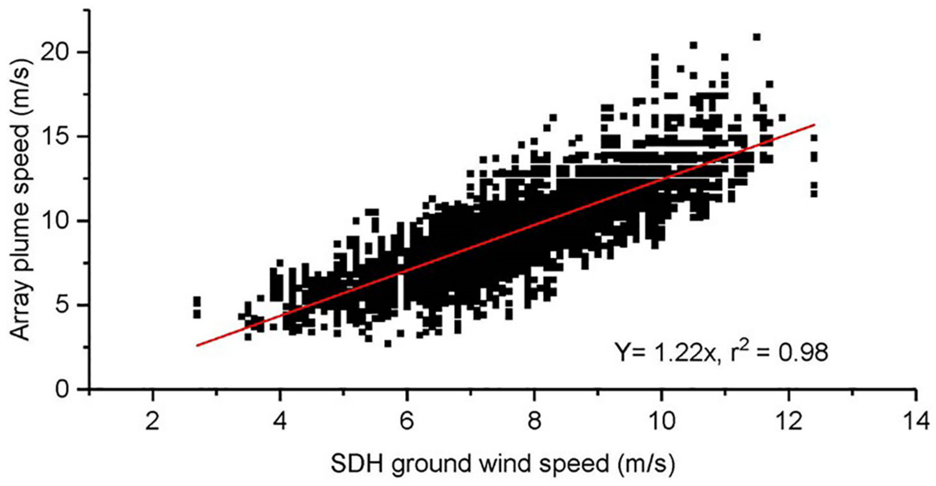

FIGURE 4 | Plume speed calculated from peak correlation using two along-axis FLYSPEC instruments versus 3-m agl wind speed measured with an ultrasonic anemometer (station SDH; **Figure 2**) for June–September 2017. Data is filtered to include only plume speeds used to calculate emission rates (see section "Spectrometer Array").

as ± 2% at 12 m/s, while the total uncertainty in the cross-correlation plume speed determination for instruments separated by 100 m is < 5% (Williams-Jones). For our configuration and conditions, this error is expected to be larger due to imperfectly synchronized computer clocks, indirect plume travel from array station 0 to 1, and imperfect plume feature correlation by the automated algorithm.

The difference between array plume speed and 3-m agl anemometer wind speed is not unexpected given likely variability of the vertical wind profile. Horizontal mean wind speeds measured by the SDH anemometer are affected by friction and surface roughness as air passes over the ground. Under moderate trade wind conditions, the top of the plume typically reached 500–800 m agl (Patrick et al., 2018); thus, plume speeds tracked by the array are expected to be somewhat larger, depending on the altitude of the plume.

Errors Due to Location of Plume SO_2 Maximum Between Array Sensors

The track of the summit SO_2 plume is quite predictable during typical trade wind conditions. Stations located toward the statistical center of the plume are spaced more closely together (250–400 m), while the stations most likely to be at the edges of the plume are spaced further apart (450–880 m). Strong winds result in a narrow plume, and the plume's core can fall between adjacent sensors, particularly when the plume is located toward the edges of the array where instrument spacing is greater. In these instances, the peak of the plume can go undetected and the shape of the plume is inaccurately captured, resulting in an underestimation of the emission rate. The effects of this issue can be seen in the comparison of the helicopter traverse and array data (see section "Validation of Array Emission Rates Using Other Measurement Strategies"). We estimate that under-reporting of emission rate is most likely to occur during wind directions between 0 and 20° and >50°, which occurred ∼15% of the time for our data set. Based on our case study, we estimate the magnitude of the under-reporting of the emission rate is on the order of 30–50% for data collected during periods when the plume maximum falls between the sensors, but this will vary depending on the location and width of the plume.

RESULTS

SO_2 Emissions From Kīlauea Volcano 2014–2017

The SO_2 budget for Kīlauea during this period includes emissions from both the summit Overlook vent and the ERZ (primarily the Puʻu ʻŌʻo vent). While SO_2 release from the ERZ was dominant from 1983 until the opening of the Overlook vent in 2008 (Elias and Sutton, 2017), summit emissions were an order of magnitude greater than those released from the rift during 2014–2017. For historical context, the road-based SO_2 emissions collected downwind of the Puʻu ʻŌʻo vent are included here, although they represent less than 10% of the total Kīlauea emissions for the reported era. The ERZ SO_2 values were all measured using an upward looking mobile FLYSPEC ∼10 km downwind of the gas emission source, where the plume is relatively weak and homogeneous, with column amounts generally < 500 ppmm. Thus, the complexities caused by very high plume optical depths are not a factor for ERZ measurements.

Long-Term SO_2 Output

Figure 5 presents the 10-s, daily-, and monthly mean SO_2 emission rates calculated using summit FLYSPEC array measurements. Averages are presented for days with at least 2 h of valid 10-s data, which reduces the likelihood of atypical conditions influencing the average. Emission rates averaged over a month used all valid 10-s values for the period. Emission rates calculated using SDH wind speeds (<10% of the data set) have been adjusted by +22% to account for the systematic underestimation of the ground-based wind measurements for plumes aloft (section "The Impact of Plume Speed Source on Calculated Array Emission Rates"). The uncertainties in the array values are based on the uncertainty in SO_2 column amounts (∼22%), plume speeds (∼5–30%), and underestimation due to plume maxima occurring between sensors (30–40% -see section "Errors Due to Location of Plume SO_2 Maximum Between Array Sensors"). These factors result in individual emission rate value uncertainties of ∼30–50%.

The average monthly Kīlauea East Rift Zone emission rates are included in **Figure 5B**. Although a minor contribution to total emissions, fluctuations in ERZ emissions are correlated with notable changes in the eruption during the period of interest (e.g., Global Volcanism Program, 2014). The emission rate data presented in this paper are given in Elias et al. (2018).

For 2014–2017, Kīlauea released an average of 5100 t/d, or 1.9 ± 0.1 Tg/yr. This is consistent with the space-based OMI SO_2 inventory performed by Carn et al. (2017), which ranks Kīlauea as the second highest passively degassing SO_2 producer (behind Ambrym) for the period 2005–2015. Kīlauea emissions represent 8% of the total SO_2 released from the 91 persistently degassing volcanic sources consistently detected from space by OMI (Carn et al., 2017).

SO_2 Short-Term Variability Reflects Lava Lake Dynamics

The short-term summit SO_2 release is highly variable and depends on the spattering or non-spattering condition of the lava lake (Elias and Sutton, 2012; Nadeau et al., 2015; Patrick et al., 2016a,b, 2017, 2018). Stagnant lake conditions resulted in decreased SO_2 release, while vigorous lake spattering was reflected in increased SO_2 emissions The SO_2 signature is consistent with lava lake fluctuations driven by cycles of activity at shallow depth, close to the lake surface. The high resolution SO_2 FLYSPEC array measurements have helped confirm the types of seismicity that are associated with shallow outgassing processes, with seismic energy < 0.2 HZ most clearly correlated with the outgassing signature (**Figure 6**).

A record of SO_2 emissions separated into spattering and non-spattering lava lake conditions is presented in **Figure 6**, and shows that on an annual basis, non-spattering lava lake phases correspond to SO_2 emission rates that are on average 20–50% of

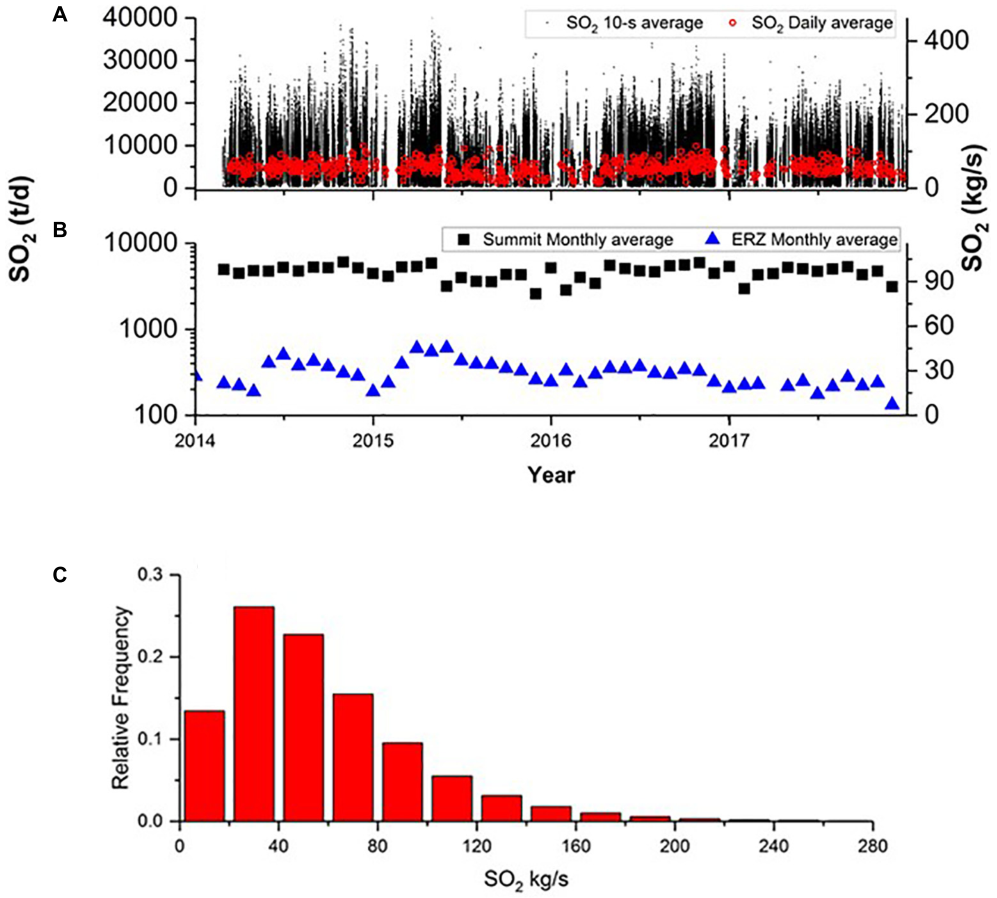

FIGURE 5 | (A) SO_2 10-s (black dots) and daily (red circles) average emission rate time series from Kīlauea Volcano summit array measurements 2014–2017. Daily means are reported for days with at least 2 h of data. For display purposes, infrequent values (<0.5% of data) above 40000 t/d are not shown. **(B)** Average SO_2 release over a month (black square) was calculated using all valid 10-s values during the period. East Rift Zone average monthly SO_2 (blue triangles) were measured by vehicle traverse of Chain of Craters Road downwind of the Puʻu ʻŌʻō vent (**Figure 2**). **(C)** Frequency distribution of summit array 10-s emission rate values show that 99% of the values are less than 200 kg/s (~17,000 t/d), with emission rates most commonly between 20 and 60 kg/s.

those during spattering phases. This is consistent with findings of Patrick et al. (2016a,b). While the gas release during spattering phases was similar for 2014–2017, SO_2 emissions associated with non-spattering intervals began to decrease in 2015, with a marked decrease in the occurrence of non-spattering events in 2016 (Patrick et al., 2018). This suggests changes in the permeability in the upper portions of the lava lake, possibly due to changes in circulation patterns, magma reservoir pressure, and/or magma supply rates. Oppenheimer et al. (2018) showed that the spattering regime releases larger gas bubbles, which may support the observation of more efficient decoupling of gas from the lake during spattering activity.

VALIDATION OF ARRAY EMISSION RATES USING OTHER MEASUREMENT STRATEGIES

Kīlauea has a long history of emission rate measurements (Elias et al., 1998; Elias and Sutton, 2002, 2007, 2012) and the spectrometer array represents the latest technological upgrade. Based on careful analysis of sources of error and comparison with other methods discussed in this paper, we consider emission rates recorded by the array as our best SO_2 estimates for 2014–2017. However, since the array represents a new methodology for measuring emission rates at Kīlauea, the next section presents results of several experiments aimed at validation of this new technique.

Comparison of Array Emission Rates With Helicopter Traverses

We attempted to validate the array-based emission rates by traversing the plume using an upward looking DOAS mounted on a helicopter above the array, and ~3 km further downwind. A range of plausible emission rates were calculated using the spectral retrieval methods as described in section "The Impact of Fit Window," and the mobile DOAS reduction software. The array calculated plume speed was not available during the period of the helicopter traverses, therefore the wind speed

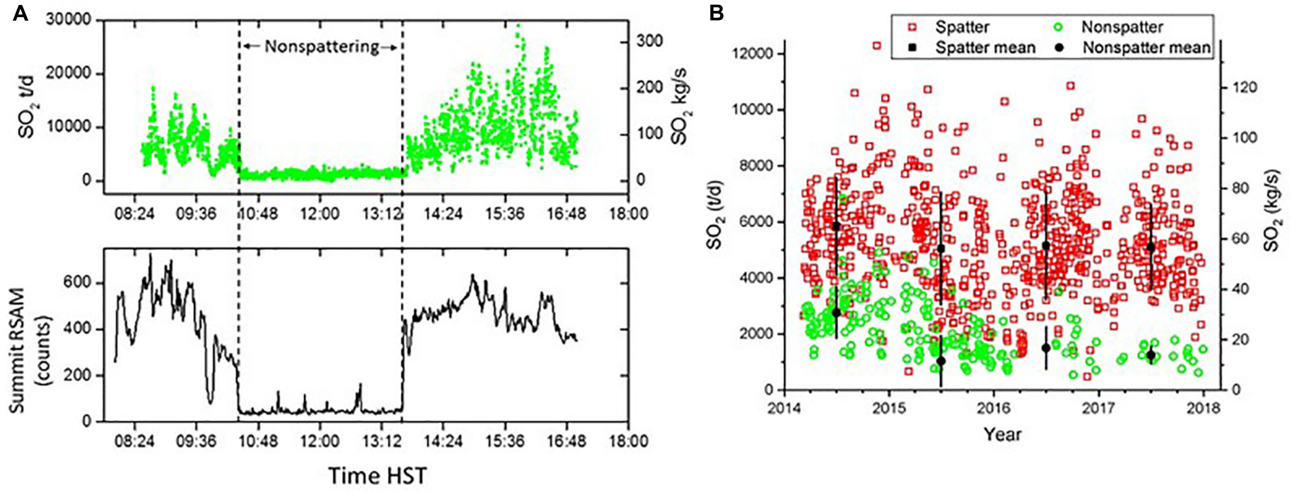

FIGURE 6 | (A) SO_2 emission rates (green) and relative seismic amplitude (RSAM, frequency > 0.2 Hz, black) during a transition between spattering and non-spattering lava lake conditions (marked by dashed lines) at Kīlauea Overlook vent on 9/9/2016. **(B)** Daily average SO_2 emissions for lava lake spattering (red) and non-spattering (green) periods lasting > 1 h for 2014–2017. Non-spattering episodes are defined by RSAM level <100 counts. Annual mean and standard deviation are shown by black symbols for spattering (square) and non-spattering (circle) episodes. The sparser data at the beginning of each year reflects the seasonal nature of the trade winds. A lack of trade winds during the winter months results in fewer measurable plume configurations.

from the 3 m agl SDH anemometer (location in **Figure 2**) was used. The traverse and array data were scaled up using the correction factor detailed in section "Long-Term SO_2 Output." A meteorological station located ~5.5 km downwind of the vent (PKE) measures wind vector at 3 m agl (analogous to the SDH station) and showed that wind speeds near the location of the more distal traverses were less than 10% different than those measured by the SDH sensor near the location of the array.

For this case study, the DOAS helicopter traverse emission rates were higher, on average, than those reported by the array (**Figure 7** and **Table 2**). **Figure 7A** presents the SO_2 column amounts as measured by the helicopter traverse and reveals that the plume maximum fell between adjacent sensors F7 and F9 (odd numbered sensors are adjacent and span the east side of the array), and thus caused the array to miss the plume maximum and underestimate the total emission rate. The range of helicopter values represent minimum and maximum emission rates calculated using the 319–340 nm, SLFB, and DFW retrievals.

This experiment exposes a potential weakness in characterizing an eruption plume using discrete sensors. While the column amount retrievals themselves agree well with other techniques, certain wind directions/plume positions will result in an underestimation of the emission rate. Some of the observed scatter in the array emission rates is likely due to this issue. However, averaged over time, the data provide a reasonable estimate of emission rates since prevailing trade winds generally blow the plume to the more densely instrumented center of the array. Helicopter measurements reduced using a retrieval algorithm equivalent to the array algorithm, return emission rates that significantly overlap the array 10-s values. The 2 techniques differ in measurement time-base, viewing geometry of the instruments, and measured plume transect. The dynamic nature of gas release and uncertainty in the maximum column amount position contribute to general agreement between the traverse and array data, rather than quantitative alignment. A single helicopter traverse performed at the array location on 3/30/2017 yielded an emission rate within 24% of the coincident array measurement.

Comparison of Array Emission Rates With Road Traverses

Before the establishment of the spectrometer array, HVO mainly relied on road-based FLYSPEC and DOAS traverses beneath the summit plume to assess the SO_2 emission rate (Elias et al., 1998; Elias and Sutton, 2002, 2007, 2012). However, road traverses conducted on Crater Rim Drive have been challenging to interpret since 2008, with the onset of the current phase of activity at Kīlauea's summit. Two significant factors, discussed below, are the retrieval of accurate column densities for the optically dense plume, and the measurement of an accurate plume speed. While the road-based data provide useful qualitative information on SO_2 outgassing, they provide only general guidance on the quality of the array's measurements.

Comparison of Different SO_2 Retrievals for Road Traverses

At Kīlauea, Crater Rim Drive is the most accessible road that allows vehicle-based traverses to pass completely below the summit plume during the prevailing trade wind conditions. Its relative proximity to the location of the Overlook vent (<500 m) means that the overhead plume is more concentrated than at the location of the array further downwind. The much higher SO_2 column densities and aerosol optical depths encountered on the road greatly increase the impact of radiative transfer in and around the plume. Therefore, conventional algorithms for

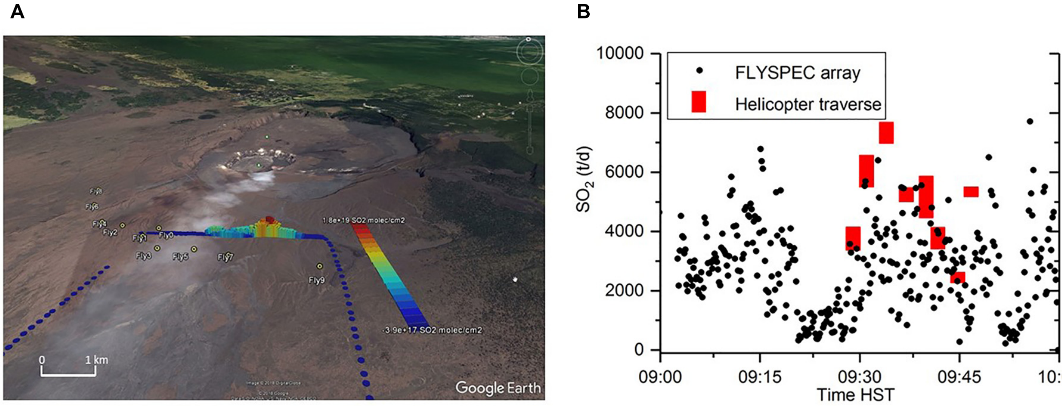

FIGURE 7 | (A) SO_2 column amounts during helicopter traverses measured with an upward-looking DOAS between 09:26 and 09:51 HST on 29 June 2017. The tracks are 3∼ km downwind of the vent and the warmer colors (yellow, orange, red) indicate higher SO_2 column amounts. Note that the plume center is located between array stations F7 and F9, likely contributing to underestimated values by the array as compared to the helicopter traverse.Image ©2018 DigitalGlobe. ©2018 Google. **(B)** Time series of 10-s SO_2 emission rates measured by the spectrometer array (black dots) between 09:00 and 10:00 HST on 29 June 2017. Red bars indicate the range of plausible SO_2 emission rates derived from upward-looking DOAS traverses on a helicopter at the location of the array (first five measurements) and ∼3 km farther downwind (last 3 measurements) using the various spectral retrieval methods described in section "Calculating SO_2 Column Densities From UV-Spectral Data." The plotted times for the 3 downwind measurements were adjusted to account for plume travel time.

retrieving SO_2 column density may give inaccurate results (Kern et al., 2012) and careful treatment of the complexities of light scattering and attenuation is required.

TABLE 2 | Summary of average emission rates obtained from the array and by DOAS helicopter traverses above the array and 3 km downwind of the array between 09:29 and 09:53 Hawai'i Standard Time (HST) on 29 June 2017.

Data source	Average SO_2 emission rate	Standard Deviation
Spectrometer array	2925 t/d	1020 t/d
Heli-traverses (upper limit)	5246 t/d	1581 t/d
Heli-traverses (mean)	4890 t/d	1519 t/d
Heli-traverses (lower limit)	4531 t/d	1478 t/d

The three values reported for the DOAS helicopter traverses correspond to the range of plausible emission rates resulting from the 319–340 nm, SLFB, and DFW retrievals. The standard deviation is representative of the true variability of the emission rate over time, not the errors associated with the measurements.

TABLE 3 | Summary of average emission rates obtained from the array and by DOAS vehicle traverses on Crater Rim Drive between 11:05 and 11:52 HST on 30 March 2017.

Data source	Average SO_2 emission rate	Standard Deviation
Spectrometer array	2721 t/d	1201 t/d
Road traverses (upper limit)	4695 t/d	3213 t/d
Road traverses (mean)	3754 t/d	2299 t/d
Road traverses (lower limit)	2813 t/d	1448 t/d

The three values reported for the DOAS traverses correspond to the range of plausible emission rates resulting from the various spectral retrieval methods discussed in the section "Comparison of Different SO_2 Retrievals for Road Traverses," with the minimum and maximum values retrieved using the 319–340 nm fit window and SRT DOAS, respectively. The standard deviation is representative of the true variability of the emission rate over time, not the errors associated with the measurements.

To obtain an estimate of the uncertainty we may expect in SO_2 column density measurements from Crater Rim Drive, we examined results of ten upward-looking Mobile DOAS traverses on 30 March 2017 using a variety of spectral analysis methods. In addition to applying all the DOAS retrievals used for comparison of the DFW technique at the location of the array (see section "The Impact of Fit Window" and **Figure 3**), we also analyzed the traverse data in the very extended wavelength fit window at 360–390 nm, as first suggested by Bobrowski et al. (2010) since SO_2 column densities greater than 2,500 ppmm are frequently encountered (see section "Long UV Wavelength SO_2 Fit Window").

We also implemented a DFW retrieval analogous to that used to analyze the FLYSPEC array and applied this to the mobile DOAS spectra. **Figure 8** shows how the results from various DOAS retrievals compare to those of the DFW method applied to the mobile DOAS data. Note that this plot encompasses column densities of up to 25,000 ppmm, a factor of 5 higher than the column densities measured at the location of the array. The road traverse column density comparison mirrors the general trend of the array column density comparison (section "The Impact of Fit Window").

As expected, the conventional DOAS analysis in the 310–325 nm wavelength range returns significantly lower SO_2 column densities than all other methods once column amounts exceed around 1000 ppmm. The very strong absorption of SO_2 in this wavelength range causes complex radiative transfer effects at higher column amounts (Kern et al., 2012), that are not well captured by this simple approach. Therefore, this retrieval method is not considered further in our comparison.

The 319–340 nm window, SLFB, and DFW all return similar results, though for very low column amounts the signal-to-noise of the 319–340 nm retrieval is inferior to that of the other two approaches. For column densities above 2,500 ppmm, the DOAS

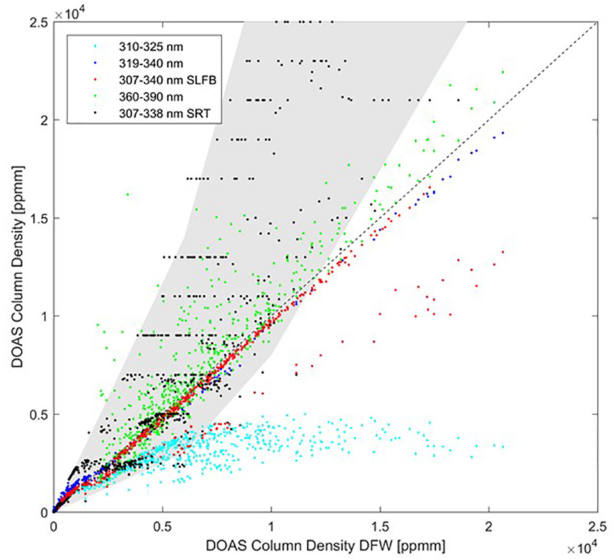

FIGURE 8 | SO_2 column densities obtained from ten road traverse measurements on Crater Rim Drive on 03 March 2017 between 10:50 and 11:55 HST. Column densities were evaluated with 6 different retrieval methods. In this plot, all column densities are plotted against the results obtained using a Dual Fit Window (DFW) approach that is equivalent to the spectral analysis procedure used to evaluate FLYSPEC mobile or upward looking array data.

fit in the 360–390 nm wavelength region returns slightly higher (about 20%) SO_2 columns than the DFW method, with more observed scatter.

Finally, the more complex SRT method returns a range of SO_2 column densities (gray shaded region) that overlaps with the DFW results up to about 5,000 ppmm, but then returns column densities that are up to a factor of 2 higher. The horizontal spread in the SRT data apparent in the plot is caused by variability in the retrieved plume aerosol optical depth (AOD). In the SRT retrieval, an estimate of the AOD is derived together with the SO_2 column density (Kern et al., 2012). In this case, however, the retrieval returned a relatively large uncertainty for the AOD, which causes a relatively large uncertainty for the SO_2 column density (hence the wide range of reported values in the gray area). In the vertical direction, the discrete values for SO_2 column density (i.e., horizontal lines) are artifacts that stem from the limited resolution of the SRT lookup table.

It is challenging to ascertain which of the applied retrievals generally yields the most accurate results overall, since each has advantages and disadvantages. The 319–340 nm, SLFB and DFW methods are all similar in that they include areas of the spectrum where the SO_2 absorption is weaker than in the standard DOAS 310–325 nm window. In this manner, they avoid issues related to non-linear instrument sensitivity caused by strong SO_2 absorption, but they do not account for potential changes of the effective light path in and around the volcanic plume due to scattering on aerosols, which as noted, can be significant. The SRT-DOAS retrieval does account for complex radiative transfer, but it relies on the accuracy of assumptions used to generate precomputed lookup tables which are then compared to the measurement spectra (see **Table 1**). For a limited case study such as presented here, these assumptions should be quite good, but short-term variability in atmospheric and plume conditions may still compromise the results. While SRT-DOAS provides insight into the potential magnitude of the errors, it is much more difficult to use this technique for routine monitoring.

Regardless of which method is most accurate in this scenario, the comparison shows that there is a much larger uncertainty associated with the column density retrieval for the large SO_2 abundances encountered on Crater Rim Drive than for the more dilute plume at the location of the array, 3 km downwind (compare **Figure 3**). For the traverse case study, the retrieved column amounts from the various analysis methods range between about −30 to +100% of the DFW results as compared to −6 to +22% of the DFW results derived at the location of the array.

Comparison of Plume Speed Measurements for Analyzing Road Traverses

As discussed in section "Determining Plume Speed," plume speed is a direct multiplier for deriving emission rate, and traditionally represents the largest overall uncertainty in SO_2 flux measurements. HVO has several sources available for measuring plume speed in proximity to the Overlook vent. Plume speed can be taken from SO_2 camera imagery, or the wind speed recorded by a ground-based anemometer can be used (section "Anemometers").

To examine the uncertainty of our plume speed assumptions for the traverse measurements, we compared wind data from 3 days on which we have anemometer data, SO_2 camera images, and coincident traverse measurements on Crater Rim Drive. On all 3 days, the traverse measurements were used to determine the wind direction, which then feeds into the determination of plume speed from the SO_2 camera imagery. The wind speed comparisons for the individual days are shown in **Figures 9A–C**.

On all 3 days, the average wind speeds obtained from the OBS and NPT anemometers were within 12% of one another, while the SO_2 camera plume speed was systematically higher. The camera plume speeds also appear to be more variable than those reported by the anemometers; however, this is an artifact of different averaging methods for the anemometers (internal averaging over the 10–15-min interval) and the camera (discrete 10-s measurements averaged over the period of a single 3–5-min traverse.

The absolute difference between SO_2 camera plume speed and anemometer wind speed appears to grow with increasing wind speeds. This is consistent with the expected vertical wind profile for plume speeds measured by the camera at 50–200 m agl. This discrepancy is expected to increase for larger wind speeds, and a power law is often used to describe the increasing horizontal mean wind speeds with altitude (also see section "Determining Plume Speed"). A reasonable agreement can be achieved between the anemometer and SO_2 camera plume speeds by correcting the anemometer wind data, as is shown in **Figure 10**.

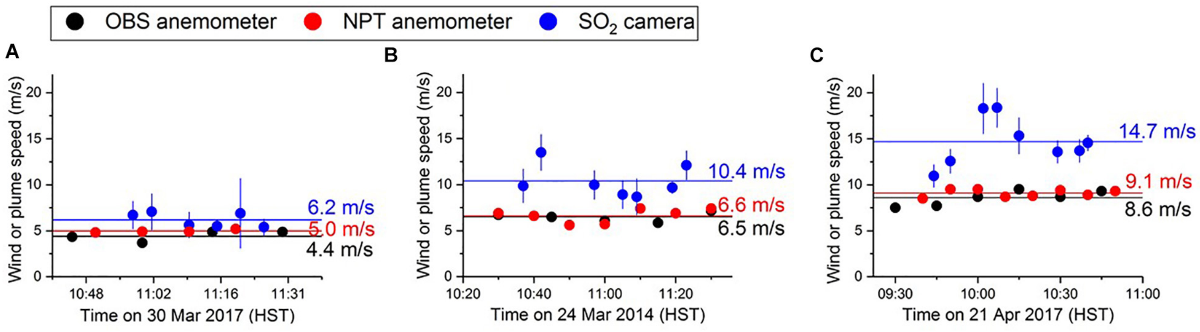

FIGURE 9 | (A–C) Comparison of wind speeds derived from SO_2 camera with wind speeds from meteorological stations OBS (10 m agl on rim of caldera) and NPT (3 m agl on floor of caldera; **Figure 2**) on three different days. Anemometer wind speeds are averaged over the intervals at which they are plotted. The SO_2 camera wind speed was derived and plotted at times only coincident with DOAS vehicle traverse measurements performed on Crater Rim Drive.

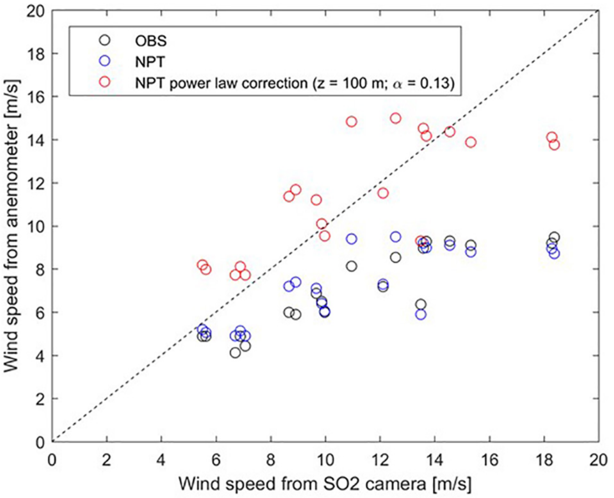

FIGURE 10 | Comparison of wind speeds derived from the SO_2 camera (horizontal axis) with wind speeds from anemometers at HVO and NPT. Data are from March 24, 2014, April 21, 2014, and March 30, 2017. Anemometer data is interpolated to timing of SO_2 camera measurements. The wind speed calculated with SO_2 camera data plot systematically higher than the anemometer data, with differences increasing for larger wind speeds. Applying a power law correction to the NPT data (red circles) brings them into the same range as the camera wind speeds.

Such a correction is extremely sensitive to the chosen model parameters (in this case the exponent), which depends on the surface roughness, a complex parameter and one that is especially difficult to estimate for the anemometer perched on the rim of the caldera. Applying a power law correction of the form v(z) = v(3m) *(z/3m)^α with z = 100m and α = 0.13 to the 3 m agl NPT wind speeds, brings them into the same range as the camera plume speeds, which were generally derived for a plume about 100 m above ground level. The α used here lies between values that characterize conditions over open water (0.11) and open land surfaces (0.143).

We also note that none of the measurement techniques, including the SO_2 camera, measure plume speed at the exact location of Crater Rim Drive where the traverse measurements are made. Prior to 2008, gas emissions were characterized by a low ground-hugging plume which was predominantly influenced by wind speed. However, since the onset of the summit eruption, the plume buoyancy, rise rate, and horizontal speed are affected by both the local wind and lava lake conditions, which are extremely dynamic (Patrick et al., 2018). Therefore, it is not straightforward to correct the anemometer data to obtain accurate plume speeds for use in calculating emission rates from the road traverses. Instead, we interpret the discrepancy between our various methods of plume speed determination as an indicator of our measurement uncertainty. Based on the results obtained in the 3-day case study shown here, we expect that our wind measurements are within 30–40% of the true plume speed.

Comparison of Road Traverse and Array Emission Rates

We have shown that errors associated with obtaining accurate column densities and plume speed contribute to significant uncertainties in measuring SO_2 emission rates by vehicle traverse on Crater Rim Drive under 2014–2017 degassing conditions. Here, we present examples of coincident traverse and array measurements to characterize the range of values that can arise with the noted uncertainties.

Figure 11 shows the time series of SO_2 emission rates obtained from the spectrometer array (black dots) and by coincident mobile DOAS traverses (red bars) on Crater Rim Drive on March 30, 2017. The red bars indicate the range of values calculated for the DOAS traverses from the various SO_2 spectral retrieval methods discussed in section "Comparison of Different SO_2 Retrievals for Road Traverses." The traverse measurements are shifted by +7 min to account for the time it took the plume to travel the 2.5 km from Crater Rim Drive to the array. The array values were calculated using the cross-correlation method for determining plume speed, and the traverses were analyzed assuming a plume speed of 4.4 m/s. This corresponds to the average wind speed measured by the OBS anemometer during the measurement interval, and based on the case study for this day, is assumed to be accurate within about 30–40%. The OBS station (**Figure 2**) wind speed value has historically been used to calculate road-based emission rates.

On the day presented here, the DOAS traverse and array emission rates agree broadly, with some notable outliers, which may be related to plume heterogeneities. As the plume emitted from the Overlook vent drifts downwind, it is mixed with background air by turbulent diffusion. This process reduces spatial gradients in SO_2 concentration. Road traverses might pass directly under clouds of concentrated volcanic gas, then pass between such clouds in the next measurement. By the time the plume reaches the array, concentrated gas clouds are diluted, and gaps between such features have been at least partially filled in by gas from surrounding clouds. Therefore, the array will measure a more homogeneous plume. Road traverse results that are higher than array results may also be due to plume maxima falling between array sensors, yielding underestimation of emission rates by the array (see section "Errors Due to Location of Plume SO_2 Maximum Between Array Sensors").

The road traverse results on this day show atypical agreement with the array data (**Figure 11** and **Table 3**). In general, the long-term road data record underestimates the emissions as compared to the array – on average, by about 60%. We attribute this to a combination of underestimated plume speeds and underreporting of column amounts due to radiative transfer issues. There may be a maximum threshold for the column amounts measured close to the vent, and thus, consistent under-reporting of emission rates calculated for Crater Rim Drive road traverses.

Figure 12 presents a general comparison of FLYSPEC array and road traverse daily average emission rates from 2014 to 2017 separated into spattering and non-spattering lava lake conditions. A non-spattering lake condition is defined by relative seismic amplitude (RSAM) < 100 counts (see section "SO_2 Short-Term Variability Reflects Lava Lake Dynamics"). The traverse data were collected and analyzed using a mobile FLYSPEC and DFW algorithm, or mobile DOAS and extended fit-window (319–340 nm); each traverse took 3–5 min to collect. These data show that on average, the road-based method returns emission rates that are about 60% less than those calculated from the FLYSPEC array for both the spattering and non-pattering cases. While the non-spattering lava lake condition produces a more translucent and gas-poor plume (Patrick et al., 2018), and errors due to radiative transfer effects should have less impact on calculated column densities, the data for both lava lake conditions are not significantly different. Maximum column densities for the non-spattering condition are still greater than 2500 ppmm, so the less opaque plume associated with more quiescent lake conditions can still cause significant errors in retrieved column amounts due to scattering effects. Although on average the road traverse data significantly underestimates emission rates as compared to the FLYSPEC array, as shown in the specific examples in this study, cases of parity, and even traverse values greater than array values do occur. This supports the general observation that the multiple uncertainties impacting the summit road-based data set are difficult to resolve.

Comparison of Array Emission Rates With Space-Based SO_2 Measurements

The array emission rates agree well with OMI space based SO_2 measurements. For 2014–2017, Kīlauea released an average of 5100 t/d, or 1.9 ± 0.1 Tg/yr according to array DFW results. This is consistent with Carn et al. (2017) who calculate a daily average of 5518 t/d for Kīlauea for the same period (Carn, 2018, pers. comm., 1 october).

CONCLUSION AND FUTURE WORK

Long-lasting eruptions at the summit and East Rift Zone of Kīlauea Volcano have provided a testing ground for novel gas measurement techniques. Traditional SO_2 UV spectroscopy measurements via road traverses, performed 10 km downwind of the East Rift Zone eruption accurately measure the generally low emissions from this area. However, the dense volcanic plume produced by the summit lava lake was challenging to quantify using traditional traverse or scanning measurements. Summit emissions during the reported period were best measured using an array of 10 upward looking UV spectrometers (FLYSPECs) spanning the width of the plume $\sim$3 km downwind of the vent. The FLYSPEC array provides 10-s SO_2 emission rate data during daylight hours and prevailing trade wind conditions. To validate these novel measurements, we examined both column density values and calculated emission rates from the array. For column densities, we compared a variety of retrieval techniques with the array's dual fit window (305–315 and 319.5–330 nm) approach. Comparing fits from (1) conventional DOAS 310–325 nm window, (2) 319–340 nm extended wavelength window, (3) 307–340 nm sliding lower bound (SLFB) window, and (4) Simulated Radiative Transfer DOAS treatment, we found the various methods returned column densities from -6 to $+22\%$ of the array values. We consider these results to confirm the validity of the FLYSPEC dual fit window treatment.

To confirm the emission rate values, we investigated the wind and plume speed measurements used to calculate emission rates. We found 3 m agl wind speeds adjacent to the array to be 22% less on average than plume speeds measured with 2 spectrometers located along the plume axis. Thus, the SO_2 summit emission rates calculated using the ground-based wind speeds have been adjusted to account for this discrepancy.

Comparing array measurements with helicopter-traverses performed 3 and 6 km downwind of the vent show broad agreement with coincident array measurements with some notable outliers. Helicopter traverse measurements analyzed using a comparable fit window were within $+24$ and $+55\%$ of the array measurements. This discrepancy reflects the underestimation by the array due to the plume maxima being positioned between sensors, as well as the dynamic nature of the plume, differences in time base, viewing angle, and uncertainty of the wind speed for the downwind plume.

Our 1-day detailed case study comparing emission rates from the FLYSPEC array and road traverses shows reasonable agreement (**Figure 11**). However, the accuracy of the road-based measurements is severely limited by the large discrepancy

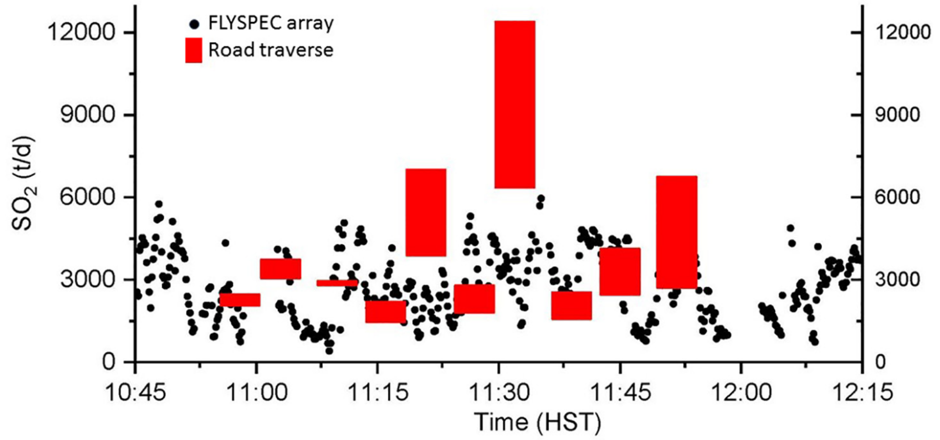

FIGURE 11 | Comparison of SO_2 emission rates from the FLYSPEC array (black dots) and the road- traverses (red bars) on March 30, 2017. The red bars indicate the range of values obtained from the various analysis methods described in section "Comparison of Different SO_2 Retrievals for Road Traverses." A constant wind speed of 4.4 m/s was assumed in analyzing the traverse data, which corresponds to the average wind speed measured by the OBS anemometer during the measurement period.

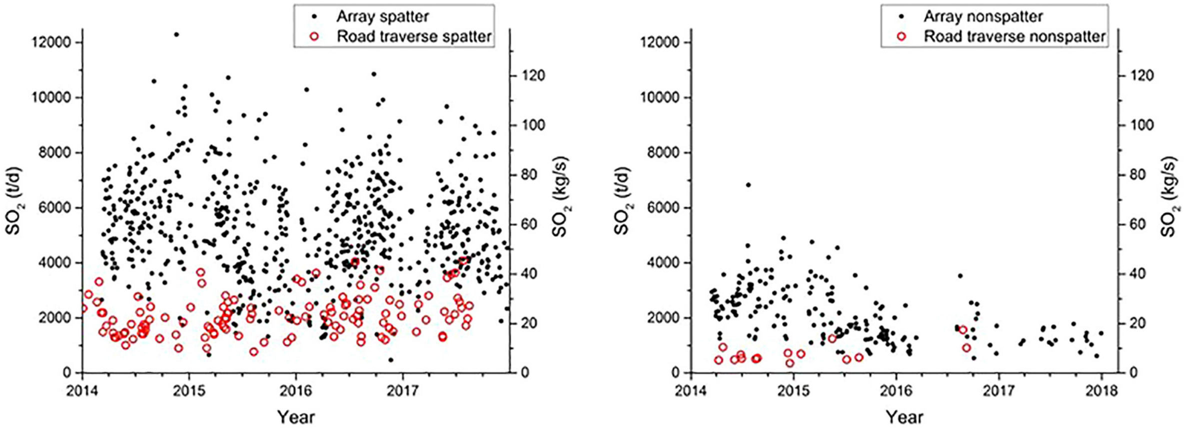

FIGURE 12 | Emission rates from FLYSPEC array (black dots) and road traverses (red circles) separated into spattering **(Left)** and non-spattering **(Right)** lava lake conditions. On average, the road-based method returns emission rates that are about 60% less than those calculated from the FLYSPEC array for both lava lake conditions. Non-spattering episodes are defined by RSAM level < 100 counts.

found between results from different spectral retrieval methods (−30 to +100%, **Figure 8**). Looking at a longer time series comparison of emission rates shows that the road traverse results differ from the array emission rate values, on average, by a factor of ∼2.5 when using similar retrieval methods for both analyses. The multiple errors for the road-traverse data due to radiative transfer, plume geometry, and wind speed uncertainties create challenging measurement conditions which are difficult to address. The use of SRT-DOAS retrievals can help address the radiative transfer effects for the road data, but the dynamic nature and variable geometry of the plume as well as varying meteorological conditions during the 2014–2017 period creates challenges in the practical application of SRT-DOAS. We surmise that the accuracy of the road-data is insufficient to quantitatively validate the array emission rates for the period in question.

Agreement between SO_2 emissions measured from space by OMI and the FLYSPEC array for 2014–2017 are exceptionally good. Daily SO_2 values for the two datasets are 5518 t/d and 5100 t/d, respectively. The discrepancy of < 10% between the techniques suggests that space-based emission rates calculated using the new OMI planetary boundary layer SO_2 column dataset is a good option for tracking emission rates during periods of vigorous outgassing at Kīlauea.

Technical issues contribute to uncertainties in the array SO_2 measurements which could be considered for the future. These include improvements in plume speed calculation, calibration spectra, computer time synchronization, real-time emission rate filters, and spatial resolution of plume features as discussed below.

Plume speed: plume speeds are generated every 1.5 min, or ground based wind speed reported every 10 min, while 1-s column densities are used to calculate 10 s emission rates. The short-term variability in plume motion may not be captured by this treatment. Calibration spectra: we show that column densities retrieved with the array DFW are consistent with conventional and novel fit window comparisons; however, the reference and cell calibration spectra used for these fits could more accurately represent the conditions during sample spectra collection. Since the array is generally in the volcanic plume, there are limited opportunities to collect new calibration spectra for use in analyzing sample spectra. Exploring the use of synthetic reference spectra or use of the conventional modeled DOAS approach could be considered. Time synchronization: accurate and reliable emission rates, and importantly, plume speed calculations, depend on the synchronization of the 10 computer clocks. A robust algorithm for *in situ* clock checks is critical for accurate emission rate calculations. Emission rate filters: with the large number of instruments and high rate of data collection, spurious data points can occur due to time of day/sun angle and spectrometer inconsistencies. More refined real-time data could be achieved through improved emission rate filtering algorithms. Plume features: spatial resolution could be improved by incorporating scanning spectrometers with $\leq 45°$ scan angle. While this would provide more plume structure detail and could help avoid missing major plume features passing between stations, it would significantly increase the complexity and cost of the system.

The FLYSPEC array approach may be useful for other volcano observatories requiring high time resolution emission rate measurements. Advantages of the approach include straightforward measurements due to the simple upward looking geometry. The system is particularly useful in locations with a prevailing plume direction coupled with low altitude, inaccessible, or optically dense plumes. Depending on plume column densities, the array can be located at a distance downwind to minimize errors due to light scattering but provide sufficient signal for accurate retrievals. The dual window approach allows flexibility in retrieving variable column amounts accurately and thus can accommodate changes in eruptive activity and outgassing vigor. Disadvantages include the expense and challenge of maintaining multiple field spectrometer systems, the need for robust telemetry, and reduced spatial resolution as compared to scanning systems.

AUTHOR CONTRIBUTIONS

TE collected, analyzed, and interpreted data, contributed to development of FLYSPEC array hardware and software, prepared manuscript. CK collected, analyzed, and interpreted data, co-wrote manuscript. KH and HG developed FLYSPEC array system, analyzed data, contributed to manuscript. AS collected and analyzed data, contributed to development of FLYSPEC array hardware and software.

ACKNOWLEDGMENTS

Past and current HVO Volunteers Mike Cappos, Gail Ferguson, Howard Hoshide, Isabelle Taylor, Anne Fulton, Tracee Fukunaga, Mary Barr, Jennifer Lennon, and Lora Beatty are deeply thanked for assistance in field data collection and analysis. Thanks to Matt Patrick and Russell Atkinson for programming help, and Matt Patrick for valuable discussion. The Institute of Advanced Studies and the Durham COFUND fellowship scheme (funded by Durham University, United Kingdom, and the European Union) are thanked for providing the opportunity for this manuscript to come to fruition. Authors would also like to acknowledge that this work is conducted inside Hawai‘i Volcanoes National Park with permission from the National Park Service. Any use of trade, firm, or product names is for descriptive purposes only and does not imply endorsement by the U.S. Government.

SUPPLEMENTARY MATERIAL

The Supplementary Material for this article can be found online at: https://www.frontiersin.org/articles/10.3389/feart.2018.00214/full#supplementary-material

REFERENCES

Aiuppa, A., Federico, C., Giudice, G., Gurrieri, S., Liuzzo, M., Shinohara, H., et al. (2006). Rates of carbon dioxide plume degassing from Mount Etna volcano. *J. Geophys. Res.* 111:B09207. doi: 10.1029/2006JB004307

Andres, R., Kyle, P. R., Stokes, J. B., and Rose, W. I. (1989). SO_2 from episode 48A eruption, Hawaii: sulfur dioxide emissions from the episode 48A East Rift Zone eruption of Kilauea volcano, Hawaii. *Bull. Volcanol.* 52, 113–117. doi: 10.1007/BF00301550

Beirle, S., Horman, C., Penning de Vries, M., Dorner, S., Kern, C., and Wagner, T. (2013). Estimating the volcanic emission rate and atmospheric lifetime of SO_2 from space: a case study for Kīlauea Volcano, Hawai‘i. *Atmos. Chem. Phys. Discuss.* 13:28631. doi: 10.5194/acpd-13-28695-2013

Beirle, S., Hörmann, C., Penning de Vries, M., Dörner, S., Kern, C., and Wagner, T. (2014). Estimating the volcanic emission rate and atmospheric lifetime of SO_2 from space: a case study for Kilauea volcano, Hawai‘i. *Atmos. Chem. Phys.* 14, 8309–8322. doi: 10.5194/acp-14-8309-2014

Bluth, G. J. S., Shannon, J. M., Watson, M., Prata, A. J., and Realmuto, V. J. (2007). Development of an ultra-violet digital camera for volcanic SO_2 imaging. *J. Volcanol. Geothermal Res.* 161, 47–56. doi: 10.1016/j.jvolgeores.2006.11.004

Bobrowski, N., Kern, C., Platt, U., Hörmann, C., and Wagner, T. (2010). Novel SO_2 spectral evaluation scheme using the 360–390 nm wavelength range. *Atmos. Meas. Tech.* 3, 879–891. doi: 10.5194/amt-3-879-2010

Bogumil, K., Orphal, J., Homann, T., Voigt, S., Spietz, P., Fleischmann, O. C., et al. (2003). Measurements of molecular absorption spectra with the SCIAMACHY pre-flight model: instrument characterization and reference data for atmospheric remote-sensing in the 230–2380 nm region. *J. Photochem. Photobiol. A Chem.* 157, 167–184. doi: 10.1016/S1010-6030(03)00062-5

Businger, S., Huff, R., Pattantyus, A., and Horton, K. (2015). Observing and forecasting Vog dispersion from Kīlauea volcano, Hawaii. *Bull. Am. Meteorol. Soc.* 96, 1667–1686. doi: 10.1175/BAMS-D-14-00150.1

Carlsen, H. K., Hauksdottir, A., Valdimarsdottir, U. A., Gíslason, T., Einarsdottir, G., Runolfsson, H., et al. (2012). Health effects following the Eyjafjallajökull volcanic eruption: a cohort study. *BMJ Open* 2:e001851. doi: 10.1136/bmjopen-2012-001851

Carn, S. A., Fioletov, V. E., McLinden, C. A., Li, C., and Krotkov, N. A. (2017). A decade of global volcanic SO_2 emissions measured from space. *Sci. Rep.* 7:44095. doi: 10.1038/srep44095

Casadevall, T. J., Stokes, J. B., Greenland, L. P., Malinconico, L. L., Casadevall, J. R., and Furukawa, B. T. (1987). "SO_2 and CO_2 emission rates at Kilauea Volcano, 1979–1984," in *Volcanism in Hawaii: U.S. Geological Survey Professional Paper 1350*, Vol. 1, Chap. 29, eds R. W. Decker, T. L. Wright, and P. H. Stauffer, 771–780. Available at: https://pubs.usgs.gov/pp/1987/1350/

Chartier, T. A., Rose, W. I., and Stokes, J. B. (1988). Detailed record of SO_2 emissions from Pu'u ‘O‘o between episodes 33 and 34 of the 1983–86 ERZ eruption, Kilauea, Hawaii. *Bull. Volcanol.* 50, 215–228. doi: 10.1007/BF01047485

Cronin, S. J., and Sharp, D. S. (2002). Environmental impacts on health from continuous volcanic activity at Yasur (Tanna) and Ambrym, Vanuatu. *Int. J. Environ. Health Res.* 12, 109–123. doi: 10.1080/09603120220129274

de Moor, J. M., Aiuppa, A., Pacheco, J., Avard, G., Kern, C., Liuzzo, M., et al. (2016). Short-period volcanic gas precursors to phreatic eruptions: insights from Poás Volcano, Costa Rica. *Earth Planet. Sci. Lett.* 442, 218–227. doi: 10.1016/j.epsl.2016.1002.1056

Delmelle, P., Stix, J., Baxter, P. J., Garcia-Alvarez, J., and Barquero, J. (2002). Atmospheric dispersion, environmental effects and potential health hazard associated with the low-altitude gas plume of Masaya volcano, Nicaragua. *Bull. Volcanol.* 64, 423–434. doi: 10.1007/s00445-002-0221-6

Edmonds, M., Herd, R. A., Galle, B., and Oppenheimer, C. M. (2003). Automated, high time-resolution measurements of SO_2 flux at Sourfriére Hills Volcano, Montserrat. *Bull. Volcanol.* 65, 578–586. doi: 10.1007/s00445-003-0286-x

Eguchi, K., Uno, I., Yumimoto, K., Takemura, T., Nakajima, T. Y., Uematsu, M., et al. (2011). Modulation of cloud droplets and radiation over the North Pacific by sulfate aerosol erupted from Mount Kilauea. *Sola* 7, 77–80. doi: 10.2151/sola.2011-020

Elias, T., Kern, C., Horton, K. A., Garbeil, H., and Sutton, A. J. (2018). *SO_2 Emission Rates from Kilauea Volcano, Hawaii (2014-2017)*. Washington, DC: U.S. Geological Survey data Release, doi: 10.5066/F7794402

Elias, T., and Sutton, A. J. (2002). *Sulfur Dioxide Emission Rates of Kīlauea Volcano, Hawai‘i, an Update: 1998–2001. U.S. Geological Survey Open-File Report* 02–460, 29. Available at: https://pubs.usgs.gov/of/2002/of02-460/

Elias, T., and Sutton, A. J. (2007). *Sulfur Dioxide Emission Rates from Kīlauea Volcano, Hawai‘i, an Update: 2002–2006. U.S. Geological Survey Open-File Report 2007–1114, Version 1.0*, 37. Available at: https://pubs.usgs.gov/of/2007/1114/

Elias, T., and Sutton, A. J. (2012). *Sulfur Dioxide Emission Rates from Kīlauea Volcano, Hawai‘i, 2007–2010. U.S. Geological Survey Open-File Report* 2012–1107, 25. Available at: https://pubs.usgs.gov/of/2012/1107/

Elias, T., and Sutton, A. J. (2017). *Volcanic Air Pollution Hazards in Hawaii. U.S. Geological Survey Fact Sheet* 2017–3017. Available at: https://pubs.er.usgs.gov/publication/fs20173017

Elias, T., Sutton, A. J., Oppenheimer, C., Horton, K. A., Garbeil, H., Tsanev, V., et al. (2006). Comparison of COSPEC and two miniature ultraviolet spectrometer systems for SO_2 measurements using scattered sunlight. *Bull. Volcanol.* 68, 313–322. doi: 10.1007/s00445-005-0026-5

Elias, T., Sutton, A. J., Stokes, J. B., and Casadevall, T. J. (1998). *Sulfur Dioxide Emission Rates of Kīlauea Volcano, Hawai‘i, 1979–1997. U.S. Geological Survey Open-File Report 98–462*. Available at: http://pubs.usgs.gov/of/1998/of98-462/

Fickel, M., and Delgado Granados, H. (2017). On the use of different spectral windows in DOAS evaluations: effects on the estimation of SO_2 emission rate and mixing ratios during strong emission of Popocatépetl volcano. *Chem. Geol.* 462, 67–73. doi: 10.1016/j.chemgeo.2017.05.001

Galle, B., Johansson, M., Rivera, C., Zhang, Y., Kihlman, M., Kern, C., et al. (2010). Network for observation of volcanic and atmospheric change (NOVAC): a global network for volcanic gas monitoring: network layout and instrument description. *J. Geophys. Res.* 115:D05304. doi: 10.1029/2009JD011823

Galle, B., Oppenheimer, C., Geyer, A., McGonigle, A. J. S., Edmonds, M., and Horrocks, L. (2003). A miniaturized ultraviolet spectrometer for remote sensing of SO_2 fluxes: a new tool for volcano surveillance. *J. Volcanol. Geothermal Res.* 119, 241–254. doi: 10.1016/S0377-0273(02)00356-6

Gerlach, T. M., McGee, K. A., Sutton, A. J., and Elias, T. (1998). Rates of volcanic CO_2 degassing from airborne determinations of SO_2 emission rates and plume CO_2/SO_2: test study at Pu'u 'O'o cone, Kilauea volcano, Hawaii. *Geophys. Res. Lett.* 25, 2675–2678. doi: 10.1029/98GL02030

Gliß, J., Stebel, K., Kylling, A., and Sudbø, A. (2018). Improved optical flow velocity analysis in SO_2 camera images of volcanic plumes – implications for emission-rate retrievals investigated at Mt Etna, Italy and Guallatiri, Chile. *Atmos. Meas. Tech.* 11, 781–801. doi: 10.5194/amt-11-781-2018

Global Volcanism Program (2014). "Report on Kilauea (United States)," in *Bulletin of the Global Volcanism Network*, Vol. 39, ed. R. Wunderman (Washington, DC: Smithsonian Institution), 12. doi: 10.5479/si.GVP.BGVN201412-332010

Grainger, J. F., and Ring, J. (1962). A photoelectric grating spectrometer. *Mon. Not. R. Astron. Soc.* 125, 93–104. doi: 10.1093/mnras/125.2.93

Halliday, T. J., Lynham, J., and de Paula, A. (2018). VOG: using volcanic eruptions to estimate the health costs of particulates. *Econ. J.* doi: 10.1111/ecoj.12609

Halmer, M. M., Schmincke, H.-U., and Graf, H.-F. (2002). The annual volcanic gas input into the atmosphere, in particular into the stratosphere: a global data set for the past 100 years. *J. Volcanol. Geothermal Res.* 115, 511–528. doi: 10.1016/S0377-0273(01)00318-3

Horton, K. A., Garbeil, H., Sutton, A. J., Elias, T., and Businger, S. (2012). "Early monitoring results from the Halema‘uma‘u vog measurement and prediction FLYSPEC array," in *Proceedings of the Conferences on Extended Abstracts, AGU Chapman Hawaiian Volcanoes: From Source to Surface*, (Waikoloa, HI: American Geophysical Union).

Horton, K. A., Williams-Jones, G., Garbeil, H., Elias, T., Sutton, A. J., Mouginis-Mark, P., et al. (2006). Real-time measurement of volcanic SO_2 emissions: validation of a new UV correlation spectrometer (FLYSPEC). *Bull. Volcanol.* 68, 323–327. doi: 10.1007/s00445-005-0014-9

Kern, C., Deutschmann, T., Werner, C., Sutton, A. J., Elia, T., and Kelly, P. J. (2012). Improving the accuracy of SO_2 column densities and emission rates obtained from upward-looking UV-spectroscopic measurements of volcanic plumes by taking realistic radiative transfer into account. *J. Geophys. Res.* 117:D20302. doi: 10.1029/2012JD017936

Kern, C., Kick, F., Lübcke, P., Vogel, L., Wöhrbach, M., and Platt, U. (2010). Theoretical description of functionality, applications, and limitations of SO_2 cameras for the remote sensing of volcanic plumes. *Atmos. Meas. Tech.* 3, 733–749. doi: 10.5194/amt-3-733-2010

Kern, C., Sutton, J., Elias, T., Lee, L., Kamibayashi, K., Antolik, L., et al. (2015). An automated SO_2 camera system for continuous, real-time monitoring of gas emissions from Kīlauea Volcano's summit Overlook Crater. *J. Volcanol. Geothermal Res.* 300, 81–94. doi: 10.1016/j.jvolgeores.2014.12.004

Kern, C., Werner, C., Elias, T., Sutton, A. J., and Lubcke, P. (2013). Applying UV cameras for SO_2 detection to distant or optically thick volcanic plumes. *J. Volcanol. Geothermal Res.* 262, 80–89. doi: 10.1016/j.jvolgeores.2013.06.009

Klein, A., Lübcke, P., Bobrowski, N., Kuhn, J., and Platt, U. (2017). Plume propagation direction determination with SO_2 cameras. *Atmos. Meas. Tech.* 10, 979–987. doi: 10.5194/amt-10-979-2017

Mather, T. A., Pyle, D. M., Tsanev, V. I., McGonigle, A. J. S., Oppenheimer, C., and Allen, A. G. (2006). A reassessment of current volcanic emissions from the Central American arc with specific examples from Nicaragua. *J. Volcanol. Geothermal Res.* 149, 297–311. doi: 10.1016/j.jvolgeores.2005.07.021

Millan, M. M. (1980). Remote sensing of air pollutants. A study of some atmospheric scattering effects. *Atmos. Environ.* 14, 1241–1253. doi: 10.1016/0004-6981(80)90226-7

Millán, M. M., and Chung, Y. S. (1977). Detection of a plume 400 km from the source. *Atmos. Environ.* 11, 939–944. doi: 10.1016/j.jconhyd.2010.09.009

Moffat, A. J., and Millan, M. M. (1971). The application of optical correlation techniques to the remote sensing of SO_2 plumes using skylight. *Atmos. Environ.* 5, 677–690. doi: 10.1016/0004-6981(71)90125-9

Moré, J. (1978). "The levenberg-marquardt algorithm: implementation and theory," in *Numerical Analysis*, Vol. 630, ed. G. A. Watson (Berlin: Springer-Verlag).

Mori, T., Hirabayashi, J., Kazahaya, K., Mori, T., Ohwada, M., Miyashita, M., et al. (2007). A Compact Ultraviolet Spectrometer System (COMPUSS) for monitoring volcanic SO_2 emission: validation and preliminary observation. *Bull. Volcanol. Soc. Jan.* 52, 105–112.

Mori, T., Mori, T., Kazahaya, K., Ohwada, M., Hirabayashi, J., and Yoshikawa, S. (2006). Effect of UV scattering on SO_2 emission rate measurements. *Geophys. Res. Lett.* 33:L17315. doi: 10.1029/2006GL026285

Nadeau, P. A., Werner, C. A., Waite, G. P., Carn, S. A., Brewer, D., Elias, T., et al. (2015). Using SO_2 camera imagery and seismicity to examine degassing and gas accumulation at Kīlauea Volcano, May 2010. *J. Volcanol. Geothermal Res.* 300, 70–80. doi: 10.1016/j.jvolgeores.2014.12.005

Oppenheimer, C., Scaillet, B., Woods, A., Sutton, A. J., Elias, T., and Moussallam, Y. (2018). Influence of eruptive style on volcanic gas emission chemistry and temperature. *Nat. Geosci.* 11, 678–681. doi: 10.1038/s41561-018-0194-5

Patrick, M., Orr, T., Sutton, J. A., Elias, T., and Swanson, D. (2013). *The First Five Years of Kīlauea's Summit Eruption in Halema'uma'u Crater, 2008–2013: U.S. Geological Survey Fact Sheet* 2013–3116. Available at: https://pubs.er.usgs.gov/publication/fs20133116

Patrick, M. R., Orr, T., Sutton, A. J., and Lev, E. (2016a). Shallow and deep controls on lava lake surface motion at Kīlauea Volcano. *J. Volcanol. Geothermal Res.* 328, 247–261. doi: 10.1016/j.jvolgeores.2016.11.010

Patrick, M. R., Orr, T., Sutton, A. J., Lev, E., Thelen, W., and Fee, D. (2016b). Shallowly driven fluctuations in lava lake outgassing, Kīlauea Volcano, Hawai'i. *Earth Planet. Sci. Lett.* 433, 326–338. doi: 10.1016/j.epsl.2015.10.052

Patrick, M. R., Orr, T., Swanson, D., Elias, T., and Shiro, B. (2018). *Lava Lake Activity at the Summit of Kīlauea Volcano in 2016: U.S. Geological Survey Scientific Investigations Report* 2018–5008, 58. Available at: https://pubs.er.usgs.gov/publication/sir20185008

Perner, D., and Platt, U. (1979). Detection of nitrous acid in the atmosphere by differential optical absorption. *Geophys. Res. Lett.* 7, 1053–1056. doi: 10.1029/GL007i012p01053

Peters, N., Hoffmann, A., Barnie, T., Herzoga, M., and Oppenheimer, C. (2015). Use of motion estimation algorithms for improved flux measurements using SO_2 cameras. *J. Volcanol. Geothermal Res.* 300, 58–69. doi: 10.1016/j.jvolgeores.2014.08.031

Platt, U. (1994). "Differential optical absorption spectroscopy (DOAS)," in *Air Monitoring by Spectroscopic Techniques Chemical Analysis Series*, Vol. 127, ed. M. W. Sigrist (Hoboken, NJ: Wiley), 27–84.

Platt, U., and Stutz, J. (2008). *Differential Optical Absorption Spectroscopy - Principles and Applications*. Berlin: Springer. doi: 10.1007/978-3-540-75776-4

Robock, A. (2000). Volcanic eruptions and climate. *Rev. Geophys.* 38, 191–219. doi: 10.1029/1998RG000054

Stoiber, R. E., Malinconico, L. L., and Williams, S. N. (1983). "Use of the correlation spectrometer at volcanoes," in *Forecasting Volcanic Events*, eds H. Tazieff and J. C. Sabroux (Amsterdam: Elsevier), 424–444.

Sutton, A. J., and Elias, T. (2014). "One hundred volatile years of volcanic gas studies at the Hawaiian Volcano Observatory," in *U.S. Geological Survey Professional Paper* 1801, (Reston, VA: USGS).

Sutton, A. J., Elias, T., Gerlach, T. M., and Stokes, J. B. (2001). Implications for eruptive processes as indicated by sulfur dioxide emissions from Kilauea Volcano, Hawai'i, 1979-1997. *J. Volcanol. Geothermal Res.* 108, 283–302. doi: 10.1016/S0377-0273(00)00291-2

Symonds, R. B., Rose, W. I., Bluth, G. J. S., and Gerlach, T. M. (1994). "Volcanic-gas studies: methods, results, and applications," in *Volatiles in Magmas*, eds M. R. Carroll and J. R. Hollaway (Chantilly, VA: Mineralogical Society of America), 1–66.

Tam, E., Miike, R., Labrenz, S., Sutton, A. J., Elias, T., Davis, J., et al. (2016). Volcanic air pollution over the Island of Hawai'i; emissions, dispersal, and composition. Association with respiratory symptoms and lung function in Hawai'i Island school children. *Environ. Int.* 92–93, 543–552. doi: 10.1016/j.envint.2016.03.025

Uno, Eguchi, K., and Yumimoto, K. (2013). "Eruption of Mt. Kilauea impacted cloud droplet and radiation budget over North Pacific," in *Western Pacific Air-Sea Interaction Study*, eds M. Uematsu, Y. Yokouchi, Y. W. Watanabe, S. Takeda, and Y. Yamanaka (Tokyo: TERRAPUB), 83–87.

van Manen, S. (2014). Perception of a chronic volcanic hazard: persistent degassing at Masaya volcano, Nicaragua. *J. Appl. Volcanol.* 3:1. doi: 10.1186/s13617-014-0009-3

Vandaele, A. C., Hermans, C., and Fally, S. (2009). Fourier transform measurements of SO_2 absorption cross sections: II. Temperature dependence in the 29 000–44 000 cm-1 (227–345 nm) region. *J. Quant. Spectrosc. Radiat. Transf.* 110, 2115–2126. doi: 10.1016/j.jqsrt.2009.05.006

Wilson, D., Elias, T., Orr, T., Patrick, M., Sutton, J., and Swanson, D. (2008). Small explosion from new vent at Kilauea's summit. *Eos Trans. Am. Geophys. Union* 89:203. doi: 10.1029/2008EO220003

Williams-Jones, G., Horton, K. A., Elias, T., Garbeil, H., Mouginis-Mark, P., Sutton, A. J., et al. (2006). Accurately measuring volcanic plume velocity with multiple UV spectrometers. *Bull. Volcanol.* 68, 328–332. doi: 10.1007/s00445-005-0013-x

Conflict of Interest Statement: KH does business as FLYSPEC, Inc., and sells spectrometer systems.

The remaining authors declare that the research was conducted in the absence of any commercial or financial relationships that could be construed as a potential conflict of interest.

frontiers in Earth Science

ORIGINAL RESEARCH
published: 11 January 2019
doi: 10.3389/feart.2018.00247

Insights Into the Mechanisms of Phreatic Eruptions From Continuous High Frequency Volcanic Gas Monitoring: Rincón de la Vieja Volcano, Costa Rica

Angelo Battaglia [1]*, ***J. Maarten de Moor*** [2], ***Alessandro Aiuppa*** [1], ***Geoffroy Avard*** [2], ***Henriette Bakkar*** [3], ***Marcello Bitetto*** [1], ***M. M. Mora Fernández*** [4,5], ***Peter Kelly*** [6], ***Gaetano Giudice*** [7], ***Dario Delle Donne*** [1] ***and Hairo Villalobos*** [2]

[1] Dipartimento DiSTeM, Università di Palermo, Palermo, Italy, [2] Observatorio Vulcanológico y Sismológico de Costa Rica, Universidad Nacional, Heredia, Costa Rica, [3] ICE, Sabana Norte, San José, Costa Rica, [4] Escuela Centroamericana de Geología, Universidad de Costa Rica, San José, Costa Rica, [5] Red Sismológica Nacional (RSN: UCR-ICE), Universidad de Costa Rica, San José, Costa Rica, [6] United States Geological Survey, Cascades Volcano Observatory, Vancouver, DC, United States, [7] Sezione di Palermo, Istituto Nazionale di Geofisica e Vulcanologia, Palermo, Italy

OPEN ACCESS

Edited by:
Jacob B. Lowenstern,
Volcano Disaster Assistance Program (USGS), United States

Reviewed by:
Hiroshi Shinohara,
Geological Survey of Japan (AIST), Japan
Paul Wallace,
University of Oregon, United States

***Correspondence:**
Angelo Battaglia
angelo.battaglia03@unipa.it

Specialty section:
This article was submitted to Volcanology, a section of the journal Frontiers in Earth Science

Received: *26 June 2018*
Accepted: *18 December 2018*
Published: *11 January 2019*

Citation:
Battaglia A, de Moor JM, Aiuppa A, Avard G, Bakkar H, Bitetto M, Mora Fernández MM, Kelly P, Giudice G, Delle Donne D and Villalobos H (2019) Insights Into the Mechanisms of Phreatic Eruptions From Continuous High Frequency Volcanic Gas Monitoring: Rincón de la Vieja Volcano, Costa Rica. Front. Earth Sci. 6:247. doi: 10.3389/feart.2018.00247

Understanding the trigger mechanisms of phreatic eruptions is key to mitigating the effects of these hazardous but poorly forecastable volcanic events. It has recently been established that high-rate volcanic gas observations are potentially very suitable to identifying the source processes driving phreatic eruptions, and to eventually detecting precursory changes prior to individual phreatic blasts. In February-May 2017, we deployed a Multi-GAS instrument to continuously monitor gas concentrations in the crater lake plume of Rincón de la Vieja, a remote and poorly monitored active volcano in Costa Rica, site of frequent phreatic/phreatomagmatic eruptions. Forty-two phreatic/phreatomagmatic eruptions were seismically recorded during our investigated period, 9 of which were also recorded for gas by the Multi-GAS. To the best of our knowledge, these represent the first instrumentally measured gas compositions during individual phreatic/phreatomagmatic explosions at an active volcano. Our results show that during background quiescent degassing the Rincón de la Vieja crater lake plume was characterized by high CO_2/SO_2 ratios of 64 ± 59 and H_2S/SO_2 ratios of 0.57 ± 0.20. This composition is interpreted as reflecting hydrothermal (re)processing of magma-sourced gas in the sub-limnic environment. Phreatic blasts were recorded by the Multi-GAS as brief (1–2 min long) pulses of elevated gas mixing ratios (up to ~52 ppmv SO_2 and >3,000 ppmv CO_2), or more than an order of magnitude higher than during background degassing (~1 ppmv SO_2 and ~450 ppmv CO_2). During the phreatic eruption(s), the H_2S/SO_2 ratio was systematically lower (<0.18) than during background degassing, but the CO_2/SO_2 ratio remained high (and variable), ranging from 37 to 390. These S-poor compositions for the eruptive gas imply extensive processing of the source magmatic gas during pre-eruptive hydrothermal storage, likely by deposition of native S and/or sulfate. Our gas results are thus overall consistent with a mechanism of phreatic eruptions triggered by accumulation of magmatic-hydrothermal gases beneath a hydrothermal seal. We claim that real-time Multi-GAS monitoring is urgently needed at other crater lake-hosting volcanoes (e.g., Ruapehu, Aso), where phreatic eruptions may similarly be preceded by phases of reduced S degassing at the surface.

Keywords: volcanic gases, crater lakes, Rincón de la Vieja, phreatic eruption, Multi-GAS, Costa Rica

INTRODUCTION

Phreatic eruptions are among the most unpredictable and hazardous volcanic phenomena (Mastin and Witter, 2000; Browne and Lawless, 2001). These blasts involve the violent, explosive discharge of pressurized pockets of external (non-volcanic, mostly meteoric) water, and are therefore particularly common at "wet" volcanoes whose summits are topped by crater lakes (Rouwet and Morrissey, 2015; Stix and de Moor, 2018). In addition to the large availability of exogenous water, active crater lakes are especially prone to developing phreatic eruptions owing to the presence of a persistent heat source (conductive/convective heating from shallow magma, and/or rising magmatic volatiles), and the frequent formation of permeability barriers at the lake bottom (e.g., impermeable layers of precipitated native sulfur or alteration minerals) that favor gas accumulation (Christenson et al., 2010; Christenson and Tassi, 2015; Delmelle and Bernard, 2015, and references cited therein). The exact mechanisms driving crater lake breaching eruptions are still not entirely understood, and the respective roles of the magmatic and sublimnic hydrothermal systems in triggering the eruptions are still a matter of debate (Takano et al., 1994; Christenson and Tassi, 2015; Rouwet and Morrissey, 2015).

Phreatic eruptions have typically occurred in the past without being preceded by any obvious precursor, as recently dramatically demonstrated by the deadly Ontake (in 2014, Oikawa et al., 2016) and Kusatsu-Shirane (in 2018) eruptions in Japan. The recent technical advances in real-time observation of lake plume gas compositions (Di Napoli et al., 2013; Shinohara et al., 2015; Tamburello et al., 2015; de Moor et al., 2016a; Gunawan et al., 2016) bring a new perspective on eruption forecasting. Using measurements from a permanently installed "lake" Multi-GAS (Multi-component Gas Analyser System; Aiuppa et al., 2006, 2010; Aiuppa, 2015), de Moor et al. (2016a) identified for the first time systematic short-term (days to weeks) variations in plume gas compositions prior to individual phreatic explosions at Laguna Caliente crater lake, Poás volcano (Costa Rica). These observations indicated an increase of magmatic volatiles input prior to individual phreatic blasts, which demonstrates the potential of high-frequency real-time gas monitoring.

Here, we report on the results of 3 months of instrumental monitoring of volcanic gas composition at Rincón de la Vieja volcano (10.49 N, 85.19 W), in the Costa Rican segment of the Central American volcanic arc (CAVA). Rincón de la Vieja is one of the most active and remote volcanoes in Costa Rica (Barquero and Segura, 1983; Alvarado et al., 1992), and hosts a highly acidic crater lake (Tassi et al., 2005, 2009), the source of recurrent phreatomagmatic to phreatic eruptions (Boudon et al., 1996). The intense ($SO_2 > 60$ tons/day; de Moor et al., 2017) gas emissions have only occasionally been studied in the past (Tassi et al., 2005, 2009; Aiuppa et al., 2014; de Moor et al., 2017), due to the limited accessibility of the volcano summit. Our study here provides the first near-continuous gas dataset taken during a period of recurrent phreatic activity at Rincon de la Vieja, including the first measurement of the syn-explosive gas phase. The aim is to use our novel gas observations to derive new insights into the mechanisms driving crater lake phreatic explosions and assess the potential for forecasting eruptions at Rincón de la Vieja.

RINCÓN DE LA VIEJA VOLCANO

Rincón de la Vieja volcano is part of the Guanacaste volcanic range (**Figure 1**), a Quaternary magmatic range related to subduction of the Cocos plate underneath the Caribbean plate (Carr, 1984; Carr et al., 1990; DeMets, 2001; DeMets et al., 2010). The Guanacaste volcanic range consists of four andesitic central edifices (Orosí-Cacao, Rincón de la Vieja-Santa María, Miravalles, and Tenorio-Montezuma). Before construction of the Quaternary andesitic chain, intense explosive silicic volcanism generated a series of collapse events and associated calderas (Molina et al., 2014). The Rincón de la Vieja-Santa María volcanic complex (maximum elevation 1,916 m) was constructed within one of these calderas, the 120 km^2 Cañas Dulces Caldera (Molina and Martí, 2016). The Cañas Dulce caldera hosts several hydrothermal fields (Giggenbach and Correales, 1992), including several thermal manifestations on the Rincón de la Vieja massif itself (Tassi et al., 2005), aligned along a NW-SE trend running roughly parallel to the volcano's axis.

Rincón de la Vieja (10.49 N, 85.19 W) is the only currently active andesitic stratovolcano in the Guanacaste Cordillera. The volume of the massif is estimated at 130 km^3 (Carr, 1984). The most recent magmatic eruption (with significant juvenile component) took place ∼3,500 years B.P. (Alvarado et al., 1992). This eruption left the dacitic Rio Blanco tephra deposit (volume, 0.25 km^3), which also includes a small fraction ($<3\%$) of andesitic scoria and pumice indicating a mixed magma reservoir (Kempter, 1997). The historically active crater has produced frequent phreatic to phreatomagmatic eruptions since 1851 (Boudon et al., 1996). Major eruptions in the mid-1990s caused large lahars and significant damage to local communities. The 1995, 1991, 1983, 1967, 1966, and 1922 eruptions expelled part of the crater lake, producing acidic lahars (Barquero and Segura, 1983; OVSICORI, 1995; Kempter, 1997; Kempter and Rowe, 2000), mostly breaching through the topographically lower northern crater rim.

FIGURE 1 | Structural and volcanological setting of the Costa Rica segment of the Central American Volcanic Arc (CAVA). Modified from Brandes et al. (2007). Map data: Google, Landsat/Copernicus image, SIO, NOAA, U.S. Navy, NGA, GEBCO.

Rincón de la Vieja is monitored by Observatorio Vulcanológico y Sismológico de Costa Rica-Universidad Nacional (OVSICORI-UNA) and the Instituto Costaricense de Electricidad (ICE). Volcano monitoring is complicated by remote location and extreme field conditions (high rainfall, frequent fog and extremely windy). The active crater today hosts a large hyper-acidic lake (pH = 0.7–1 and T = 26–30°C in February-March 2017) (**Figure 2**), characterized by vigorous degassing and continuous overturning (Tassi et al., 2005, 2009; de Moor et al., 2017). Dark-gray spherules of colloidal sulfur are widespread on the lake's surface (**Figure 2**), while fumarolic emissions up to 130°C are observed on the inner crater walls (Tassi et al., 2005; Aiuppa et al., 2014).

Phreatic/phreatomagmatic activity resumed in September 2011, after 13 years of quiescence. During 2012–2013, Rincón de la Vieja exhibited low seismicity and very infrequent eruptions. From September 2014, eruptive activity escalated to an average of 25 phreatic-phreatomagmatic events per month, peaking in October 2015 and March 2016 when 43 and 220 eruptions were recorded, respectively. Visual binocular microscope observations (made by G. Avard at OVSICORI-UNA, following the procedure described in Alvarado et al., 2016) revealed that erupted ash fragments (250–500 μm portion) contain well-preserved greenish minerals and a small portion (∼5%) of fresh-looking glassy and vesicular shards. These observations were interpreted as indicative of the involvement of shallow magma in 2015–2016, as is the case at many volcanoes with phreatic eruptions (e.g., Stix and de Moor, 2018). Native sulfur fragments were also systematically observed in the erupted products of 2015–2017, especially in the 1–2 mm ash grain-size fraction (G. Avard, pers. comm.). Sulfur-rich minerals were also repeatedly observed as veins and fillings in fractures of large ejecta and blocks dispersed throughout the crater. The frequency and seismic energy of eruptions increased in early 2017. During our gas monitoring interval (February 3–May 9, 2017) 42 seismic signals associated to phreatic/phreatomagmatic eruptions were recognized, and 9 of these eruptions were also identified geochemically (**Table 1**; see below). Some of these 9 eruptions (eruptions 1–3 and 9; **Figure 3**) were preceded by a long period (LP) seismic signal several seconds before the explosion. In almost all cases (eruptions 1, 3, 4–7), pulses of spasmodic tremor occurred a few hours before the eruption. Two major phreatic/phreatomagmatic eruptions (generating hot lahars that traveled outside the crater to the north) took place on May 23 and on June 11 (Global Volcanism Program, 2017), just a few weeks after our Multi-GAS stopped acquiring. The explosion on June 11 generated a 1–2 km high plume, and ejected coarse materials to the W and NW onto the upper N flank. This event, the largest (based on seismic energy) registered during 2011–2018, was preceded by a LP swarm 2 h before the explosion. Material collected from the May 23 lahar down the river contained only ∼1% juvenile component, but fragments erupted from the June 11 eruption (also collected from a lahar) contained ∼44% juvenile material (OVSICORI-UNA). Phreatic activity has intermittently continued until the time of writing (late 2018).

MATERIALS AND METHODS

The gas dataset we report on in this study was recorded using two distinct fully autonomous Multi-GAS instruments, one

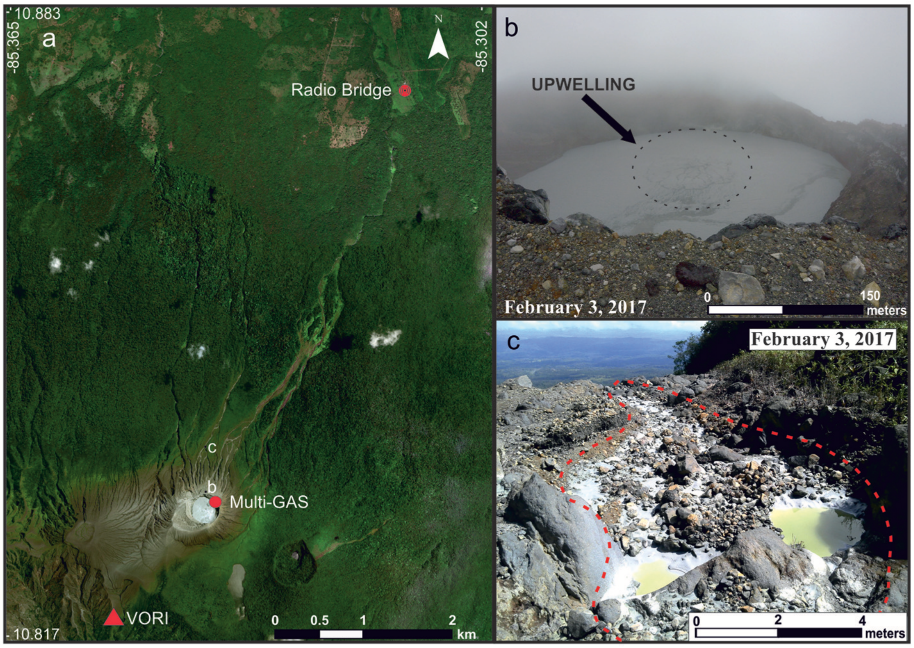

FIGURE 2 | (a) Satellite image of Rincón de la Vieja volcano showing location of the Multi-GAS measurement site, the VORI seismic station, and the Radio Bridge, map data: Google, Landsat/Copernicus image, SIO, NOAA, U.S. Navy, NGA, GEBCO; **(b)** The Rincón de la Vieja active crater, with convection cells and abundant gray sulfur spherules floating on the lake surface; **(c)** Water and sulfur deposits in a canyon on the northern slope of Rincón de la Vieja.

designed by the Instituto Nazionale di Geofisica e Vulcanologia (INGV) and one designed by the U.S. Geological Survey (USGS). The two instruments (INGV and USGS-campaign) operated sequentially at the same site, located on the northern inner wall of the active crater ~1 m downwind the lake shore (Lat. 10.8327 Long. −85.3355; see **Figure 2**). This site was selected because its position ensured regular fumigation by the lake gas plume, while minimizing any potential gas contribution from low-temperature crater fumaroles (not observed at the measurement site during our study). The Multi-GAS instruments were powered by an external (12 V, 40 Ah) battery and 3 solar panels in order to ensure proper operation in all climatic conditions. A PVC tube with two filters served as gas inlet, and allowed gas to be pumped (at 1.2 L/m) inside the Multi-GAS instruments. The first (INGV-type) Multi-GAS was installed on February 3, 2017 and operated until March 17, 2017, when it was dismantled (for use at a different volcano) and replaced by a second (USGS-campaign type; Gunawan et al., 2016) Multi-GAS. This latter operated until May 09, 2017, when it stopped transmitting data before being finally destroyed during the May 23 lahar-producing phreatic blast (Global Volcanism Program, 2017).

The two Multi-GAS instruments used very similar sensor kits (see below) and were re-calibrated at OVSICORI with the same standard gases before the installation, showing very similar response. The INGV-type Multi-GAS was recalibrated after returning from the field (in late March 2017), and the original calibration was reproduced within sensor precision. Both Multi-GAS instruments measured SO_2 and H_2S mixing ratios (precision within ± 15% at 2σ; Lewicki et al., 2017) with the same specific electrochemical sensors (models TD2G-1A and TC4E-1A, respectively; all from City Technology and with ± 5% repeatability). Interference of SO_2 gas on the H_2S sensor (15 %) was determined during calibration procedure and corrected with the Ratiocalc software. CO_2 mixing ratios were measured using an on-board spectrometer (INGV-type: Gascard EDI030102NG, measurement range = 0–3,000 ppmv, precision, ± 3% at 2σ; USGS-type LI-COR LI-840A, measurement range = 0–5,000 ppmv, precision, ± 1.5% at 2σ). The INGV-type Multi-GAS instrument, controlled by an arduino2 datalogger, acquired data at 0.1 Hz rate during 4 sampling periods per day, of 30 min duration each. In the USGS-type Multi-GAS, all data acquisition and scheduling was controlled by a Campbell Scientific data logger (CR1000 with NL115 module) outfitted with 2 GB of onboard memory. The station completed four data acquisition cycles per day, in which data were acquired for 1 h at a 1 Hz rate. Before and after each measurement cycle, the station performed sensor baseline checks by activating two miniature 3-way teflon solenoid valves (Cole-Parmer WU-01540-11) that formed a closed-loop and recirculated trapped sample gases through soda lime and desiccant for 3 min to remove acid gases and water vapor in order to provide a measure of within-run baseline drift and to clean and dry the instrument prior to shutting down. For both Multi-GAS instruments, data were telemetered (at the end of each acquisition cycle) via radio modem (Xetawave) to OVSICORI using a radio bridge installed on the northern base of the volcano (**Figure 2**). The acquired gas mixing ratios data were post-processed using the Ratiocalc software (Tamburello,

TABLE 1 | Time (in GMT), duration (in s), and associated energy (in J) of the phreatic-phreatomagmatic eruptions occurring during February-May 2017.

Date	Time eruption (GMT)	Duration (s)	Seismic energy (J)	Multi-GAS peak time (GMT)	Eruption number
05/02/2017	7:47:50	42	18.42		
07/02/2017	12:53:06	52	56.03		
07/02/2017	18:19:29	72	28.67		
08/02/2017	22:44:32	61	48.58		
09/02/2017	17:49:41	51	7.74		
13/02/2017	2:59:04	16	9.16		
13/02/2017	9:16:49	138	9.69	9:12:06 - 9:16:35	1
14/02/2017	17:47:42	62	5.96		
16/02/2017	7:12:50	112	42.73		
16/02/2017	13:27:24	173	20.07		
19/02/2017	1:56:00	88	12.86		
19/02/2017	5:49:24	198	7.38		
20/02/2017	15:22:06	106	17.43	15:23:04	2
23/02/2017	3:34:16	94	7.80	03:34:50	3
25/02/2017	12:56:36	106	8.42		
26/02/2017	5:30:48	175	16.94		
27/02/2017	n/a	n/a	n/a	03:16:20	4
02/03/2017	21:24:35	n/a	n/a	21:25:56 – 21:26:50	5
11/03/2017	22:49:17	342	18.88		
14/03/2017	20:53:19	155	8.69		
18/03/2017	23:34:14	272	50.12		
20/03/2017	n/a	n/a	n/a	06:16:00	6
20/03/2017	19:03:50	227	73.83		
26/03/2017	10:11:07	174	18.73		
26/03/2017	10:28:39	115	54.56		
26/03/2017	10:55:42	88	52.67		
26/03/2017	15:49:39	124	80.15		
27/03/2017	10:15:39	70	26.25		
29/03/2017	9:31:17	253	23.58		
31/03/2017	12:46:49	n/a	40.95		
31/03/2017	14:10:50	n/a	38.31		
04/04/2017	14:48:20	122	24.00		
04/04/2017	15:03:49	90	128.66		
06/04/2017	7:48:06	606	103.30		
12/04/2017	17:46:18	175	48.14	17:53:00	7
19/04/2017	0:38:16	200	234.62		
19/04/2017	1:49:19	195	89.22		
20/04/2017	00:02:00	n/a	n/a	00:05:00	8
23/04/2017	5:12:41	111	9.74		
25/04/2017	6:18:40	114	11.47	06:21:00	9
28/04/2017	1:26:16	381	46.28		
09/05/2017	14:59:47	312	24.02		

*Nine of these eruptions were also recorded by the Multi-GAS (the "Multi-GAS peak Time" identifies the temporal window of Multi-GAS over which the syn-explosive gas was detected). The nine eruptions are numbered as in **Figure 3**.*

2015) to derive gas ratios between volatile couples (CO_2/SO_2 and H_2S/SO_2) using linear regression. In order to derive accurate gas ratios, the different response time (∼2–4 s) between the spectroscopic sensor and the electrochemical sensors was corrected for during data processing with the Ratiocalc software. No pressure correction was applied to the electrochemical sensors owing to very similar altitude between calibration site (Heredia, ∼1,200 m) and Rincon's summit (∼1,500 m). Based on laboratory tests with standard gases, errors in the derived ratios are typically ≤15%. Unfortunately, the plume was condensing at all conditions encountered during observations, so it was not possible to determine a robust volcanic H_2O signal.

Seismic activity was characterized using the reference station VORI, operated by the Observatorio Sismológico y Vulcanológico de Arenal y Miravalles (OSIVAM) of the Instituto Costarricense de Electricidad (ICE). This station is located 1.8 km

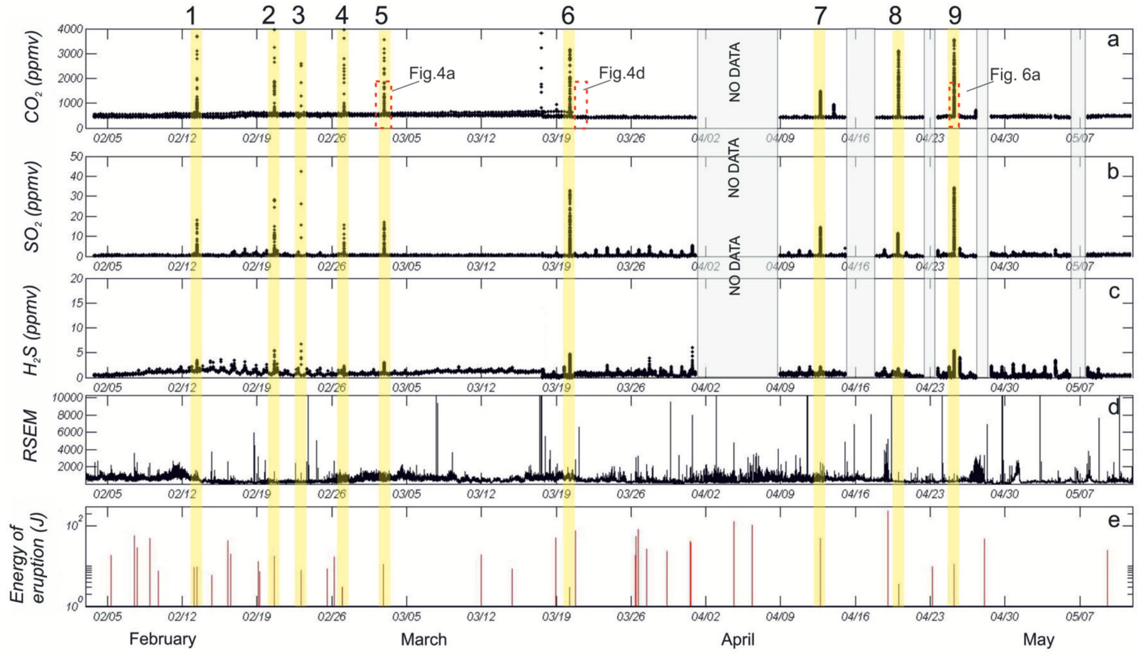

FIGURE 3 | Time-series of **(a–c)** gas mixing ratios (in ppmv); **(d)** RSEM, **(e)** eruptive energy. Note that Multi-GAS data (CO_2, SO_2, and H_2S mixing ratios) are not continuous but obtained during 4 daily cycles, each 30–60 min long. The shaded yellow bands identify the 9 explosions (numbered #1 to #9) during which the Multi-GAS was operating, allowing the *syn-explosive* gas composition to be determined. The five light gray areas identify all periods with no MultiGAS data. The small red insets in the CO_2 plot identify the expanded portions shown in **Figures 4**, **6**.

SW of the active crater, and is equipped with a digital 3-component broadband TRIMBLE REFTEK 151B sensor with flat response from 0.016 (60 s) to 50 Hz. Signals were sampled at 100 Hz. Close inspection of seismic records was carried out to extract discrete events and, in the particular case of eruptive signals, to estimate the associated seismic energy ($E_{seismic}$). Seismic energy was calculated using the relation for bodywaves generated by an isotropic source at the top of a homogeneous half space (Boatwright, 1980; Arámbula-Mendoza et al., 2011):

$$E_{seismic} = 2\pi r^2 \rho_{earth} c_{earth} \frac{1}{A} \int S^2 U(t)^2 dt \qquad (1)$$

where r is the distance from the source to the seismic station, ρ is rock density, c is the P wave velocity, S is the site effect, U is seismic amplitude and A is attenuation. We used $r = 1{,}800$ m, $c = 1{,}500$ m/s, $\rho = 2{,}600$ kg/m^3. The site and attenuation effects were neglected for simplicity.

The temporal evolution of seismic activity was explored using Real-time Seismic Energy Measurement, or RSEM (De la Cruz-Reyna and Reyes-Davila, 2001), which considers the square of the amplitude (directly related to seismic energy). The seismic signal was filtered in the band of 1–10 Hz in order to avoid strong ambient noise present in the records.

RESULTS

Figure 3 is a temporal record of CO_2, SO_2, and H_2S concentrations measured by the two Multi-GAS instruments. The RSEM time-series is shown in **Figure 3d** for comparison, along with **Figure 3e** the timing of each of the seismically-identified phreatic explosions.

The temporal plots exhibit a sequence of gas peaks (numbered #1 to #9 in **Figure 3**) that clearly emerge above a persistent background (characterized by low concentration of all gases). By comparison with seismic data (**Figures 3d,e**, **4a**), we find that each of the gas peaks corresponds to a Multi-GAS recording of a phreatic explosion, i.e., the peaks are records of the composition of the gas released during a phreatic blast (referred as *syn-explosive gas*). CO_2 and SO_2 (**Figures 3a,b**, **4a**) exhibit the most pronounced peaks in the *syn-explosive gas*, with peak concentrations of >3,000 ppmv and ~52 ppmv, respectively. H_2S peaks are more moderate (typically < 5 ppmv).

Nine (**Figure 3**) of the 42 phreatic events that occurred during February 3-May 9, 2017 are captured by our Multi-GAS record (the remaining explosions took place outside the four daily Multi-GAS acquisition cycles). The background gas mixing ratios thus correspond to continuous passive degassing between the explosions, in what we refer to as the *quiescent gas*. The *quiescent gas* is typically characterized by low SO_2 and H_2S mixing ratios (<2 ppmv), and CO_2 (<500 ppmv) slightly above atmospheric background values.

As in other recent work (Aiuppa et al., 2017, 2018; de Moor et al., 2017), the Multi-GAS-derived gas mixing ratios data are post-processed to calculate the ratios between the various volatiles using the procedure of Tamburello (2015).

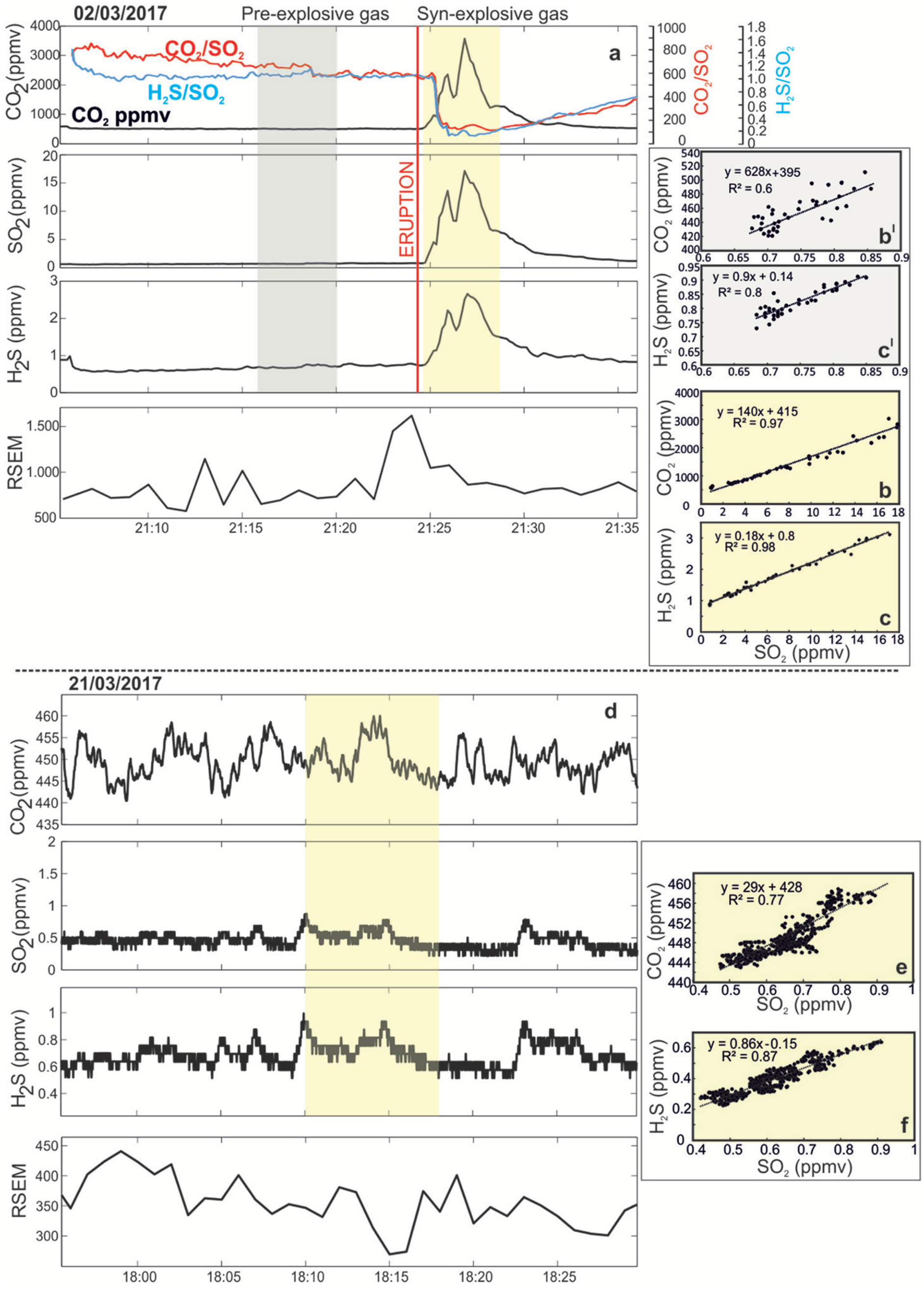

FIGURE 4 | (a) Detail of gas and seismic records taken on March 02, 2017 between ~21:05 and ~21:35 GMT. The eruption (event #5 in **Figure 3**, see inset) occurred at ~21:24 GMT. Mixing ratios increase after the blast, starting at ~21:24 GMT. The yellow-colored area corresponds to the sub-interval (identified with Ratiocalc) where CO_2, SO_2, and H_2S are positively correlated at statistically significant level ($R^2 > 0.6$). These subsets of CO_2, SO_2, and H_2S mixing ratios are used to draw **(b)** CO_2 vs. SO_2 and **(c)** H_2S vs. SO_2 correlation plots, and to calculate the time-averaged CO_2/SO_2 and H_2S/SO_2 ratios (within the yellow-colored temporal windows) from the slopes of the best-fit regression lines (listed in **Table 2**). In **(a)** the red and blue lines are high-resolution (1 Hz) records of CO_2/SO_2 and H_2S/SO_2 ratios, respectively, calculated by taking the ratio of individual couples of co-acquired mixing ratios. This point-to-point ratios (e.g., Pering et al., 2014) have large (~ 50 %) associated errors at the ppm level [e.g., before the explosion, **(a)**], so they should only be viewed as semi-quantitative estimates. Nevertheless, the contrasting gas signatures for *pre-explosive* and *syn-explosive gas* are clearly observed. Example of CO_2 vs. SO_2 and H_2S vs. SO_2 correlation plots for the *pre-explosive gas* [built from data within the gray-colored temporal windows in **(a)**], shown in **(b')** and **(c')**, confirm a very CO_2-rich (or SO_2-poor) gas composition prior to the blast. Gas ratios progressively return to the pre-eruptive levels toward the end of the Multi-GAS acquisition. **(d)** Example of gas and seismic records taken during a quiescent phase (March 21, 2017 between ~17:55 and ~18:30 GMT). Very low gas mixing ratios are observed throughout, as characteristic of the *quiescent gas*. The yellow-colored area corresponds to the only sub-interval (identified with Ratiocalc) where CO_2, SO_2, and H_2S are positively correlated at statistically significant level ($R^2 > 0.6$). These subsets of CO_2, SO_2, and H_2S mixing ratios are used to construct **(e)** CO_2 vs. SO_2 and **(f)** H_2S vs. SO_2 correlation plots, from which the time-averaged CO_2/SO_2 and H_2S/SO_2 ratios (within the yellow-colored temporal windows) are calculated (listed in **Table 2**).

To this aim, the gas mixing ratios time-series are sequentially examined with Ratiocalc to identify individual temporal windows (of $\geq$250 s, corresponding to subsets of $\geq$ 30 data points) with high correlation coefficients ($R^2 > 0.6$) between gas couples.

The procedure is illustrated in **Figures 4a,d** are temporal plots of mixing ratios recorded during a single explosion (**Figures 4a–c**), and during a typical quiescent degassing phase (**Figures 4d–f**) (see insets in **Figure 4**). By sequentially scanning the two sub-datasets, we identify the temporal intervals where the best correlations ($R^2 > 0.6$) between gas mixing ratio pairs are observed (yellow bands in **Figures 4a,d**). These subsets of CO_2, SO_2, and H_2S mixing ratios are then used to build CO_2 vs. SO_2 (**Figures 4b,e**) and H_2S vs. SO_2 (**Figures 4c,f**) correlation plots, and to calculate the time-averaged CO_2/SO_2 and H_2S/SO_2 ratios (within the yellow-colored temporal windows) from the slopes of the best-fit regression lines. The procedure is repeated for the entire dataset, and all the obtained gas ratio pairs are listed in **Table 2**.

Our gas ratios, listed in **Table 2** and illustrated in **Figure 5**, show contrasting H_2S/SO_2 ratios composition for the *quiescent gas* and the *syn-explosive gas*. The *quiescent gas* composition is characterized by H_2S/SO_2 ratios of 0.57 ± 0.2 (1 σ) (range, 0.01–1.5), or well above the H_2S/SO_2 of the gas released during the phreatic eruptions. This *syn-explosive gas* exhibits H_2S/SO_2 ratios of 0.04 ± 0.06 (range, 0.0003–0.18) (**Figure 5**). The *quiescent gas* H_2S/SO_2 ratio exhibits a weak but appreciable declining trend, from February (∼1) to early May (∼0.5) (**Figure 5B**), but remains systematically above the *syn-explosive gas* range (which shows no systematic trend).

Table 2 shows that *quiescent gas* and *syn-explosive gas* released by the lake have overlapping CO_2/SO_2 ratio compositions (64 ± 59 and 136 ± 110 at 1σ; **Figure 5A**). Both show a tendency of decreasing CO_2/SO_2 ratios from February (∼120 ± 51) to early May (∼70 ± 20).

Prior to each individual explosion, the CO_2, SO_2, and H_2S mixing ratios are typically very low (see **Figures 4a**, **6a**). Thus, the composition of the *quiescent gas* released in the minutes/seconds before an explosion, here refereed as *pre-explosive gas*, is not well constrained. One important aspect is, however, that the compositional change from *pre-explosive gas* to *syn-explosive gas* is large and abrupt at the onset of eruption (**Figures 4a**, **6a**). To highlight this observation, we show in **Figure 4a** the CO_2/SO_2 and H_2S/SO_2 ratios calculated by simply taking the ratio of individual couples of co-acquired mixing ratios. This point-to-point ratio approach (e.g., Pering et al., 2014) provides high-resolution (1 Hz) records of CO_2/SO_2 and H_2S/SO_2 ratios, see **Figures 4a**, **6a**. The errors associated with this methodology are potentially very large (∼ 50%, as based on laboratory tests) at the few ppm level (e.g., before the explosions), so the ratios displayed in **Figures 4a**, **6a** should only be viewed as semi-quantitative estimates. However, for the specific example shown in **Figure 4a**, the ratios calculated with the point-to-point ratio technique (respectively of 640 and 1.1 for CO_2/SO_2 and H_2S/SO_2) are reasonably close to those obtained with the scatter plot methodology described above (respectively of 628 and 0.9 for CO_2/SO_2 and H_2S/SO_2). A comparable similarity of point-to-point-derived and scatter plot-derived ratios is obtained for the explosion detailed in **Figure 6a** (see **Table 2**). We thus argue that the abrupt changes in CO_2/SO_2 and H_2S/SO_2 ratios at eruption onsets (**Figures 4a,e**, **6a**) are real, and point to very distinct gas signatures for *pre-explosive gas* and *syn-explosive gas*, with the former being typically more SO_2-poor. Very similar abrupt variations in gas ratios are observed for all 9 recorded explosions, followed by a gradual return to *quiescent gas* compositions over timescales of minutes (**Figures 4a**, **6a**). The point-to-point-derived compositions of the *pre-explosive gas* are listed in **Table 2**.

DISCUSSION

Our Multi-GAS results, in tandem with previous results (Aiuppa et al., 2014; de Moor et al., 2017), constrain the composition of the gas plume released by the Rincón de la Vieja crater lake (**Figure 7**). Our 2017 results confirm that SO_2 is the prevalent S gas species in the Rincón de la Vieja crater lake plume during both quiescent and explosive degassing, with H_2S/SO_2 <1 in all except six cases (**Table 2**). This is in line with previous reports (all Multi-Gas measurements) of Aiuppa et al. (2014) (1 survey in April 2013; H_2S/SO_2 = 0.9 ± 0.15) and (de Moor et al., 2017) (3 surveys between April 2014 and March 2016; H_2S/SO_2 of 0.05–0.3) (**Figure 7**). In contrast, low-temperature (<80°C) fumaroles, scattered on the inner crater walls, and around the lake shore, typically exhibit high H_2S/SO_2 ratios of ∼4 (Tassi et al., 2005). In these weaker hydrothermal manifestations, S re-equilibration (e.g., SO_2 conversion to H_2S) during cooling and reaction with wall-rocks in the fumarole's feeding conduits is very likely. Similarly, de Moor et al. (2016b) showed that Poas fumaroles have higher H_2S/SO_2 than the plume from the acid crater lake.

The 2017 crater lake plume is richer in CO_2 (CO_2/SO_2 ratios of 64 ± 59 to 136 ± 110 for *quiescent gas* and *syn-explosive gas, respectively*) than in 2013 (CO_2/SO_2 = 27 ± 15; Aiuppa et al., 2014) and 2014–2016 (CO_2/SO_2 of 4.3–9.5; de Moor et al., 2017) (a period over which Rincón's activity was progressively intensifying) (**Figure 7**). Thus, degassing at Rincón de la Vieja appears to be highly dynamic on yearly time scales in terms of gas compositions. Our continuous record from 2017 has much improved temporal resolution than past (campaign) surveys, and thus allows evaluation of the extent to which gas composition responds to high-frequency changes in volcanic activity. Three key observations emerge:

i) the plume H_2S/SO_2 ratio varied little during quiescent lake degassing in 2017: 0.57 ± 0.20 (**Figures 5B**, **7**); this limited variability is suggestive of S speciation buffering by fluid + solid phase reaction(s) (at least partially) (Giggenbach, 1987, 1996);
ii) during phreatic blasts, the gas emissions shift to more oxidized conditions (H_2S/SO_2 <0.18) than during quiescent degassing (**Figures 5B**, **6**); the compositional change at the eruption

TABLE 2 | Multi-GAS-derived (molar) CO_2/SO_2 and H_2S/SO_2 ratios in the Rincon de la Vieja crater lake plume.

Time	Ratio	Ratio value	R^2	Ratio	Ratio value	R^2	SO_2max (ppmv)	Eruption number
04/02/2017 09:05	CO_2/SO_2	100	0.65	H_2S/SO_2	0.54	0.62	0.68	
05/02/2017 03:05	CO_2/SO_2	115	0.68	H_2S/SO_2	0.69	0.65	0.70	
05/02/2017 09:05	CO_2/SO_2	109	0.67	H_2S/SO_2	1.07	0.60	0.69	
06/02/2017 03:05	CO_2/SO_2	102	0.65	H_2S/SO_2	0.75	0.70	0.67	
06/02/2017 21:05	CO_2/SO_2	137	0.70	H_2S/SO_2	0.83	0.68	0.67	
10/02/2017 21:05	CO_2/SO_2	193	0.64	H_2S/SO_2	0.91	0.63	0.63	
13/02/2017 09:08	CO_2/SO_2	502		H_2S/SO_2	1.03	0.94	0.66	PRE-EXPL
13/02/2017 09:12	CO_2/SO_2	131	0.78	H_2S/SO_2	0.0003	0.84	18.17	1
13/02/2017 15:05	CO_2/SO_2	99	0.70	H_2S/SO_2	0.61	0.75	0.86	
14/02/2017 09:05	CO_2/SO_2	51	0.70	H_2S/SO_2	0.82	0.70	0.97	
14/02/2017 15:05	CO_2/SO_2	320	0.65	H_2S/SO_2	0.94	0.68	0.59	
15/02/2017 03:05	CO_2/SO_2	90	0.64	H_2S/SO_2	0.65	0.60	0.58	
17/02/2017 03:05	CO_2/SO_2	198	0.60	H_2S/SO_2	0.74	0.64	0.47	
17/02/2017 15:05	CO_2/SO_2	118	0.62	H_2S/SO_2	0.37	0.70	1.08	
17/02/2017 21:05	CO_2/SO_2	38	0.65	H_2S/SO_2	0.43	0.65	3.71	
18/02/2017 15:05	CO_2/SO_2	144	0.60	H_2S/SO_2	0.52	0.60	1.52	
18/02/2017 21:05	CO_2/SO_2	59	0.65	H_2S/SO_2	0.49	0.62	2.34	
19/02/2017 21:05	CO_2/SO_2	41	0.65	H_2S/SO_2	0.41	0.67	3.16	
20/02/2017 03:05	CO_2/SO_2	101	0.68	H_2S/SO_2	0.46	0.63	0.87	
20/02/2017 15:17	CO_2/SO_2	567		H_2S/SO_2	0.40	0.79	1.08	PRE-EXPL
20/02/2017 15:23	CO_2/SO_2	99	0.82	H_2S/SO_2	0.08	0.93	28.38	2
20/02/2017 21:05	CO_2/SO_2	33	0.65	H_2S/SO_2	0.45	0.92	2.98	
21/02/2017 15:05	CO_2/SO_2	84	0.63	H_2S/SO_2	0.70	0.94	1.60	
21/02/2017 21:05	CO_2/SO_2	59	0.81	H_2S/SO_2	0.44	0.83	1.06	
22/02/2017 03:05	CO_2/SO_2	232	0.75	H_2S/SO_2	0.86	0.97	0.49	
22/02/2017 15:05	CO_2/SO_2	101	0.80	H_2S/SO_2	0.74	0.84	1.02	
22/02/2017 21:05	CO_2/SO_2	246	0.75	H_2S/SO_2	0.22	0.90	2.19	
23/02/2017 03:12	CO_2/SO_2	1296		H_2S/SO_2	1.30	0.60	0.40	PRE-EXPL
23/02/2017 03:34	CO_2/SO_2	38	0.68	H_2S/SO_2	0.0003	0.86	52.61	3
23/02/2017 15:05	CO_2/SO_2	113	0.62	H_2S/SO_2	1.06	0.75	1.14	
23/02/2017 21:05	CO_2/SO_2	118	0.65	H_2S/SO_2	0.90	0.86	1.00	
24/02/2017 15:05	CO_2/SO_2	167	0.74	H_2S/SO_2	1.17	0.84	0.96	
24/02/2017 21:05	CO_2/SO_2	95	0.69	H_2S/SO_2	0.36	0.90	1.99	
25/02/2017 15:05	CO_2/SO_2	286	0.65	H_2S/SO_2	1.54	0.80	0.59	
26/02/2017 03:05	CO_2/SO_2	62	0.70	H_2S/SO_2	0.54	0.83	1.08	
27/02/2017 03:11	CO_2/SO_2	730		H_2S/SO_2	0.90	0.89	0.75	PRE-EXPL
27/02/2017 03:16	CO_2/SO_2	231	0.97	H_2S/SO_2	0.010	0.89	15.70	4
28/02/2017 21:05	CO_2/SO_2	204	0.98	H_2S/SO_2	0.64	0.83	0.97	
02/03/2017 15:05	CO_2/SO_2	105	0.70	H_2S/SO_2	0.91	0.78	0.79	
02/03/2017 21:16	CO_2/SO_2	640 (628)	0.60	H_2S/SO_2	1.1 (0.9)	0.82	0.85	PRE-EXPL
02/03/2017 21:25	CO_2/SO_2	140	0.97	H_2S/SO_2	0.18	0.98	17.14	5
03/03/2017 21:05	CO_2/SO_2	216	0.68	H_2S/SO_2	0.85	0.80	0.70	
11/03/2017 03:05	CO_2/SO_2	86	0.85	H_2S/SO_2	0.92	0.89	0.74	
12/03/2017 21:05	CO_2/SO_2	118	0.82	H_2S/SO_2	0.63	0.85	0.95	
14/03/2017 21:05	CO_2/SO_2	62	0.70	H_2S/SO_2	0.90	0.84	0.91	
15/03/2017 03:05	CO_2/SO_2	217	0.75	H_2S/SO_2	0.97	0.86	0.70	
17/03/2017 17:58	CO_2/SO_2	67	0.66	H_2S/SO_2	0.56	0.66	0.60	
17/03/2017 23:57	CO_2/SO_2	38	0.63	H_2S/SO_2	0.97	0.74	0.44	
18/03/2017 00:20	CO_2/SO_2	270	0.70	H_2S/SO_2	0.53	0.60	0.45	
18/03/2017 11:59	CO_2/SO_2	170	0.65	H_2S/SO_2	0.86	0.63	0.45	

(Continued)

TABLE 2 | Continued

Time	Ratio	Ratio value	R^2	Ratio	Ratio value	R^2	SO_2max (ppmv)	Eruption number
18/03/2017 12:02	CO_2/SO_2	106	0.62	H_2S/SO_2	0.88	0.75	0.45	
18/03/2017 12:21	CO_2/SO_2	50	0.62	H_2S/SO_2	0.75	0.63	0.53	
18/03/2017 17:55	CO_2/SO_2	82	0.61	H_2S/SO_2	0.74	0.61	0.54	
18/03/2017 23:59	CO_2/SO_2	98	0.64	H_2S/SO_2	0.62	0.62	0.73	
19/03/2017 00:03	CO_2/SO_2	86	0.52	H_2S/SO_2	1.05	0.77	0.63	
19/03/2017 05:58	CO_2/SO_2	93	0.69	H_2S/SO_2	0.51	0.76	0.45	
19/03/2017 06:16	CO_2/SO_2	167	0.62	H_2S/SO_2	0.43	0.62	0.53	
19/03/2017 06:19	CO_2/SO_2	115	0.61	H_2S/SO_2	0.78	0.73	0.64	
19/03/2017 12:07	CO_2/SO_2	103	0.67	H_2S/SO_2	0.56	0.63	0.64	
19/03/2017 12:14	CO_2/SO_2	39	0.61	H_2S/SO_2	0.66	0.89	0.73	
19/03/2017 00:27	CO_2/SO_2	116	0.68	H_2S/SO_2	0.66	0.60	0.50	
19/03/2017 12:19	CO_2/SO_2	83	0.60	H_2S/SO_2	0.78	0.72	0.50	
19/03/2017 18:14	CO_2/SO_2	37	0.63	H_2S/SO_2	0.66	0.94	0.80	
20/03/2017 06:13	CO_2/SO_2	1265	0.98	H_2S/SO_2	0.81	0.60	0.44	PRE-EXPL
20/03/2017 06:16	CO_2/SO_2	70	0.98	H_2S/SO_2	0.004	0.99	32.80	6
21/03/2017 18:14	CO_2/SO_2	29	0.77	H_2S/SO_2	0.86	0.90	0.90	
23/03/2017 00:17	CO_2/SO_2	30	0.68	H_2S/SO_2	0.63	0.70	0.70	
24/03/2017 12:19	CO_2/SO_2	69	0.61	H_2S/SO_2	0.50	0.75	0.70	
26/03/2017 00:25	CO_2/SO_2	18	0.74	H_2S/SO_2	0.50	0.69	0.90	
26/03/2017 00:27	CO_2/SO_2	10	0.68	H_2S/SO_2	0.57	0.94	1.00	
27/03/2017 00:17	CO_2/SO_2	11	0.64	H_2S/SO_2	0.56	0.93	1.01	
27/03/2017 12:19	CO_2/SO_2	12	0.61	H_2S/SO_2	0.46	0.83	0.85	
28/03/2017 06:17	CO_2/SO_2	32	0.79	H_2S/SO_2	0.20	0.74	0.80	
28/03/2017 18:25	CO_2/SO_2	32	0.61	H_2S/SO_2	0.43	0.79	1.00	
29/03/2017 00:10	CO_2/SO_2	43	0.61	H_2S/SO_2	0.46	0.97	0.50	
29/03/2017 00:26	CO_2/SO_2	10	0.69	H_2S/SO_2	0.51	0.96	1.40	
30/03/2017 18:09	CO_2/SO_2	15	0.62	H_2S/SO_2	0.61	0.76	1.02	
30/03/2017 18:24	CO_2/SO_2	44	0.65	H_2S/SO_2	0.71	0.79	0.50	
31/03/2017 00:12	CO_2/SO_2	17	0.64	H_2S/SO_2	0.57	0.85	0.61	
31/03/2017 00:29	CO_2/SO_2	32	0.71	H_2S/SO_2	0.57	0.92	1.10	
31/03/2017 06:24	CO_2/SO_2	32	0.75	H_2S/SO_2	0.89	0.74	0.77	
31/03/2017 18:06	CO_2/SO_2	79	0.68	H_2S/SO_2	0.61	0.96	0.30	
31/03/2017 18:14	CO_2/SO_2	10	0.71	H_2S/SO_2	0.70	0.92	1.40	
31/03/2017 18:26	CO_2/SO_2	46	0.75	H_2S/SO_2	0.55	0.67	0.85	
31/03/2017 23:53	CO_2/SO_2	24	0.62	H_2S/SO_2	0.42	0.79	1.02	
09/04/2017 12:24	CO_2/SO_2	18	0.77	H_2S/SO_2	0.46	0.77	1.00	
09/04/2017 18:12	CO_2/SO_2	24	0.62	H_2S/SO_2	0.58	0.92	0.70	
10/04/2017 00:08	CO_2/SO_2	48	0.82	H_2S/SO_2	0.51	0.75	0.50	
11/04/2017 00:02	CO_2/SO_2	19	0.62	H_2S/SO_2	0.59	0.92	0.80	
11/04/2017 12:21	CO_2/SO_2	16	0.75	H_2S/SO_2	0.52	0.86	0.90	
11/04/2017 18:10	CO_2/SO_2	16	0.69	H_2S/SO_2	0.68	0.99	0.70	
11/04/2017 18:13	CO_2/SO_2	8	0.64	H_2S/SO_2	0.39	0.75	1.00	
11/04/2017 18:15	CO_2/SO_2	23	0.80	H_2S/SO_2	0.60	0.92	0.92	
11/04/2017 18:23	CO_2/SO_2	15	0.89	H_2S/SO_2	0.62	0.83	0.93	PRE-EXPL
12/04/2017 17:53	CO_2/SO_2	85	0.91	H_2S/SO_2	0.03	0.92	12.34	7
12/04/2017 18:15	CO_2/SO_2	20	0.70	H_2S/SO_2	0.46	0.88	0.93	
13/04/2017 00:20	CO_2/SO_2	20	0.80	H_2S/SO_2	0.49	0.91	0.90	
13/04/2017 06:18	CO_2/SO_2	28	0.61	H_2S/SO_2	0.45	0.73	1.10	
13/04/2017 06:25	CO_2/SO_2	33	0.63	H_2S/SO_2	0.46	0.48	0.80	
13/04/2017 12:16	CO_2/SO_2	52	0.67	H_2S/SO_2	0.60	0.94	0.70	

(Continued)

TABLE 2 | Continued

Time	Ratio	Ratio value	R^2	Ratio	Ratio value	R^2	SO_2max (ppmv)	Eruption number
13/04/2017 18:01	CO_2/SO_2	35	0.67	H_2S/SO_2	0.54	0.86	0.68	
14/04/2017 00:09	CO_2/SO_2	14	0.69	H_2S/SO_2	0.03	0.79	0.80	
14/04/2017 00:11	CO_2/SO_2	26	0.66	H_2S/SO_2	0.39	0.88	0.80	
14/04/2017 00:19	CO_2/SO_2	124	0.94	H_2S/SO_2	0.63	0.91	0.91	
18/04/2017 00:19	CO_2/SO_2	32	0.60	H_2S/SO_2	0.52	0.86	0.76	
18/04/2017 12:27	CO_2/SO_2	21	0.60	H_2S/SO_2	0.59	0.78	0.90	
18/04/2017 18:06	CO_2/SO_2	21	0.61	H_2S/SO_2	0.57	0.95	0.70	
18/04/2017 18:11	CO_2/SO_2	17	0.60	H_2S/SO_2	0.69	0.72	0.90	
18/04/2017 18:20	CO_2/SO_2	22	0.86	H_2S/SO_2	0.56	0.90	1.20	
19/04/2017 00:15	CO_2/SO_2	16	0.86	H_2S/SO_2	0.31	0.57	1.17	
19/04/2017 05:58	CO_2/SO_2	19	0.67	H_2S/SO_2	0.60	0.82	0.93	
19/04/2017 18:09	CO_2/SO_2	29	0.68	H_2S/SO_2	0.61	0.88	0.40	
19/04/2017 18:24	CO_2/SO_2	12	0.60	H_2S/SO_2	1.06	0.90	0.36	
20/04/2017 00:01	CO_2/SO_2	118	0.76	H_2S/SO_2	0.53	0.88	0.44	
20/04/2017 00:01	CO_2/SO_2	628		H_2S/SO_2	0.70	0.74	0.75	PRE-EXPL
20/04/2017 00:05	CO_2/SO_2	390	0.98	H_2S/SO_2	0.014	0.95	6.00	8
20/04/2017 06:02	CO_2/SO_2	15	0.71	H_2S/SO_2	0.71	0.90	0.76	
20/04/2017 06:19	CO_2/SO_2	71	0.71	H_2S/SO_2	0.74	0.87	1.00	
20/04/2017 12:11	CO_2/SO_2	34	0.71	H_2S/SO_2	0.49	0.74	0.60	
20/04/2017 23:55	CO_2/SO_2	51	0.76	H_2S/SO_2	0.49	0.95	0.60	
23/04/2017 18:02	CO_2/SO_2	34	0.75	H_2S/SO_2	0.58	0.98	0.40	
24/04/2017 12:11	CO_2/SO_2	13	0.68	H_2S/SO_2	0.54	0.98	0.80	
24/04/2017 12:23	CO_2/SO_2	19	0.72	H_2S/SO_2	0.56	0.89	1.20	
24/04/2017 17:58	CO_2/SO_2	19	0.81	H_2S/SO_2	0.53	0.89	1.20	
24/04/2017 18:17	CO_2/SO_2	43	0.69	H_2S/SO_2	0.62	0.91	0.61	
25/04/2017 00:21	CO_2/SO_2	17	0.89	H_2S/SO_2	0.25	0.60	1.50	
25/04/2017 06:01	CO_2/SO_2	53	0.65	H_2S/SO_2	0.12	0.74	0.85	
25/04/2017 06:02	CO_2/SO_2	241	0.81	H_2S/SO_2	0.44	0.90	0.84	
25/04/2017 06:08	CO_2/SO_2	119	0.64	H_2S/SO_2	0.01	0.99	1.15	
25/04/2017 06:15	CO_2/SO_2	638 (489)	0.71	H_2S/SO_2	0.54 (0.38)	0.99	1.13	PRE-EXPL
25/04/2017 06:21	CO_2/SO_2	55	0.77	H_2S/SO_2	0.004	0.99	34.42	9
25/04/2017 18:11	CO_2/SO_2	28	0.60	H_2S/SO_2	0.67	0.96	1.40	
25/04/2017 18:19	CO_2/SO_2	74	0.95	H_2S/SO_2	0.50	0.95	7.62	
26/04/2017 00:10	CO_2/SO_2	19	0.77	H_2S/SO_2	0.55	0.96	1.01	
26/04/2017 00:27	CO_2/SO_2	16	0.67	H_2S/SO_2	0.65	0.93	1.20	
27/04/2017 00:01	CO_2/SO_2	21	0.66	H_2S/SO_2	0.60	0.93	0.77	
27/04/2017 06:07	CO_2/SO_2	49	0.94	H_2S/SO_2	0.47	0.77	0.30	
28/04/2017 18:13	CO_2/SO_2	16	0.62	H_2S/SO_2	0.33	0.76	0.70	
29/04/2017 00:21	CO_2/SO_2	106	0.67	H_2S/SO_2	0.49	0.98	0.40	
29/04/2017 00:08	CO_2/SO_2	38	0.63	H_2S/SO_2	0.52	0.89	1.20	
29/04/2017 12:25	CO_2/SO_2	7	0.65	H_2S/SO_2	0.41	0.88	1.30	
29/04/2017 18:00	CO_2/SO_2	17	0.90	H_2S/SO_2	0.41	0.73	1.42	
29/04/2017 18:20	CO_2/SO_2	35	0.62	H_2S/SO_2	0.48	0.89	1.34	
30/04/2017 00:10	CO_2/SO_2	35	0.84	H_2S/SO_2	0.69	0.96	0.80	
30/04/2017 18:14	CO_2/SO_2	45	0.70	H_2S/SO_2	0.57	0.81	1.20	
30/04/2017 18:00	CO_2/SO_2	27	0.65	H_2S/SO_2	0.43	0.82	1.18	
30/04/2017 18:19	CO_2/SO_2	39	0.63	H_2S/SO_2	0.50	0.92	1.20	
01/05/2017 12:06	CO_2/SO_2	54	0.68	H_2S/SO_2	0.16	0.38	1.20	
01/05/2017 17:55	CO_2/SO_2	40	0.70	H_2S/SO_2	0.52	0.92	1.26	
01/05/2017 18:10	CO_2/SO_2	51	0.90	H_2S/SO_2	0.55	0.97	1.08	

(Continued)

TABLE 2 | Continued

Time	Ratio	Ratio value	R^2	Ratio	Ratio value	R^2	SO_2max (ppmv)	Eruption number
02/05/2017 00:04	CO_2/SO_2	10	0.75	H_2S/SO_2	0.50	0.99	1.20	
02/05/2017 00:09	CO_2/SO_2	16	0.77	H_2S/SO_2	0.55	0.99	0.91	
02/05/2017 00:21	CO_2/SO_2	27	0.82	H_2S/SO_2	0.58	0.92	1.25	
02/05/2017 12:10	CO_2/SO_2	35	0.74	H_2S/SO_2	0.43	0.88	1.01	
02/05/2017 12:25	CO_2/SO_2	63	0.81	H_2S/SO_2	0.42	0.95	1.10	
02/05/2017 18:14	CO_2/SO_2	56	0.84	H_2S/SO_2	0.29	0.78	1.00	
03/05/2017 00:05	CO_2/SO_2	56	0.82	H_2S/SO_2	0.33	0.92	0.80	
03/05/2017 00:13	CO_2/SO_2	54	0.84	H_2S/SO_2	0.50	0.88	0.92	
03/05/2017 00:22	CO_2/SO_2	34	0.82	H_2S/SO_2	0.44	0.96	1.09	
03/05/2017 06:01	CO_2/SO_2	50	0.67	H_2S/SO_2	0.37	0.86	0.80	
03/05/2017 06:05	CO_2/SO_2	60	0.64	H_2S/SO_2	0.37	0.89	0.75	
03/05/2017 06:10	CO_2/SO_2	56	0.70	H_2S/SO_2	0.43	0.82	0.68	
03/05/2017 06:18	CO_2/SO_2	72	0.63	H_2S/SO_2	0.34	0.79	0.76	
04/05/2017 00:00	CO_2/SO_2	26	0.65	H_2S/SO_2	0.42	0.86	0.70	
04/05/2017 00:15	CO_2/SO_2	37	0.82	H_2S/SO_2	0.64	0.93	0.77	
04/05/2017 06:09	CO_2/SO_2	22	0.67	H_2S/SO_2	0.42	0.93	1.00	
04/05/2017 06:17	CO_2/SO_2	38	0.63	H_2S/SO_2	0.53	0.91	0.76	
04/05/2017 18:21	CO_2/SO_2	38	0.87	H_2S/SO_2	0.52	0.91	1.10	
04/05/2017 17:57	CO_2/SO_2	19	0.63	H_2S/SO_2	0.46	0.88	1.25	
05/05/2017 00:04	CO_2/SO_2	14	0.60	H_2S/SO_2	0.62	0.89	0.50	
05/05/2017 12:02	CO_2/SO_2	3	0.74	H_2S/SO_2	0.56	0.97	1.20	
05/05/2017 18:26	CO_2/SO_2	4	0.90	H_2S/SO_2	0.52	0.98	1.20	
08/05/2017 00:15	CO_2/SO_2	6	0.80	H_2S/SO_2	0.64	0.97	1.41	
08/05/2017 00:22	CO_2/SO_2	17	0.76	H_2S/SO_2	0.27	0.52	1.01	
08/05/2017 12:07	CO_2/SO_2	68	0.61	H_2S/SO_2	0.35	0.83	0.80	
08/05/2017 12:27	CO_2/SO_2	116	0.62	H_2S/SO_2	0.35	0.71	0.76	
08/05/2017 18:18	CO_2/SO_2	38	0.77	H_2S/SO_2	0.49	0.92	1.26	
08/05/2017 17:57	CO_2/SO_2	127	0.69	H_2S/SO_2	0.54	0.92	0.69	
09/05/2017 00:23	CO_2/SO_2	67	0.65	H_2S/SO_2	0.41	0.81	1.20	
09/05/2017 06:05	CO_2/SO_2	86	0.60	H_2S/SO_2	0.44	0.67	0.40	

The R^2 values ($\geq$ 0.6 in all cases) identify the regression coefficients in the CO_2 vs. SO_2 and H_2S vs. SO_2 scatter plots that concurred to determine each ratio. SO_2 max identifies the peak SO_2 concentration within each measurement interval. All data refer to quiescent gas except for those associated with an eruption number (which correspond to the syn-explosive gas). The quiescent gas measured prior to each explosion is referred as pre-explosive gas (PRE-EXPL in the table). The quoted compositions for the pre-explosive gas are 20-min averages of point-to-point ratios, e.g., calculated by taking the ratios of individual co-acquired gas concentration couples. Based on laboratory tests, we estimate error in these point-to-point ratios at ~50%, so the quoted values should only be viewed as semi-quantitative estimates. Only in 2 cases (out of 9 explosions), gas mixing rates were correlated to significant levels (R^2 > 0.6) to allow ratios to be derived with the correlation plot methodology also (see ***Figures 4a**, **6a***). *The scatter plot-derived gas ratios are listed in parenthesis for comparison in the table.*

onset is rapid and abrupt, as indicated by the gas ratio contrast between the *pre-explosive gas* and *explosive gas* (**Figures 4a**, **6a**);

iii) both the *quiescent gas* and *syn-explosive gas* are similarly CO_2-rich (relative to S;) compared to magmatic gases in Costa Rica and Nicaragua (see **Figure 7** and reference therein).

iv) The quiescent gas vented prior to an explosion (the *pre-explosive gas*) has systematically higher CO_2/SO_2 ratios than the corresponding *explosive gas* (**Figures 4**, **6**). This difference can only partially reflect the different data processing technique (point-to-point vs. scatter plot, see **Figures 4**, **6**). Thus, also in view of the H_2S/SO_2 records discussed above (see point ii), we conclude that the *explosive gas* is especially SO_2-rich.

These peculiar features of the Rincón de la Vieja crater lake plume have implications for the nature of the magmatic-hydrothermal system producing the emissions, and for the trigger mechanisms of the recurrent explosions, as detailed below.

Rincon de la Vieja Gas Signature: Magmatic or Hydrothermal?

In contrast to the less active (e.g., less acidic) volcanic lakes fed by hydrothermal H_2S only (e.g., Hasselle et al., 2018), the low (typically <1) H_2S/SO_2 ratios in the Rincón de la Vieja crater lake gas suggest supply of oxidized (SO_2-dominated) magmatic fluids into the lake system (Christenson et al., 2010; Christenson and Tassi, 2015). Magmatic gases typically display equilibrium H_2S/SO_2 ratios buffered by redox conditions in the coexisting

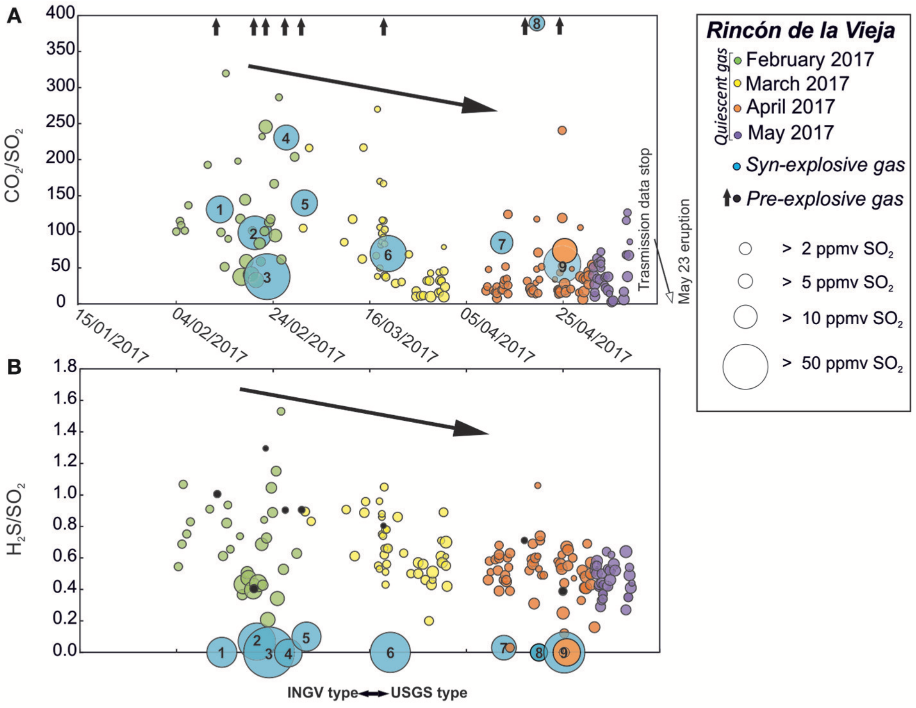

FIGURE 5 | Time-series of gas **(A)** CO_2/SO_2 and **(B)** H_2S/SO_2 (molar) ratios. *Quiescent gases, pre-explosive gases* and *syn-explosive gases* are plotted with different colors. Symbol size is proportional to SO_2 mixing ratios. In **(A)**, all *pre-explosive gases* plot at higher CO_2/SO_2 ratios (as shown by the arrows).

silicate melt, according to Giggenbach (1987):

$$SO_2 + 3H_2 = H_2S + 2H_2O \tag{2}$$

This magma-inherited H_2S/SO_2 ratio is then generally preserved during rapid ascent and cooling of magmatic gases, unless hydrothermal storage and re-equilibration occurs (Giggenbach, 1987). Resolving Equation (2) over a range of magmatic temperatures, and at redox conditions (e.g., H_2/H_2O ratios) buffered by the silicate melt at QFM (quartz-fayalite-magnetite) and NNO (Nickel-Nickel oxide) buffers (Carmichael and Ghiorso, 1986), a range of equilibrium H_2S/SO_2 ratios can be obtained (as illustrated in **Figure 8**), well encompassing the Rincón de la Vieja crater lake gas range. For example, gases separating from magma at ~900°C and QFM will have equilibrium H_2S/SO_2 of ~1 (constituting the so-called magmatic gas H_2S/SO_2 buffer of Giggenbach, 1987), similar to gases from the Rincón de la Vieja crater lake (**Figures 7**, **8**).

A continuous supply of SO_2-rich magmatic gases to the lake is also consistent with the dissolved ion composition of the crater lake water, placing Rincón de la Vieja in the field of high-activity volcanic lakes according to the classification of Pasternack and Varekamp (1997) and Varekamp et al. (2000). Tassi et al. (2005, 2009) argue that the high Cl^-/Na^+ ratio in the Rincón de la Vieja crater lake requires supply of magmatic HCl into the lake, a process also responsible for the high SO_4^{2-} and F^- concentrations (from the dissolution of magmatic SO_2, H_2S, and HF). The hyper-acidic chloride–sulfate brine filling the crater lake is also rich in aluminum, iron, zinc, copper, and boron (because of elemental input via both magmatic gases and enhanced rock dissolution), and is thus compositionally similar to the magmatic gas-fed Laguna Caliente Crater Lake, Poás volcano (Tassi et al., 2009).

Whereas, S speciation and lake chemistry clearly support magmatic gas feeding the lake, the high CO_2/SO_2 signature of the Rincón de la Vieja crater lake gas is inconsistent with a "pure magmatic" hypothesis. **Figure 7** compares the Rincón de la Vieja gas compositions (this work and previous studies) with gases emitted by other recently active Costa Rican volcanoes (Poás and Turrialba; de Moor et al., 2016a,b, 2017). Both Poás and Turrialba datasets show a spread of volcanic gas compositions, which have been interpreted as reflecting variable extents of mixing between magmatic and hydrothermal end-members (Fischer et al., 2015; de Moor et al., 2016a,b). The magmatic CO_2/SO_2 end-members (see stars in **Figure 7**) have been estimated at ~0.3–0.5 (Poás) and ~1–2 (Turrialba), well below the Rincón de la Vieja crater lake gas range for both quiescent and syn-explosive gas types. Similarly, gas observations at nearby Nicaraguan volcanoes Masaya and Momotombo imply a magmatic gas CO_2/SO_2 ratio of ~3–6 (Aiuppa et al., 2014, 2017; de Moor et al., 2017), again implying that the Rincón de la Vieja crater lake gas in 2017 has too high CO_2/SO_2 to be interpreted as pure magmatic (see **Figure 7**).

The CO_2-rich composition of Rincón de la Vieja crater lake gases also does not agree with magmatic degassing models (Moretti et al., 2003) using input conditions relevant to Costa Rica-like magma (see de Moor et al., 2016b for details).

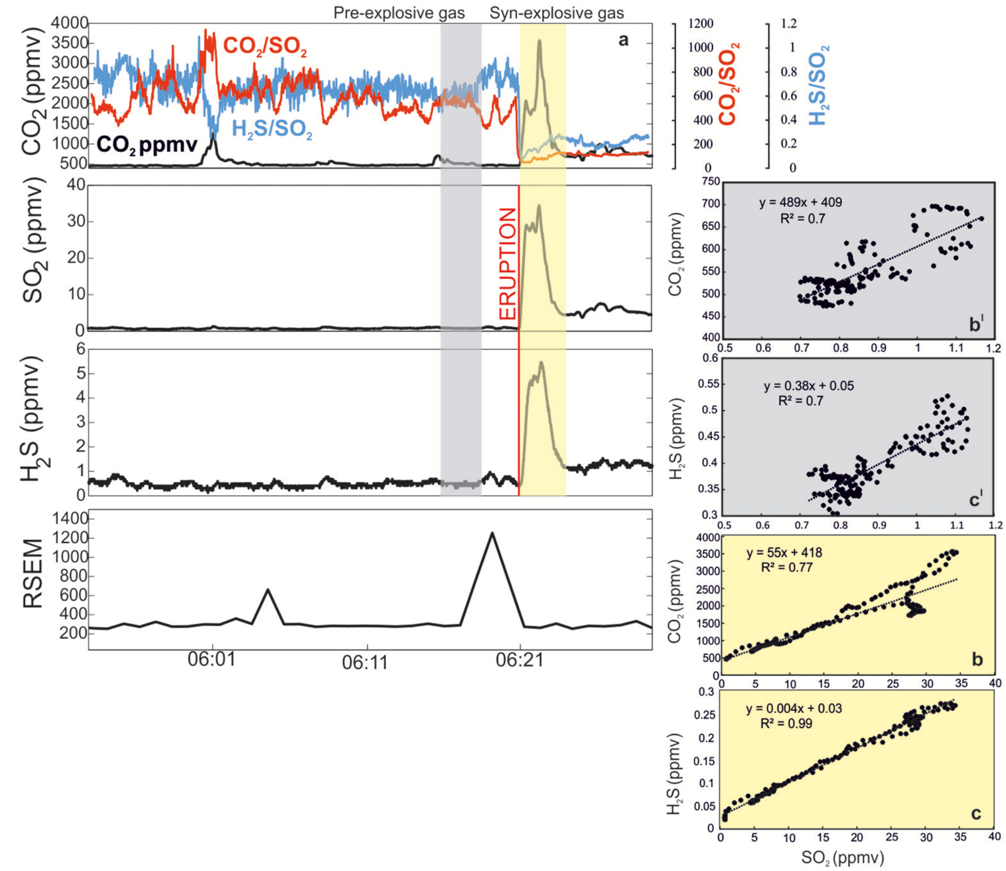

FIGURE 6 | (a) Detail of gas and seismic records taken on April 25, 2017 between ∼5:51 and ∼6:31 GMT. The eruption (event #9 in **Figure 3**, see inset) occurred at ∼6.21 GMT. Mixing ratios increase after the blast. The yellow-colored area corresponds to the sub-interval (identified with Ratiocalc) where CO_2, SO_2, and H_2S are positively correlated at statistically significant level ($R^2 > 0.6$). These subsets of CO_2, SO_2, and H_2S mixing ratios are used to draw **(b)** CO_2 vs. SO_2 and **(c)** H_2S vs. SO_2 correlation plots, and to calculate the time-averaged CO_2/SO_2 and H_2S/SO_2 ratios (within the yellow-colored temporal windows) from the slopes of the best-fit regression lines (listed in **Table 2**). In **(a)** the red and blue lines are high-resolution (1 Hz) records of CO_2/SO_2 and H_2S/SO_2 ratios, respectively, calculated by taking the ratio of individual couples of co-acquired mixing ratios. This point-to-point ratios suggest contrasting gas signatures for *pre-explosive* and *syn-explosive gas*. Example of CO_2 vs. SO_2 and H_2S vs. SO_2 correlation plots for the *pre-explosive gas* [built from data within the gray-colored temporal windows in **(a)**], shown in **(b')** and **(c')**.

These numerical simulations (see **Figure 7**) predict equilibrium CO_2/SO_2 ratios of 20 to 0.07 for gases exsolved from a Turrialba-like andesitic magma (at redox condition of QFM +1 to +3 and temperatures of 900–1,100°C) decompressed from 250 MPa to 0.1 MPa pressure. The measured CO_2/SO_2 ratios in Rincón de la Vieja crater lake gas (64±59 and 136±110 for the *quiescent* and *syn-explosive gas*, respectively) are clearly higher than the typical magmatic range, unless very high gas-melt separation pressures ($>> 250$ MPa, equivalent to > 9 km depth) are assumed. Such a deep magma source is unlikely, however, because heat pipes typically sustaining intense degassing and convective overturning at crater lakes require shallow magma (**Figure 9**; Christenson and Tassi, 2015). Also, magma involvement in the recent Rincón de la Vieja eruptions (implicated by the small but ubiquitous juvenile fragments in the eruption deposits) is indicative of shallow storage (**Figure 9**).

To summarize, the CO_2-rich gas compositions with low H_2S/SO_2 ratios (**Figure 7**) are incompatible with a direct shallow magmatic source for the gas vented by the Rincón de la Vieja crater lake. We propose that the pristine chemical composition of deep magmatic gases is altered during upward migration by gas-water-rock reactions within the (sub)limnic hydrothermal system.

The Role of the Sublimnic Hydrothermal System

The interactions of magmatic gases with either the crater lake or the subjacent hydrothermal system are the most obvious candidates for generating the observed CO_2-rich (S-depleted) Rincón de la Vieja gas. Magmatic gas-lake and/or magmatic-hydrothermal reactions, if occurring, could also effectively control S partitioning between reduced and oxidized forms, thus modifying the original magmatic H_2S/SO_2 ratio (Christenson et al., 2010; Christenson and Tassi, 2015).

One often-invoked mechanism of magmatic SO_2 dissolution into active volcanic lakes is via disproportionation reactions such

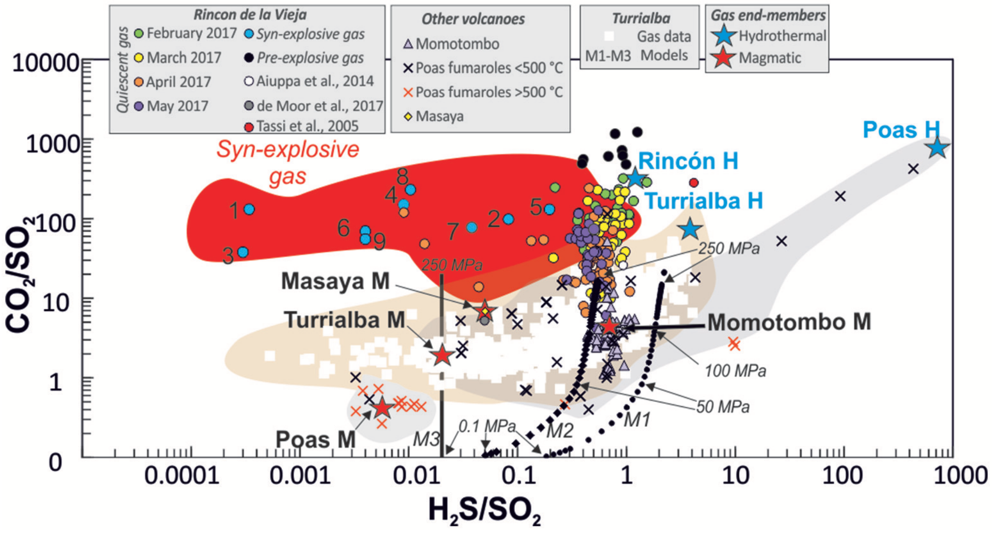

FIGURE 7 | H_2S/SO_2 vs.CO_2/SO_2 scatter plot of Costa Rica and Nicaraguan volcanic gases. The Rincón de la Vieja gas (both *quiescent gas* and *syn-explosive gas*; same symbols as in **Figure 5**) is contrasted with the composition of volcanic gases from other volcanoes of the Costa Rica-Nicaragua arc segment. Momotombo and Masaya: (Aiuppa et al., 2014, 2017; de Moor et al., 2017); Poas: (Aiuppa et al., 2017; de Moor et al., 2017). Estimated compositional fields for hydrothermal (H) and magmatic (M) end-members are indicated (this study; based on averaging of magmatic and hydrothermal compositions quoted in the previous studies). The hypothetical composition of the Rincón hydrothermal pole (H) was estimated by averaging composition of the two measurements of *quiescent gases* with the lowest SO_2 concentrations (e.g., the most hydrothermal endmember). Numbers alongside the *syn-explosive gas* data-points identify the explosions (see **Figure 3**). The curves labeled M1 to M3 indicate the model-derived H_2S/SO_2 vs.CO_2/SO_2 compositions obtained by model simulations of degassing upon decompression (from 250 to 0.1 MPa) for a Turrialba-like magma (taken from de Moor et al., 2016b). M1 and M2 models have been initialized at slightly different H_2O contents (3 and 2 wt. %, respectively). In model M3, gas compositions obtained in runs M1-M2 are re-calculated at surface discharge conditions (QFM+3, 0.1 MPa, 650°C), yielding H_2S/SO_2 ratio of ~0.02 (see the original work of de Moor et al., 2016b for further details).

as (Kusakabe et al., 2000):

$$3SO_2 + 2H_2O \rightarrow 2HSO_{4^-} + S_{(e)} + 2H^+ \quad (3a)$$

$$4SO_2 + 4H_2O \rightarrow 3HSO_{4^-} + H_2S + 3H^+ \quad (3b)$$

The two relationships can be combined into the following equilibrium:

$$SO_2 + S_{(e)} + 2H_2O = H_2S + H^+ + HSO_{4^-} \quad (4)$$

To assess the role played by magmatic gas-lake water reactions, we test if the measured H_2S/SO_2 ratios in the Rincón de la Vieja gas (**Figures 4–8**) are consistent with the equilibrium ratio predicted by Equation (4) at lake water conditions, i.e., if the measured gas S speciation is controlled/buffered by dissolved S species in the crater lake water. In the Rincón de la Vieja crater lake, oxidized (exavalent) dissolved S species prevail (Tassi et al., 2005), and sulfur spherules are always observed on the lake surface (**Figure 2**), implying that all of the ingredients for reaction 4 are available in abundance. Solving Equation (4) for the H_2S/SO_2 gas ratio, at crater lake water conditions (T = 30–50°C; $H_2SO_4 = 8.16 \times 10^{-12}$ M at pH = 0.77 and $SO_4^{2-} = 0.146$ M), and using the thermodynamic data from HSC thermochemical software (http://www.hsc-chemistry.com/), we obtain the curve labeled "*Lake*" in **Figure 8**. The H_2S/SO_2 gas ratios predicted by reaction (4) are, however, H_2S-dominated, pointing against a lake-buffered H_2S/SO_2 ratio hypothesis (**Figure 8**). Our calculations thus suggest that either a kinetic process prevails (e.g., that Equation 4 does not go to completion in the lake, leading to only partial conversion of magmatic SO_2 into H_2S) (Ohmoto and Lasaga, 1982; Rye, 2005), or that magmatic gas-water interactions occur deeper in the system, such as in the hotter sublimnic hydrothermal system (**Figure 9**).

A variety of magmatic gas-water-rock reactions have been proposed to occur in sublimnic hydrothermal systems (Christenson and Tassi, 2015; Shinohara et al., 2015). These hydrothermal reactions, typically occurring in the upper portion of a heat pipe (**Figure 9**), invariably enrich the gas phase in CO_2 relative to more reactive SO_2 and H_2S (Symonds et al., 2001, 2003), and may thus generate the high CO_2/SO_2 ratios in Rincón de la Vieja crater lake gas. In addition to leading to S depletion, these reactions can also act as controls on the H_2S/SO_2 ratio (see below).

In addition to the reaction described by Equation (4), S scrubbing can occur via (Giggenbach, 1987; Christenson and Tassi, 2015):

$$2H_2S_{(g)} + SO_{2(g)} = 3S_{(e)} + 2H_2O \quad (5)$$

This reaction scavenges H_2S and SO_2 in 2:1 proportions, and can thus (at least partially) justify the oxidized nature ($SO_2 > H_2S$) of the Rincón de la Vieja gas. In fact, the situation is more complicated, because as pointed out by Shinohara et al. (2011), S deposition via Equation (5) can either increase or decrease

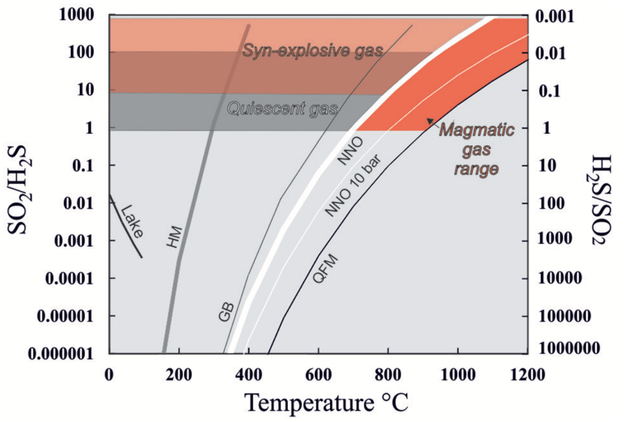

FIGURE 8 | Temperature dependence of the SO_2/H_2S ratio, as predicted by the common magmatic and hydrothermal redox buffers (modified from Aiuppa et al., 2005). The solid lines represent the H_2S/SO_2 ratios at equilibrium with redox conditions (oxygen fugacity, fO_2) fixed by QFM (Quartz-Fayalite-Magnetite), NNO (Nickel-Nickel oxide), and HM (Hematite-magnetite) redox buffers (Giggenbach, 1987, 1996). The magmatic gas range is from Aiuppa et al. (2005). The curve labeled GB and Lake illustrate the equilibrium H_2S/SO_2 ratios at redox conditions fixed by the Giggenbach (1987) FeO-$FeO_{1.5}$ hydrothermal buffer (Equation 6) and dissolved S species in the lake buffer water (Equation 2), respectively. Pressure is 1 bar except where specified. The measured H_2S/SO_2 ranges for both the *quiescent* and *syn-explosive* gas are indicated by gray and red bands, respectively.

the gas H_2S/SO_2 ratio, depending on the original S speciation (SO_2-dominated or H_2S-dominated) in the feeding magmatic gas entering the hydrothermal system (unconstrained for Rincón). Also, concurrently with hydrothermal S deposition, iron minerals in the hydrothermal rock matrix can contribute buffering redox conditions (e.g., the gas H_2/H_2O ratio), via (Giggenbach, 1987):

$$4FeO_{1.5} + 2H_2 = 4(FeO) + 2H_2O \tag{6}$$

$$4Fe_3O_4 + 2H_2O = 6Fe_2O_3 + 2H_2 \tag{7}$$

These reactions can then buffer, via Equation (2), the residual (after S deposition) hydrothermal gas H_2S/SO_2 ratio. For example, the H_2S/SO_2 gas ratios predicted (as a function of temperature) from Equation (2), and redox conditions buffered by either the Fe(II)-Fe(III) hydrothermal buffer (Equation 6; Giggenbach, 1987) or the Hematite-Magnetite buffer (HM) hydrothermal (Equation 7), are graphically illustrated in **Figure 8**. The figure shows that the measured H_2S/SO_2 ratios in the Rincón de la Vieja gas would be consistent with those imposed by hydrothermal buffering at HM redox conditions, 290–400°C, and 1 bar (**Figure 8**). Coexistence of oxidized (hematite) and reduced (magnetite, pyrite) iron forms is suggested at both Rincón de la Vieja (Tassi et al., 2005) and in the nearby Borinquen and Miravalles hydrothermal fields (Gherardi et al., 2002; Molina and Martí, 2016). However, since a second independent redox couple (e.g., the H_2/H_2O ratio; Aiuppa et al., 2011) is not measured in the Rincón gas, evidence for hydrothermal (HM) buffering of S speciation remains speculative.

In summary, available gas information at Rincón de la Vieja is suggestive of extensive hydrothermal processing of magmatic gases within the sublimnic hydrothermal system. These hydrothermal reactions consume S (compared to relatively inert C, thus explaining the high observed CO_2/S ratio), but the exact S deposition mechanisms (Equations 3–5), and perhaps the role of hydrothermal redox buffering (Equation 7), cannot be quantitatively constrained with the present data. However the observed difference in H_2S/SO_2 between the *quiescent gas* (0.57 ± 0.20) and the *syn-explosive gas* (0.04 ± 0.06), and the abrupt gas ratio changes at eruption onsets (**Figures 4a**, **6a**), clearly imply less hydrothermal interaction (e.g., less SO_2 deposition) during the phreatic blasts (**Figure 9**). This can be explained by a combination of faster gas transit, transient disruption of the sublimnic hydrothermal envelop, and/or deeper (hotter) gas source during the explosions (**Figure 9**).

The Eruption Trigger

Whatever the exact process (Equations 3–6), S scrubbing reactions are likely to lead to rapid and effective formation of native S seals (Christenson and Tassi, 2015). The presence of S spherules in the Rincón de la Vieja crater lake points to the existence of a native sulfur layer at the lake bottom (Hurst et al., 1991; Takano et al., 1994; Christenson et al., 2010) (**Figure 9**).

The physical state of this S pool is known to be dependent on temperature, with a ∼2000-times viscosity increase upon heating in the 150–200°C temperature range (Hurst et al., 1991; Oppenheimer, 1992; Takano et al., 1994). It is possible that magmatic-hydrothermal gases, while persistently fluxing through the Rincón de la Vieja sublimnic hydrothermal system, progressively heat the S pool, thus ultimately creating the conditions for the development of a viscous impermeable seal (**Figure 9A**).

We envision a mechanism in which, during quiescence (**Figure 9A**), the feeding magmatic gas interacts with the sublimnic hydrothermal system, undergoes S deposition (± buffering by hydrothermal minerals) and develops a CO_2-rich gas. A fraction of this gas, perhaps after further S deposition into the lake, is emitted to the surface as *quiescent gas*, but the remaining fraction is accumulated at depth as the impermeable S seal develops (**Figure 8a**). The *quiescent gas* released shortly prior to explosions, e.g., the *pre-explosive gas*, is characterized by low gas mixing ratios and especially high CO_2/SO_2 ratios, consistent with a reduction of gas transfer from underneath the seal, and extensive S loss to hydrothermal minerals (**Figures 4a**, **6a**).

Ultimately, gas accumulation underneath the seal leads to pressure buildup and seal failure to trigger a phreatic explosion (**Figure 9B**). This mechanism is also supported by the recurrent observation in the erupted products, especially in the 1–2 mm ash grain-size fraction, of native sulfur fragments. We argue that, during the phreatic blasts, rapid gas ascent reduces hydrothermal interactions as supported by the observed short-term variations in gas chemistry. In fact, our high-resolution (1 Hz) of CO_2/SO_2 and H_2S/SO_2 records (see **Figures 4a**, **6a**) show that both ratios suddenly decrease at the eruption onset, implying the each *syn-eruptive gas* is SO_2-richer than its corresponding *pre-explosive gas*. Rapid gas ascent, perhaps combined with gas ascent from

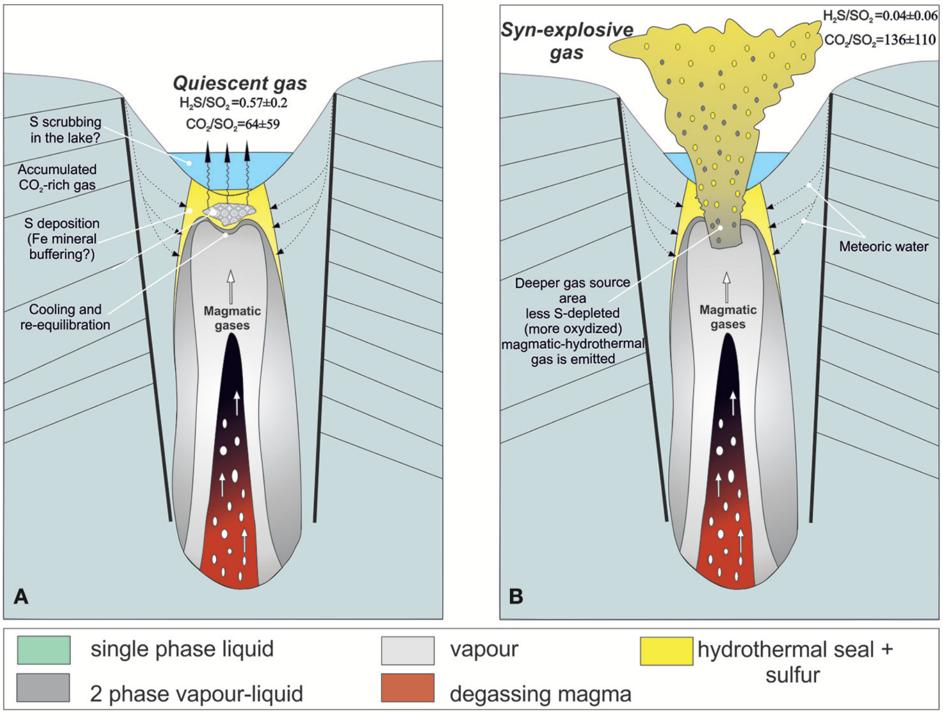

FIGURE 9 | A schematic model for the Rincón de la Vieja volcano shallow feeding system, detailing the structure of the sublimnic hydrothermal/magmatic system (modified from Christenson et al., 2010). **(A)** During quiescence, the feeding magmatic gas undergoes S deposition (± buffering by hydrothermal minerals) within the sublimnic hydrothermal system. The resulting CO_2-rich gas is partially surface-vented as *quiescent gas*, and partially accumulated beneath an impermeable S seal; **(B)** pressure buildup below the S seal triggers a phreatic explosion, characterized by rapid gas ascent, limited hydrothermal interaction, and deeper gas source. This *syn-explosive gas* retains a C-rich signature, implying a magmatic-hydrothermal nature.

deeper/hotter portions of the magmatic-hydrothermal vapor zone (**Figure 9B**), are likely implicated in producing the relatively SO_2-richer *syn-explosive gas*.

We caution that our interpretation is based on only ~3 months of observations and the capturing of only 9 out of 42 explosions in that time interval. Thus, longer observations are required to draw more concrete conclusions. However, our results confirm that continuous instrumental geochemical monitoring, in tandem with seismic monitoring, can contribute to understanding the mechanisms that drive the Rincón de la Vieja magmatic system toward potentially hazardous critical states. It is interesting to note that both the H_2S/SO_2 and CO_2/SO_2 ratios in the Rincón de la Vieja *quiescent gas* decreased from February to early May (**Figures 5**, **7**), implying a decreasing extent of hydrothermal re-equilibration of the feeding magmatic gases. This trend toward more magmatic-like gas composition may tentatively be interpreted as reflecting an increase in the magmatic gas supply to the lake conduit, and thus a more unstable magmatic system leading to the major lahar-generating phreatic eruption of May 23 (Global Volcanism Program, 2017), which occurred just a few weeks after our Multi-GAS dataset ended (and actually destroyed the instrument). As stated above, this event (and the following June 11 event) erupted a sizeable juvenile fragment component, claiming for escalating magmatic activity.

Implications for Monitoring of Active Crater Lakes

Our measurements of the syn-explosive gas, the first of their nature at an active volcano, provide observational evidence for that formation of hydrothermal S seals may strongly be implicated in the generation of phreatic eruptions, as originally proposed at Ruapehu volcano in New Zeeland (Hurst et al., 1991; Takano et al., 1994; Christenson et al., 2010). It is arguable that hydrothermal seal formation may fuel phreatic/phreatomagmatic activity at other recurrently erupting volcanic lakes worldwide (Christenson and Tassi, 2015; Stix and de Moor, 2018). As our Rincón de la Vieja dataset shows, continuous gas records may help tracking such seal formation events, as marked by phases of reduced surface S degassing (see the low SO_2 and H_2S mixing ratios, and high CO_2/SO_2 ratios, in the *pre-explosive gas*; **Figures 4a**, **6a**, **7**). To test this hypothesis further, our results thus claim for the need of augmenting the number of volcanic crater lakes that are monitored by permanent gas instrumentation.

It is also interesting to note that the rapid and abrupt transition between *pre-explosive* and *explosive gas* at Rincón de la Vieja (**Figures 4a**, **6a**), pointing to reduced surface S outgassing prior to each blast, is in stark contrast with what recurrently reported at Poás, where precursory trends toward more magmatic (more S-rich) gas composition are observed instead (de Moor et al., 2016a). We argue this difference may imply an overall lower magmatic gas input, or a more effective seal (or both), at Rincón de la Vieja, compared to the more active Poás volcano (where the magmatic system appears more implicated as eruption trigger). This comparison suggests that distinct trigger mechanisms, with different relative roles played by hydrothermal sealing vs. magmatic as influx, may in fact be operating at active crater lakes. This diversity in potential trigger mechanisms (Stix and de Moor, 2018) reinforces the need for more robust (and temporally continuous) gas records at volcanic crater lakes.

CONCLUSIONS

This study investigates degassing dynamics of Rincón de la Vieja during a period of intense phreatic activity. For the first time at any volcano, the composition of the gas released during discrete phreatic events (confirmed seismically) was resolved using Multi-GAS. Our results demonstrate chemically distinct gas compositions during quiescent degassing vs. explosive eruptive degassing. The *quiescent* gas is characterized by very low concentrations of sulfur gas species (SO_2 and $H_2S < 2$ ppmv) and relatively high H_2S/SO_2 ratios (mean 0.57), whereas the *syn-explosive* gas shows much higher gas mixing ratios of SO_2 and CO_2 and a systematic decrease of H_2S/SO_2 ratio (mean, 0.04). Both the *quiescent* and *syn-explosive* gases exhibit high CO_2/S ratios relative to regional magmatic gases, but each *explosive gas* has lower CO_2/S ratio than its corresponding *pre-explosive gas*.

These C-rich gases, if interpreted as magmatic, would require a very deep ($P > 250$ MPa) magmatic source, which is unlikely in view of the recent magma involvement in the 2017 Rincón phreatomagmatic eruptions. We thus favor a mechanism in which magmatic gas-water-rock reactions in the sublimnic hydrothermal system lead to deposition of native S and sulfate formation, and thus enrich the gas phase in C relative to SO_2 and H_2S. The presence of abundant native sulfur spherules in the lake is consistent with this scenario, as the presence of S spherules suggests a native sulfur layer at the lake bottom. We propose that continuous gas fluxing may progressively lead to development of an impermeable seal near the lake/hydrothermal system interface. Gas accumulates underneath the seal, and ultimately ruptures this seal resulting in phreatic eruptions. The trend of decreasing *quiescent* CO_2/SO_2 and H_2S/SO_2 ratios from February to May 2017 can be interpreted as an increase in the magmatic gas supply, providing a precursor to the major eruption of 23 May.

These results, the first volcano reports for the gas phase released by discrete phreatic eruptions, confirm (Christenson and Tassi, 2015) that the complex interplay between rising magmatic gases and the sublimnic hydrothermal system likely plays a decisive role in triggering the explosions.

DATA AVAILABILITY STATEMENT

The raw data supporting the conclusions of this manuscript will be made available by the authors, without undue reservation, to any qualified researcher.

AUTHOR CONTRIBUTIONS

AB, JMdM, and AA conceived the idea. AB, JMdM, GA, HB, HV, MB, GG, and PK prepared the instrumentation and conducted the field experiment. AB, MM, HB, and DD processed the data. AB and AA drafted the article with help from JMdM, PK, GA, HB, and MM.

ACKNOWLEDGMENTS

We wish to thank Franco Tassi, Orlando Vaselli, Giulio Bini, and ICE staff for help during Multi-GAS installation. We gratefully acknowledge OVSICORI for logistical support. We also thank Bill Evans (USGS), Ryunosuke Kazahaya, Hiroshi Shinohara, Paul Wallace, and Jacob Lowenstern, whose thoughtful comments improved the quality of this work. This research has been funded by the Deep Carbon Observatory via the DECADE research initiative (Grant no. 10759-1238, AA). JMdM gratefully acknowledges support through the Deep Carbon Observatory's Biology Meets Subduction project. Any use of trade, firm, or product names is for descriptive purposes only and does not imply endorsement by the U.S. Government.

REFERENCES

Aiuppa, A. (2015). "Volcanic-gas monitoring," in *Volcanism and Global Environmental Change*, eds A. Schmidt, K. Fristad, and L. Elkins-Tanton (Cambridge: Cambridge University Press), 81–96. doi: 10.1017/CBO9781107415683.009

Aiuppa, A., Bertagnini, A., Métrich, N., Moretti, R., Di Muro, A., Liuzzo, M., et al. (2010). A model of degassing for Stromboli volcano. *Earth Planet. Sci. Lett.* 295, 195–204. doi: 10.1016/j.epsl.2010.03.040

Aiuppa, A., de Moor, J. M., Arellano, S., Coppola, D., and Francofonte, V., Galle, B., et al. (2018). Tracking formation of a lava lake from ground and space: Masaya volcano (Nicaragua), 2014–2017. *Geochem. Geophys. Geosyst.* 19, 496–515. doi: 10.1002/2017GC007227

Aiuppa, A., Federico, C., Giudice, G., Gurrieri, S., Liuzzo, M., Shinohara, H., et al. (2006), Rates of carbon dioxide plume degassing from Mount Etna volcano. *J. Geophys. Res. Solid Earth* 111, 1–8. doi: 10.1029/2006JB004307

Aiuppa, A., Fischer, T. P., Plank, T., Robidoux, P., and Di Napoli, R. (2017), Along-arc, inter-arc and arc-to-arc variations in volcanic gas CO2/ST ratios reveal dual source of carbon in arc volcanism. *Earth Sci. Rev.* 168, 24–47. doi: 10.1016/j.earscirev.2017.03.005

Aiuppa, A., Inguaggiato, S., McGonigle, A. J. S., O'Dwyer, M., Oppenheimer, C., Padgett, M. J., et al. (2005), H_2S fluxes from Mt. Etna, Stromboli, and Vulcano (Italy) and implications for the sulfur budget at volcanoes. *Geochim. Cosmochim. Acta* 69, 1861–1871. doi: 10.1016/j.gca.2004.09.018

Aiuppa, A., Robidoux, P., Tamburello, G., Conde, V., Galle, B., Avard, G., et al. (2014), Gas measurements from the Costa Rica-Nicaragua volcanic segment suggest possible along-arc variations in volcanic gas chemistry. *Earth Planet. Sci. Lett.* 407, 134–147. doi: 10.1016/j.epsl.2014.09.041

Aiuppa, A., Shinohara, H., Tamburello, G., Giudice, G., Liuzzo, M., and Moretti, R. (2011). Hydrogen in the gas plume of an open-vent volcano, Mount Etna Italy. *J. Geophys. Res. Solid Earth* 116, 1–8. doi: 10.1029/2011JB008461

Alvarado, G. E., Kussmaul, S., Chiesa, S., Gillot, P. Y., Appel, H., Worner, G., et al. (1992). Resumen cronoestratigrafico de las rocas igneas de Costa Rica basado en dataciones radiometricas. *J. South Am. Earth Sci.* 6, 151–168. doi: 10.1016/0895-9811(92)90005-J

Alvarado, G. E., Mele, D., Dellino, P., de Moor, J. M., and Avard, G. (2016). Are the ashes from the latest eruptions (2010–2016) at Turrialba volcano (Costa Rica) related to phreatic or phreatomagmatic events? *J. Volcanol. Geotherm. Res.* 327, 407–415. doi: 10.1016/j.jvolgeores.2016.09.003

Arámbula-Mendoza, R., Lesage, P., Valdés-González, C., Varley, N., Reyes-Dávila, G., and Navarro, C. (2011). Seismic activity that accompanied the effusive and explosive eruptions during the 2004–2005 period at Volcán de Colima, Mexico. *J. Volcanol. Geotherm. Res.* 205, 30–46. doi: 10.1016/j.jvolgeores.2011.02.009

Barquero, J., and Segura, J. (1983). La actividad del volcán Rincón de la Vieja. *Bol. Vulcanol.* 13, 5–10.

Boatwright, J. (1980). A spectral theory for circular seismic sources: Simple estimates of source dimension, dynamic stress drop, and radiated seismic energy. *Bull. Seismol. Soc. Am.* 70, 1–27.

Boudon, G., Rancon, J. P., Kieffer, G., Soto, G. J., Traineau, H., and Rossignol, J. C. (1996). Les eruptions de 1966–1970 et 1991–1992 du volcan Rincón de la Vieja, Costa Rica: exemple d'activité recurrente d'un systéme hydromagmatique. *C.R. Acad. Sci. Paris* 322-IIa, 101–108.

Brandes, C., Astorga, A., Back, S., Littke, R., and Winsemann, J. (2007). Deformation style and basin-fill architecture of the offshore Limón back-arc basin (Costa Rica). *Marine Petrol. Geol.* 24, 277–287, doi: 10.1016/j.marpetgeo.2007.03.002

Browne, P. R. L., and Lawless, J. V. (2001). Characteristics of hydrothermal eruptions, with examples from New Zealand and elsewhere. *Earth Sci. Rev*. 52, 299–331. doi: 10.1016/S0012-8252(00)00030-1

Carmichael, I. S. E., and Ghiorso, M. S. (1986), Oxidation-reduction relations in basic magma: a case for homogeneous equilibria. *Earth Planet. Sci. Lett*. 78, 200–210. doi: 10.1016/0012-821X(86)90061-0

Carr, M. J. (1984), Symmetrical and segmented variation of physical and geochemical characteristics of the Central American volcanic front. *J. Volcanol. Geotherm. Res*. 20, 231–252.

Carr, M. J., Feigenson, M. D., and Bennett, E. A. (1990), Incompatible element and isotopic evidence for tectonic control of source mixing and melt extraction along the Central American arc. *Contrib. Mineral. Petrol*. 105, 369–380.

Christenson, B. W., Reyes, A. G., Young, R., Moebisd, A., Sherburne, S., Cole-Bakere, J., et al. (2010). Cyclic processes and factors leading to phreatic eruption events: Insights from the 25 September 2007 eruption through Ruapehu Crater Lake, New Zealand. *J. Volcanol. Geother. Res.* 191, 15–32. doi: 10.1016/j.jvolgeores.2010.01.008

Christenson, B. W., and Tassi, F. (2015). "Gases in volcanic lake environments," in *Volcanic Lakes*, eds D. Rouwet, B. W. Christenson, F. Tassi, and J. Vandemeulebrouck (Heidelberg: Springer).

De la Cruz-Reyna, S., and Reyes-Davila, G. A. (2001). A model to describe precursory material-failure phenomena: applications to short-term forecasting at Colima volcano, Mexico. *Bull. Volcanol*. 63, 297–308. doi: 10.1007/s004450100152

de Moor, J. M., Aiuppa, A., Avard, G., Wehrmann, H., Dunbar, N., Muller, C., et al. (2016b). Turmoil at turrialba volcano (Costa Rica): degassing and eruptive processes inferred from high-frequency gas monitoring. *J. Geophys. Res. Solid Earth* 121, 5761–5775. doi: 10.1002/2016JB013150

de Moor, J. M., Aiuppa, A., Pacheco, J., Avard, G., Kern, C., Liuzzo, M., et al. (2016a). Short-period volcanic gas precursors to phreatic eruptions: Insights from Poás Volcano, Costa Rica. *Earth Planet. Sci. Lett.* 442, 218–227. doi: 10.1016/j.epsl.2016.02.056

de Moor, J. M., Kern, C., Avard, G., Muller, C., Aiuppa, A., Saballos, A., et al. (2017). A new sulfur and carbon degassing inventory for the southern central american volcanic arc: the importance of accurate time-series data sets and possible tectonic processes responsible for temporal variations in arc-scale volatile emissions. *Geochem. Geophys. Geosystems*. 18, 4437–4468. doi: 10.1002/2017GC007141

Delmelle, P., and Bernard, A. (2015). "The remarkable chemistry of sulfur in volcanic acid crater lakes: a scientific tribute to Bokuichiro Takano and Minoru Kusakabe," in *Volcanic Lakes,* eds D. Rouwet, F. Tassi J. Vandemeulebrouck, and B. Christenson (Berlin: Springer), 238–259. doi: 10.1007/978-3-642-36833-2_10

DeMets, C. (2001). A new estimate for present- day Cocos-Caribbean plate motion: Implication for slip along the Central American volcanic arc. *Geophys. Res. Lett.* 28, 4043–4047. doi: 10.1029/2001GL013518

DeMets, C., Gordon, R. G., and Argus, D. F. (2010). Geologically current plate motions. *Geophys. J. Int.* 181, 1–80. doi: 10.1111/j.1365-246X.2009.04491

Di Napoli, R., Federico, C., Aiuppa, A., D'Antonio, M., , and Valenza, M. (2013). Quantitative models of hydrothermal fluid–mineral reaction: the Ischia case, *Geochim. Cosmochim. Acta* 105, 108–129. doi: 10.1016/j.gca.2012.11.039

Fischer, T. P., Ramírez, C., Mora-Amador, R. A., Hilton, D. R., Barnes, J. D., Sharp, Z. D., et al. (2015). Temporal variations in fumarole gas chemistry at Poas volcano, Costa Rica. *J. Volcanol. Geotherm. Res*. 294, 56–70. doi: 10.1016/j.jvolgeores.2015.02.002

Gherardi, F., Panichi, C., Yock, A., and Gerardo-Abaya, J. (2002). Geochemistry of the surface and deep fluids of the Miravalles volcano geothermal system (Costa Rica). *Geothermics* 31, 91–128. doi: 10.1016/S0375-6505(01)00030-X

Giggenbach, W. F. (1987). Redox processes governing the chemistry of fumarolic gas discharges from White Island, New Zealand. *Appl. Geochem*. 2, 141–161.

Giggenbach, W. F. (1996). "Chemical composition of volcanic gas," in *IAVCEI-UNESCO: Monitoring and Mitigation of Volcanic Hazards*, ed R. Tilling (Berlin: Springer), 221–256.

Giggenbach, W. F., and Correales, R. S. (1992). Isotopic and chemical composition of water and steam discharges from volcanic-magmatic-hydrothermal systems of the Guanacaste geothermal province, Costa Rica. *Appl. Geochem*. 7, 309–332.

Global Volcanism Program, (2017). "Report on Rincon de la Vieja (Costa Rica)," in *Bulletin of the Global Volcanism Network, 42:8 Smithsonian Institution*, ed E. Venzke (Washington, DC: Global Volcanism Program).

Gunawan, H., Caudron, C., Pallister, J., Primulyana, S., Christenson, B., McCausland, W., et al. (2016). New insights into KawahIjen's volcanic system from the wet volcano workshop experiment. *Geol. Soc. Lond. Spec. Publ.* 437, 35–56. doi: 10.1144/SP437.7

Hasselle, N., Rouwet, D., Aiuppa, A., Jácome-Paz, M. P., Pfeffer, M., Taran, Y., et al. (2018). Sulfur degassing from steam-heated crater lakes: El Chichón (Chiapas, Mexico) and Víti (Iceland). *Geophys. Res. Lett.* 45, 7504–7513. doi: 10.1029/2018GL079012

Hurst, A. W., Bibby, H. M., Scott, B. J., and McGuiness, M. J. (1991). The heat source of ruapehu crater lake; deductions from the energy and mass balances. *J. Volcanol. Geother. Res.* 46, 1–11.

Kempter, K. (1997). *Geologic evolution of the Rincón de la Vieja volcanic complex, northwestern Costa Rica - 159 págs.* Ph. D. Thesis. University of Texas, Austin, TX.

Kempter, K. A., and Rowe, G. L. (2000). Leakage of Active Crater lake brine through the north flank at Rincon de la Vieja volcano, northwest Costa Rica, and implications for crater collapse. *J. Volcanol. Geother. Res.* 97, 143–159. doi: 10.1016/S0377-0273(99)00181-X

Kusakabe, M., Komoda, Y., Takano, B., and Abiko, T. (2000). Sulfur isotopic effects in the disproportionation reaction of sulfur dioxide in hydrothermal fluids: implications for the δ34S variations of dissolved bisulfate and elemental sulfur from active crater lakes. *J. Volcanol. Geotherm. Res.* 97, 287–307. doi: 10.1016/S0377-0273(99)00161-4

Lewicki, J. L., Kelly, P. J., Bergfeld, D., Vaughan, R. G., and Lowenstern, J. B. (2017). Monitoring gas and heat emissions at Norris Geyser Basin, Yellowstone National Park, USA based on a combined eddy covariance and Multi-GAS approach. *J. Volcanol. Geother. Res.* 347, 312–326. doi: 10.1016/j.jvolgeores.2017.10.001

Mastin, L. G., and Witter, J. B. (2000). The hazards of eruptions through lakes and seawater. *J. Volcanol. Geother. Res.* 97, 195–214. doi: 10.1016/S0377-0273(99)00174-2

Molina, F., and Martí, J. (2016). The Borinquen geothermal system (Cañas Dulces caldera, Costa Rica). *Geothermics* 64, 410–425. doi: 10.1016/j.geothermics.2016.07.001

Molina, F., Martì J., Aguirre, G., Vega, E., and Chavarria, L. (2014). Stratigraphy and structure of the Canas Dulces caldera (Costa Rica). *Geol. Soc. Am. Bull*. 126, 1448–1466. doi: 10.1130/B31012.1

Moretti, R., Papale, P., and Ottonello, G. (2003). A model for the saturation of C–O–H–S fluids in silicate melts. *Geol. Soc. Lond. Spec. Publ.* 213, 81–101. doi: 10.1144/GSL.SP.2003.213.01.06

Ohmoto, H., and Lasaga, A. C. (1982). Kinetics of reactions between aqueous sulfates and sulfides in hydrothermal systems. *Geochim. Cosmochim. Acta* 46, 1727–1745.

Oikawa, T., Yoshimoto, M., Nakada, S., Maeno, F., Komori, J., and Shimano, T. (2016). Reconstruction of the 2014 eruption sequence of Ontake Volcano from recorded images and interviews. *Earth Planet. Space* 68:79. doi: 10.1186/s40623-016-0458-5

Oppenheimer, C. (1992). Sulphur eruptions at Volcan Poas, Costa Rica. *J. Volcanol. Geother. Res.* 49, 1–21.

OVSICORI (Observatorio Vulcanologico y Sismologico de Costa Rica), (1995). *Actividad Eruptiva del Volcan Rincon de la Vieja durante los dias 6–13 de noviembre, 1995.* Open report, OVSI- CORI-UNA, p. 42.

Pasternack, G. B., and Varekamp, J. C. (1997). Volcanic lake systematics I. Physical constraints. *Bull. Volcanol.* 58, 528–538.

Pering, T. D., Tamburello, G., McGonigle, A. J. S., Aiuppa, A., Cannata, A., Giudice, G., et al. (2014). High time resolution fluctuations in volcanic carbon dioxide degassing from Mount Etna. *J. Volcanol. Geotherm. Res.* 270, 115–121. doi: 10.1016/j.jvolgeores.2013.11.014

Rouwet, D., and Morrissey, M. M. (2015). "Mechanisms of crater lake breaching eruptions," in *Volcanic Lakes*, eds D. Rouwet, B. W. Christenson, F. Tassi, and J. Vandemeulebrouck (Heidelberg: Springer).

Rye, R. O. (2005). A review of the stable-isotope geochemistry of sulfate minerals in selected igneous environments and related hydrothermal systems. *Chem. Geol.* 215, 5–36. doi: 10.1016/j.chemgeo.2004.06.034

Shinohara, H., Hirabayashi, J., Nogami, K., and Iguchi, M. (2011). Evolution of volcanic gas composition during repeated culmination of volcanic activity at Kuchinoerabujima volcano, Japan. *J. Volcanol. Geotherm. Res.* 202, 107–116. doi: 10.1016/j.jvolgeores.2011.01.011

Shinohara, H., Yoshikawa, S., and Miyabuchi, Y. (2015). "Degassing activity of a volcanic crater lake: volcanic plume measurements at the yudamari crater lake, aso Volcano, Japan," in *Volcanic Lakes, Advances in Volcanology*, eds D. Rouwet, B. Christenson, F. Tassi, and J. Vandemeulebrouck (Berlin; Heidelberg: Springer).

Stix, J., and de Moor, J. M. (2018). Understanding and forecasting phreatic eruptions driven by magmatic degassing. *Earth Planet. Space* 70:83. doi: 10.1186/s40623-018-0855-z

Symonds, R. B., Gerlach, T. M., and Reed, M. H. (2001). Magmatic gas scrubbing: implications for volcano monitoring. *J. Volcanol. Geother. Res.* 108, 303–341. doi: 10.1016/S0377-0273(00)00292-4

Symonds, R. B., Janik, C. J., Evans, W. C., Ritchie, B. E., Counce, D., Poreda, R. J., et al. (2003). Scrubbing masks magmatic degassing during repose at Cascade-Range and Aleutian-Arc volcanoes. *US Geol. Surv. Open File Rep.* 3, 3–435. Available online at: http://pubs.usgs.gov/of/2003/0435/

Takano, B., Ohsawa, S., and Glover, R. B. (1994). Surveillance of Ruapehu Crater Lake, New Zealand, by aqueous polythionates. *J. Volcanol. Geother. Res.* 60, 29–57. doi: 10.1016/0377-0273(94)90096-5

Tamburello, G. (2015). Ratiocalc: Software for processing data from multicomponent volcanic gas analyzers. *Comput. Geosci.* 82, 63–67. doi: 10.1016/j.cageo.2015.05.004

Tamburello, G., Agusto, M., Caselli, A., Tassi, F., Vaselli, O., Calabrese, S., et al. (2015). Intense magmatic degassing through the lake of Copahue volcano, 2013–2014. *J. Geophys. Res. Solid Earth* 120, 6071–6084. doi: 10.1002/2015JB012160

Tassi, F., Vaselli, O., Capaccioni, B., Giolito, C., Duarte, E., Fernandez, E., et al. (2005), The hydrothermal-volcanic system of Rincón de la Vieja volcano (Costa Rica): a combined (inorganic and organic) geochemical approach to understanding the origin of the fluid discharges and its possible application to volcanic surveillance. *J. Volcanol. Geother. Res.* 148, 315–333. doi: 10.1016/j.jvolgeores.2005.05.001

Tassi, F., Vaselli, O., Fernandez, E., Duarte, E., Martinez, M., Delgado, A., et al. (2009). Morphological and geochemical features of crater lakes in Costa Rica: an overview. *J. Limnol.* 68, 193–205. doi: 10.3274/JL09-68-2-04

Varekamp, J. C., Pasternack, G. B., and Rowe, G. L. Jr. (2000). Volcanic lake systematics II. Chemical constraints. *J. Volcanol. Geother. Res.* 97, 161–179. doi: 10.1016/S0377-0273(99)00182-1

Conflict of Interest Statement: The authors declare that the research was conducted in the absence of any commercial or financial relationships that could be construed as a potential conflict of interest.

frontiers in Earth Science

ORIGINAL RESEARCH
published: 13 February 2019
doi: 10.3389/feart.2018.00241

A Rapidly Convecting Lava Lake at Masaya Volcano, Nicaragua

Tom D. Pering[1]*, **Tehnuka Ilanko**[1], **Thomas C. Wilkes**[1], **Rebecca A. England**[1], **Siân R. Silcock**[1], **Leigh R. Stanger**[2], **Jon R. Willmott**[2], **Robert G. Bryant**[1] and **Andrew J. S. McGonigle**[1,3]

[1] Department of Geography, University of Sheffield, Sheffield, United Kingdom, [2] Department of Electronic and Electrical Engineering, University of Sheffield, Sheffield, United Kingdom, [3] School of Geosciences, The University of Sydney, Sydney, NSW, Australia

Lava lakes provide a rare opportunity to study conduit flow processes through direct observation of the exposed magma surface. The recent lava lake activity at Masaya volcano (Nicaragua), which commenced in 2015, displayed several unusual phenomena. We report on the dynamics of this rapidly convecting lake, which, to the best of our knowledge manifested the highest lava flow velocities ever reported for a lava lake: 13.7–16.4 m s^{-1}, in addition to unusual fluid dynamic behavior involving alteration in surface flow direction. We studied this system with multiparametric and high time resolution remote sensing measurements, performed during June 2017, including ultraviolet camera observations of SO_2 emission rates, near infrared thermal camera measurements and video analyses of the lake surface. Median SO_2 emission rates of 3.1 (±0.8) and 3.7 (±0.9) kg s^{-1} were found, which are lower than previously published estimates, and could represent challenging remote sensing conditions or a waning in lava lake activity. Video analyses enabled characterization of frequent bursts of approximately hemispherical spherical-cap bubbles on the surface with diameters ranging 0.6–8.5 m (median of 2.6 m), and calculation of individual bubble masses, which contribute to active bubble bursting values estimated at 1.9 to 3.9 kg s^{-1}. We show that only a small fraction, 7–17%, of total emission volumes are contributed by these bubbles, based on estimated emission rates of 22.5 and 26.9 kg s^{-1}. Furthermore, periodicity analysis reveals regular 200–300 s oscillations in SO_2 emissions. These are not shared by any of our other datasets and particularly during the contemporaenously acquried thermal data, hence, we tentatively assign an atmospheric causal generation mechanism, driven by atmospheric transport and turbulence phenomena, such as eddying. Overall, we highlight the uniquely high velocity and fluid dynamic behavior of Masaya lava lake.

Keywords: lava lake, sulfur dioxide emissions, spherical-cap bubble, rapid convection, multiparametric, lake velocity

OPEN ACCESS

Edited by:
Franco Tassi,
Università degli Studi di Firenze, Italy

Reviewed by:
Dmitri Rouwet,
National Institute of Geophysics and Volcanology (INGV), Italy
Mark Thomas,
University of Leeds, United Kingdom

***Correspondence:**
Tom D. Pering
t.pering@sheffield.ac.uk

Specialty section:
This article was submitted to Volcanology,
a section of the journal
Frontiers in Earth Science

Received: 03 September 2018
Accepted: 13 December 2018
Published: 13 February 2019

Citation:
Pering TD, Ilanko T, Wilkes TC, England RA, Silcock SR, Stanger LR, Willmott JR, Bryant RG and McGonigle AJS (2019) A Rapidly Convecting Lava Lake at Masaya Volcano, Nicaragua.
Front. Earth Sci. 6:241.
doi: 10.3389/feart.2018.00241

INTRODUCTION

Lava lakes are one of the most spectacular volcanic phenomena, providing the opportunity to observe actively convecting magmatic systems. However, the rarity of these lakes, coupled with logistic and accessibility issues, limit our ability to study them. Between December 2015 and March 2016, a lava lake emerged at Masaya volcano in Nicaragua (Global Volcanism Program, 2017; Aiuppa et al., 2018), manifesting a rapidly convecting and turbulent lava surface.

This provided a valuable opportunity to study the dynamics of this vigorously convecting lava lake, which appeared to share some characteristic surface behaviors with those at Villarrica (Chile; Moussallam et al., 2016) and Ambrym (Vanuatu; Allard et al., 2016a,b), i.e.; turbulent surfaces punctuated by frequent bubble bursts, which cover a significant proportion of the lake surface. Such behavior is in direct contrast with the prolonged slower surface motions and cooled plates exhibited at Halema'uma'u Crater, Kilauea (USA; Patrick et al., 2016), Erta Ale (Ethiopia; Jones et al., 2006), and Nyiragongo (Congo; Burgi et al., 2014). **Table 1** summarizes key characteristics of lava lakes across the globe.

The dynamics of lava lakes can be investigated through the study of gas emissions (e.g., Nadeau et al., 2015; Moussallam et al., 2016), gas ratios (e.g., Ilanko et al., 2015; Allard et al., 2016a,b), thermal fluxes (e.g., Spampinato et al., 2008; Peters et al., 2014a; Radebaugh et al., 2016), seismicity (e.g., Palma et al., 2008; Richardson et al., 2014), infrasound (e.g., Bouche et al., 2010) and visible video imagery (e.g., Harris et al., 2005). Of these, gas studies can provide information on the style of magma convection through identification of temporal trends in emission and ratio data. Moussallam et al. (2016) identified three broad models to explain lava lake behaviors: (1) fluctuating uni-directional flow (e.g., Witham et al., 2006) where upward and downward magma flow alternate, (2) bi-directional flow (e.g., Kazahaya et al., 1994) where both upward and downward flow occur at the same time, i.e., via convection, and (3) bubble flux driving heat transfer into a lava lake (e.g., Bouche et al., 2010). These models can, in combination or in isolation, help explain variations in visible lava lake behaviors such as the movement of lava lake surfaces, changes in lake level, and surface activities, e.g., spattering, bubble bursting and fountaining (Moussallam et al., 2016).

TABLE 1 | An overview of current and past lava lakes, their dimensions, lake surface velocities (where available) and degassing characteristics associated with those.

Volcano	Diameter (m)	Velocity (m s^{-1})	SO$_2$ ER (kg s^{-1})	References
Ambrym (Benbow)	25	–	75	1, 2
Ambrym (Marum)	50	5	25	1, 3
Erebus	30	<0.1	0.9	4, 5
Erta Ale	34–100	0.01–0.4	0.7	6, 7, 8, 9, 10
Kilauea	180 by 250*	0.3	10.1 ± 8.4	11, 12
Masaya	50	13.7–16.4	0–17	13, This Study
Nyamulagira	20–200	–	162	14
Nyiragongo	~50–240^	–	13 ± 9	15, 16
Villarrica	22 by 32*	–	1.6–1.9	17

*Non-circular lake; ^;since 2002. References: (1) Allard et al. (2016a); (2) Allard et al. (2016b); (3) Radebaugh et al. (2016); (4) Peters et al. (2014a,b); (5) Oppenheimer and Kyle (2008); (6) Oppenheimer et al. (2004); (7) Harris et al. (2005); (8) Jones et al. (2006); (9) Spampinato et al. (2008); (10) Vergniolle and Bouche (2016); (11) Nadeau et al. (2015); (12) Patrick et al. (2016); (13) Aiuppa et al. (2018); (14) Bobrowski et al. (2017); (15) Arellano et al. (2017); (16) Burgi et al. (2014); and (17) Moussallam et al. (2016).

Masaya is an open vent, basaltic volcano (Walker et al., 1993; Stix, 2007), which has four pit craters at its summit, with recent activity concentrated solely within the Santiago crater (Rymer et al., 1998). The very recent appearance of the lava lake at Masaya, which was initiated in the latter half of 2015 (Global Volcanism Program, 2017), has produced a number of publications (Stephens et al., 2017; Aiuppa et al., 2018; Stephens and Wauthier, 2018; Wilkes et al., 2018). Of these reports, Aiuppa et al. (2018) give a thorough overview of gas emissions and ratios between 2014 and 2017. These authors identified an initial CO$_2$-rich plume composition prior to lake formation, which then became more SO$_2$-rich as the lake appeared at the surface, however, their data only extended to early 2017, prior to our own field study, performed in June of that year.

Here, using a multiparametric dataset captured from ultraviolet camera, thermal, and visible measurements performed during June 2017, we present a study into the high temporal resolution dynamics of Masaya lava lake.

METHODS, RESULTS, AND ANALYSIS

In order to study the behavior associated with the lava lake at Masaya we applied a range of high time resolution remote sensing imaging approaches to capture visual, thermal and degassing phenomena. Our fieldwork on Masaya volcano was conducted between the 12th and 18th June 2017. We note that our observations only provide information about the lava lake behavior during this period. Indeed, the lava lake activity has changed significantly since its inception, in terms of magma level within the crater, the number of active vents (Global Volcanism Program, 2017), and in the fluid behavior of the lake (see **Supplementary Table 1** for video links).

Figure 1 shows the characteristics of the lake during our fieldwork period. The lake exhibited rapid surface motion, with lava moving from an inflow in the southeast toward the northwest. As this material hit the crater walls, it overturned, creating vigorous splashbacks that threw individual lava clots onto the lake surface and walls. In addition, near-circular burst events were observed to occur with high frequently (several per second) across the lake surface. We hypothesize that these correspond to the release of spherical-cap bubbles, given the burst dimensions and presence within a wider fluid, i.e., the bubbles are not constrained within a narrow conduit (Wegener and Parlange, 1973; Bhaga and Weber, 1981). From our observation position on the crater rim (11.983043°, −86.168961°) it was not possible to observe the entire lake. Where the lava first entered the field of view it appeared to travel at high horizontal velocities. However, the portion not visible from our vantage point was visible from the opposite side of the crater, where the lava appears to be traveling at slower horizontal velocities. Unfortunately, it was not possible to measure the velocity of the lake from that point as only a small fraction of the lake was visible.

All location data are provided in the **Supplementary Material** Google Earth File. Where central values are given for datasets, we report either the mean or the median depending on the statistical distribution. The mean is given for normally distributed and

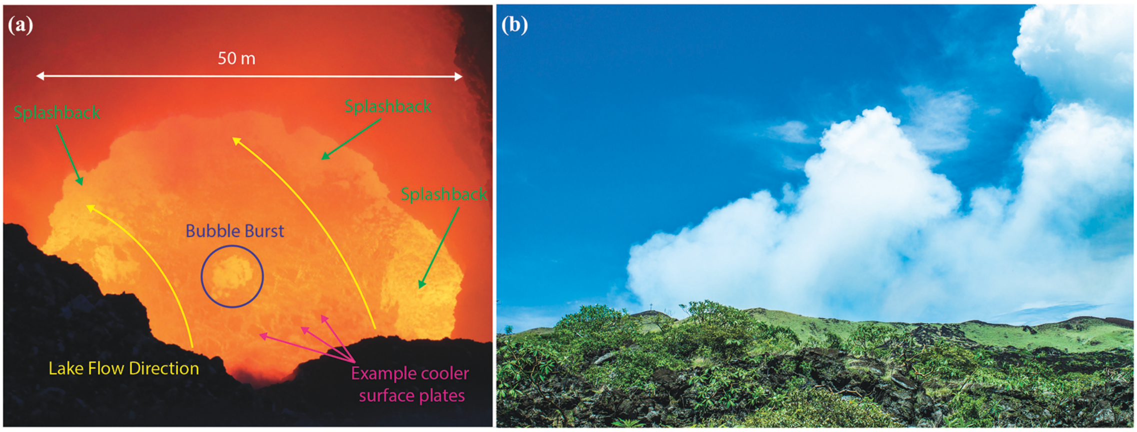

FIGURE 1 | (a) An overview of the features of Masaya lava lake during our period of measurement in June 2017, and **(b)** an image of typical conditions during the measurements.

the median for non-normally distributed data, as assessed using Skewness and Kurtosis. The presence of periodicity within the datasets was also investigated using: Fast Fourier transform (FFT) via Welch's method (Welch, 1967), Lomb-Scargle analysis for unevenly sampled data (Lomb, 1976; Scargle, 1982), and the continuous wavelet transform (CWT) using the Morlet wavelet (Morlet et al., 1982; Torrence and Compo, 1998; Grinsted et al., 2004). All of these approaches are commonly used for detecting periodicity in environmental datasets (Pering et al., 2014a) and were implemented in this study using Matlab® routines.

UV Camera Data

UV camera data were acquired from the flanks of Masaya on 15 and 18 June 2017 (Local Time) using the low-cost "PiCam" instrumentation of Wilkes et al. (2016, 2017). For full hardware details of these units please see Wilkes et al. (2016, 2017). Here we give a brief synopsis of UV camera acquisition and processing protocols, which are discussed in detail elsewhere (e.g., Kantzas et al., 2010; McGonigle et al., 2017).

The two deployed cameras have filters (produced by Edmund Optics Inc.) with full width at half maxima of 10 nm, centered on 310 and 330 nm, respectively. These are the two wavelengths where SO_2 absorbs and does not absorb, respectively. Images from the cameras were taken synchronously at a rate of 0.25 Hz. The data were linearly interpolated to 1 Hz timeseries after processing, to facilitate comparison with other datasets. Dark and clear sky images were taken to correct for sensor noise and inhomogeneous illumination (vignetting) of the sensor. The images were aligned to correct for small offsets between the camera alignment, and the pixel intensities were converted to uncalibrated absorption values, using the Beer-Lambert law. These data were then converted to column amount values, on the basis of calibration with gas cells of known concentration (0, 304 ± 31 and 1,257 ± 58 ppm m). To calculate each SO_2 emission rate the integrated column amount (ICA) along a defined line (see **Figure 2a**) was multiplied by the plume speed, calculated using cross correlation, which has associated errors of $<10\%$ (McGonigle et al., 2005; Williams-Jones et al., 2006).

The plume at Masaya was optically thick above a certain height. We therefore selected integration lines across the plume width as close as possible to the crater rim during processing. Cross correlation was used rather than optical flow for plume speed determination, as at this ICA location optical flow methods did not sufficiently register the plume motion, likely a failure of the optical flow algorithm used. The optical thickness also causes a deviation from the Beer-Lambert law, leading to errors in retrievals of SO_2 emission rates. Kern et al. (2013) studied the effects of varying plume optical thicknesses and plume SO_2 column amounts (ranging 0–10,000 ppm·m). For conditions in the plume at Masaya with approximate maximum SO_2 column amounts of 2000 ppm·m at a viewing distance of <2 km from the gas, the authors suggested a 20% deviation from Beer-Lambert law, and we therefore take this as our error arising from this effect. Furthermore, given our proximity to the plume, error from light dilution is expected to be low—at the lower end of the 20–80% quoted by Campion et al. (2015). Overall, therefore, the root-mean-square error (assuming a lower light dilution error of +20% (i.e., a systematic underestimation of SO_2 content), plume speed error of ±10%, deviation from Beer-Lambert law of ±20%, and accuracy of ±10% on gas cell concentrations) associated with our UV camera measurements is estimated at ∼25%.

UV camera data for 18 June 2017 are displayed in **Figure 2b**, and for 15 June 2017 in **Figure S1**. See **Supplementary Video 1**, where puffing behavior of the plume is evident. Our UV camera emission rate data had medians of $\sim 3.1 \pm 0.8$ and 3.7 ± 0.9 kg s^{-1} and ranged ∼0.9–5.7 kg s^{-1} and ∼0.8–5.6 kg s^{-1}, on the 15th and 18th, respectively. Aiuppa et al. (2018) report median daily SO_2 emission rates of 0–17 kg s^{-1} between March 2014 and March 2017, with an average median daily emission rate of 7.8 kg s^{-1} on the basis of data from the NOVAC network (Johansson et al., 2009; Galle et al., 2010). The temporal difference between the data from Aiuppa et al. (2018) and our study

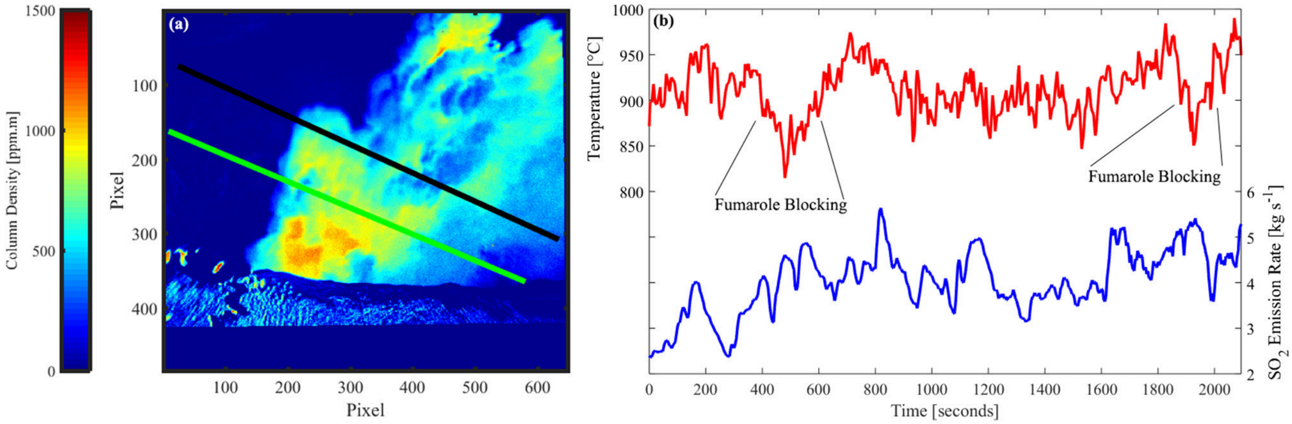

FIGURE 2 | (a) an example absorption image from 18th June with indicated integration lines for determining integrated column amount (green line) and plume speed via cross correlation (black line), **(b)** example temperature (red line) and SO_2 emission rate (blue line) traces through time during a period of synchronous acquisition on the 18th June.

precludes a direct comparison. However, our data fits within their general reported range. Although, it is possible that SO_2 emissions are too low because of the optically thick plume (Kern et al., 2013).

NIR Thermal Measurements

We used a Raspberry Pi near infrared (NIR) system identical to that described in Wilkes et al. (2018). The camera system operates on the principle of Planck's law, which is that all objects radiate according to their temperature. Hotter objects radiate with greater power and with a peak wavelength that becomes shorter at higher temperatures. If an object is hotter than approximately 600°C then it radiates with significant power that can be measured by silicon cameras. This enables thermal imaging to be undertaken with the very mature technology used in consumer cameras; achieving low cost, high resolution and high frame rates. Daylight can interfere with the measurements and so 850 nm filters are used to virtually eliminate the daylight, whilst leaving significant sensitivity in the NIR region that silicon technology is sensitive to. This unit operated in the ∼850–1,100 nm wavelength region, by virtue of an installed 850 nm long pass filter (Thorlabs, RG850), to provide sensitivity at magmatic temperatures. The camera had a 10° field of view, achieved using a 3D printed lens holder and custom optical system (a Cooke Triplet lens specifically designed for the application), and was situated above the lava lake on the crater terrace. Images were taken on 12, 14, 15, 17, and 18 June 2017 (full datasets are provided in the **Supplementary Material**). There are a number of sources of uncertainty with this technique, including calibration, sensor noise, flat-field, emissivity, and path transmission. For full details of camera construction, calibration and discussion of uncertainty calculation, see Wilkes et al. (2018). On the basis of this article we consider the error in temperature to be ∼10–15°C, in the range of reported temperatures ∼800–1,100°C.

Post-acquisition, the images were stabilized for camera motion and then interrogated for temperature fluctuations across the whole lake area, indicating a median temperature range of ∼911–994°C, as detailed in **Table 2**. An example thermal flux trace is displayed alongside contemporaneous UV camera time series data from 18 June 2017 in **Figure 2b**. Visible dips in thermal flux, associated with obscuration by a fumarole which obscured the lake surface sporadically, are indicated. See **Figure S2** for example calibrated images, and an example acquisition sequence is available via **Supplementary Video 2**.

TABLE 2 | An overview of median temperatures acquired from near infrared acquisitions on indicated dates.

Date (UTC)	Time start (UTC)	Time finish (UTC)	Median temperature (°C)
12/06/17	17:44:42	18:11:57	982
12/06/17	18:12:20	18:44:48	980
14/06/17	16:49:46	18:18:38	980
14/06/17	18:19:26	18:58:38	994
16/06/17	00:00:04	00:16:46	996
16/06/17	00:20:32	00:54:02	980
17/06/17	23:46:09	00:34:51	930
18/06/17	00:36:36	00:55:42	930
18/06/17	18:20:15	18:55:09	911

DSLR Camera

Visible video capture of the lava lake dynamics was conducted using a Canon EOS 1100D DSLR camera, which recorded video at 25 fps at a resolution of 1,280 by 720 pixels, using a 75–300 mm focal length lens. Videos were recorded on the 12, 14, 15, and 17 June 2017 (local date), and we selected videos from the 17th for analysis based on their length and clarity (see **Supplementary Video 3**). Lake velocity was calculated using particle image velocimetry (PIV) with a Matlab GUI (PIVlab) detailed by Thielicke and Stamhuis (2014). PIV is a common method for mapping fluid flow velocities (Raffel et al., 2007).

Our images were pre-processed using the in-built PIVlab CLAHE (contrast limited adaptive histogram equalization) method, which sharpened the contrast between different regions of the lake surface (e.g., the cooler plates). During analysis, PIVlab splits each image into a matrix of cells (interrogation areas), and then calculates the offset between subsequent images in

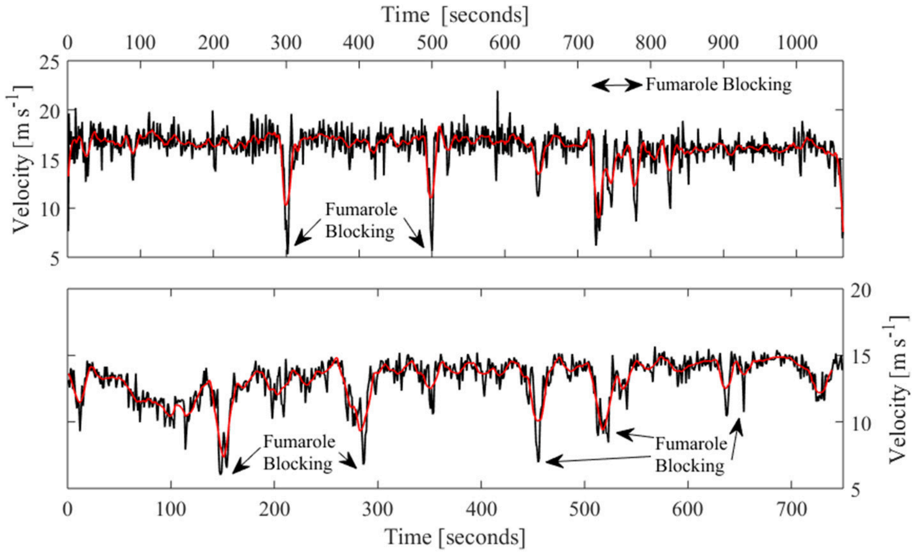

FIGURE 3 | Two separate examples of average lake surface velocity (on the region of interest) through time. Arrows indicate where fumaroles significantly blocked the view of the lava lake and affected the velocity analysis.

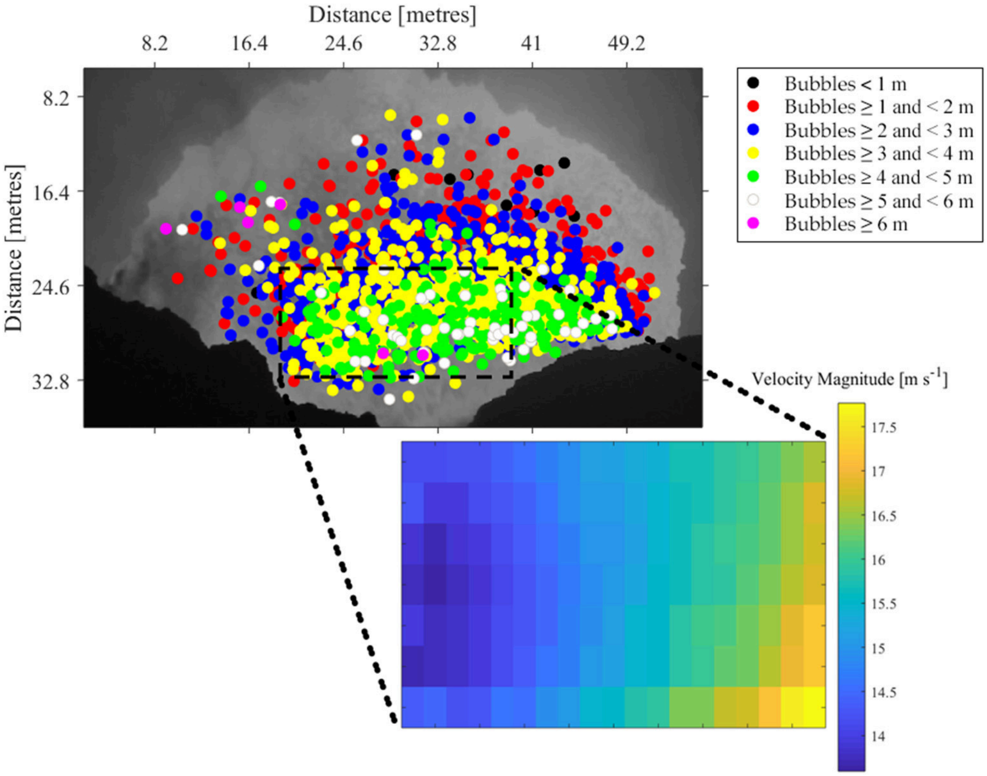

FIGURE 4 | Monochrome image of the lava lake with bubble burst positions indicated, highlighting the general trend that as bubbles get larger their median "Y-axis" position moves closer to the point at which the lavas arrive at the lake surface. Dashed rectangle indicates the region of interest used to calculate averaged pixel area velocity.

time. We used a fast Fourier transform (FFT) option for this to reduce computational burden. A region of interest (ROI) on the lake surface was selected that did not overlap with the area of vigorous splashback, and, as far as possible, avoided obscuration by fumarolic gas (see **Figures 1a**, **4**). The direction of lake motion was determined by manually tracking cooled surface plates using ImageJ (https://imagej.nih.gov/ij/) and software plugin MTrackJ (Meijering et al., 2012; https://imagescience.org/meijering/software/mtrackj/).

The calculated median lake surface velocities (**Figure 3**) of 13.7–16.4 m s^{-1} (49.3–59.0 km h^{-1}) are to the best of our knowledge, by far the highest ever reported for a lava lake: see **Table 1** for data for other lava lakes across the globe. In addition, this velocity was observed to vary across the lake. **Figure 4** shows

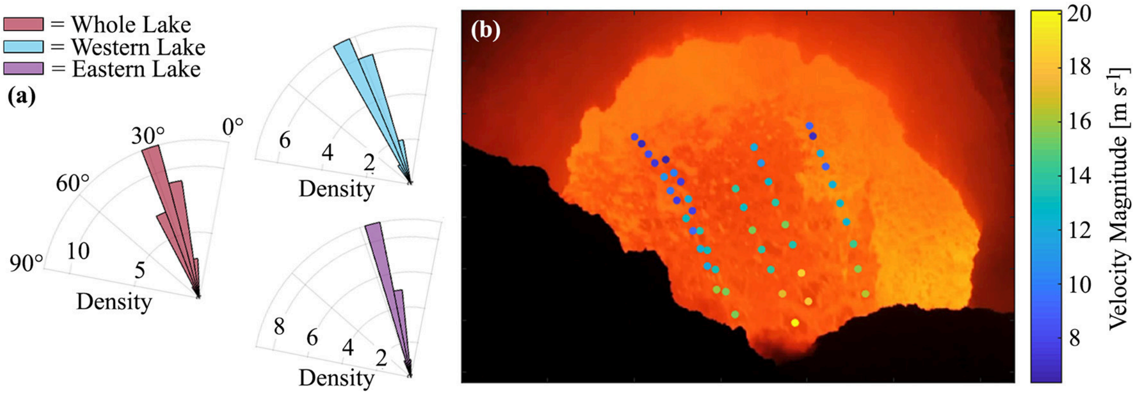

FIGURE 5 | (a) Direction of tracked plates from first appearance to disappearance across the whole lake, and the right and left sides. Left and right were determined by splitting the lake in half. **(b)** representative plate tracks, with each dot color coded by its measured velocity. A clear curving and reduction in velocity is highlighted.

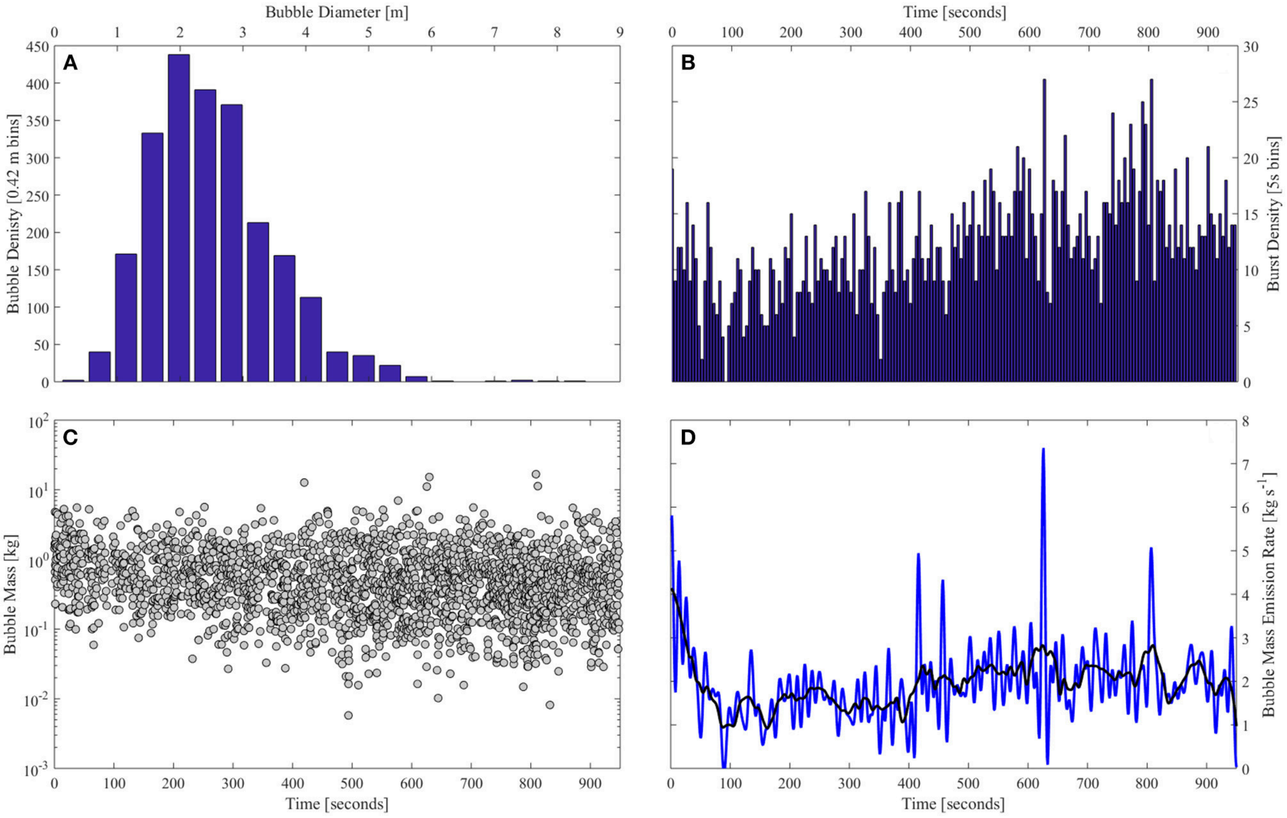

FIGURE 6 | (A) the distribution of bubble burst diameters on the lake surface, **(B)** the number of bursts in 5 s bins, **(C)** the mass of each bubble burst through time, and **(D)** bubble mass emission rate with a superimposed savitzy golay filter of 1 min.

averaged velocity values for segments of the ROI indicated by the dashed box. There is a clear difference in flow velocity from the point the lava first enters our imagery, at >17.5 m s^{-1}, to the western portions of the lake where velocities slow to <14 m s^{-1}. There is also a clear difference between lake velocity and curvature on the western and eastern portion of the lake, i.e., the eastern portion is faster by 1–2 m s^{-1}, while the western and eastern portions were angled at >30° and <30°, respectively (see **Figure 5**). This highly unique behavior is reminiscent of the cresting of water in a waterfall or a river rapid, i.e., a change in the vertical gradient of the magma causes an acceleration of the fluid.

MtrackJ was also used to map the surface positions, diameters, and time of bubble bursts, these phenomena were readily resolvable given their clear circular imprint on the lake surface (see **Figure 1a**). Given the reasonable assumption that each bursting bubble is of spherical-cap morphology, i.e., the bubble is not constrained within a narrow conduit, which would promote Taylor bubble formation (e.g., a similar analysis was performed on Erta 'Ale by Bouche et al., 2010; see also Pering and McGonigle, 2018), we can then calculate the masses of individual bubbles. We use the constant 0.57 and our measured bubble diameter d_b to convert to the term d_e (a characteristic length scale of a cap bubble), the equivalent diameter, as per Davies and Taylor (1950):

$$d_b = \frac{d_e}{0.57}$$

We then used d_e, to calculate the volume of the bubble (V_b) at burst, after Joseph (2003):

$$d_e = \left(\frac{6V_b}{\pi}\right)^{\frac{1}{3}}$$

The number of moles in each bubble can then be derived from the ideal gas law ($PV = nRT$), where P is atmospheric pressure

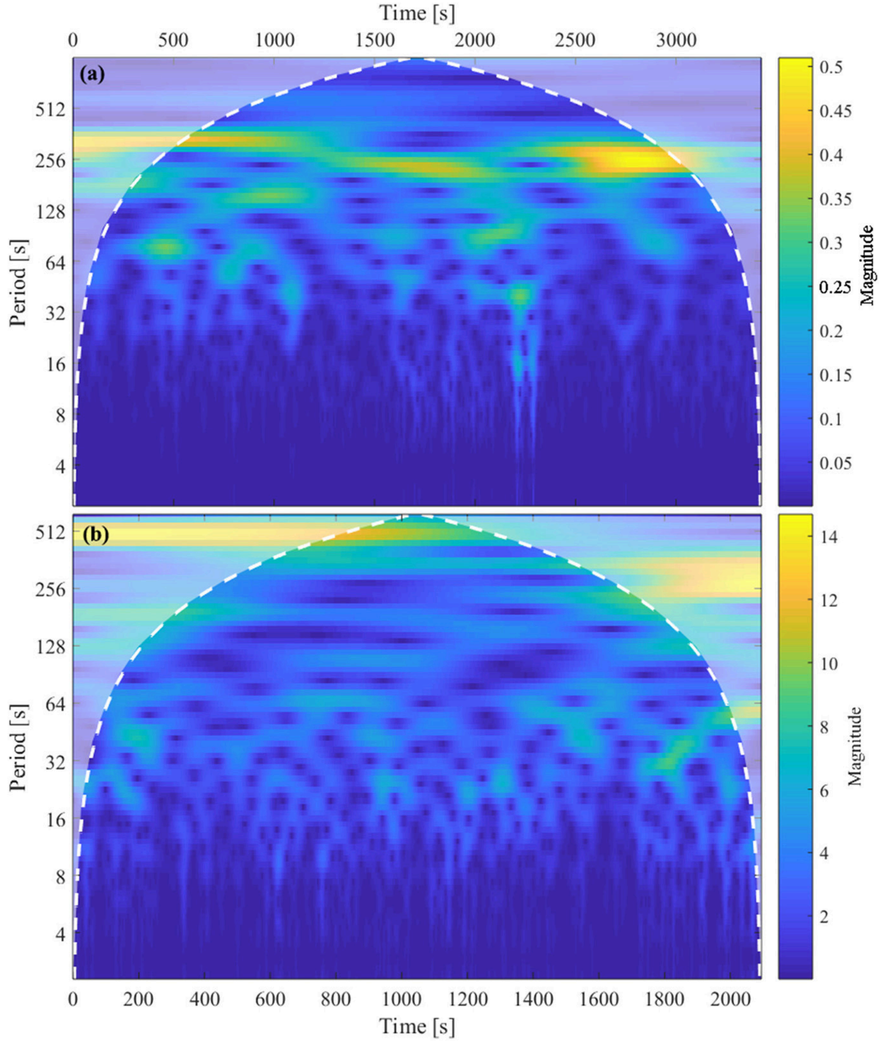

FIGURE 7 | Wavelet power spectrum analysis of synchronous data from 18/06/17 of **(a)** UV camera emission rates and **(b)** the thermal camera data, showing a potential periodicity at ~200–300 s in the UV data which isn't shared in the thermal time series. Dashed white line indicates the wavelet cone of influence. Note differing times on the x axes.

(Pa), V is volume (m^3), n are the number of moles in the bubble, R is the real gas constant (8.314 J^{-1} mol^{-1}), and T is the temperature in Kelvin (taken to be 1,238 K, e.g., 965°C, which was the average surface temperature recorded from our thermal camera images during the entire measurement period). Here, we have used atmospheric pressure to approximate the bursting pressure of all bubbles. In reality, the rheological characteristics of the magma mean that the pressure threshold for bursting will be above atmospheric values (e.g., Del Bello et al., 2012); pressure is therefore a key source of error in our estimates of number of moles per bubble. Using the molar gas ratios from Aiuppa et al. (2018), ($CO_2/SO_2 = 5$ and $H_2O/SO_2 = 10$), we can calculate the following molar proportions for the major volcanic gases: 6% SO_2; 31% CO_2; and 63% H_2O. These ratios are from data reported for the latter part of 2016 and early 2017, which are the most contemporaneously available data for our measurement period (see Figures 2b,f in Aiuppa et al. (2018)) and best available given the lack of direct measurement of bubble molar composition. These molar proportions can then be converted to mass of each gas species in the bubble, and thus total mass. Assuming atmospheric pressure at burst, the median total bubble mass is therefore 0.5 kg, with a range of 5×10^{-3}-15.4 kg. In total, 1,830 kg was released from 2,351 bubble bursts over the 948 s observation sequence, corresponding to a bubble flux of ~1.9 kg s^{-1} (**Figures 6C,D**). However, in an approximate sensitivity analysis we can estimate the effect of a change in pressure on our results. For example, a doubling in burst pressure would give a median total bubble mass of 1.0 kg, with 3,741 kg released in total, and a bubble flux of 3.9 kg s^{-1}. Based on both these burst pressure scenarios bubble flux accounts for 7% to 17% of the total emission rates of 22.5 and 26.9 kg s^{-1} for 15 and 18 June 2017, estimated from the UV camera SO_2 data combined with ratios from Aiuppa et al. (2018). This indicates that a relatively low proportion of emissions are derived from these active bubble bursts.

Bubble burst diameters ranged from 0.6 to 8.5 m, with a median of 2.6 m (**Figure 6A**). There is no clear temporal pattern in bubble bursts behavior (**Figure 6B**). There is, however, a significant difference between the median "Y-axis" positions of bubble bursts when considering ranged steps of 1 m up to 6 m in diameter (t-tests significant at the 0.05 significance level for steps of 1 m), with a strong trend for larger diameter bubbles bursting closest to the lake entrance area, which probably reflects the faster ascent time of large diameter spherical-cap bubbles (Joseph, 2003). In the western portion of the lava lake there are four bubble bursts of >6 m, which could result from the collection of multiple smaller bubbles against the crater wall.

Periodicity and Regression Analysis

All of the acquired datasets (UV emission rate, thermal, lake surface velocity, bubble burst frequency, bubble location, bubble diameter, and bubble mass) were investigated for potential periodicities and relationships through use of regression. The one interval of overlap between the UV and thermal data (18/06/18) revealed no clear linkage between the two datasets (see **Figure 7**), although the UV data contain potential periodicities on timescales of 200–300 s. There were no clear periodicities in any of the analyzed thermal data, and those in the bubble burst and velocity data were only evident at short periods, <20 s, and likely driven by random fluctuations. Furthermore, there were no clear relationships between the thermal and velocity datasets.

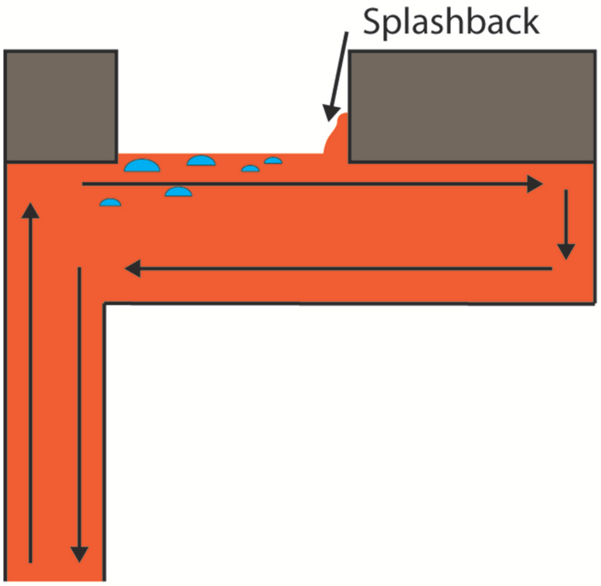

FIGURE 8 | An illustration of hypothetical lava lake behavior at Masaya. Arrows indicated possible directions of fluid flow. The deflection of rapidly ascending magma into a surface chamber could drive the processes measured at the surface, through the "window" available to observers.

In the field, puffs of gas were visibly emanating from the crater area at regular intervals (see **Figure 1B**) during the acquisition periods, and we cannot rule out a volcanogenic cause for this activity. However, given the lack of apparent correlation between the UV camera and thermal data, we tentatively posit an atmospheric causal mechanism for the periodicity in the former dataset. An atmospheric mechanism could relate to micro-climatological conditions around the volcano and/or atmospheric transport and turbulence phenomena, such as eddying, which could be driven by crater geometry. This said, we cannot rule out at this stage that a magmatic or an alternative volcanogenic mechanism (e.g., through CO_2 or H_2O rich pulses) could drive this puffing given the short period of overlapping thermal and UV camera data. In order to investigate these hypotheses, contemporaneous gas ratio data would be required (e.g., Multi-GAS, as in Pering et al., 2014b).

DISCUSSION AND CONCLUSION

Here we highlight the dynamics of the recent lava lake at Masaya volcano, which manifested, to the best of our knowledge, the highest surface velocities (13.7–16.4 m s^{-1}) ever reported for a lava lake. In comparison, despite its turbulent surface motion and comparatively high gas emissions, even the surface velocities at Ambrym volcano are two to three times lower than those for Masaya (**Table 1**). Whilst the lake surface at Villarrica volcano appeared to also manifest rapid lateral motion (see Supplementary Videos of Moussallam et al., 2016), its velocity was not quantified in that article. The flow velocities at Masaya lava lake are indeed more reminiscent of lava flow behavior rather than convective overturn in a lava lake, but even the infamous flows of Nyiragongo in 2002 only reached 2.8–5.6 m s^{-1} (Favalli et al., 2009) and lava streams within lava tubes at Kilauea have only been observed to flow at velocities up to 4.2 m s^{-1} by Kauahikaua et al. (1998). Velocities comparable to those reported here may be theoretically possible for the longest basaltic lava flows on Earth (of over 100 km in length), e.g., >4–12 m s^{-1} (Keszthelyi and Self, 1998), further highlighting the uniqueness of our observations. It should, however, be noted that at the first point of the lava appearing at the surface, i.e., further to the southeast than visible in the imagery used for our analyses, the lava surface appeared to be traveling at visibly reduced velocities (see videos in **Supplementary Table 1**). This intimates some mechanism whereby the lava velocity increases, and then, as observed in our velocity analysis, begins to slow. We also observed a curvature in lake motion that was more pronounced on the western than eastern side (**Figure 5**). **Figure 8** highlights a possible causal mechanism, involving the deflection of rapidly ascending magma into a surface chamber, where observers see only a window into this process.

Our gas data, with SO_2 emission rates of 3.1–3.7 kg s^{-1}, are similar to those reported by Aiuppa et al. (2018), but are toward the lower range of reported values, during an earlier stage of the lava lake (with data ending in early 2017). This is consistent with the general waning in activity throughout 2017 as seen in our video, but measurements were potentially hampered by an optically thick plume, so are likely an underestimation (Kern et al., 2013). **Supplementary Table 1** shows videos from different stages of the lake's activity, highlighting that early on in the lake's existence, the rapid lateral motion of its surface was punctuated by visibly larger bursts, which were not present during our measurement period. This reduction in explosion rates, and potentially lava lake level, is entirely consistent with the lower SO_2 emission rates reported here.

Periodicity analysis only revealed oscillations in the SO_2 emission dataset (of period 200–300 s), and not in any of the other datasets, suggesting that as per Moussallam et al. (2016) at Villarrica, turbulent mixing of the magma within the conduit disrupts any potential periodicity, and that the detected periodicity in the degassing data was of atmospheric origin. Specifically, any large puffs of gas, which would likely be driven by the bursting of large bubbles, were not observed on the lake surface. Furthermore, the absence of clear periodicity in thermal data suggests that a gas-rich and higher temperature pulse could also not drive the periodic behavior. The range of bubble diameters was 0.6–8.5 m, a wider range than the 3–6 m observed at Erta 'Ale by Bouche et al. (2010), but with a lower median value at Masaya of 2.6 m. We suggest that these bursting bubbles have little influence on the dynamics of the lake, given their small contribution to total gas emissions (∼7–17%; figures which are likely lower given possible underestimation of SO_2 emissions). It is likely that they are formed within the conduit, as this would explain the observation that larger diameter bubbles burst closer to the lake entrance area than those of smaller diameters; i.e., a larger diameter spherical-cap bubble will ascend at a faster velocity than a smaller one (Joseph, 2003) and therefore appear sooner at the surface than smaller bubbles, which are transported further into the lake by the rapid convection before bursting. In contrast, if bubbles were formed within the lake their size distribution ought not to vary according to location.

This study highlights the wealth of information that can be gained through the combination of visible, thermal, and gas emission imaging data, revealing a lava lake with a uniquely high flow velocity with lake surface punctuated by the bursting of spherical-cap bubbles. Similar approaches at other volcanoes could provide further refinement on our understanding of how degassing processes drive the dynamics of lava lakes and other basaltic classes of activity.

DATA AVAILABILITY STATEMENT

Access to the supplementary information "Locations.kmz" Google Earth locations file is available on request from the corresponding author.

AUTHOR CONTRIBUTIONS

TP, TW, and RE conducted the fieldwork. JW, AM, RB, and LS provided significant technical help with instrumentation. TI, RE, SS, and TP conducted analysis. TP wrote the manuscript.

FUNDING

TP acknowledges funding from the Royal Society (RG170226). RE and TP were supported by a University of Sheffield GLOSS studentship. AM acknowledges funding from a Leverhulme Research Fellowship (RF-2016-580) and The Rolex Institute. JW acknowledges support of a EPSRC Fellowship (EP/M009106/1).

ACKNOWLEDGMENTS

Thanks to INETER (Istituto Nicaraguense de Estudios Territoriales), in particular Wilfried Strauch, and the Masaya National Park for providing help with access to the volcano.

SUPPLEMENTARY MATERIAL

The Supplementary Material for this article can be found online at: https://www.frontiersin.org/articles/10.3389/feart.2018.00241/full#supplementary-material

REFERENCES

Aiuppa, A., Maarten de Moor, J., Arellano, S., Coppola, D., Francofonte, V., Galle, B., et al. (2018). Tracking formatino of a lava lake from ground and space: Masaya volcano (Nicaragua), 2014–2017. *Geochem. Geophys. Geosyst.* 19, 496–414. doi: 10.1002/2017/GC007227

Allard, P., Aiuppa, A., Bani, P., Métrich, N., Betagnini, A., Gauthier, P.-J., et al. (2016a). Prodigious emission rates and magma degassing budget of major, trace and radioactive volatile species from Ambrym basaltic volcano, Vanuatu island Arc. *J. Volcanol. Geother. Res.* 322, 119–143. doi: 10.1016/j.volgeores.2015.10.004

Allard, P., Burton, M., Sawyer, G., and Bani, P. (2016b). Degassing dynamics of basaltic lava lake at a top-ranking volatile emitter: Ambrym volcano, Vanuatu arc. *Earth Planet. Sci. Lett.* 448, 69–80. doi: 10.1016/j.epsl.2016.05.014

Arellano, S., Yalire, M., Galle, B., Bobrowski, N., Dingwell, A., et al. (2017). Long-term monitoring of SO_2 quiescent degassing from Nyiragongo's lava lake. *J. Afr. Earth Sci.* 134, 866–873. doi: 10.1016/j.afrearsci.2016.07.002

Bhaga, D., and Weber, M. E. (1981). Bubbles in viscous liquids: shapes, wakes, and velocities. *J. Fluid Mech.* 105, 61–85.

Bobrowski, N., Giuffrida, G. B., Arellano, S., Yalire, M., Liotta, M., Brusca, L., et al. (2017). Plume composition and volatile flux of Nyamulagira volcano, Democratic Republic of Congo, during birth and evolution of the lava lake, 2014–2015. *Bull. Volcanol.* 79:90. doi: 10.1007/s00445-017-1174-0

Bouche, E., Vergniolle, S., Staudacher, T., Nercessian, A., Delmont, J.-C., Frogneux, M., et al. (2010). The role of large bubbles detected from acoustic measurements on the dynaics of Erta 'Ale lava lake (Ethiopia). *Earth Planet. Sci. Lett.* 295, 37–48. doi: 10.1016/j.epsl.2010.03.020

Burgi, P.-Y., Darrah, T. H., Tedesco, D., and Eymold, W. K. (2014). Dynamics of the Mount Nyiragongo lava lake. *J. Geogr. Res. Solid Earth* 119, 4106–4122. doi: 10.1002/2013JB010895

Campion, R., Delgado-Granados, H., and Mori, T. (2015). Image-based correction of the light dilution effect for SO_2 camera measurements. *J. Volcanol. Geother. Res.* 300, 48–57. doi: 10.1016/j.volgeores.2015.01.004

Davies, R. M., and Taylor, G. I. (1950). The mechanics of large bubbles rising through extended liquids and through liquids in tubes. *Proc. R. Soc. Lond. A* 200, 375–390. doi: 10.1098/rspa.1950.0023

Del Bello, E., Llewellin, E. W., Taddeucci, J., Scarlato, P., and Lane, S. J. (2012). An analytical model for gas overpressure in slug-driven explosions: insights into Strombolian volcanic eruptions. *J. Geophys. Res. Solid Earth* 117. doi: 10.1029/2011JB008747

Favalli, M., Chirico, G. D., Papale, P., Pareschi, M. T., and Boschi, E. (2009). Lava flow hazard at Nyiragongo volcano, D.R.C. *Bull. Volcanol.* 71, 363–374. doi: 10.1007/s00445-008-0233-y

Galle, B., Johansson, M., Rivera, C., Zhang, Y., Kihlman, M., Kern, C., et al. (2010). Network for Observation of Volcanic and Atmospheric Change (NOVAC)—A global network for volcanic gas monitoring: network layout and instrument description. *J. Geophys. Res.* 115:D05304. doi: 10.1029/2009JD011823

Global Volcanism Program (2017). *Masaya*. Available online at: https://volcano.si.edu/volcano.cfm?vn=344100#bgvn_201709 (Accessed August 1, 2018).

Grinsted, A., Moore, J. C., and Jevrejeva, S. (2004). Application of the cross wavelet transform and wavelet coherence to geophysical time series. *Nonlinear Processes Geophys.* 11, 561–566. doi: 10.5194/npg-11-561-2004

Harris, A. J. L., Carniel, R., and Jones, J. (2005). Identification of variable convective regimes at Erta Ale Lava Lake. *J. Volcanol. Geother. Res.* 142, 207–223. doi: 10.1016/j.volgeres.2004.11.011

Ilanko, T., Oppenheimer, C., Burgisser, A., and Kyle, P. (2015). Cyclic degassing of Erebus volcano, Antarctica. *Bull. Volcanol.* 77:56. doi: 10.1007/s00445-015-0941-z

Johansson, M., Galle, B., Zhang, Y., Rivera, C., Chen, D., and Wyser, K. (2009). The dual-beam mini-DOAS technique—measurements of volcanic gas emission, plume height and plume speed with a single instrument. *Bull. Volcanol.* 71, 747–751. doi: 10.1007/s00445-008-0260-8

Jones, J., Carniel, R., Harris, A. J. L., and Malone, S. (2006). Seismic characteristics of variable convection at Erta 'Ale lava lake, Ethiopia. *J. Volcanol. Geother. Res.* 153, 64–79. doi: 10.1016/j.volgeores.2005.08.004

Joseph, D. D. (2003). Rise velocity of a spherical cap bubble. *J. Fluid Mech.* 488, 213–223. doi: 10.1017/S0022112003004968

Kantzas, E. P., McGonigle, A. J. S., Tamburello, G., Aiuppa, A. and Bryant, R. G. (2010). Protocols for UV camera volcanic SO2 measurements. *J. Volcanol. Geotherm. Res.* 194, 55–60. doi: 10.1016/j.jvolgeores.2010.05.003

Kauahikaua, J., Cashman, K. V., Mattox, T. N., Heliker, C. C., Hon, K. A., Mangan, T. M., et al. (1998). Observations on basaltic lava streams in tubes from Kilauea Volcano, island of Hawai'i. *J. Geophys. Res.* 103, 27303–27323.

Kazahaya, K., Shinhara, H., and Saito, G. (1994). Excessive degassing of Izu-Oshima volcano: magma convection in a conduit. *Bull. Volcanol.* 56, 207–216. doi: 10.1007/BF00279605

Kern, C., Werner, C., Elias, T., Sutton, A. J., and Lubcke, P. (2013). Applying UV camera for SO2 detection to distant or optically thick volcanic plumes. *J. Volcanol. Geotherm. Res.* 262, 80–89. doi: 10.1016/j.volgeores.2013.06.009

Keszthelyi, L., and Self, S. (1998). Some physical requirements for the emplacement of long basaltic lava flows. *J. Geophys. Res.* 103, 27447–27464.

Lomb, N. R. (1976). Least-squares frequency analysis of unequally spaced data. *Astrophys. Space Sci.* 39, 447–462. doi: 10.1007/BF00648343

McGonigle, A. J. S., Hilton, D. R., Fischer, T. P., and Oppenheimer, C. (2005). Plume velocity determination for volcanic SO_2 flux measurements. *Geophys. Res. Lett.* 32:L11302. doi: 10.1029/2005GL022470

McGonigle, A. J. S., Pering, T. D., Wilkes, T. C., Tamburello, G., D'Aleo, R., Bitetto, M., et al. (2017). Ultraviolet imagine of volcanic plumes: a new paradigm in volcanology. *Geosciences* 7:68. doi: 10.3390/geosciences7030068

Meijering, E., Dzyubackyk, O., and Smal, I. (2012). "Methods for cell and particle tracking," In: *Imaging and Spectroscopic Analysis of Living Cells, Methods in Enzymology*, ed P. M. Conn. 183–200.

Morlet, J., Arens, G., Fourgeau, E., and Giard, D. (1982). Wave propagation and sampling theory—Part 1: complex signal and scattering in multilayered media. *Geophysics* 47, 203–221. doi: 10.1190/1.1441328

Moussallam, Y., Bani, P., Curtis, A., Barnie, T., Moussallam, M., Peters, N., et al. (2016). Sustaining persistent lava lakes: observations from high-resolution gas measurements at Villarrica volcano, Chile. *Earth Planet. Sci. Lett.* 454, 237–247. doi: 10.1016/j.epsl.2016.09.012

Nadeau, P. A., Werner, C. A., Waite, G. P., Carn, S. A., Brewer, I. D., Elias, T., et al. (2015). Using SO_2 camera imagery and seismicity to examine degassing and gas accumulation at Kilauea Volcano, May 2010. *J. Volcanol. Geother. Res.* 300, 70–80. doi: 10.1016/j.volgeores.2014.12.005

Oppenheimer, C., and Kyle, P. R. (2008). Probing the magma plumbing of Erebus volcano, Antarctica, by open-path FTIR spectroscopy of gas emissions. *J. Volcanol. Geother. Res.* 177, 743–754. doi: 10.1016/j.volgeores.2007.08.022

Oppenheimer, C., McGonigle, A. J. S., Allard, P., Wooster, M. J., and Tsanev, V. (2004). Sulfur, heat, and magma budget of Erta 'Ale lava lake, Ethiopia. *Geology* 32, 509–512. doi: 10.1130/G20281.1

Palma, J. L., Calder, E. S., Basualto, D., Blake, S., and Rothery, D. A. (2008). Correlations between SO_2 flux, seismicity, and outgassing activity at the open vent of Villarrica volcano, Chile. *J. Geophys. Res.* 113:B10201. doi: 10.1029/2008JB005577

Patrick, M. R., Orr, T., Swanson, D. A., and Lev, E. (2016). Shallow and deep controls on lava lake surface motion at Kilauea Volcano. *J. Volcanol. Geother. Res.* 328, 247–261. doi: 10.1016/j.volgeores.2016.11.010

Pering, T. D., and McGonigle, A. J. S. (2018). Combining spherical-cap and taylor bubble fluid dynamics with plume measruements to characterize basaltic degassing. *Geosciences* 8:42. doi: 10.3390/geosciences8020042

Pering, T. D., Tamburello, G., McGonigle, A. J. S., Aiuppa, A., Cannata, A., Giudice, G., et al. (2014a). High time resolution fluctuations in volcanic carbon dioxide degassing from Mount Etna. *J. Volcanol. Geother. Res.* 270, 115–121. doi: 10.1016/j.volgeores.2013.11.014

Pering, T. D., Tamburello, G., McGonigle, A. J. S., Hanna, E., and Aiuppa, A. (2014b). Correlation of oscillatory behaviour in Matlab using wavelets. *Computers Geosci.* 70, 206–212. doi: 10.1016/j.cageo.2014.06.006

Peters, N., Oppenheimer, C., Killingsworth, D. R., Frechette, J., and Kyle, P. (2014b). Correlation of cycles in Lava Lake motion and degassing at Erebus Volcano, Antarctica. *Geochem. Geophys. Geosyst.* 15, 3244–3257. doi: 10.1002/2014GC005399

Peters, N., Oppenheimer, C., Kyle, P., and Kingsbury, N. (2014a). Decadal persistence of cycles in lava lake motion at Erebus volcano, Antarctica. *Earth Planet. Sci. Lett.* 395, 1–12. doi: 10.1016/j.epsl.2014.03.032

Radebaugh, J., Lopes, R. M., Howell, R. R., Lorenz, R. D., and Turtle, E. P. (2016). Eruptive behavior of the Marum/Mbwelesu lava lake, Vanuatu and comparisons with lava lakes on Earth and Io. *J. Volcanol. Geother. Res.* 322, 105–118. doi: 10.1016/j.volgeores.2016.03.019

Raffel, M., Willert, C. E., Wereley, S. T., and Kompenhans, J. (2007). *Particle Image Velocimetry: A Practical Guide, 2nd Edn.* New York, NY: Springer.

Richardson, J. P., Waite, G. P., and Palma, J. L. (2014). Varying seismic-acoustic properties of the fluctuating lava lake at Villarrica volcano, Chile. *J. Geophys. Res. Solid Earth* 119, 5560–5573. doi: 10.1002/2014JB011002

Rymer, H., van Wyk de Vries, B., Stix, J., and Williams-Jones, G. (1998). Pit crater structure and processes governing persistent activity at Masaya Volcano, Nicaragua. *Bull. Volcanol.* 59, 345–355.

Scargle, J. D. (1982). Studies in astronomical time series analysis. II—Statistical aspects of spectral analysis of unevenly spaced data. *Astrophys. J.* 263, 835–853. doi: 10.1086/160554

Spampinato, L., Oppenheimer, C., Calvari, S., Cannata, A., and Montalto, P. (2008). Lava lake surface characterization by thermal imaging: Erta 'Ale volcano (Ethiopia). *Geochem. Geophys. Geosyst.* 9:e2164. doi: 10.1029/2008GC002164

Stephens, K. J., Ebmeier, S. K., Young, N. K., and Biggs, J. (2017). Transient deformation associated with explosive eruption measured at Masaya volcano (Nicaragua) using Interferometric Synthetic Aperture Radar. *J. Volcanol. Geother. Res.* 344, 212–223. doi: 10.1016/j.volgeores.2017.05.014

Stephens, K. J., and Wauthier, C. (2018). Satellite geodesy captures offset magma supply associated with lava lake appearance at Masaya volcano, Nicaragua. *Geophys. Res. Lett.* 45, 2669–2678. doi: 10.1002/2017GL076769

Stix, J. (2007). Stability and instability of quiescently active volcanoes: the case of Masaya, Nicaragua. *Geology* 35, 535–538. doi: 10.1130/g23198a.1

Thielicke, W., and Stamhuis, E. J. (2014). PIVlab—Towards user-friendly, affordable and accurate digital particle image velocimetry in MATLAB. *J. Open Res. Softw.* 2:e30. doi: 10.5334/jors.bl

Torrence, C., and Compo, G. P. (1998). A practical guide to wavelet analysis. *Bull. Am. Meteorol. Soc.* 79, 61–78. doi: 10.1175/1520-0477(1998)079

Vergniolle, S., and Bouche, E. (2016). Gas-driven lava lake fluctuations at Erta'Ale volcano (Ethiopia) revealed by MODIS measurements. *Bull. Volcanol.* 78:60. doi: 10.1007/s00445-016-1047-y

Walker, J. A., Williams, S. N., Kalamarides, R. I., and Feigenson, M. D. (1993). Shallow open-system evolution of basaltic magma beneath a subduction zone volcano—The Masaya Caldera Complex, Nicaragua. *J. Volcanol. Geother. Res.* 56, 379–400.

Wegener, P. P., and Parlange, J. (1973). Spherical-cap bubbles. *Ann. Rev. Fluid Mech.* 5, 79–100.

Welch, P. D. (1967). The use of fast fourier transform for the estimation of power spectra: a method based on time averaging over short, modified periodograms. *IEEE Transac. Audio Electroacoust.* 15, 70–73. doi: 10.1109/TAU.1967.1161901

Wilkes, T. C., McGonigle, A. J. S., Pering, T. D., Taggart, A. J., White, B. S., Bryant, R. G., et al. (2016). Ultraviolet imaging with low cost smartphone sensors: development and application of a Raspberry Pi-based UV camera. *Sensors* 16:1649. doi: 10.3390/s16101649

Wilkes, T. C., Pering, T. D., McGonigle, A. J. S., Tamburello, G., and Willmott, J. R. (2017). A low-cost smartphone sensor-based UV camera for volcanic SO_2 emission measurements. *Rem. Sens.* 9:27. doi: 10.3390/rs9010027

Wilkes, T. C., Stanger, L. R., Willmott, J. R., Pering, T. D., McGonigle, A. J. S., and England, R. A. (2018). The development of a low-cost, near infrared high-temperature thermal imaging system and its application to the retrieval of accurate lava lake temperatures at Masaya volcano, Nicaragua. *Rem. Sens.* 10:450. doi: 10.3390/rs10030450

Williams-Jones, G., Horton, K. A., Elias, T., Garbeil, H., Mouginis-Mark, P. J., Sutton, A. J., et al. (2006). Accurately measuring volcanic plume velocity with multiple UV spectrometers. *Bull. Volcanol.* 68, 328–332. doi: 10.1007/s00445-005-0013-x

Witham, F., Woods, A. W., and Gladstone, C. (2006). An analogue experimental model of depth fluctuations in lava lakes. *Bull. Volcanol.* 69, 51–56. doi: 10.1007/s00445-006-0055-8

Conflict of Interest Statement: The authors declare that the research was conducted in the absence of any commercial or financial relationships that could be construed as a potential conflict of interest.

frontiers in Earth Science

ORIGINAL RESEARCH
published: 26 February 2019
doi: 10.3389/feart.2019.00009

Multi-year Satellite Observations of Sulfur Dioxide Gas Emissions and Lava Extrusion at Bagana Volcano, Papua New Guinea

Brendan T. McCormick Kilbride[1]*, Kila Mulina[2], Geoffrey Wadge[3], R. Wally Johnson[4], Ima Itikarai[2] and Marie Edmonds[1]

[1] COMET, Department of Earth Sciences, University of Cambridge, Cambridge, United Kingdom, [2] Rabaul Volcanological Observatory, Rabaul, Papua New Guinea, [3] COMET, Department of Meteorology, University of Reading, Reading, United Kingdom, [4] School of Asia and the Pacific, Australian National University, Canberra, ACT, Australia

Bagana, arguably the most active volcano in Papua New Guinea, has been in a state of near-continuous eruption for over 150 years, with activity dominated by sluggish extrusion of thick blocky lava flows. If current extrusion rates are representative, the entire edifice may have been constructed in only 300–500 years. Bagana exhibits a remarkably high gas flux to the atmosphere, with persistent sulfur dioxide (SO_2) emissions of several thousand tons per day. This combination of apparent youth and high outgassing fluxes is considered unusual among persistently active volcanoes worldwide. We have used satellite observations of SO_2 emissions and thermal infrared radiant flux to explore the coupling of lava extrusion and gas emission at Bagana. The highest gas emissions (up to 10 kt/day) occur during co-extrusive intervals, suggesting a degree of coupling between lava and gas, but gas emissions remain relatively high ($\sim$2,500 t/d) during inter-eruptive pauses. These passive emissions, which clearly persist for decades if not centuries, require a large volume of degassing but non-erupting magma beneath the volcano with a substantial exsolved volatile phase to feed the remarkable SO_2 outgassing: an additional $\sim$1.7–2 km^3 basaltic andesite would be required to supply the excess SO_2 emissions we observe in our study interval (2005 to present). That this volatile phase can ascend freely to the surface under most conditions is likely to be key to Bagana's largely effusive style of activity, in contrast with other persistently active silicic volcanoes where explosive and effusive eruptive styles alternate.

Keywords: Bagana volcano, satellite remote sensing, sulfur dioxide, lava extrusion, OMI, MODIS

Edited by:
Andrew McGonigle,
University of Sheffield,
United Kingdom

Reviewed by:
Hiroshi Shinohara,
Geological Survey of Japan (AIST),
Japan
Alessandro Tibaldi,
Università degli studi di Milano
Bicocca, Italy

***Correspondence:**
Brendan T. McCormick Kilbride
brendanvolc@gmail.com

Specialty section:
This article was submitted to
Volcanology,
a section of the journal
Frontiers in Earth Science

Received: 27 April 2018
Accepted: 18 January 2019
Published: 26 February 2019

Citation:
McCormick Kilbride BT, Mulina K,
Wadge G, Johnson RW, Itikarai I and
Edmonds M (2019) Multi-year Satellite
Observations of Sulfur Dioxide Gas
Emissions and Lava Extrusion at
Bagana Volcano, Papua New Guinea.
Front. Earth Sci. 7:9.
doi: 10.3389/feart.2019.00009

1. INTRODUCTION

Long-lived eruptions from silicic volcanoes are a common and hazardous mode of volcanism. Over two hundred volcanoes have exhibited cycles of lava dome-building and destruction in the Holocene (Global Volcanism Program, 2013), and two thirds of the fatalities caused by volcanic activity since 1600 CE are attributed to eruptions at these volcanoes (Auker et al., 2013). The characteristics of persistent silicic volcanism include: the emplacement of lava flows and domes composed of crystal-rich, high viscosity lava (10^6–10^{11} Pa s); strongly cyclic behavior with episodes of lava extrusion punctuated by violent Vulcanian or sub-Plinian explosive eruptions; and relatively slow extrusion rates (10^{-2}–10^{-1} km^3 year^{-1}) that may persist for months or years (Druitt and Kokelaar, 2002; Sherrod et al., 2008; Power et al., 2010; Wadge et al., 2014; Sheldrake et al., 2016). Many persistently active silicic volcanoes are also major sources of volcanic gas, with outgassing fluxes remaining high even during pauses between eruptive phases (Delgado-Granados et al., 2001; Edmonds et al., 2003; Arellano et al., 2008; Lopez et al., 2013b).

Few volcanoes worldwide are so persistently active as Bagana, Papua New Guinea, which has many of the traits outlined above (long-lived eruptions, crystal-rich magmas, slow extrusion rate, substantial outgassing) yet seems to lack the classic episodic extrusive/explosive eruption cycle so characteristic of dome-building volcanoes (Barmin et al., 2002; Sheldrake et al., 2016). Bagana has exhibited near-continuous extrusion of andesitic lava flows since it was first observed by scientists in the 1840s (Bultitude et al., 1978; Wadge et al., 2012) and is a remarkable emitter of sulfur dioxide (SO$_2$) with the highest persistent outgassing flux of any volcano worldwide without a lava lake (McGonigle et al., 2004b; McCormick et al., 2012; Carn et al., 2017). The volcano's remote location precludes regular visits and satellite remote sensing has emerged as a key tool for studying Bagana (McCormick et al., 2012; Wadge et al., 2012, 2018). Many aspects of Bagana's activity remain enigmatic, including the mechanisms of its prodigious gas output and the key processes controlling the timing and intensity of lava extrusion.

In this contribution we use satellite observations to explore the activity of Bagana over the last decade with a particular focus on lava extrusion and SO$_2$ gas emissions. We show that Bagana's activity is strongly episodic, with phases of lava extrusion and elevated gas emissions lasting for several months, separated by pauses of similar duration where extrusion may cease. We find clear evidence for strong co-eruptive coupling between gas and magma, but also for substantial passive gas emissions during inter-eruptive pauses. We consider it likely that a substantial exsolved volatile phase is present in the shallow plumbing system (Wallace, 2005; Wallace and Edmonds, 2011; Parmigiani et al., 2016; Edmonds and Woods, 2018), comprising a large proportion of the co-eruptive gas flux and dominating the inter-eruptive passive emissions. This volatile-rich phase could exert a strong influence on eruptive style: a permeability drop in the upper conduit impeding gas escape is an important mechanism for triggering explosive eruptions (Stix et al., 1993; Edmonds et al., 2003; Geirsson et al., 2014). Explosive eruptions do occur infrequently at Bagana and threaten surrounding isolated villages with ashfall, debris avalanche and pyroclastic flow inundation. Deeper insight into volcanic processes at Bagana will benefit from careful analyses of recent erupted products, and dedicated ground-based monitoring. At a minimum we advocate continued satellite surveillance of this active and potentially dangerous volcano.

2. GEOLOGICAL CONTEXT

2.1. Tectonic Setting and Volcanism on Bougainville

Bagana is located on Bougainville Island, geographically part of the Solomon archipelago but politically an autonomous region of Papua New Guinea (PNG). PNG lies in a complex tectonic buffer zone between the southwest–northeast converging Australian continent and the Ontong-Java plateau in the Pacific Ocean (**Figure 1a**). The interactions of rotating microplates—the Woodlark, Adelbert, North and South Bismarck, and Solomon Sea plates—control the volcanic and seismic activity in the region. Volcanism on Bougainville is a consequence of the Solomon Sea plate being subducted beneath the Pacific plate. Total convergence across the boundary is rapid (93–110 mm/yr), earthquake locations point to a steeply dipping ($\sim 70^o$) slab, and water depths in the adjacent trench exceed 8,000 m (Tregoning et al., 1998; Syracuse and Abers, 2004; Holm and Richards, 2013; Holm et al., 2016).

Blake (1968) identifies seventeen post-Miocene volcanoes on Bougainville, running southeast along the mountainous central spine of the island (**Figure 1b**). Two caldera-forming eruptions at Billy Mitchell, of VEI 5 and 6, respectively, are dated to 1030 ± 25 and 1580 ± 20 Common Era (Global Volcanism Program, 2013). Balbi and Loloru exhibit fumarolic activity and are considered dormant. The remainder of Bouganville's volcanoes show no signs of activity and are considered extinct. Bougainville and the other Solomon Islands are largely formed of Tertiary and Quaternary volcanic rocks, derived sediments, and subordinate limestones (Blake and Miezitis, 1967; Blake, 1968). The highest point on Bougainville is the summit of Balbi (2,591 m); Bagana's summit elevation is currently 1,897 m (Wadge et al., 2018).

2.2. Bagana Volcano

Bagana is an andesitic lava cone, a stratovolcano dominantly built of overlapping lava flows with only small volumes of pyroclastics. Reliable observations date to 1842 and the characteristic activity comprises the extrusion of slow-moving blocky lava flows persisting for weeks to months (Blake, 1968; Bultitude, 1976, 1981; Cooke and Johnson, 1978; Bultitude and Cooke, 1981). The lava flows are tens of meters thick and exhibit prominent levee-bound margins on the volcano's steep upper and medial slopes and extensive lateral spread into steep-fronted lobes at lower elevations (**Figure 2**). Satellite radar observations of lava extrusion during 2010-11 revealed strongly pulsatory extrusion rates, with a 14-month mean of 0.92 m^3 s^{-1} (Wadge et al., 2012). By digital elevation model (DEM) differencing over timescales from years to decades, Wadge et al. (2018) calculated a mean extrusion rate of ∼1.0 m^3 s^{-1} for 1945–2014. If these extrusion rates are representative, the entire Bagana edifice—estimated by Wadge et al. (2018) to have volume of 5.1–9.6 km^3—could have been built in only 300–500 years.

Bagana's shallow summit crater can be occupied by a small lava dome but this is frequently obscured by a dense gas plume emanating from numerous fumaroles on the dome surface (**Figure 2**). Infrequent explosive eruptions destroy the dome,

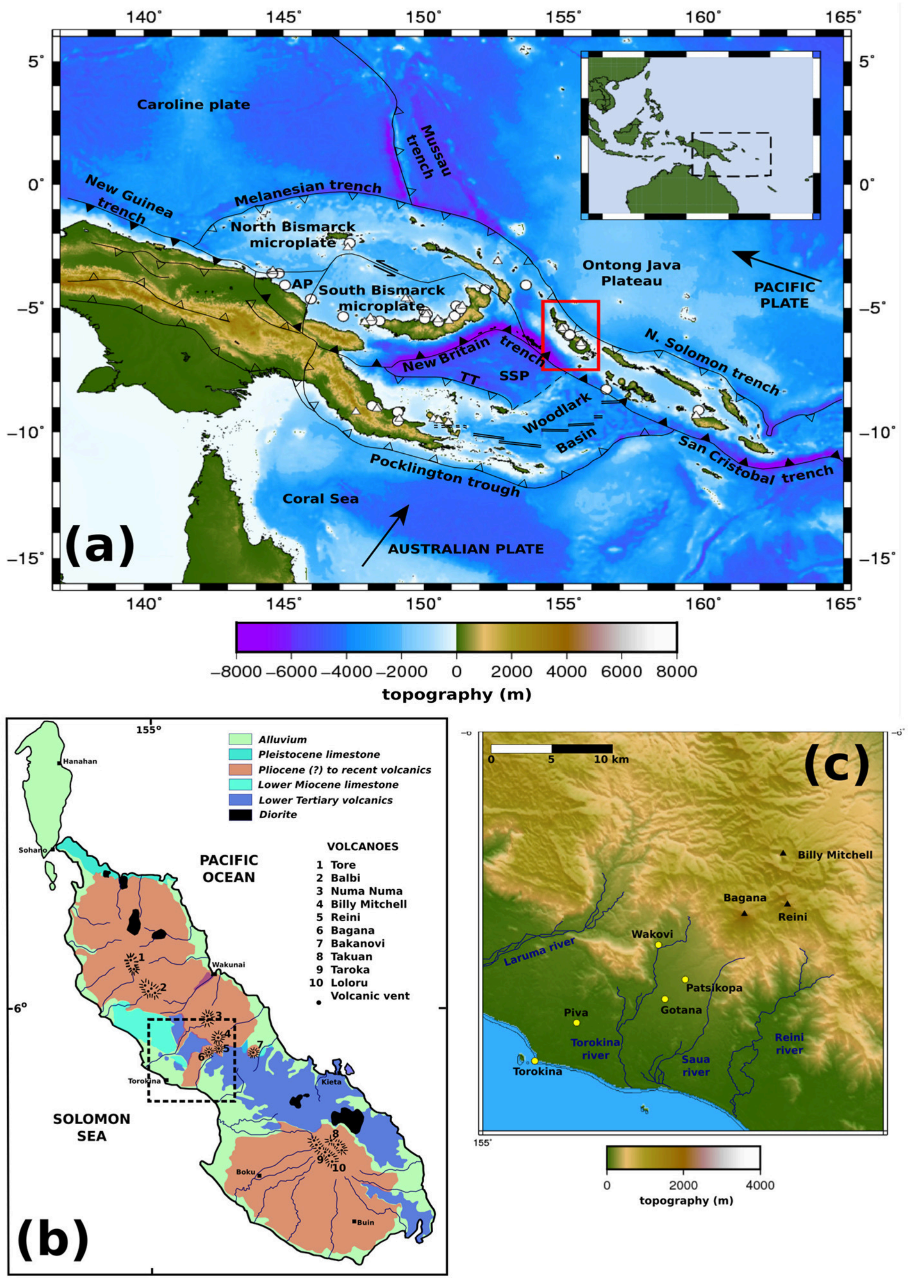

FIGURE 1 | (a) Tectonic setting of Papua New Guinea. Topography and bathymetry from EOAA ETOPO1 Global Relief Model (doi: 10.7289/V5C8276M). Plate names, boundaries and arrows indicating rate and direction of motion from Holm et al. (2016). AP, Adelbert Microplate; TT, Trobriand Trough; SSP, Solomon Sea Plate. Ticked boundaries are subduction zones, with active (black triangles) and inactive (open triangles) margins distinguished. **(b)** Sketch geological map of Bougainville showing major lithologies and known volcanoes, redrawn from Blake (1968). **(c)** Bagana environs with settlements, rivers and neighboring volcanoes indicated. Topography from Shuttle Radar Topography Mission, USGS, 2000.

modify the geometry of the crater rim, and may influence the downslope direction of lava flows. There are extensive scree and talus deposits on the volcano flanks sourced from lava flows, pyroclastic density currents and debris avalanches. We (BMK) visited Bagana in September 2016 and recent debris flow deposits extended 4.5 km from the summit. Ephemeral hot springs are reported around the base of the cone, and we noted high water temperatures (∼60°C) in tributaries of the Torokina river close to the volcano.

Bagana lavas are porphyritic basaltic andesites, with 30–50 volume % phenocrysts of plagioclase, augite, magnetite and hornblende, and a matrix of plagioclase microlites,

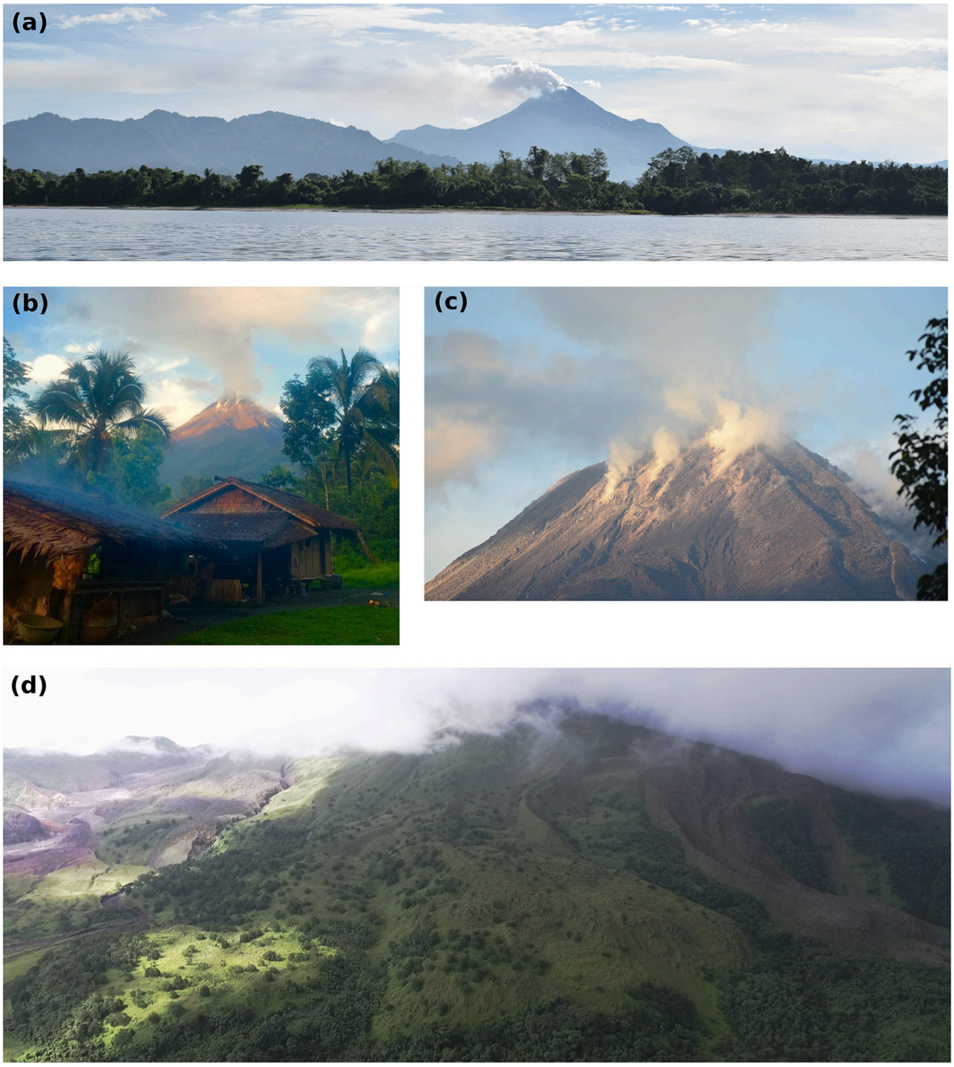

FIGURE 2 | (a) Bagana viewed from off-shore to the west-southwest. Note strong summit gas plume. Distance to summit ∼25 km. **(b)** A rare clear view of Bagana's summit, as seen from Patsikopa village (**Figure 1c**), ∼7 km to the southwest **(c)** Zoom to summit region, highlighting strongly degassing fumaroles and steep, levee-bound upper reaches of the 2000–2008 lava flow field. **(d)** Aerial photograph (taken by DJI Phantom drone onboard camera) of lower western slopes of Bagana, with 2000–2008 lava flow field to the right of the image and heavily vegetated lava flows dating from 1952–1966 in the center. Far left of the image shows distal ends of 2010–2012 lava flow, and recent debris avalanche deposits reported to have been emplaced in August 2016. Upper slopes are obscured by low altitude cloud. All photographs by B.T. McCormick Kilbride, September 2016.

hypersthene, magnetite, and glass (Blake, 1968; Bultitude, 1976; Bultitude et al., 1978). Analyzed lavas fall into three groups, chemically distinct and erupted during different periods of activity. Pre-1943 lavas, termed Group 1 by Bultitude et al. (1978), are the most evolved products of the volcano, with SiO_2 contents of ∼56–58 wt%. Lavas erupted during 1943-53 (Group 2) are the most primitive products sampled (SiO_2 ∼53–54 wt%), while Group 3 lavas, erupted during 1959–1975, are intermediate in composition, with SiO_2 ∼55-56 wt%. Lavas erupted in 1988–1989 (Rogerson et al., 1989) and recent lavas erupted post-2005 also appear to be compositionally similar to Group 3 (B. McCormick Kilbride, unpublished data).

2.3. Recent Activity of Bagana

Bagana's historical activity has been comprehensively reviewed by Bultitude et al. (1978), Bultitude (1981) and Bultitude and Cooke (1981). Prior to the Second World War, when air traffic in the region increased significantly, observations of the volcano were very rare. Wadge et al. (2018) drew on several decades of pilot reports, ground-based observations and, in particular, satellite remote sensing, to construct the most complete account of Bagana's activity to date. Here, we review only the activity during our study interval, 2000 to 2017, summarized in **Figure 3**. Other accounts of Bagana's activity can be found in the Bulletins of the Global Volcanism Program [http://volcano.si.edu/volcano.cfm?vn=255020], drawn from information provided by Rabaul

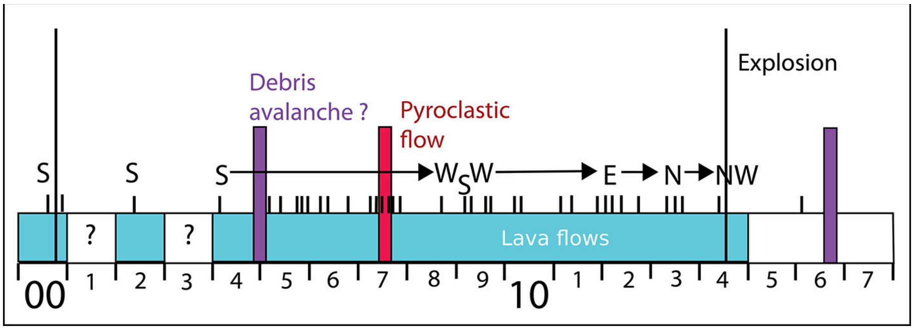

FIGURE 3 | Summary of activity reported at Bagana for our study interval, 2000–2017, after Wadge et al. (2018). Light blue shading corresponds to reports of active lava extrusion. Vertical purple and red bars indicate timing of known major debris avalanches or pyroclastic flows, and long vertical black lines indicate known large explosive eruptions. Short vertical black tick marks indicate timing of ASTER acquisitions where lava flow direction, shown as cardinal and ordinal letters, on the volcano's flanks can be distinguished.

Volcanological Observatory (RVO) and the Darwin Volcanic Ash Advisory Centre (VAAC).

Figure 3 is largely based on ASTER observations (Advanced Spaceborne Thermal Emissions and Reflection Radiometer carried on the NASA Terra satellite, Pieri and Abrams, 2004). ASTER makes observations with high (sub-100 m) spatial resolution in both visible/near-infrared (VNIR) and thermal infrared (TIR) and is particularly valuable for Bagana in that the radiative portion of active lava flows can be imaged at sufficient resolution to determine the direction of flow away from the summit crater. Our catalog of ASTER images is available in the **Supplementary Material** accompanying this manuscript. The timing and directional information (e.g., S = south) of these observations are shown by short black vertical lines in **Figure 3**; the limited number of observations over several years is a consequence of ASTER's infrequent observations as well as clouds obscuring lava flow thermal emissions. From 2000 to 2008 lava flowed south, though there is no positive evidence of this for 2001 and 2003. From 2008 to 2014 lava flowed successively west, south, west, east, north and northwest. There is no ASTER evidence of flank lava flows since 2014 though there have been radiant signals from the summit crater. Other significant events are recorded in **Figure 2**, two debris avalanches (late 2004 and 2016), two large explosions (late 2000 and mid 2014), and a pyroclastic flow in mid 2007. This may not be a complete record of activity at Bagana. RVO visits to the volcano are infrequent and although local observers make nominally daily reports to the Observatory, these are limited to clear views of the western slopes of the volcano.

All reported activity at Bagana includes reference to a dense and persistent summit gas plume. To date, only SO_2 emissions have been measured at Bagana, with recent attempts to quantify plume gas chemistry using UAV-based sensors proving inconclusive [S. Arellano, personal communication]. SO_2 emissions were first measured by COSPEC in 1983 and 1989 and were reported as 36 and 37 kg s^{-1}, respectively, equivalent to ~3,100–3,200 t d^{-1} or 1,130–1,170 kt y^{-1} (Global Volcanism Program, 1983, 1989; Andres and Kasgnoc, 1998). An airborne DOAS survey in 2003 measured SO_2 emissions of 23 kg s^{-1}, equivalent to ~2,000 t d^{-1} or 725 kt y^{-1} (McGonigle et al., 2004b). OMI observations during 2004-2008 measured a total of 455 kt but this is likely to be an underestimate of true SO_2 emissions caused by rapid plume processing and the low altitude of Bagana's plume (McCormick et al., 2012). Recent global inventories of volcanic emissions reported Bagana's mean annual SO_2 flux for the period 2005–2015 as 1,380 kt y^{-1}, making it the third highest persistent volcanic SO_2 source after Ambrym and Kilauea (Fioletov et al., 2016; Carn et al., 2017).

3. MATERIALS AND METHODS

3.1. Remote Sensing of SO_2 Emissions

3.1.1. The Ozone Monitoring Instrument

The Ozone Monitoring Instrument (OMI) is a hyperspectral UV/visible spectrometer launched in 2004 aboard the Aura satellite in NASA's A-train constellation (Levelt et al., 2006a,b). OMI observations have been widely used to study volcanic SO_2 emissions, both from discrete eruptions (Thomas et al., 2009; Carn and Prata, 2010; Lopez et al., 2013a) and over multi-year intervals on the regional and global scale (McCormick et al., 2012, 2015; Carn et al., 2016, 2017; Fioletov et al., 2016). OMI measures backscattered solar radiation from Earth's surface and atmosphere and SO_2 column concentrations have been calculated using a series of increasingly sophisticated retrieval algorithms (Krotkov et al., 2006; Yang et al., 2007, 2009; Li et al., 2013, 2017). All OMI mission data are archived online [https://mirador.gsfc.nasa.gov/] and the entire dataset has recently been re-analyzed using the latest retrieval algorithm, based on principal component analysis, PCA (Li et al., 2013, 2017; Carn et al., 2017).

The PCA-retrieved background SO_2 has a standard deviation of ~0.5 Dobson units (DU, 1 DU = 2.69×10^{26} molec km^{-2}), a factor of two reduction in retrieval noise over the preceding linear fit algorithm (Fioletov et al., 2016; Krotkov et al., 2016). The total error for a single retrieval may be 70–150% (Krotkov et al., 2016) but a comprehensive error analysis of the OMSO2VOLCANO product, encompassing retrieval noise, plume altitude, cloud cover, latitude, and other factors has not yet been published. Systematic errors in the SO_2 Jacobians used in the retrieval arise where local observational conditions differ widely from those assumed in the Jacobian calculations. SO$_2$ column concentration is likely to be overestimated in scenes with snow, ice or cloud cover, or in the free troposphere over the open ocean. Certain precautions can be made to reduce error, such as rejecting pixels from the outermost two rows of the OMI swath, which are subject to elevated noise levels and have significantly larger area than more central pixels, and high-reflectivity pixels with cloud fractions in excess of 0.3. Cloud cover can be extensive in tropical locations such as Papua New Guinea and further work is certainly needed to accommodate spatially and temporally variable cloud cover in SO$_2$ retrievals.

Time-averaging has been widely used for its significant effect in reducing uncertainties due to retrieval noise. For example, uncertainties fall to 10–15% of the signal on an annual basis (Krotkov et al., 2016). Generally, we have avoided the use of individual retrievals in this study pending further quantitative evaluation of the data quality and focussed largely on annual or monthly summing and averaging of SO$_2$ retrievals. Overall, the PCA algorithm's significantly reduced noise and regional biases relative to earlier operational products make it substantially better suited to quantifying lower altitude (i.e., planetary boundary layer, PBL) SO$_2$ emissions than earlier operational data products (Fioletov et al., 2016; Krotkov et al., 2016; Carn et al., 2017).

3.1.2. SO$_2$ Mass Loading, Lifetime and Emission Rates

The PCA retrieval algorithm yields atmospheric SO$_2$ column concentrations for every pixel in the OMI swath. Given the area of each pixel and by summing pixels, we compute a total SO$_2$ mass loading in each field-of-view (FOV) "scene." Different estimates of column concentration are provided according to the SO$_2$ plume altitude. The PBL SO$_2$ column concentration assumes a plume center of mass altitude (CMA) of 1.0 km, somewhat lower than Bagana's summit altitude of ~1.8 km. Following Fioletov et al. (2016) and Carn et al. (2017) we perform a correction on the retrieved SO$_2$ vertical column densities by using a local air mass factor (AMF, 0.547) rather than the default effective AMF of 0.36 used in the full PCA retrieval. This AMF correction reduces scene mass loadings by ~33%. We lack reliable measurements of plume altitude at Bagana but given the dominantly passive or co-extrusive character of the emissions we do not envisage a strong thermal lofting effect and therefore consider the vent altitude a reasonable estimate of long-term mean plume altitude. The lower troposphere SO$_2$ data (TRL, with CMA ~2.5 km) yield scene mass loadings around 65% lower than the PBL data and probably underestimate SO$_2$ mass loading over Bagana.

We calculate mass loadings for a roughly 2^o latitude/longitude domain centered on Bagana, adjusting this domain manually to capture the full extent of elongate plumes, or to avoid incursions from drifting SO$_2$ from nearby passive degassing volcanoes (e.g., Rabaul, Ulawun) or regional eruptions (e.g., Manam in January 2005). These total SO$_2$ mass loadings represent the volcano's emissions since the previous satellite overpass, less any SO$_2$ that has been advected beyond the margins of the box or has been removed by chemical or physical processes. Single orbit SO$_2$ mass loadings are unlikely to be equal to at-source daily SO$_2$ emission rates, unless SO$_2$ lifetime is close to 24 h (i.e., 1 day). SO$_2$ can be removed from the atmosphere by oxidation to SO_4^{2-} or direct physical processes, such as wet deposition. The lifetime of SO$_2$ in the tropical boundary layer or troposphere is thought to be ~1–2 days but estimates of SO$_2$ lifetime vary widely and depend on a host of factors: gas-phase oxidation is limited by hydroxyl availability; wet deposition and aqueous-phase oxidation by atmospheric humidity and cloud cover; other aerosol reaction pathways by pH or the availability of particulate reaction surfaces (Eatough et al., 1994; Faloona, 2009). Volcanic plumes are highly heterogenous in their chemistry, particle content and humidity and consequently lifetime estimates of volcanic SO$_2$ vary more widely (Oppenheimer et al., 1998; McGonigle et al., 2004a; Rodriguez et al., 2008; Boichu et al., 2013; Beirle et al., 2014; McCormick et al., 2014).

Lopez et al. (2013a) and Carn et al. (2016) presented simple methods to calculate SO$_2$ emission rate (tons per day) by multiplying scene SO$_2$ mass loading (tons SO$_2$) by plume speed (kilometers per hour, or day) and dividing by the plume length (km). This method can be extended to calculate the scene SO$_2$ lifetime, which is equal to the mass loading divided by the emission rate. The main caveats of this approach are the need for an accurate local wind speed and also for plumes of a linear geometry, where SO$_2$ column concentration decreases downwind and steady state emissions can be reasonably assumed. We identified 75 such SO$_2$ plumes in our OMI observations and performed these calculations to obtain SO$_2$ emission rate and lifetimes from our measured mass loadings. Our plume speed estimates come from NCEP Renanalysis 2 data (provided by the NOAA/OAR/ESRL PSD, Boulder, USA, available online: https://www.esrl.noaa.gov/psd) for a plume altitude of ~2 km. We calculate SO$_2$ lifetime ranging from 9 to 43 h, with a mean of 22.5 h and a standard deviation of 7.6 h. Binning our data into months of the year, we find a similar mean of 23.1 h and a decreased standard deviation of 4.5 h. There is no compelling evidence for a seasonal variation in SO$_2$ lifetime. These results bear out the suggestion that tropospheric volcanic plumes are complex environments and SO$_2$ lifetime can vary widely.

Incorporating SO$_2$ lifetime into our results is not trivial. Without some assumption of lifetime, a mass loading time series cannot strictly be interpreted in terms of changing at-source emission rate. However, lifetime demonstrably varies widely and we do not have an accurate daily record of this variation. Herein, we have opted for a constant lifetime of 22.5 h in order to convert our mass loading data into emission rates. To acknowledge the uncertainty introduced by this assumption of constant lifetime, we also present higher and lower bound emission rates calculated by shorter (14.9 h) and longer (30.1 h) lifetimes, respectively. Our approach is not fully adequate to characterize the variability of SO$_2$ lifetime but this is a formidable challenge and one that requires extensive atmospheric physical and chemical modeling of a range of volcanic plume settings in order to be overcome.

3.1.3. The OMI Row Anomaly

The early years of the OMI SO_2 dataset have complete daily global coverage, achieved by the instrument's wide swath and 14/15 daily orbits (Levelt et al., 2006b). Since late 2008, coverage has been diminished due to the OMI Row Anomaly (ORA), a blockage in the sensor's field of view that renders a variable fraction of the swath unuseable (Carn et al., 2013; Flower et al., 2016). Flower et al. (2016) showed that the ORA imposes periodicities of 3.2 and 7.9 days in OMI observations, akin to the 2.3-day cycles typical of polar-orbiting satellite datasets caused by changing sensor viewing angle. Applying a running average to the data can suppress the effect of these cycles–if the averaging window used is greater in length than the cycle period–but this also reduces the dynamic range of the data. In this study, we are interested mostly in the long-term behavior of Bagana and have largely binned our satellite observations on an annual or monthly basis, effectively reducing the influence of the ORA or changing viewing geometry.

A consequence of the ORA is that gaps in an SO_2 emissions time series result in an underestimate of the true emissions budget. To treat these gaps as true null values–where no SO_2 was emitted from the volcano–is misleading and inconsistent with the largely continuous daily emissions observed in the early years of our dataset. Accordingly, we fill these data gaps using either averaging or linear interpolation based on preceding or following observations. For gaps of 1–5 days, we calculate the missing SO_2 mass as the mean of two closest preceding and two closest following OMI observations. When the gap between consecutive observations is greater than 5 days (n = 67), we use linear interpolation between the two observations before and after the gap. On the ten occasions where data gaps exceed 10 days, we treat the null values as real null values (i.e., SO_2 mass = 0), judging that an attempted correction here would be too poorly constrained by the unavailability of surrounding observations. The consequence of this correction for null values is a 56% increase in total OMI-observed SO_2 mass loading over the course of our study period.

3.2. Remote Sensing of Thermal Emissions and Lava Extrusion

The Moderate Resolution Imaging Spectroradiometer (MODIS) is an infrared sensor carried by two NASA satellites, Terra and Aqua, launched in 1999 and 2004. MODIS has been used in many Earth Observation applications, notably the detection of thermal anomalies (or "hotspots") such as wildfires and lava or pyroclastic debris from erupting volcanoes (Wright et al., 2002; Rothery et al., 2005; Wright, 2016). MODVOLC is an algorithm developed for the automated detection of volcanic hotspots and the quantification of their emitted thermal infrared (TIR) radiation (Wright et al., 2002, 2004; Wright, 2016). The MODVOLC database has full daily coverage from 2000 to the present day, can be searched and visualized online [http://modis.higp.hawaii.edu/], and provides hotspot pixel counts, spectral radiance and radiant flux for every active volcano on Earth. Other thermal monitoring algorithms exist (e.g., MIROVA, Coppola et al. (2016)) but the great advantage of MODVOLC, justifying our use of it here, is consistency of data quality and coverage over a multi-year timeframe and the care taken to avoid false positives in the data (Wright, 2016).

We have used data from both MODIS instruments, resulting in four potential daily observations of Bagana's spectral radiance. However, we restricted our analysis to nighttime observations, in order to minimize any sunglint effects. This had the effect of removing 26 alerts across the duration of our study period, leaving 1314 separate hotspot detections. The low number of daytime observations at Bagana is likely a consequence of reduced thermal contrast between the volcanic edifice and its surroundings during sunlit hours. The number of hot pixels detected within each alert varies between 1 and 8, though most alerts comprise only 1 (63%), 2 (27%), or 3 (7%) pixels. In general, the global MODVOLC database is dominated by radiant emissions from basaltic lava flows, given their tendency for high width-to-thickness ratios and high eruption temperatures (Wright, 2016). Given Bagana's basaltic andesite composition (and therefore lower temperature) and narrow, strongly channelized lava flows, the typically low number of hot pixels in any single MODIS overpass is within expectations.

Radiant flux (ϕ_e, measured in W, or J s^{-1}) can be estimated from MODIS observations using an empirical relationship based on observed spectral radiance at 3.959 μm, $L_{3.959}$ (after Kaufman et al., 1998; Wooster et al., 2003):

$$\phi_e = 1.89 \times 10^7 (L_{3.959} - L_{3.959,bg})$$

where $L_{3.959,bg}$ is the spectral radiance of adjacent pixels without anomalous thermal emissions. Uncertainties on individual measurements of radiant flux should not exceed 30% (Wright, 2016). We calculate the total radiant flux for each Terra or Aqua overpass by summing the radiant flux measured from each hotspot pixel. On longer (e.g., monthly or annual) timescales, we calculate the total radiated energy (J) by integration beneath the curve. After Wright (2016), we treat data gaps exceeding 7 days as real null values, where eruptive activity bringing hot lava to the Earth's surface has ceased. Shorter data gaps may be a result of clouds obscuring radiant surfaces and these gaps are accounted for in our calculations of total radiated energy by the use of linear interpolation between preceding and consecutive MODVOLC alerts.

3.3. Volcanic Ash Advisories

Volcano Ash Advisories (VAAs) resulting from activity at Bagana are issued by the Darwin VAAC, and have been mainly based on observations by the following satellites: GMS-5 (launched March 1995, decommissioned July 2005); MTSAT-1R (or Himawari-6, launched 26 February 2005, decommissioned 4 December 2015); MTSAT-2 (or Himawari-7, launched 18 February 2006, and still operational, though mostly occupying a stand-by mode); and Himawari-8 (launched 7 October 2014, and operational 7 July 2015). In addition to these Japanese-operated instruments, Darwin VAAC has used observations from the US GOES-9 satellite (reactivated between 2003 and and November 2005 to provide coverage after the failure of MTSAT-1 to reach orbit) and Defense Meteorological Satellite Program (DMSP) missions, and pilot observations from a range of regional airlines. Data reported in VAAs include: the date and time of ash cloud detection; an identification of the source volcano; information on the altitude and direction of volcanic clouds; and forecasts of where the ash will disperse based on current wind fields. The Darwin archive of VAAs (June 1998 to present) is hosted online by the Australian Bureau of Meteorology [ftp://ftp.bom.gov.au/anon/gen/vaac/].

3.4. Rabaul Volcanological Observatory Reports

Bagana occupies a remote location in the heavily forested interior of Bougainville (**Figure 1c**), roughly 20 km northeast of Torokina, one of very few anchorages on the island's southwest coast. Several small villages lie between the volcano and the coast, with a population of roughly 8,000 in a 30 km radius (Global Volcanism Program, 2013). RVO retain a local observer to provide daily reports on activity at the volcano; the present observer is based in Gotana (9.5 km SW of the summit, 6.201°S 155.136°E) though some reports have been obtained from Wakovi (7.5 km to WSW, 6.161°S 155.132°E). The reports are variable in content but can provide useful constraint on the timing of changes in activity including whether lava flows are active, nighttime incandescence can be seen at the volcano's summit, or ashfall is reported on the villages. Reports are available fairly regularly but gaps in the record are common owing to the absences by the observer from Bougainville or clouds obscuring the volcano summit from view. The highly directional nature of Bagana's extrusive activity means that reports of lava extrusion are particularly fragmentary.

4. RESULTS

4.1. Inter-Annual Satellite Observations

4.1.1. Comparison With Earlier Work on SO_2 Emissions

We generated an inter-annual time series of Bagana SO_2 emissions (**Figure 5A**), by first filling the null values in our scene mass loading data and performing an AMF correction, secondly by converting individual scene mass to daily emission rates using estimates of SO_2 lifetime, and finally by integrating these emission rates to calculate annual emissions. Assuming a lifetime of 22.5 h is accurate, annual emissions vary from a peak of 1,284 kt in 2005 to around 350–700 kt in most other years. Emissions are lower in 2004 and 2017 where our data does not extend to the full year. Our upper range lifetime estimate (30.1 h) reduces annual emissions by ∼25% while our lower range lifetime estimate (14.5 h) increases annual emissions by ∼51% (**Figure 5A**). Following 2005, Bagana's annual emissions generally decrease but with clear secondary peaks in 2012 and 2015–2016.

A recent global OMI survey of persistent volcanic emissions (Carn et al., 2017) derived annual SO_2 emission rates for Bagana for 2005–2015. Their approach was to align all detected SO_2 pixels into a common wind direction and fit a modified Gaussian to the generated composite plume in order to estimate the per-year SO_2 emission rates, shown alongside our data in **Figure 5A**. There are two important features to note in this comparison: (i) the large difference (∼40–100%) in magnitude of the Carn et al. (2017) emissions and our data; and (ii) the two time series have relatively similar trends, aside from 2010 and 2012.

These differences are not straightforward to understand but seem likely to be a combined consequence of our different ways of handling the OMI data and differences in SO_2 lifetime. Carn et al. (2017) derive emissions consistent with a composite plume generated by combining all detected OMI pixels while we have individually processed all scenes and derived an SO_2 mass burden or emission rate on a per-scene basis. One possibility is that truncation of larger gas plumes by the OMI row anomaly will cause major reductions in scene mass loadings and therefore annual totals, whereas calculated emission rates may be less affected if near-source pixels with higher SO_2 column density are preserved and have a greater significance to the Gaussian fitting. There are likely to be consequences of different tolerances for cloud cover or the obscuring effects of the row anomaly, our handling of null data, and different sources of plume speed estimates. Conclusively determining the accuracy of two different approaches to estimating SO_2 emissions is challenging and, given the limitations imposed by row anomaly and the different temporal and spatial resolution of each approach, perhaps insurmountable.

One approach to reduce the discrepancy between our data and that of Carn et al. (2017) would be to consider our estimates of SO_2 lifetime as maxima. For each year in 2005–2015, the common interval of our studies, we can calculate mean scene SO_2 mass loadings and daily emission rates, and by combining these compute rough estimates of lifetime. This results in a mean SO_2 lifetime of 10.1 h (±2.4), considerably shorter than the lifetimes we calculated above. 10.1 h is toward the faster end of published estimates of SO_2 lifetime in volcanic plumes but may be reasonable for low altitude (boundary layer) conditions in a humid tropical setting. Support for short SO_2 lifetimes comes from our visual inspection of Bagana plumes in OMI field-of-view scenes: using reasonable local wind speed estimates from NCEP Renanalysis 2 data we estimate a likely downwind range of 400–500 km for Bagana plumes to reach before the subsequent OMI overpass. On the basis of these criteria we can assess whether observed SO_2 is fresh or relict. We find that relict plumes are rarely seen. Our analysis is generally aided by most Bagana plumes clearly emanating from the volcano (**Figure 4**).

Throughout the remainder of this study, we will quote SO_2 emissions based on our previously described conversion of mass loading to emission rate assuming a 22.5 h lifetime. We ask the reader to bear in mind the potential uncertainty (+51%, -25%) as described above, arising from longer or shorter lifetimes, and moreover that under certain conditions even shorter lifetimes may result in scene mass loadings being underestimates of Bagana's true at-source emissions.

4.1.2. Overview of Bagana's Activity, 2000–2017: Radiant Flux, SO_2 Emissions, Ash Plumes

From low levels in 2000-01, our MODVOLC data show a steady increase in integrated annual radiant flux to a peak of 3.6 $\times 10^{14}$ J in 2005, paralleling the peak in SO_2 emissions described above (**Figures 5A,B**). During 2006–2011, radiant flux and SO_2

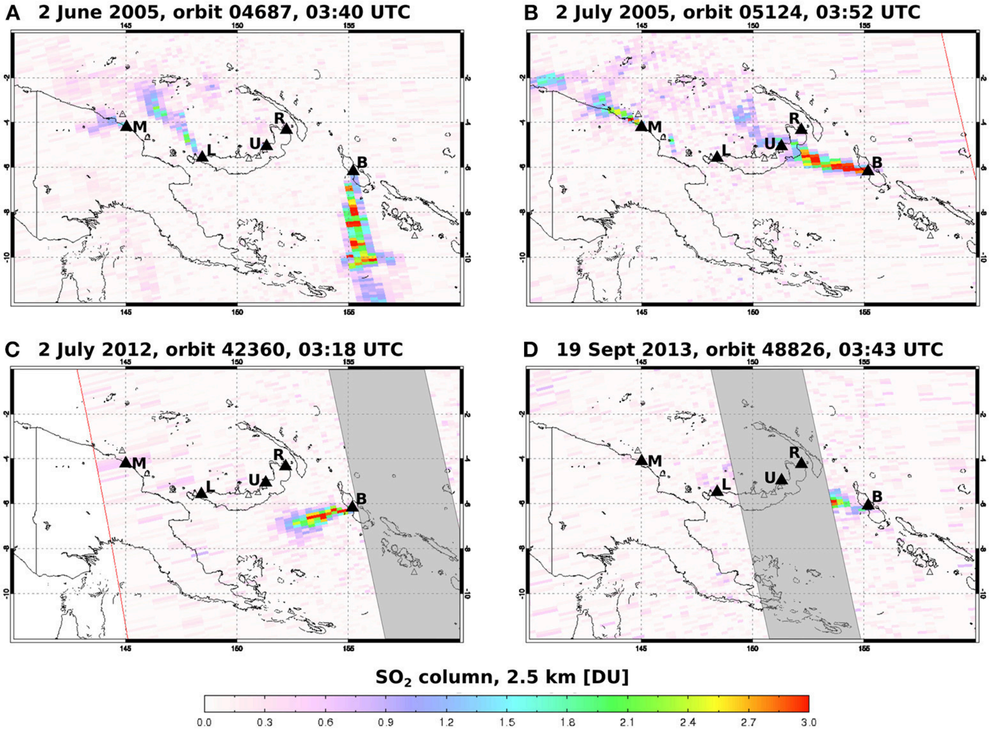

FIGURE 4 | Examples of individual scene SO_2 observations by OMI, mapped using OMIplot software (Carn, 2011). Volcanoes across Papua New Guinea that have been identified as detectable SO_2 sources (McCormick et al., 2012) in OMI data are indicated: M, Manam; L, Langila; U, Ulawun; R, Rabaul (Tavurvur); B, Bagana. **(A,B)** Shows strong SO_2 emissions from Manam, Ulawun, and Langila in addition to Bagana, with **(B)** illustrating the care that must be taken to correctly attribute emissions when volcanoes are closely spaced. In **(C,D)**, the area of the OMI swath affected by the Row Anomaly is shaded in light gray. In **(C)**, the full extent of the Bagana SO_2 plume can be mapped, whereas in **(D)**, the plume is truncated by the Row Anomaly, and the retrieved scene SO_2 mass must therefore be considered a minimum estimate.

emissions decrease following similar trends, though the range of 1.6–2.8 $\times 10^{14}$ J remains above 2000-04 levels. In 2012, a second strong peak is recorded in radiant flux (3.4 $\times 10^{14}$ J), comparable to the 2005 peak, and again matching the SO_2 emissions data. During 2013–2017, radiant flux and total SO_2 mass decrease to levels comparable to pre-2005, again with very similar trends.

The radiant flux emitted from a volcanic edifice is proportional to the temperature and areal extent of some hot feature, mostly likely a lava flow or dome or an active vent (Wright, 2016). At Bagana, the features most likely to be triggering MODVOLC alerts are active lava flows on the edifice flanks; the summit dome itself may be too small for consistent detection. Therefore, we interpret the trend in radiant flux (**Figure 5B**) as follows: (i) low level extrusion only in 2000, increasing steadily in the following 4 years; (ii) a major peak in extrusive activity centered on 2005, decreasing thereafter through 2006–2011; (iii) a second major peak in extrusive activity centered on 2012, decreasing thereafter to low level extrusion comparable to pre-2004.

The inter-annual trend in SO_2 mass loading detected by OMI over Bagana (**Figure 5A**) also suggests continuous but variable activity, and is broadly similar in trend to the radiant flux time series (**Figure 5B**). The principal differences are the lack of OMI observations prior to 2004 and the relative magnitude of the 2012 secondary peak in activity. The two satellite datasets correlate reasonably well ($R^2 = 0.77$, **Figure 5D**). Our interpretation is that increased lava extrusion, indicated by high radiant flux, occurs periodically, notably in 2005 and 2012, and is accompanied by elevated SO_2 mass loadings. There are years with reduced lava extrusion, notably 2000–2001 and 2015–2016, but the non-zero radiant flux data suggest that extrusive activity occurred to some extent in every year between 2000–2017. This fits our existing perspective of Bagana as a persistently active volcano. The non-zero intercept of the regression line in **Figure 5D** may indicate that SO_2 emissions, though correlated, continue when radiant flux drops to zero, a suggestion that we will explore further below.

Figure 5E records the number of VAAs issued for Bagana each year. Since 1998 Darwin VAAC has issued over 19,000 VAAs for volcanoes across Indonesia, the southern Philippines, Papua New Guinea, and Vanuatu, with 1459 VAAs (7.5% of total) issued for Bagana (dating from May 2004 to September 2017), a remarkable number for a volcano whose activity is dominantly effusive. Over half (56%) of VAAs issued for Bagana date from 2015-17 but this increase over previous years is strongly related to changing satellite capability. After September 2015, satellite-based ash detection for Darwin VAAC switched from MTSAT-1R and MTSAT-2 observations (hourly frequency) to higher spatial resolution observations by Himawari-8 every 10 min. It

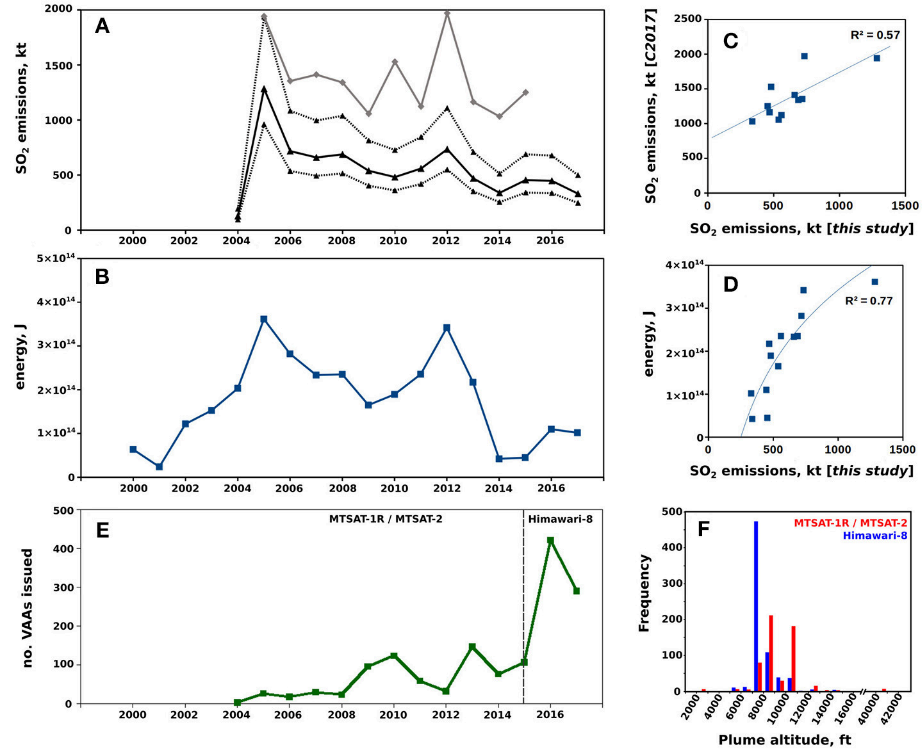

FIGURE 5 | Satellite observations of Bagana's activity, binned annually: **(A)** annual SO_2 emissions (black solid curve), derived from our OMI daily observations, with dashed black lines illustrating potential range in emissions due to uncertainty over SO_2 lifetime. Gray line is annual SO_2 emission rates reported by Carn et al. (2017); **(B)** total thermal energy radiated from Bagana, derived from MODIS observations and the MODVOLC algorithm; **(C)** scatterplot of integrated thermal energy vs. SO_2 emissions [this study]; **(D)** scatterplot of total SO_2 emissions from this study vs. Carn et al. (2017); **(E)** total annual Volcanic Ash Advisories (VAAs) issued for Bagana; **(F)** histogram showing frequency of VAAs binned by altitude, with MTSAT (2004–2015) and Himawari-8 (2015–2017) eras separated.

is difficult to distinguish changes in activity from changes in satellite sensitivity, so we interpret the MT-SAT (2004–2015) and Himawari-8 (2015–2017) eras of the VAA dataset separately.

In the MT-SAT era, MODVOLC radiant flux data suggest substantial lava extrusion in 2005 and 2012, with reduced extrusion in the surrounding years (**Figure 5B**). The time series of total VAAs issued is anti-correlated with this trend, most notably in 2008–2014 (**Figure 5E**). When extrusion is most active (e.g., 2005 and 2012), it appears that explosive activity and the production of ash plumes is relatively low, and that during intervals of decreased lava extrusion (e.g., 2008–2011) the production of ash plumes increases. Ash-producing explosions of varying intensity are a common feature of inter-extrusive pauses at dome-forming volcanoes (e.g., Norton et al., 2002). The anti-correlation between the number of VAAs issued and total radiant flux does not continue in the Himawari-8 era (**Figures 5B,E**). This may be a consequence of the dramatic increase in frequency of ash detection or, alternatively, a shift to a different style of activity: ash venting is also known to occur periodically during extrusive episodes (e.g., Cole et al., 2014). Given uncertainty over short timescale variations in activity at Bagana and a lack of direct ground-based observations, we cannot confidently infer the processes which give rise to the various VAAs issued.

The aviation color code, also recorded in VAAs, comprises four levels from green, through yellow and orange, to red that signify levels of unrest at the volcano in question (Guffanti and Miller, 2013). Activity at Bagana, as reported in VAAs, is dominantly tagged at the level of orange, that is, "volcanic eruption is underway with no or minor ash emission." In the MTSAT era, 85% of the VAAs issued were tagged orange, with the majority of the remainder tagged yellow; in the Himawari-8 era, 99% of the VAAs were tagged orange. Based on these color codes, Bagana's ash venting activity falls within a relatively limited range of intensity: alerts tagged red were only issued on 4 separate occasions (total of 11 alerts) and never persisted for more than a day. Further insight can be gleaned from the ash plume altitude reported in each VAA. The altitude range of ash plumes differs strongly between the MTSAT and Himawari eras. The MTSAT data show a bimodal distribution, with two peaks of similar magnitude centered on 8,000 and 10,000 feet (roughly 2.4 and 3 km), whereas 69% of Himawari-8 observations are of plumes at 7,000 feet (2.1 km). These altitude bins are of course close together, but a key observation is that many more ash plumes were reported at 10000 feet or higher in the MTSAT era (210, 39% of total) than in the Himawari era (47, or 7% of total). We consider this good evidence for a long-term decrease in the intensity of ash venting activity at Bagana, noting that the actual frequency of ash plume detection increases through time due to the heightened sensitivity of Himawari-8. The great majority of VAAs issued for Bagana are likely to correspond to low level ash venting activity, and not larger explosive eruptions or dome collapse events. We infer this from the generally low altitude of the plumes detected (<1% of plumes exceeded 5 km in altitude), for example in relation to typical ash venting altitudes reported at Soufrière Hills (up to 6 km, Cole et al., 2014).

4.2. Monthly Satellite Observations

4.2.1. Eruptive Intervals of Several Months Duration

The tendency for coincident peaks in radiant flux and SO_2 emissions that we observed in our annual time series is still clearly apparent when we integrate our OMI and MODVOLC data over monthly intervals (**Figure 6**). Coincidence of peaks and troughs in the two time series can be seen for the majority of our study period, with the exception of mid-2016 and mid-2017 when the peaks are slightly offset. The relative magnitude of the changes in the two time series do not match well and there is no overall correlation between monthly radiant flux and SO_2 mass loading ($R^2 = 0.47$ can be attributed to a positive skewing caused by the extreme values of radiant flux and SO_2 mass in May 2005; without this pair of points R^2 falls to 0.23). Given the different temporal sampling and resolution of the two satellite datasets we do not expect a strong quantitative correlation here, despite the good correspondence in topology of the two time series.

We interpret coincident peaks as eruptive intervals, with high radiant flux signifying active lava extrusion, and higher levels of detected SO_2 indicating elevated accompanying degassing. Based on our data, the most notable eruptive episodes, with highest radiant flux and SO_2 emissions, are: (i) May 2005 to December 2006; (ii) December 2007 to April 2008; (iii) October 2011 to December 2012. In May to July 2005 monthly radiant flux ranged from 6.7 to 14.0 to 3.0 $\times 10^{14}$ J and the integrated SO_2 emissions for the three months was ~680 kt. The nature of this large yet short-lived SO_2 release remains enigmatic, as noted previously by McCormick et al. (2012). Darwin VAAC reported that ash plumes in mid-2005 did not exceed 10,000 ft (~3.3 km, **Figure 7**) and there was no report relayed to RVO of a large explosive eruption or dome collapse from local observers on the ground. We suggest that this interval represents an intense episode of lava extrusion at Bagana and is indicative of highly variable activity over short timescales. Based on radiant flux or SO_2 emissions, this appears to have been the most intense eruptive episode at Bagana in recent years.

A further major eruptive episode occurred in 2010–2012. From Wadge et al. (2012), who analyzed 14 months of TerraSar-X satellite radar observations (11–55 day revisit time) we know there was persistent eruption of lava from October 2010 to December 2011, with a variable extrusion rate (from 0.26 m^3s^{-1} to 1.8 m^3s^{-1}; mean = 0.92 ± 0.35 m^3s^{-1}). Wadge et al. (2012) argued that Bagana's lava extrusion can be strongly pulsatory on a sub-monthly basis based on their observations of four successive pulses of lava advancing down a single channelized flow. From Wadge et al. (2012)'s semi-quantitative analysis of OMI data, no conclusive argument could be made regarding systematic trends in gas emissions at the onset or through the duration of these pulses in extrusion.

We have analyzed SO_2 emissions and radiant flux alongside Wadge et al. (2012)'s extrusion rate data (**Figure 8**). There is not a convincing correspondence between peaks and troughs in the three datasets, though SO_2 emissions do appear to increase in the wake of elevated radiant flux at the beginning of Wadge et al. (2012)'s Pulse 1 and Pulse 3. The onsets of each pulse in lava extrusion, as defined by Wadge et al. (2012), are not accurately known but the likely onset intervals do coincide with increased SO_2 mass loading (for example, late October 2010, late January 2011) and radiant flux (late January 2011, mid September 2011). This adds some credence to the notion that the onset of each pulse is marked by higher lava extrusion and SO_2 emission rates, though the differing spatial resolution and coverage of our datasets precludes a definitive evaluation of this suggestion. Inter-comparison is limited by the temporally sparse nature of the TerraSar-X dataset as well as the fact that OMI observations are exclusively daytime while the MODIS observations we have selected to use here are exclusively nighttime.

We can re-calculate SO_2 emissions and radiant flux at the sampling rate of Wadge et al. (2012)'s study, that is computing total mass loading or radiant flux corresponding to each 11–55 day interval. **Figures 8D-F** shows that there is a reasonable positive correlation between SO_2 mass loading, radiant flux, and erupted lava volume when each dataset is binned to the same temporal scale. These relationships support our earlier assertion, when looking at longer-duration datasets, that there is a general first-order coupling between lava extrusion and gas emission at Bagana, with episodes of elevated extrusion (and therefore radiant flux) being generally accompanied by increased SO_2 emissions.

It is unfortunate that Wadge et al. (2012) only had access to TerraSar-X data until December 2011. As **Figure 8** shows, SO_2 emissions and radiance reached considerably higher levels in 2012 than in October 2010 to December 2011 (see also **Figure 6**). There is a clear sense in both SO_2 and radiant flux data of strongly pulsatory gas and thermal emissions. From this limited perspective, we consider it likely that obtaining a larger satellite radar dataset will enable a fuller evaluation of Bagana's eruptive behavior.

4.2.2. Inter-Eruptive Pauses

In addition to coincident peaks, our monthly time series of radiant flux and SO_2 mass (**Figure 6**) show coincident minima. Near-zero radiant flux can be seen throughout 2001 and the early part of 2002 (before OMI's launch) and also in early 2009, much of 2014–2015, and late 2017. In these three latter intervals, integrated SO_2 emissions are also reduced, often falling below the long-term mean. We consider these intervals to be periods of greatly reduced or halted lava extrusion. The near-zero radiant fluxes measured by MODIS are likely to indicate low thermal emissions from cooling lava flows or perhaps a dome in the summit crater. Notwithstanding this decrease in extrusion rate, SO_2 emissions seem to continue, albeit at reduced levels, suggesting that in addition to co-eruptive degassing there may be a significant passive degassing component

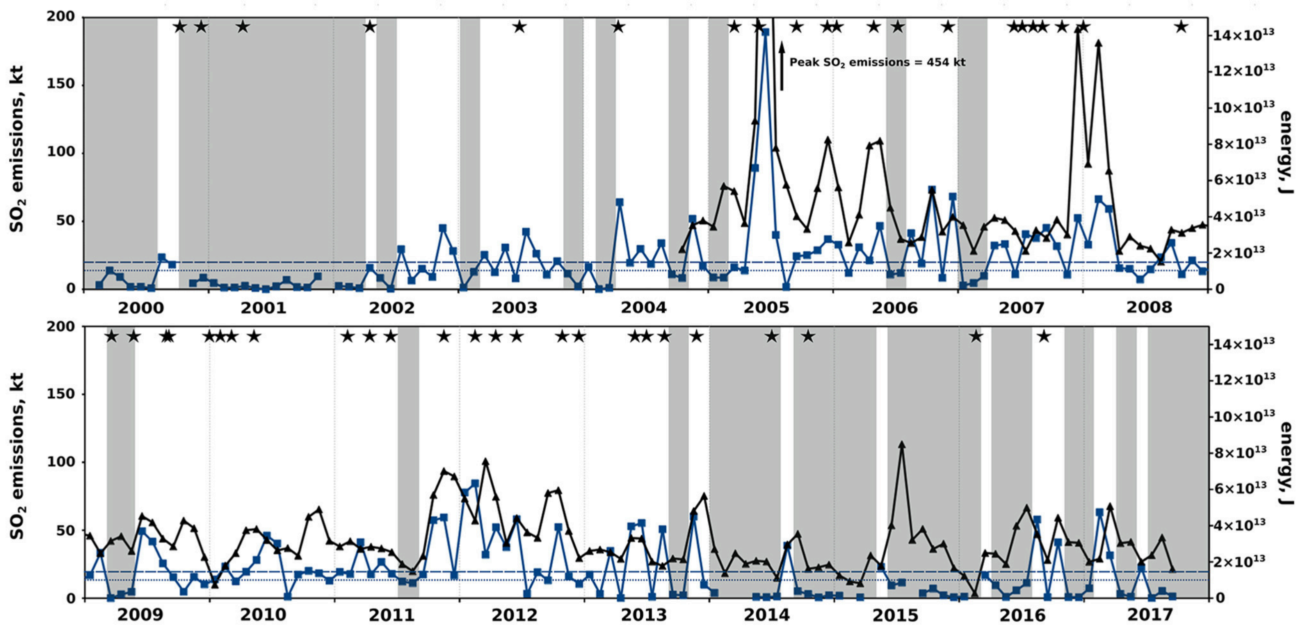

FIGURE 6 | Satellite observations of Bagana's activity, binned monthly, from January 2000 through September 2017. Blue curve indicates integrated monthly thermal energy calculated from MODVOLC data; black curve shows integrated monthly SO$_2$ emissions (note the truncated ordinate). The blue dashed line corresponds to the mean monthly radiated energy (1.5×10^{13} J); the blue dotted line shows the 1.0×10^{13} J threshold used in definition of phase and pause transitions. Co-extrusive phases are indicated by white vertical shading; non-extrusive pauses are indicated by gray vertical shading. Black stars indicate timing of ASTER detections of thermal anomalies on the Bagana edifice.

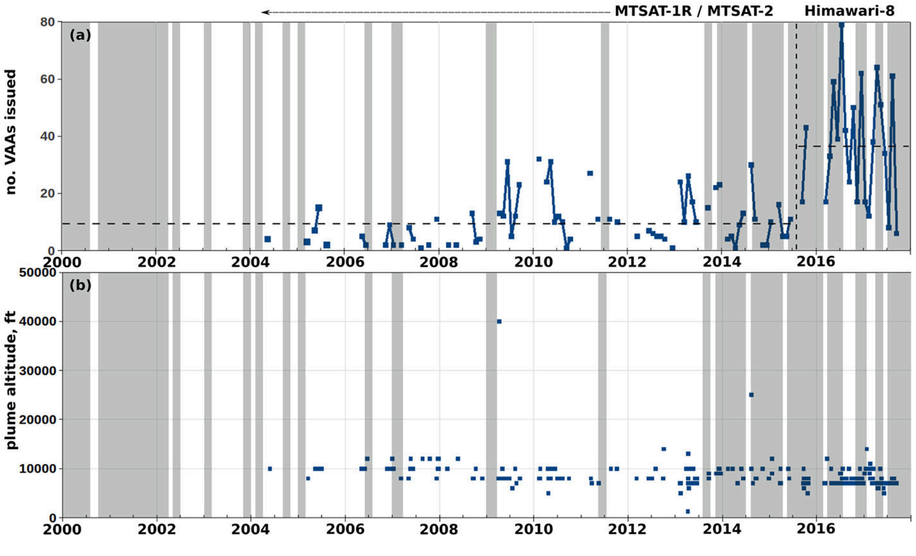

FIGURE 7 | Monthly total Volcanic Ash Advisories (VAAs) **(a)** issued for Bagana between 2000 and 2017 and the altitude of the ash plume **(b)**. Vertical black dashed line in mid-2015 indicates transition to high-resolution and more regular Himawari-8 observations of ash plumes. Horizontal black dashed lines indicate the mean number of VAAs issued per month for the MTSAT and Himawari-8 eras. Vertical white and gray shading indicates phases of lava extrusion and inter-eruptive pauses, respectively.

to Bagana's overall emissions budget. Monthly emissions of 30–50 kt correspond to mean daily emission rates of 1,000–1,600 td^{-1}, higher than is observed at most non-erupting volcanoes worldwide.

4.2.3. Timing and Intensity of Ash Emissions

As discussed earlier, the notable increase in the number of VAAs issued for Bagana in our 2000–2017 study window is in large part due to the improved sensitivity of the satellite instruments

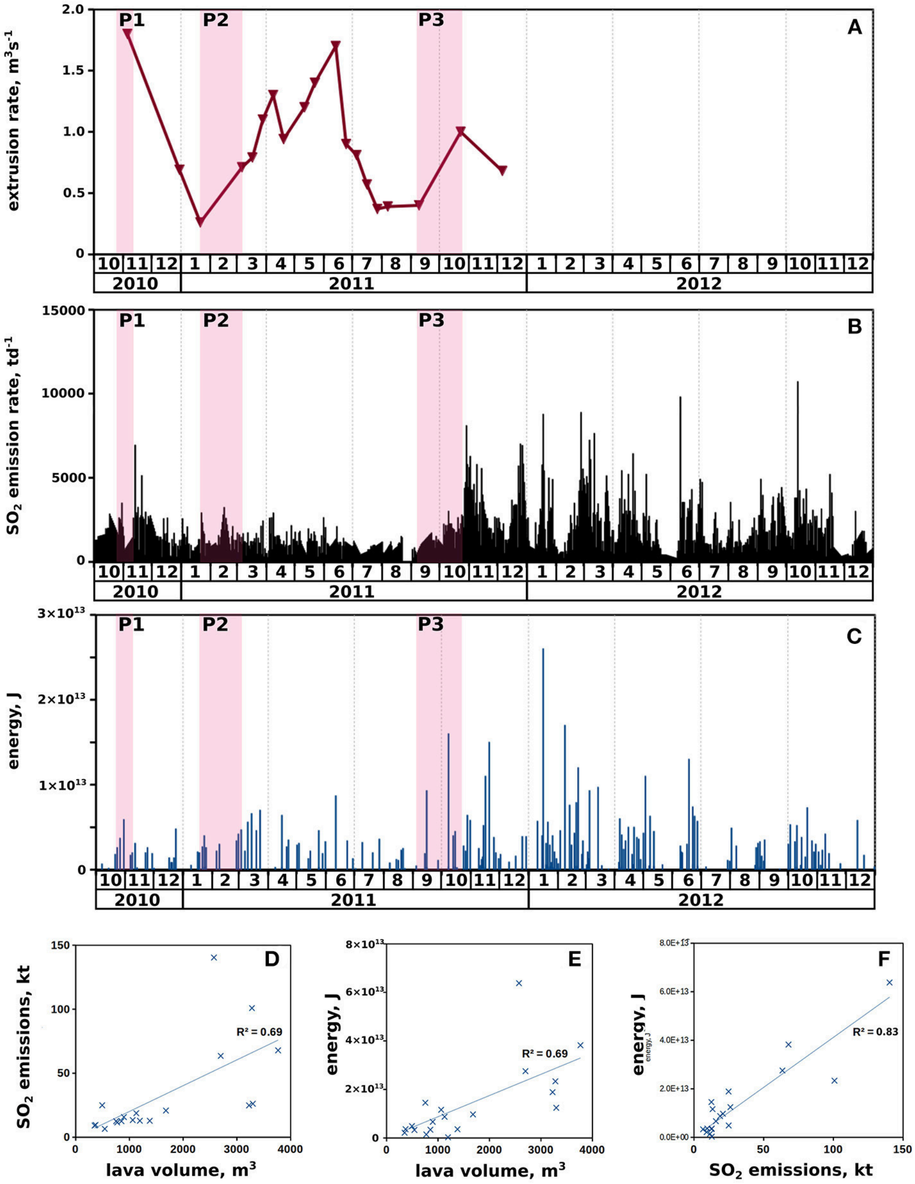

FIGURE 8 | (A) Bagana's lava extrusion rate as measured by satellite radar, TerraSar-X (Wadge et al., 2012). **(B)** Daily SO_2 emission rate calculated from our OMI measurements. **(C)** Daily integrated thermal calculated from MODVOLC data. In all three time series panels, pink vertical shading indicates the approximate onset of each pulse in lava extrusion reported by Wadge et al. (2012). Scatterplots **(D–F)** compare TerraSar-X measurements of lava volume (Wadge et al., 2012)with SO_2 emissions and thermal energy, with the latter two integrated over the same measurement intervals as TerraSar-X observations.

providing data to Darwin VAAC. **Figure 7** summarizes the detection of ash plumes from Bagana in terms of total VAAs per month as well as the altitude distribution of the full dataset (1,459 events). The MTSAT and Himawari eras are again distinguished, with the latter era seeing a major increase in detection frequency, notably of lower altitude ash plumes.

In the MTSAT era, there is a tendency for increased ash emissions to occur during periods of active lava extrusion. The number of VAAs issued rises above the MTSAT era mean (10 alerts per month) in 32 months, and 22 (69%) of these fall into intervals we judge to be co-eruptive. The single most intense ash emission event, based on plume altitude, occurred in August 2009, during a short-lived eruptive phase. In the Himawari-8 era, we make a contrary observation: the mean (36 alerts per month) is exceeded in 11 months, of which 8 (73%) fall into inter-eruptive pauses.

If the general tendency for lower altitude ash plumes in the Himawari-8 era (**Figure 5F**) is a true volcanic phenomenon, and not solely a result of improved detection capability, we could present a cautious interpretation. Based on the low altitude reported in VAAs, most of the events that cause ash emission at Bagana are low intensity ash venting or puffing events that occur during extrusive episodes due to short-lived drops in permeability in the shallow conduit, perhaps due to variable gas/magma ascent rates. Such events are more common during extrusive periods when there is a high magma flux up Bagana's conduit. We might term these Type I ash emission events. Inter-eruptive ash venting may then be controlled by periodic sealing of gas escape pathways through cooling, non-ascending magma in the conduit. These Type II events are likely to have a lesser intensity owing to reduced gas flux from depth (consistent with our general trend of lower SO_2 emissions in pause intervals). The detection of ash plumes resulting from this lower intensity venting activity was not possible in the MTSAT era, but following the switch to Himawari lower altitude ash plumes are now more frequently detected and tend to occur in inter-eruptive pauses.

5. DISCUSSION

5.1. Co-eruptive and Passive SO_2 Emissions

Distinguishing two alternating activity states, co-extrusive "phases" and inter-eruptive "pauses," has been successful as a framework for interpreting long-term behavior of persistently active silicic volcanoes, notably Soufrière Hills, Montserrat (Edmonds et al., 2003; Cole et al., 2014; Wadge et al., 2014). Herein, we have shown that Bagana's activity can be similarly characterized as alternating intervals of (i) active lava extrusion and high SO_2 emissions (*phases*) and (ii) halted extrusion and lower, but still substantial, passive SO_2 emissions (*pauses*). In order to explore how the volcano's SO_2 emissions are partitioned between these two types of activity, we have color coded (**Figures 6**, **7**) to distinguish eruptive phases (vertical white shading) and quiescent pauses (vertical gray shading).

We lack reliable direct observations of extrusion on a multi-year basis—contrast with 14-month TerraSar-X survey of Wadge et al. (2012)—and have therefore used our radiant flux observations from MODIS to define the timing and duration of phases and pauses. We define an eruptive phase to begin when radiant flux exceeds a chosen threshold, and consider extrusion to be persisting until radiant flux falls below our threshold for at least 2 months, whereupon we deem an inter-eruptive pause to have begun. A reasonable threshold to use for defining phases and pauses might be the long-term monthly mean of our radiant flux dataset, which is 1.5×10^{14} J. However, since the distribution of monthly radiant flux is not normal, but skewed positively with a long tail, we also consider a lower threshold of 1.0×10^{14} J.

Changing the threshold from 1.5×10^{14} J to 1.0×10^{14} J (**Table 1**) reduces the number of both phases and pauses and increases the proportion of time that Bagana spends in an extrusive state (from 45% to 60% of our study interval). In addition, the lower threshold results in a greater proportion of the total radiant flux (81–90%) and SO_2 emissions (61–76%) occurring in phases, i.e., being co-eruptive. The mean daily SO_2 emission rate between phases and pauses varies relatively little when we change the threshold because the greater duration of phases than pauses offsets the increased total phase emissions. For the greater proportion of gas and thermal emissions falling in the co-eruptive phases, we prefer the 1.0×10^{14} J threshold and have shaded (**Figure 6**) on this basis.

We have limited independent verification of the timing of active lava extrusion with which to test our defined pauses and phases, partly from the 14-month TerraSar-X study of Wadge et al. (2012) but mostly from ASTER imagery. ASTER observations of the world's volcanoes are archived and freely accessible online in the ASTER Volcano Archive [https://ava.jpl.nasa.gov/]. Observations of Bagana are relatively infrequent but this is offset by ASTER's high spatial resolution which detects sub-km thermal anomalies with greater reliability than sensors such as MODIS with relatively coarse spatial resolution. ASTER observations of active lava flows are shown in **Figure 6** by the black stars. 81% of ASTER-detected active lava flows fall within intervals we have defined as co-eruptive phases. ASTER thermal anomalies during our quiescent pauses may indicate cooling lava flows, rather than active extrusion, but we cannot rule out the possibility that extrusive episodes are slightly longer or shorter in length than our criteria (based on MODIS observations alone) would suggest. We consider this a relatively minor uncertainty.

Our OMI data indicate that the majority of SO_2 emissions occur in eruptive phases rather than in pauses (**Table 1**), with mean co-eruptive emission rates of 3,290–3,390 td^{-1} around 30% higher than mean quiescent emission rates of 2,530–2,660 td^{-1}. These daily emission rates are comparable to previously reported SO_2 emissions from Bagana, whether satellite- (Carn et al., 2017) or ground-based measurements (Global Volcanism Program, 1983, 1989; McGonigle et al., 2004b), and confirm Bagana's place among the very largest volcanic SO_2 sources worldwide (Shinohara, 2013; Carn et al., 2017). No estimates yet exist of volcanic CO_2 emissions from Papua New Guinea (Burton et al., 2013) and given the high SO_2 emissions reported throughout the region (McCormick et al., 2012) this is considered a significant gap in our global dataset. Recent studies (Aiuppa et al., 2017; Mason et al., 2017) debate the importance of crustal or subducted carbon in modulating magmatic CO_2/S_{TOTAL} ratios, and thefore CO_2 emissions, and given the lack of constraint on these variables for the New Britain–Bougainville subduction system we cannot speculate too far. However, if our estimated SO_2 emission rates are correct, even a "carbon-poor" scenario (CO_2/S_{TOTAL} ∼1-2) could result in a daily CO_2 emissions from Bagana of 2.5–6.8 ktd^{-1}, or 0.9–2.5 Mt yr^{-1}, comparable to known major sources such as Ambrym, Etna, or Popocatépetl (Burton et al., 2013; Allard et al., 2016).

5.2. Explaining Bagana's High SO_2 Emissions

In common with many other arc volcanoes, lava and gas fluxes at Bagana initially seem strongly coupled, in that degassing of ascending and erupting magma supplies a strong co-eruptive gas plume. However, our discovery of substantial passive emissions at Bagana requires an additional source of gas, other than decompression-driven degassing of magma during eruption. One possibility is that the Bagana plumbing system stores a larger

TABLE 1 | Table summarizing the characteristics of co-eruptive phases and inter-eruptive pauses at Bagana, with alternative thresholds used to define phase-pause transition.

	1.5 $\times10^{14}$ J threshold		**1.0 $\times10^{14}$ J threshold**	
	Phases	*Pauses*	Phases	*Pauses*
No. episodes	24	*25*	19	*20*
Total duration (months)	95	*118*	127	*86*
Total radiant flux ($\times10^{14}$ J)	25.2	*6.0*	28.4	*2.6*
Total SO_2 emissions (kt)	4,776	*3,048*	5,941	*1,884*
Mean SO_2 emissions (td^{-1})	3,389	*2,662*	3,286	*2,525*

volume of basaltic andesite magma than is erupted, and sulfur-rich vapor exsolving from this magma is continually free to ascend to the surface, regardless of the prevailing state of activity. Alternatively, this excess vapor phase could be supplied by a more primitive, deeper-stored magma, generating a substantial fraction of exsolved magmatic vapor (Wallace, 2001, 2005; Gerlach et al., 2008; Wallace and Edmonds, 2011). Underplating by more primitive magmas is well established in many arc volcanoes and there is often chemical or textural evidence for interaction between a deeper reservoir and the shallow-stored magma that supplies eruptions (Bacon, 1986; Clynne, 1999; Murphy et al., 2000; Coombs et al., 2003; Humphreys et al., 2006; Plail et al., 2018). At Bagana, detailed textural or chemical analyses of erupted products might offer a way of distinguishing these scenarios. In the meantime, our study offers the first good evidence for an excess gas phase.

The interval over which we have the best estimate of erupted volume is October 2010 to December 2011, thanks to the Wadge et al. (2012)'s TerraSar-X survey. The total extruded volume in this interval was 33×10^6 m^3, with an estimated mass of 92.4×10^6 t based on a reasonable density for basaltic andesite of 2.8 g cm^{-3}. Assuming a phenocryst content of 42% (the mean value across 33 analyzed Bagana lavas, Bultitude et al., 1978), the mass of degassing melt is $\sim 53.6 \times 10^6$ tons. Integrated SO_2 emissions through this interval was 7.2×10^5 t, of which 3.6×10^5 t is sulfur. As a first approximation, we can calculate the concentration of sulfur in the melt, $[S_{MELT}]$, by dividing the emitted sulfur mass by the erupted lava mass, yielding an estimate for $[S_{MELT}]$ of 6,340 ppm. Given the previously discussed uncertainty on the SO_2 lifetime used to convert scene mass loadings into emission rates, the range of potential $[S_{MELT}]$ calculated for this interval is 4,760–10,260 ppm.

We can repeat this calculation for the full duration of our SO_2 dataset, 13 years from October 2004 to end September 2017. We assume that the long-term, that is inter-annual, mean extrusion rate at Bagana is ~ 1.0 m^3s^{-1} (Wadge et al., 2018). From **Figure 6** we calculate that Bagana was in an eruptive state for 127 months of our full OMI SO_2 time series (note this calculation uses the data based on the 1.0 $\times10^{14}$ J threshold in **Table 1**). Combining these data, we estimate the erupted lava volume in this window to be 340×10^6 m^3, equal to a degassing melt mass of 552×10^6 t. Our total co-eruptive SO_2 mass loading in 2004–2017 was 5.9 $\times$ 10^6 t SO_2, of which 2.95×10^6 t sulfur. From these data, we estimate $[S_{MELT}]$ to be 5340 ppm (with a potential range, due to uncertainty on integrated SO_2 emissions of 3,990–8,700 ppm).

We consider these estimates of $[S_{MELT}]$ to be implausible. Sulfur concentration of melts can vary widely, but for andesitic magma at shallow crustal pressures (below 200 MPa) and relatively oxidizing conditions (around ΔFMQ 1-2) we would not anticipate more than a few hundred ppm, while island arc basalts may hold percent-level sulfur at sulfide saturation (Liu et al., 2007; Jugo, 2009). More likely, volatiles are supplied from additional non-erupted magma. If this were of similar basaltic andesite composition to the erupted lavas, we would require volumes of non-erupting but degassing magma to be a factor of 5-6 greater than the total erupted volume, in order to bring our calculated $[S_{MELT}]$ from ∼5,000–6,000 ppm below at least ∼1,000 ppm. From this, we might infer significant endogenic growth of the volcanic edifice, thus-far undetected as focussed TerraSar-X surveys (e.g., Wadge et al., 2012, 2018) may not be sensitive to topographic change of the entire edifice relative to a surrounding regional baseline. Alternatively, there may be a long-lived, established reservoir where exsolved volatiles accumulate with relatively evolved lavas near the roof zone (Huber et al., 2012; Parmigiani et al., 2016; Edmonds and Woods, 2018). The upper reaches of the reservoir are tapped periodically by eruption and the reservoir is fed over longer timescales by underplating mafic magma that supplies the observed excess volatile phase. Chemical and textural analyses of Bagana's erupted products could shed light on magma intensive parameters and pre-eruptive reservoir processes.

5.3. Influence of Gas Emissions on Eruptive Style

The first quantitative reports of Bagana's extreme SO_2 emissions date to the 1980s (Global Volcanism Program, 1983, 1989) and given historical reports and photographs of thick gas plumes emanating from the summit (Bultitude, 1976, 1981; Bultitude et al., 1978; Bultitude and Cooke, 1981) it is a reasonable assumption that open system degassing is a persistent characteristic of the volcano's activity. This open system behavior—whether controlled by a permeable bubble network within the rising magma or by fractures around the conduit—is likely to be an important control on Bagana's dominantly effusive mode of eruption (Edmonds et al., 2003; Cashman, 2004; Gonnermann and Manga, 2007; Farquharson et al., 2015). If permeability were to be compromised and gas escape impeded, the resulting overpressure could trigger Vulcanian-style explosive eruptions or dome collapse events, yielding pyroclastic flows and ballistic fallout around the edifice. Such phenomena have been reported from Bagana (Bultitude, 1976; Bultitude and Cooke, 1981). Explosive damage to the crater rim may influence the flow direction of subsequent lava extrusion. Sudden transitions to explosive activity change the nature of volcanic hazard at Bagana and modify the risk to surrounding populations. Although the threatened population is relatively small (8,000, as of 2013), several villages lie in river valleys downslope of the volcano and could be at risk from density current hazards. Given the limited monitoring onsite, mitigating for these potential higher risk scenarios is a significant challenge.

6. CONCLUSIONS

Earlier studies of Bagana volcano have described persistent lava extrusion and a strong sustained summit gas plume over several decades, if not centuries (Bultitude, 1976, 1981; Bultitude et al., 1978; Bultitude and Cooke, 1981; McGonigle et al., 2004b). Our multi-year satellite observations of SO_2 mass loading and thermal infrared radiant flux expand our previous work on this volcano (McCormick et al., 2012; Wadge et al., 2012, 2018) and demonstrate that although lava extrusion and gas emissions are indeed persistent, they are also highly variable on inter-annual and sub-annual timescales. We contend that a first-order coupling exists between lava extrusion and gas emissions, with peak SO_2 mass loadings identified during episodes or "phases" of active extrusion lasting several months. In addition, we find evidence for inter-eruptive "pauses," of similar duration, where extrusion may largely cease, radiant flux emissions are restricted to the cooling of fresh lava flows or the volcano's small summit dome, and yet passive SO_2 emissions continue. This pattern of activity—peak gas emissions during extrusive episodes, yet substantial emissions continuing during quiescence—is consistent with that seen at other persistently active silicic volcanoes, such as Bezymianny, Tungurahua, Soufrière Hills, and Popocatépetl (Delgado-Granados et al., 2001; Edmonds et al., 2003; Arellano et al., 2008; Lopez et al., 2013b).

Based on satellite-based OMI data, we have calculated, over multi-year timescales, daily mean SO_2 emissions at Bagana of $\sim$3,300 td^{-1} in co-eruptive phases and $\sim$2,500 td^{-1} in inter-eruptive pauses. Converting observed SO_2 mass loadings into at-source emission rates remains subject to significant uncertainties, chiefly over SO_2 lifetime, and future work must engage with the challenge of quantifying temporal variation in lifetime with local atmospheric conditions. These uncertainties notwithstanding, our results confirm that Bagana is among the largest global volcanic SO_2 sources. We explore the reasons for the extremely high SO_2 emissions and conclude that either the magma is unusually sulfur-rich, or there is significant "excess" sulfur degassing from magma that does not erupt, whether the same basaltic-andesite that supplies the lava extrusion or a deeper body that may or may not interact chemically and physically with the erupted magma. Distinguishing these scenarios could be accomplished by geochemical and petrographic methods and is a key goal of our future work. Meanwhile, we highlight that the open system degassing of Bagana is very likely to be critical for its generally effusive behavior. Sudden loss of conduit or magma permeability to ascending gas may result in explosive eruptions, far larger than the mild ash venting activity we have described herein. Such explosive eruptions are known from the historical record. Mitigating for these higher risk events at such a remote volcano is a formidable challenge to in-country hazard management authorities.

AUTHOR CONTRIBUTIONS

BM conceived of the study, analyzed and interpreted satellite data, prepared the figures, and wrote the manuscript with further interpretation of the data contributed by the other authors. GW analyzed the ASTER imagery. KM provided data from Rabaul Volcanological Observatory reports. All authors read, reviewed and approved all versions of the manuscript.

FUNDING

The research leading to these results has received funding from the NERC Centre for Observation and Modeling of Earthquakes, Volcanoes and Tectonics (COMET); from the Deep Carbon Observatory programme DECADE (DEep CArbon DEgassing); from the British Geological Survey; and from the Isaac Newton Trust at the University of Cambridge. All satellite data used in this study are provided by NASA and are in the public domain.

ACKNOWLEDGMENTS

BM, GW, and ME acknowledge funding from NERC COMET. BM acknowledges further financial support from the British Geological Survey, the Isaac Newton Trust at the University of Cambridge, and the Deep Carbon Observatory. BM acknowledges valuable discussions with Lois Salem, Peter Webley, Simon Carn, Fred Prata, and particularly Adele Bear-Crozier. We thank two reviewers for their careful and perceptive comments and Andrew McGonigle for his editorial handling.

SUPPLEMENTARY MATERIAL

The Supplementary Material for this article can be found online at: https://www.frontiersin.org/articles/10.3389/feart.2019.00009/full#supplementary-material

REFERENCES

Aiuppa, A., Fischer, T., Plank, T., Robidoux, P., and Napoli, R. D. (2017). Along-arc, inter-arc and arc-to-arc variations in volcanic gas co_2/s_t ratios reveal daul source of carbon in arc volcanism. *Earth Sci. Rev.* 168, 24–47. doi: 10.1016/j.earscirev.2017.03.005

Allard, P., Aiuppa, A., Bani, P., Metrich, N., Bertagnini, A., Gauthier, P.-J., et al. (2016). Prodigious emission rates and magma degassing budget of major, trace and radioactive volatile species from Ambrym basaltic volcano, Vanuatu island arc. *J. Volcanol. Geother. Res.* 322, 119–143. doi: 10.1016/j.jvolgeores.2015.10.004

Andres, R., and Kasgnoc, A. (1998). A time-averaged inventory of subaerial volcanic sulphur emissions. *J. Geophys. Res.* 103, 25251–25261. doi: 10.1029/98JD02091

Arellano, S., Hall, M., Samaniego, P., Pennec, J.-L. L., Ruiz, A., Molina, I., et al. (2008). Degassing patterns of Tungurahua volcano (Ecuador) during the 1999-2006 eruptive period, inferred from remote spectroscopic measurements of SO_2 emissions. *J. Volcanol. Geother. Res.* 176, 151–162. doi: 10.1016/j.jvolgeores.2008.07.007

Auker, M., Sparks, R., Siebert, L., Crosswellen, H., and Ewert, J. (2013). A statistical analysis of the global historical volcanic fatalities record. *J. Appl. Volcanol.* 2:2.

Bacon, C. (1986). Magmatic inclusions in silicic and intermediate volcanic rocks. *J. Geophys. Res.* 91, 6091–6112. doi: 10.1029/JB091iB06p06091

Barmin, A., Melnik, O., and Sparks, R. (2002). Periodic behaviour in lava dome eruptions. *Earth Planet. Sci. Lett.* 199, 173–184. doi: 10.1016/S0012-821X(02)00557-5

Beirle, S., Hörmann, C., de Vries, M. P., Dörner, S., Kern, C., and Wagner, T. (2014). Estimating the volcanic emission rate and atmospheric lifetime of SO$_2$ from space: a case study for Kīlauea volcano, Hawai'i. *Atmosph. Chem. Phys.* 14, 8309–8322. doi: 10.5194/acp-14-8309-2014

Blake, D. (1968). Post Miocene volcanoes on Bougainville Island, territory of Papua and New Guinea. *Bull. Volcanol.* 32, 121–138. doi: 10.1007/BF02596588

Blake, D., and Miezitis, Y. (eds.). (1967). *Geology of Bougainville and Buka Islands, New Guinea*. Canberra: Bureau of Mineral Resources, Geology and Geophysics Bulletin No. 93.

Boichu, M., Menut, L., Khvorostayanov, D., Clarisse, L., Clerbaux, C., Turquety, S., et al. (2013). Inverting for volcanic SO$_2$ flux at high temporal resolution using spaceborne plume imagery and chemistry-transport modelling: the 2010 Eyjafjallajökull eruption case study. *Atmosph. Chem. Phys.* 13, 8569–8584. doi: 10.5194/acp-13-8569-2013

Bultitude, R. (1976). "Eruptive history of Bagana volcano, Papua New Guinea, between 1882 and 1975," in *Volcanism in Australasia*, ed R. Johnson (Amsterdam: Elsevier), 317–336.

Bultitude, R. (1981). "Literature search for pre-1945 sightings of volcanoes and their activity on Bougainville Island," in *Cooke-Ravian Volume of Volcanological Papers*, Vol. 10, ed R. Johnson (Geological Survey of Papua New Guinea Memoir), 227–242.

Bultitude, R., and Cooke, R. (1981). "Note on activity from Bagana volcano from 1975 to 1980," in *Cooke-Ravian Volume of Volcanological Papers*, Vol. 10, ed R. Johnson (Port Moresby: Geological Survey of Papua New Guinea Memoir), 243–248.

Bultitude, R., Johnson, R., and Chappell, B. (1978). Andesites of Bagana volcano, Papua New Guinea: chemical stratigraphy, and a reference andesite composition. *BMR J. Aust. Geol. Geophys.* 3, 281–295.

Burton, M., Sawyer, G., and Granieri, D. (2013). Deep carbon emissions from volcanoes. *Rev. Mineral. Geochem.* 75, 323–354. doi: 10.2138/rmg.2013.75.11

Carn, S. (2011). *Omiplot Software*. Available online at: https://vhub.org/resources/682

Carn, S., Clarisse, L., and Prata, A. (2016). Multi-decadal satellite measurements of global volcanic degassing. *J. Volcanol. Geother. Res.* 311, 99–134. doi: 10.1016/j.jvolgeores.2016.01.002

Carn, S., Fioletov, V., McLinden, C., Li, C., and Krotkov, N. (2017). A decade of global volcanic SO$_2$ emissions measured from space. *Sci. Rep.* 7:44095. doi: 10.1038/srep44095

Carn, S., Krotkov, N., Yang, K., and Krueger, A. (2013). "Measuring global volcanic degassing with the Ozone Monitoring Instrument (OMI)," in *Remote Sensing of Volcanoes and Volcanic Processes: Integrating Observation and Modeling*, Vol. 380, eds D. Pyle, T. Mather, and J. Biggs (Geological Society of London Special Publications), 229–257.

Carn, S., and Prata, F. (2010). Satellite-based constraints on explosive SO$_2$ release from Soufrière Hills Volcano, Montserrat. *Geophys. Res. Lett.* 37:L00E22. doi: 10.1029/2010GL044971

Cashman, K. (2004). "Volatile controls on magma ascent and eruption," in *The State of the Planet: Frontiers and Challenges in Geophysics*, eds R. Sparkes and C. Hawkesworth (Washington, DC: IUGG Geophysical Monograph), 109–124. doi: 10.1029/150GM10

Clynne, M. (1999). A complex magma mixing origin for rocks erupted in 1915, Lassen Park, California. *J. Petrol.* 40, 105–132. doi: 10.1093/petroj/40.1.105

Cole, P., Smith, P., Komorowski, J.-C., Alfano, F., Bonadonna, C., Stinton, A., et al. (2014). "Ash venting occurring both prior to and during lava extrusion at Soufrière Hills Volcano, Montserrat, from 2005 to 2010," in *The Eruption of Soufrière Hills Volcano, Montserrat from 2000 to 2010*, Vol. 39, eds G. Wadge, R. Robertson, and B. Voight (London: Geological Society of London Memoirs), 71–92.

Cooke, R., and Johnson, R. (1978). *Volcanoes and Volcanology in Papua New Guinea*. Geological Survey of Papua New Guinea Reports, 78/2.

Coombs, M., Eichelberger, J., and Rutherford, M. (2003). Experimental and textural constraints on mafic enclave formation in volcanic rocks. *J. Volcanol. Geother. Res.* 119, 125–144. doi: 10.1016/S0377-0273(02)00309-8

Coppola, D., Laiolo, M., Cigolini, C., Donne, D. D., and Ripepe, M. (2016). "Enhanced volcanic hot-spot detection using MODIS IR data: results from the MIROVA system," in *Detecting, Modeling and Responding to Effusive Eruptions*, Vol. 426, eds A. Harris, T. de Groeve, F. Garel, and S. Carn (London: Geological Society of London Special Publications), 181–205.

Delgado-Granados, H., González, L., and Sánchez, N. (2001). Sulfur dioxide emissions from Popocatépetl volcano (Mexico): case study of a high-emission rate, passively degassing erupting volcano. *J. Volcanol. Geother. Res.* 108, 107–120. doi: 10.1016/S0377-0273(00)00280-8

Druitt, T., and Kokelaar, B., editors (2002). *The Eruption of Soufrière Hills Volcano, Montserrat, from 1995 to 1999*. Geological Society of London Memoir No. 21.

Eatough, D., Caka, F., and Farber, R. (1994). The conversion of SO$_2$ to sulfate in the atmosphere. *Israeli J. Chem.* 34, 301–314. doi: 10.1002/ijch.199400034

Edmonds, M., Oppenheimer, C., Pyle, D., Herd, R., and Thompson, G. (2003). SO$_2$ emissions from Soufrière Hills Volcano and their relationship to conduit permeability, hydrothermal interaction and degassing regime. *J. Volcanol. Geother. Res.* 124, 23–43. doi: 10.1016/S0377-0273(03)00041-6

Edmonds, M., and Woods, A. (2018). Exsolved volatiles in magma reservoirs. *J. Volcanol. Geother. Res.* 368, 13–30. doi: 10.1016/j.jvolgeores.2018.10.018

Faloona, I. (2009). Sulfur processing in the marine atmospheric boundary layer: a review and critical assessment of modeling uncertainties. *Atmospher. Environ.* 43, 2841–2854. doi: 10.1016/j.atmosenv.2009.02.043

Farquharson, J., Heap, M., Varley, N., Baud, P., and Reuschlé, T. (2015). Permeability and porosity relationships of edifice-forming andesites: a combined field and laboratory study. *J. Volcanol. Geother. Res.* 297, 52–68. doi: 10.1016/j.jvolgeores.2015.03.016

Fioletov, V., McLinden, C., Krotkov, N., Li, C., Joiner, J., Theys, N., et al. (2016). A global catalogue of large SO$_2$ sources and emissions derived from the Ozone Monitoring Instrument. *Atmospher. Chem. Phys.* 16, 11497–11519. doi: 10.5194/acp-16-11497-2016

Flower, V., Carn, S., and Wright, R. (2016). The impact of satellite sensor viewing geometry on time-series analysis of volcanic emissions. *Remote Sens. Environ.* 183, 282–293. doi: 10.1016/j.rse.2016.05.022

Geirsson, H., Rodgers, M., LaFemina, P., Witter, M., Roman, D., Muñoz, A., et al. (2014). Multidisciplinary observations of the 2011 explosive eruption of telica volcano, nicaragua: implications for the dynamics of low-explosivity ash eruptions. *J. Volcanol. Geother. Res.* 271, 55–69. doi: 10.1016/j.jvolgeores.2013.11.009

Gerlach, T., McGee, K., and Doukas, M. (2008). Emission rates of CO$_2$, SO$_2$, and H$_2$S, scrubbing, and preeruption excess volatiles at Mount St. Helens, 2004-2005. *US Geol. Survey Professional Paper* 1750, 543–572. doi: 10.3133/pp175026

Global Volcanism Program (1983). Report on Bagana (Papua New Guinea). *Sci. Event Alert Network Bull.* 8:9.

Global Volcanism Program (1989). Report on Bagana (Papua New Guinea). *Scientific Event Alert Network Bull.* 14:7.

Global Volcanism Program (2013). Smithsonian Institution Volcanoes of the World, v. 4.6.0.

Gonnermann, H., and Manga, M. (2007). The fluid mechanics inside a volcano. *Annu. Rev. Fluid Mech.* 39, 321–356. doi: 10.1146/annurev.fluid.39.050905.110207

Guffanti, M., and Miller, T. (2013). A volcanic activity alert-level system for aviation: review of its development and application in Alaska. *Nat. Hazards* 69, 1519–1533. doi: 10.1007/s11069-013-0761-4

Holm, R., and Richards, S. (2013). A re-evaluation of arc-continent collision and along-arc variation in the Bismarck Sea region, Papua New Guinea. *Aust. J. Earth Sci.* 60, 605–619. doi: 10.1080/08120099.2013.824505

Holm, R., Rosenbaum, G., and Richards, S. (2016). Post 8 Ma reconstruction of Papua New Guinea and Solomon Islands: microplate tectonics in a convergent plate boundary setting. *Earth Sci. Rev.* 156, 66–81. doi: 10.1016/j.earscirev.2016.03.005

Huber, C., Bachmann, O., Vigneresse, J., Dufek, J., and Parmigiani, A. (2012). A physical model for metal extraction and transport in shallow magmatic systems. *Geochem. Geophys. Geosyst.* 13:Q08003. doi: 10.1029/2012GC004042

Humphreys, M., Blundy, J., and Sparks, R. (2006). Magma evolution and open-system processes at Shiveluch volcano: insights from phenocryst zoning. *J. Petrol.* 47, 2303–2334. doi: 10.1093/petrology/egl045

Jugo, P. (2009). Sulfur content at sulfide saturation in oxidized magmas. *Geology* 37, 415–418. doi: 10.1130/G25527A.1

Kaufman, Y. J., Justice, C. O., Flynn, L. P., Kendall, J. D., Prins, E. M., Giglio, L., et al. (1998). Potential global fire monitoring from EOS-MODIS. *J. Geophys. Res.* 103, 32215–32238. doi: 10.1029/98JD01644

Krotkov, N., Carn, S., Krueger, A., Bhartia, P., and Yang, K. (2006). Band residual difference algorithm for retrieval of SO_2 from the AURA Ozone Monitoring Instrument (OMI). *IEEE Trans. Geosci. Remote Sens.* 44, 1259–1266. doi: 10.1109/TGRS.2005.861932

Krotkov, N. A., McLinden, C. A., Li, C., Lamsal, L. N., Celarier, E. A., Marchenko, S. V., et al. (2016). Aura OMI observations of regional SO_2 and NO_2 pollution changes from 2005 to 2015. *Atmosph. Chem. Phys.* 16, 4605–4629. doi: 10.5194/acp-16-4605-2016

Levelt, P., Hilsenrath, E., Leppelmeier, G., van den Oord, G., Bhartia, P., Tamminen, J., et al. (2006a). Science objectives of the Ozone Monitoring Instrument. *IEEE Trans. Geosci. Remote Sens.* 44, 1199–1208. doi: 10.1109/TGRS.2006.872336

Levelt, P., van den Oord, G., Dobber, M., Mlkki, A., Visser, H., de Vries, J., et al. (2006b). The ozone monitoring instrument. *IEEE Trans. Geosci. Remote Sens.* 44, 1093–1100. doi: 10.1109/TGRS.2006.872333

Li, C., Joiner, J., Krotkov, N., and Bhartia, P. (2013). A fast and sensitive new satellite SO_2 retrieval algorithm based on principal component analysis: application to the Ozone Monitoring Instrument. *Geophys. Res. Lett.* 40, 1–5. doi: 10.1002/2013GL058134

Li, C., Krotkov, N., Carn, S., Zhang, Y., Spurr, R., and Joiner, J. (2017). New-generation NASA Aura Ozone Monitoring Instrument (OMI) volcano SO_2 dataset: algorithm description, initial results, and continuation with the Suomi-NPP Ozone Mapping and Profiler Suite (OMPS). *Atmosph. Meas. Techniq.* 10, 445–458. doi: 10.5194/amt-10-445-2017

Liu, Y., Samaha, N.-T., and Baker, D. (2007). Sulfur concentration at sulfide saturation (SCSS) in magmatic silicate melts. *Geochim. Cosmochim. Acta* 71, 1783–1799. doi: 10.1016/j.gca.2007.01.004

Lopez, T., Carn, S., Werner, C., Fee, D., Kelly, P., Doukas, M., et al. (2013a). Evaluation of Redoubt volcano's sulfur dioxide emissions by the Ozone Monitoring Instrument. *J. Volcanol. Geother. Res.* 259, 290–307. doi: 10.1016/j.jvolgeores.2012.03.002

Lopez, T., Ushakov, S., Izbekov, P., Tassi, F., Cahill, C., Neill, O., et al. (2013b). Constraints on magma processes, subsurface conditions, and total volatile flux at Bezymianny Volcano in 2007-2010 from direct and remote volcanic gas measurements. *J. Volcanol. Geother. Res.* 263, 92–107. doi: 10.1016/j.jvolgeores.2012.10.015

Mason, E., Edmonds, M., and Turchyn, A. (2017). Remobilization of crustal carbon may dominate arc volcanic emissions. *Science* 357, 290–294. doi: 10.1126/science.aan5049

McCormick, B., Edmonds, M., Mather, T., and Carn, S. (2012). First synoptic analysis of volcanic degassing in Papua New Guinea. *Geochem. Geophys. Geosyst.* 13:Q03008. doi: 10.1029/2011GC003945

McCormick, B., Herzog, M., Yang, J., Edmonds, M., Mather, T., Carn, S., et al. (2014). A comparison of satellite- and ground-based measurements of SO_2 emissions from Tungurahua volcano, Ecuador. *J. Geophys. Res.* 119, 4264–4285.

McCormick, B., Popp, C., Andrews, B., and Cottrell, E. (2015). Ten years of satellite observations reveal highly variably sulphur dioxide emissions at Anatahan Volcano, Mariana Islands. *J. Geophys. Res.* 120, 7258–7282. doi: 10.1002/2014JD022856

McGonigle, A., Delmelle, P., Oppenheimer, C., Tsanev, V., Delfosse, T., Williams-Jones, G., et al. (2004a). SO_2 depletion in tropospheric volcanic plumes. *Geophys. Res. Lett.* 31:L13201. doi: 10.1029/2004GL019990

McGonigle, A., Oppenheimer, C., Tsanev, V., Saunders, S., Mulina, K., Tohui, S., et al. (2004b). Sulphur dioxide fluxes from papua new guinea's volcanoes. *Geophys. Res. Lett.* 31:L08606. doi: 10.1029/2004GL019568

Murphy, M., Sparks, R., Barclay, J., Carroll, M., and Brewer, T. (2000). Remobilization of andesite magma by intrusion of mafic magma at the Soufrière Hills Volcano, Montserrat, West Indies. *J. Petrol.* 41, 21–42. doi: 10.1093/petrology/41.1.21

Norton, G., Watts, R., Voight, B., Mattioli, G., Herd, R., Young, S., et al. (2002). Pyroclastic flow and explosive activity at soufrière hills volcano, montserrat, during a period of virtually no magma extrusion (march 1998 to november 1999). *Geol. Soc. Memoir* 21, 467–481. doi: 10.1144/GSL.MEM.2002.021.01.21

Oppenheimer, C., Francis, P., and Stix, J. (1998). Depletion rates of sulfur dioxide in tropospheric volcanic plumes. *Geophys. Res. Lett.* 25, 2671–2674. doi: 10.1029/98GL01988

Parmigiani, A., Faroughi, S., Huber, C., Bachmann, O., and Su, Y. (2016). Bubble accumulation and its role in the evolution of magma reservoirs in the upper crust. *Nature* 532, 492–495. doi: 10.1038/nature17401

Pieri, D., and Abrams, M. (2004). ASTER watches the world's volcanoes: a new paradigm for volcanological observations from orbit. *J. Volcanol. Geother. Res.* 135, 13–28. doi: 10.1016/j.jvolgeores.2003.12.018

Plail, M., Edmonds, M., Woods, A., Barclay, J., Humphreys, M., Herd, R., et al. (2018). Mafic enclaves record syn-eruptive basalt intrusion and mixing. *Earth Planet. Sci. Lett.* 484, 30–40. doi: 10.1016/j.epsl.2017.11.033

Power, J., Coombs, M., and Freymueller, J., editors (2010). "The 2006 eruption of Augustine Volcano, Alaska," in *U.S Geological Society Professional Paper 1769*.

Rodriguez, L., Watson, I., Edmonds, M., Ryan, G., Hards, V., Oppenheimer, C., et al. (2008). SO_2 loss rates in the plume emitted by Soufrière Hills volcano, Montserrat. *J. Volcanol. Geother. Res.* 173, 135–147. doi: 10.1016/j.jvolgeores.2008.01.003

Rogerson, R. J., Hilyard, D. B., Finlayson, E. J., Johnson R. W., and McKee, C. O. (1989). *The Geology and Mineral Resources of Bougainville and Buka Islands, Papua New Guinea, Vol 16*. Port Moresby: Geological Survey of Papua New Guinea Memoir, 217.

Rothery, D., Coppola, D., and Saunders, C. (2005). Analysis of volcanic activity patterns using MODIS thermal alerts. *Bull. Volcanol.* 67, 539–556. doi: 10.1007/s00445-004-0393-3

Sheldrake, T., Sparks, R., Cashman, K., Wadge, G., and Aspinall, W. (2016). Similarities and differences in the historical records of lava dome-building volcanoes: Implications for understanding magmatic processes and eruption forecasting. *Earth Sci. Rev.* 160, 240–263. doi: 10.1016/j.earscirev.2016.07.013

Sherrod, D., Scott, W., and Stauffer, P., editors (2008). "A Volcano Rekindled; The Renewed Eruption of Mount St. Helens, 2004-2008," in *U.S Geological Society Professional Paper 1750*.

Shinohara, H. (2013). Volatile flux from subduction zone volcanoes: insights from a detailed evaluation of the fluxes from volcanoes in Japan. *J. Volcanol. Geother. Res.* 268, 46–63. doi: 10.1016/j.jvolgeores.2013.10.007

Stix, J., Zapata, J. A., Calvache, M. V., Cortés, G. P., Fischer, T. P., Gómez, D., et al. (1993). A model of degassing at Galeras Volcano, Colombia, 1988-1993. *Geology* 21, 963–967. doi: 10.1130/0091-7613(1993)021<0963:AMODAG>2.3.CO;2

Syracuse, E., and Abers, G. (2004). Global compilation of variations in slab depth beneath arc volcanoes and implications. *Geochem. Geophys. Geosyst.* 7:Q05017.

Thomas, H., Watson, I., Kearney, C., Carn, S., and Murray, S. (2009). A multi-sensor comparison of sulphur dioxide emissions from the 2005 eruption of Sierra Negra volcano, Galápagos Islands. *Remote Sens. Environ.* 113, 1331–1342. doi: 10.1016/j.rse.2009.02.019

Tregoning, P., Lambeck, K., Stoltz, A., Morgan, P., McClusky, S., van der Beek, P., et al. (1998). Estimation of current plate motions in Papua New Guinea from Global Positioning System observations. *J. Geophys. Res.* 103, 12181–12203. doi: 10.1029/97JB03676

Wadge, G., McCormick Kilbride, B. T., Edmonds, M., and Johnson, R. (2018). Persistent growth of a young andesite lava cone: Bagana Volcano, Papua New Guinea. *J. Volcanol. Geother. Res.* 356, 304–315. doi: 10.1016/j.jvolgeores.2018.03.012

Wadge, G., Robertson, R., and Voight, B., editors (2014). *The Eruption of Soufrière Hills Volcano, Montserrat from 2000 to 2010*. Geological Society of London Memoir No. 39. doi: 10.1144/M39.1

Wadge, G., Saunders, S., and Itikarai, I. (2012). Pulsatory andesite lava flow at Bagana volcano, Papua New Guinea. *Geochem. Geophys. Geosyst.* 13:Q11011.

Wallace, P. (2001). Volcanic SO_2 emissions and the abundance and distribution of exsolved gas in magma bodies. *J. Volcanol. Geother. Res.* 108, 85–106. doi: 10.1016/S0377-0273(00)00279-1

Wallace, P. (2005). Volatiles in subduction zone magmas: concentrations and fluxes based on melt inclusion and volcanic gas data. *J. Volcanol. Geother. Res.* 140, 217–240. doi: 10.1016/j.jvolgeores.2004.07.023

Wallace, P., and Edmonds, M. (2011). The sulfur budget in magmas: evidence from melt inclusions, submarine glasses, and volcanic gas emissions. *Rev. Mineral. Geochem.* 73, 215–246. doi: 10.2138/rmg.2011.73.8

Wooster, M., Zhukov, B., and Oertel, D. (2003). Fire radiative energy for quantitative study of biomass burning: derivation from the BIRD experimental satellite and comparison to MODIS fire products. *Remote Sens. Environ.* 86, 83–107. doi: 10.1016/S0034-4257(03)00070-1

Wright, R. (2016). MODVOLC: 14 years of autonomous observations of effusive volcanism from space. *Geol. Soc. Lond. Spec. Publ.* 426, 23–53. doi: 10.1144/SP426.12

Wright, R., Flynn, L., Garbeil, H., Harris, A., and Pilger, E. (2002). Automated volcanic eruption detection using MODIS. *Remote Sens. Environ.* 82, 135–155. doi: 10.1016/S0034-4257(02)00030-5

Wright, R., Flynn, L., Garbeil, H., Harris, A., and Pilger, E. (2004). MODVOLC: near-real-time thermal monitoring of global volcanism. *J. Volcanol. Geother. Res.* 135, 29–49. doi: 10.1016/j.jvolgeores.2003.12.008

Yang, K., Krotkov, N., Krueger, A., Carn, S., Bhartia, P., and Levelt, P. (2007). Retrieval of large volcanic SO_2 columns from the Aura Ozone Monitoring Instrument: comparison and limitations. *J. Geophys. Res.* 112:D24S43. doi: 10.1029/2007JD008825

Yang, K., Krotkov, N., Krueger, A., Carn, S., Bhartia, P., and Levelt, P. (2009). Improving retrieval of volcanic sulfur dioxide from backscattered UV satellite observations. *Geophys. Res. Lett.* 36:L03102. doi: 10.1029/2008GL036036

Conflict of Interest Statement: The authors declare that the research was conducted in the absence of any commercial or financial relationships that could be construed as a potential conflict of interest.

frontiers
in Earth Science

TECHNOLOGY REPORT
published: 13 March 2019
doi: 10.3389/feart.2019.00026

Non-dispersive UV Absorption Spectroscopy: A Promising New Approach for *in-situ* Detection of Sulfur Dioxide

Jan-Lukas Tirpitz[1]*, **Denis Pöhler**[1], **Nicole Bobrowski**[2], **Bruce Christenson**[3], **Julian Rüdiger**[4], **Stefan Schmitt**[1] and **Ulrich Platt**[1,2]

[1] Department of Physics and Astronomy, Institute of Environmental Physics, University of Heidelberg, Heidelberg, Germany, [2] Max-Planck Institute for Chemistry, Mainz, Germany, [3] National Isotope Centre, GNS Science, Lower Hutt, New Zealand, [4] Atmospheric Chemistry, BayCEER, University of Bayreuth, Bayreuth, Germany

A new type of instrument for *in-situ* detection of volcanic sulfur dioxide is presented on the basis of non-dispersive UV absorption spectroscopy. It is a promising alternative to presently used compact and low-cost SO_2 monitoring techniques, over which it has a series of advantages, including an inherent calibration, fast response times (< 2 s to reach 90 % of the applied concentration), a measurement range spanning about 5 orders of magnitude and small, well-known cross sensitivities to other gases. Compactness, cost-efficiency and detection limit (< 1 ppm, few ppb under favorable conditions) are comparable to other presently used *in-situ* instruments. Our instrument prototype has been extensively tested in comparison studies with established methods. In autumn 2015, diverse volcanic applications were investigated such as fumarole sampling, proximal plume measurements and airborne measurements several kilometers downwind from the vent on Mt. Etna and White Island. General capabilities and limitations of the measurement principle are discussed, considering different instrument configurations and future applications.

Keywords: Sulfur dioxide, optical measurement, UV spectroscopy, volcanic degassing, NDUV

Edited by:
Andrew McGonigle,
University of Sheffield,
United Kingdom

Reviewed by:
Manuel Queisser,
University of Manchester,
United Kingdom
Robin Campion,
National Autonomous University of
Mexico, Mexico

***Correspondence:**
Jan-Lukas Tirpitz
jtirpitz@iup.uni-heidelberg.de

Specialty section:
This article was submitted to
Volcanology,
a section of the journal
Frontiers in Earth Science

Received: 31 July 2018
Accepted: 05 February 2019
Published: 13 March 2019

Citation:
Tirpitz J-L, Pöhler D, Bobrowski N,
Christenson B, Rüdiger J, Schmitt S
and Platt U (2019) Non-dispersive UV
Absorption Spectroscopy: A
Promising New Approach for in-situ
Detection of Sulfur Dioxide.
Front. Earth Sci. 7:26.
doi: 10.3389/feart.2019.00026

1. INTRODUCTION

Volcanoes emit a variety of gases [in order of typical abundance the major compounds are: water vapor (H_2O), carbon dioxide (CO_2), sulfur dioxide (SO_2), hydrogen sulphide (H_2S), hydrogen halides; Textor et al., 2004]. Today emission rate estimates and composition measurements of different gas species in volcanic plumes are used for diagnosing volcanic processes and activity (e.g., Aiuppa et al., 2007; Burgisser and Scaillet, 2007; Oppenheimer et al., 2014). In studies of this kind, SO_2 is one of the most prominent gases to measure. Beside the dependence of its gas fraction and emission rate on sub surface magmatic processes, it features properties like a high abundance in volcanic plumes, a low atmospheric background, a relatively long (typically days) atmospheric lifetime and favorable optical absorption properties, which make it easy to detect and an excellent plume tracer (Caroll and Holloway, 1994; Oppenheimer et al., 2011; Platt et al., 2018). Remote sensing of SO_2 has become well-established among volcanologists to determine abundance and total emission rate from safe distance and at low logistic effort (e.g., Moffat and Millan, 1971; Oppenheimer et al., 1998; Galle et al., 2003; Horton et al., 2006; Mori and Burton, 2006), however, its *in-situ* detection remains a crucial complemental tool, e.g., to achieve high spatial resolution or more accurate measurements and for the validation of remote sensing instruments. There are a series of high precision SO_2 monitors commercially available, but typically they are rather bulky, heavy, and relatively complex setups, which restricts their applicability for volcanic gas measurements for different reasons: (1) In many cases, sampling sites are not easy to access and lack any kind of infra-structure, such that instruments including the necessary peripherals have to be carried over long distances or even mounted to UAVs (unmanned aerial vehicles) with typical payloads of few kg. (2) Instrument lifetimes are often affected by harsh environmental conditions and corrosive sample gases, which is particularly problematic for automatized long-term monitoring stations. Thus, compact, rugged, and cost effective instrument designs with low power consumption and low maintenance requirements are desirable. Electrochemical air quality sensors (most prominently applied in Multi-GAS instruments as described by Shinohara, 2005 or Aiuppa et al., 2005) meet these requirements well but come along with drawbacks in the data quality. The typically applied miniature sensors (size: few centimeters at a side, weight: 20–30 g) achieve suitable detection limits (few 100 ppb) when frequently calibrated but suffer from long-term calibration drifts (reported between few %/year and 10 %/hour, strongly dependent on field conditions; Shinohara, 2005; Kelly et al., 2013; Lewicki et al., 2017), variable cross sensitivities to other volcanic and atmospheric gases, a limited detectable concentration range (about 3 orders of magnitude) and slow response times (10 to 30 s to reach 90 % of signal, dependent on absolute signal and different for rise and fall; Roberts et al., 2014).

On the basis of a newly developed prototype—the "PITSA" (**P**ortable ***In-siTu*** **S**ulfur dioxide **A**nalyser)—here we present an alternative method for *in-situ* detection of SO_2. The prototype is based on the principle of non-dispersive ultra violet absorption spectroscopy (NDUV). Detection limit, compactness and cost-efficiency remain comparable to other small scale solutions, while significant improvements are achieved regarding long-term accuracy, cross sensitivities, and temporal response behavior. Therefore, it is expected to lead to improvements particularly in the domains of long-term monitoring, high frequency investigations, and UAV applications, and therefore investigation of remote volcanoes. The prototype has been extensively tested in intercomparison studies with instruments based on established methods like electrochemistry and UV fluorescence.

2. MEASUREMENT PRINCIPLE AND PROTOTYPE SETUP

2.1. Measurement Principle

The principle of non-dispersive absorption spectroscopy itself has already been developed in the 1930's (Lehrer and Luft, 1938) but has mainly been applied in the infra red (NDIR). Its cost-effective and compact application for SO_2 has been nearly impossible until the recent developments in the field of ultra violet (UV) light emitting diodes (LEDs). NDUV makes use of the fact that different gas species absorb light at different wavelengths. Therefore, guiding light through a sample gas and measuring its attenuation at suitable wavelengths, provides information on the gas composition. The absorption efficiency of a gas species at wavelength λ is typically described by its "absorption cross-section" $\sigma(\lambda)$, which is well-known for most atmospheric constituents and can be found in data bases like by Keller-Rudek et al. (2013). The characteristic absorption properties of each gas originate from its molecular-atomic structure and the resulting allowed quantum state transitions. In many applications the spectral absorption patterns of different gases overlap and spectrally resolved ("dispersive") measurements of the attenuation have to be performed to separate the contribution of different absorbers. On the other hand, in a few cases the gas of interest is the only—or at least the dominant—absorber in a distinct wavelength range. Then, a single ("non-dispersive") measurement of the light's attenuation in this range is sufficient to determine its concentration. For SO_2 in volcanic plumes, this is the case in the ultra violet (UV) at wavelengths around 285 nm (see **Figure 1A**).

Figure 1B shows the basic setup of the PITSA prototype. Gas is pumped through an aerosol filter into a sample cell of length $L = 27\,\text{cm}$, where it is exposed to the parallelized beam of a UV-LED (UV-TOP 280) with a well-known emission spectrum in the desired wavelength range around 285 nm (see **Figure 1A**). The aerosol filter is a 200 nm pore filter and prevents scattering and absorption of light on particles (see section 3.1.5 for details), assuring that SO_2 absorption is the dominant light attenuating process in the gas. A detector (silicon photodiode with appropriate amplifier and readout electronics, see section 2.3 below) is located behind the cell, measuring the spectrally integrated intensity

$$I = \int_{\lambda_1}^{\lambda_2} I(\lambda)\,\mathrm{d}\lambda \tag{1}$$

The integration limits $\lambda_1 \approx 200\,\text{nm}$ and $\lambda_2 \approx 1,100\,\text{nm}$ are confined by the sensitivity range of the photodiode but generously bracket the wavelength interval where the emission spectrum of the LED $I_0(\lambda)$ has non-zero intensity. A solenoid valve allows to occasionally pump the sample air through an SO_2 scrubber (an off the shelf gas mask cartridge), which removes the SO_2 from the sample cell such that the reference intensity

$$I_0 = \int_{\lambda_1}^{\lambda_2} I_0(\lambda)\,\mathrm{d}\lambda \tag{2}$$

(which is unaffected by SO_2 absorption) can be recorded with the same detector. In the following this procedure will be referred to as "zero point measurement." By comparing the two intensities I_0 and I, the SO_2 concentration in the cell is calculated (see below).

For a setup with a single detector behind a measurement cell, LED intensity fluctuations and drifts were observed to be the limiting factor for the instrument's detection limit, as they cannot be distinguished from actual changes in the SO_2 concentration in the cell. To overcome this, in the PITSA a part of the light is measured over a "monitoring channel" with no variable absorber

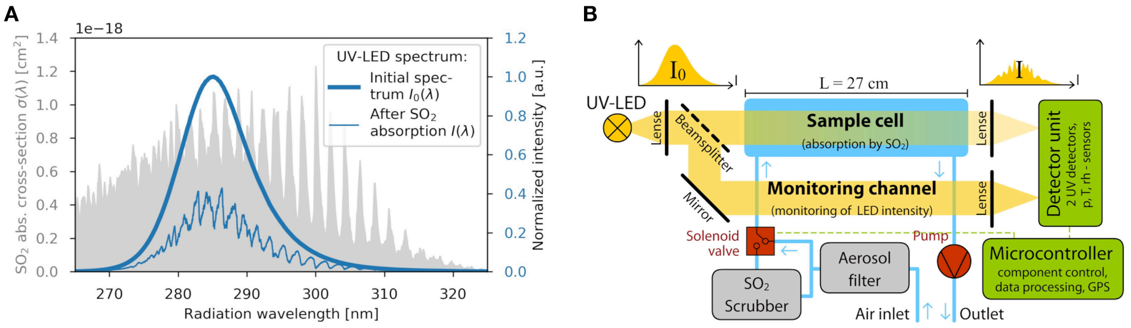

FIGURE 1 | (A) Wavelength dependence of the SO$_2$ absorption cross section (gray shaded area) and the spectrum of the UV-LED (thick blue line), as determined with a spectrometer. The thin blue line exemplarily shows the LED spectrum having passed a 27 cm sample cell (as applied in the PITSA prototype) containing 1,000 ppm SO$_2$ (volume mixing ratio). **(B)** Schematic of the PITSA prototype setup. The UV light in the sample cell is solely attenuated due to SO$_2$ absorption. By comparing the light intensities I_0 and I, the amount of SO$_2$ in the cell can be calculated.

in the light path. It allows to monitor the LED intensity and to correct for its variations, which improves the detection limit by a factor of ≈ 5. If not stated otherwise, this correction has been applied to data shown in this article.

From the two intensities I_0 and I the spectrally integrated "optical density"

$$\tau = \log(I_0/I) \tag{3}$$

of the sample gas can be calculated. τ is a convenient measure for the light attenuation, since it is in first approximation proportional to the SO$_2$ number concentration (see Equation 6). It can therefore be regarded as a kind of uncalibrated instrument signal.

2.2. Inherent Calibration of the Instrument

The PITSA setup is exceptional in a way, that it is possible to theoretically derive the relationship between τ and the actual SO$_2$ concentration to very high precision, hence, a calibration curve can be calculated without feeding test gases to the instrument. The light intensity after passing the cell at a distinct wavelength λ, is given according to the Beer-Lambert-Law (Swinehart, 1962) to:

$$I(\lambda) = I_0(\lambda) \cdot \exp\left(-\sigma(\lambda)\, c\, L\right) \tag{4}$$

Here, $I_0(\lambda)$ is the intensity of the incident UV radiation, which is multiplied by an attenuation factor, that depends on the wavelength dependent absorption cross section $\sigma(\lambda)$, the SO$_2$ number concentration c (molecules per unit volume) and the absorption path length L. Equivalent to the definition before (Equation 3), the optical depth at a distinct wavelength λ is given by:

$$\tau(\lambda) = \log\left(\frac{I_0(\lambda)}{I(\lambda)}\right) = \sigma(\lambda)\, L\, c \tag{5}$$

To obtain the relation between c and the actual instrument response τ (calculated from the integrated intensities I and I_0, as defined in Equations 1 and 2, Equation 5) has to be integrated. Since there are no analytical expressions for either $\sigma(\lambda)$ nor $I_0(\lambda)$, the integrals have to be calculated numerically. However, for small optical depths, (Equation 5) can be linearized, to obtain an approximate analytic expression (detailed derivation in **Supplementary Material**):

$$\tau = \log\left(\frac{I_0}{I}\right) = \sigma_{eff}\, L\, c \tag{6}$$

Here, σ_{eff} is the "effective absorption cross section," defined as

$$\sigma_{eff} = \int_0^\infty \frac{I_0(\lambda)}{I_0}\, \sigma(\lambda)\, \mathrm{d}\lambda \tag{7}$$

which is the average value of $\sigma(\lambda)$, weighted with the normalized LED emission spectrum $I_0(\lambda)/I_0$, both shown in **Figure 1A**. In practice, it is sufficient to perform the integration over the non-zero region of $I_0(\lambda)$. For the results presented below, we chose 250 and 330 nm as the lower and upper integration limit respectively.

Finally, the SO$_2$ number concentration c can be converted to a volume mixing ratio [in the following referred to as "VMR," given in parts per million (ppm) or parts per billion (ppb)], by applying the ideal gas law, yielding:

$$VMR = \frac{k_B\, T}{p} \cdot c \tag{8}$$

with k_B, T, and p being the Boltzmann constant, temperature, and pressure, respectively. To assure an accurate conversion in the PITSA, T, and p are continuously monitored by corresponding sensors on the detector circuit board in the optical setup. For theoretical calculations and error estimations within this article normal temperature and pressure (NTP) conditions are assumed, which are $T = 293.15\,\mathrm{K}$ and $p = 1013.25\,\mathrm{hPa}$. For other conditions, VMRs have to be scaled according to Equation (8).

For a quantitative solution of the sensor response, the SO$_2$ absorption cross section $\sigma(\lambda)$ is taken from Vandaele et al. (2009). Further, the shape of the LED spectrum $I_0(\lambda)/I_0$ is required. It was observed to be very stable over time and a wide range of

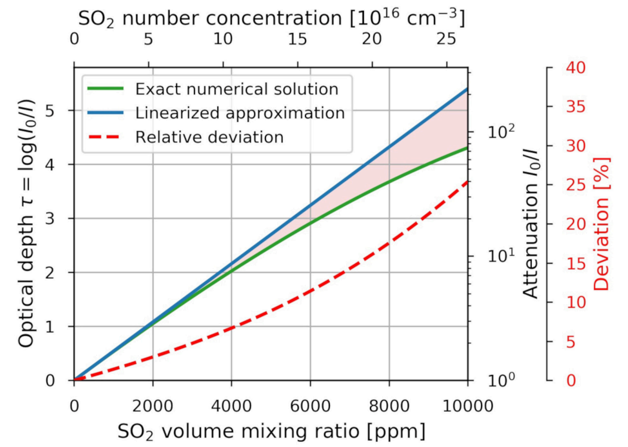

FIGURE 2 | Calculated response curves of the PITSA to SO$_2$ number concentration/volume mixing ratio expressed in observed optical depth/light attenuation. Shown are the curves for the exact numerical calculation and the linearized approach (Equation 6). For the relative deviation between them (red dashed line) the third y-axis on the right applies.

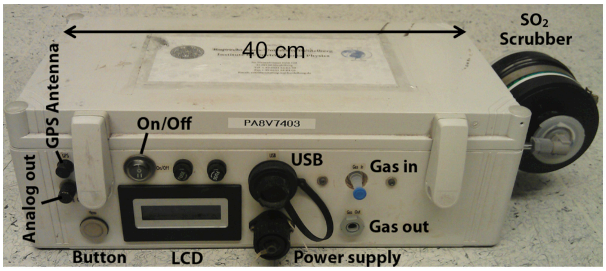

FIGURE 3 | Exterior view of the PITSA instrument. The front panel features: gas in- and outlet, on/off switch for main power (with protective fuses to its right), an LAD screen showing preliminary real time data (SO$_2$, CO$_2$, temperature and pressure), a programmable push button (typically used to manually trigger zero point measurements) and connectors for USB (real time digital data output, firmware programming), power (battery charging and external power supply), external GPL antenna and analog output (2 channels for SO$_2$ and CO$_2$ for application with analog data loggers).

conditions (see section 2.2 and **Supplementary Material**), it is therefore sufficient to determine it once with a scientific grade spectrometer. Insertion of these values into Equation (6) and the numerical integration of Equation (5), respectively, yields the two response curves shown in **Figure 2**. Equation (7) yields $\sigma_{eff} \approx 7.6 \cdot 10^{-19}\text{cm}^2$, meaning that intensity variations $< 10^{-4}$ have to be resolved to achieve detection limits $<$ 0.2 ppm in the SO$_2$ VMR. The linear approximation is sufficient (deviation $<$ 1 %) for VMRs up to $\approx$700 ppm, which is suitable for most volcanic applications. For higher VMRs (up to 10 000 ppm), a higher order analytical solution of Equation (5) or the numerical approach should be applied. As discussed in section 3.1.2, the calculated responses are sufficient to single digit percent accuracies in the measurement. With offset drifts being corrected through the automated zero point measurements with SO$_2$ scrubbed air, the instrument features an inherent and stable calibration. In fact, all data shown in this article were evaluated without ever applying an experimental SO$_2$ gas calibration to the instrument.

2.3. Mechanical Design and Electronics of the PITSA Instrument

The optical cell basically consists of a glass tube (27 cm length, 11 mm diameter, 26 ml volume), with air in- and outlets and UV transmissive fused silica windows at each end. A lens in front of the UV-LED parallelizes the light before a beam splitter and a mirror distribute it to the measurement cell and the monitoring channel, respectively. Lenses in front of each detector channel focus the light again (compare **Figure 1B**). To minimize the impact of mechanical strain (vibration, shock, ...) on the measurement (see section 3.1.6), the whole optical setup is mounted on a common aluminum bracket, which is in turn placed on damping feet, for its mechanical decoupling from the housing and less sensitive instrument components. The optical bench is equipped with heating resistors (switchable between 4 and 8 W heating power, to obtain a typical temperature rise above ambient of 10 and 20 K, respectively), which can be activated to prevent condensation (see section 3.1.4). An image of the optical bench can be found in the **Supplementary Material**. Teflon and Tygon (type 2375) tubings were used to guide the air through the setup. The pump is a diaphragm pump of type TM22-A12 from Topsflow. An off-the-shelf gas mask cartridge (type Eurfilter A2-B2-E2-K2-P3 R from Panarea) served as SO$_2$ scrubber and Millex-FG filters from Merck Millipore with pore size of 220 nm were used for particle filtering at the inlet.

The LT3092 current source from Linear Technologies (an integrated circuit of few millimeter outline) was used to generate a stable supply current of 7 mA for the UV-LED from the battery voltage, resulting in an optical output power around 0.3 mW. Higher currents up to 40 mA can be applied to the LED to achieve optical output powers >1.5 mW, but were not used in the PITSA, as they decrease the LED's lifetime.

A single detector channel consists of following components: A silicon photodiode (type PC10-2-TO5 by Pacific Silicon Sensor Inc.) produces a photo current ($\approx$0.7 μA at negligible absorption in the cell) proportional to the number of photons hitting the diode's active area. A transimpedance amplifier implemented by using a chopper operational amplifier (AD8552 by Analog Devices) with a 3 MΩ feedback resistor converts the photo current to a voltage of $\approx$2 V. A 22-Bit analog to digital converter (MCP3551) converts the analog signal to a digital value. The minimum integration time of the detector is 75 ms, which is the conversion time of the analog to digital converter. A sketch of the detector circuitry can be found in the **Supplementary Material**.

Detector unit and solenoid valve are controlled by a microcontroller (Arduino Mega 2560 R3) with GPS-capability, which also performs data processing and logging. The recorded data is written to a memory card. For external logging, e.g., in multi sensor systems, data are simultaneously sent to the instrument's USB port and an analog output. The whole setup is integrated into a polycarbonate housing (see **Figure 3**) together

TABLE 1 | Overview on the measurement error sources and their approximative impact on the detected SO_2 VMR.

Error	Kind	Error source	Order of magnitude	Subsection
Offset error (absolute)	Random:	Photon shot noise	$4\,\text{ppb s}^{1/2}/\sqrt{t_{int}}$	3.1.1
		Electronic readout noise	$4\,\text{ppb s}^{1/2}/\sqrt{t_{int}}$	3.1.1
		Detector drift	$3\,\text{ppb min}^{-1/2} \cdot \sqrt{T_{ref}}$	3.1.1
		Mechanical impact	0–200 ppb	3.1.6
	Systematic:	Interference to other gases	0–400 ppb	3.1.3
		Aerosol scattering	$<$ 10 ppb	3.1.5
		Condensation and humidity	0–1000 ppm	3.1.4
Sensitivity error (relative)	Random:	T and p in the cell	$<$ 2 %	3.1.2
		Change in LED spectral shape	$<$ 1 %	3.1.2
	Systematic:	Error in literature cross section	$<$ 3 %	3.1.2
		Absorption path	$<$ 1 %	3.1.2
		Scrubber leakage	$<$ 0.2 %	3.1.2

"Offset error" comprises all error sources which induce absolute deviations (independent of instrument reading) from the true value. "Sensitivity error" comprises all error sources, which affect the instrument sensitivity (see section 2.2), hence, whose absolute impact scales with instrument reading. The impact of noise and drifts are dependent on the detector integration time t_{int} and the intervals T_{ref}, in which zero point measurements are performed.

with a 120 Wh rechargeable battery (HE-12V-10Ah-LiMn by Hellpower Industries). Remaining free space in the housing allowed to add a small commercial CO_2 detector (Senseair K30-FR) to the setup, which — in combination with the PITSA — allows to determine (approximate) CO_2/SO_2 ratios. A small LCD screen at the outside of the box (see **Figure 3**) shows preliminary real-time data. With a power consumption $<$ 5 W (heating disabled), the instrument runs autonomously without any further peripheral equipment for about 24 h. The footprint of the housing (without scrubber) are 40 x 20 x 13 cm, the total weight is ≈ 8 kg.

3. INSTRUMENT PERFORMANCE

3.1. Measurement Accuracy

The total accuracy of the PITSA is restricted by a series of error sources, which are summarized in **Table 1** and discussed in detail in the following subsections. Since the impact of some error sources depends on the measurement parameters and conditions, the total accuracy has to be estimated individually for a given application from information in this chapter.

3.1.1. Instrument Noise and Zero Drift

A fundamental constraint for the detection limit are noise and drift in the instrument's zero signal (regarded here without considering the interferences listed in sections 3.1.3–3.1.6). As mentioned above and shown in the following, linear zero drift is not an immediate problem, since it can be detected during zero point measurements and corrected, whereas the rate of zero drift is of concern. **Figure 4** shows the PITSA signal during a measurement with no SO_2 in the laboratory at two different time periods (10 and 180 min). A detector integration time of $t_{int} = 0.5$ s per data point was chosen in this example. The ordinate axis on the right is the optical density $\tau = \log(I_0/I)$, the left axis shows corresponding deviations of the SO_2 VMR in ppb. The light blue curve shows the signal, without performing zero point measurements. It basically consists of high frequency noise and long-term offset drift. The noise can be explained by regarding the noise contribution from the different detector components (analog-to-digital converter, operational amplifier, and thermal noise of feedback resistor, see section 2.3) and the photon shot noise, which can be estimated from the photo current. They make up about 40 and 60 %, respectively, of the observed noise. The long-term drifts originate from drifts of the two intensity measuring channels (sample cell channel and monitoring channel) against each other. Its ultimate cause could not be unambiguously identified. A correlation with temperature was clearly visible but showed ambiguities and proved not to be sufficient to predict the drifting behavior. Drifting is therefore corrected by performing zero point measurements as described in section 2 in regular intervals T_{ref}. They yield zero points from

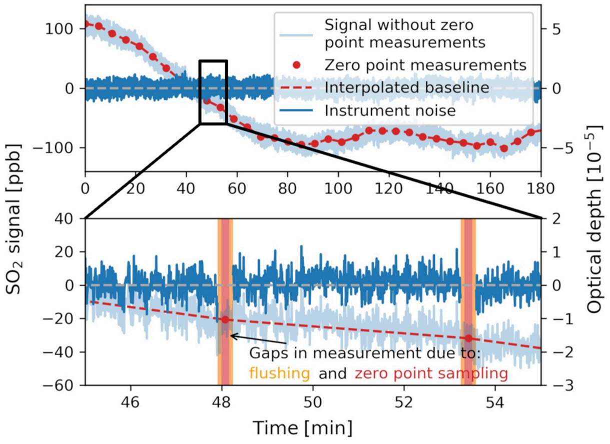

FIGURE 4 | Instrument noise (dark blue curve) at a detector integration time $t_{int} = 0.5$ s and a reference interval $T_{ref} = 5$ min. Red dots indicate zero point measurements from which drift can be inferred and subtracted. **Top**: 180 min time interval, **Bottom**: zoom into a 9 min section. Additional graphs are for explanatory reason (see text for details).

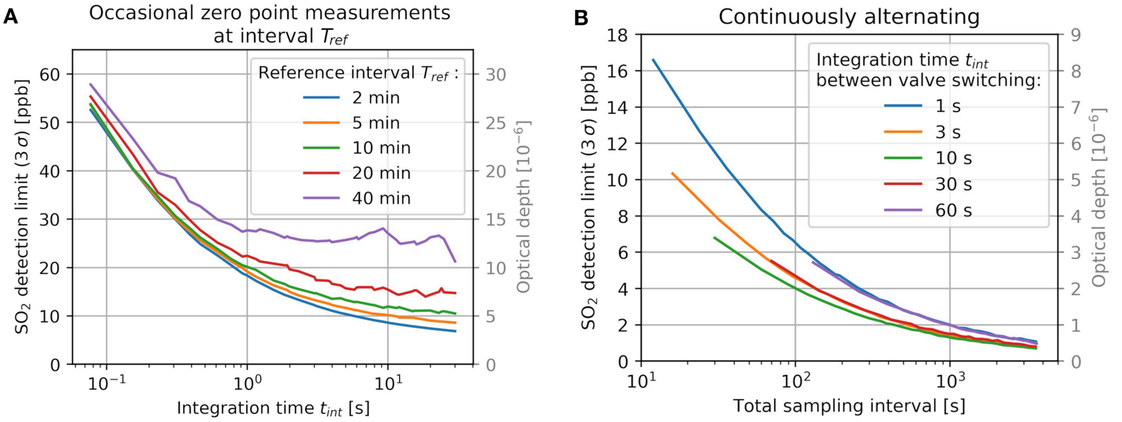

FIGURE 5 | Instrument detection limit (3×RMS of instrument noise) for different measurement protocols. **(A)** As a function of the detector integration time t_{int} for different reference intervals T_{ref}. For sufficiently short T_{ref} a $1/\sqrt{t_{int}}$ behavior is observed. **(B)** In case of continuous alternation between measurement and zero point measurement. Here an optimum is seen for 10 seconds integration time between switching.

which a new baseline can be interpolated. In the example in **Figure 4**, T_{ref} was chosen to 5 min. The zero point measurements and the resulting baseline are indicated by the red dots and the dashed line, respectively. After subtraction of the baseline, the dark blue curve remains, which is the actual instrument zero signal after post processing. It is obvious, that it is dependent on t_{int} and T_{ref}, since t_{int} affects the short term noise, whereas T_{ref} determines how well drift can be eliminated. Note that each zero point measurement leaves a data gap, as it takes time (typically 10–20 s) to (1) flush the cell with scrubbed air, (2) to perform the actual zero point sampling and (3) to flush the cell with sample air again. T_{ref} is therefore always a trade-off between drift elimination and data coverage. In the lower (zoomed) panel of **Figure 4**, the gaps are well-visible and indicated by the colored (orange and red) areas. The left of **Figure 5** shows the instrument resolution (4×RMS of instrument noise) as a function of t_{int} for different T_{ref}. A flushing time of 5 s was assumed. For large T_{ref}, the drift cannot be accurately corrected anymore and increase of t_{int} cannot effectively improve the resolution.

For applications where low temporal resolutions are sufficient, continuous alternation between measurement and zero point measurement is recommended. In that case, only a single measurement data point with integration time t_{int} is recorded before another zero point measurement is initiated. Due to the flushing time of the cell (here 5 s) with this technique the temporal resolution is limited to $>$ 10 s, but drifts are most efficiently removed.

The detection limit can then be further improved by averaging over a series of such measurement-zero point cycles. The right side of **Figure 5** shows the detection limits for this measurement algorithm as a function of the number of averaged cycles N (in units of the resulting temporal resolution) for different integration times between valve switching. The curves decrease in good approximation with $1/\sqrt{N}$, as it is theoretically predicted for statistical noise, which indicates that the drift is nearly perfectly eliminated. For the integration times there is an optimum at 10 s. For shorter integration times, noise becomes large, while for higher integration times, the gap between measurement and reference increases and drift correction becomes worse.

Regarding **Figure 5**, following aspects shall be noted: measurements presented in this section were performed in the laboratory. When encountering harsh field conditions, drift of the instrument may be more variable and detection limits for high values of T_{ref} might degrade significantly. Further, the resolution given here was determined by only considering noise and drifting of the instrument. The detection limit is mostly determined by other systematic effects, which are discussed separately in sections 3.1.3–3.1.6.

3.1.2. Sensitivity Error

As demonstrated in section 2, the instrument's response curve (hence, the sensitivity) was theoretically calculated instead of performing an experimental calibration with test gases. When calculating SO_2 number concentrations, the systematic uncertainty (neglecting random noise) of the sensitivity is determined by the uncertainties of the factors in Equation 6, namely the effective absorption cross section σ_{eff}, the absorption path length L and the integrated optical depth τ. L can easily be determined to better than 1 % relative accuracy. The impact of errors in τ on the instrument sensitivity are negligible, as detector offsets can be corrected to $\approx 10^{-5}$ (of total signal) and combined non-linearities of all detector components are $< 10^{-4}$. The SO_2 leakage of a new gas mask cartridge used as the scrubber was measured to be less than 0.2 % (see section 3.4). The impact of changes in the shape of the LED emission spectrum $I_0(\lambda)/I_0$ on σ_{eff} were observed to be $<$ 1 % over the LED's lifetime and a temperature range of -10 to 50 °C (see **Supplementary Material**). Therefore, the uncertainty of σ_{eff} is dominated by the error of the literature cross section. According to Vandaele et al. (2009) the uncertainty in $\sigma(\lambda)$ originates mainly from systematic errors which are specified to 6 %. The impact of

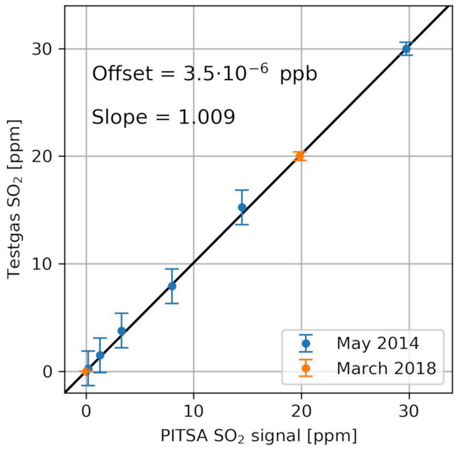

FIGURE 6 | Comparison of the theoretically calculated PITSA response curve with calibration gases of known SO_2 concentrations in N_2. The black line is an error weighted linear regression. This plot demonstrates the high accuracy of the theoretically calculated PITSA calibration and its long-term stability.

pressure and temperature dependencies of $\sigma(\lambda)$ was calculated to $< 0.2\,\%$ for $T = -10\ldots50\,^\circ\mathrm{C}$ and $p = 500\ldots1013$ Pa.

For the conversion from number concentrations to VMRs, temperature T and pressure p and related uncertainties have to be taken into account (see Equation 8). In the PITSA, the absolute accuracy of the applied combined sensor for p and T are 200 Pa and 1 K, respectively, as specified by the supplier. Since their measurements inside the instrument's housing are not necessarily representative for the sample gas (temperatures not acclimatized, pressure variations dependent on pump performance), enhanced uncertainties of 5 K and 1000 Pa were assumed instead. These uncertainties can be improved in future setups by installing the temperature sensor closer to the sample cell and the pressure sensor with a direct connection to the air flow path.

Summing up these uncertainties yields a total systematic error in sensitivity for SO_2 VMRs of $\approx 7\,\%$. The sensitivity was validated in the lab with different calibration gases (SO_2 in N_2) and ambient air [assumed to contain (0 ± 5) ppb SO_2] in 2015 and 2018. The results are shown in **Figure 6**. The error weighted linear regression deviates from the ideal 1:1 line only by 1 %. This suggests, that the average error of $\sigma(\lambda)$ over the LED emission range is much smaller than specified by Vandaele. From this validation we estimate the uncertainty in the PITSA's sensitivity to be better than 5 % over the instrument lifetime.

3.1.3. Cross Sensitivities to Other Gaseous Species

In the spectral range of the UV-LED, SO_2 is the dominant but not the only absorber in volcanic plumes. Even though negligible in most applications, optical densities of other gases can cause significant false signals, when going to low detection limits (see for instance section 4.2). **Table 2** shows the most prominent interfering species and their impact on PITSA measurements. **Figure 7** shows their absorption cross section in comparison to SO_2. The most critical gas is ozone (O_3), due to its variable tropospheric background, which is typically depleted in volcanic plumes by chemical reactions (Lee et al., 2005; Roberts et al., 2009; Vance et al., 2010). Since it is at least partly absorbed by the SO_2 scrubber, it induces offsets in the signal, even at stable O_3 concentrations. In remote areas O_3 backgrounds are of the order of $1-100$ ppb (Vingarzan, 2004), yielding an apparent SO_2 signal of about $3-300$ ppb. Atmospheric background chlorine monoxide (ClO) concentrations are negligible (Chang et al., 2004). ClO/SO_2 ratios around 0.05—as reported for the Mt. Etna Plume (Bobrowski et al., 2007)—would result in interferences up to 15 %, however, the authors themselves have expressed substantial doubts on the reliability of these numbers, due to difficulties in the spectral evaluation. Newer data (General, 2014; Gliss et al., 2015) point to much lower ClO/SO_2 ratios below 10^{-3}, which would result in interferences $< 0.4\,\%$. Further, ClO/SO_2 ratios around 0.05 would result in deviations $> 15\,\%$ between the PITSA and the electrochemical sensor in the measurement presented in section 4.1, which cannot be observed. Nitrogen dioxide (NO_2) is a weak absorber with negligible rural atmospheric backgrounds of 1–30 ppb (Atkins and Lee, 1995; Meng et al., 2010). But in highly polluted areas with NO_2 VMRs of more than 1 ppm measurements can still be affected. Further, dependent on the plume age, NO_2/SO_2 ratios > 0.1 are reported at Mt. Erebus (Oppenheimer et al., 2005), which would result in measurement error in the percent range. However, such high values could neither be reproduced in later measurements, nor in a repeated evaluation of the underlying dataset with an improved retrieval (Boichu et al., 2011). The cross sections of O_3 and ClO decrease faster with increasing wavelength than the SO_2 cross section. Thus, the cross interference can be minimized by choosing an LED with a higher peak emission wavelength, at cost of SO_2 sensitivity. Besides the listed gases, absorption by a series of background polycyclic aromatics and ketones can lead to up to a few ppb of apparent SO_2 VMR, depending on air quality and nearby vegetation, such that there may be conditions where detection limits below a few ppb cannot be achieved. It shall be noted that in the case of NDUV the cross sensitivities are well-predictable and stable over time and environmental conditions, which is not the case for many other measurement principles (e.g., electrochemical).

3.1.4. Condensation and Humidity Interference

When trying to resolve optical densities $< 10^{-4}$, it is obvious, that water condensation in the optical setup must be avoided. Feeding steam from boiling water to the instrument for instance easily leads to optical depth signals of ≈ 1, corresponding to $\approx 2{,}000$ ppm of apparent SO_2. To avoid condensation, the temperature of the optical setup must be kept above the sample air temperature. When heat generation of the electronic components is not sufficient in the PITSA, the setup can be actively heated to $\approx 20^\circ$C above environmental temperature. Direct sampling, e.g. at the very proximity to the vent of hot fumaroles is not possible without any further drying mechanisms or dedicated setups, withstanding the required temperatures. Even when avoiding condensation, depending on the conditions a positive offset of a few 100 ppb in the PITSA signal was

TABLE 2 | The most important cross interfering gas species.

Gas	$\sigma_{eff}/\sigma_{eff,SO2}$	Background [ppb]	Plume abundance	Max interference
O_3	3.2	1–100	Usually below background	320 ppb
ClO	3.7	< 0.1	ClO/SO_2 probably $< 10^{-2}$	$4 \cdot 10^{-4}$
NO_2	0.1	1–30	$NO_2/SO_2 \approx 10^{-1}$	10^{-4}

The ratio $\sigma_{eff}/\sigma_{eff,SO2}$ was chosen here as a measure for the interference strength. Multiplying the VMR of an interfering species by this ratio yields the corresponding apparent SO_2 signal. Background values are given for remote areas, with low anthropogenic pollution. Plume abundance values are rough estimates and can differ widely in distinct cases (see text).

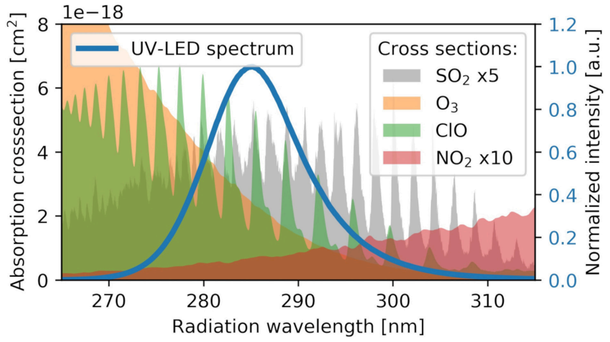

FIGURE 7 | Cross sections of the most important interfering gas species in comparison to SO_2 in the LED's spectral emission interval.

observed, which correlates with relative humidity. The reason for this interference is not yet clear. Certainly it is not UV absorption by water vapor, since water does not have absorption structures in the wavelength range of interest. Also the reaction of the PITSA to humidity is much slower than the actual flushing time of the cell. Candidates for possible causes are (1) thin water layers, which are existent on surfaces even at non-condensing conditions and whose thickness change with humidity and (2) water uptake of mechanical components like seals, which might lead to deformations in the setup. The correlation appeared to be very variable, probably since the scrubber's water uptake is dependent on its conditions and scrubbing history. Further, memory effects of the tubing and the filter system cannot be excluded. In a zero measurement during the atmospheric simulation chamber experiments described in section 4.4), the humidity interference could be observed at well-controlled conditions. The chamber was stabilized at 25 ± 1.5 °C, the PITSA was heated to 35±1.5 °C. Relative humidity was varied between 15 and 45 % over about 10 h, revealing a correlation of about 20 ppb apparent SO_2 per % relative humidity (see **Supplementary Material** for the corresponding plot). Further investigations are necessary to understand and eventually remove this effect.

3.1.5. Influence of Light Scattering by Molecules and Aerosols

Apart from absorption, the light intensity is also attenuated due to scattering away from the initial propagation direction. Scattering occurs on molecules ("Rayleigh scattering") and particles ("Mie scattering"). At 280 nm and NTP conditions, the Rayleigh scattering optical depth is $\approx 5 \cdot 10^{-6}$ (Bucholtz, 1995). This is close to the instrument's detection limit but cancels out in the optical density $\tau = I_0/I$ to negligible contributions, since measurement I and zero point measurement I_0 are both affected. Mie scattering is largely suppressed by the particle filter on the instrument's inlet. Its maximum pore size is specified to 200 nm. The filters capability to filter smaller particles (radii $R < 100$ nm) is not known. According to the Mie scattering theory, particles with radii $R < 50$ nm (approaching the Rayleigh molecule scattering regime) are very inefficient scatterers (scattering cross section σ_p becomes much smaller than the geometric cross section πR^2) and can be neglected, whereas for larger particles, σ_p can be assumed to be equal to $\approx \pi R^2$ in a first approximation (Roedel and Wagner, 2017). Hence, for the PITSA there remains a potentially critical size interval 50 nm $< R <$ 100 nm, where scattering by particles might become a significant light attenuating factor. Particle concentrations $dn/d\log_{10}(R)$ in the remaining particle size range may exceed 10^5 cm^{-3} in polluted urban areas and volcanic plumes (Roberts et al., 2018). During experiments in the atmospheric simulation chamber (see section 4.4), a corresponding scenario could be simulated with artificial aerosol (sea spray aerosol, consisting of NaCl, NaBr and H_2SO_4, injected with a Venturi-Nozzle) at zero SO_2 to investigate the impact on the PITSA measurements. **Figure 8A** shows the particle size distribution inside the chamber as measured by a scanning mobility particle sizer (SMPS), over the course of the experiment. **Figure 8B** shows time series of the PITSA and an estimated expected signal. The latter was calculated by integrating the SMPS size distributions over the critical size interval (assuming sharp cuts at 50 and 100 nm for simplicity), assuming the particle absorption cross sections σ_p to be equal to πR^2. This very simplified approximation predicts well-visible cross interference of up to 800 ppb, whereas the actual PITSA measurements do not seem to be affected ($<$ 20 ppb increase). This suggests that even particles with $R < 100$ nm are sufficiently filtered, such that aerosol cross sensitivities are negligible for common volcanic applications. Nevertheless, possible aerosol interference should be kept in mind when exposing the PITSA to extreme aerosol loads.

3.1.6. Mechanical Impact

Deformation of the optical setup due to mechanical impact (heavy vibrations, mechanical shock, ...) can lead to a change

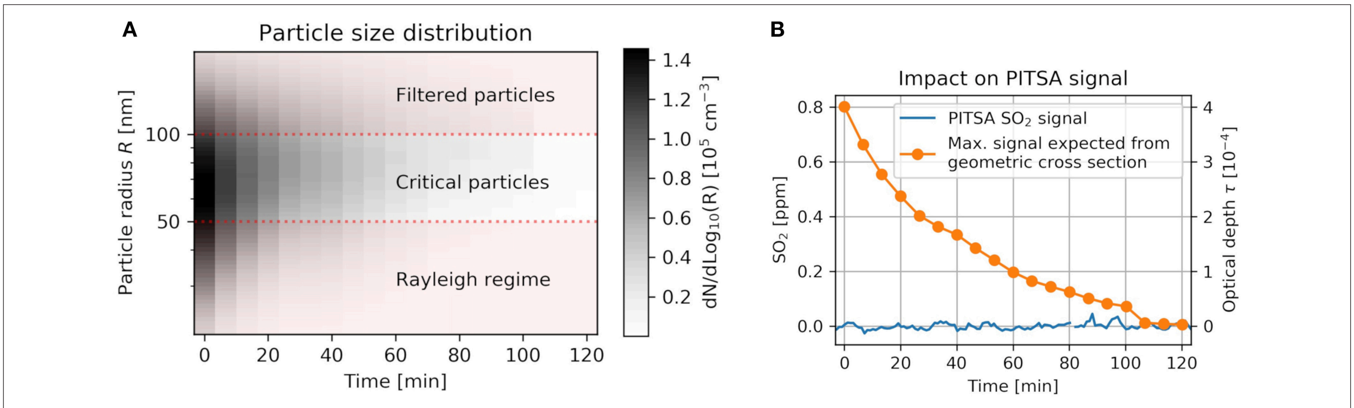

FIGURE 8 | Atmospheric simulation chamber experiment to investigate the impact of nano particles on PITSA measurements. **(A)** particle size distributions in the chamber, measured by an SMPS. Only aerosol in the "critical" size interval are of interest (see text). **(B)** time series of the PITSA signal, which is much lower than the expected signal, as estimated from the size distributions on the left, assuming geometric absorption cross sections ($\sigma_p = \pi R^2$).

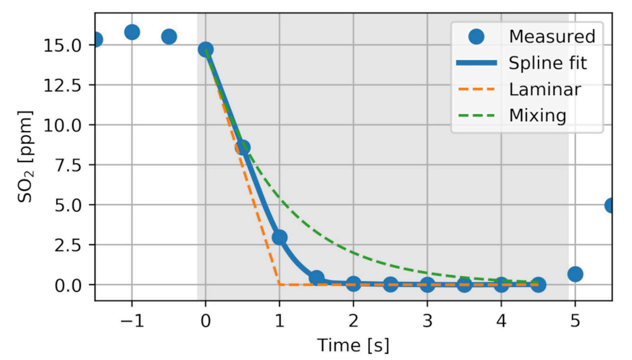

FIGURE 9 | The drop in SO$_2$ concentration after switching to reference mode (zero air, marked by the gray shaded area) during a measurement at Etna volcano. The blue points represent the actual data points, whereas the blue line is a quadratic spline interpolation, to allow determination of t_{90}. Theoretical calculations for perfect laminar flow and turbulent mixing inside the cell are depicted by the dashed lines.

in the light throughput and thus the instrument signal. This is a major drawback compared e.g., to electrochemical sensors. Despite the mechanical decoupling of the optics from the rest of the instrument (see section 2.3) slight deformations were possibly observed during the measurement flight presented in section 4.2, which caused deviations of about 15 ppb in the SO$_2$ VMR. However, we expect that this effect can be significantly reduced by optimizing the design. In particular for setups with smaller outlines, similar stability should be achievable at less effort.

3.2. Instrument Response Time

The response time of the instrument is limited by the flushing time of the sample cell. **Figure 9** shows response of the PITSA while switching from plume air with 15 ppm SO$_2$ VMR to scrubbed reference air (gray area), which causes a nearly step-shaped decrease in SO$_2$ at the sample cell inlet. From the response the flushing time can be determined to $t_{90} \approx 1.3$ s, which corresponds to the time interval in which the VMR dropped to 10 % of its initial value. Dashed lines show calculated responses for the given cell volume and air flow, assuming laminar flow and turbulent mixing, respectively. As expected, reality is a mixture of both. These short response times are a major improvement compared to conventional field sensors, as they allow to detect short time variations in volcanic gas compositions which are a recent field of research (e.g., Pering et al., 2014). Furthermore, gas compositions are often derived by evaluating data from multiple collocated instruments against each other. In such setups fast responding sensors are desirable, since long response times and different response behaviors of the individual instruments can cause severe complications and artifacts during data evaluation (Roberts et al., 2012).

3.3. Measurement Range

The measurement range is limited, mainly because for high SO$_2$ VMRs, the light intensity reaching the detector becomes too low and the contribution of electronic noise exceeds the sensitivity error specified in section 3.1.2. When applying the numerical solution of Equation 5 (which takes non-linearities of the instrument response into account), the PITSA provides reasonable results up to VMRs of about 1 % (10 000 ppm) at any data rate, which is sufficient for most volcanic applications. If desired, the measurement range can be shifted to higher VMRs by reduction of the instrument sensitivity, which can either be achieved by using shorter absorption paths or by changing the LED peak emission wavelength (see **Figure 1A**).

3.4. Maintenance Requirements

The most critical expandable parts are the scrubber, the aerosol filter, the UV-LED and the pump. For the scrubber and the particle filter, lifetimes are strongly dependent on the measurement conditions. The capacity of the gas mask cartridge (Panarea Eurfilter A2B2E2K2P3) is specified to 3 l (ca. 8 g) of pure SO$_2$. Unless this limit is exceeded, a leakage < 0.5 % is guaranteed by the supplier to meet regulatory requirements. Assuming an average SO$_2$ VMR of 10 ppm, a PITSA airflow of 1.5 l/min and typical reference measurement intervals (5 s duration, performed in 300 s intervals), a life-time of > 20 years is obtained. However, this simple scaling of the scrubber capacity neglects the impact of other gases and may not apply, since the life-time of an unused cartridge in its sealed packaging is specified to 6 years only. Our observations are not sufficient for a clearer statement: for a new scrubber the leakage was found to be < 0.2%, which is in agreement with the specifications. Further, we derived an upper limit of 2 % leakage (limited by the uncertainty of reference instrumentation), after 0.8 ml (2 mg) of SO_2 had been supplied to a single scrubber over a period of 4 months during cloud chamber experiments (see section 4.4). Further investigations are necessary in this domain. The particle filter lasts for several hundred hours of operation in quiescent degassing plumes at low background aerosol, whereas hourly exchange can be necessary when ash containing plumes are sampled (Marco Luzzio, personal communication). On the lifetime of the UV-LED, there is only sparse information given by the supplier. During the atmospheric simulation chamber (see section 4.4) experiments in the laboratory, a linear decrease in optical output power due to ageing of 40 % over 1,000 h of operation was observed, at a supply current of 7 mA and instrument temperatures of $(40 \pm 3)\,^\circ$C (heating enabled). Even though the exact scaling of lifetime with current and temperature is not known, it is likely that lifetimes of 5,000 h can be exceeded at few mA and typical environmental temperatures. The typical lifetime of higher grade miniature pumps are of the order of 10 000 h.

3.5. Cost Efficiency

This section is intended to give a rough impression on the costs of the used components. We regard this as an important aspect to consider, when it comes to the application of instruments in harsh meteorologic conditions and acidic environments as they are encountered during volcanic plume *in-situ* measurements. A fully functional setup like the PITSA instrument can be realized at material costs of about 2,500 €. At this price, for instance electrochemical sensors are already available with all necessary peripherals assembled and ready to use. Considering development and construction costs, the costs for the PITSA are estimated to about 10,000 €. However, it shall be noted that a part of the cost charges off, since the optical setup has a longer lifetime than electrochemical cells.

4. APPLICATION AND COMPARISON STUDIES

The PITSA has been successfully applied at volcanoes in Italy (Mt. Etna, Stromboli), New Zealand (White Island), Ecuador (Guagua Pichincha), Colombia (Nevado del Ruiz), and Argentina (Peteroa, Copahue). Further it was used in atmospheric simulation chamber experiments in Bayreuth (Germany). In the following a few exemplary measurements are shown, of which some were performed in parallel to other *in-situ* instruments for comparison and validation, to demonstrate the PITSA's applicability in the field and laboratory.

4.1. Crater Rim Measurements at Mt. Etna

On the 23rd of September 2015, measurements at the rim of the North East Crater of Mt. Etna (Italy) were performed in parallel to a freshly calibrated electrochemical sensor (CiTiceL 3MST/F), as it is usually applied in Multi-GAS sensor systems. **Figure 10** on the left shows an excerpt of the total 40 min time series. The light blue curve shows the original PITSA signal ($t_{int} = 0.5$ s), which reveals variation in SO_2 on very short time-scales, which are not seen by the electrochemical sensor, due to its slower response. For better comparability, the PITSA's temporal resolution was degraded by convoluting the signal with an exponential decay function (decay time of $t_{dec} = 10$ s), which mimics the pulse response of a sensor with $t_{90} = t_{dec}/\log(2) \approx 14$ s. This yields the dark blue dashed curve, which is in very good agreement with the electrochemical sensor data. The scatter plot on the right of **Figure 10** confirms the agreement. It shows 10 s average values over the whole 40 min time series.

4.2. Airborne Plume Scans at White Island Volcano

During a measurement campaign on White Island (New Zealand) in cooperation with the Institute of Geological and Nuclear Science (GNS), airborne measurements ≈ 4 km

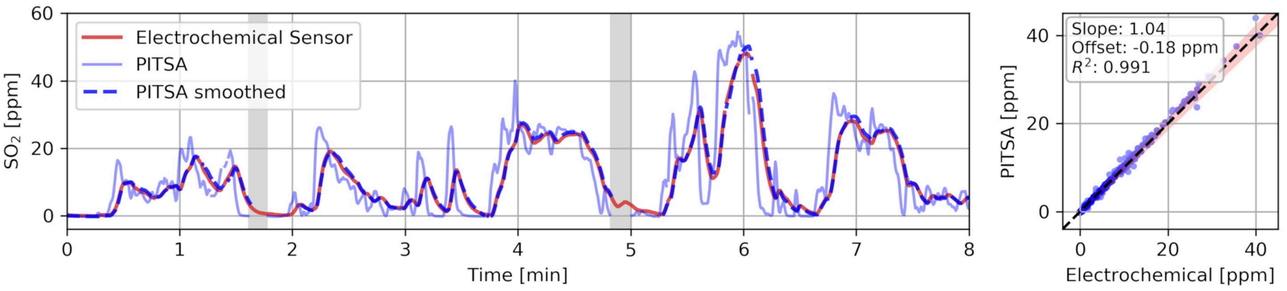

FIGURE 10 | Parallel measurements of the PITSA and a freshly calibrated electrochemical sensor on the rim of Mt. Etna. Gray shaded areas mark PITSA data gaps due to zero point measurements. **Left**: Excerpt of the time series. After artificially degrading the PITSA's response time, the two instruments are in good agreement. **Right**: Scatter plot of 10 s average values. Darkness of points represents the data point density. The red shaded area indicates the uncertainty of the electrochemical sensor as specified by the supplier.

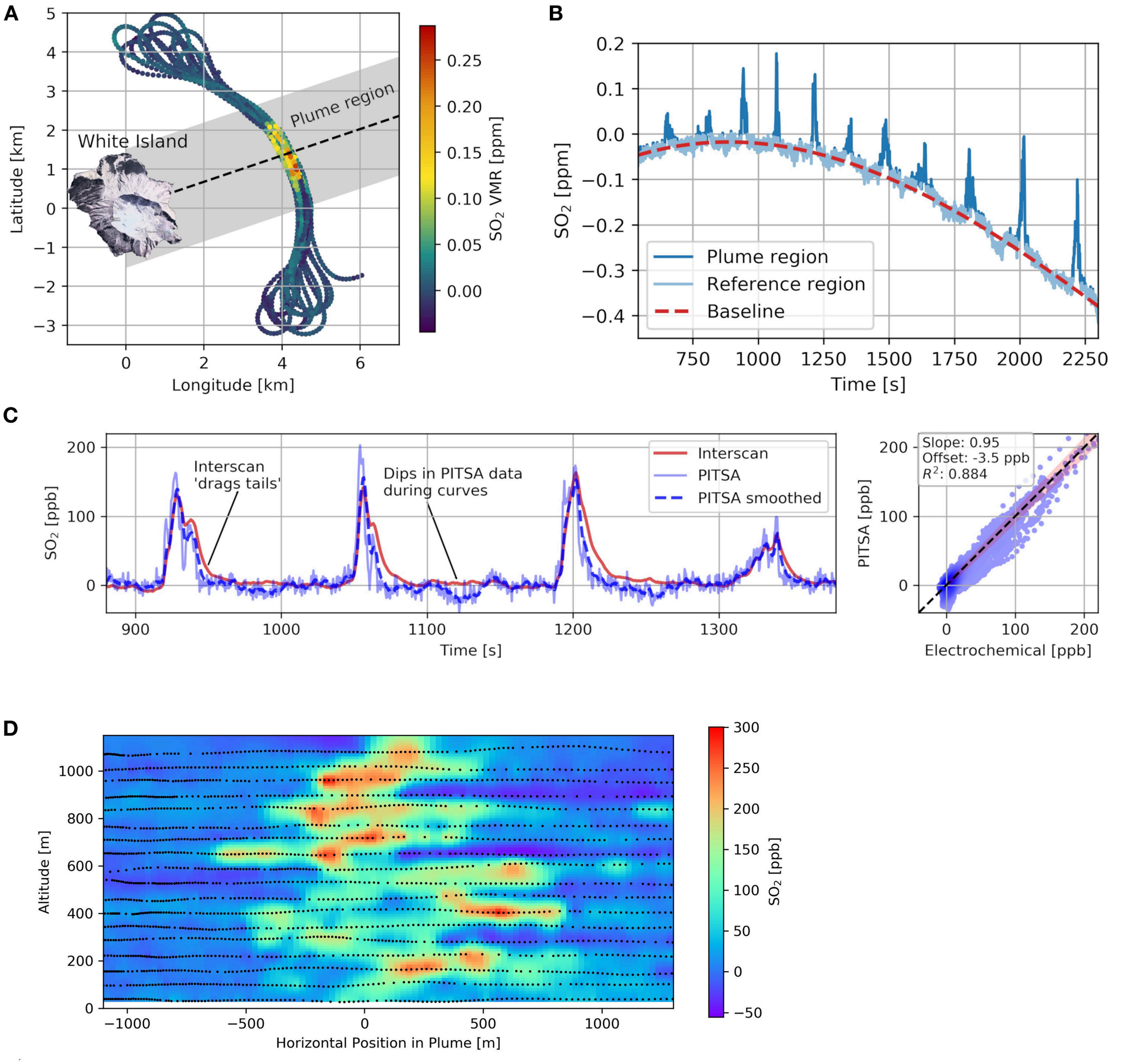

FIGURE 11 | Aircraft measurements at White Island volcano, New Zealand during December of 2015. **(A)** Flight path of the propeller machine, with respect to the position of the White Island crater. **(B)** Corresponding time series of the raw PITSA signal. The individual plume transects can be identified by the peaks on top of the baseline signal. The baseline was calculated by fitting a 4th order polynomial to the SO_2 free reference region. **(C)** Parallel measurements of the PITSA and the Interscan 4000 electrochemical sensor during the gas flight. The left plot shows an excerpt of the time series. After artificially degrading the PITSA's response time, the two instruments are in good agreement when the plane penetrates the plume. When leaving again, there are large deviations, most likely due to an asymmetric response behavior of the Interscan. The scatter plot on the right shows 10 s average values. Darkness of points represents the data point density. The red shaded area indicates the uncertainty of the Interscan as specified by the supplier. **(D)** The plume cross sectional SO_2 VMR, as measured by the PITSA. The map was interpolated from the actual sample points, which are represented by the small black dots.

downwind from the crater were performed with the PITSA on a small propeller aircraft on 8th of December 2015. At such distances from the source, plumes are already well diluted and in the case of White Island SO_2 VMRs rarely exceed 1 ppm. The flight path is shown on the left in **Figure 11A**. A series of 17 plume transects were flown perpendicular to the wind direction. Altitude was increased successively in steps of $\approx$ 60 m, to obtain cross-sectional 2D distributions of the measured gases. Among others, a very sensitive electrochemical sensor (Interscan 4000, measurement range of 2–2,000 ppb) was installed in the aircraft. In this particular case, the PITSA's automated zero point measurements were disabled, to avoid potential loss of valuable measurement time during the short plume crossings. Instead, gas free regions were identified during post processing and used to calculate a baseline (see **Figure 11B**). Compared to zero point measurements with a scrubber it has the advantage that undesired offsets caused by O_3 cross interference (see section 3.1.3) and water vapor influence (see section 3.1.4) are removed to a large extent. The baseline was determined by fitting a 4th order polynomial to the presumably gas free data. **Figure 11C** shows the baseline corrected PITSA measurements in comparison to the Interscan data. Similar as for the PITSA a

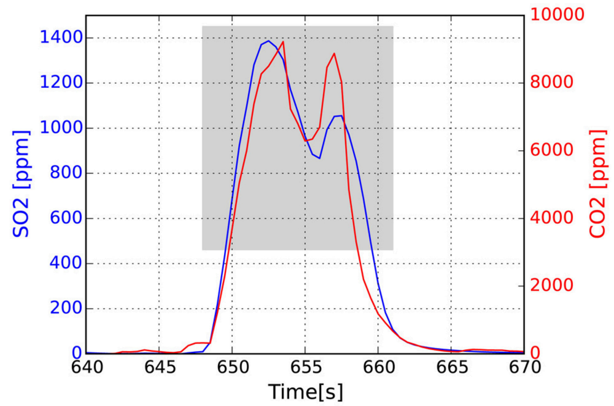

FIGURE 12 | Gas VMRs of the measurement inside the Fumarole Zero plume over time with backgrounds subtracted. From the data in the grey shaded area a CO_2/SO_2 ratio of 6.8 was derived.

baseline was also subtracted from the Interscan data (offset of $\approx$ 45 ppb). Cross sensitivities of the Interscan to hydrogen sulphide (H_2S) were avoided by scrubbing H_2S from the sampled air. The plot is equivalent to **Figure 10**. For the smoothing (see section 4.1), this time t_{dec} was chosen to only 2.5 s. Again, the PITSA is the faster instrument, but also exhibits larger noise. The slightly negative VMRs between the transects coincide with the curvature of the flight path and may indicate an influence of the force acting on the instrument, leading e.g., to slight bending of the optical setup and causing relative changes in the light throughput of $\approx 10^{-5}$. Effects of O_3 depletion and water vapor enhancement in the plume seem to be too small to be observed, such that in this particular case detection limits of $\approx$ 20 ppb were achieved. The asymmetric peak shapes in the Interscan data (independent of flight direction) suggest that the Interscan suffers an asymmetric response behavior, reacting much faster to SO_2 increases than to declines. This explains the change in instrument agreement, which gets significantly worse when leaving the plume. With the fast response a highly resolved 2D SO_2 plume cross section could be recorded, which is shown in **Figure 11D**. Wind speed and direction were obtained using the wind circle method (Doukas, 2002). Integration over plume cross section and multiplying by the wind speed yielded a total SO_2 emission rate of $280 \pm 85\,\mathrm{t\,d^{-1}}$. This is in agreement with results from simultaneously performed remote sensing measurements ($320 \pm 160\,\mathrm{t\,d^{-1}}$, derived with a zenith DOAS instrument, also installed on the plane) and reported literature values (Werner et al., 2008).

4.3. Fumarole Sampling at White Island Volcano

On the 3rd of December 2015, the plume of a fumarole on the White Island crater floor ('Fumarole Zero' with a degassing temperature of 170 °C) was sampled. To reduce the impact of condensation and the risk of damage inside the PITSA, the sample air was drawn at 5 m distance from the vent, the sampling time was limited to 10 s and the instrument's internal heater was used (see section 2.3). **Figure 12** shows the recorded time series. Here, also data of the integrated CO_2 sensor are shown (see section 2.3). Measurements outside the plume just before entering and after leaving were assumed as background and were subtracted. Observed peak values in CO_2 and SO_2 were 9,800 and 1,400 ppm, respectively. The data in the gray shaded area yield a CO_2/SO_2 ratio of 6.8. This is in good agreement with ratios measured during sampling at the crater rim on the same day (6 ± 2) and as measured by GNS on the gas flight 5 days later (8 ± 4).

4.4. Application in Atmospheric Simulation Chamber Experiments

From November 2017 to June 2018 the PITSA was applied in Bayreuth (Germany), during atmospheric simulation chamber experiments (similarly as described in detail by Buxmann et al., 2012) for the investigation of reactive halogen chemistry in volcanic plumes. The chamber consists of a 4 $\mathrm{m^3}$ PTFE bag with a diameter of 1.4 m and 2.5 m height, and with a sun simulator made of 7 x 1200 W Osram HMI lamps. Beside the PITSA, several other instruments were connected to the chamber to monitor the conditions and gas concentrations inside, among others a fluorescence SO_2 instrument by Enivronnement S.A., type AF 20M. **Figure 13** shows times series of the PITSA and the AF 20M (1 min average values) during an SO_2 injection event in the chamber. The AF 20M and the PITSA both showed offsets of −680 and −370 ppb, respectively, before SO_2 was injected. These offsets were subtracted.

5. CONCLUSIONS AND OUTLOOK

On the basis of the PITSA prototype, it has been shown, that NDUV is a promising alternative measurement technique for *in-situ* detection of SO_2 in applications where SO_2 levels exceeding 10 ppb are encountered. Beside volcanic degassing, this comprises also fields like ship or industrial plant emissions. The calculated instrument sensitivity is accurate and stable to better than 5 %. Instrument offset drifts can reliably be removed, when automatic zero point measurements are performed in regular intervals (i.e., between 10 seconds and several hours, depending on the desired offset stability). The instrument is then inherently calibrated, which is a major advantage compared to most other established techniques. Sub-ppm detection limits are easily achieved and can be further improved to few tens of ppb under favorable conditions (see section 4.2) at response times of $1-2$ s. Cross sensitivities to other gases are small, well-known, and stable over the instrument's lifetime. The fully functional PITSA is somewhat larger and heavier (50 cm, 8 kg, including batteries for 24 h operation, all required electronics for logging, and filter for automatic zero point measurements) than e.g., electrochemical sensors of similar functionality but still fits into a backpack, for easy access of remote sampling sites with logistical restrictions. The large measurement range makes the instrument very flexible in its application: as shown in section 4.3 and 4.2, respectively, the instrument is capable of sampling fumarolic

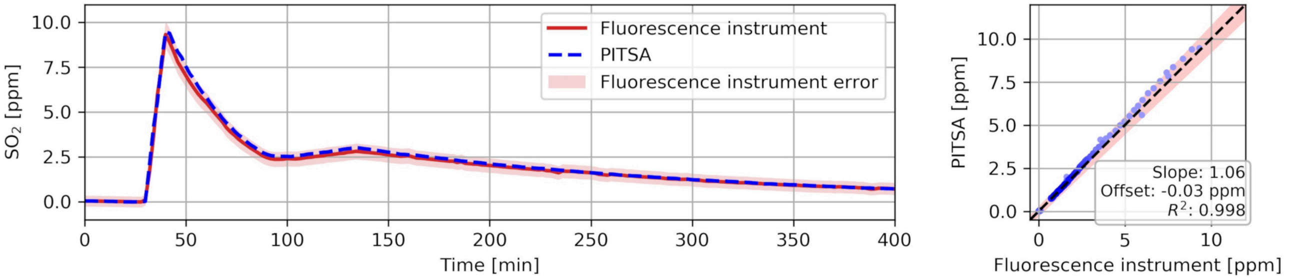

FIGURE 13 | Left: Parallel measurements of the PITSA and the AF 20M fluorescence monitor during an SO_2 injection event in the atmospheric simulation chamber. **Right**: Corresponding scatter plot. Darkness of points represents the data point density. The red shaded area indicates the uncertainty of the AF 20M, as estimated from earlier chamber experiments.

plumes with $>$1,000 ppm SO_2 VMRs, as well as carrying out airborne measurements of diluted plumes with $<$ 0.3 ppm at several kilometers distance to the vent. Possible drawbacks are data gaps due to zero point measurements, the strong influence of condensation and currently the not well-understood interference with air humidity. Performance and applicability have been validated in a series of volcanic field applications and comparison studies as described in section 4.

For future NDUV instruments a number of modified setups are conceivable, depending on the requirements. If measurements at low SO_2 VMRs ($<$ 10 ppb) are desired, a general limitation of the principle are the numerous small cross sensitivities, which become significant at detection limits of few ppb. Therefore, modifications like an enhancement of the absorption path L to increase instrument sensitivity are unlikely to lead to notable improvements. However, usually (e.g., in typical volcanic plumes) detection limits around 1 ppm are sufficient. Then shorter or folded light paths would allow much more compact and lighter devices. Since most systematic effects in first approximation scale with L and instrument noise is not the limiting factor, a reduction of L by a factor of 2–5 can probably be realized without strongly impacting on the instrument's detection limit. Photon shot noise decreases with the LED optical output power P_{LED} according to $1/\sqrt{P_{LED}}$ and can therefore be reduced by applying larger currents to the LED. Maximum values for the supply current and resulting P_{LED} of the UV-TOP280 are 40 mA and 1.6 mW, respectively, which corresponds to an increase of factor $\approx$ 6 in optical output (decrease in noise by factor 2.4), compared to the results shown in this study. A further option to reduce the instrument size at costs of performance is to remove the monitoring channel, which would degrade the instrument's detection limit by a factor of $\approx$ 5. Note, that by reducing the cell size also the response behavior improves, as flushing of the cell takes less time. If larger cells are required, an increase of the pump flow rate can be used to achieve the same effect. Regarding the scrubber, alternative approaches to zero point measurements like a partial evacuation of the sample cell should be considered. In applications, where gas free air is reliably sampled in regular intervals (e.g., section 4.2), scrubbing is not even necessary. For UAV based plume scanning for instance, scrubber and LED monitoring channel could be abandoned, such that very small (5 x 5 x 10 cm), light ($<$ 1 kg) and fast ($t_{90} < 1$ s) instruments with detection limits around 1 ppm become possible, which would be sufficiently sensitive for applications close to the vent (typical SO_2 concentrations $\gg$1 ppm) and which could be carried even by small quadcopters with little payload.

DATA AVAILABILITY

The raw data supporting the conclusions of this manuscript will be made available by the authors, without undue reservation, to any qualified researcher.

AUTHOR CONTRIBUTIONS

UP invented the instrument. He came up with the basic idea of using NDUV for volcanic SO_2 detection in the way described. He supervised and consulted J-LT throughout his work. J-LT was the executing student. He realized the instrument, measured in the field, evaluated most of the data, and wrote the first draft of this article. DP supervised the realization of the PITSA with his long-time experience in scientific instrument development. NB organized and coordinated measurement campaigns to Mt. Etna and Strobili and was strongly involved in the evaluation and scientific classification of the data shown in this article. BC organized and coordinated the measurements performed at White Island volcano in New Zealand and provided the corresponding data for instrument comparison. He had a role in motivating the project, seeing a need for such spectrometry in the application to volcanological pursuits. JR and SS performed the cloud chamber experiments during which a row of characterization and comparison measurements were conducted. All authors contributed to manuscript revision and read and approved the submitted version.

FUNDING

We acknowledge financial support by Deutsche Forschungsgemeinschaft within grant PL 193-19/1, grant PL 193 16/1 and the funding programme Open Access Publishing, by the Baden-Württemberg Ministry of Science, Research and the Arts and by Ruprecht-Karls-Universität Heidelberg.

ACKNOWLEDGMENTS

We thank Giovanni Giuffrida and Marco Liuzzo for their support. Ralph Pfeifer for the realization of the optomechanical setup. Karen Britten for the support and instrument operation during the airborne measurements. Udo Friess for the help on the theory of spectroscopy, Jonas Kuhn for taking the instrument on further campaigns, Agnes Marzot for the accommodation in New Zealand.

SUPPLEMENTARY MATERIAL

The Supplementary Material for this article can be found online at: https://www.frontiersin.org/articles/10.3389/feart.2019.00026/full#supplementary-material

REFERENCES

Aiuppa, A., Federico, C., Giudice, G., and Gurrieri, S. (2005). Chemical mapping of a fumarolic field: la fossa crater, vulcano island (aeolian islands, italy). *Geophys. Res. Lett.* 32:13. doi: 10.1029/2005GL023207

Aiuppa, A., Moretti, R., Federico, C., Giudice, G., Gurrieri, S., Liuzzo, M., et al. (2007). Forecasting etna eruptions by real-time observation of volcanic gas composition. *Geology* 35, 1115–1118. doi: 10.1130/G24149A.1

Atkins, D., and Lee, D. S. (1995). Spatial and temporal variation of rural nitrogen dioxide concentrations across the united kingdom. *Atmos. Environ.* 29, 223–239. doi: 10.1016/1352-2310(94)00229-E

Bobrowski, N., Von Glasow, R., Aiuppa, A., Inguaggiato, S., Louban, I., Ibrahim, O., et al. (2007). Reactive halogen chemistry in volcanic plumes. *J. Geophys. Res. Atmos.* 112:D6. doi: 10.1029/2006JD007206

Boichu, M., Oppenheimer, C., Roberts, T. J., Tsanev, V., and Kyle, P. R. (2011). On bromine, nitrogen oxides and ozone depletion in the tropospheric plume of Erebus volcano (Antarctica). *Atmos. Environ.* 45, 3856–3866. doi: 10.1016/j.atmosenv.2011.03.027

Bucholtz, A. (1995). Rayleigh-scattering calculations for the terrestrial atmosphere. *Appl. Opt.* 34, 2765–2773. doi: 10.1364/AO.34.002765

Burgisser, A., and Scaillet, B. (2007). Redox evolution of a degassing magma rising to the surface. *Nature* 445:194. doi: 10.1038/nature05509

Buxmann, J., Balzer, N., Bleicher, S., Platt, U., and Zetzsch, C. (2012). Observations of bromine explosions in smog chamber experiments above a model salt pan. *Int. J. Chem. Kinetics* 44, 312–326. doi: 10.1002/kin.20714

Caroll, M., and Holloway, J. (1994). Volatiles in magma. *Mineral. Soc. Am.* 30, 38–42.

Chang, C.-T., Liu, T.-H., and Jeng, F.-T. (2004). Atmospheric concentrations of the Cl atom, ClO radical, and HO radical in the coastal marine boundary layer. *Environ. Res.* 94, 67–74. doi: 10.1016/j.envres.2003.07.008

Doukas, M. P. (2002). *A New Method for GPS-Based Wind Speed Determinations During Airborne Volcanic Plume Measurements*. US Department of the Interior, US Geological Survey.

Galle, B., Oppenheimer, C., Geyer, A., McGonigle, A. J., Edmonds, M., and Horrocks, L. (2003). A miniaturised ultraviolet spectrometer for remote sensing of SO2 fluxes: a new tool for volcano surveillance. *J. Volcanol. Geothermal Res.* 119, 241–254. doi: 10.1016/S0377-0273(02)00356-6

General, S. (2014). *Development of the Heidelberg Airborne Imaging DOAS Instrument (HAIDI)*. PhD thesis, Institute of Environmental Physics: University of Heidelberg.

Gliss, J., Bobrowski, N., Vogel, L., Pöhler, D., and Platt, U. (2015). OClO and BrO observations in the volcanic plume of Mt. Etna–implications on the chemistry of chlorine and bromine species in volcanic plumes. *Atmos. Chem. Phys.* 15, 5659–5681. doi: 10.5194/acp-15-5659-2015

Horton, K. A., Williams-Jones, G., Garbeil, H., Elias, T., Sutton, A. J., Mouginis-Mark, P., et al. (2006). Real-time measurement of volcanic SO_2 emissions: validation of a new UV correlation spectrometer (FLYSPEC). *Bull. Volcanol.* 68, 323–327. doi: 10.1007/s00445-005-0014-9

Keller-Rudek, H., Moortgat, G. K., Sander, R., and Sörensen, R. (2013). The MPI-mainz UV/VIS spectral atlas of gaseous molecules of atmospheric interest. *Earth Syst. Sci. Data* 5:365. doi: 10.5194/essd-5-365-2013

Kelly, P. J., Kern, C., Roberts, T. J., Lopez, T., Werner, C., and Aiuppa, A. (2013). Rapid chemical evolution of tropospheric volcanic emissions from Redoubt Volcano, Alaska, based on observations of ozone and halogen-containing gases. *J. Volcanol. Geothermal Res.* 259, 317–333. doi: 10.1016/j.jvolgeores.2012.04.023

Lee, C., Kim, Y. J., Tanimoto, H., Bobrowski, N., Platt, U., Mori, T., et al. (2005). High ClO and ozone depletion observed in the plume of Sakurajima volcano, japan. *Geophys. Res. Lett.* 32. doi: 10.1029/2005GL023785

Lehrer, E., and Luft, K. (1938). Verfahren zur Bestimmung von Bestandteilen in Stoffgemischen mittels Strahlenabsorption. *Deutsche Patentschrift DE* 730:478.

Lewicki, J. L., Kelly, P., Bergfeld, D., Vaughan, R. G., and Lowenstern, J. B. (2017). Monitoring gas and heat emissions at Norris Geyser Basin, Yellowstone National Park, USA based on a combined eddy covariance and Multi-GAS approach. *J. Volcanol. Geothermal Res.* 347, 312–326. doi: 10.1016/j.jvolgeores.2017.10.001

Meng, Z.-Y., Xu, X.-B., Wang, T., Zhang, X.-Y., Yu, X.-L., Wang, S.-F., et al. (2010). Ambient sulfur dioxide, nitrogen dioxide, and ammonia at ten background and rural sites in China during 2007–2008. *Atmos. Environ.* 44, 2625–2631. doi: 10.1016/j.atmosenv.2010.04.008

Moffat, A. J., and Millan, M. M. (1971). The applications of optical correlation techniques to the remote sensing of SO_2 plumes using sky light. *Atmos. Environ.* 5, 677–690.

Mori, T., and Burton, M. (2006). The SO_2 camera: A simple, fast and cheap method for ground-based imaging of SO_2 in volcanic plumes. *Geophys. Res. Lett.* 33. doi: 10.1029/2006GL027916

Oppenheimer, C., Fischer, T. P., and Scaillet, B. (2014). "Volcanic degassing: process and impact," in *Treatise on Geochemistry* 2nd Edn, eds H. D. Holland and K. K. Turekian (Elsevier), 111–179. doi: 10.1016/B978-0-08-095975-7.00304-1

Oppenheimer, C., Francis, P., Burton, M., Maciejewski, A., and Boardman, L. (1998). Remote measurement of volcanic gases by Fourier transform infrared spectroscopy. *Appl. Phys. B Lasers Opt.* 67, 505–515.

Oppenheimer, C., Kyle, P., Tsanev, V., McGonigle, A., Mather, T., and Sweeney, D. (2005). Mt. Erebus, the largest point source of NO_2 in antarctica. *Atmos. Environ.* 39, 6000–6006. doi: 10.1016/j.atmosenv.2005.06.036

Oppenheimer, C., Scaillet, B., and Martin, R. S. (2011). Sulfur degassing from volcanoes: Source conditions, surveillance, plume chemistry and earth system impacts. *Rev. Mineral. Geochem.* 73:363. doi: 10.2138/rmg.2011.73.13

Pering, T., Tamburello, G., McGonigle, A., Aiuppa, A., Cannata, A., Giudice, G., et al. (2014). High time resolution fluctuations in volcanic carbon dioxide degassing from Mount Etna. *J. Volcanol. Geothermal Res.* 270, 115–121. doi: 10.1016/j.jvolgeores.2013.11.014

Platt, U., Bobrowski, N., and Butz, A. (2018). Ground-based remote sensing and imaging of volcanic gases and quantitative determination of multi-species emission fluxes. *Geosciences* 8:44. doi: 10.3390/geosciences8020044

Roberts, T., Braban, C., Martin, R., Oppenheimer, C., Adams, J., Cox, R., et al. (2009). Modelling reactive halogen formation and ozone depletion in volcanic plumes. *Chem. Geol.* 263, 151–163. doi: 10.1016/j.chemgeo.2008.11.012

Roberts, T., Braban, C., Oppenheimer, C., Martin, R., Freshwater, R., Dawson, D., et al. (2012). Electrochemical sensing of volcanic gases. *Chem. Geol.* 332, 74–91. doi: 10.1016/j.chemgeo.2012.08.027

Roberts, T., Saffell, J., Oppenheimer, C., and Lurton, T. (2014). Electrochemical sensors applied to pollution monitoring: measurement error and gas ratio bias–a volcano plume case study. *J. Volcanol. Geothermal Res.* 281, 85–96. doi: 10.1016/j.jvolgeores.2014.02.023

Roberts, T., Vignelles, D., Liuzzo, M., Giudice, G., Aiuppa, A., Coltelli, M., et al. (2018). The primary volcanic aerosol emission from Mt Etna: size-resolved particles with SO_2 and role in plume reactive halogen chemistry. *Geochim. Cosmochim. Acta* 222, 74–93. doi: 10.1016/j.gca.2017.09.040

Roedel, W., and Wagner, T. (2017). "Strahlung und energie in dem system atmosphäre/erdoberfläche," in *Physik unserer Umwelt: Die Atmosphäre* (Heidelberg; Berlin: Springer), 1–65.

Shinohara, H. (2005). A new technique to estimate volcanic gas composition: plume measurements with a portable multi-sensor system. *J. Volcanol. Geothermal Res.* 143, 319–333. doi: 10.1016/j.jvolgeores.2004.12.004

Swinehart, D. (1962). The Beer-Lambert law. *J. Chem. Educ.* 39:333. doi: 10.1021/ed039p333

Textor, C., Graf, H.-F., Timmreck, C., and Robock, A. (2004). "Emissions from volcanoes," in *Emissions of Atmospheric Trace Compounds* (Dordrecht: Springer), 269–303.

Vance, A., McGonigle, A. J., Aiuppa, A., Stith, J. L., Turnbull, K., and von Glasow, R. (2010). Ozone depletion in tropospheric volcanic plumes. *Geophys. Res. Lett.* 37:22. doi: 10.1029/2010GL044997

Vandaele, A. C., Hermans, C., and Fally, S. (2009). Fourier transform measurements of SO_2 absorption cross sections: II.: temperature dependence in the 29 000–44 000 cm^{-1} (227–345 nm) region. *J. Quant. Spectrosc. Radiat. Transfer* 110, 2115–2126. doi: 10.1016/j.jqsrt.2009.05.006

Vingarzan, R. (2004). A review of surface ozone background levels and trends. *Atmos. Environ.* 38, 3431–3442. doi: 10.1016/j.atmosenv.2004.03.030

Werner, C., Hurst, T., Scott, B., Sherburn, S., Christenson, B., Britten, K., et al. (2008). Variability of passive gas emissions, seismicity, and deformation during crater lake growth at White Island Volcano, New Zealand, 2002–2006. *J. Geophys. Res. Solid Earth* 113:B1. doi: 10.1029/2007JB005094

Conflict of Interest Statement: The authors declare that the research was conducted in the absence of any commercial or financial relationships that could be construed as a potential conflict of interest.

frontiers in Earth Science

METHODS
published: 16 April 2019
doi: 10.3389/feart.2019.00065

The PiSpec: A Low-Cost, 3D-Printed Spectrometer for Measuring Volcanic SO_2 Emission Rates

Thomas Charles Wilkes[1]*, *Tom David Pering*[1], *Andrew John Samuel McGonigle*[1,2], *Jon Raffe Willmott*[3], *Robert Bryant*[1], *Alan Lomas Smalley*[1], *Forrest Marion Mims III*[4], *Alfio V. Parisi*[5] and *Rebecca Anne England*[1]

[1] *Department of Geography, The University of Sheffield, Sheffield, United Kingdom,* [2] *School of Geosciences, The University of Sydney, Sydney, NSW, Australia,* [3] *Department of Electronic and Electrical Engineering, The University of Sheffield, Sheffield, United Kingdom,* [4] *Geronimo Creek Observatory, Seguin, TX, United States,* [5] *Faculty of Health, Engineering and Sciences, University of Southern Queensland, Toowoomba, QLD, Australia*

Spectroscopy has been used to quantify volcanic gas emission rates, most commonly SO_2, for a number of decades. Typically, commercial spectrometers costing 1000s USD are employed for this purpose. The PiSpec is a new, custom-designed, 3D-printed spectrometer based on smartphone sensor technology. This unit has ≈1 nm spectral resolution and a spectral range in the ultraviolet of ≈280–340 nm, and is specifically configured for the remote sensing of SO_2 using Differential Optical Absorption Spectroscopy (DOAS). Here we report on the first field deployment of the PiSpec on a volcano, to demonstrate the proof of concept of the device's functionality in this application area. The study was performed on Masaya Volcano, Nicaragua, which is one of the largest emitters of SO_2 on the planet, during a period of elevated activity where a lava lake was present in the crater. Both scans and traverses were performed, with resulting emission rates ranging from 3.2 to 45.6 kg s^{-1} across two measurement days; these values are commensurate with those reported elsewhere in the literature during this activity phase (Aiuppa et al., 2018; Stix et al., 2018). Furthermore, we tested the PiSpec's thermal stability, finding a wavelength shift of 0.046 nm/°C between 2.5 and 45°C, which is very similar to that of some commercial spectrometers. Given the low build cost of these units (≈500 USD for a one-off build, with prospects for further price reduction with volume manufacture), we suggest these units hold considerable potential for volcano monitoring operations in resource limited environments.

Keywords: UV spectroscopy, DOAS, sulfur dioxide, volcanic emissions, Masaya volcano, smartphone sensor, Raspberry Pi, 3D printing

Edited by:
John Stix,
McGill University, Canada

Reviewed by:
Ryunosuke Kazahaya,
Geological Survey of Japan (AIST),
Japan
J. Maarten De Moor,
OVSICORI-UNA, Costa Rica

****Correspondence:***
Thomas Charles Wilkes
tcwilkes1@sheffield.ac.uk

Specialty section:
This article was submitted to
Volcanology,
a section of the journal
Frontiers in Earth Science

Received: *14 September 2018*
Accepted: *14 March 2019*
Published: *16 April 2019*

Citation:
Wilkes TC, Pering TD, McGonigle AJS, Willmott JR, Bryant R, Smalley AL, Mims FM III, Parisi AV and England RA (2019) The PiSpec: A Low-Cost, 3D-Printed Spectrometer for Measuring Volcanic SO_2 Emission Rates. Front. Earth Sci. 7:65. doi: 10.3389/feart.2019.00065

INTRODUCTION

Ground-based remote sensing of sulfur dioxide (SO_2) emissions from volcanoes has been performed for a number of decades, aiding in both monitoring efforts and volcanic research (e.g., Young et al., 1998; Shinohara et al., 2008; Arellano et al., 2017). Differential Optical Absorption Spectroscopy (DOAS) is the most commonly applied retrieval approach, utilizing the distinct absorption features of SO_2, most commonly in the ≈300–325 nm wavelength range

(Platt and Stutz, 2008). A variety of instrument designs and deployment modes have been proposed and employed within this scientific community: Multi AXis DOAS (MAX-DOAS; e.g., Hönninger et al., 2004; Bobrowski et al., 2007; Galle et al., 2010), walking traverses (e.g., McGonigle et al., 2002), road traverses (McGonigle et al., 2002; Galle et al., 2003; Salerno et al., 2009), airborne traverses (Galle et al., 2003; McGonigle et al., 2004; Grutter et al., 2008), high time-resolution fixed field of view deployments (e.g., McGonigle et al., 2009; Tamburello et al., 2011) and satellite remote sensing (e.g., Khokhar et al., 2005; Rix et al., 2009; Theys et al., 2015). Airborne DOAS instruments have also been proposed as a means of improving aviation safety related to volcanic hazard, by providing early detection of volcanic plumes (Vogel et al., 2011). Most prominently in volcanology, the Network for Observation of Volcanic and Atmospheric Change (NOVAC) project has led to the deployment of a large number of scanning spectrometers at volcanoes across the globe, monitoring SO_2 emissions along with other gas species (Galle et al., 2010).

Recently, we have developed the PiSpec, a 3D-printed UV spectrometer based on a detector primarily designed for the smartphone market (Wilkes et al., 2017). The sensor, here packaged as part of a Raspberry Pi camera module, is modified by removal of its Bayer filter, as described in Wilkes et al. (2016), to deliver significant enhancement in UV sensitivity. This instrument provides a relatively low-cost alternative to off-the-shelf commercially available UV spectrometers ($\approx$500 USD vs. >1000 USD), with the potential to drive costs down further with mass production. Furthermore, the presented methodology allows researchers to quite easily design and build new spectrometers with spectral ranges and resolutions specifically tailored for their desired applications. The initial article (Wilkes et al., 2017) highlighted that this specific PiSpec design has the performance to facilitate DOAS retrievals of SO_2, with comparable functionality to a commercial USB2000 (Ocean Optics, Inc.) instrument. However, those relatively rudimentary tests, using SO_2 filled quartz cells, did not rigorously assess the spectrometer's performance under representative field deployment conditions, which can often be more challenging than isolated laboratory experiments, for example, involving road traverses on bumpy roads or large changes in ambient temperatures. Here, we therefore present the first deployment of the PiSpec on a volcano, in this case at Masaya volcano (11°59′3.65″ N, 86°10′5.28″ W), Nicaragua, to demonstrate its performance under "real world" field conditions. Both scanning and road traverse retrievals are presented from this campaign, which took place during a period of heightened activity, whilst a lava lake was present in the crater. Furthermore, since spectrometers can be subjected to a wide range of ambient conditions during field deployments, we also characterize the thermal stability of the spectrometer via laboratory tests.

MATERIALS AND METHODS

Measurement and Retrieval Technique

The PiSpec instrument design is described in detail in Wilkes et al. (2017). It is based on a Czerny-Turner optical bench layout, with off-the-shelf optical components mounted in a 3D-printed housing. Light enters through a slit aperture and is collimated using a mirror, before falling incident onto a diffraction grating; the dispersed light is then focused onto a detector, to provide a system spectral resolution and range of $\approx$1 nm and $\approx$280–340 nm, respectively. The detector is an Omnivision OV5647 sensor, primarily designed for the smartphone market, but here packaged as part of the Raspberry Pi v1.3 camera module (Raspberry Pi Foundation). This camera board has the advantage of greater user control, such as raw 10-bit data access and better gain control, relative to sensors incorporated into smartphone units themselves. Furthermore, this board-based configuration makes the sensor more readily accessible, such that we are able to chemically remove the Bayer filter, as described by Wilkes et al. (2016); this produces a uniformly responding sensor with enhanced UV sensitivity, both of which are crucial features for this application area. The detector acquisition is controlled by a Raspberry Pi computer, which in turn is controlled by a custom Python 3 graphical user interface run on a Windows laptop. As in Wilkes et al. (2017), all spectra captured herein have been generated by co-adding 11 rows across the PiSpec sensor, to increase the signal-to-noise ratio (SNR).

We have previously demonstrated that the instrument has $\approx$1 nm spectral resolution and a spectral range of $\approx$280–340 nm, with a 30 μm slit in place. This implementation makes it well tailored for DOAS retrievals of SO_2, following approaches which are extensively documented elsewhere (Galle et al., 2003; Platt and Stutz, 2008). In brief, the method involves collection of a clear-sky Fraunhofer spectrum, $I_0(\lambda)$, with which subsequent in-plume spectra, $I(\lambda)$, can be used to calculate the plume optical density, $D(\lambda)$:

$$D(\lambda) = \ln\left(\frac{I_0(\lambda)}{I(\lambda)}\right) \tag{1}$$

The differential optical density, $D'(\lambda)$, can then be isolated through applying a high-pass filter to $D(\lambda)$; here, we use a Butterworth high-pass filter implemented in MATLAB®. A reference spectrum of the SO_2 absorption cross-section, such as that provided by Vandaele et al. (2009), is then convolved with the instrument's line shape and high-pass filtered also. This spectrum is then fitted to $D'(\lambda)$, using a least-squares method, such that the scaling factor of the fit provides the column density of SO_2 for that spectral acquisition. An O_3 absorption spectrum (taken from the HITRAN database; Gordon et al., 2017) is similarly fitted, to remove effects from this species, which also has distinct absorption features within the spectral fitting window; SO_2 column densities retrieved with and without this O_3 correction differed by <2%. In this work, the fitting window was manually determined for each spectrum, by assessing the degree of saturation present at shorter wavelengths when large column densities of SO_2 were present; we then ensured that a sufficiently long start wavelength for the fitting window was chosen in order to avoid this saturation. Typically, for larger column densities a fit window of $\approx$314–324 nm was used, which we later show is linear up to $\approx$4000 ppm · m. Whilst fitting window determination could be automated for the PiSpec, as with any other DOAS instrument (Vogel et al., 2013), this was not the purpose of this study.

In practice, spectra $I_0(\lambda)$ and $I(\lambda)$ first must be corrected for dark current and stray light. Firstly, for the former a dark spectrum was acquired with the entrance optics blocked, in this case with a lens cap covering the lens. On Masaya, the dark acquisitions were made immediately prior to or after a full scan/traverse sequence. The dark spectrum is then subtracted from all spectra. Stray light was subsequently corrected for by subtracting the average digital number (DN) between ≈285–295 nm from the entire spectrum. At these wavelengths, the irradiance at the Earth's surface is negligible, due to strong absorption by Ozone, therefore, the signal at the detector should be ≈0. In reality this is not the case, due to stray light within the spectrometer, which is assumed to be uniform across the detector.

For the PiSpec's entrance slit we predominantly used the 30 μm slit aperture; however, for some field traverses we tested a 50 μm slit to explore the outcomes of increased light throughput, with associated reduction in required exposure times. This modification does, however, result in decreased spectral resolution, which can be detrimental to the DOAS retrievals.

Thermal Stability

Volcanoes can be located in a range of extreme environments, often found at low temperatures due to their altitude, or in hot conditions from direct sun exposure at lower latitudes. Since spectrometers can be sensitive to changes in thermal conditions, shifting and warping the line function (e.g., Platt and Stutz, 2008), it is important to address this issue as part of evaluating the PiSpec's utility in volcanic surveillance operations.

These tests were performed by acquiring spectra from a Hg-Ar lamp (Ocean Optics, Inc.) coupled to the PiSpec by an optical fiber. This setup was placed in an incubator (Panasonic MIR-254-PE), set on Low Humidity Mode, to expose it to temperatures between ≈0 and 50°C. The PiSpec was further placed inside a plastic pouch containing silica gel, to reduce humidity and prevent condensation; within this pouch the lowest temperature actually achieved was 2.5°C. Temperature was logged every minute using a LogTag® HAXO-8 recorder. At each temperature setting a repose period of ≈1 h was applied before acquisition, to allow the pouch to equilibrate with the incubator temperature. The tests spanned 2 days, 19–20 June 2018.

Field Deployment

The PiSpec was tested on Masaya volcano, Nicaragua, on the 14th (19:20 to 21:30 UTC) and 16th of June 2017 (16:40 to 18:20 UTC). At this time, a vigorously overturning lava lake was emplaced in Masaya's Santiago crater. The lake, which has been visible since late 2015 (Venzke, 2017), has been the subject of only a few published articles to date (Aiuppa et al., 2018; Stephens and Wauthier, 2018; Wilkes et al., 2018; Pering et al., 2019). SO_2 emission rates from the crater, measured with a NOVAC scanning-DOAS system, have been highly variable since the lake appeared, with measured fluxes ranging between 0 and 50 kg s^{-1} (Aiuppa et al., 2018). Between 2005 and 2015, Carn et al. (2017) listed Masaya as the 18th largest passive volcanic emitter of SO_2 on earth. Furthermore, due to the low elevation of Masaya's crater, and hence its plume, emissions can have a considerable impact on surrounding vegetation and communities (Delmelle et al., 2002).

We deployed the PiSpec to acquire under two distinct observation modes: scanning-DOAS (14th June) and road traverses (16th June). For the former set up, tests were performed close to the vent, manually scanning horizontally through the plume whilst it was still rising buoyantly from the crater. Contemporaneous visible video was acquired with a DSLR camera, allowing plume transport speed determinations by tracking the condensed plume. This was based on integrating the pixel brightness over two cross sections through the rising plume, then generating time series for each of these feeds, which were cross correlated in order to determine the temporal lag between them. This follows the commonly applied approach in both spectral and image based determinations of plume speed in volcanic SO_2 emission rate estimations (McGonigle et al., 2005; Mori and Burton, 2006). Indeed, in settings where a volcanic plume is persistently condensed, this also demonstrates that visible imagery can provide an effective low-cost method of retrieving plume speeds for a DOAS instrument.

Uncertainties associated with the cross-correlation technique are dominated by knowledge of the distance from observer to camera, and the angle of plume motion relative to the normal of the camera viewing direction, i.e., plume speed has a $1/\cos\alpha$ dependency on relative angle of plume motion, where α is the angular offset from a plume motion that is perpendicular to the camera viewing direction (Klein et al., 2017). For the scans in particular, since they were located close to the source, the relative uncertainty associated with distance to the plume dominates the total uncertainty; it was estimated to be $\approx \pm 0.2$ (20%). Conversely, even with a relatively large absolute uncertainty for the angle of plume motion (estimated to be $\approx \pm 10°$), the associated relative uncertainty is small ($\approx \pm 0.02$).

Road traverses were performed by supporting the PiSpec out of a car window and continuously acquiring GPS receiver (Adafruit Ultimate GPS breakout) geo-referenced spectra whilst driving under the plume on La Carretera a Masaya, located to the north east of the Santiago crater (see **Figure 1**). These measurements were made under rather rare conditions, with the plume blowing approximately north-north-east, making La Carretera a Masaya the optimal route for traverses; the prevailing wind direction is approximately from the east, as evidenced by the SO_2 impacts on plant growth on the western side of the volcano. At times, overhanging trees may have interfered with the traverse spectra; however, we were careful to pause acquisitions when large regions of obstruction were encountered. In general, the quality of fitted SO_2 spectra suggests that significant issues from trees were avoided. Plume speed, again, was estimated using visible video acquired shortly before we began the traverses, and using cross correlation. Traverse emission rates were then computed from the wind, GPS and spectral concentration data following the methodology outlined by McGonigle (2007).

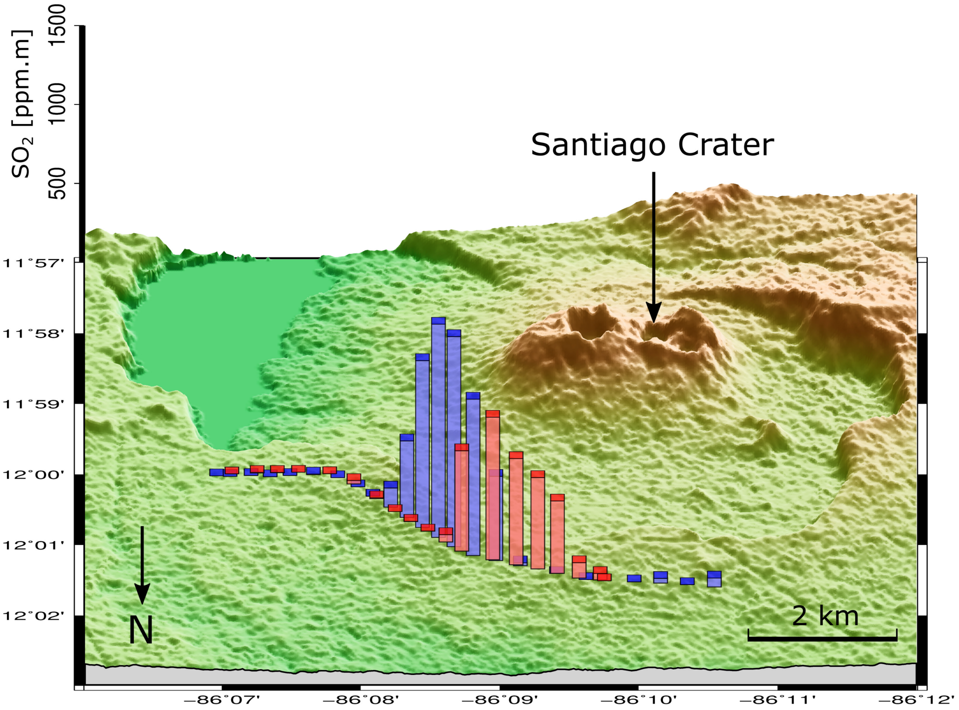

FIGURE 1 | Traverse SO_2 column densities (ppm · m) plotted in bars for two traverses started at 17:46:01 UTC (red) and 17:55:10 UTC (blue); emission rates were 16.3 and 27.2 kg s^{-1}, respectively. Traverses were performed along La Carretera a Masaya. Base map topographic data retrieved from USGS (2018). Data for this figure, and all other figures in this manuscript, are available in **Supplementary Data Sheet S1**.

RESULTS AND DISCUSSION

Comparison of the PiSpec With the USB2000

A number of commercial spectrometers are currently used for DOAS applications in volcanology. Although it has now been discontinued, the USB2000 (Ocean Optics) was once perhaps the most commonly used spectrometer (e.g., Galle et al., 2003; Mori et al., 2006; Kantzas et al., 2009; Bobrowski et al., 2010), and therefore provides a good benchmark to compare the PiSpec against. This instrument is also very similar to the USB2000+ and Flame-S spectrometers, the next generation versions of the USB2000, which are currently market available and frequently used today. **Table 1** provides some useful features of these PiSpec, USB2000 and USB2000+ spectrometers, for comparison; the Flame-S specifications are very similar to that of the USB2000+, but the former instrument is manufactured with new techniques to improve thermal stability and reduce unit-to-unit variability. As may be expected, the Ocean Optics instruments have some advantages, such as a higher bit-depth (12-/16-bit for the USB2000/2000+ vs. 10-bit for the PiSpec) and, in this configuration, a greater spectral resolution (0.65 nm for the USB2000/2000+ vs. 1 nm for the PiSpec).

Contemporaneously acquired clear-sky spectra from both the PiSpec and USB2000 are displayed in **Figure 2**. Both spectra have been corrected for dark current by subtracting a dark spectrum, and the signals have been normalized to the peak at ≈330 nm to facilitate comparison. Prior to normalization, the 330 nm signals were 2147 and 487 for the USB2000 and PiSpec, respectively; for the 12- and 10-bit A/D converters, this corresponds to saturation of 52 and 48%, respectively. Shutter speeds of approximately 1.5 and 6 s were used in this case, for the USB2000 and PiSpec respectively, highlighting the greater sensitivity of the USB2000 device, as would be expected.

In general, the spectra show similar features, although the peaks and troughs of the USB2000 spectrum are more pronounced than the PiSpec's. This is in accordance with the

TABLE 1 | A comparison of the PiSpec with the USB2000 and USB2000+ (Ocean Optics).

	PiSpec	USB2000	USB2000+
Dimensions [mm]	80 × 75 × 57	89 × 63 × 34	89 × 63 × 34
Interface	CSI port (e.g., Raspberry Pi)	USB 2.0 RS-232	USB 2.0 RS-232
Sensor	Omnivision OV5647	Sony ILX511A	Sony ILX511A
Sensor Architecture	CMOS	CCD	CCD
Senor dimensions [pixels]	2592 × 1944	2048 × 1	2048 × 1
Bit depth	10	12	16
Spectral Resolution [nm]^1	≈1.0	0.65	0.65
Spectral Range [nm]^1	≈280–340	≈250–400	≈250–400
Stray light/320 nm signal	0.034–0.13	0.031–0.12	0.050–0.069

Note the Ocean Optics spectrometers can be configured in a number of ways. This comparison presents a configuration which may be optimal for DOAS retrievals of SO_2.

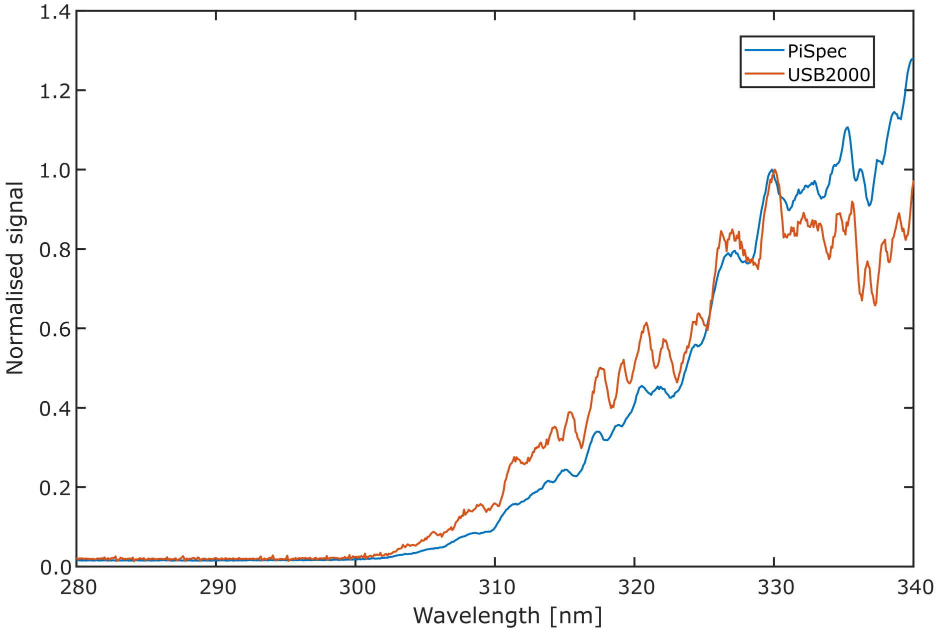

FIGURE 2 | Clear sky spectra gathered by the PiSpec and USB2000. Both spectra have been dar-subtracted and then normalized to the peak at ≈330 nm. This peak was at 48 and 52% saturation for the PiSpec and USB2000, respectively.

smaller instrument line shape (ILS) of the USB2000, which will more precisely preserve the high frequency oscillations in sky intensity. Below 330 nm, the signal in the PiSpec drops off somewhat faster than the USB2000. It is likely that this is due to the detector in the USB2000 being coated with a UV fluorescent coating, to enhance its UV sensitivity by absorbing UV radiation and emitting visible light which is sensed at the detector.

From these spectra, the stray light was quantified following the method of Kantzas et al. (2009), by taking the ratio of stray light signal at approximately 290 nm to signal at 320 nm. Here, the stray light was quantified as 0.033 and 0.034 for the USB2000 and the PiSpec, respectively. These remarkably similar values are also toward the lower end of the range of values found by Kantzas et al. (2009), who investigated three USB2000s, two USB2000+s, one USB4000 and one Avantes B.V. Avaspec-2048-USB2. Values ranged between 0.012 (Avaspec) and 0.12 (one USB2000). On a separate occasion, the PiSpec stray light was quantified as 0.13 (Wilkes et al., 2017), which remains comparable to the upper end of the aforementioned commercial spectrometers.

Of particular pertinence to this work, some comparison of the PiSpec and USB2000 was made by Wilkes et al. (2017), where DOAS retrievals of quartz-filled SO_2 cells were performed with both instruments. The analysis of sets of 10 spectra acquired by each instrument showed that both resulted in similar column density retrievals when measuring ≈300 and ≈1200 ppm · m gas cells: 304 ± 31 (±1 SD) and 1257 ± 58 ppm · m for the PiSpec; 296 ± 12 and 1184 ± 30 ppm · m for the USB2000. Shutter speeds of 6 and 1.5 s were used for the PiSpec and USB2000, respectively. Whilst the performance of the USB2000 was somewhat more consistent for each cell (smaller standard deviation), the PiSpec's performance was still quite reasonable considering its lower price. From these tests, the maximum cell uncertainty for the PiSpec was ≈10%, for the cell with the lower of the two SO_2 column densities. This value will be combined with the plume speed uncertainty to give a rough estimate of overall uncertainty in emission rate measurements presented in Section "Traverse and Scanning DOAS."

Thermal Stability

Here, we discuss thermally induced changes in ILS and spectral calibration using the 313.150 nm emission line from the Hg-Ar lamp, in order to investigate the system robustness to variations in ambient conditions during field operations. This peak is located within typical fit windows for SO_2 DOAS retrievals, which are generally somewhere in the 300–325 nm range. Our results suggest that the spectrometer calibration has a generally linear dependence on temperature across the considered range (**Figure 3**); however, a few notable deviations from this trend are also apparent. Firstly, there appears to be no change in peak location between 20 and 25°C. This may partly be a result of the pixel discretization of a continuous spectrum. There is, however, some change in line shape, in keeping with the general trend (see **Figure 4**). The second effect is apparent at the highest temperature measurements, ≈50°C. Here, there is a large shift in the peak, which jumps ≈1 nm from the 45°C spectrum. This notable displacement may be caused by a significant mechanical movement in one of the PiSpec's components, for example, the detector, via some release mechanism activated above a particular threshold. The similarity in line shape between the 45 and 50°C would corroborate this argument (**Figure 4**). The detector and associated Pi Camera board is currently mounted to the spectrometer with nuts and bolts which may allow movement, especially under changing thermal conditions. Securing this part more stringently, with glue for instance, may prevent such issues,

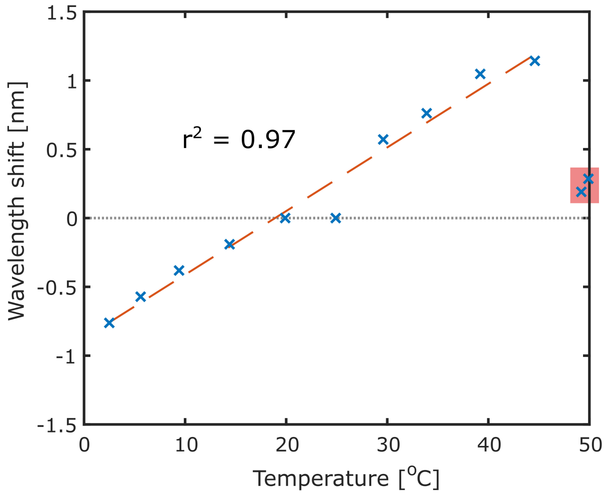

FIGURE 3 | Thermal stability of the spectrometer displayed as wavelength change of the 313.155 nm mercury emission line with temperature. Shifts are shown relative to the peak location at 25°C. A linear regression model indicates a wavelength shift dependence of 0.046 nm/°C, with a good model fit of r^2 = 0.97. The two high-temperature points, boxed in red, do not follow the linear trend, and may be caused by a larger scale shift in one of the optical components in the PiSpec. These data are not included in the regression analysis, since they are clearly associated with a different mechanism. Nevertheless, they should not be ignored, and suggest that at high temperatures > 45°C the PiSpec may begin to become unstable. In general, such high temperatures should be easily avoidable by keeping the instrument out of direct sunlight.

and it ought to be emphasized that the current hardware is very much a first version of this instrument. As we believe this issue to be independent of the general thermal stability characteristics of the spectrometer, we omit these data points from the regression analysis; we then also propose that above 45°C the PiSpec alignment may become unstable.

The linear dependence, omitting the high temperature data as discussed above, indicates that the PiSpec displays wavelength shifts of ≈0.046 nm/°C (≈0.5 pixel/°C) between ≈2.5–45°C; the coefficient of determination, r^2 = 0.97, indicates that this linear model fits the wavelength shifts well across this temperature range. This thermal stability is in extremely good agreement with shifts quoted by Platt and Stutz (2008) of 0.05 nm/°C for commercial spectrometers, indicating that in this sense there is no trade off in using this lower cost unit for these spectral measurements. In terms of pixel shifts, Platt and Stutz (2008) quote a typical value of 0.1 pixel/°C, which is lower than the 0.5 pixel/°C for the PiSpec. This should not impact the PiSpec's performance, since the shift can be corrected for using software.

Thermal instabilities of spectrometers can also lead to a stretch or squeeze of spectra which goes beyond a simple linear shift of all wavelengths across the sensor (McGonigle, 2007; Platt and Stutz, 2008). To investigate this effect, widely separated emission lines (296.728 and 334.148 nm) were tracked through the spectra captured across the studied temperature range, and their separation in numbers of pixels were recorded. For all temperatures below 40°C these two peaks were separated by exactly 393 pixels, indicating that the peaks shifted simultaneously in the same direction. For the three spectra above 40°C the pixel separation moved to 392 pixels. Since each pixel in the PiSpec represents a 0.095 nm band, this squeeze in spectra remains relatively insignificant even at the quite extreme temperatures.

There is, however, a change in the ILS of the unit across this temperature range (see **Figure 4**). In particular, at cooler temperatures the PiSpec's ILS is notably wider, with the spectral resolution, defined as the full-width-at-half-maximum of an

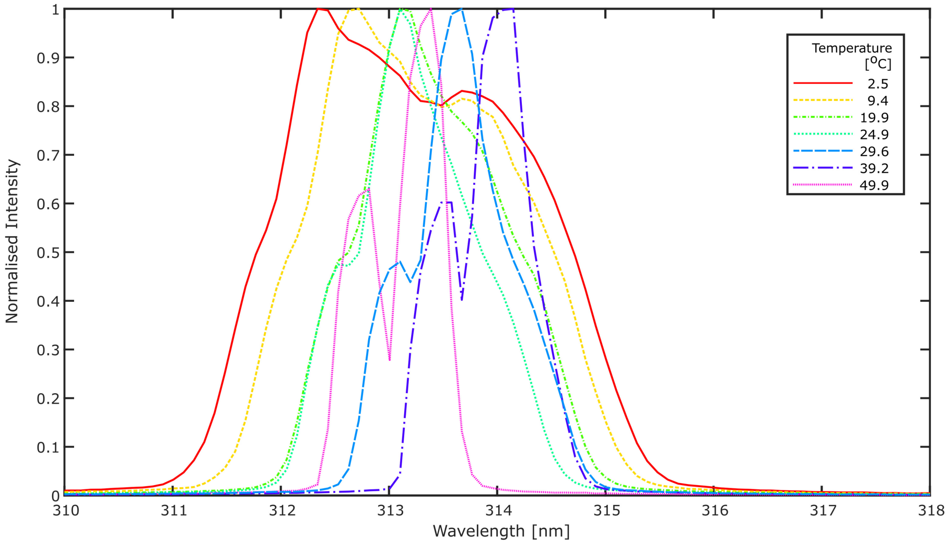

FIGURE 4 | Normalized instrument line shapes for a number of temperatures displayed in **Figure 3**. At low temperatures the line shape becomes quite broad, possibly preventing DOAS retrievals from being performed. Toward higher temperatures a double peak begins to form.

emission line, increasing markedly. At 2.5°C this increases to 2.9 nm, which would likely be too broad to enable conventional SO_2 DOAS measurements. At 25°C the spectral resolution measured here is ≈1.1 nm. An instrument with a broader ILS (lower spectral resolution) can have a lower sensitivity to SO_2, especially when the ILS approaches the line width of the SO_2 absorption structures, where response can also become non-linear (Frankenberg et al., 2005; Platt and Stutz, 2008). This is likely to be the case beyond a spectral resolution of ≈1 nm, therefore, a changing line shape induced by thermal instability could affect the PiSpec's retrievals of SO_2. Linearity/non-linearity is discussed in more detail in Section "Detection Limit and Linearity."

Kantzas et al. (2009) show that the spectral resolution of commercial units (USB2000, Ocean Optics) is also impacted by changing ambient temperatures; however, the temperature range considered therein was not as extreme as that presented here. Another point made by Kantzas et al. (2009), is that the line widths and thermal responses vary between spectrometers, even for the same model, and we note that the same should be expected of the PiSpec; to date, only one PiSpec instrument has been built and tested.

As discussed by Platt and Stutz (2008), thermostating a spectrometer is the best means of preventing thermal instabilities from affecting DOAS retrievals. As with commercial spectrometers, here we highlight that the PiSpec would similarly benefit from such measures. Nevertheless, DOAS measurements with commercial instruments are frequently made without such controls in place, and our tests described later (see Traverse and Scanning DOAS) show that the PiSpec does appear to work adequately, at least within the range of conditions encountered in this study, without thermal stabilization. To some extent post processing of spectra, by wavelength shifting and squeezing/stretching the differential optical density array such that it better fits the SO_2 reference spectrum, can account for calibration error caused by thermal instability, as can measurements of gas cells containing known column amounts of SO_2, and/or regular calibration with mercury lamps under the conditions encountered in the field. However, the change in ILS is more difficult to correct for, unless the change is well characterized. Inspecting the changes in ILS in **Figure 4**, we may, therefore, suggest that the PiSpec could function acceptably within ≈ ± 5°C of its calibration temperature; although this will still result in some error in retrieved column densities, as discussed earlier. Meroni et al. (2010) present a method for calibrating spectrometers using Fraunhofer lines and atmospheric absorption features, therefore providing a possible means of recalibration without the need for a calibration lamp in the field. In general, whilst short term deployments, such as the scans and traverses presented herein, are unlikely to be significantly affected by changing temperatures, permanent DOAS installations for automated monitoring can be subject to considerable changes in temperatures both on daily and seasonal timescales. As such, permanent installations with the PiSpec, as with commercial spectrometers, should consider measures to prevent or compensate for thermal instabilities in the instrumentation.

TABLE 2 | A summary of scan and traverse emission rates measured with the PiSpec.

Start Time (UTC)	End Time	Retrieval Mode	Plume Speed (m/s)	Emission Rate (kg/s)
19:22:25	19:32:27	Scan	3.9 ± 0.8	3.2 ± 0.7
19:33:50	19:41:05	Scan	3.9 ± 0.8	4.0 ± 0.9
19:43:08	19:51:01	Scan	3.9 ± 0.8	4.6 ± 1.0
19:51:59	20:01:31	Scan	3.9 ± 0.8	3.6 ± 0.8
20:02:30	20:07:37	Scan	3.9 ± 0.8	5.6 ± 1.3
21:04:22	21:15:42	Scan	3.9 ± 0.8	7.3 ± 1.7
21:16:37	21:25:47	Scan	3.9 ± 0.8	7.1 ± 1.6
16:42:26	16:54:37	Traverse	5.3 ± 0.7	45.6 ± 7.6
17:02:39	17:12:18	Traverse	5.3 ± 0.7	17.8 ± 2.9
17:28:11	17:35:27	Traverse	5.3 ± 0.7	20.5 ± 3.4
17:46:01	17:54:33	Traverse	5.3 ± 0.7	16.3 ± 2.7
17:55:10	18:03:27	Traverse	5.3 ± 0.7	27.2 ± 4.5
18:08:21	18:17:39	Traverse	5.3 ± 0.7	11.3 ± 1.9

Traverse and Scanning DOAS

Seven spectrometer scans (**Table 2**) were performed on the Santiago crater rim. A typical scan and example DOAS retrieval are displayed in **Figure 5**. The estimated plume rise speed of 3.9 ± 0.8 m s^{-1}, obtained through cross-correlation, resulted in emission rates of between 3.2 ± 0.7 and 7.3 ± 1.7 kg s^{-1}, with a mean of 5.1 kg s^{-1}. Within these scans, column densities of up to ≈2000 ppm · m SO_2 were measured. SO_2 emission rates from six road traverses ranged between 11.3 ± 1.9 and 45.6 ± 7.6 kg s^{-1} (**Figure 1** shows two typical traverses); the mean traverse rate was 23.1 kg s^{-1}. In this case, a plume speed of 5.3 ± 0.7 m s^{-1} was estimated, again from video imagery. Considering both the scan and traverse data, our mean recorded emission rate was 13.4 ± 12.3 kg s^{-1} (±1 standard deviation).

Other available data to compare our emission rates against come from Aiuppa et al. (2018) and Stix et al. (2018). The former data are derived from the NOVAC network scanning spectrometers in the period 19/07/2016–01/03/2017, and range widely from ≈0–50 kg s^{-1}; however, most emission rates are below 25 kg s^{-1}. The mean emission rate is 7.9 ± 3.5 kg s^{-1} (±1 standard deviation), with significant day to day variability in this period and no clear overall trend over this timescale. The work of Stix et al. (2018) implemented a drone-mounted DOAS system (DROAS) for traversing the Masaya plume between 04/05/2017 and 06/04/2017. Their measured fluxes ranged between 15 and 22 kg s^{-1}, with a mean of 18 kg s^{-1}. These measurements, which were made closer to the time of the work presented herein, are significantly higher than those of Aiuppa et al. (2018) on average, although they are comfortably within the extremes presented by the latter.

In general, our data are commensurate with the above fluxes from other authors, which were captured in the same activity period, in which Masaya's crater contained the lava lake. Notwithstanding the potential for changes in degassing between the three observation periods, the datasets do compare rather favorably, with all bar two of our fluxes falling within the range 0–25 kg s^{-1}, which encompassed the majority of the

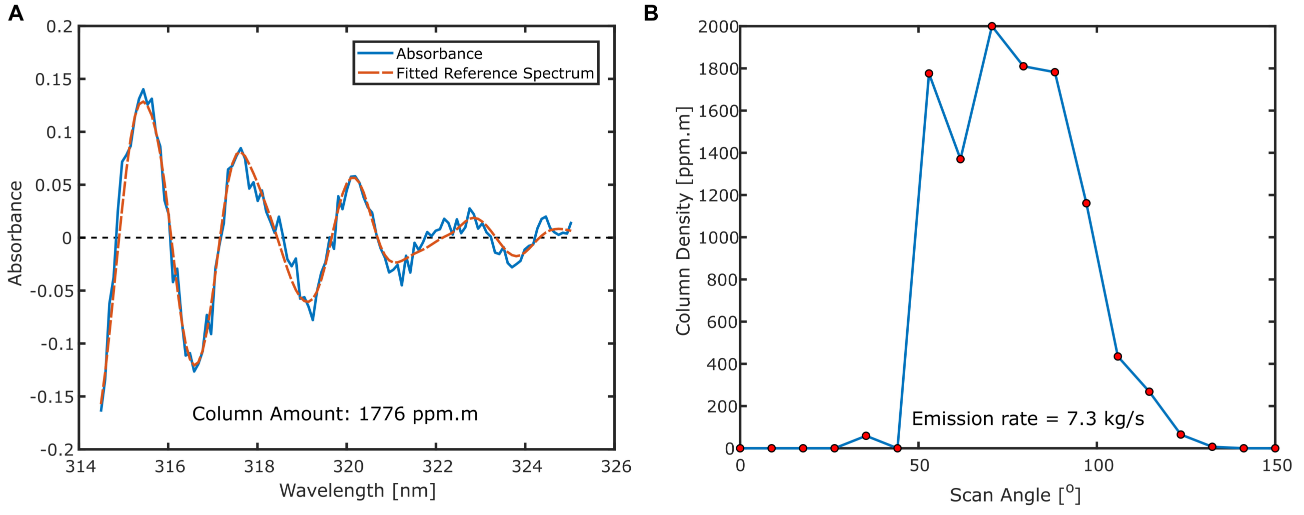

FIGURE 5 | (A) Example DOAS retrieval (fit window of 314.5–325 nm) from the scan presented in **(B)**. **(B)** A full PiSpec scan taken from the Santiago crater rim between 21:04 UTC and 21:15 UTC, on 14th June 2017. The resulting emission rate computed from the scan was 7.3 kg s^{-1}.

Aiuppa et al. (2018) fluxes; all emission rates herein fall below their quoted maximum flux of 50 kg s^{-1} in this interval. Our traverse values are also in quite good agreement with the traverses of Stix et al. (2018), with mean values of 23 and 18 kg s^{-1}, respectively.

Our scan data correspond to the quoted Aiuppa et al. (2018) fluxes rather better than the traverse data, with 4 of 7 scans falling within one standard deviation of their quoted mean; the further 3 are comfortably within 2 standard deviations. This might be expected given the comparison of scan to scan data, however, pushing this comparison further is perhaps tenuous in the sense that the scan orientations are rather different, e.g., the NOVAC scans are from a rather different vantage point; there is also the difference in the acquisition period. Our scan emission rates are rather lower than those from the traverse observations, which might be simply a manifestation of considerable and rapid (timescales of hours to days) variation in emission rate from the volcano, which is also apparent in the NOVAC fluxes reported in Aiuppa et al. (2018). The traverse data are more commensurate with the traverses of Stix et al. (2018), with both datasets containing notably larger average fluxes than the average of scans presented in Aiuppa et al. (2018). Recently, de Moor et al. (2017) also found that a scanning-DOAS system systematically retrieved lower SO_2 fluxes than traverses when studying emissions from Turrialba in Costa Rica. It is not clear whether this is simply coincidental or whether it is caused by fundamental differences in how the scan/traverse retrieval modes are performed and processed. In their Supplementary Information, de Moor et al. (2017) provide a good discussion of possible causes for discrepancies, such as ash on the optics or sub-optimal scanning position; for a permanent station the latter is of course impossible to always prevent since wind direction is changeable. Some systematic over-/under-estimation in our data may also come from the plume speed scalar, since all scan emission rates are derived from a single plume speed and, likewise, all traverse emission rates are derived from a separate single plume speed. Any error in this calculated speed will therefore be propagated through all emission rates of that retrieval mode.

In concordance with our earlier vindication of the capacity of the PiSpec to accurately constrain cell SO_2 column amounts, via comparison with a USB2000 spectrometer (Wilkes et al., 2017), we suggest that the comparisons with NOVAC and DROAS data demonstrate the capability of the PiSpec to accurately retrieve volcanic SO_2 emission rates. Following the substantial contribution to volcano monitoring and research made by the NOVAC project in recent years (e.g., Galle et al., 2010; Lübcke et al., 2014; Granieri et al., 2015; Hidalgo et al., 2015; Dingwell et al., 2016; Aiuppa et al., 2018), we suggest that the low-cost self-built PiSpec could augment efforts to assess and mitigate volcanic hazards globally, by enabling further dissemination of DOAS measurement systems on active volcanoes.

Due to the relatively modest UV sensitivity of the low-cost PiSpec sensor, as we highlighted in Wilkes et al. (2017), relatively long shutter speeds are required to provide the high SNR required for sensitive DOAS measurements. In the case of these scans and traverses, shutter speeds of up to 6 s were used when the unit was fitted with the 30 μm slit. This, coupled with apparently large overheads in the camera module's image capture, means that acquisition and transfer of each spectrum took ≈30–40 s. Whilst there is likely to be a software fix for this issue, at present this means that a scan takes some ≈10 min to complete. This current performance would preclude the PiSpec from being used for high time resolution (≈1 Hz) applications, such as that presented by McGonigle et al. (2009) for integration of SO_2 fluxes with other high time resolution geophysical data. Traverse temporal durations are unaffected by this issue, but it will act to reduce the spatial resolution in comparison with what could be achieved with a commercial spectrometer, for a given traverse speed.

One hardware solution to capturing spectra faster is to implement a larger 50 μm slit aperture, which allowed shutter speeds to be reduced from 4.5–6.0 s to 2.5–4.0 s, with a considerable reduction in acquisition rate (capturing every 15–20 s). This configuration was implemented in the final three traverses of the day. Both instrument setups measured similar emission rates, with no trend of over- or under-estimation for the larger aperture; this suggests that, at least in this context, the larger aperture configuration is a suitable solution to this issue. A further approach could be to co-add more rows of the sensor, e.g., essentially co-adding spectra, which could also result in significant increases in SNR, and hence the prospect to obtain higher acquisition rates by reducing shutter speeds (Wilkes et al., 2017). Such improvements to this system should be investigated further in the future.

Detection Limit and Linearity

Many volcanoes emit much smaller quantities of SO_2 than those measured here on Masaya volcano, whilst others can emit far more. It is therefore important that DOAS instruments are able to detect low column densities of SO_2 accurately, with a high SNR, and that the DOAS retrieval remains linear for higher column densities. Here we provide a quantitative assessment of the PiSpec's performance for detection of both low and high column densities of SO_2.

As with other spectrometers, the PiSpec's ability to resolve SO_2 will depend on the measurement conditions and acquisition settings. This is highlighted by **Figure 6**, which displays retrievals of relatively low column densities (86 and 112 ppm · m) from a PiSpec traverse (**Figure 6A**) and scan (**Figure 6B**) captured during the Masaya campaign. The scan retrieval shows much noisier absorbances, which is a result of lower signal during these measurements. The clear sky spectrum associated with this scan had a DN of just 50 at 311 nm, whilst the DN of the traverse clear spectrum was 326 at 311 nm. The latter will have a considerably larger SNR, which is preserved in the absorbance spectrum. Both spectra were acquired at the upper limit of the PiSpec's shutter speed range, i.e., with 6 s exposures; therefore, the lower signal in the scan could be caused by the time of day (≈3 pm local for the scan vs. ≈11 am for the traverse), different sky conditions between these acquisition periods, and/or different viewing orientations.

More exact determination of the instrument's detection limit was performed by analyzing the noise in an absorbance spectrum generated from two clear-sky images. Following Stutz and Platt (1996), an estimation of the detection limit can be made with:

$$\bar{D}_{\text{limit}} \approx \sigma \times \frac{6}{(n-1)^{1/2}} \tag{2}$$

where σ is the standard deviation of an absorbance spectrum generated from two spectra containing no absorbing species and n is the number of pixels in the spectrum. $\bar{D}_{\text{limit}}$ is the detection limit of the average optical density, which itself is defined by Stutz and Platt as three times the standard deviation of the reference spectrum; it provides a measure of the absorption strength of a given spectrum. It should be noted that the detection limit presented here is somewhat simplified; a much more complex procedure is discussed by Stutz and Platt (1996) and Platt and Stutz (2008), however, this simplified algorithm has been shown to provide a relatively accurate estimation (within 10–20% of the more complex method).

From clear sky spectra acquired in Masaya on the end of a traverse sequence, the absorbance noise σ was 3.10×10^{-3}. In a fitting window of 85 pixels, such as that used in the DOAS fits in **Figure 6**, this noise corresponds to a detection limit $\bar{D}_{\text{limit}}$ of 2.03×10^{-3}. In the presence of residual structures, from unknown gas species or the instrument itself, the detection limit must be scaled by a correction factor of 3–4 (Platt and Stutz, 2008).

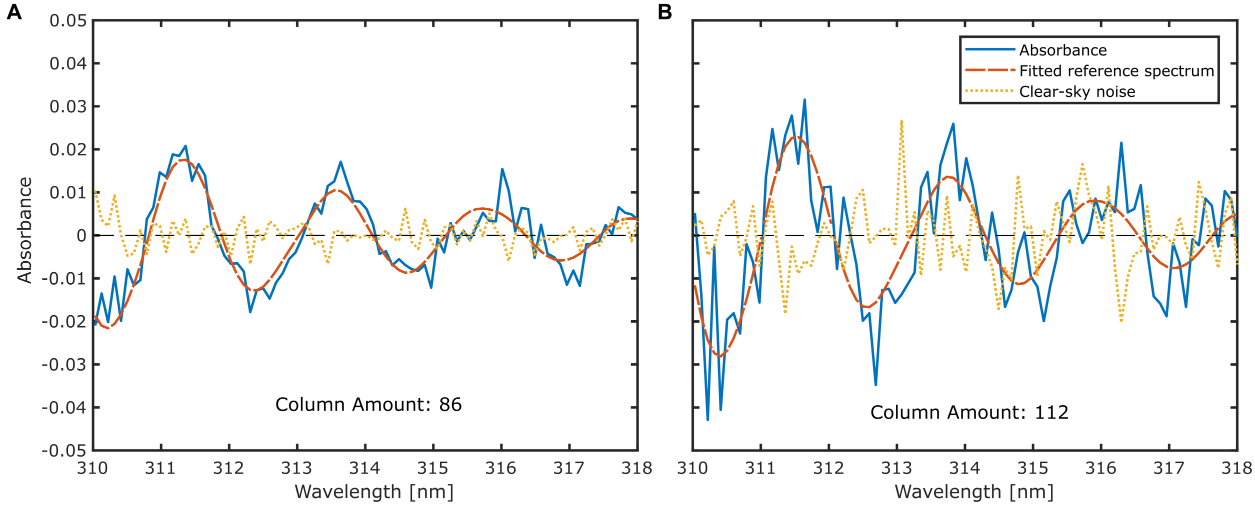

FIGURE 6 | Relatively low column density DOAS fits for **(A)** traverse and **(B)** scan modes on Masaya volcano. Also shown are noise spectra generated using a second clear-sky spectrum as $I(\lambda)$, as opposed to an in-plume spectrum (see Equation 1). Differences in noise levels results from different viewing geometries and conditions for the traverse and scan measurements.

Here, we conservatively use 4, therefore, the average optical density detection limit is 8.11×10^{-3}. The resulting column density detection limit is 26 ppm · m SO_2. Following the same methodology for the scan associated with **Figure 6B**, a detection limit of 50 ppm · m was estimated. As can be seen, these values are case-specific and it is not possible to generate a single detection limit for the PiSpec instrument for all scenarios. Indeed, $\bar{D}_{\text{limit}}$ will depend on field conditions, PiSpec acquisition settings and the DOAS fitting procedure. Nevertheless, the conservative detection limits presented here are quite reasonable.

The detection limits are an order of magnitude larger than the 2.5 ppm · m quoted by Galle et al. (2003) for a mini-DOAS instrument; however, it is not clear how they have defined the limit in their work. The limits discussed for the PiSpec are quite conservative, since they include a factor of four increase in $\bar{D}_{\text{limit}}$ associated with the potential presence of residual structures in the spectra, following Platt and Stutz (2008). Omitting this factor, the detection limit for the traverse discussed above would be 6.5 ppm · m, which is quite similar to the mini-DOAS. We suggest, however, that the more conservative estimate, 26 ppm · m in this case, is likely to be more realistic. This general picture of the PiSpec providing a somewhat reduced performance in terms of resolving gas column densities is also borne out in the prior work of Wilkes et al. (2017), which is discussed in Section 3.1. Therein a series of 10 measurements of gas cells were made, with both a USB2000 and PiSpec unit, and the standard deviations of the retrieved column densities were assessed. In this case, the variability in gas column densities from the USB2000 was typically a factor of two below that of the PiSpec. This was for instrument integration times of 1.5 and 6 s for the USB2000 and PiSpec, respectively, which provided very similar levels of detector saturation at 330 nm (52 and 48%, respectively).

Conversely, at large column densities DOAS retrievals can become non-linear due to the spectral resolution of the spectrometer not perfectly resolving high frequency variations in the SO_2 absorption cross-section, and due to the fact that the natural logarithm and convolution with the ILS are not commutative operations (Frankenberg et al., 2005; Wenig et al., 2005; Bobrowski et al., 2010). Linearity of PiSpec DOAS retrievals was assessed by modeling the instrument response following Wagner et al. (2003) and Kern et al. (2017). First a column density of SO_2 was assumed. This was used to generate an absorption spectrum through the Beer-Lambert law and use of a high resolution absorption cross-section from Vandaele et al. (2009). This absorption spectrum was convolved with the PiSpec ILS and the natural logarithm taken; the resultant spectrum was then down-sampled to the pixel resolution of the PiSpec. Finally, a typical DOAS fit procedure was applied to this spectrum, using the ILS-convolved high resolution absorption cross-section spectrum.

The results of this model are displayed in **Figure 7**, run for column densities of 0–10000 ppm · m, in 1000 ppm · m increments, and for a fit window of 314–324 nm. Up to 4000 ppm · m the fit is extremely linear, producing a retrieval of 3957 ppm · m for a true SO_2 column density of 4000 ppm · m. This indicates that for the majority of volcanic applications the PiSpec will perform linearly. In particular, all PiSpec measurements made on Masaya were comfortably within this extremely linear response interval. Since non-linearity becomes more pronounced at higher optical densities, shifting to longer wavelengths, where SO_2 is less strongly absorbing, is one method which could account for this saturation effect where necessary (Bobrowski et al., 2010); alternatively, the modeled response can be used to correct retrievals (Wagner et al., 2003; Kern et al., 2017).

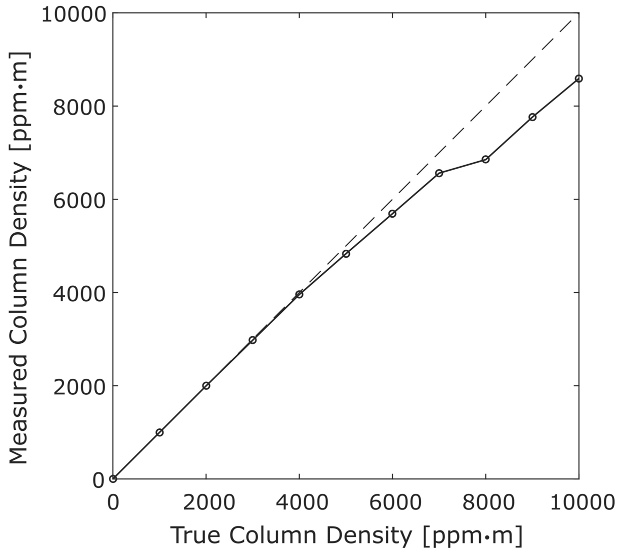

FIGURE 7 | Modeled PiSpec response to SO_2 in the fit window 314–324 nm. The response shows the saturation effect, whereby larger optical depths become non-linearly related to column densities, becomes significant above ≈4000 ppm · m. This model can be used to correct for retrieved column densities, or the DOAS fit window can be shifted to longer wavelengths to minimize the effect.

CONCLUSION

We have presented the first deployment of a custom-built spectrometer (PiSpec) for the retrieval of volcanic SO_2 emission rates. Both scanning and driving traverse DOAS modes were performed on Masaya volcano in June 2017, with both sets of results lying within the bounds of rates measured by NOVAC spectrometers in early 2017 (Aiuppa et al., 2018) and DROAS traverses in May 2017 (Stix et al., 2018). Furthermore, we show that the thermal stability of the PiSpec is similar to commercial units quoted by Platt and Stutz (2008), with a wavelength shift of ≈0.046 nm/°C within the range 2.5–45°C. The PiSpec's line shape is seen to change markedly across this temperature range, as would be expected. Whilst detection limits depend on a number of external (e.g., weather) as well as internal instrumental factors, typically the PiSpec's detection limit was found to be less than ≈50 ppm · m during its deployment on Masaya; in some idealistic scenarios, a limit of less than 10 ppm · m may be possible. These results demonstrate the utility of the PiSpec to deliver broadly comparable performance to commercial DOAS systems in terms of volcanic plume observations. This is significant given the low cost of the PiSpec and the potential for further cost reduction, with mass production, in that this unit could be particularly useful in resource-poor settings to provide valuable data for monitoring and fundamental science applications. We therefore suggest that dissemination of these instruments should be a principal forthcoming objective. Future work on this instrument should also focus on assessing its long-term performance in the field, as well as improvements to the mounting of components in the PiSpec, which may improve the instrument's thermal stability.

AUTHOR CONTRIBUTIONS

TW primarily wrote the manuscript and performed the analyses. AM co-wrote the manuscript. TW, TP, and RE performed the field work. TW, AM, and JW designed the PiSpec instrument. RB co-supervised the project. AS assisted in thermal stability tests. AP and FM assisted in preparation of this manuscript.

FUNDING

TW was supported by a scholarship from the Department of Geography, University of Sheffield. TP and RE were supported by a University of Sheffield GLOSS studentship. JW acknowledges the support of an Engineering and Physical Sciences Research Council grant (EP/M009106/1).

ACKNOWLEDGMENTS

We would like to thank reviewers RK and MDM, and editor JS, for their detailed comments on the initial manuscript, which we feel have greatly improved the quality of the article. We would like to thank Ulrich Platt for a number of useful discussions pertinent to this work. We would also like to thank the Laboratory Staff in the Department of Geography, University of Sheffield, for their continued support of our research needs. We acknowledge the use of the Generic Mapping Tool (Wessel et al., 2013) for drawing **Figure 1**.

SUPPLEMENTARY MATERIAL

The Supplementary Material for this article can be found online at: https://www.frontiersin.org/articles/10.3389/feart.2019.00065/full#supplementary-material

DATA SHEET S1 | Data for the 7 figures included in the manuscript.

REFERENCES

Aiuppa, A., de Moor, J. M., Arellano, S., Coppola, D., Francofonte, V., Galle, B., et al. (2018). Tracking formation of a lava lake from ground and space: masaya volcano (Nicaragua), 2014-2017. *Geochem. Geophys. Geosyst.* 19, 2014–2017. doi: 10.1002/2017GC007227

Arellano, S., Yalire, M., Galle, B., Bobrowski, N., Dingwell, A., Johansson, M., et al. (2017). Long-term monitoring of SO2quiescent degassing from Nyiragongo's lava lake. *J. Afr. Earth Sci.* 134, 866–873. doi: 10.1016/j.jafrearsci.2016.07.002

Bobrowski, N., Kern, C., Platt, U., Hörmann, C., and Wagner, T. (2010). Novel SO2 spectral evaluation scheme using the 360-390 nm wavelength range. *Atmos. Meas. Tech.* 3, 879–891. doi: 10.5194/amt-3-879-2010

Bobrowski, N., von Glasow, R., Aiuppa, A., Inguaggiato, S., Louban, I., Ibrahim, O. W., et al. (2007). Reactive halogen chemistry in volcanic plumes. *J. Geophys. Res. Atmos.* 112, 1–17. doi: 10.1029/2006JD007206

Carn, S. A., Fioletov, V. E., McLinden, C. A., Li, C., and Krotkov, N. A. (2017). A decade of global volcanic SO2 emissions measured from space. *Sci. Rep.* 7:44095. doi: 10.1038/srep44095

de Moor, J. M., Kern, C., Avard, G., Muller, C., Aiuppa, A., Saballos, A., et al. (2017). A new sulfur and carbon degassing inventory for the southern central american volcanic arc: the importance of accurate time-series data sets and possible tectonic processes responsible for temporal variations in arc-scale volatile emissions. *Geochem. Geophys. Geosyst.* 18, 4437–4468. doi: 10.1002/2017GC007141

Delmelle, P., Stix, J., Baxter, P., Garcia-Alvarez, J., and Barquero, J. (2002). Atmospheric dispersion, environmental effects and potential health hazard associated with the low-altitude gas plume of Masaya volcano, Nicaragua. *Bull. Volcanol.* 64, 423–434. doi: 10.1007/s00445-002-0221-6

Dingwell, A., Rutgersson, A., Claremar, B., Arellano, S., Yalire, M. M., and Galle, B. (2016). Seasonal and diurnal patterns in the dispersion of SO2 from Mt. Nyiragongo. *Atmos. Environ.* 132, 19–29. doi: 10.1016/j.atmosenv.2016.02.030

Frankenberg, C., Platt, U., and Wagner, T. (2005). Iterative maximum a posteriori (IMAP)-DOAS for retrieval of strongly absorbing trace gases: model studies for CH4 and CO2 retrieval from near infrared spectra of SCIAMACHY onboard ENVISAT. *Atmos. Chem. Phys.* 5, 9–22. doi: 10.5194/acpd-4-6067-2004

Galle, B., Johansson, M., Rivera, C., Zhang, Y., Kihlman, M., Kern, C., et al. (2010). Network for observation of volcanic and atmospheric change (NOVAC)—a global network for volcanic gas monitoring: network layout and instrument description. *J. Geophys. Res.* 115:D05304. doi: 10.1029/2009JD011823

Galle, B., Oppenheimer, C., Geyer, A., McGonigle, A. J. S., Edmonds, M., and Horrocks, L. A. (2003). A miniaturised ultraviolet spectrometer for remote sensing of SO2 fluxes: a new tool for volcano surveillance. *J. Volcanol. Geotherm. Res.* 119, 241–254. doi: 10.1016/S0377-0273(02)00356-6

Gordon, I. E., Rothman, L. S., Hill, C., Kochanov, R. V., Tan, Y., Bernath, P. F., et al. (2017). The HITRAN2016 molecular spectroscopic database. *J. Quant. Spectrosc. Radiat. Transf.* 203, 3–69. doi: 10.1016/j.jqsrt.2017.06.038

Granieri, D., Salerno, G. G., Liuzzo, M., La Spina, A., Giuffrida, G., Caltabiano, T., et al. (2015). Emission of gas and atmospheric dispersion of SO2 during the December 2013 eruption at san miguel volcano (El Salvador, Central America). *Geophys. Res. Lett.* 42, 5847–5854. doi: 10.1002/2015GL064660

Grutter, M., Basaldud, R., Rivera, C., Harig, R., Junkerman, W., Caetano, E., et al. (2008). SO 2 emissions from Popocatépetl volcano: emission rates and plume imaging using optical remote sensing techniques. *Atmos. Chem. Phys. Atmos. Chem. Phys.* 8, 6655–6663. doi: 10.5194/acp-8-6655-2008

Hidalgo, S., Battaglia, J., Arellano, S., Steele, A., Bernard, B., Bourquin, J., et al. (2015). SO2 degassing at Tungurahua volcano (Ecuador) between 2007 and 2013: transition from continuous to episodic activity. *J. Volcanol. Geotherm. Res.* 298, 1–14. doi: 10.1016/j.jvolgeores.2015.03.022

Hönninger, G., von Friedeburg, C., and Platt, U. (2004). Multi axis differential optical absorption spectroscopy (MAX-DOAS). *Atmos. Chem. Phys.* 4, 231–254. doi: 10.5194/acp-4-231-2004

Kantzas, E. P., McGonigle, A. J. S., and Bryant, R. G. (2009). Comparison of low cost miniature spectrometers for volcanic SO2 emission measurements. *Sensors* 9, 3256–3268. doi: 10.3390/s90503256

Kern, C., Masias, P., Apaza, F., Reath, K. A., and Platt, U. (2017). Remote measurement of high preeruptive water vapor emissions at Sabancaya volcano by passive differential optical absorption spectroscopy. *J. Geophys. Res. Solid Earth* 122, 3540–3564. doi: 10.1002/2017JB014020

Khokhar, M. F., Frankenberg, C., Van Roozendael, M., Beirle, S., Kühl, S., Richter, A., et al. (2005). Satellite observations of atmospheric SO2from volcanic eruptions during the time-period of 1996-2002. *Adv. Space Res.* 36, 879–887. doi: 10.1016/j.asr.2005.04.114

Klein, A., Lübcke, P., Bobrowski, N., Kuhn, J., and Platt, U. (2017). Plume propagation direction determination with SO2 cameras. *Atmos. Meas. Tech.* 10, 979–987. doi: 10.5194/amt-10-979-2017

Lübcke, P., Bobrowski, N., Arellano, S., Galle, B., Garzón, G., Vogel, L., et al. (2014). BrO/SO2 molar ratios from scanning DOAS measurements in the NOVAC network. *Solid Earth* 5, 409–424. doi: 10.5194/se-5-409-2014

McGonigle, A. J. S. (2007). Measurement of volcanic SO2 fluxes with differential optical absorption spectroscopy. *J. Volcanol. Geotherm. Res.* 162, 111–122. doi: 10.1016/j.jvolgeores.2007.02.001

McGonigle, A. J. S., Aiuppa, A., Ripepe, M., Kantzas, E. P., and Tamburello, G. (2009). Spectroscopic capture of 1 Hz volcanic SO2 fluxes and integration with volcano geophysical data. *Geophys. Res. Lett.* 36:L21309. doi: 10.1029/2009GL040494

McGonigle, A. J. S., Hilton, D. R., Fischer, T. P., and Oppenheimer, C. (2005). Plume velocity determination for volcanic SO 2 flux measurements. *Geophys. Res. Lett.* 32:L11302. doi: 10.1029/2005GL022470

McGonigle, A. J. S., Oppenheimer, C., Galle, B., Mather, T. A., and Pyle, D. M. (2002). Walking traverse and scanning DOAS measurements of volcanic gas emission rates. *Geophys. Res. Lett.* 29, 46-1–46-4. doi: 10.1029/2002GL015827

McGonigle, A. J. S., Oppenheimer, C., Tsanev, V. I., Saunders, S., Mulina, K., Tohui, S., et al. (2004). Sulphur dioxide fluxes from papua new guinea's volcanoes. *Geophys. Res. Lett.* 31, 1–4. doi: 10.1029/2004GL019568

Meroni, M., Busetto, L., Guanter, L., Cogliati, S., Crosta, G. F., Migliavacca, M., et al. (2010). Characterization of fine resolution field spectrometers using solar fraunhofer lines and atmospheric absorption features. *Appl. Opt.* 49, 2858–2871. doi: 10.1364/AO.49.002858

Mori, T., and Burton, M. R. (2006). The SO2 camera: a simple, fast and cheap method for ground-based imaging of SO 2 in volcanic plumes. *Geophys. Res. Lett.* 33:L24804. doi: 10.1029/2006GL027916

Mori, T., Mori, T., Kazahaya, K., Ohwada, M., Hirabayashi, J., and Yoshikawa, S. (2006). Effect of UV scattering on SO_2 emission rate measurements. *Geophys. Res. Lett.* 33, 3–7. doi: 10.1029/2006GL026285

Pering, T. D., Ilanko, T., Wilkes, T. C., England, R. A., Silcock, S. R., Stanger, L. R., et al. (2019). A rapidly convecting Lava Lake at Masaya Volcano, Nicaragua. *Front. Earth Sci.* 6:241. doi: 10.3389/feart.2018.00241

Platt, U., and Stutz, J. (2008). *Differential Optical Absorption Spectroscopy, Principles and Applications, Series: Physics of Earth and Space Environments*. Heidelberg: Springer, doi: 10.1007/978-3-540-75776-4

Rix, M., Valks, P., Hao, N., van Geffen, J., Clerbaux, C., Clarisse, L., et al. (2009). Satellite monitoring of volcanic sulfur dioxide emissions for early warning of volcanic hazards. *IEEE J. Sel. Top. Appl. Earth Obs. Remote Sens.* 2, 196–206. doi: 10.1109/JSTARS.2009.2031120

Salerno, G. G., Burton, M. R., Oppenheimer, C., Caltabiano, T., Tsanev, V. I., and Bruno, N. (2009). Novel retrieval of volcanic SO2 abundance from ultraviolet spectra. *J. Volcanol. Geotherm. Res.* 181, 141–153. doi: 10.1016/j.jvolgeores.2009.01.009

Shinohara, H., Aiuppa, A., Giudice, G., Gurrieri, S., and Liuzzo, M. (2008). Variation of H2O/CO2 and CO2/SO2 ratios of volcanic gases discharged by continuous degassing of mount etna volcano, Italy. *J. Geophys. Res. Solid Earth* 113, 1–11. doi: 10.1029/2007JB005185

Stephens, K. J., and Wauthier, C. (2018). Satellite geodesy captures offset magma supply associated with lava lake appearance at masaya volcano, nicaragua. *Geophys. Res. Lett.* 45, 2669–2678. doi: 10.1002/2017GL076769

Stix, J., De Moor, J. M., Rüdiger, J., Alan, A., Corrales, E., D'Arcy, F., et al. (2018). Using drones and miniaturized instrumentation to study degassing at turrialba and masaya volcanoes, central america. *J. Geophys. Res. Solid Earth* 123, 6501–6520. doi: 10.1029/2018JB015655

Stutz, J., and Platt, U. (1996). Numerical analysis and estimation of the statistical error of differential optical absorption spectroscopy measurements with least-squares methods. *Appl. Opt.* 35, 6041–6053. doi: 10.1364/AO.35.006041

Tamburello, G., McGonigle, A. J. S., Kantzas, E. P., and Aiuppa, A. (2011). Recent advances in ground-based ultraviolet remote sensing of volcanic SO2 fluxes. *Ann. Geophys.* 54, 199–208. doi: 10.4401/ag-5179

Theys, N., De Smedt, I., van Gent, J., Danckaert, T., Wang, T., Hendrick, F., et al. (2015). Sulfur dioxide vertical column DOAS retrievals from the ozone monitoring instrument: global observations and comparison to ground-based and satellite data. *J. Geophys. Res. Atmos.* 120, 2470–2491. doi: 10.1002/2014JD022417.Received

USGS (2018). *Advanced Spaceborned Thermal Emission and Reflection Radiometer 1 arc-Second. ASTER DEM is a Product of METI and NASA*. Available at: https://earthexplorer.usgs.gov/ (accessed May 20, 2018).

Vandaele, A. C., Hermans, C., and Fally, S. (2009). Fourier transform measurements of SO2 absorption cross sections: II. Temperature dependence in the 29 000-44 000 cm-1 (227-345 nm) region. *J. Quant. Spectrosc. Radiat. Transf.* 110, 2115–2126. doi: 10.1016/j.jqsrt.2009.05.006

Venzke, E. (ed.) (2017). *Bulletin of the Global Volcanism Network*. Available at: https://volcano.si.edu.

Vogel, L., Galle, B., Kern, C., Delgado Granados, H., Conde, V., Norman, P., et al. (2011). Early in-flight detection of SO2 via differential optical absorption spectroscopy: a feasible aviation safety measure to prevent potential encounters with volcanic plumes. *Atmos. Meas. Tech.* 4, 1785–1804. doi: 10.5194/amt-4-1785-2011

Vogel, L., Sihler, H., Lampel, J., Wagner, T., and Platt, U. (2013). Retrieval interval mapping: a tool to visualize the impact of the spectral retrieval range on differential optical absorption evaluations. *Atmos. Meas. Tech.* 6, 275–299. doi: 10.5194/amt-6-275-2013

Wagner, T., Heland, J., Zöger, M., and Platt, U. (2003). A fast H2O total column density product from GOME - validation with in-situ aircraft measurements. *Atmos. Chem. Phys.* 3, 651–663. doi: 10.5194/acp-3-651-2003

Wenig, M., Jähne, B., and Platt, U. (2005). Operator representation as a new differential optical absorption spectroscopy formalism. *Appl. Opt.* 44, 3246–3253. doi: 10.1364/AO.44.003246

Wessel, P., Smith, W. H. F., Scharroo, R., Luis, J., and Wobbe, F. (2013). Generic mapping tools: improved version released. *EOS* 94, 409–410. doi: 10.1002/2013EO450001

Wilkes, T. C., McGonigle, A. J. S., Pering, T. D., Taggart, A., White, B., Bryant, R., et al. (2016). Ultraviolet imaging with low cost smartphone sensors: development and application of a raspberry pi-based UV camera. *Sensors* 16:1649. doi: 10.3390/s16101649

Wilkes, T. C., McGonigle, A. J. S., Willmott, J. R., Pering, T. D., and Cook, J. M. (2017). Low-cost 3D printed 1 nm resolution smartphone sensor-based spectrometer: instrument design and application in ultraviolet spectroscopy. *Opt. Lett.* 42, 4323–4326. doi: 10.1364/OL.42.004323

Wilkes, T. C., Stanger, L., Willmott, J., Pering, T. D., McGonigle, A. J. S., and England, R. (2018). The development of a low-cost, near infrared, high-temperature thermal imaging system and its application to the retrieval of accurate lava lake temperatures at masaya volcano, nicaragua. *Remote Sens.* 10:450. doi: 10.3390/rs10030450

Young, S. R., Francis, P. W., Barclay, J., Casadevall, T. J., Gardner, C. A., Daroux, B., et al. (1998). Monitoring SO2 emission at the Soufrière Hills Volcano: implications for changes in eruptive conditions. *Geophys. Res. Lett.* 25, 3681–3684. doi: 10.1029/98GL01406

Conflict of Interest Statement: The authors declare that the research was conducted in the absence of any commercial or financial relationships that could be construed as a potential conflict of interest.

frontiers
in Earth Science

ORIGINAL RESEARCH
published: 07 June 2019
doi: 10.3389/feart.2019.00114

Variability in the Gas Composition of the Popocatépetl Volcanic Plume

Noémie Taquet[1]*, Wolfgang Stremme[1], Michel Grutter[1], Jorge Baylón[1], Alejandro Bezanilla[1], Benedetto Schiavo[1], Claudia Rivera[1,2], Robin Campion[3], Thomas Boulesteix[4], Amiel Nieto-Torres[5], Ramón Espinasa-Pereña[5], Thomas Blumenstock[6] and Frank Hase[6]

[1] Centro de Ciencias de la Atmósfera, Universidad Nacional Autónoma de México, Mexico City, Mexico, [2] Facultad de Química, Universidad Nacional Autónoma de México, Mexico City, Mexico, [3] Departamento de Vulcanologia, Instituto de Geofisica, Universidad Nacional Autónoma de México, Mexico City, Mexico, [4] Laboratorio Nacional de Geoquímica y Mineralogía, Universidad Nacional Autónoma de México, Mexico City, Mexico, [5] Centro Nacional de Prevención de Desastres, Mexico City, Mexico, [6] Institute of Meteorology and Climate Research, Karlsruhe Insitute of Technology, Karlsruhe, Germany

OPEN ACCESS

Edited by:
Nicole Bobrowski,
Universität Heidelberg, Germany

Reviewed by:
Giancarlo Tamburello,
National Institute of Geophysics and Volcanology (INGV), Italy
Michael Robert Carroll,
University of Camerino, Italy

***Correspondence:**
Noémie Taquet
noemi.taquet@gmail.com

Specialty section:
This article was submitted to Volcanology, a section of the journal Frontiers in Earth Science

Received: *06 October 2018*
Accepted: *30 April 2019*
Published: *07 June 2019*

Citation:
Taquet N, Stremme W, Grutter M, Baylón J, Bezanilla A, Schiavo B, Rivera C, Campion R, Boulesteix T, Nieto-Torres A, Espinasa-Pereña R, Blumenstock T and Hase F (2019) Variability in the Gas Composition of the Popocatépetl Volcanic Plume. Front. Earth Sci. 7:114. doi: 10.3389/feart.2019.00114

Long-term time series of volcanic plumes composition constitute valuable indicators of the evolution of the magmatic and volcanic systems. We present here a 4-years long time series of molecular ratios of HF/HCl, HCl/SO_2, SiF_4/SO_2, HF/SiF_4 measured in the Popocatépetl's volcanic plume using ground-based solar absorption FTIR spectroscopy. The instrument, based in the Altzomoni NDACC (Network for the Detection of Atmospheric Composition Change) station, facing the Popocatépetl volcano, provides an unrivaled precision. The computed mean and standard deviation of the HF/HCl and HCl/SO_2 ratios for this period were found to be 0.24 ± 0.03 and 0.11 ± 0.03, respectively. SiF_4 was detected in three occasions and the SiF_4/SO_2 ratios ranged between $(1.9 \pm 0.5) \times 10^{-3}$ and $(9.9 \pm 0.4) \times 10^{-3}$. The HBr/HCl and HBr/$SO_2$ ratios remained below their detection limits (1.25×10^{-4} and 1.25×10^{-5}, respectively), given that a part of the HBr has already been converted to other bromine species (e.g., BrO, Br_2) a few kilometers downwind of the crater. Combining our time series with satellite SO_2 fluxes and seismic data, we explain the significant long-term HCl/SO_2 variations by changes in the conduit and edifice permeabilities, impacting the deep and shallow degassing processes. The high temporal resolution of the data also allows capturing the variation of the volcanic plume composition preceding and induced by a common moderate explosion at Popocatépetl volcano. We interpret the observed variations of the HCl/SO_2 ratio during the explosion in terms of changes in the contribution of the deep/shallow degassing. We additionally report the detection of an increase of SiF_4 after the explosion, likely explained by in-plume HF-ash interaction. During this event, SiF_4/HCl vs. HF/HCl was found to have a linear relation with a slope of −1/4, which implies a conservation of fluorine.

Keywords: SO_2, HCl, SiF_4, solar absorption, FTIR spectroscopy, volcanic gas, Popocatépetl

1. INTRODUCTION

Changes in the eruptive dynamics (passive degassing, dome extrusion, or destruction) of dome-capped volcanic systems are mainly controlled by the gas content in the magma, directly affecting its viscosity and ascending speed (Martel and Schmidt, 2003; Boudon et al., 2015; Manga et al., 2018). Magma mixing in the storage reservoir (Witter et al., 2005), assimilation of the volcanic edifice basement (Goff et al., 2001), gas redox reactions and gas-rock interactions (Love et al., 1998; Mori et al., 2002; Stremme et al., 2011; Battaglia et al., 2019), conduit permeability changes (Edmonds et al., 2001; Taquet et al., 2017; Campion et al., 2018), or hydrothermal activity and gas interactions in the volcanic gas plume (Bagnato et al., 2013) are important processes contributing to changes in the gas composition from the deep to the shallow system. The identification and estimation of the contribution of each of these individual processes require an ample database from long-term gas measurements. Ground-based FTIR spectroscopy allows long-term monitoring of the volcanic plumes composition (SO_2, HCl, HF, SiF_4) during both quiescent and eruptive periods and with sufficient temporal resolution to relate the composition change with both intrusive and eruptive processes.

The contrast in solubilities between the gas species (e.g., CO_2, SO_2, and halogens) and their variations during magma ascent are widely used to decipher the effusive-explosive transitions in eruptive processes (Aiuppa et al., 2009; Lee et al., 2018). Prior studies, some of which are also based on FTIR spectroscopic measurements, have already reported long-term but discontinuous time series of the halogen and sulfur contents in volcanic plumes. The long-term variability of the HCl/SO_2 ratio was previously related to both the deep and shallow disturbances of the volcanic activity, such as changes in the hydrothermal contribution (Hirabayashi et al., 1982; Mori and Notsu, 2008; Shinohara et al., 2015) or changes in the composition of the magmatic source (Oppenheimer et al., 2002). The short-term variations were rather explained by variations in the permeability of the magma column (Oppenheimer et al., 2002), lava domes growth or change in the lava extrusion rate (Edmonds et al., 2001). Trace gases such as SiF_4 in volcanic plumes were also studied (Francis et al., 1996; Love et al., 1998; Mori et al., 2002; Stremme et al., 2012; Taquet et al., 2017) for the understanding of the lava dome destruction episodes.

Considering the volcanic/magmatic factors likely to influence the plume composition, an open question is the extent to which variations in gas composition reflect the changes in the intrusive/extrusive contributions. Andesitic volcanoes with lava domes often behave cyclically, alternating magmatic episodes of extrusion and potentially hazardous episodes of dome destruction by volcanic explosions. Popocatépetl volcano has been one of the strongest permanent emitters of volcanic gases over its now 23-year long ongoing eruptive activity, and represents a potential risk for the 25 M inhabitants in its immediate neighborhood. As for most of the andesitic volcanoes, its regularly strong explosive activity impedes frequent direct observations and proximal gas composition measurements. The gas plume thus constitutes one of the only magmatic information purveyors.

In this contribution, we present a 4-years long time series of the HCl/SO_2, HF/HCl, and SiF_4/SO_2 ratios obtained from a high spectral resolution (HR) FTIR spectrometer, which forms part of the Network for the Detection of Atmospheric Composition Change (NDACC)[1], facing the Popocatépetl volcano. The variability of these time series is interpreted in the light of the SO_2 OMI-derived fluxes and of the volcanic activity described by both seismic records and visual observations.

2. BACKGROUND

The Popocatépetl volcano is an andesitic-dacitic stratovolcano (5,426 m a.s.l.) of the trans-Mexican volcanic belt, located 70 km SE of Mexico City (21 M inhabitants) and 43 km west of Puebla (3.2 M inhabitants). Although some historical plinian eruptions occurred in its past (the latest between 675 and 1095 A.D.; Siebe et al., 1996), its activity in the last century essentially consisted in the alternation of effusive and explosive phases with the extrusion of andesitic to dacitic lava domes until their destructions through series of vulcanian explosions (Gómez-Vazquez et al., 2016). The most recent historical eruptive phase before the current one started in 1919 and ended in 1927 (Gómez-Vazquez et al., 2016). The current eruptive phase started at the end of 1993, after 70 years of quiescence, with manifestations of phreatic activity related to the crater lake, which disappeared on December 1994 with the first important explosion. The first intra-crater lava dome was observed during March 1996, and since then at least 38 succeeded each other in the summit crater. Their growth is spasmodic, and occurs during very short extrusive episodes several hours to several days long, generally accompanied by low frequency harmonic tremor (Arambula et al., 2016) and explosive events. During an activity cycle, the lava dome endures multiple phases of successive inflation, degassing, deflation, and compaction, occasionally punctuated by its partial destruction. These processes lead to a progressive weakening of the dome structure, until the final destructive phase (days to weeks in duration), generally evidenced by series of consecutive moderate explosions. The Popocatépetl lava domes can reach highly variable volumes, estimated from 10^5 to 7×10^6 m^3 (Gómez-Vazquez et al., 2016), the most recent being smaller than those observed 20 years ago. Knowledge on the dome cycles of the current eruption only stems from seismic monitoring and the aerial photographs taken during rare overflights of the crater (Gómez-Vazquez et al., 2016), with the support of distant visible and infrared cameras. Only a few *in-situ* measurements were performed since the appearance of the first lava dome in 1996 (Goff et al., 1998, 2001), the composition measurements are thus principally based on remote sensing techniques.

The typical eruptive gas columns or passive degassing at Popocatépetl volcano are characterized by the presence of H_2O, CO_2, SO_2, HCl, HF, and SiF_4, the abundance of which was only sparsely measured since the volcanic reawakening in 1996 (**Table 3**). The most recent SO_2 fluxes estimations range from

---

[1] https://www2.acom.ucar.edu/irwg

3,000 to 5,000 ton/day for quiescent periods, and are higher than 25,000 ton/day for eruptive events (Delgado-Granados et al., 2001; Grutter et al., 2008; Campion et al., 2018) and show that the Popocatépetl′s conduit system is essentially permeable (Campion et al., 2018). Ultimately, the variability of the SiF_4/SO_2 ratio was explored on the basis of high temporal resolution measurements (Taquet et al., 2017) to reveal the causes of transient permeability changes, highlighting the role of lava dome destruction episodes and short-term sudden drops in SO_2 fluxes preceding explosions (Campion et al., 2018).

These studies essentially provided snap shots of the composition of the Popocatépetl volcanic plume, but did not allow studying its variability over prolonged eruptive or passive degassing periods.

3. MEASUREMENTS AND METHODS

3.1. The Altzomoni Atmospheric Observatory

The measurements were performed between 2012 and 2016 from the Altzomoni Atmospheric Observatory (3,985 m a.s.l) (**Figure 1**), 12 km north of the Popocatépetl′s crater. The site location has been chosen to comply with a number of spectroscopic and safety requirements, such as an open view to the volcano, a high altitude to minimize the water vapor and the anthropogenic contamination, a safe distance from the crater and the abundant ash-falls, the availability of power supply, communication and a convenient access (Stremme et al., 2011; Schiavo et al., 2019). In March 2012, a container equipped with a high resolution FTIR spectrometer coupled with a solar tracker was installed in the observatory. The instrument, the measurements and the retrieval products comply with the NDACC quality requirements, and provide high precision total columns and profiles of a wide range of atmospheric gases (Baylon et al., 2017). The site became an official NDACC station in 2015. Since October 2012, remote solar absorption measurements are performed every time the meteorologic and geometric conditions required for measurements are fulfilled. Solar occultation measurements of the Popocatépetl′s plume can be performed on days with clear sky conditions and only during favorable wind conditions, which are typically fulfilled after the sunrise when the wind is toward the NE direction, so that the volcanic plume and the instrument are aligned with the sun (**Figure 1D**). More than one hundred measurement days out of the 591 recorded show a clear signal of the volcanic plume. Typically, the part of the volcanic plume measured by the instrument has traveled 10–20 km downwind from the crater and was recorded from a few minutes up to 1 h after being exhaled.

3.2. Instrumentation

The Bruker HR120/5 FTIR spectrometer (**Figure 1B**) is capable of measuring with a maximal optical path difference (OPDmax) and resolution (res) of 257 cm and 0.0035 cm^{-1}, respectively (res = 0.9/OPDmax). The spectrometer operates with either KBr or CaF_2 beam splitters, 3 different detectors (MCT, InSb, and InGaAs) and a set of 7 optical filters installed in a rotating wheel. The instrument is equipped with a precise solar tracker (Camtracker; Gisi et al., 2012) based on a commercial telescope mount as can be seen in **Figure 1A**. The system is equipped with an automated solar-tracker cover and liquid-nitrogen filling systems, which, together with a microwave communication system (50 km line of sight to the university campus), allows a fully-remote control of the instrument.

In general, the measurement sequence includes the acquisition of a pair of "low resolution" (0.1 cm^{-1}) spectra lasting several seconds and one with "high-resolution" (0.005 cm^{-1}), which can take as long as 7 min. In one sequence, this is repeated for each optical filter to cover the different spectral regions. The spectral resolution and filters used for each of the analyzed gases are reported in the **Table 1**. When the volcanic plume is detected, we can choose an alternative sequence that only consists of low resolution measurements, having NDACC filters 3 and 6 and near infrared (NIR) spectra measured with a higher frequency (**Table 1**). All the NIR spectra in both sequences are also measured with a "moderate resolution" (0.02 cm^{-1}), each of them taking 37 s.

3.3. Spectral Analysis

The analysis of SO_2, HCl, HF, SiF_4, HBr is optimized depending on the different optical filters used to measure the spectra and adapting the spectral resolution and the range for each of the different species (**Table 1**). HF and HCl are analyzed from NIR measurements (without filter) with moderate spectral resolution (0.02 cm^{-1}) and the InGaAS detector in DC (Direct Current) operation mode. HCl and SO_2 are retrieved together in the mid infrared (MIR) spectral range covered by the filter 3. SiF_4 and SO_2 are measured in the long wave IR spectral range using filter 6 with a spectral resolution of 0.1 cm^{-1}. The gas column amounts are retrieved from the measured spectra using the PROFFIT v.9.6 retrieval code (Hase et al., 2004). It solves the ray tracing and provides a forward simulation of the expected transmission spectra with line-by-line calculations using the cross sections and a priori profiles of each atmospheric constituent. The code makes the inversion by constrained least-squares fitting and the resulting vertical profiles and columns of the target gases are reported with a corresponding error analysis.

The retrieval strategies used for the analysis of the volcanic plume aimed specifically at optimizing the total column averaging kernel in the altitude of the volcanic layer between 5,500 and 6,000 m a.s.l. Therefore, a strategy for each specie is chosen depending if the gas has a stratospheric background or not, if more than one degree of freedom is allowed or if the available information is limited for its retrieval. SO_2 and SiF_4 do not have any atmospheric background and are retrieved as a simple scaling with contributions only on the lower levels. HF and HCl in the MIR region are retrieved adjusting the VMR-profile using a Tikhonov constraint on a logarithmic scale and an a priori which consists in the averaged profile of 41 years run of the Whole Atmospheric Community Climate Model (WACCM), as commonly done in the NDACC community, but with an increased concentration in the lower troposphere between 4 and 6 km. This strategy gives an initial sensitivity to the volcanic layer and allows adjusting both the stratospheric background and the volcanic plume. The HCl retrieval in the

FIGURE 1 | Presentation of the measurement site: The NDACC Altzomoni Atmospheric Observatory **(A)** Automated solar tracker installed on the roof of the station. **(B)** Picture of the high resolution FTIR spectrometer inside the container. **(C)** Location of the Altzomoni observatory, the seismic Canario station, and the Popocatépetl volcano. **(D)** A typical geometry for solar occultation measurements of the volcanic plume.

NIR region does not contain more than one independent portion of information and uses therefore a block-Tikhonov constraint shifting the VMR concentration below 6 km, while keeping the concentrations above 6 km fixed to the a priori calculated from the WACCM model.

For this study, a filter was applied to the data in order to only include the spectra that contain information of the volcanic plume. Measurements with SO_2 columns below 1.1×10^{16} molecules cm^{-2}, a baseline calculated over the 4 years of the record, were discarded. For the selected data, the HCl/SO_2 (Filter 3), HF/HCl (Open = no Filter) and SiF_4/SO_2 (Filter 6) ratios were determined for each day (or volcanic event) from the correlation plots of each pair of gases. The slopes were calculated when a good correlation is obtained (Pearson's coefficient $R \geqslant 0.8$). When the error in the slope (corresponding to 99% confidence intervals) is higher than 50%, the data are discarded. HF and SiF_4 columns were retrieved from spectra measured with different filters so that their ratios (SiF_4/HF) were derived from the SiF_4/HCl ratios (product of SiF_4/SO_2 and SO_2/HCl ratios) and HF/HCl ratios using interpolation in time. The retrieved slant columns within a volcanic plume are very sensitive to small movements of the plume with respect to the line of sight, but the interpolation of the gas ratios will not change as much as the individual columns. A calibration factor of 0.86 was applied to correct the HF/HCl ratio to account for spectroscopic inconsistency between the used line intensities of the fundamental and the first overtone of the HCl bands reported in the HITRAN 2004 spectral data base (Rothman et al., 2005).

3.4. OMI Fluxes

The SO_2 flux measurements used in this study were obtained by processing the standard NASA OMSO2 v2 product (Yang et al., 2007) with the traverse method (Bluth et al., 1994; Campion, 2014). The data from the OMSO2 product, downloaded from the Mirador server (https://mirador.gsfc.nasa.gov/), report SO_2 vertical column densities for each pixel of the image, obtained with four different SO_2 vertical distribution profiles (PBL: center of mass = 0.7 km; TRL: center of mass = 2.6 km; TRM: center of mass = 7.5 km; STL: center of mass = 15 km). The SO_2 content of the plume was interpolated for each pixel at the plume altitude between these four a priori values. Traverses are defined as rows or columns of pixels crossing the plume at increasing distances downwind from the crater. The SO_2 flux is calculated for each traverse as:

$$F = V.\cos(\theta).\sum_{i} C_i.L_i \tag{1}$$

Where V is the wind speed, θ is the angle between the traverse and the plume direction, C_i is the SO_2 column interpolated at the plume height for the ith pixel of the traverse, L_i is its length (or width depending on the plume direction). OMI's pixel size is 13 × 24 km at nadir, and stretches with increasing viewing angle, until reaching 16 × 140 km at the edge of the 2,500 km wide swath. The application of the traverse method requires two conditions in order to produce reliable results, which are a coherent plume transport direction and the absence of a cloud coverage above the volcanic plume. The fulfilling of the former condition can be assessed by a visual inspection of the SO_2 plume shape. The cloud top pressure and the cloud fraction, reported for each pixel as an ancillary information in the OMSO2 product, allow to assess the latest one. The values of SO_2 fluxes reported in **Figure 2C** are the average value of the fluxes measured on images fulfilling these two conditions. Despite taking the highest care in processing the OMI data, a systematic difference is observed between the OMI-derived SO_2 fluxes and those obtained using ground-based instruments such as COSPEC traverses. The ground-based measurements are in average 2.5 times higher than those of OMI but generally follow the same trends (Campion, in preparation). McCormick et al. (2014) compared such datasets for Tungurahua volcano, where roughly similar trends can be observed. The precise causes of this discrepancy are still under investigation although we suspect that the SO_2 column might be either underestimated by the

TABLE 1 | Filters, detectors, and spectroscopic parameters used for the analysis of SO_2, HCl, HF, SiF_4, and HBr in the Popocatépetl's plume from solar absorption measurements (LN2 = liquid nitrogen cooled).

Gas	Filter	Detector	Resolution (cm^{-1})	Spectral ranges (cm^{-1})
SO_2	3 & 4	InSb(LN2,DC)	0.1 & 0.005	2480.0–2520.0
SO_2	6	MCT(LN2,AC/DC)	0.1 & 0.005	1120.0–1180.0
HCl	3	InSb(LN2,DC)	0.1 & 0.005	2727.0–2728.5; 2775.0–2776.50; 2818.75–2820.35; 2820.75–2822.35; 2843.0–2844.4; 2903.35–2904.85; 2923.0–2924.50; 2925.0–2926.75; 2942.0–2943.5; 2960.3–2961.825; 2962.3–2964.0; 2995.0–2996.5
HCl	Open	InGaAs	0.02	5738.0–5740.0; 5767.0–5767.8; 5779.2–5779.9
HF	1, Open	InGaAs	0.1, 0.0075 & 0.02	3999.0–4003.5; 4036.5–4041.0
SiF_4	6	MCT(LN2,AC/DC)	0.1	1015.0–1035.0
HBr	3 & 4	InSb(LN2,DC)	0.005	2412.0–2413.75; 2432.0–2433.0; 2451.25–2453.00; 2488.0–2491.0; 2505–2510; 2541.0–2542.75; 2574.0–2576.0; 2589.95–2591.5; 2619.5–2623.0; 2634.0–2636.5; 2661.5–2664.0; 2673.9–2676.15; 2686.33–2688.05; 2697.4–2700.0; 2709.6–2710.7

OMI retrieval due to the high turbidity of the atmosphere over central Mexico or overestimated by the ground-based COSPEC measurements maybe due to a problem of calibration.

3.5. Seismic Data

Popocatépetl′s seismic monitoring is operated by 3 triaxial broadband seismic stations of the CENAPRED (National Center for Disaster Prevention). The Canario station (2.1 km from the crater, 4,200 m.a.s.l.; **Figure 1C**), provides the data used in this study. We computed the Real-time Seismic Amplitude Measurement (RSAM) (Endo and Murray, 1991), consisting in the average amplitude of ground movements caused by volcanic events at 10 min intervals. As the RSAM does not differentiate between volcanic activity and other sources of ground vibration (wind, rain, thunder, or tectonic earthquakes), the data from Canario were filtered by manually removing non-volcanic signals from their waveform and frequency spectra. We manually reviewed more than 170,000 values for the study period comprising the period 2012–2016.

4. RESULTS

4.1. Variability of the Popocatépetl Plume Composition Over 4 Years

The complete time series of the HCl/SO_2, HF/HCl, and SiF_4/SO_2 ratios (error ⩽50%) and their linear fit weighting-based errors are reported in **Figures 2A,B** concurrently with the SO_2 fluxes (**Figure 2C**) and seismic activity (**Figure 2D**).

4.1.1. HF/HCl

The measured HF and HCl columns are both detected and mutually sufficiently well correlated (Pearson's R ⩾0.80, error ⩽50%) in 77 out of 591 days of measurements and the corresponding slopes (HF/HCl) were reported with their error bars in **Figure 2A**. Gray and black colors distinguish data with an error lower than 10% (black, 34 measurement days) from the others with higher errors (gray, 43 measurement days). The following calculations are realized only selecting datapoints with an error lower than 10%. The HF/HCl ratios are distributed around an average value of 0.24 and a standard deviation of 0.03 (**Figure 3A**). Only 7% of the values are outside the standard deviation from the average. These values are essentially concentrated over short time periods (a maximum of 2 days) and do not systematically coincide with the RSAM "spikes" characterizing volcanic explosions in the seismic record or with shifts in the RSAM cumulative curve.

4.1.2. HCl/SO_2

The measured HCl and SO_2 columns are both detected and mutually sufficiently well correlated (Pearson's R ⩾0.80, error ⩽ 50%) in 129 out of 591 days of measurements, and their slopes (HCl/SO_2) are reported in **Figure 2B** with their error bars. As previously described for HCl/HF, data with error lower than 10% are represented in black (90 measurement days) and the other data in gray (39 measurement days) and the following statistical calculations are realized only using data with error lower than 10%. The mean and standard deviation obtained for the complete time series are 0.11 ± 0.03. The repartition of the HCl/SO_2 ratios relatively to the average (**Figure 3B**) shows at least three distinguishable periods, labeled period I (Nov. 2012–May 2013), II (Nov. 2013–Mar. 2014), and III (Sep. 2014–Dec. 2016), with different HCl/SO_2 averages reported in **Table 2**.

About 90% of the HCl/SO_2 ratios obtained during period I (Nov. 2012–May 2013) are below the overall average (0.11) with a mean ratio and standard deviation of 0.07 ± 0.02. A zoom of this period is presented in **Figure 4**. This period, displaying the most intense volcanic activity of the whole survey, is characterized by a monotonously declining trend of the ratio between values of 0.09 and 0.04, independent of the volcanic activity. The HCl/SO_2 declining trend (slope = −0.34%/day and R^2 = 0.70) was calculated after excluding iteratively outliers using the Chauvenet's criterion. Therefore, in each iteration a straight line is fitted and only the data with differences within the two

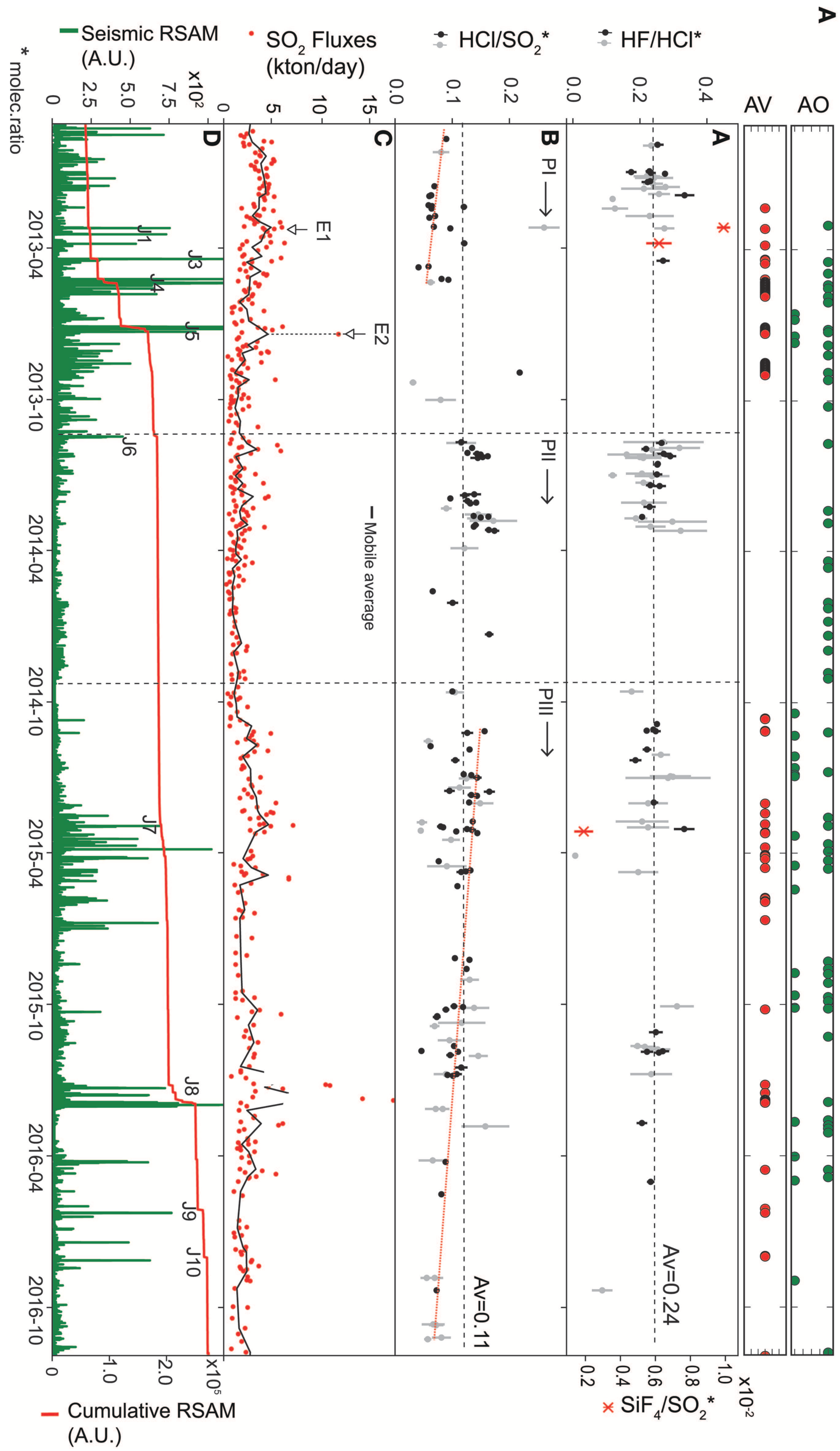

FIGURE 2 | Time series of the Popocatépetl plume composition between 2012 and 2017 for **(A)** SiF_4/SO_2 (red) and HF/HCl molecular ratios (black for datapoints with error ⩽10% and gray for those with error ⩾10%) **(B)** HCl/SO_2 molecular ratios (black for datapoints with error ⩽10% and gray for those with error ⩾10%), obtained from FTIR solar absorption measurements. The vertical dashed lines represent the beginning of each of the period PI, PII and PIII defined in **Table 2**. **(C)** SO_2 fluxes obtained from the OMI satellite measurements (red) and their moving average (black) over 5 points **(D)** seismic RSAM (green) and its cumulative curve (red) obtained from the Canario seismic station. J1–J10 indicate the main cumulative RSAM shifts. Top of the figure: AO, Aerial observations including overflights of the Popocatépetl crater and satellite observations from USGS. The presence of a lava dome is indicated by the position of the point (Top = Yes, Bottom = No). AV, Ash Venting episodes.

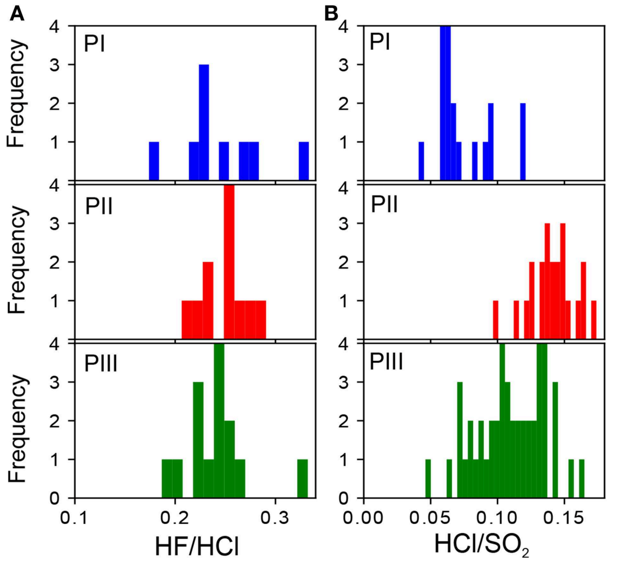

FIGURE 3 | Histogram of the **(A)** HF/HCl and **(B)** HCl/SO_2 ratios for each periods depicted in **Figure 2**.

TABLE 2 | Statistics of the HCl/SO_2 molecular ratios measured in the Popocatépetl plume over the 4-year record.

HCl/SO_2	Total	Period I Nov.2012–May 2013	Period II Nov.2013–Mar. 2014	Period III Sep. 2014– Dec. 2016
Average	0.11	0.07	0.14	0.11
Max	0.22	0.12	0.17	0.17
Min	0.04	0.04	0.10	0.05
STD	0.03	0.02	0.02	0.03

standard deviations interval are selected for the next iteration and a new trend-line is fitted. Convergence was reached after four iterations. Five outliers were identified, numbered 1–5 in **Figure 4B**, where they clearly coincide (within 1 day) with the main RSAM peaks. Most of them even match with the shifts observed in the RSAM cumulative curve on March 07th, 2013 (J1), March 26th, 2013 (J3), and May 8–9th, 2013 (J5).

These five events are characterized by high HCl/SO_2 ratios (**Figure 4B**), and moderate to high SO_2 fluxes ($\geqslant$3,100 ton/day, **Figure 4A**) compared to the global average over our 4-year record (2,790 ton/day). They occur within 24 h after harmonic and spasmodic tremor crisis and almost continuous explosive activity over several hours (explosions or exhalation trains), which correspond to sporadic dome growth episodes. The extreme high HCl/SO_2 ratio value (0.218 ± 0.004) obtained on August 30th, 2013 coincides with the end of an intense period of seismic and volcanic activity.

During our period II (Nov.2013–Mar.2014), 95% of the HCl/SO_2 ratios are higher than the overall average (0.11), with a mean value of 0.14 (**Table 2**). The variability of the HCl/SO_2 ratio is significant during this period which is characterized by a quiet and rather stable volcanic and seismic activity, with relatively low SO_2 fluxes (mean of 1,990 ton/day). The latter can explain the especially high HCl/SO_2 ratio during this period. During the period III (Sep.2014–Dec.2016) another decreasing trend (slope $= -0.08\%$/day and $R^2 = 0.78$) of the HCl/SO_2 ratio is observed, starting with values very similar to those obtained for the period II (around 0.16), and ending with low values similar to those measured during the period I (around 0.06). This decreasing trend started a few weeks before a renewal of the seismic activity after about a year of very low activity.

4.1.3. SiF_4/SO_2

In our time series, SiF_4/SO_2 was higher than the detection limit for only three eruptive events on March 7th and 26th, 2013 and on March 6th, 2015 (**Figure 2A**-red). The values ranged between $(1.9 \pm 0.5) \times 10^{-3}$ and $(9.9 \pm 0.4) \times 10^{-3}$. SiF_4 was previously measured at Popocatépetl volcano with similar abundances (**Table 3**). It is assumed that SiF_4 is formed in the shallow volcanic system from the reaction: $SiO_2(s) + 4HF(g) \rightarrow SiF_4(g) + 2H_2O$ (1), under low temperature conditions ($\leqslant$600°C), when the exsolved HF reacts with the silicate rocks of the conduit or in the plume by ash-gas interaction during explosions. Though, SiF_4 being seldom measured, the precise context favoring its formation remains to be fully depicted.

Here, we find that every detection of SiF_4 took place while a lava dome obstructed the main crater (based on seismic records, webcams observations of ash venting episodes, CENAPRED reports, and photographs taken during crater overflights). The first SiF_4 event detected (on March 7th, 2013) coincides with an important harmonic and spasmodic tremor episode (**Figures 2, 4**), associated with a 6 h sustained ash venting episode (exhalation train). It likely corresponds to a sporadic growth phase of the lava dome observed during an overflight on March 4th, 2013, probably initially emplaced around February 10th, 2013 (Gómez-Vazquez et al., 2016). The second SiF_4 event (on March 26th, 2013) coincides with another sustained volcanic activity period (**Figure 2**), with similar characteristics (episode of sustained ash venting and explosive activity) probably reflecting a new growth phase of the above mentioned lava dome. The third SiF_4 event, recorded on March 06th, 2015, also coincides with an important active volcanic phase, punctuated by some episodes of harmonic and spasmodic tremor (the last observed on March 06th, 2015 before the dome destruction) and explosive activity. On March 07th, 2015, a $\geqslant$1h-long explosive crisis (train of explosions), ejected incandescent blocks more than 500 m away from the crater. This phase corresponds to a growth episode of the dome emplaced around February 11th, 2015 (CENAPRED Reports; Gómez-Vazquez et al., 2016) and observed during an overflight on February 27th, 2015 with a diameter of 250 m and at least 40 m in thickness (1.96×10^6 m^3).

4.1.4. HBr/HCl and HBr/SO_2

HBr is too dilute in the plume to be properly detected. We however propose its detection limit as an upper limit for its ratio with HCl and SO_2. For this, a set of 15 spectral windows including the HBr lines R8 to R1 and P1 to P7 of the R and P branches were used in the retrieval strategy, typically consisting

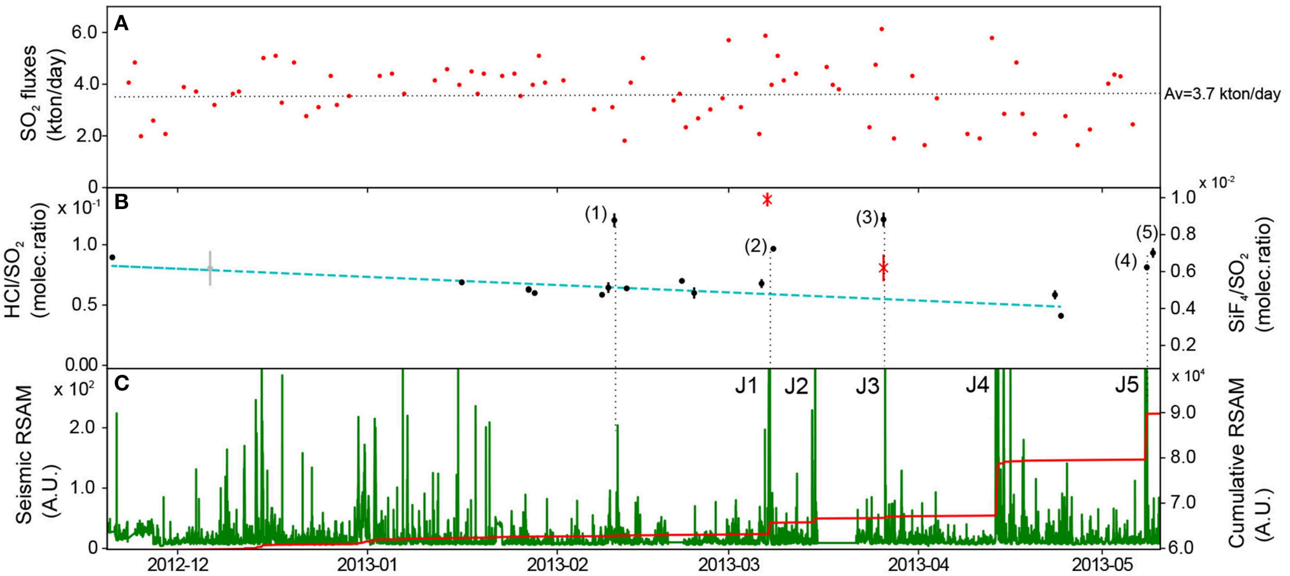

FIGURE 4 | Zoom of the **(A)** SO_2 fluxes, **(B)** HCl/SO_2 (in black and gray), and SiF_4/SO_2 (in red) ratios and **(C)** seismic RSAM time series shown in **Figure 2** from December 2012 to May 2013. In **(B)** the (1–5) points are outliers from the HCl/SO_2 declining trend (cyan) and correspond to ash venting episodes. In **(C)** J1–J5 denote main cumulative RSAM shifts.

in a set of various rather narrow spectral windows (Echle et al., 2000). The error analysis of PROFFIT9.6 includes the estimation of random and systematic errors, and is therefore helpful to estimate the detection limit, either of an individual spectrum or from the analysis of the whole time series. In the high resolution spectra with the highest SO_2 slant columns, we estimated the random error in the HBr retrieval to be about 5.0×10^{14} molec. cm^{-2} and an anomaly can only be detected if the column of a single event exceeds this amount. From this number, the corresponding SO_2 column (4×10^{19} molec. cm^{-2}) and HCl column (4×10^{18} molec. cm^{-2}), we estimated upper limits for the HBr/SO_2 and HBr/HCl ratios, respectively equal to 1.25×10^{-5} and 1.25×10^{-4}.

Assuming a mean Br/Cl ratio of $(2.2 \pm 2.0) \times 10^{-3}$ for arc volcanoes (Gerlach, 2004), we calculated a speculative primitive HBr/SO_2 mean for Popocatépetl from our mean HCl/SO_2 long-term ratio (0.11 ± 0.03). We obtained a HBr/SO_2 range from 1.6×10^{-5} to 5.9×10^{-4} considering the standard deviations. This is surprisingly in the range of the recently reported BrO/SO_2 at Popocatépetl volcano, from 4×10^{-5} to 4×10^{-4} (Fickel and Delgado Granados, 2017), measured at 4 km from the crater using DOAS spectroscopy. Therefore, a significant part of the HBr might have converted into BrO and other bromine species, such as Br_2 (Bani et al., 2009; Gutmann et al., 2018), before our detection.

Such calculations have deeper implications for the halogens degassing at Popocatépetl volcano. Using the maximum of both the theoretical HBr/SO_2 and the measured BrO/SO_2 ratios, we found that if such Br/Cl characterized the Popocatépetl emissions, 68% of HBr would be converted into BrO. This is close to the highest values reported in the literature, for measurements performed at 14 km from the crater of the Ambrym volcano (Bani et al., 2009; Gutmann et al., 2018). This value is abnormally high for measurements at 4 km from the crater (Gutmann et al., 2018), which suggests higher primary Br/Cl and HBr/SO_2 ratios at least for some degassing events at Popocatépetl volcano.

4.2. Variations of the Plume Composition Induced by a Moderate Explosion

Our frequent measurements allow capturing changes in the plume composition preceding and induced by one of the common moderate explosions (mentioned as type 1 in Campion et al., 2018) recorded on March 6th, 2015. **Figures 5A–C**, **6A–C** report the time series of the HF/HCl, HCl/SO_2, and SiF_4/SO_2 ratios and the corresponding correlation plots, which were recalculated point by point from each spectrum. Our measurements started 15 min after the explosion reported by the CENAPRED at 07:30 (local time), and continued up to 6 h afterwards. The explosion was preceded by weak passive degassing and followed by gas puffs (one of the most important occurred at 8:47) punctuating the continuous degassing regime. These degassing regimes were defined in Campion et al. (2018). Using the pictures from the visible camera (taken every minute from the Altzomoni station), the respective arrival times for (i) the first (07:30) explosion plume and (ii) the most important puff (08:47) plume in the instrument optical path are 07:54 (about 10 min after the beginning of the record) and 9:11 (i.e., 24 min travel time for both plumes between emission at the volcano and measurement).

The correlation plots (**Figures 6A–C**) of the different measured gas pairs and the time series of their ratios (**Figures 5A–C**) allow distinguishing different phases during our record. We observe that the pre-explosive and explosive phases (Pa1 and Pa2) are characterized by 10% higher HCl/SO_2

TABLE 3 | Previous measurements of the HCl/SO_2, HF/HCl, SiF_4/SO_2 ratios and SO_2 and HCl fluxes in the Popocatépetl plume.

Date	HCl/SO_2	HF/HCl[a]	$SiF_4/SO_2 \times 10^{-3}$	SO_2 fluxes (ton/day)	HCl fluxes (ton/day)	References
02/19/94	0.14	0.98	–	1,200	100	(Goff et al., 1998, 2001)—alkaline traps
05/04/94	0.21	0.80	–	900	110	(Goff et al., 1998, 2001)—alkaline traps, (Delgado-Granados et al., 2001; Roberge et al., 2009)
07/02/94	0.13	1.37	–	3,100	220	(Goff et al., 1998, 2001)—alkaline traps
11/05/94	0.12	0.64	–	1,260	90	(Goff et al., 1998, 2001)—alkaline traps
12/21/94	0.14	0.18	–	–	–	(Goff et al., 1998, 2001)—alkaline traps
12/21/94 – 06/30/95	–	–	–	3,470	–	(Delgado-Granados et al., 2001)—COSPEC
12/24/94	0.18	0.58	–	3,960	400	(Goff et al., 1998, 2001)—alkaline traps
03/05/96[b]	0.16	0.018	–	–	–	(Goff et al., 1998, 2001)—alkaline traps
03/07/96	0.37	0.18	–	12,900	2,700	(Goff et al., 1998, 2001)—alkaline traps
Average 96	0.17	0.29	–	–	–	(Goff et al., 1998, 2001)—alkaline traps
03/25/96 – 12/29/96	–	–	–	11,000	–	(Delgado-Granados et al., 2001)— COSPEC
02/21/97	–	–	1.0	–	–	(Goff et al., 1998, 2001; Love et al., 1998)—FTIR
02/23/97	0.19	0.73	1.7	–	–	(Goff et al., 1998, 2001; Love et al., 1998)—FTIR
02/24/97	–	–	2.4	2,000	260	(Goff et al., 1998, 2001; Love et al., 1998)—FTIR
02/26/97	–	–	1.0	60,000	7,800	(Goff et al., 1998, 2001; Love et al., 1998)—FTIR
02/27/97	0.23	0.27	–	13,000	1,700	(Goff et al., 1998, 2001)—FTIR
01/17/97 – 05/15/97	–	–	–	12,930	–	(Delgado-Granados et al., 2001)—COSPEC
02/12/98	0.32	0.34	–	1,030	190	(Goff et al., 1998, 2001)—FTIR
02/13/98	0.28	0.32	–	2,710	430	(Goff et al., 1998, 2001)—FTIR
12/01/07	0.05 ± 0.001	0.08 ± 0.01	–	–	–	(Stremme et al., 2011), (Erupt. event)
12/01/07	–	0.04 ± 0.02	–	–	–	(Stremme et al., 2011), (Erupt. event)
12/01/07	–	0.16 ± 0.01	–	–	–	(Stremme et al., 2011), (Erupt. event)
11/17/08	0.15 ± 0.002	0.24 ± 0.01	0.39 ± 0.02–2.56 ± 0.30	–	–	(Stremme et al., 2011, 2012) (Passive degassing)
05/12	0.10	–	–	–	–	Stremme (unpublished data)
01-06/15	–	–	0.1-1.2	–	–	(Taquet et al., 2017)
2012-2016	0.11 ± 0.03	0.24 ± 0.03	1.9 ± 0.5–9.9 ± 0.4	2,790	–	This work
2012-2013(P1)	0.07 ± 0.02	0.24 ± 0.04	6.2 ± 0.7–9.9 ± 0.4	3,680	150	This work (Active period with extrusive activity)
2013-2014(P2)	0.14 ± 0.02	0.25 ± 0.02	–	1,990	160	This work (Quiet episode)
2014-2016(P3)	0.11 ± 0.02	0.24 ± 0.03	1.9 ± 0.5	2,702	167	This work (Active period with renewal of extrusive activity)

[a] *Between 1994 and 1998 HF/HCl is estimated from SO_2/HCl and SO_2/HF ratios.*

[b] *Renewal of extrusive activity (first lava dome observed in March 1996).*

ratios [**Figures 5A**, **6A**, slope (a) = 0.121 ± 0.002, $R^2 = 0.997$] than those of the post explosive phases (Pa3 and Pa4) [slope (b) = 0.110 ± 0.001, $R^2 = 0.997$], which suggests that the post explosive plume is richer in SO_2. HF/HCl variation rates (slope) are similar during Pa1, Pa2, and Pa4 (**Figure 6B**). The post explosive phase (Pa3) is distinguished from the others by much higher SiF_4/SO_2 ratios and variation rates [slope (f) = 0.022 ± 0.005, $R^2 = 0.94$, **Figures 6C**, **5C**] than those of the other phases [slope (e) = 0.0006 ± 0.0006, $R^2 = 0.46$] and comparatively 50% lower HF columns for equivalent HCl columns. The SiF_4/HF ratio is indirectly calculated from the previously reported ratios. The correlation plot of the SiF_4/HCl vs. HF/HCl ratios and the SiF_4/HF time series are reported in **Figures 6D**, **5D**, respectively. A good correlation [trend (f), $R^2 = 0.94$] is found between these ratios, defining a variation rate (slope) of −0.24 ± 0.02, in agreement with the molar balance of the reaction (1) (see section 4.1.3), indicating that the fluorine species are conserved. This result suggests that over the complete record no appreciable quantities of other F-species (e.g., CaF_2, $CaSiF_6$, NaF; Delmelle et al., 2018) than HF and SiF_4 are implied in the fluorine transformation.

5. DISCUSSION

5.1. Insights Into the Origin of the Moderate Explosions at Popocatépetl Volcano

The triggering mechanisms of one of the most common type of explosions at Popocatépetl are explored here, using our daily HCl/SO_2, SiF_4/SO_2, HF/HCl, and SiF_4/HF time series. These

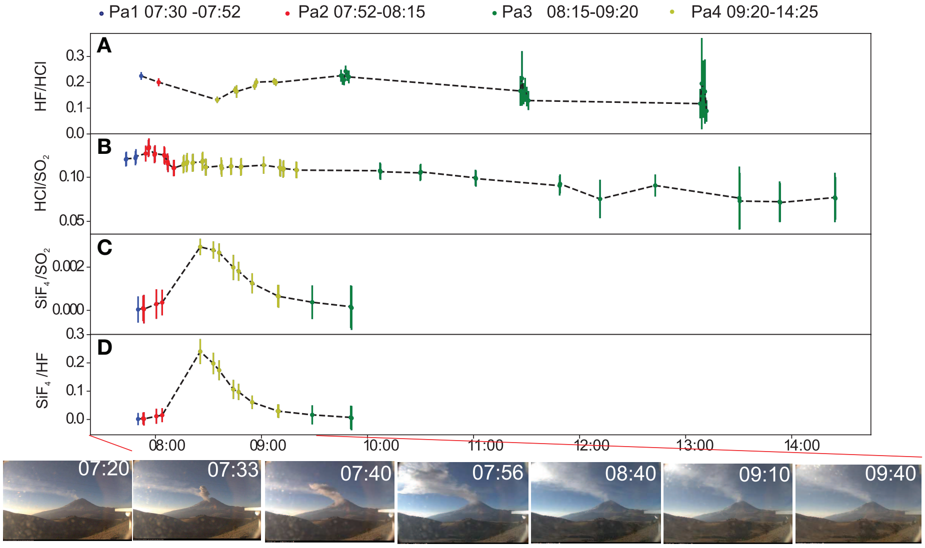

FIGURE 5 | Time series of **(A)** HF/HCl, **(B)** HCl/SO_2, and **(C)** SiF_4/SO_2 ratios acquired on March 6th, 2015 at Popocatépetl volcano. The time axis corresponds to the measurement time, where the plume of the 07:30 a.m. explosion was measured at 07:54. The different colors correspond to the different periods mentioned in the text, Pa1 (07:30–07:52) in blue, Pa2 (07:52–08:15) in red, Pa3 (08:15–09:20) in yellow, and Pa4 (09:20–14:25) in green. **(D)** SiF_4/HF time series calculated from the previously mentioned ratios for the different periods.

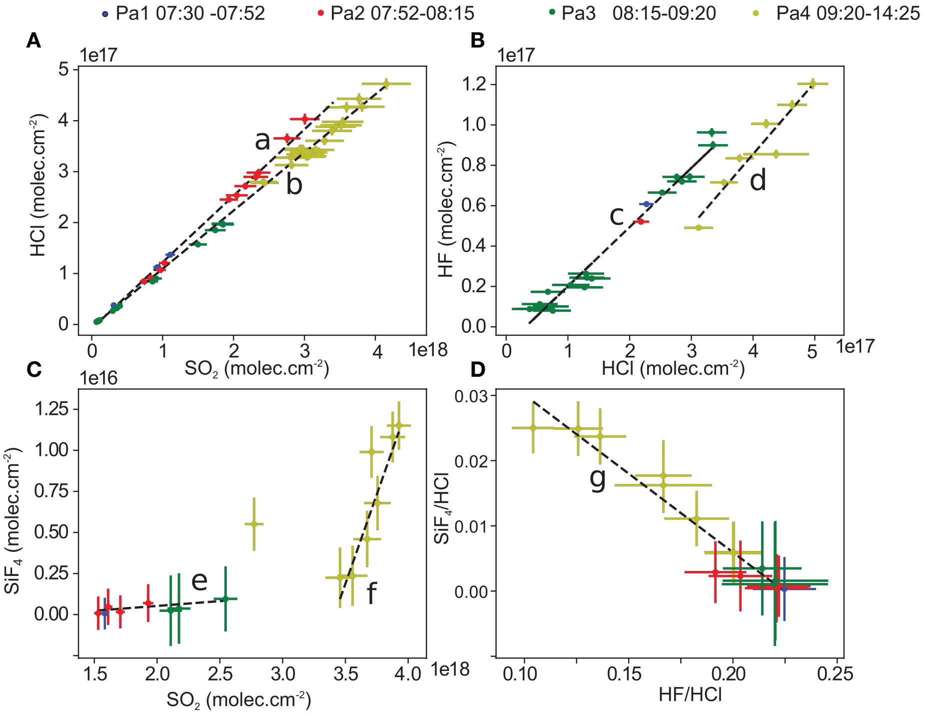

FIGURE 6 | Correlation plots of **(A)** HCl vs. SO_2, **(B)** HF vs. HCl, **(C)** SiF_4 vs. SO_2, and **(D)** SiF_4/HCl vs. HF/HCl several minutes preceding, during and several hours after the detection of an explosion occurring on March 6th, 2015 at 07:30 a.m. The different colors correspond to the periods mentioned in **Figure 5**.

events generally mark important breakdowns in the lava domes growth, causing their partial or total destruction. Some recent geochemical studies have used the SiF_4/HF ratios as a proxy to detect changes in the gas temperature beneath lava domes (Love et al., 1998; Stremme et al., 2012). A common hypothesis is that the dome cooling and an overpressure beneath the dome should drive the vulcanian explosions at the Popocatépetl volcano (Love et al., 1998; Stremme et al., 2012). Such hypothesis has recently been challenged by high temporal resolution measurements of proxies to the permeability of Popocatépetl domes (Taquet et al., 2017; Campion et al., 2018), showing that the SO_2 fluxes only decreased minutes before explosions, a time frame incompatible with the cooling and solidifying of lava domes. High temporal resolution measurements such as those presented here during March 6th, 2015 provide valuable information on the variability of the HF/HCl, SO_2/HCl, SiF_4/SO_2, and SiF_4/HF ratios several minutes before and up to several hours after typical explosive events. The four correlation plots (**Figure 6**) and the time series (**Figure 5**) presented suggest the existence of various regimes during the same episode, in which different physical and chemical processes predominate:

(i) The first two phases (Pa1 and Pa2) have higher HCl/SO_2 ratios (**Figures 5**, **6**) than the later phases (Pa3 and Pa4). Therefore, the halogen species, which predominate in the volcanic plume at the beginning of the explosion, reveal a momentaneously higher contribution of the shallow degassing.

(ii) The lower HCl/SO_2 ratios observed during the last two phases (Pa3 and Pa4), following the trend (b) in **Figure 6A**, reflect a higher contribution of the deeper exsolved SO_2-rich gas. This explosive phase releases more ash and a large quantity of condensed gases, visible in the fourth photograph in **Figure 5**.

(iii) The measurements performed in the concentrated plume (Pa3) display a specific trend in the HF/HCl (d) and SiF_4/SO_2 (f) correlation plots, which we explain by the formation of SiF_4 from HF.

(iv) The SiF_4/HCl and HF/HCl correlation observed in **Figure 6D** reflects the conservation of fluorine during the whole record.

The presence of SiF_4 in the Popocatépetl's explosion plumes was mainly explained by the release of SiF_4-enriched gas pockets produced by the HF percolation through the lava dome obstructing the crater (Love et al., 1998; Stremme et al., 2011; Taquet et al., 2017). Taquet et al. (2017) observed both prolonged periods (several hours) with a higher base level of SiF_4/SO_2 ratios (likely supporting such a primary production), occasionally preceding the explosions, and sharp SiF_4/SO_2 spikes within periods of high conduit permeability (which rather support the gas-ash interactions). The detection of the primary SiF_4 production (HF percolation through the conduit vs. secondary ash-gas interaction) with our measurements configuration would require the combination of various factors such as an initial strong HF degassing, a little permeable lava dome to improve the HF-silicate interaction (Taquet et al., 2017) and an efficient transport toward the measurement locus. In the case of March 06th measurements, the delay (more than 20 minutes) between the detection of the explosive plume and our significant detection of SiF_4 would imply a special wind scenario (gradient with altitude generating the late arrival of the early emitted SiF_4-rich gas) and low gas mixing to consider SiF_4 as resulting from a primary production. However the delay is more likely explained by the in-plume SiF_4 production from ash.

5.2. Long-Term Evolution of the Popocatépetl Plume Composition

The 4-year time series of HCl/SO_2, HF/HCl, and SiF_4/SO_2 ratios of the Popocatépetl′s plume presented here give an overview of its long-term variability during both eruptive and quiescent episodes. **Table 3** summarizes the results from this work together with previous studies using direct sampling, alkaline traps and FTIR techniques. The fairly constant HF/HCl ratio over our record, averaging 0.24 ± 0.03 (min = 0.17; max = 0.33) complies with the HF/HCl average reported by Goff et al. (1998) in 1996 using alkaline traps, and FTIR measurements performed between 1997 and 2008 (average = 0.24; min = 0.02; max = 0.73). These ratios belong to the range defined by Aiuppa et al. (2009) for volatile-rich arc volcanism. The HCl/SO_2 ratios, averaging 0.11 ± 0.03 (min = 0.04; max = 0.22) are also very close to the vast majority of the previous measurements since 1994 (average = 0.17; min = 0.05; max = 0.37; **Table 3**). The SiF_4/SO_2 ratios found for this study (from $(1.9 \pm 0.5) \times 10^{-3}$ to $(9.9 \pm 0.4) \times 10^{-3}$) are in the same order of magnitude as the previously reported values (**Table 3**). The small number of SiF_4 detections during our 4-years time series, compared to that reported in a previous study (Taquet et al., 2017), is probably due to the SiF_4 dilution downwind. The atmospheric chemistry, as well as gas-ash-aerosols interactions, have been proposed to alter the magmatic composition of volcanic plumes (Notsu and Mori, 2010; Martin et al., 2012; Maters et al., 2016). Each individual gas ratio of our dataset corresponds to the slope of well linearly correlated ($R \geqslant 0.8$) gas columns pairs of specific degassing events, thus gas plumes with highly inhomogeneous composition would be filtered out.

The high HCl/SO_2 ratios (averaging 0.14) recorded during the period II, are associated with the lowest SO_2 fluxes and coincide with the unique prolonged low seismic and volcanic activity period of our record (**Figure 2**). The lowest ratios (average $\leqslant 0.1$) observed during the period I and at the end of period III are the lowest since 1994, together with one measurement performed on December 2007 during an eruptive event. The five high HCl/SO_2 ratios, odd to the period I trend, correspond to short extrusive episodes (spasmodic tremor and trains of explosions reported by the CENAPRED, the seismograms are available in http://www.ssn.unam.mx/sismogramas/ppig/). Such events have been characterized by Campion et al. (2018) as strong degassing events with the highest SO_2 fluxes of their survey period. Here, our moderate to high OMI-derived fluxes do not necessarily capture the high SO_2 fluxes of the extrusion phases (generally a few hours long). In any case, the anomalously high HCl/SO_2 ratios (for high to moderate SO_2 fluxes) reflect the shallow exsolution of the halogens during the magma ascent. This observation is in agreement with previous observations for other volcanoes during dome growth episodes (Edmonds et al., 2001).

The HCl/SO_2 decreasing trend observed during the period I (**Figure 2B**) reaches the lowest ratios of the whole time series in April 2013, and coincides with important SO_2 fluxes (average of 3,680 ton/day, **Figure 2C**) compared to those of the period II (average of 1,990 ton/day). This period of higher SO_2 fluxes is part of a more global progressive increase, initiated mid 2011, representing the most important long-term SO_2 flux variation since 2005 (Carn et al., 2017). The SO_2 fluxes reached and maintained a maximum of around 4,750 ton/day between December 2012 and March 2013, declining to a base-level on September 2013, which is at least twice that of 2006. The injection and mixing of a mafic gas-rich magma in the deep system, eventually assisted by basement assimilation (Goff et al., 1998), is a plausible hypothesis to explain such a global increase of the SO_2 fluxes after 2011, associated with the above-described low HCl/SO_2 ratios (period I). This hypothesis is supported in Espinasa Pereña (2012), describing the main activity steps at Popocatépetl volcano since 1994. The declining trend of the ratio from November 2012 to April 2013 likely reflects a progressive HCl depletion of the gas plume post-2011 magma melange.

From the SO_2 fluxes and the HCl/SO_2 average ratios, the HCl fluxes are estimated to be around 150 and 160 ton/day for periods I and II, respectively and the increase of the HCl/SO_2 ratio observed between the period I and II is due to the reduction of the SO_2 fluxes. The SO_2 fluxes began to decline after an important prolonged peak (E1) between March 7th and 16th, 2013. The E1 peak coincides with a period of intense vulcanian explosions and sometimes trains of explosions, probably reflecting the ultimate extrusive phase of a lava dome growth initiated in February 2013, and which was destroyed several days after (Gómez-Vazquez et al., 2016). We interpret the sharp decline in SO_2 fluxes after E1 as the result of the self-compaction of the plug and/or collapse of parts of the shallow conduit after its strong degassing. The overall declining trend of SO_2 fluxes is finalized by an important prolonged peak (E2), observed between July 3th and August 11th, 2013. This period initiates with the strongest seismic crisis and shift of cumulative RSAM (J5) of our record (between July 3rd and 17th, 2013) and coincides with the destructive phase of a lava dome observed for the last time on July 7th, 2013, followed by the formation of a new crater 200 m wide and 30 m deep observed on July 15th, 2013. The new inner crater remained similar until October 2014 (CENAPRED reports).

The integration of the E2 degassing peak roughly represents 70% of the "missing" SO_2 flux during the progressive obstruction of the conduit between mid-March and June 30th 2013 (difference between the measured SO_2 fluxes and a hypothetical degassing scenario, assuming a constant amount of emissions, based on the fluxes measured between December 2012 and March 2013). Considering the uncertainties on both the OMI-derived SO_2 fluxes and the duration of the periods taken into account for this calculation, the SO_2 peak release (E2) is of the same order of magnitude as the estimated missing SO_2 flux. The E2 SO_2 peak corresponds to the sudden release of the gas accumulated beneath the less permeable plug during the conduit obstruction. The formation of the deep crater after the strong SO_2 discharge (peak E2) probably reflects the main phase of the plug subsidence and the conduit collapse. We speculate that the conduit edges were previously progressively weakened by alternating gas compression and decompression cycles, generating stress and rock alteration during the sustained degassing period.

The sudden decrease of pressure after the main release of accumulated gases (E2) between mid-March and June 30th of 2013 likely provoked the conduit to collapse, and momentarily diminished the shallow system permeability and the SO_2 fluxes between July 17th and August 11th, 2013. We expect that the long-term low SO_2 base-level, combined with high HCl/SO_2 observed during the period II, and coinciding with the low seismic and volcanic activity would rather reflect a late stage degassing of the post-2011 melange. The magma degassing at shallow depth (a shallow reservoir was estimated at a depth of 6 km by Roberge et al., 2009) progressively increases its viscosity and density, damping the magmatic ascension and extrusive activity. The volcanic activity indeed remained at very low levels until the end of 2014, with the extrusion of only a few domes of small volumes (CENAPRED reports; Gómez-Vazquez et al., 2016). The renewal of degassing on October 20th, 2014 is coeval with a short exhalation train and tremor ($\leqslant$4 h long), associated with the growth phase of a new lava dome, the largest of 2014 (Gómez-Vazquez et al., 2016), observed on November 6th during an overflight. The internal pressure of the magmatic system has apparently increased sufficiently to open a new pathway toward the surface. This is highlighted by a renewed degassing consisting in moderate SO_2 fluxes and high HCl/SO_2 ratios similar to those observed during the period II.

The very high HCl/SO_2 ratios exhibited at the beginning of this degassing event, in spite of moderate SO_2 fluxes, indicate that (1) the degassing takes place at a rather shallow level in the magmatic system, and/or (2) the magma is depleted in SO_2 with respect to the period I. In our opinion, this is consistent with the very low seismic activity over the preceding year and indicates that the emitted gases proceed from the 2013 stalling magma batch. The uppermost part of the magma column is the most readily cooled down and prone to crystallization. We speculate that the lesser activity over the year 2014 and the stalling of the magma column enhanced crystallization, which might have resulted in a second boiling episode (Blake, 1984). The latter would have considerably modified the physical properties of the magma (temperature, density, viscosity, vesicularity) and allowed the renewal of degassing. The highest HCl/SO_2 ratios were maintained until the actual resumption of the extrusive activity, dragging the whole magma column toward the surface, and thus progressively implying deeper magmas in the degassing, resulting in the observed declining trend in the HCl/SO_2 time series and the moderate SO_2 fluxes over the years 2015–2016. The exceptionally high SO_2 peak fluxes observed in January 2016 coincide with some of the most violent ash venting episodes of the survey period.

6. CONCLUDING REMARKS

In this work we present a 4-year study on the chemical composition of a volcanic plume with high frequency measurements. The variability of the HCl/SO_2, HF/HCl and SiF_4/SO_2 molecular ratios of the Popocatépetl volcano was determined from solar absorption infrared spectra recorded from a fixed site. The results are in good agreement with measurements reported previously since 1996. However, our long-term time series combined with seismic data and SO_2 fluxes records allowed us deciphering the symptoms of variations in the volcanic activity. While the HF/HCl ratio does not significantly vary for our dataset, the long-term variability of the HCl/SO_2 ratio highly depends on the volcanic (and seismic) activity.

Combining these results with satellite SO_2 fluxes, seismic RSAM and visual observations we suggest that the long-term variability of the HCl/SO_2 ratios results from changes in the shallow plumbing system following the inferred 2011 mafic magma injection. Our study started at the end of 2012, during the late degassing of the post-2011 melange, characterized by a decreasing HCl/SO_2 ratio and strong SO_2 fluxes over several months. Following this period, both the SO_2 fluxes and the volcanic activity drastically decreased for more than a year, reflecting, in our opinion, the progressive densification and crystallization of the melange, damping the extrusive activity. The activity resumes at the end of 2014 with moderate SO_2 fluxes and high HCl/SO_2, progressively decreasing over 2015–2016.

The high temporal resolution of these measurements also captures the plume composition changes preceding and induced by an explosive event at Popocatépetl volcano. Two phases were distinguished, for which different HCl/SO_2 slopes were measured. We propose that the first phase of the explosion implied a higher contribution of the shallow plug degassing while the second phase released an increased contribution of the deeper system. Lava dome-HF or ash-HF interactions within the volcanic plume after the explosion may explain the measured SiF_4/SO_2 and HCl/HF ratios during and after the event. The anti-correlation between SiF_4/HCl and HF/HCl and their slope of $-\frac{1}{4}$ proves the conservation of the fluorine species ($SiF_4 + HF$). This expected result ($0 = -0.25 \times 4 + 1$) confirms the high quality of the individual solar absorption measurements providing a valid basis for further volcanological interpretations. Future work will aim to validate all these observations using complementary techniques, such as a UV-camera to monitor the SO_2 flux more precisely and with higher temporal resolution and more detailed seismic analysis (Salerno et al., 2018). Moreover, attempts to retrieve the emitted CO_2 using solar absorption measurements (Butz et al., 2017) could help to decipher the deeper origin of the variability in the gas composition data measured in the volcanic plume.

AUTHOR CONTRIBUTIONS

NT and WS: gas measurements, gas retrievals, solar absorption spectroscopy, and manuscript writing. JB, AB, BS, CR, and MG: gas retrieval and gas absorption spectroscopy. RC: SO_2 fluxes and discussion. TBo: discussion and contribution to the manuscript writing. AN-T and RE-P: seismic data process. TBl and FH: gas retrieval and gas absorption spectroscopy.

ACKNOWLEDGMENTS

We acknowledge the reviewers G. Tamburello and M. Caroll, the editor N. Bobrowski, and the Chief editor V. Acocella for their thorough review which contributed to significantly improve the quality of the manuscript. We acknowledge the technical personnel of the Centro de Ciencias de la Atmósfera (CCA-UNAM) for maintaining the instruments, in particular H. Sotto, D. Flores, O. López, A. Rodriguez, W. Gutiérrez López, L.M. García y Espinosa de los Reyes. We wish to thank D. Legrand from the Institute of Geophysics (UNAM, Mexico) for fruitful discussions and CENAPRED for providing the seismic data. The financial support through UNAM-DGAPA IN107417 & IN112216 and CONACYT 275239 & 290589 grants is acknowledged. NT and TBo also thank the stipend given by the Mexican Foreign Affairs Department (Secretaría de Relaciones Exteriores) and its AMEXCID program.

REFERENCES

Aiuppa, A., Baker, D., and Webster, J. (2009). Halogens in volcanic systems. *Chem. Geol.* 263, 1–18. doi: 10.1016/j.chemgeo.2008.10.005

Arambula, R., Valdes-Gonzalez, C., Varley, N., Reyes-Pimentel, T. A., and Juarez-Garcia, B. (2016). Tremor and its duration-amplitude distribution at Popocatépetl volcano, Mexico. *Geophys. Res. Lett.* 43, 8994–9001. doi: 10.1002/2016GL070227

Bagnato, E., Aiuppa, A., Bertagnini, A., Bonadonna, C., Cioni, R., Pistolesi, M., et al. (2013). Scavenging of sulphur, halogens and trace metals by volcanic ash: the 2010 Eyjafjallajökull eruption. *Geoch. Cosmochim. Acta* 103, 138–160. doi: 10.1016/j.gca.2012.10.048

Bani, P., Oppenheimer, C., Tsanev, V., Carn, S., Cronin, S., Crimp, R., et al. (2009). Surge in sulphur and halogen degassing from ambrym volcano, Vanuatu. *Bull. Volcanol.* 71, 1159–1168. doi: 10.1007/s00445-009-0293-7

Battaglia, A., de Moor, J. M., Aiuppa, A., Avard, G., Bakkar, H., Bitetto, M., et al. (2019). Insights into the mechanisms of phreatic eruptions from continuous high frequency volcanic gas monitoring: Rincón de la Vieja volcano, Costa Rica. *Front. Earth Sci.* 6:247. doi: 10.3389/feart.2018.00247

Baylon, J. L., Stremme, W., Grutter, M., Hase, F., and Blumenstock, T. (2017). Background CO_2 levels and error analysis from ground-based solar absorption IR measurements in Central Mexico. *Atmos. Measure. Tech.* 10, 2425–2434. doi: 10.5194/amt-10-2425-2017

Blake, S. (1984). Volatile oversaturation during the evolution of silicic magma chambers as an eruption trigger. *J. Geophys. Res.* 89, 8237–8244. doi: 10.1029/JB089iB10p08237

Bluth, G., Casadevall, T., Schnetzler, C., Doiron, S., Walter, L., Krueger, A., et al. (1994). Evaluation of sulfur dioxide emissions from explosive volcanism: the 1982-1983 eruptions of Galunggung, Java, Indonesia. *J. Volcanol. Geother. Res.* 63, 243–256. doi: 10.1016/0377-0273(94)90077-9

Boudon, G., Balcone-Boissard, H., Villemant, B., and Morgan, D. J. (2015). What factors control superficial lava dome explosivity? *Sci. Rep.* 5:14551. doi: 10.1038/srep14551

Butz, A., Dinger, A. S., Bobrowski, N., Kostinek, J., Fieber, L., Fischerkeller, C., et al. (2017). Remote sensing of volcanic CO_2, HF, HCl, SO_2, and BrO in the downwind plume of Mt. Etna. *Atmos. Measure. Tech.* 10, 1–14. doi: 10.5194/amt-10-1-2017

Campion, R. (2014). New lava lake at Nyamuragira volcano revealed by combined ASTER and OMI SO_2 measurements. *Geophys. Res. Lett.* 41, 7485–7492. doi: 10.1002/2014GL061808

Campion, R., Delgado-Granados, H., Legrand, D., Taquet, N., Boulesteix, T., Pedraza-Espitía, S., et al. (2018). Breathing and coughing: the extraordinarily high degassing of Popocatépetl volcano investigated with an SO_2 camera. *Front. Earth Sci.* 6:163. doi: 10.3389/feart.2018.00163

Carn, S., Fioletov, V., McLinden, C., Li, C., and Krotkov, N. (2017). A decade of global volcanic SO_2 emissions measured from space. *Sci. Rep.* 7:44095. doi: 10.1038/srep44095

Delgado-Granados, H., Cardenas Gonzalez, L., and Piedad Sanchez, N. (2001). Sulfur dioxide emissions from Popocatépetl volcano (Mexico): case study of a high-emission rate, passively degassing erupting volcano. *J. Volcanol. Geotherm. Res.* 108, 107–120. doi: 10.1016/S0377-0273(00)00280-8

Delmelle, P., Wadsworth, F. B., Maters, E. C., and Ayris, P. M. (2018). High temperature reactions between gases and ash particles in volcanic eruption plumes. *Rev. Mineral. Geochem.* 84, 285–308. doi: 10.2138/rmg.2018.84.8

Echle, G., von Clarmann, T., Dudhia, A., Flaud, J.-M., Funke, B., Glatthor, N., et al. (2000). Optimized spectral microwindows for data analysis of the michelson interferometer for passive atmospheric sounding on the environmental satellite. *Appl. Opt.* 39, 5531–5540. doi: 10.1364/AO.39.005531

Edmonds, M., Pyle, D., and Oppenheimer, C. (2001). A model for degassing at the Soufrière Hills volcano, Montserrat, West Indies, based on geochemical data. *Earth Planet. Sci. Lett.* 186, 159–173. doi: 10.1016/S0012-821X(01)00242-4

Endo, E. T., and Murray, T. (1991). Real-time seismic amplitude measurement (RSAM): a volcano monitoring and prediction tool. *Bull. Volcanol.* 53, 533–545. doi: 10.1007/BF00298154

Espinasa Pereña, R. (2012). *Historia de la Actividad del Volcán Popocatépetl 17 Años de Erupciones.* Mexico: CENAPRED.

Fickel, M., and Delgado Granados, H. (2017). On the use of different spectral windows in DOAS evaluations: effects on the estimation of SO_2 emission rate and mixing ratios during strong emission of Popocatépetl volcano. *Chem. Geol.* 462, 67–73. doi: 10.1016/j.chemgeo.2017.05.001

Francis, P., Chaffin, C., Maciejewski, A., and Oppenheimer, C. (1996). Remote determination of SiF_4 in volcanic plumes: a new tool for volcano monitoring. *Geophys. Res. Lett.* 23, 249–252. doi: 10.1029/96GL00022

Gerlach, T. M. (2004). Volcanic sources of tropospheric ozone-depleting trace gases. *Geochem. Geophys. Geosyst.* 5:Q09007. doi: 10.1029/2004GC000747

Gisi, M., Hase, F., Dohe, S., Blumenstock, T., Simon, A., and Keens, A. (2012). XCO_2-measurements with a tabletop FTS using solar absorption spectroscopy. *Atmos. Measure. Tech.* 5, 2969–2980. doi: 10.5194/amt-5-2969-2012

Goff, F., Janik, C. J., Delgado, H., Werner, C., Counce, D., Stimac, J. A., et al. (1998). Geochemical surveillance of magmatic volatiles at Popocatépetl volcano, Mexico. *Geol. Soc. Am. Bull.* 110, 695–710. doi: 10.1130/0016-7606(1998)110<0695:GSOMVA>;2.3.CO;2

Goff, F., Love, S. P., Warren, R., Counce, D., Obenholzner, J., Siebe, C., et al. (2001). Passive infrared remote sensing evidence for large, intermittent CO_2 emissions at Popocatépetl volcano, Mexico. *Chem. Geol.* 177, 133–156. doi: 10.1016/S0009-2541(00)00387-9

Gómez-Vazquez, A., De la Cruz-Reyna, S., and Mendoza-Rosas, A. T. (2016). The ongoing dome emplacement and destruction cyclic process at Popocatépetl volcano, central mexico. *Bull. Volcanol.* 78:58. doi: 10.1007/s00445-016-1054-z

Grutter, M., Basaldud, R., Rivera, C., Harig, R., Junkerman, W., Caetano, E., et al. (2008). SO_2 emissions from Popocatépetl volcano: emission rates and plume imaging using optical remote sensing techniques. *Atmos. Chem. Phys.* 8, 6655–6663. doi: 10.5194/acp-8-6655-2008

Gutmann, A., Bobrowski, N., Roberts, T., Rüdiger, J., and Hoffmann, T. (2018). Advances in bromine speciation in volcanic plumes. *Front. Earth Sci.* 6:24. doi: 10.3389/feart.2018.00213

Hase, F., Hannigan, J., Coffey, M., Goldman, A., Hopfner, M., Jones, N., et al. (2004). Intercomparison of retrieval codes used for the analysis of high-resolution, ground-based FTIR measurements. *J. Quant. Spectrosc. Radiat. Transfer* 87, 25–52. doi: 10.1016/j.jqsrt.2003.12.008

Hirabayashi, J., Ossaka, J., and Ozawa, T. (1982). Relationship between volcanic activity and chemical composition of volcanic gases; a case study on the Sakurajima Volcano. *Geochem. J.* 16, 11–21. doi: 10.2343/geochemj.16.11

Lee, S., Kang, N., Park, M., Hwang, J. Y., Yun, S. H., and Jeong, H. Y. (2018). A review on volcanic gas compositions related to volcanic activities and non-volcanological effects. *Geosci. J.* 22, 183–197. doi: 10.1007/s12303-017-0056-y

Love, S. P., Goff, F., Counce, D., Siebe, C., and Delgado, H. (1998). Passive infrared spectroscopy of the eruption plume at Popocatépetl volcano, Mexico. *Nature* 396, 563–567. doi: 10.1038/25109

Manga, M., Mitchell, S. J., Degruyter, W., and Carey, R. J. (2018). Transition of eruptive style: pumice raft to dome-forming eruption at the havre submarine volcano, Southwest Pacific Ocean. *Geology* 46, 1075–1078. doi: 10.1130/G45436.1

Martel, C., and Schmidt, B. C. (2003). Decompression experiments as an insight into ascent rates of silicic magmas. *Contrib. Mineral. Petrol.* 144, 397–415. doi: 10.1007/s00410-002-0404-3

Martin, R., Wheeler, J., Ilyinskaya, E., Braban, C., and Oppenheimer, C. (2012). The uptake of halogen (HF, HCl, HBr and HI) and nitric (HNO_3) acids into acidic sulphate particles in quiescent volcanic plumes. *Chem. Geol.* 296, 19–25. doi: 10.1016/j.chemgeo.2011.12.013

Maters, E. C., Delmelle, P., and Bonneville, S. (2016). Atmospheric processing of volcanic glass: effects on iron solubility and redox speciation. *Environ. Sci. Technol.* 50, 5033–5040. doi: 10.1021/acs.est.5b06281

McCormick, B. T., Herzog, M., Yang, J., Edmonds, M., Mather, T. A., Carn, S. A., et al. (2014). A comparison of satellite-and ground-based measurements of so^2 emissions from tungurahua volcano, ecuador. *J. Geophys. Res.* 119, 4264–4285. doi: 10.1002/2013JD019771

Mori, T., and Notsu, K. (2008). Temporal variation in chemical composition of the volcanic plume from Aso volcano, Japan, measured by remote FT-IR spectroscopy. *Geochem. J.* 42, 133–140. doi: 10.2343/geochemj.42.133

Mori, T., Sato, M., Shimoike, Y., and Notsu, K. (2002). High SiF_4/HF ratio detected in Satsuma-Iwojima volcano's plume by remote FT-IR observation. *Earth Planets Space* 54, 249–256. doi: 10.1186/BF03353024

Notsu, K., and Mori, T. (2010). Chemical monitoring of volcanic gas using remote FT-IR spectroscopy at several active volcanoes in Japan. *Appl. Geochem.* 25, 505–512. doi: 10.1016/j.apgeochem.2010.01.008

Oppenheimer, C., Edmonds, M., Francis, P., and Burton, M. (2002). Variation in HCl/SO_2 gas ratios observed by fourier transform spectroscopy at Soufrière Hills volcano, Montserrat. *Geol. Soc. Lond. Memoirs* 21, 621–639. doi: 10.1144/GSL.MEM.2002.021.01.31

Roberge, J., Delgado-Granados, H., and Wallace, P. J. (2009). Mafic magma recharge supplies high CO_2 and SO_2 gas fluxes from Popocatépetl volcano, Mexico. *Geology* 37:107. doi: 10.1130/G25242A.1

Rothman, L. S., Jacquemart, D., Barbe, A., Benner, D. C., Birk, M., Brown, L., et al. (2005). The HITRAN 2004 molecular spectroscopic database. *J. Quant. Spectrosc. Radiat. Trans.* 96, 139–204. doi: 10.1016/j.jqsrt.2004.10.008

Salerno, G. G., Burton, M., Di Grazia, G., Caltabiano, T., and Oppenheimer, C. (2018). Coupling between magmatic degassing and volcanic tremor in basaltic volcanism. *Front. Earth Sci.* 6:157. doi: 10.3389/feart.2018.00157

Schiavo, B., Stremme, W., Grutter, M., Campion, R., Guarin, C. A., Rivera, C., et al. (2019). Characterization of a UV camera system for So2 measurements from popocatépetl volcano. *J. Volcanol. Geother. Res.* 370, 82–94. doi: 10.1016/j.jvolgeores.2018.09.001

Shinohara, H., Ohminato, T., Takeo, M., Tsuji, H., and Kazahaya, R. (2015). Monitoring of volcanic gas composition at Asama volcano, Japan, during 2004-2014. *J. Volcanol. Geother. Res.* 303, 199–208. doi: 10.1016/j.jvolgeores.2015.07.022

Siebe, C., Abrams, M., Macias, J. L., and Obenholzner, J. (1996). Repeated volcanic disasters in Prehispanic time at Popocatépetl, central Mexico: past key to the future? *Geology* 24:399. doi: 10.1130/0091-7613(1996)024<0399:RVDIPT>2.3.CO;2

Stremme, W., Krueger, A., Harig, R., and Grutter, M. (2012). Volcanic SO_2 and SiF_4 visualization using 2-D thermal emission spectroscopy - Part 1: Slant-columns and their ratios. *Atmos. Measure. Tech.* 5, 275–288. doi: 10.5194/amt-5-275-2012

Stremme, W., Ortega, I., Siebe, C., and Grutter, M. (2011). Gas composition of Popocatépetl Volcano between 2007 and 2008: FTIR spectroscopic measurements of an explosive event and during quiescent degassing. *Earth Planet. Sci. Lett.* 301, 502–510. doi: 10.1016/j.epsl.2010.11.032

Taquet, N., Hernández, I. M., Stremme, W., Bezanilla, A., Grutter, M., Campion, R., et al. (2017). Continuous measurements of SiF_4 and SO_2 by thermal emission spectroscopy: insight from a 6-month survey at the Popocatépetl volcano. *J. Volcanol. Geotherm. Res.* 341, 255–268. doi: 10.1016/j.jvolgeores.2017.05.009

Witter, J. B., Kress, V. C., and Newhall, C. G. (2005). Volcan Popocatépetl, Mexico. Petrology, magma mixing, and immediate sources of volatiles for the 1994 present eruption. *J. Petrol.* 46, 2337–2366. doi: 10.1093/petrology/egi058

Yang, K., Krotkov, N. A., Krueger, A. J., Carn, S. A., Bhartia, P. K., and Levelt, P. F. (2007). Retrieval of large volcanic SO_2 columns from the aura ozone monitoring instrument: comparison and limitations. *J. Geophys. Res. Atmospheres* 112, 24–43. doi: 10.1029/2007JD008825

Conflict of Interest Statement: The authors declare that the research was conducted in the absence of any commercial or financial relationships that could be construed as a potential conflict of interest.

The handling editor declared a past co-authorship with one of the authors FH.

frontiers in Earth Science

ORIGINAL RESEARCH
published: 02 July 2019
doi: 10.3389/feart.2019.00132

Variation of the BrO/SO_2 Molar Ratio in the Plume of Tungurahua Volcano Between 2007 and 2017 and Its Relationship to Volcanic Activity

Simon Warnach[1,2], Nicole Bobrowski[1,2], Silvana Hidalgo[3], Santiago Arellano[4], Holger Sihler[1,2], Florian Dinger[1,2], Peter Lübcke[2], Jean Battaglia[5], Alexander Steele[6], Bo Galle[4], Ulrich Platt[1,2] and Thomas Wagner[1]*

[1] Max Planck Institute for Chemistry, Satellite Remote Sensing, Mainz, Germany, [2] Institute of Environmental Physics, University of Heidelberg, Heidelberg, Germany, [3] Instituto Geofísico, Escuela Politécnica Nacional, Quito, Ecuador, [4] Department of Space, Earth and Environment, Chalmers University of Technology, Gothenburg, Sweden, [5] Laboratoire Magmas et Volcans, Observatoire de Physique du Globe de Clermont-Ferrand (OPGC), IRD, CNRS, Université Clermont Auvergne, Aubière, France, [6] UCL Hazard Centre, Department of Earth Sciences, University College London, London, United Kingdom

Recent long-term observations of the bromine monoxide (BrO) to sulphur dioxide (SO_2) molar ratio in volcanic plumes have suggested a link between changes in the BrO/SO_2 ratio and the volcanic activity. Nevertheless, understanding of the mechanisms determining this link is still limited due to the lack of studies on volcanic bromine release from the melt into the atmosphere. We present the results of 10 years (2007–2017) of observations of the BrO/SO_2 molar ratio in the volcanic plume of Tungurahua volcano, Ecuador. Following the nearly continuous eruptive activity from 1999 to 2008, Tungurahua showed alternating phases of eruptive activity separated by periods of quiescence between late 2008 and March 2016, after which degassing intensity decreased below detection. By comparing the BrO/SO_2 molar ratios collected from 13 eruptive phases to volcanic activity, this study aims to broaden the global observational database investigating their link. For this purpose, we combine three different methods to retrieve the BrO/SO_2 molar ratio to analyse variations over different timescales. We identify a cyclic pattern in BrO/SO_2 molar ratios for 11 of the 13 eruptive phases. The phases are initialised by low BrO/SO_2 molar ratios between 2 and 6 $\times 10^{-5}$ coinciding with vulcanian-type activity followed by a strong increase to ratios ranging between 4 and 17 $\times 10^{-5}$ when eruptive dynamism shifts to strombolian. For five phases, we additionally observe a progressive decrease to the initial values of 2 to 5 $\times 10^{-5}$ toward the end of the phase. This clear pattern indicates a connection between the BrO/SO_2 molar ratio and eruptive dynamics. Based on our new data, we propose a conceptual model of the volcanic processes taking place at Tungurahua during the eruptive phases. Our data furthermore indicate that maximal BrO/SO_2 molar ratios observed during each phase could be related to the input of volatile-rich magma into the active part of the volcanic system of Tungurahua. This study shows that long-term BrO/SO_2 molar ratios can be used as a proxy for the volatile status as well as temporal evolution of the volcanic system.

Keywords: Tungurahua, SO_2, BrO, ratio, degassing, volcano, DOAS, NOVAC

Edited by:
Alessandro Aiuppa,
University of Palermo, Italy

Reviewed by:
Mattia Pistone,
Université de Lausanne, Switzerland
Stefan Bredemeyer,
Helmholtz Centre Potsdam, Germany

***Correspondence:**
Simon Warnach
s.warnach@mpic.de

Specialty section:
This article was submitted to Volcanology, a section of the journal Frontiers in Earth Science

Received: 31 July 2018
Accepted: 14 May 2019
Published: 02 July 2019

Citation:
Warnach S, Bobrowski N, Hidalgo S, Arellano S, Sihler H, Dinger F, Lübcke P, Battaglia J, Steele A, Galle B, Platt U and Wagner T (2019) Variation of the BrO/SO_2 Molar Ratio in the Plume of Tungurahua Volcano Between 2007 and 2017 and Its Relationship to Volcanic Activity. Front. Earth Sci. 7:132. doi: 10.3389/feart.2019.00132

INTRODUCTION

The molar ratios of gas species in volcanic plumes offer crucial information about volcanic processes. Sulphur dioxide (SO_2) emissions have in some cases proven to be a good forecasting tool for volcanic eruptions (e.g. Malinconico, 1979; Olmos et al., 2007; Hidalgo et al., 2018). Moreover, the halogen to sulphur ratios have been used for detecting changes in volcanic activity due to the different melt-fluid partitioning coefficients of these elements (Noguchi and Kamiya, 1963; Carrol and Holloway, 1994).

Changes in the chlorine to sulphur ratio have been suggested to forecast eruptions (Menyailov, 1975) and to distinguish different types of activity (Pennisi and Cloarec, 1998; Allard et al., 2005; Aiuppa, 2009; Spina et al., 2015). Several studies interpreting these measurements advocated preferred release of chlorine and fluorine at low pressures corresponding to shallow depth beneath the volcanic vent (Noguchi and Kamiya, 1963; Villemant and Boudon, 1999; Aiuppa et al., 2002; Burton et al., 2007; Edmonds et al., 2009). For bromine in contrast, the degassing processes are still not fully understood and lack comparison of measurements with model data. Several studies investigated melt-fluid partitioning of bromine with respect to sulphur using artificial melts (Bureau et al., 2000, 2010; Cochain et al., 2015) and concluded that the partition coefficient highly depends on the melt composition. A recent study using natural melts suggested efficient degassing of bromine at shallow depths beneath the volcanic vent similar to chlorine behaviour (Cadoux et al., 2018).

Since the first detection of bromine monoxide (BrO) inside a volcanic plume (Bobrowski et al., 2003), BrO as well as the BrO/SO_2 molar ratio have been retrieved at various volcanoes using ground-based measurements (e.g. Oppenheimer et al., 2006; Bobrowski and Platt, 2007; Kern et al., 2009; Boichu et al., 2011; Kelly et al., 2013) as well as from satellite (Theys et al., 2009; Hörmann et al., 2013). In addition, bromine chemistry in volcanic plumes has also been investigated through plume-chemistry models (e.g. Bobrowski et al., 2007; von Glasow, 2010; Roberts et al., 2014). A review of the current knowledge of bromine chemistry in volcanic plumes as well as a collection of all volcanic bromine measurements since 2003 was reported by Gutmann et al. (2018).

Recent studies of long-term BrO/SO_2 datasets have revealed changes in connection with varying volcanic activity at Mount Etna (Bobrowski and Giuffrida, 2012) and Nevado del Ruiz (Lübcke et al., 2014), or due to external forcing such as Earth tides (Dinger et al., 2018). The advantage of the BrO/SO_2 molar ratio compared to other halogen/sulphur ratios is that both species can be measured simultaneously via automated remote-sensing using scattered sunlight spectra applying the Differential Optical Absorption Spectroscopy (DOAS) technique (Platt and Stutz, 2008). This allows for continuous long-term data retrieval throughout different states of volcanic activity (Galle et al., 2010).

This study focuses on Tungurahua volcano, an andesitic subduction volcano located 120 km south of Quito, Ecuador. The average magma supply rates for this volcano have been estimated at $\approx 1.5 \times 10^6$ m^3yr^{-1} over the last 2300 years (Hall et al., 1999). Regular eruptions occurred at least once per century (Pennec et al., 2008; Bablon et al., 2018). Hence, Tungurahua is among the most active volcanoes in the northern Andes in recent times (Hall et al., 1999; Wright et al., 2012). The most recent eruptive cycle started in September 1999. From 1999 until late 2008 Tungurahua exhibited long periods of continuous eruptive activity (Arellano et al., 2008; Samaniego et al., 2011; Hidalgo et al., 2015), with typical SO_2 emission rates of the order of 1000 t/d derived from ground-based measurements (Arellano et al., 2008; Galle et al., 2010) and from satellite (Carn et al., 2008; McCormick et al., 2014). From 2008 to 2016, however, the activity has been characterised by alternating eruptive phases and relative quiescence. Eruptive phases have displayed strombolian to vulcanian explosions, which were accompanied by persistent ash and gas emissions, and sporadic pyroclastic flows and lava effusion (Hidalgo et al., 2015).

We investigate the variation of the BrO/SO_2 molar ratio in the plume of Tungurahua from the spectral data recorded by a network of four autonomous scanning-DOAS stations over the period March 2007 to January 2017. To improve readability, we will refer to all ratios by omitting "molar" in the rest of the manuscript, e.g. BrO/SO_2 ratio. The different eruptive phases are decomposed into different stages, in order to identify characteristic patterns in the BrO/SO_2 ratio. We identify a pattern which was repeatedly observed throughout phases over the whole period of investigation. We interpret it with respect to magmatic processes and volcanic activity and derive a conceptual model of the eruptive dynamic representative for each eruptive phase. Lastly, we also discuss the behaviour of the BrO/SO_2 ratios in relation to different types of explosive activity.

MATERIALS AND METHODS

Measurement Setup

At Tungurahua volcano, four stations were run during the study period by the IG-EPN (Instituto Geofísico – Escuela Politécnica Nacional), all of which operated with NOVAC (Network for Observation of Volcanic and Atmospheric Change) version 1 instruments (Galle et al., 2010). The instruments were located 6–11 km from the volcanic vent, with three stations to the west of the crater, in the direction of the prevalent plume direction, and one to the north-east (for a detailed description of the location of the instruments see Hidalgo et al., 2015).

NOVAC currently comprises automatic scanning DOAS instruments at more than 40 volcanoes. The instruments measure volcanic plume constituents by performing a scan across the sky, which is comprised typically of 51 spectra obtained in steps of 3.6°. The scanning plane intersects the volcanic plume under favourable wind conditions. Furthermore, the intersection of simultaneous measurements by different instruments is used to derive plume height and direction, allowing – with knowledge of the wind speed – for the calculation of fluxes (Galle et al., 2010). However, these variables are not needed to extract BrO/SO_2 ratios, which purely depend on the spectral measurements.

Spectroscopic Retrieval

The amount of SO_2 and BrO in the plume was retrieved via a DOAS analysis comparing the spectra measured in the direction of the volcanic plume with spectra in a direction not intercepting the volcanic plume. To improve the signal-to-noise ratio in this work the co-adding retrieval algorithm was used as described in Lübcke et al. (2014): The algorithm identifies 10 plume spectra (having the highest SO_2 values) and 10 reference spectra (having the lowest SO_2 values) in each scan. The algorithm then co-adds these spectra, respectively from four consecutive scans (i.e. 40 spectra of each type in total). The resulting spectra, which are from now on referred to as "co-added" spectra, are then used as measurement and reference spectrum in the DOAS fitting algorithm, respectively (Platt and Stutz, 2008). This yielded one co-added BrO as well as one SO_2 mean slant column density (SCD) roughly every 30 min.

Fit Parameter

In addition to the co-added plume and reference spectra, the DOAS fitting algorithm also included absorption cross-sections for SO_2 (Vandaele et al., 2009) and O_3 (Burrows et al., 1999) in the SO_2 spectral fit region (314.8–326.8 nm) and SO_2, BrO (Fleischmann et al., 2004), O_4 (Hermans et al., 2003), NO_2 (Vandaele et al., 1998) and CH_2O (Meller and Moortgat, 2000) in the BrO spectral fit region (330.6–352.75 nm) as well as a third-order polynomial to account for broadband absorption structures, Mie, and Rayleigh scattering. Two spectra were included to account for the Ring effect (Grainger and Ring, 1962) – the standard Ring spectrum as well as a wavelength dependent Ring spectrum (derived from the original Ring spectrum by multiplication with λ^4, where λ represents wavelength; Wagner et al., 2009). The fit settings were chosen as an outcome of the study by Vogel et al. (2013).

The detection limit can be derived as a multiple of the DOAS fit error based on Platt and Stutz (2008). In our study we used three times the fit error – which is usually a quite conservative estimate – yielding here a mean detection limit of 4.9×10^{16} molecules/cm^2 (SO_2) and 4.9×10^{13} molecules/cm^2 (BrO). The latter fits very well to the random fluctuations of BrO around zero when SO_2 SCDs are close to zero (i.e. no gas emissions), which similarly span roughly $\pm 5 \times 10^{13}$ molecules/cm^2. For SO_2 this fluctuation is hardly visible, because the signal is up to two orders of magnitude larger than the detection limit.

Determining the BrO/SO_2 Ratio

The BrO/SO_2 ratio for a series of simultaneous measurements of both species inside a volcanic plume is usually obtained by performing a linear regression for BrO as a function of SO_2 (e.g. Bobrowski et al., 2003, 2007; Bobrowski and Giuffrida, 2012; Hörmann et al., 2013). The linear regression was performed using the error-weighted orthogonal regression algorithm developed by Cantrell (2008).

For this study, it was employed in two ways:

1. Daily regression: This regression takes all co-added BrO and SO_2 data of a particular day to retrieve daily BrO/SO_2 ratios in order to observe short-term changes in the BrO/SO_2 ratio. To ensure the quality of the retrieved BrO/SO_2 ratio, days were considered only if at least one data point exceeded SO_2 SCDs of 5×10^{17} molecules/cm^2 and the regression fit error was below 1.5×10^{-5}.
2. Period regression: Data acquired over the period of several days/weeks were evaluated using the same methodology as for the daily regression. The beginning and end of these periods were chosen when a change in the daily BrO/SO_2 ratios could be detected. For long periods without significant change, the beginning and end of these periods were additionally chosen when changes in the classification of explosive activity from Hidalgo et al. (2015) occurred. Only those periods where at least five co-added SO_2 SCDs exceeded 5×10^{17} molecules/cm^2, the maximum SO_2 SCD exceeded 7×10^{17} molecules/cm^2, and the regression fit error was below 1×10^{-5} were taken into account.

We also calculated the BrO/SO_2 ratio by taking the BrO/SO_2 ratio of every co-added data point with high SO_2 signal (SO_2 SCD $> 7 \times 10^{17}$ molecules/cm^2). In a second step, the daily mean BrO/SO_2 ratio was calculated as the error-weighted daily mean over these single BrO/SO_2 ratios. To ensure robust results we calculated the daily mean BrO/SO_2 ratio only if there were at least five data points above the SO_2 threshold. An example of the results obtained by this algorithm for 28 December 2010 is given in **Figure 1A**. This method was used by Lübcke et al. (2014) for NOVAC data and we will refer to it as "daily means" in this study.

In this study, we introduce a scheme including all three methods, the daily means method as well as the two linear regression methods to achieve a sufficient set of BrO/SO_2 ratios. They are presented in **Figure 1**. The daily mean method yielded BrO/SO_2 ratios on 277 days, while the daily regression was successful on 425 days. Of the 276 days, in which both methods yielded a BrO/SO_2 ratio, we observed a good correlation between the two methods. However, the daily mean method consistently yielded slightly lower ratios (we retrieved a slope of 0.86 ± 0.05; see **Figure 2**). The results of all daily mean and daily regression BrO/SO_2 ratios as a function of time are plotted in **Figure 3C**.

Volcanic Activity Classification

We used the classification criteria of volcanic activity described by Hidalgo et al. (2015), which includes the eruptive and quiescent phases from 2007 to 2013. We extended this classification in order to cover our study period following the same criteria (i.e. seismo-acoustic records and visual observations).

Three types of activity were distinguished during the study period: (1) Quiescence, (2) Low explosive activity and (3) High explosive activity. Episodes of high explosive activity are those in which discrete vulcanian explosions occurred, with the explosions themselves being classified as vulcanian when their mean acoustic excess pressures were greater than 100 Pa at a distance of 1 km from the vent (Johnson, 2003). Episodes of low explosive activity are those in which no vulcanian explosions were present. These episodes were

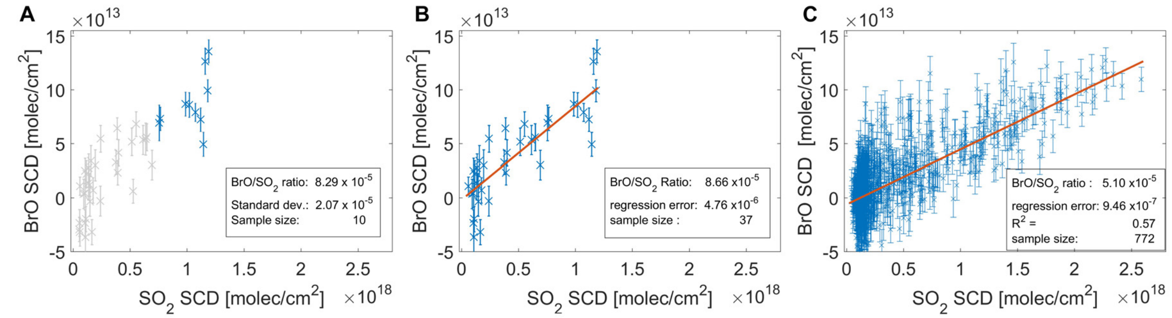

FIGURE 1 | Examples for the three different methods to calculate the BrO/SO_2 ratio: **(A)** "daily mean" method for 28 December 2010. The complete set of retrieved BrO and SO_2 SCDs during this day is plotted in grey. The daily mean BrO/SO_2 ratio is calculated as the mean from all values exceeding the SO_2 threshold of 7×10^{17} molecules/cm^2 (blue). Calculated ratio: 8.29×10^{-5}. **(B)** Daily regression for 28 December 2010. Retrieved ratio: 8.66×10^{-5}. **(C)** Period regression for the period from 22 November–25 December 2010, Retrieved ratio: 5.10×10^{-5}.

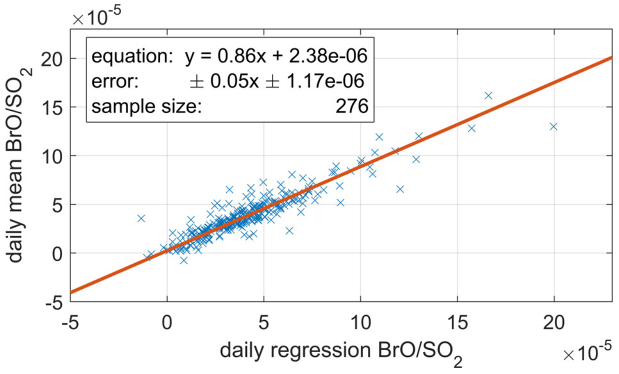

FIGURE 2 | Error-weighted linear regression plot (using the method from Cantrell, 2008) between the daily mean and the daily regression BrO/SO_2 ratios of the 276 acquisition days, in which both methods yielded a BrO/SO_2 ratio. The fit result is written in the upper left corner and plotted by a red line. Error bars have been omitted for the sake of clarity.

instead characterised by Strombolian-type activity, during which the explosions had excess pressures smaller than the 100 Pa threshold (Johnson, 2003). In both cases, explosive activity is commonly accompanied by intense gas and ash emissions. During quiescent episodes, the seismic activity was generally weak and merely a few long period and volcano-tectonic earthquakes were detected.

RESULTS

BrO and SO_2 SCDs From Tungurahua

Over the study period between 2007 and 2017, 18 phases of high SO_2 SCDs (of the order of 10^{18} molecules/cm^2) could be identified from the NOVAC data. They were separated by periods of weak SO_2 degassing, where the SO_2 SCDs generally did not exceed 1.6×10^{17} molecules/cm^2. BrO SCDs exceeded the detection limit of 4.8×10^{13} molecules/cm^2 only during phases where high SO_2 SCDs were measured. In those phases typical BrO SCDs around 8×10^{13} molecules/cm^2 were observed. During the phases of weak SO_2, BrO fluctuated around zero and was below detection. The results of BrO and SO_2 from Tungurahua are displayed in **Figures 3A,B**.

BrO/SO_2 Ratios

BrO/SO_2 ratios typically ranged between 2 and 8×10^{-5}, which is similar to ratios observed at other arc volcanoes in the Northern Volcanic Zone of the Andes, such as Nevado del Ruiz (Lübcke et al., 2014) and Cotopaxi (Dinger et al., 2018). In 2009 and the first half of 2010, relatively constant BrO/SO_2 ratios of 2 to 6×10^{-5} were observed. This contrasts with periods in 2008 and after 2010, where a larger range of ratios between 2 and 20×10^{-5} were detected. During the intermitting periods of weak SO_2 degassing, we could only infer an upper limit for the BrO/SO_2 ratio, calculated as the ratio between the BrO detection limit and the maximal SO_2 SCD during these periods:

$$\left(\frac{\mathrm{BrO}}{\mathrm{SO_2}}\right)_{\text{upper limit}} = \frac{\mathrm{BrO\ SCD_{detection\ limit}}}{\mathrm{SO_2\ SCD_{max,\ during\ low\ SO_2\ periods}}} \approx \frac{4.8 \times 10^{13}}{1.6 \times 10^{17}} = 3 \times 10^{-4}$$

Since this value far exceeds even the largest BrO/SO_2 ratios observed during phases of high SO_2 SCDs, we are not able to draw any conclusion from BrO/SO_2 ratios during these phases of low SO_2 at Tungurahua.

Dynamic of the BrO/SO_2 Ratio at Tungurahua

We identified changing BrO/SO_2 ratios during 11 phases of high SO_2 SCDs, which we number with roman numerals in chronological order (see **Figure 3A**). We identified a characteristic pattern in the BrO/SO_2 ratio over the course of each phase. For two phases (I and VII) the pattern is observed more than once and we separate this by adding the suffix a and b to the phase numbering, thus adding up to 13 phases, where we observe the BrO/SO_2 pattern. This pattern can be divided into

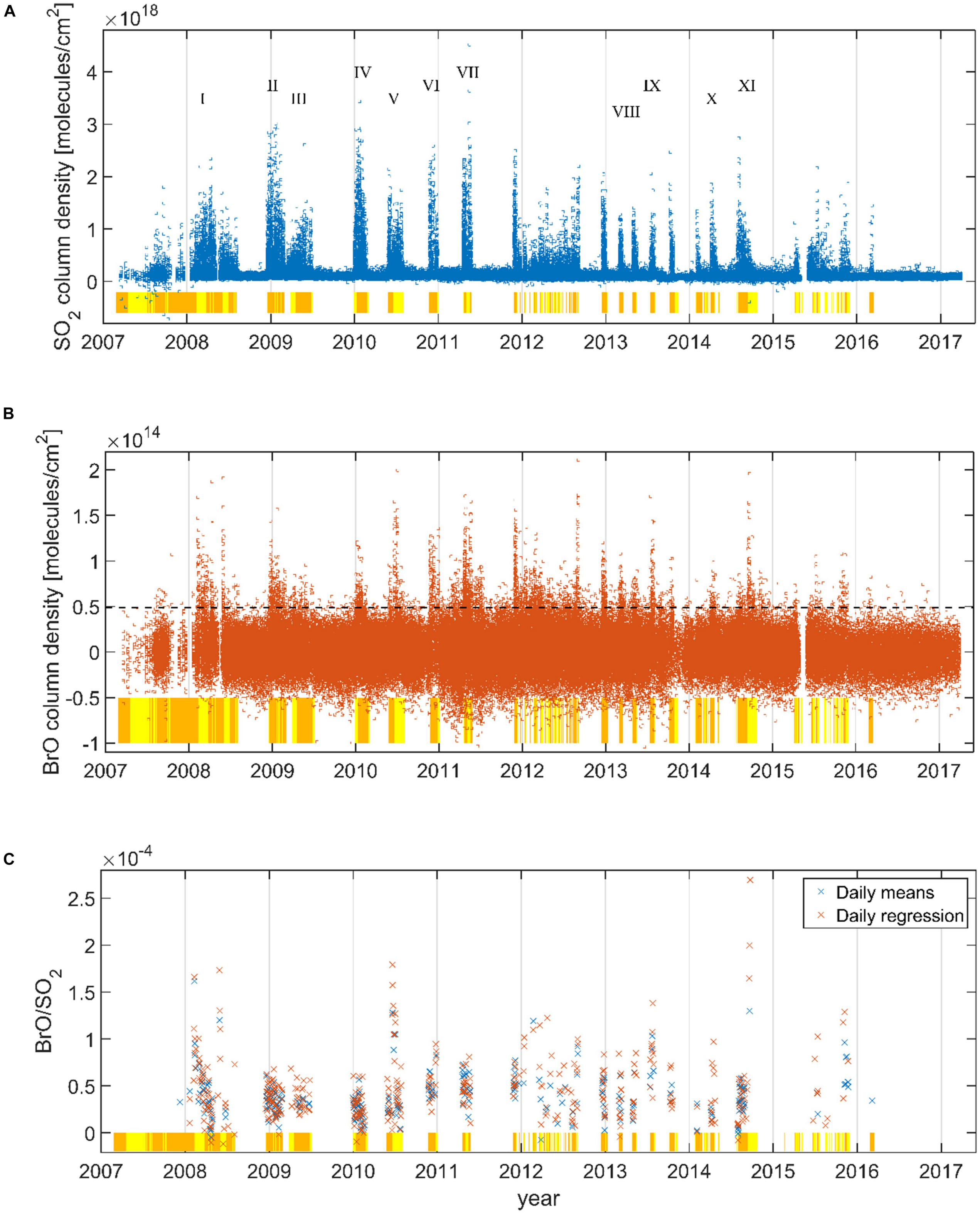

FIGURE 3 | Time-series of the co-added results for **(A)** SO_2 SCDs and **(B)** BrO SCDs for the NOVAC stations at Tungurahua volcano from March 2007 until March 2017. **(C)** the daily mean BrO/SO_2 ratios are plotted for both calculation methods. The coloured areas at the bottom of each plos indicates the volcanic activity derived from seismo-acoustic data (Hidalgo et al., 2015): high explosive activity (orange) and low explosive activity (yellow). The SO_2 detection limit is 4.9×10^{16} molecules/cm^2 and the BrO detection limit is 4.9×10^{13} molecules/cm^2 (indicated by the dashed line). The 11 eruptive phases discussed later in the manuscript are included with roman numerals in **(A)**.

four stages, consisting of two initial stages (0 and 1), followed by an intermediate stage 2 and an ending stage 3. The separation of the initial stages into stage 0 and 1 could only be derived for four phases.

Stage 0 exclusively occurred in phases II, III, IV, and VII and typically lasted for periods of time between 2 and 21 days. We observed BrO and SO_2 degassing and BrO/SO_2 ratios between 3 and 6×10^{-5}, with a mean ratio of 4.31×10^{-5}.

Stage 1 was present in every phase. We observed a constant baseline BrO/SO_2 ratio of typically less than 5×10^{-5} (only for phase IX was it significantly higher at 6.20×10^{-5}). Mean ratio: 3.58×10^{-5}.

Stage 2 generally started with a strong increase in bromine emissions, which resulted in a BrO/SO_2 ratio of up to 17×10^{-5}, often twice as high as the ratio during stage 1. If stage 2 continued for more than a week, the ratio progressively decreased until it reached the former baseline level from stage 1. We will denote the latter part of this stage as stage 2b and the former as stage 2a. Stage 2 was observed in 11 phases (see **Table 1**). Mean ratio: 9.22×10^{-5}.

Stage 3 started when the BrO/SO_2 ratio decreased to low BrO/SO_2 ratios, similar to the ones observed in stage 1 ($2–5 \times 10^{-5}$). It could be seen in 5 phases (Ia, Ib, II, V, and X). Mean ratio: 3.44×10^{-5}.

The most significant feature is the strong increase in the BrO/SO_2 ratios from stage 1 to stage 2. This increase was lowest for phases II and VII and highest for phases Ia, Ib, V, and XI. The evolving pattern of BrO/SO_2 ratios through the four stages can be clearly recognised for every phase (see **Figure 4** and **Table 1**).

Evolution of the BrO/SO_2 Ratio Over the Course of Each Phase

Here, we discuss in detail the evolution of the BrO/SO_2 ratio through every phase in chronological order. Phase V – serving as an example – will be discussed in more detail.

Phase I: During phase I (from 19 January to 22 July 2008), we observed the pattern twice. We will refer to them as phase Ia and phase Ib. Phase Ia started with a BrO/SO_2 ratio of 4.54×10^{-5} during the initialisation from 19 January 2008 (stage 1), lasting until an increase to 1.7×10^{-4} was observed on 8 February (stage 2a, lasting for 5 days). The BrO/SO_2 ratio decreased over the following weeks (stage 2b) until baseline levels were reached in March/April 2008 (stage 3, see **Figure 5**). Phase Ib started on 28 April 2008 with a ratio of 2.86×10^{-5}, reaching a short intermediate stage 2 on 28 May 2008, lasting only 6 days. It then decreased to 3.26×10^{-5} until 27 July 2008.

Phases II and III: The pattern is less clear for these phases, where only a small enhancement in the BrO/SO_2 ratio could

TABLE 1 | Overview over all 13 phases: Name, period, stages observed and their respective duration (in days), and the BrO/SO_2 ratio for each of the stages (if present). The evolution of the BrO/SO_2 ratio during the phases is also depicted in **Figure 4**.

Phase	Period (dd.mm.yy)	Stages observed (duration in d)	BrO/SO_2 stage 0	BrO/SO_2 stage 1	BrO/SO_2 stage 2	BrO/SO_2 stage 3
Ia	19.01.08–25.03.08	1- 2- 3 (20- 18- 29)	Below detection	3.88×10^{-5}	1.06×10^{-4}	5.18×10^{-5}
Ib	28.04.08–04.08.08	1- 2- 3 (30- 6- 26)	Below detection	2.86×10^{-5}	1.22×10^{-4}	3.26×10^{-5}
II	16.12.08–01.03.09	0- 1- 2- 3 (2- 32- 8- 5)	3.07×10^{-5}	3.56×10^{-5}	5.57×10^{-5}	2.12×10^{-5}
III	28.03.09–03.07.09	0- 1- 2 (21- 69- 8)	4.84×10^{-5}	3.19×10^{-5}	4.17×10^{-5}	Below detection
IV	30.12.09–04.03.10	0- 1 (12- 45)	3.04×10^{-5}	2.28×10^{-5}	Below detection	Below detection
V	26.05.10–04.08.10	1- 2- 3 (24- 22- 25)	Below detection	2.80×10^{-5}	9.49×10^{-5}	3.16×10^{-5}
VI	22.11.10–25.12.10	1- 2 (34- 9)	Below detection	5.10×10^{-5}	9.00×10^{-5}	Below detection
VIIa	20.04.11–08.05.11	0- 1- 2 (2- 12- 5)	6.31×10^{-5}	4.32×10^{-5}	6.57×10^{-5}	below detection
VIIb	16.05.11–26.05.11	1 (11)	Below detection	4.36×10^{-5}	Below detection	Below detection
VIII	28.04.13–16.05.13	1- 2 (8- 11)	Below detection	2.24×10^{-5}	8.29×10^{-5}	Below detection
IX	14.07.13–05.08.13	1- 2 (6- 17)	Below detection	6.20×10^{-5}	9.19×10^{-5}	Below detection
X	02.04.14–24.04.14	1- 2- 3 (13- 6- 4)	Below detection	2.63×10^{-5}	8.54×10^{-5}	3.27×10^{-5}
XI	02.08.14–25.10.14	1- 2 (41- 44)	Below detection	3.11×10^{-5}	1.78×10^{-4}	Below detection

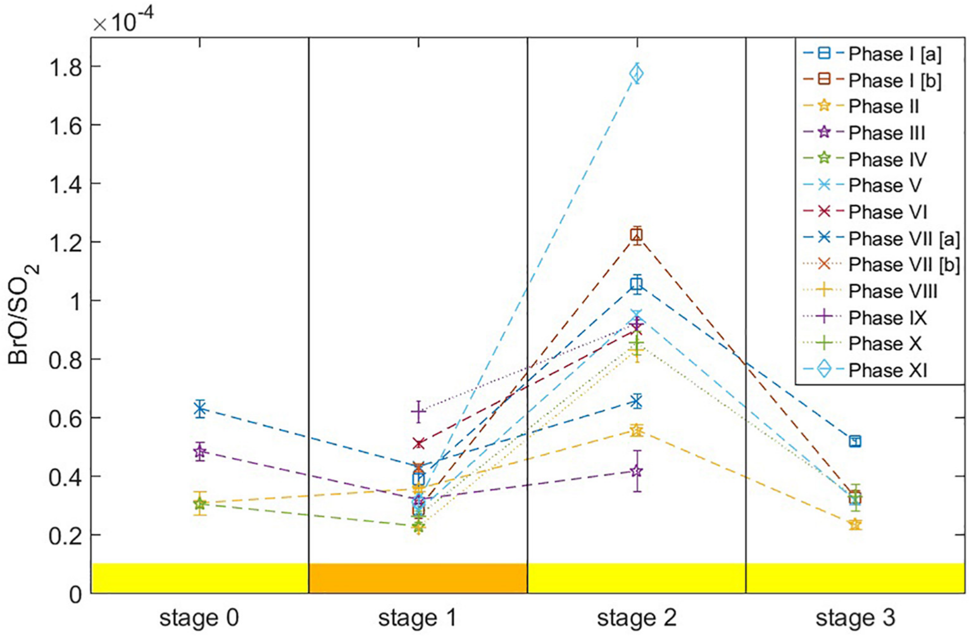

FIGURE 4 | The evolution of the BrO/SO$_2$ ratio during the stages of the different phases. Depicted are the mean BrO/SO$_2$ ratios (period regression) for each of the four stages: stage 0, stage 1, stage 2, and stage 3. The colour at the bottom indicates the most predominant activity classification during each stage (Hidalgo et al., 2015). Detailed discussion in the text.

be observed on 19 January 2009 (phase II) and on 26 June 2009 (phase III).

Phase IV: This phase exclusively consisted of the initial stages 0 and 1 with low BrO/SO$_2$ ratio (2–3 $\times$ 10^{-5}). After stage 1, the gas signal decreased below the detection limit and no BrO/SO$_2$ ratio could be retrieved for stage 2.

Phase V: This phase took place from 29 May until 4 August 2010 and comprised stages 1 to 3. Stage 1, spanning from 29 May until 18 June, was characterised by high SO$_2$ emissions with SO$_2$ SCDs of up to 2 $\times$ 10^{18} molecules/cm^2 while BrO SCDs did not exceed 1 $\times$ 10^{14} molecules/cm^2 (see **Figure 6**, bottom left). During this stage, a mean BrO/SO$_2$ ratio of 2.80 $\times$ 10^{-5} was retrieved. Stage 2 started on 19 June with a strong increase in the BrO/SO$_2$ ratio by more than 1 $\times$ 10^{-4} to 1.7 $\times$ 10^{-4} as a result of a sharp rise in BrO SCDs up to 2 $\times$ 10^{14} molecules/cm^2 (see **Figure 6**, bottom middle). As stage 2 progressed, the BrO/SO$_2$ ratio slowly decreased (stage 2b), reaching previous baseline levels of roughly 3 $\times$ 10^{-5} by 11 July (after 22 days), where it remained throughout stage 3 until the gas emission dropped below the detection limit on 4 August. Both the BrO/SO$_2$ ratio as well as the linear regression results for the three stages of phase V are plotted in **Figure 6**. The period regression of each of these three stages reveals that the gas composition was similar during stages 1 and 3. While the SO$_2$ SCDs were similar for all three stages, BrO SCDs were higher during stage 2, if compared to stages 1 and 3 (**Figure 6**, bottom).

Phases VI to IX and XI exhibited only the initial stages and the intermediate stage 2, with a varying increase in strength from initialisation to stage 2 of 2.3 $\times$ 10^{-5} (during phase VII) to 1.4 $\times$ 10^{-4} (during phase XI).

Phase X: This phase behaved similar to phases VI-IX, but also had a short stage 3.

The detailed depiction of the co-added SO$_2$ and BrO SCDs as well as the BrO/SO$_2$ ratios for every phase can be found in the **Supplementary Materials**.

In 2012, in the second half of 2015, and for six phases between 2013 and 2016, only short periods with few BrO SCDs above the detection limit could be observed and longer period of BrO/SO$_2$ ratios could not be identified. For the six phases between 2013 and 2016 constant BrO/SO$_2$ ratio were calculated, with values ranging from 1.8 to 5.2 $\times$ 10^{-5}, similar to the range during stages 0 and 1.

Relation of the BrO/SO$_2$ Ratio With Explosive Activity

The observed changes in the BrO/SO$_2$ ratio between the different stages in the cycle observed during each phase at Tungurahua can be linked to changes in the explosive activity classification. The classification is closely related to the pattern of the BrO/SO$_2$ ratio in the following way: Stage 0 was typically related to low explosive activity. During Stage 1 – characterised by low BrO/SO$_2$ ratios – explosive activity was always defined as high. The subsequent increase in BrO/SO$_2$ ratios between stage 1 and 2 coincides with a change from high to low explosive activity. Only phases VIII, IX, and X (all after 2012), which are the shortest phases, did not exhibit this change in the classification. For these phases the activity classification remained high throughout stage 2. Stage 3 was generally governed by low explosive activity.

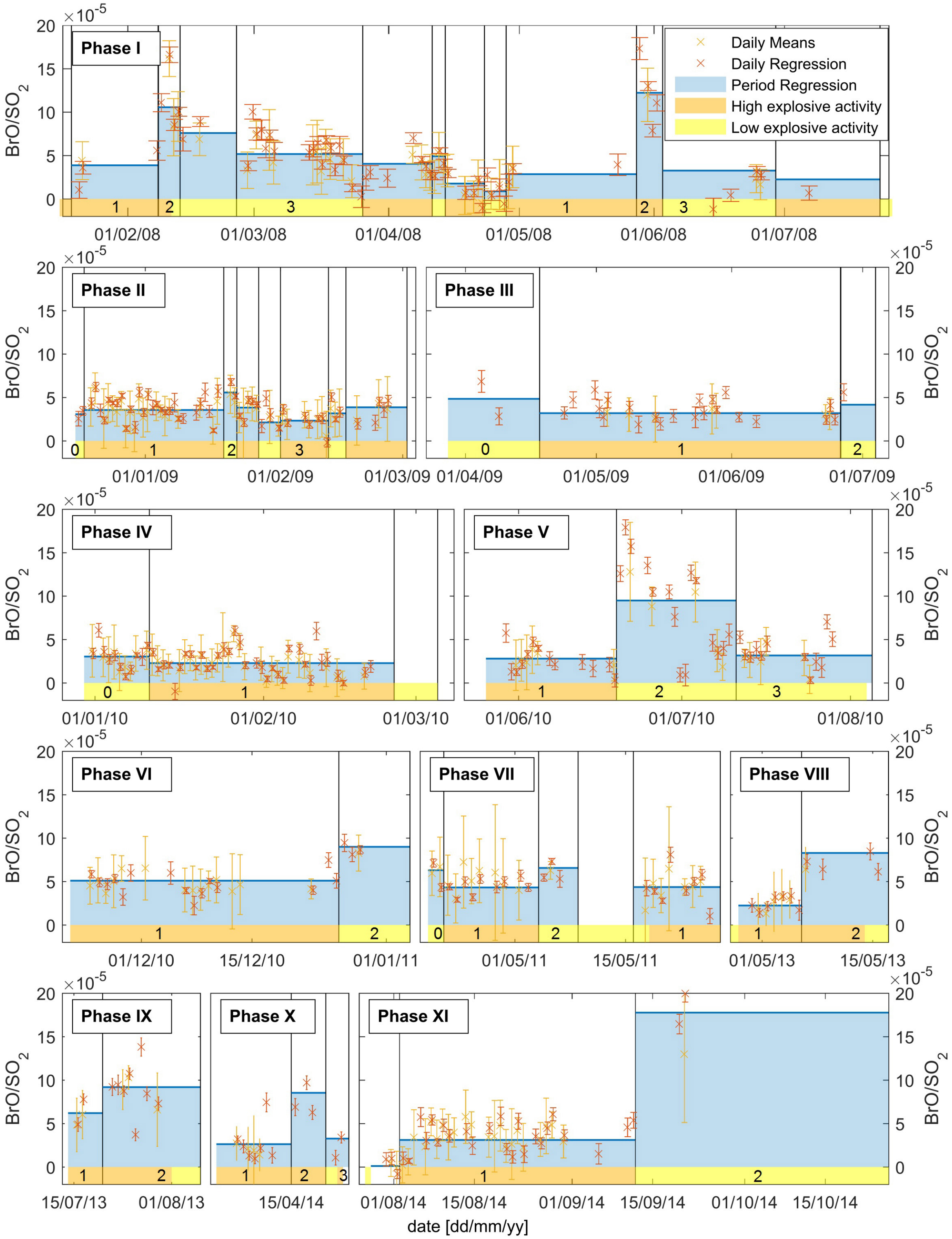

FIGURE 5 | BrO/SO$_2$ ratio over the course of each phase. Mean BrO/SO$_2$ ratio of the different periods (blue area, separated by black lines), the corresponding stage number is marked below the blue area. Furthermore, daily BrO/SO$_2$ from daily regression (red crosses) as well as from daily mean method (yellow crosses) are included. Explosivity classification is marked by yellow (low explosive) and orange area (high explosive).

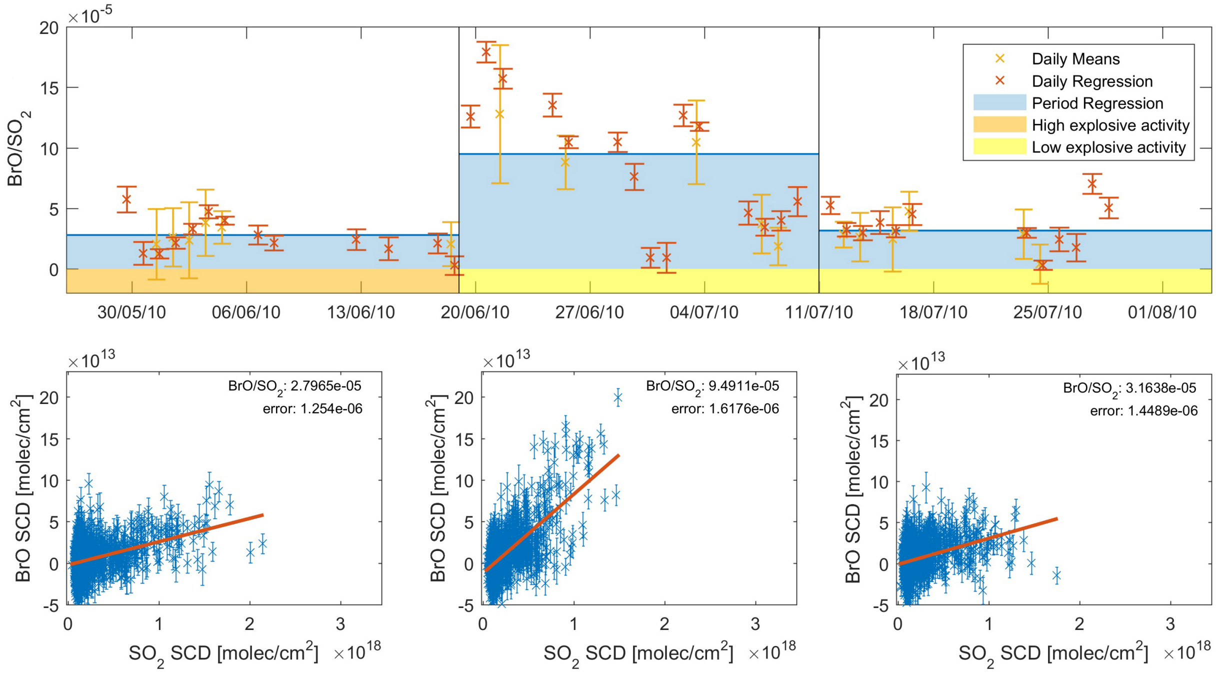

FIGURE 6 | NOVAC data observed during eruptive phase V (26 May–4 August 2010). The three stages (stages 1–3) are separated by vertical lines. Top: The BrO/SO_2 ratio calculated by a period regression for each stage (blue area). Also, the results for the daily regression (red) and daily means method (yellow) are plotted. Activity classification (Hidalgo et al., 2015) is indicated with orange (high explosive) and yellow (low explosive). Bottom: Period regression of the BrO to SO_2 plotted for the three stages.

The fact that for most of the phases the change in activity from high to low explosive activity was linked to an increase in the BrO/SO_2 ratio suggests that this might be inherent to the volcanic system of Tungurahua during the study period. In order to compare the explosive activity classification with the BrO/SO_2 ratio throughout the whole dataset, we performed period regressions for every period of high and low explosive activity. The results are shown in **Figure 7**. While the mean of all BrO/SO_2 ratio during high explosive activity (3.87×10^{-5}) is slightly lower than the mean of all BrO/SO_2 ratios during low explosive activity (5.19×10^{-5}), there is large variance caused by other parameters and thus this difference seems to be not statistically significant.

DISCUSSION

In **Figure 4**, a recurring temporal pattern in the eruptive phases of Tungurahua can be observed. We can summarise our observations as follows:

1. Initiation of degassing with low BrO/SO_2 ratios is observed during the initial stages. These are associated with high SO_2 emissions and strong seismicity, i.e. vulcanian explosions, occurring at the beginning of the eruptive phases.
2. After the initial stages, increased BrO values and nearly unchanged SO_2 emissions are observed in the plume, leading to an increased BrO/SO_2 ratio (observed for 11 of 13 eruptive phases). This typically coincided with the termination of high explosive activity.
3. For five phases, BrO/SO_2 decreased afterward and remained low until SO_2 SCDs decreased below detection. For the other eight phases, degassing had decreased already to a point that SO_2 and BrO were below the limit to calculate meaningful BrO/SO_2 ratios.

Changes of the BrO/SO_2 ratio in the plume of a single volcano have previously been linked to changes in volcanic processes (Bobrowski and Giuffrida, 2012; Lübcke et al., 2014; Dinger et al., 2018), when observing 3 to 20 min old volcanic plumes (e.g. Platt and Bobrowski, 2015; Gutmann et al., 2018). This was assumed to be caused by different melt-fluid partitioning of bromine and sulphur in magmatic melts. Moreover, differences in the BrO/SO_2 ratio among different volcanoes have been attributed to differences in magmatic composition (Platt and Bobrowski, 2015).

The melt-fluid partitioning of halogens (especially of chlorine and fluorine) with respect to sulphur has been the subject of multiple studies (e.g. Spilliaert et al., 2006; Burton et al., 2007). They found lower melt-fluid partitioning of chlorine compared to sulphur and thus concluded that (1) sulphur is usually released from magma earlier than chlorine (Carrol and Holloway, 1994; Spilliaert et al., 2006; Aiuppa, 2009; Webster et al., 2009) and (2) that the Cl/S ratio decreases with increasing degassing source depth (e.g. Burton et al., 2007). Measurements of chlorine and sulphur suggest that chlorine is more significantly released only

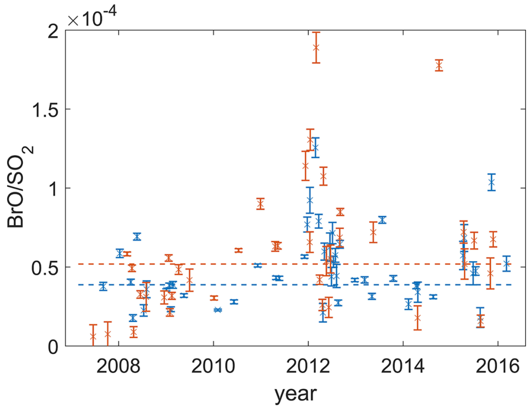

FIGURE 7 | BrO/SO$_2$ ratio calculated for the periods of low explosive activity (red) and high explosive activity (blue) as determined by Hidalgo et al. (2015) throughout the whole dataset 2007–2017. The respective mean ratios are indicated by coloured lines (high explosive activity: 3.87×10^{-5}; low explosive activity: 5.19×10^{-5}).

at shallow depth (typically less than 2 km; Allard et al., 2005; Spina et al., 2015).

However, the melt-fluid partitioning of bromine with respect to sulphur is still not very well constrained. Laboratory studies using natural silicate glasses suggested lower melt-fluid partitioning coefficients for bromine compared to sulphur also (Cadoux et al., 2018). They found melt-fluid partitioning coefficients between 3.8 and 20.8, which are similar to estimates derived from melt inclusions (0.3 to 21; Kutterolf et al., 2015) and from experimental data (2.18 to 9.2 and 17.5; Bureau et al., 2000, 2010).

This is similar to chlorine, where melt-fluid partitioning coefficients were found between 0.3 and 50 (Alletti et al., 2009; Webster et al., 2009; Zajacz et al., 2012). Thus, Cadoux et al. (2018) argue that bromine should behave similarly to chlorine and should be released predominantly during later degassing stages in comparison to sulphur. They assumed sulphur melt-fluid partitioning to be ≈15–20 times larger compared to bromine, based on sulphur melt-fluid partitioning ranging between 3 and 236 (Beermann et al., 2015), and a factor of ≈9 between the chlorine and sulphur partitioning coefficients (Aiuppa, 2009).

Following these studies, and assuming no change in magmatic composition, higher BrO/SO$_2$ ratios should be associated with degassing from magma at shallow depths and lower BrO/SO$_2$ ratios released from magma degassing at deeper levels in the volcanic system.

Conceptual Model of the Evolution of BrO/SO$_2$ During Tungurahua's Eruptive Phases

Based on the BrO/SO$_2$ patterns observed in our study and on the recent studies of Cadoux et al. (2018), we propose a conceptual model that aims to explain the eruptive phases at Tungurahua.

Increasing SO$_2$ and BrO SCDs in combination with low BrO/SO$_2$ ratios are observed at the beginning of the explosive phases (stage 0 and 1). In agreement with increased SO$_2$ fluxes calculated by Hidalgo et al. (2015), we therefore interpret the initialisation of the phase as being driven by the intrusion of gas-rich magma into the upper part of the volcanic system with degassing signature dominated by deep degassing sources.

The increase in the BrO/SO$_2$ ratios on the transition to stage 2 indicates that bromine can partition from the melt more efficiently. SO$_2$ SCDs are similar during stages 1 and 2 (also observed in the SO$_2$ fluxes Hidalgo et al., 2015), implying that the increase in the BrO/SO$_2$ ratio was unlikely to be caused by depletion of SO$_2$ in the melt, but rather caused by a change of the degassing source depth. We thus propose that the magma was degassing at shallower depths during stage 2 (compared to stage 1), promoting bromine partitioning from the melt.

We further propose that the efficient degassing over the course of stage 2 resulted in a faster Br depletion due to its lower abundance in the melt. This led to the decrease in the BrO/SO$_2$ ratios toward the end of stage 2. Together with the corresponding decrease in the SO$_2$ SCDs this implies the interruption of magma intrusion. Stage 3 was thus governed by the degassing from gas-depleted magma until the gas emissions decreased below detection and the phase ends. The proposed conceptual model for the four stages is illustrated in **Figures 8A–D**, respectively.

Based on our observations and data from previous studies (Cadoux et al., 2018), we therefore suggest that each eruptive phase is driven by an intrusion of gas-rich magma, which subsequently degasses under different conditions. However, the amount of magma driving the phase might vary between the different eruptive phases.

Comparison of the Conceptual Model to Petrological Studies

Petrological studies showed that major eruptive phases at Tungurahua, like August 2006 (VEI 3) and May 2010 (phase V in this study), have been triggered by the input of new, hot, volatile-rich magma into a long-lived magmatic reservoir (Samaniego et al., 2011; Myers et al., 2014). Both studies propose an andesitic magma reservoir located at 8–10 km depth, which is coupled to a deeper mafic reservoir, probably located at depth of 15–16 km (Andújar et al., 2017). Myers et al. (2014) suggest that phase V was driven by the ascent of volatile-rich magma from the deeper basaltic andesite magma reservoir resulting in mixing with the upper andesitic, degassed, reservoir. This mechanism can account for the major eruptive phases documented at Tungurahua, and is in agreement with our conceptual model, which proposes the intrusion of volatile-rich magma (at least sulphur- and bromine-rich) as the main triggering process.

The lowest BrO/SO$_2$ ratios are observed for phases III (June 2009) and IV (February 2010), where the BrO/SO$_2$ ratios varied only between 2 and 4×10^{-5}. Thus, the high ratio recorded for phase V (18×10^{-5} at the beginning of stage 2) could indicate a comparatively high input of mafic magma leading toward this eruption (as proposed by Myers et al., 2014) and reciprocally the low BrO/SO$_2$ ratios during phase III and IV indicate low

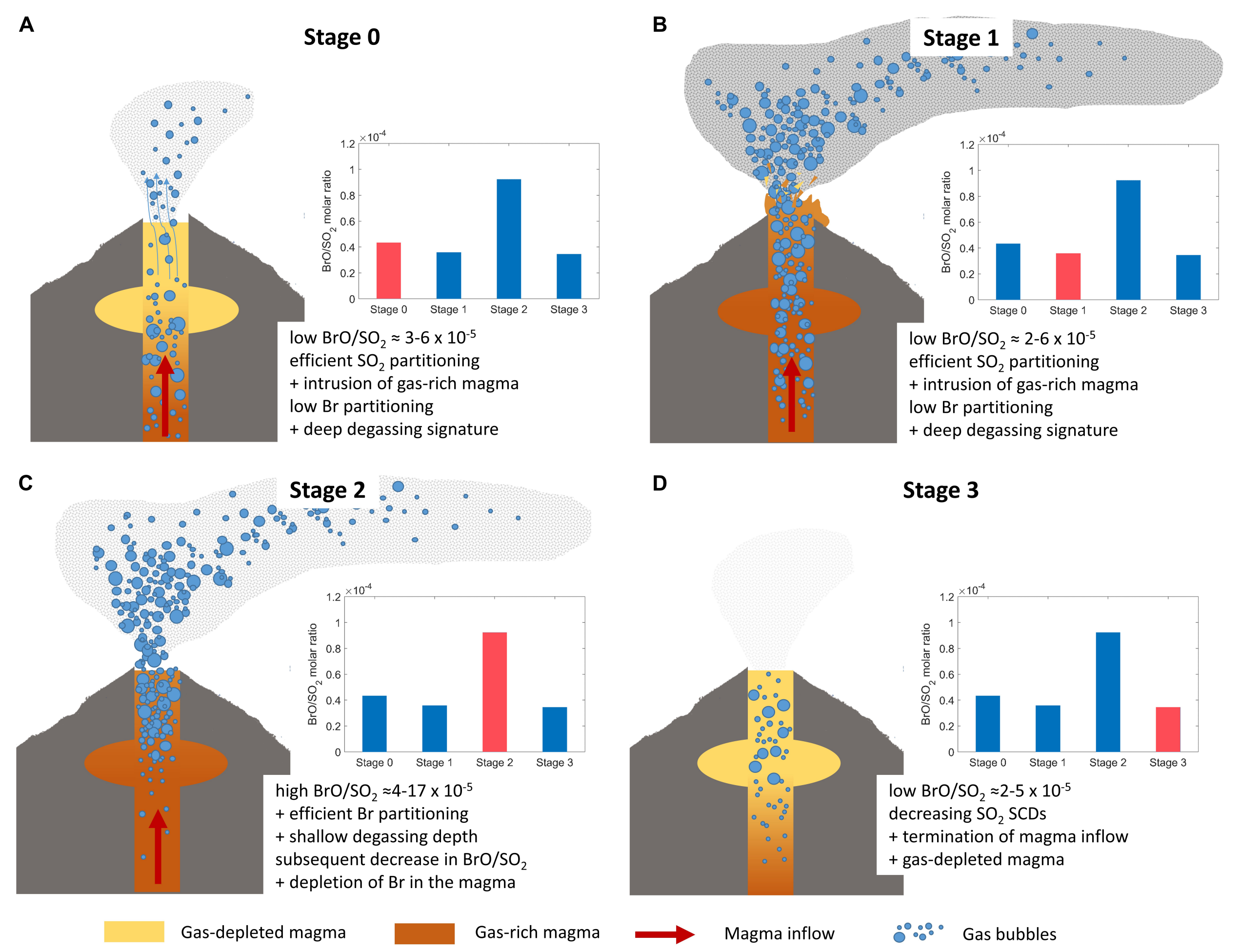

FIGURE 8 | Conceptual model for each of the 13 eruptive phases observed at Tungurahua. **(A,B)** Low BrO/SO$_2$ ratios during initialisation indicate degassing at depth, interpreted as the intrusion of gas-rich magma and deep degassing signature. BrO/SO$_2$ ratios typically between 3 and 6 × 10^{-5} (stage 0, mean ratio: 4.31 × 10^{-5}), and 2 and 6 × 10^{-5} (stage 1, mean ratio: 3.58 × 10^{-5}) were observed. **(C)** Strong increase in the BrO SCDs indicates degassing at shallow depth. BrO/SO$_2$ ratio increased to 4 to 17 × 10^{-5} (stage 2, mean ratio: 9.22 × 10^{-5}). The subsequent decrease in the BrO/SO$_2$ ratio indicates depletion of first Br in the magmatic melt. **(D)** Degassing from magma depleted in gas during stage 3 with low BrO/SO$_2$ ratios between 2 and 5 × 10^{-5} (stage 3: mean ratio: 3.44 × 10^{-5}). Detailed description given in the text.

or no input of volatile-rich mafic magma. Therefore, we can potentially link the BrO/SO$_2$ ratios observed during efficient degassing (stage 2) of the eruptive phases to the respective volatile status of the degassing magma.

Furthermore, it is important to note that during phase V, the energy of the vulcanian explosions was extremely high (Hidalgo et al., 2015) and larger than for the other eruptive phases between 2007 and 2016.

Comparison to Other Studies With Respect to Volcanic Activity

There are other studies similarly discussing long-term trends of BrO/SO$_2$ ratios with respect to changes in volcanic activity. Similar to our study, Bobrowski and Giuffrida (2012) found lower BrO/SO$_2$ ratios during periods of higher volcanic activity at Mount Etna during an observation period of more than 3 years including two long lasting periods of effusive eruptive activity and several more violent events (e.g. lava fountaining). Lübcke et al. (2014) obtained a continuous 3-year time-series of BrO/SO$_2$ ratios at the andesitic arc volcano Nevado del Ruiz. They observed low BrO/SO$_2$ ratios of ≈ 2 × 10^{-5} during a period of high seismic activity and an increase of the BrO/SO$_2$ ratios to ≈5 × 10^{-5} when the seismicity later decreased. This is similar to the behaviour which we observed during the eruptive phases of Tungurahua between the high explosive stage 1 and the low explosive stage 2.

In contrast to the laboratory measurements from Cadoux et al. (2018), Bobrowski and Giuffrida (2012) assumed an earlier bromine melt-fluid partitioning in comparison to sulphur as an interpretation of the spectral measurements, i.e. higher BrO/SO$_2$ ratios during the intrusion of gas-rich magma into the system. A similar hypothesis was proposed by Lübcke (2014), who associated the low BrO/SO$_2$ ratios to shallow degassing during a period of increased seismicity. The increase in BrO/SO_2 ratios during the activity of Cotopaxi in 2015 (Dinger et al., 2018) were, like our study, similarly interpreted in terms of efficient degassing of rising magma in the conduit following the opening of the volcanic system by four phreato-magmatic explosions (Hidalgo et al., 2018).

In contrast to our measurements, the data of Bobrowski and Giuffrida (2012) and Lübcke et al. (2014) additionally enabled to determine BrO/SO_2 ratios during non-eruptive periods and to include those in their interpretation, which could be a reason for the divergence in the interpretation to our study. In order to resolve this divergence in the interpretation of the BrO/SO_2 ratio with respect to magmatic processes and partitioning of gas constituents from the melt, further field studies as well as laboratory studies should be undertaken. For such field studies, we therefore recommend even more comprehensive data collection, including seismic tomography to better determine source regions from a geophysical standpoint.

Multiple studies have investigated the behaviour of other halogens with respect to volcanic activity, predominantly through Cl/S ratio or HCl/SO_2 ratios. Measurements at Mount Etna revealed a decrease in the Cl/S ratio when strombolian activity followed a period of violent lava fountaining, and even lower Cl/S during a phase of passive degassing (Aiuppa et al., 2004). Furthermore, Spina et al. (2015) suggested a correlation with eruption intensity derived from FTIR measurements of HCl/SO_2 ratios at Mount Etna. This contrasts to what we found for the BrO/SO_2 ratio, which could potentially be an indication that bromine and chlorine do not behave similarly as has been assumed here and in several previous studies (Seo and Zajacz, 2016; Cadoux et al., 2018). However, other measurements at Mount Etna did display an increase in the HCl/SO_2 ratio, when explosive activity subsided (Allard et al., 2005).

To our knowledge there is only one study with simultaneous measurements of BrO/SO_2 and Cl/S (Bobrowski et al., 2017). In this work the authors find a positive correlation of both ratios during a one-week period at Nyiragongo volcano in June 2011. Both ratios change concurrently with a significant decrease (several tens of metre) in the height of the lava lake. Another study by Aiuppa et al. (2005), investigating Br/S and Cl/S ratios during the transition from quiescence to eruption at Mount Etna starting in October 2004, does not demonstrate a clear change of either ratio, both staying within the variance of the measurements. Further studies will be essential to confirm or disprove the assumptions made regarding the similarities of fluid-melt partitioning of chlorine and bromine.

CONCLUSION

We successfully retrieved BrO/SO_2 ratios for 13 eruptive phases at Tungurahua volcano between 2007 and 2017. The data show typical values of BrO/SO_2 ratios between 2 and 8×10^{-5}, similar to other andesitic arc volcanoes.

For 11 of the 13 eruptive phases, we identified an evolutionary pattern in the BrO/SO_2 ratio, which we interpret as characteristic of the volcano's eruptive phases. We propose a conceptual eruptive model for Tungurahua linking this pattern in the BrO/SO_2 ratio to the eruptive dynamics of the volcanic system. The appearance of low BrO/SO_2 ratios in the plume at the beginning of the eruptive phases is directly linked to a volatile-rich magma intrusion, which acts as a trigger for the eruptive activity and is initially characterised by high explosivity. A following increase in molar ratios is associated with a shift to shallower depth at which efficient bromine degassing occurs, and is typically associated with a sustained period of low explosive activity. The subsequent depletion in volatiles in the degassing magma body finally leads to a decrease in BrO/SO_2 ratios altogether, and an end to the eruptive phase. The evolutionary pattern of the BrO/SO_2 ratios is thus linked to the explosive activity of the volcano, with low BrO/SO_2 ratios associated to high explosive activity later evolving to high ratios during a period of low explosive activity.

High BrO/SO_2 ratios observed after a reported high input of volatile-rich magma into the upper volcanic system could infer a relationship between bromine degassing to the amount of volatiles in the active system. The BrO/SO_2 can thus potentially be used as a proxy for the degree of depletion of volatiles. This study therefore demonstrates the increasing potential of long-term measurements of the BrO/SO_2 molar ratio to reveal important information about status as well as temporal evolution of the volcanic system.

AUTHOR CONTRIBUTIONS

NB, SW, PL, and UP contributed conception and design of the study. SW performed the data evaluation. NB, HS, and SW performed the statistical analysis. SW wrote the draft of the manuscript. NB, SH, FD, SA, UP, TW, and SW contributed to the interpretation of the data. All authors contributed to manuscript revision, read and approved the submitted version.

FUNDING

The publication costs of this study were kindly provided by the Max Planck Institute for Chemistry (MPIC).

ACKNOWLEDGMENTS

We thank the reviewers for their valuable time, input, and critical remarks. We thank the reviewer, MP, for the persistence in criticism which helped to make the discussion more concise and coherent. We would especially like to thank the reviewer, SB, for the detailed remarks and suggestions, which improved the manuscript significantly both with respect to overall message and conciseness of the interpretation. Both reviewers helped to improve the manuscript significantly. We thank the editor, AA, for his input and managing during the publishing process. We kindly thank the staff of the Instituto Geofísico – Escuela Politécnica Nacional (IG-EPN) – especially the Observatory at

Tungurahua – for maintaining the NOVAC instruments and for providing the spectral data. We thank the European Commission for funding of the NOVAC project under Framework 6 Research Program and DFG for financial support under project DFG PL 193/14-1.

SUPPLEMENTARY MATERIAL

The Supplementary Material for this article can be found online at: https://www.frontiersin.org/articles/10.3389/feart.2019.00132/full#supplementary-material

REFERENCES

Aiuppa, A. (2009). Degassing of halogens from basaltic volcanism: insights from volcanic gas observations. *Chem. Geol.* 263, 99–109. doi: 10.1016/j.chemgeo.2008.08.022

Aiuppa, A., Federico, C., Antonio, P., Giovannella, P., and Mariano, V. (2002). S, Cl and F degassing as an indicator of volcanic dynamics: the 2001 eruption of Mount Etna. *Geophys. Res. Lett.* 29, 54-1–54-4. doi: 10.1029/2002GL015032

Aiuppa, A., Federico, C., Franco, A., Giudice, G., Gurrieri, S., Inguaggiato, S., et al. (2005). Emission of bromine and iodine from Mount Etna volcano. *Geochem. Geophys. Geosyst.* 6:Q08008. doi: 10.1029/2005GC000965

Aiuppa, A., Federico, C., Giudice, G., Gurrieri, S., Paonita, A., and Valenza, M. (2004). Plume chemistry provides insights into mechanisms of sulfur and halogen degassing in basaltic volcanoes. *Earth Planet. Sci. Lett.* 222, 469–483. doi: 10.1016/j.epsl.2004.03.020

Allard, P., Burton, M., and Muré, F. (2005). Spectroscopic evidence for a lava fountain driven by previously accumulated magmatic gas. *Nature* 433, 407–410. doi: 10.1038/nature03246

Alletti, M., Baker, D., Scaillet, B., Aiuppa, A., Moretti, R., and Ottolini, L. (2009). Chlorine partitioning between a basaltic melt and H_2O–CO_2 fluids at Mount Etna. *Chem. Geol.* 263, 37–50. doi: 10.1016/j.chemgeo.2009.04.003

Andújar, J., Martel, C., Pichavant, M., Samaniego, P., Scaillet, B., and Molina, I. (2017). Structure of the plumbing system at Tungurahua volcano, Ecuador: insights from phase equilibrium experiments on July–August 2006 eruption products. *J. Petrol.* 58, 1249–1278. doi: 10.1093/petrology/egx054

Arellano, S., Hall, M., Samaniego, P., Pennec, J.-L. L., Ruiz, A., Molina, I., et al. (2008). Degassing patterns of Tungurahua volcano (Ecuador) during the 1999–2006 eruptive period, inferred from remote spectroscopic measurements of SO_2 emissions. *J. Volcanol. Geotherm. Res.* 176, 151–162. doi: 10.1016/j.jvolgeores.2008.07.007

Bablon, M., Quidelleur, X., Samaniego, P., Le Pennec, J.-L., Lahitte, P., Liorzou, C., et al. (2018). Eruptive chronology of Tungurahua volcano (Ecuador) revisited based on new K-Ar ages and geomorphological reconstructions. *J. Volcanol. Geotherm. Res.* 357, 378–398. doi: 10.1016/j.jvolgeores.2018.05.007

Beermann, O., Botcharnikov, R., and Nowak, M. (2015). Partitioning of sulfur and chlorine between aqueous fluid and basaltic melt at 1050°C, 100 and 200 MPa. *Chem. Geol.* 418, 132–157. doi: 10.1016/j.chemgeo.2015.08.008

Bobrowski, N., and Giuffrida, G. (2012). Bromine monoxide / sulphur dioxide ratios in relation to volcanological observations at Mt. Etna 2006 - 2009. *Solid Earth* 3, 433–445. doi: 10.5194/se-3-433-2012

Bobrowski, N., Giuffrida, G., Yalire, M., Lübcke, P., Arellano, S., Balagizi, C., et al. (2017). Multicomponent gas emission measurements of the active lava lake of Nyiragongo, DR Congo. *J. Afr. Earth Sci.* 134, 856–865. doi: 10.1016/j.jafrearsci.2016.07.010

Bobrowski, N., Hönniger, G., Galle, B., and Platt, U. (2003). Detection of bromine monoxide in a volcanic plume. *Nature* 423, 273–276. doi: 10.1038/nature0162

Bobrowski, N., and Platt, U. (2007). SO_2/BrO ratios studied in five volcanic plumes. *J. Volcanol. Geotherm. Res.* 166, 147–160. doi: 10.1016/j.jvolgeores.2007.07.003

Bobrowski, N., von Glasow, R., Aiuppa, A., Inguaggiato, S., Louban, I., Ibrahim, O. W., et al. (2007). Reactive halogen chemistry in volcanic plumes. *J. Geophys. Res.* 112:D06311. doi: 10.1029/2006JD007206

Boichu, M., Oppenheimer, C., Roberts, T. J., Tsanev, V., and Kyle, P. R. (2011). On bromine, nitrogen oxides and ozone depletion in the tropospheric plume of Erebus volcano (Antarctica). *Atmos. Environ.* 45, 3856–3866. doi: 10.1016/j.atmosenv.2011.03.027

Bureau, H., Foy, E., Raepsaet, C., Somogyi, A., Munsch, P., Simon, G., et al. (2010). Bromine cycle in subduction zones through in situ Br monitoring in diamond anvil cells. *Geochim. Cosmochim. Acta* 74, 3839–3850. doi: 10.1016/j.gca.2010.04.001

Bureau, H., Keppler, H., and Métrich, N. (2000). Volcanic degassing of bromine and iodine: experimental fluid/melt partitioning data and applications to stratospheric chemistry. *Earth Planet. Sci. Lett.* 183, 51–60. doi: 10.1016/S0012-821X(00)00258-2

Burrows, J., Richter, A., Dehn, A., Deters, B., Himmelmann, S., Voigt, S., et al. (1999). Atmospheric remote-sensing reference data from GOME-2. Temperature-dependent absorption cross sections of O_3 in the 231-794 nm range. *J. Quant. Spectrosc. Radiat. Transf.* 61, 509–517. doi: 10.1016/S0022-4073(98)00037-5

Burton, M., Allard, P., Muré, F., and La Spina, A. (2007). Magmatic gas composition reveals the source depth of slug-driven strombolian explosive activity. *Science* 317, 227–230. doi: 10.1126/science.1141900

Cadoux, A., Iacono-Marziano, G., Scaillet, B., Aiuppa, A., Mather, T. A., Pyle, D. M., et al. (2018). The role of melt composition on aqueous fluid vs. silicate melt partitioning of bromine in magmas. *Earth Planet. Sci. Lett.* 498, 450–463. doi: 10.1016/j.epsl.2018.06.038

Cantrell, C. A. (2008). Technical note: review of methods for linear least-squares fitting of data and application to atmospheric chemistry problems. *Atmos. Chem. Phys.* 8, 5477–5487. doi: 10.5194/acp-8-5477-2008

Carn, S., Krueger, A., Arellano, S., Krotkov, N., and Yang, K. (2008). Daily monitoring of Ecuadorian volcanic degassing from space. *J. Volcanol. Geotherm. Res.* 176, 141–150. doi: 10.1016/j.jvolgeores.2008.01.029

Carrol, M. R., and Holloway, J. R. (1994). *Volatiles in Magmas*, Vol. 30. Washington, D.C: Mineralogical Society of America.

Cochain, B., Sanloup, C., de Grouchy, C., Crépisson, C., Bureau, H., Leroy, C., et al. (2015). Bromine speciation in hydrous silicate melts at high pressure. *Chem. Geol.* 404, 18–26. doi: 10.1016/j.chemgeo.2015.03.015

Dinger, F., Bobrowski, N., Warnach, S., Bredemeyer, S., Hidalgo, S., Arellano, S., et al. (2018). Periodicity in the BrO/SO_2 molar ratios in the volcanic gas plume of Cotopaxi and its correlation with the Earth tides during the eruption in 2015. *Solid Earth* 9, 247–266. doi: 10.5194/se-9-247-2018

Edmonds, M., Gerlach, T. M., and Herd, R. A. (2009). Halogen degassing during ascent and eruption of water-poor basaltic magma. *Chem. Geol.* 263, 122–130. doi: 10.1016/j.chemgeo.2008.09.022

Fleischmann, O. C., Hartmann, M., Burrows, J. P., and Orphal, J. (2004). New ultraviolet absorption cross-sections of BrO at atmospheric temperatures measured by time-windowing Fourier transform spectroscopy. *J. Photochem. Photobiol. A Chem.* 168, 117–132. doi: 10.1016/j.jphotochem.2004.03.026

Galle, B., Johansson, M., Rivera, C., Zhang, Y., Kihlman, M., Kern, C., et al. (2010). Network for observation of volcanic and atmospheric change (NOVAC) - a global network for volcanic gas monitoring: network layout and instrument description. *J. Geophys. Res.* 115:D05304. doi: 10.1029/2009JD011823

Grainger, J. F., and Ring, J. (1962). Anomalous Fraunhofer line profiles. *Nature* 193, 762–762. doi: 10.1038/193762a0

Gutmann, A., Bobrowski, N., Roberts, T. J., Rüdiger, J., and Hoffmann, T. (2018). Advances in bromine speciation in volcanic plumes. *Front. Earth Sci.* 6:213. doi: 10.3389/feart.2018.00213

Hall, M. L., Robin, C., Beate, B., Mothes, P., and Monzier, M. (1999). Tungurahua volcano, Ecuador: structure, eruptive history and hazards. *J. Volcanol. Geotherm. Res.* 91, 1–21. doi: 10.1016/S0377-0273(99)00047-5

Hermans, C., Vandaele, A., Fally, S., Carleer, M., Colin, R., Coquart, B., et al. (2003). "Absorption cross-section of the collision-induced bands of oxygen from the UV to the NIR," in *Weakly Interacting Molecular Pairs: Unconventional Absorbers of Radiation in the Atmosphere*, Vol. 27, eds C. Camy-Peyret and A. Vigasin (Netherlands: Springer), 193–202. doi: 10.1007/978-94-010-0025-3_16

Hidalgo, S., Battaglia, J., Arellano, S., Sierra, D., Bernard, B., Parra, R., et al. (2018). Evolution of the 2015 Cotopaxi eruption revealed by combined geochemical & seismic observations. *Geochem. Geophys. Geosyst.* 19, 2087–2108. doi: 10.1029/2018GC007514

Hidalgo, S., Battaglia, J., Arellano, S., Steele, A., Bernard, B., Bourquin, J., et al. (2015). SO$_2$ degassing at Tungurahua volcano (Ecuador) between 2007 and 2013: transition from continuous to episodic activity. *J. Volcanol. Geotherm. Res.* 298, 1–14. doi: 10.1016/j.jvolgeores.2015.03.022

Hörmann, C., Sihler, H., Bobrowski, N., Beirle, S., Penning de Vries, M., Platt, U., et al. (2013). Systematic investigation of bromine monoxide in volcanic plumes from space by using the GOME-2 instrument. *Atmos. Chem. Phys.* 13, 4749–4781. doi: 10.5194/acp-13-4749-2013

Johnson, J. (2003). Generation and propagation of infrasonic airwaves from volcanic explosions. *J. Volcanol. Geotherm. Res.* 121, 1–14. doi: 10.1016/S0377-0273(02)00408-0

Kelly, P. J., Kern, C., Roberts, T. J., Lopez, T., Werner, C., and Aiuppa, A. (2013). Rapid chemical evolution of tropospheric volcanic emissions from Redoubt volcano, Alaska, based on observations of ozone and halogen-containing gases. *J. Volcanol. Geotherm. Res.* 259, 317–333. doi: 10.1016/j.jvolgeores.2012.04.023

Kern, C., Sihler, H., Vogel, L., Rivera, C., Herrera, M., and Platt, U. (2009). Halogen oxide measurements at Masaya volcano, Nicaragua using active long path differential optical absorption spectroscopy. *Bull. Volcanol.* 71, 659–670. doi: 10.1007/s00445-008-0252-8

Kutterolf, S., Hansteen, T. H., Freundt, A., Wehrmann, H., Appel, K., Krüger, K., et al. (2015). Bromine and chlorine emissions from Plinian eruptions along the Central American Volcanic Arc: from source to atmosphere. *Earth Planet. Sci. Lett.* 429, 234–246. doi: 10.1016/j.epsl.2015.07.064

Lübcke, P. (2014). *Optical Remote Sensing Measurements of Bromine and Sulphur Emissions: Investigating their Potential as Trace of Volcanic Activity*. Ph.D. thesis. Heidelberg: Universität Heidelberg.

Lübcke, P., Bobrowski, N., Arellano, S., Galle, B., Garzón, G., Vogel, L., et al. (2014). BrO/SO$_2$ molar ratios from scanning DOAS measurements in the NOVAC network. *Solid Earth* 5, 409–424. doi: 10.5194/se-5-409-2014

Malinconico, L. L. (1979). Fluctuations in SO$_2$ emission during recent eruptions of Etna. *Nature* 278, 43–45. doi: 10.1038/278043a0

McCormick, B., Herzog, M., Yang, J., Edmonds, M., Mather, T. A., Carn, S. A., et al. (2014). A comparison of satellite- and ground-based measurements of SO$_2$ emissions from Tungurahua volcano, Ecuador. *J. Geophys. Res. Atmos.* 119, 4264–4285. doi: 10.1002/2013JD019771

Meller, R., and Moortgat, G. K. (2000). Temperature dependence of the absorption cross sections of formaldehyde between 223 and 323K in the wavelength range 225 - 375 nm. *J. Geophys. Res. Atmos.* 105, 7089–7101. doi: 10.1029/1999JD901074

Menyailov, I. A. (1975). Prediction of eruptions using changes in composition of volcanic gases. *Bull. Volcanol.* 39, 112–125. doi: 10.1007/BF02596951

Myers, M. L., Geist, D. J., Rowe, M. C., Harpp, K. S., Wallace, P. J., and Dufek, J. (2014). Replenishment of volatile-rich mafic magma into a degassed chamber drives mixing and eruption of Tungurahua volcano. *Bull. Volcanol.* 76, 872–888. doi: 10.1007/s00445-014-0872-0

Noguchi, K., and Kamiya, H. (1963). Prediction of volcanic eruption by measuring the chemical composition and amounts of gases. *Bull. Volcanol.* 26, 367–378. doi: 10.1007/BF02597298

Olmos, R., Barrancos, J., Rivera, C., Barahona, F., López, D. L., Henriquez, B., et al. (2007). Anomalous emissions of SO$_2$ during the recent eruption of Santa Ana volcano, El Salvador, Central America. *Pure Appl. Geophys.* 164, 2489–2506. doi: 10.1007/s00024-007-0276-6

Oppenheimer, C., Tsanev, V. I., Braban, C. F., Cox, R. A., Adams, J. W., Aiuppa, A., et al. (2006). BrO formation in volcanic plumes. *Geochim. Cosmochim. Acta* 70, 2935–2941. doi: 10.1016/j.gca.2006.04.001

Pennec, J.-L. L., Jaya, D., Samaniego, P., Ramón, P., Yánez, S. M., Egred, J., et al. (2008). The AD 1300–1700 eruptive periods at Tungurahua volcano, Ecuador, revealed by historical narratives, stratigraphy and radiocarbon dating. *J. Volcanol. Geotherm. Res.* 176, 70–81. doi: 10.1016/j.jvolgeores.2008.05.019

Pennisi, M., and Cloarec, M.-F. L. (1998). Variations of Cl, F, and S in Mount Etna's plume, Italy, between 1992 and 1995. *J. Geophys. Res.* 103, 5061–5066. doi: 10.1029/97JB03011

Platt, U., and Bobrowski, N. (2015). "Quantification of volcanic reactive halogen emissions," in *Volcanism and Global Environmental Change*, eds A. Schmidt, K. Fristad, and L. Elkins-Tanton (Cambridge: Cambridge University Press), 115–132. doi: 10.1017/cbo9781107415683.011

Platt, U., and Stutz, J. (2008). *Differential Optical Absorption Spectroscopy: Physics of Earth and Space Environments*. Berlin: Springer. doi: 10.1007/978-3-540-75776-4

Roberts, T. J., Martin, R. S., and Jourdain, L. (2014). Reactive bromine chemistry in Mount Etna's volcanic plume: the influence of total Br, high-temperature processing, aerosol loading and plume–air mixing. *Atmos. Chem. Phys.* 14, 11201–11219. doi: 10.5194/acp-14-11201-2014

Samaniego, P., Pennec, J.-L. L., Robin, C., and Hidalgo, S. (2011). Petrological analysis of the pre-eruptive magmatic process prior to the 2006 explosive eruptions at Tungurahua volcano (Ecuador). *J. Volcanol. Geotherm. Res.* 199, 69–84. doi: 10.1016/j.jvolgeores.2010.10.010

Seo, J. H., and Zajacz, Z. (2016). Fractionation of Cl/Br during fluid phase separation in magmatic–hydrothermal fluids. *Geochim. Cosmochim. Acta* 183, 125–137. doi: 10.1016/j.gca.2016.04.009

Spilliaert, N., Métrich, N., and Allard, P. (2006). S–Cl–F degassing pattern of water-rich alkali basalt: modelling and relationship with eruption styles on Mount Etna volcano. *Earth Planet. Sci. Lett.* 248, 772–786. doi: 10.1016/j.epsl.2006.06.031

Spina, A. L., Burton, M., Allard, P., Alparone, S., and Muré, F. (2015). Open-path FTIR spectroscopy of magma degassing processes during eight lava fountains on Mount Etna. *Earth Planet. Sci. Lett.* 413, 123–134. doi: 10.1016/j.epsl.2014.12.038

Theys, N., Roozendael, M. V., Dils, B., Hendrick, F., Hao, N., and Mazière, M. D. (2009). First satellite detection of volcanic bromine monoxide emission after the Kasatochi eruption. *Geophys. Res. Lett.* 36:L03809.

Vandaele, A., Hermans, C., and Fally, S. (2009). Fourier transform measurements of SO$_2$ absorption cross sections: II.: temperature dependence in the 29 000 - 44 000 cm^{-1} (227 - 345 nm) region. *J. Quant. Spectrosc. Radiat. Transf.* 110, 2115–2126. doi: 10.1016/j.jqsrt.2009.05.006

Vandaele, A., Hermans, C., Simon, P., Carleer, M., Colin, R., Fally, S., et al. (1998). Measurements of the NO$_2$ absorption cross-section from 42 000 cm^{-1} to 10 000 cm-1 (238-1000 nm) at 220K and 294 K. *J. Quant. Spectrosc. Radiat. Transf.* 59, 171–184. doi: 10.1016/S0022-4073(97)00168-4

Villemant, B., and Boudon, G. (1999). H$_2$O and halogen (F, Cl, Br) behaviour during shallow magma degassing processes. *Earth Planet. Sci. Lett.* 168, 271–286. doi: 10.1016/S0012-821X(99)00058-8

Vogel, L., Sihler, H., Lampel, J., Wagner, T., and Platt, U. (2013). Retrieval interval mapping: a tool to visualize the impact of the spectral retrieval range on differential optical absorption spectroscopy evaluations. *Atmos. Meas. Tech.* 6, 275–299. doi: 10.5194/amt-6-275-2013

von Glasow, R. (2010). Atmospheric chemistry in volcanic plumes. *Proc. Natl. Acad. Sci. U.S.A.* 107, 6594–6599. doi: 10.1073/pnas.0913164107

Wagner, T., Beirle, S., and Deutschmann, T. (2009). Three-dimensional simulation of the Ring effect in observations of scattered sun light using Monte Carlo radiative transfer models. *Atmos. Meas. Tech.* 2, 113–124. doi: 10.5194/amt-2-113-2009

Webster, J., Sintoni, M., and Vivo, B. D. (2009). The partitioning behavior of Cl, S, and H$_2$O in aqueous vapor- saline-liquid saturated phonolitic and trachytic melts at 200 MPa. *Chem. Geol.* 263, 19–36. doi: 10.1016/j.chemgeo.2008.10.017

Wright, H. M., Cashman, K. V., Mothes, P. A., Hall, M. L., Ruiz, A. G., and Le Pennec, J. (2012). Estimating rates of decompression from textures of erupted ash particles produced by 1999–2006 eruptions of Tungurahua volcano, Ecuador. *Geology* 40, 619–622. doi: 10.1130/G32948.1

Zajacz, Z., Candela, P. A., Piccoli, P. M., and Sanchez-Valle, C. (2012). The partitioning of sulfur and chlorine between andesite melts and magmatic volatiles and the exchange coefficients of major cations. *Geochim. Cosmochim. Acta* 89, 81–101. doi: 10.1016/j.gca.2012.04.039

Conflict of Interest Statement: The authors declare that the research was conducted in the absence of any commercial or financial relationships that could be construed as a potential conflict of interest.

The handling Editor is currently editing a Research Topic with one of the authors NB, and confirms the absence of any other collaboration.

frontiers in Earth Science

ORIGINAL RESEARCH
published: 03 July 2019
doi: 10.3389/feart.2019.00154

Reaction Rates Control High-Temperature Chemistry of Volcanic Gases in Air

Tjarda Roberts[1], Guillaume Dayma[2] and Clive Oppenheimer[3]*

[1] CNRS UMR7328, Laboratoire de Physique et de Chimie de l'Environnement et de l'Espace, Université d'Orléans, Orléans, France, [2] CNRS, Institut de Combustion Aérothermique Réactivité et Environnement, Université d'Orléans, Orléans, France, [3] Department of Geography, University of Cambridge, Cambridge, United Kingdom

When volcanic gases enter the atmosphere, they encounter a drastically different chemical and physical environment, triggering a range of rapid processes including photochemistry, oxidation, and aerosol formation. These processes are critical to understanding the reactivity and evolution of volcanic emissions in the atmosphere yet are typically challenging to observe directly due to the nature of volcanic activity. Inferences are instead drawn largely from observations of volcanic plumes as they drift across a crater's edge and further downwind, and the application of thermodynamic models that neglect reaction kinetics as gas and air mix and thermally equilibrate. Here, we foreground chemical kinetics in simulating this critical zone. Volcanic gases are injected into a chain-of-reactors model that simulates time-resolved high-temperature chemistry in the dispersing plume. Boundary conditions of decreasing temperature and increasing proportion of air interacting with volcanic gases are specified with time according to an offline plume dynamics model. In contrast to equilibrium calculations, our chemical kinetics model predicts that CO is only partially oxidized, consistent with observed CO in volcanic plumes downwind from source. Formation of sulfate precursor SO_3 at $SO_3/SO_2 = 10^{-3}$ mol/mol is consistent with the range of reported sulfate aerosol to SO_2 ratios observed close to crater rims. High temperature chemistry also forms oxidants OH, HO_2, and H_2O_2. The H_2O_2 will likely augment volcanic sulfate yields by reacting with $SO_{2(aq)}$ in the cooled-condensed plume. Calculations show that high-temperature OH will react with volcanic halogen halides (HBr and HCl) to yield reactive halogens (Br and Cl) in the young plume. Strikingly, high-temperature production of radical oxidants (including HO_x) is enhanced by volcanic emissions of reduced gases (CO, H_2, and H_2S) due to chemical feedback mechanisms, although the kinetics of some reactions are uncertain, especially regarding sulfur. Our findings argue strongly that the chemistry of the hot near-source plume cannot be captured by equilibrium model assumptions, and highlight the need for development of more sophisticated, kinetics-based, high-temperature CHONS-halogen reaction models.

Keywords: thermodynamic equilibrium model HSC, combustion kinetics model chemkin, high-temperature, magmatic gas emission, at-source primary sulfate, volcano plume, volcanic eruption, sulfuric acid

Edited by:
Alessandro Aiuppa,
University of Palermo, Italy

Reviewed by:
Taryn Lopez,
University of Alaska Fairbanks,
United States
J. Maarten De Moor,
OVSICORI-UNA, Costa Rica

***Correspondence:**
Tjarda Roberts
Tjarda.Roberts@cnrs-orleans.fr

Specialty section:
This article was submitted to
Volcanology,
a section of the journal
Frontiers in Earth Science

Received: *06 October 2018*
Accepted: *03 June 2019*
Published: *03 July 2019*

Citation:
Roberts T, Dayma G and
Oppenheimer C (2019) Reaction
Rates Control High-Temperature
Chemistry of Volcanic Gases in Air.
Front. Earth Sci. 7:154.
doi: 10.3389/feart.2019.00154

INTRODUCTION

Volcanoes release gases and aerosols to the atmosphere through both quiescent (passive) degassing, and effusive and explosive eruptions. Volcanic emissions of SO_2 to the stratosphere are well known to impact climate through the atmospheric oxidation of SO_2 to form radiatively active sulfate aerosol particles. In fact, volcanoes release a wide range of highly reactive gases that can impact atmospheric composition and climate. Volcanic bromine and chlorine emissions undergo plume atmospheric chemistry that can destroy both tropospheric and stratospheric ozone. In descending order of typical abundance (which varies with volcano setting, magma redox conditions, and eruptive style) volcanic gas emissions consist of: H_2O, CO_2, SO_2, HCl, HF, H_2S, OCS, CO, and HBr, as well as other trace species e.g., metals. Observations of volcanic plumes identify several additional species (e.g., NO, NO_2, HNO_3, BrO, OClO, $SO_4{}^{2-}$, HO_2NO_2, and H_2O_2), (Allen et al., 2000; Mather et al., 2004b; Bobrowski et al., 2007; Oppenheimer et al., 2010; Carn et al., 2011; Martin et al., 2012; Kern and Lyons, 2018). These species are formed by oxidizing chemical reactions as the magmatic gases mix with air, first at high temperatures near to the source and then at low temperatures as the cooled plume disperses further into the background atmosphere. Numerical models of low-temperature atmospheric chemistry of the plume have been developed (e.g., Bobrowski et al., 2007; Roberts et al., 2009; von Glasow, 2010; Jourdain et al., 2016) that are able to reproduce some – but not all – of these observed oxidized species. This points to an important role of high-temperature chemistry. Current approaches apply thermodynamic equilibrium models to represent the high-temperature chemistry of the near-source plume (e.g., Gerlach, 2004; Martin et al., 2006). However, thermodynamic equilibrium calculations may be misleading if the chemistry is limited by kinetics (rates of reactions) in the rapidly cooling volcanic gas and air mixture within seconds of emission. Here, a chemical kinetics approach is developed to simulate the time-varying chemical processing of C-H-O-S gases in the hot near-source plume on its release and mixing with background air.

High-Temperature Products in Volcanic Plumes: Observations and Modeling

Observational evidence for the high-temperature production of oxidants in volcanic plumes includes SO_{xy}, HO_{xy}, NO_{xy}, and rapid formation of reactive halogens. Sulfate-rich aerosols have been observed at the crater-rim or in very near-downwind plumes of many volcanoes (exception: volcanic domes), **Table 1**. Sulfate is reported relative to co-measured SO_2 which serves as a convenient yet only approximate plume tracer, allowing observations to be normalized for dilution effects. The sulfate:SO_2 ratios typically range from 0.00002 up to around 0.01 mol/mol, **Table 1** and references therein. Many of the ratios are too high to be explained by atmospheric oxidation of SO_2 at low-temperatures on the plume transport timescale of seconds to minutes (e.g., Galeazzo et al., 2018). Instead, the observations indicate a sulfate-rich aerosol formed very close to source. One hypothesized pathway to its formation is high-temperature oxidation of a small fraction of SO_2 in the near-source plume to produce sulfate precursor SO_3 (Allen et al., 2000). For volcanic domes, sulfate formation may be enhanced by circulation of air inside the dome (Zelenski et al., 2015). The range in observed $SO_4{}^{2-}$:SO_2 indicates variability in the near-source sulfate formation processes at different volcanoes, as well as possibly some measurement uncertainty. In all cases sulfate contributes a minor fraction to the total sulfur emission that is typically dominated by SO_2 and H_2S (the proportion depending strongly on magma redox conditions; Oppenheimer et al., 2014). Nevertheless, at source (or so-called "primary") volcanic sulfate is critical to plume processes such as multi-phase halogen reactions (discussed further below) and acts as a condensational sink that can inhibit new particle formation (Sahyoun et al., 2019).

There exist few measurements of volcanic HO_{xy}. Carn et al. (2011) report in-cloud processing of SO_2 from the Huila volcanic plume by H_2O_2, with plume H_2O_2 abundance elevated above background by about 0.5 ppbv. This volcanic H_2O_2 might have

TABLE 1 | Observational evidence for at-source sulfate aerosol in volcanic plumes.

Volcano	**$SO_4{}^{2-}$/SO_2 mol/mol**	**References**
Kilauea	0.005	Naughton et al., 1975;
	0.077, 0.016, and 0.001	Kroll et al., 2015
Erta Ale	0.005, 0.008, 0.006, 0.007, 0.001, 0.007, and 0.006	de Moor et al., 2013
Lascar	0.01	Mather et al., 2004b
Masaya	0.0006–0.007, average: 0.0015 (0.0008–0.0105 mass ratio)	Allen et al., 2002
	0.006, 0.006, 0.01, and 0.013	Mather et al., 2003
	0.0055, 0.0053, 0.0064, 0.0108, 0.0052, 0.0074, 0.0493, 0.0003, 0.0058, 0.0052, 0.0046, and 0.0684 (0.0053 regression)	Martin et al., 2010
	0.023, 0.036	de Moor et al., 2013
Etna	0.017, 0.049, and 0.05	Martin et al., 2008;
	0.01–0.02	Roberts et al., 2018
Villarrica	0.02	Mather et al., 2004b
Redoubt (1990 eruptions)	0.001	Hobbs et al., 1991
Montserrat (crater-edge)	0.03 (0.04 mass ratio)	Allen et al., 2000
Montserrat (dome)	0.5 (0.7 mass ratio)	
Bezymianny (dome)	0.43	Zelenski et al. (2015)
Eyjafjallajökull 2010 fire-fountaining	0.00002, 0.0014, and 0.0044	Ilyinskaya et al., 2012
Eyjafjallajökull 2010 cooling lava flow	0.063	

Lascar and Monsterrat mass ratios were converted into molar ratios assuming masses of SO_4 and SO_2.

originated from the self-reaction of volcanic HO_2. Oppenheimer et al. (2010) measured elevated HO_2NO_2 in the (cooled and dilute) Mt Erebus plume where the cold Antarctic atmosphere likely contributed to its thermal stability. HO_2NO_2 is formed by the reaction of HO_2 with NO_2 therefore its presence provides evidence for volcanogenic sources of both HO_x and NO_x. Volcanogenic HO_x has also been observed by a chance encounter of an instrumented aircraft with the Hekla 2000 eruption plume in the lower stratosphere (Rose et al., 2006). Observations showed OH and HO_2 were elevated at up to 0.5 and 15 pptv above background in 33–34 h aged volcanic cloud during night. These measurements have eluded any explanation given the lack of photochemistry, a cooled plume, and anticipated fast HO_x destruction by reaction with volcanic SO_2 and halogens (both in excess abundances). In general, the reported elevated abundances of HO_{xy} in volcanic plumes compared to the background atmosphere are surprising because low-temperature volcanic plume chemistry is expected to deplete HO_{xy} (Galeazzo et al., 2018). Volcanic HO_{xy} may originate from high-temperature chemistry of the near-source plume.

Elevated concentrations of NO, NO_2, and HNO_3 have been measured in several volcanic plumes in the troposphere in addition to the HO_2NO_2 observed in the Mt Erebus plume: a review is given by Martin et al. (2012) and references therein, reporting a typical molar ratio for NO_y/H_2O of 10^{-5}. Whilst filter pack sampling identified HNO_3 in crater-rim plumes from several volcanoes (e.g., Mather et al., 2004a), on other occasions there was no evidence for HNO_3, even at the same volcano (e.g., Martin et al., 2010). This may point to variability in emissions-processing or reliability of measurement technique. Nevertheless, real-time aircraft-based measurements by Atmospheric Chemical Ionization Mass Spectrometer confirm volcanic HNO_3 in plumes downwind from Mt Etna at $HNO_3/SO_2 = 0.02$ (Voigt et al., 2014), and in the Mt Erebus plume (Oppenheimer et al., 2010). Sources of volcanic NO_{xy} are uncertain. Martin et al. (2012) present a kinetic model of CHON chemistry that demonstrates high-temperature formation of thermal NO_x is too slow to occur in the near-source plume that rapidly disperses and cools over seconds-minutes. Volcanic lightning is a likely source of NO_x in clouds from explosive eruptions. It has also been hypothesized that NO_x may sometimes be formed by oxidation of ammonia, for example in the stratospheric cloud from the Hekla 2000 eruption (Rose et al., 2006).

The need to characterize high-temperature chemistry in the near-source plume is underlined by model studies of volcanic halogen transformations in the plume (Bobrowski et al., 2007; von Glasow, 2010; Roberts et al., 2014). Halogens are emitted as hydrogen halides (HBr and HCl) from volcanoes but are transformed into reactive halogens (BrO and OClO) in the tropospheric plume via a multi-phase autocatalytic "bromine-explosion" chemistry occurring at low-temperatures. However, numerical models of the plume atmospheric halogen chemistry can only reproduce the observed magnitude and rate of formation of BrO if the volcanic emission is modified to include radicals believed to form at high-temperatures in the near-source plume (the so-called "effective source region"). Radicals such as OH (that react with HBr, HCl to produce Br, and Cl) provide an initial source of reactive bromine to initiate the low-temperature bromine explosion cycles. Furthermore, high-temperature production of sulfate-precursor SO_3 generates near-source (so-called "primary") sulfate aerosols that promote heterogeneous reactions that drive the bromine explosion chemistry. Observations of BrO (and occasionally OClO) in tropospheric volcanic plumes globally (e.g., Bobrowski et al., 2007; Boichu et al., 2011; Hörmann et al., 2013; Donovan et al., 2014; Kern and Lyons, 2018) indicate pervasive emissions of volcanic halogens to the troposphere accompanied by both high- and low-temperature chemistry in volcanic plumes.

The high-temperature region of the plume also facilitates gas-ash interactions including adsorption of gases such as SO_2 and HCl onto ash particles that may then fall-out (Delmelle et al., 2018 and references therein). High-temperature SO_3 is a precursor to sulfate that can condense as the eruption column cools and could change ash properties (e.g., Hoshyaripour et al., 2015) and ash-related atmospheric impacts e.g., regarding plume lightning or ice nuclei. Whilst such heterogeneous interactions are outside the scope of our study, quantifying the high-temperature oxidizing chemistry occurring in the gas-phase as volcanic gases mix with air is a fundamental first-step to characterising the near-source plume composition and its possible influence on gas-ash interactions.

Thermodynamic models such as HSC have been applied to calculate the equilibrium compositions of mixtures of magmatic gases with air, and HSC output has been used in numerical model studies of the plume atmospheric chemistry and impacts (e.g., Gerlach, 2004; Martin et al., 2006, 2007, 2009, 2011; Aiuppa et al., 2007; Bobrowski et al., 2007, 2015; Roberts et al., 2009, 2014, 2018; von Glasow, 2010; Martin and Ilyinskaya, 2011; Hoshyaripour et al., 2012; Ilyinskaya et al., 2012; Surl et al., 2015; Jourdain et al., 2016). HSC is used to calculate the composition of the near-source plume for temperatures above 600°C according to Gibbs free energy minimization. The emission is released at magmatic temperatures and as the magmatic gases entrain air, the mixture cools toward background temperature. The calculation assumes thermodynamic equilibrium composition is reached at a specified temperature and degree of mixing of air with magmatic gases (often expressed as a volumetric or molar ratio, VA:VM where VA is air volume and VM is magmatic gas volume). Plume composition is then assumed to be "quenched" with respect to high-temperature chemistry upon further mixing with air. Choice of the VA:VM "quenching-point" for the HSC calculation is rather uncertain and may vary with eruption/emission type. For studies of passively degassing volcanoes it was found that a high VA:VM = 40:60 (Bobrowski et al., 2007) yielded extremely high SO_3 relative to SO_2 (much greater than observed sulfate/SO_2 ratios, see **Table 1**), therefore more recent studies chose lower VA:VM = 10:90 or 5:95 (e.g., Roberts et al., 2014) as the point where high-temperature chemistry is quenched. Conceivably, large eruptions might sustain high-temperature conditions over longer periods allowing the chemistry to reach equilibrium conditions at higher VA:VM. Hoshyaripour et al. (2012) simulated the high-temperature chemistry in an eruption column by co-varying VA:VM from 0 to 1 with temperature decreasing

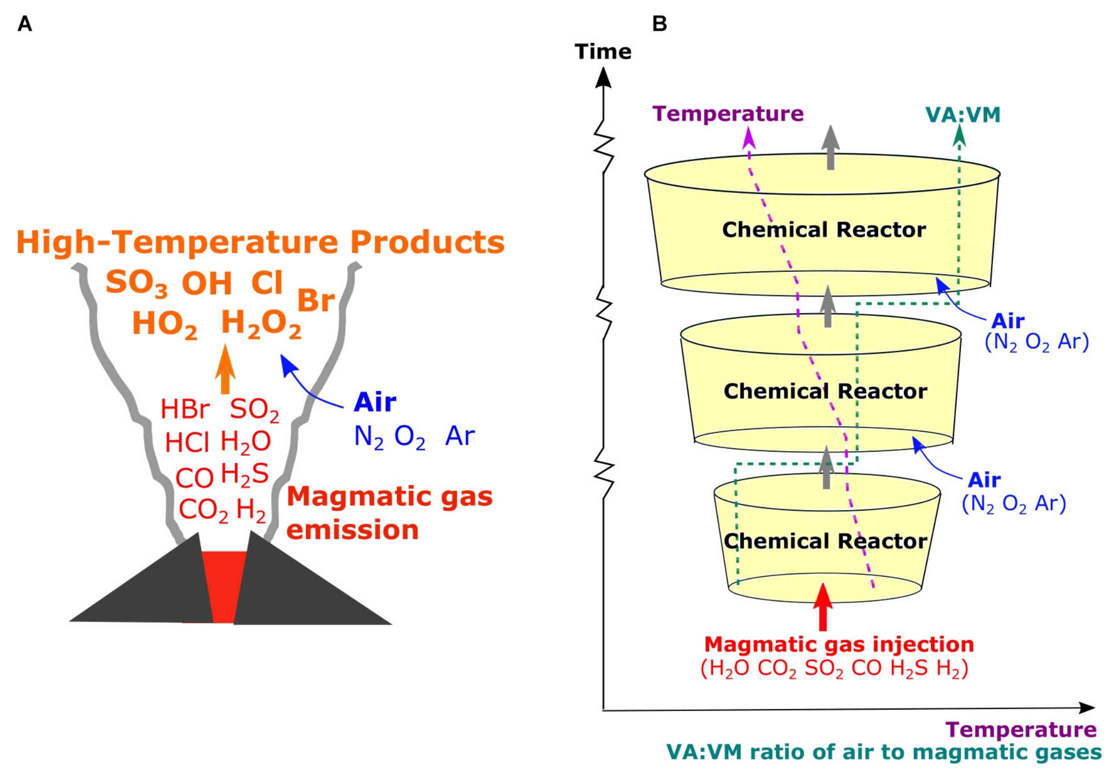

FIGURE 1 | Schematics of **(A)** high-temperature plume chemistry that generates radicals and oxidized products in the plume and **(B)** our chain-of-reactors approach to simulate the processes based on chemical kinetics under time-varying temperature (T) and proportion of mixing of air with magmatic gases (VA:VM).

from 1273 K to 873 K (1000°C to 600°C), predicting that the eruption column acts as a hot oxidizing reactor for S species.

In general, volcanic plume applications of thermodynamic equilibrium models such as HSC yield elevated abundances of SO_x (dominated by SO_3), HO_x (dominated by OH) and NO_x (dominated by NO), and halogen radicals Br, Cl (e.g., Martin et al., 2006). The relative abundances of these oxidized products increase with increasing VA:VM. The equilibrium models also predict near-complete oxidation of reduced gases emitted from volcanoes (e.g., CO, H_2S, and H_2), yet these gas species are often detected at the crater-rim or in downwind (cooled) plumes (e.g., Aiuppa et al., 2005; Schumann et al., 2011; Moussallam et al., 2012; Roberts et al., 2012; de Moor et al., 2016). This suggests that some gas species may not always be under equilibrium control (Martin et al., 2009). Plume observations of reduced gases relative to major gases (e.g., CO/CO_2, H_2/H_2O, and H_2S/SO_2) are used to infer emission properties such as temperature and oxidative state, but such inferences cannot hold true if there is substantial oxidation of the reduced gases following emission, as predicted by HSC. Here, a method is developed to evaluate how reaction rates control high-temperature chemistry of volcanic gases in air as a function of time-varying plume dynamics, **Figure 1**.

Our model uses a chemical kinetics rather than thermodynamics approach, and requires time-resolved boundary conditions in both temperature and degree of mixing of magmatic gases with air (VA:VM), as well as the composition of the volcanic gases emitted as model input. The temperature of the volcanic gas emission is uncertain. It is typically assumed to be identical to petrological magmatic estimates (600–1200°C), although analysis of gas compositions measured at Kilauea, Hawaii (Oppenheimer et al., 2018) and Mt Etna, Italy (Aiuppa et al., 2011) show that gases may cool prior to emission into the atmosphere. Introduction of surface waters may also cool the gas emission. Physical properties of the plume are poorly constrained for the few seconds following release from the eruptive vent (or other emission sources e.g., lava lake or dome), as there are few direct measurements or dedicated model studies. A study of gas-puffing dynamics at passively degassing volcano Masaya yielded estimates of mean dilutions of 0.09 and 0.24 between emission and detection by thermal radiometer about 5–10 m above the vent, for gas puffs with mean velocities 2.5 and 4.3 m/s (Branan et al., 2008).

One way to estimate temperature and VA:VM in the near-source plume can be through dynamical model simulations of plume rise (e.g., Mastin, 2007; Aubry et al., 2017). This study relies on one such eruptive case to supply physical boundary conditions: the PlumeRise model applied to the 2010 Eyjafjallajökull eruption plume (Woodhouse et al., 2013), for which observations of volcanic gases including CO/SO_2 have also been reported both close to the source and far downwind (Allard et al., 2011; Schumann et al., 2011). This Eyjafjallajökull case forms the basis for an exploratory investigation into the chemical kinetics of gas-phase reactions occurring at high-temperatures in volcanic plumes.

MATERIALS AND METHODS

Our approach to simulate high-temperature chemical reactions in the near-source plume includes three components: (i) the chemical kinetics model (chain-of-reactors), (ii) physical boundary conditions applied to the model, and (iii) the volcanic gas emissions injection as model input.

Chemical Kinetic Model (Chain-of-Reactors)

Chemkin is a fortran-based tool for incorporating complex chemical kinetics into model simulations of fluid dynamics (Kee et al., 2000 and related references from Reaction Design). Gas species and (reversible) reactions are first declared, as well as initial conditions (such as initial gas concentrations, temperature, pressure), and then the reactions are simulated in a plug-flow reactor (PFR) to evaluate temporal changes in gas composition.

Rates of progressions of reactions are quantified as the difference between the rate of the forward and reverse reactions, for example E1 for the reversible reaction A + B = C + D (where gases A, B, C, and D may also be involved in other reactions, each with its corresponding differential equation).

$$\text{E1} \quad d[C]/dt = k_f \times [A] \times [B] - k_r \times [C] \times [D]$$

The rate constants for forward reactions, k_f, are described in the form, E2, where *R* is the gas constant and T the gas temperature. The pre-exponential factor, A, the temperature exponent, β, and activation energy E, are specified in the mechanism file (see Glarborg and Marshall, 2013).

$$\text{E2} \quad k_f = A \times T^{\beta} \times \exp[-E/(R \times T)]$$

The reverse reaction rate constant, k_r, is given by E3 where K is the equilibrium constant that is determined by thermodynamic properties (molar enthalpies and entropies as a function of temperature); these properties are specified in the thermodynamic data file (see Glarborg and Marshall, 2013).

$$\text{E3} \quad k_r = k_f/K$$

The Chemkin model also accounts for third-body, unimolecular, chemically activated reactions, and pressure-dependencies of reaction rates. The resulting system of ordinary differential equations and initial conditions is solved by Chemkin to quantitatively predict how the gas composition in the chemical reactor evolves as a function of time according to the kinetics-based reaction scheme and the thermodynamic conditions.

The reaction mechanism applied within ChemKin is user-specified. There are very few studies at high-temperature dealing with sulfur species oxidation and their interactions with carbon, nitrogen oxides, or halogens. Here, the mechanism proposed by Glarborg and Marshall (2013) was selected for its good performance in comparison to laboratory shock-tube experiments, as recently highlighted by Mathieu et al. (2017). It includes 38 species involved in 161 reversible reactions. This reaction mechanism, and corresponding thermodynamic properties, relies on earlier works on sulfur chemistry and was updated to model the oxidation of carbonyl sulfide (OCS). A full list of gas species and chemical reactions is given in **Supplementary Tables S1**, **S2**. This version does not include halogens or NO_x chemistry. The interactions between sulfur, carbon, halogens, and nitrogen oxides are beyond the scope of this work, but will need to be addressed in future. Also, all the species considered were in the gas-phase; heterogeneous reactions or photochemical reactions were not included. This is a clear limitation of the present study which should be seen as a preliminary step needed to account for time evolution of chemicals in a near-source plume. Whilst the chemical scheme is one of the most complete regarding sulfur compounds, there exist some uncertainties in the high-temperature reaction kinetics, in particular related to H_2S (Mathieu et al., 2017). A single PFR simulates the high-temperature chemistry for given starting conditions in gas composition and temperature. A time-varying temperature can be introduced by applying a temperature gradient in the PFR and imposing an initial velocity of the reactor gases. However, air cannot be added as a function of time into a single reactor, i.e., the proportion of air to magmatic gases in the simulation is held constant according to the initial composition.

Therefore, a chain-of-reactors approach was developed using the Chemkin Pro software to simulate the chemical evolution of a near-source plume that simultaneously cools (decreasing T) and entrains air (increasing VA:VM) as it dilutes, **Figure 1**. Thirty PFRs were placed in a chain. A continuous decreasing trend in plume temperature was imposed across the chain by defining the start and end temperatures for each PFR according to our chosen boundary conditions (details in the next section). The starting composition for each reactor was defined by taking the output from the preceding one and diluting it with air (78% N_2, 21% O_2, 1% Ar) according to time-varying VA:VM boundary conditions. The pressure decrease was also considered even if it was not found to be significant. This alternate simulation of the plume chemistry (within reactor boxes) and mixing-dilution steps (between reactor boxes) is similar to the approach used in kinetics-based modeling of the low-temperature atmospheric chemistry of volcanic plumes e.g., PlumeChem (Roberts et al., 2009).

Boundary Conditions to the Chain-of-Reactors Provided by PlumeRise Model

The chain-of-reactors model requires time-resolved boundary conditions for plume temperature and VA:VM as the emitted volcanic gases rapidly mix with air. Here, output from the 1D PlumeRise model is used. PlumeRise describes the ascent of a turbulent buoyant plume composed of solid pyroclasts, magmatic gases, and air and includes the effects of cross-wind on turbulent entrainment of air into the plume. The PlumeRise dynamics model approximates volcanic gases as entirely H_2O (a more complex emission composition provides input to the chain-of-reactors model, see Section "Magmatic Gas Emissions" below).

Output from the PlumeRise model includes the plume temperature (T, in K), the total mass flux (Q in kg/s), the gas mass fraction (n), the vertical velocity, U (m/s), the mass fraction of water (liquid+gas) in the plume (φ), specific humidity (C), and altitude (z in m), each provided at a resolution (dz) of a few meters. These variables can be used to derive temperature and VA:VM as a function of time. The time, in seconds is given by E4, and integrating dt.

$$\text{E4} \quad dt = dz/U$$

The plume total mass (gases and solids), M in kg, in the discrete volume at each time-step is given by E5.

$$\text{E5} \quad M = dz \times Q/U$$

The mass of all gases (volcanic H_2O and air) in the plume, $M_{(g)}$ is the product of M and the gas mass fraction, n, E6.

$$\text{E6} \quad M_{(g)} = n \times M$$

Under high temperature plume conditions, all H_2O in the plume is in gaseous form, whose mass $M_{(w)}$ is the product of M and φ, E7.

$$\text{E7} \quad M_{(w)} = M \times \varphi$$

The mass of dry air in the plume, $M_{(da)}$ is the difference between $M_{(g)}$ and $M_{(w)}$, E8. The mass of background water in the plume, $M_{(bw)}$ is the product of $M_{(da)}$ with the specific humidity, C, E9. The mass of volcanic gases (here: entirely as H_2O), $M_{(vg)}$, is the difference between $M_{(w)}$ and $M_{(bw)}$, E10.

$$\text{E8} \quad M_{(da)} = M_{(g)} - M_{(w)}$$

$$\text{E9} \quad M_{(bw)} = M_{(da)} \times C$$

$$\text{E10} \quad M_{(vg)} = M_{(w)} - M_{(bw)}$$

The masses $M_{(vg)}$, $M_{(da)}$, and $M_{(bw)}$ in kg are converted into moles of volcanic gases, dry air, and background water, $m_{(vg)}$, $m_{(da)}$, $m_{(bw)}$, by dividing by their respective molecular weights (18×10^{-3} for H_2O and 29×10^{-3} for dry air containing N_2, O_2, and Ar, expressed as kg/mol), E11,12,13. The total moles of entrained wet air, $m_{(air)}$, is calculated by the sum of $m_{(da)}$ and $m_{(bw)}$, E14.

$$\text{E11} \quad m_{(da)} = M_{(da)}/(29 \times 10^{-3})$$

$$\text{E12} \quad m_{(vg)} = M_{(vg)}/(18 \times 10^{-3})$$

$$\text{E13} \quad m_{(bw)} = M_{(bw)}/(18 \times 10^{-3})$$

$$\text{E14} \quad m_{(air)} = m_{(da)} + m_{(bw)}$$

Finally, the ratio VA:VM is the moles of wet air divided by moles of volcanic gases, E15.

$$\text{E15} \quad VA : VM = m_{(air)}/m_{(vg)}$$

The calculation yields VA:VM as a function of dz or time when performed for each row of output from the 1D plume dynamics model. Assumptions that water exists purely in the gas phase and that water content is dominated by the volcanic emission are valid for the hot and concentrated plume region investigated in this study. The resulting trend in temperature with VA:VM is consistent with simple specific-heat calculations for the magmatic-air-ash mixture. Plume temperature and VA:VM depend strongly on the T, n, U starting conditions used for the PlumeRise model.

Several PlumeRise 1D model results showing decreasing temperature and increasing VA:VM with time or distance from the source are shown in **Supplementary Figure S1**, for the Eyjafjallajökull eruption April 14–17, 2010. These are based on the model runs of Woodhouse et al. (2013) that used meteorological data from local balloon soundings[1]. The model input parameters are only partially constrained, but Woodhouse et al. (2013) found good predictive capability of the model to reproduce plume height for starting parameter ranges of temperature T = 600–1000 K, vertical velocity U = 50–100 m/s, gas mass fraction n = 0.030–0.086 (Woodhouse et al., 2013; **Supplementary Table S3**). Notably, the model runs are highly diverse in their starting temperatures and predicted VA:VM. The starting temperatures are all substantially lower than petrological estimates of the magmatic temperature, (Keiding and Sigmarsson, 2012) who reported 1443 K (1170 ± 25°C) for the early flank eruption, and 1273–1333 K (1000-1060°C) for benmoritic products related to the main summit eruption that are pertinent to this study. Reasons for this are unclear but could be due to decoupling of magmatic and gas temperatures or a cooling effect of incorporated water. The Introduction Section "High-Temperature Products in Volcanic Plumes: Observations and Modeling" highlighted considerable uncertainty in the physical conditions (temperature, VA:VM) of the near-source plume.

In this exploratory study we use output from the PlumeRise simulation with starting temperature at 1000 K as example boundary conditions in time-varying T and VA:VM as a basis for chemical kinetics modeling of the hot plume chemistry. This chosen PlumeRise dynamics scenario from Woodhouse et al. (2013) combined with magmatic gas emissions based on Allard et al. (2011; **Table 2**) yields an SO_2 flux of 5.5 kt/hr SO_2, that is consistent with the range of SO_2 fluxes derived from satellite observations during the Eyjafjallajökull eruption (Boichu et al., 2013).

Magmatic Gas Emissions

A volcanic gas emission composition is input to the chain-of-reactors model, based on reported observations. It should be emphasized that available observations are an imperfect basis for the initialization of model of high-temperature chemistry in the near-source plume. First, no individual measurement technique can observe all gases in a volcanic plume. Available observations may not fully characterize all magmatic gases in the emission, nor any temporal evolution in their release as a function of volcanic activity. Second, observations of the cooled or partially cooled plume necessarily already incorporate any high-temperature modification of the emissions. Our use of such observations inherently assumes that preceding plume chemistry has only slightly modified the volcanic gas emission. This is indeed the prevalent assumption behind near-source monitoring

---

[1] http://weather.uwyo.edu/upperair/sounding.html

TABLE 2 | Magmatic gas compositions (mole fraction) used as input to the chain-of-reactors model simulations.

Volcanic gas	Eyja CO	Eyja CO-H_2S-H_2
H_2O	0.916	0.916
CO_2	0.08	0.08
SO_2	0.002	0.002
H_2S	–	0.00000145
HCl	X (0.0013)	X (0.0013)
HF	–	–
HBr	–	–
H_2	–	0.00237
CO	0.00035	0.00035

X means that the gas was replaced by Ar. The emission composition is based on field-observations of Eyjafjallajökull's summit 2010 eruption (Allard et al., 2011). A second Eyjafjallajökull emission scenario includes theoretical estimates of H_2 and H_2S. A sensitivity study also investigated emissions excluding CO or SO_2.

of volcanic gas emissions (with the exception of volcanic BrO, e.g., Guttmann et al., 2018). Unfortunately, sources such as lava bodies are typically hazardous and inaccessible, therefore few direct measurements are available of the gas emission prior to any mixing with air.

In this study the composition of the Eyjafjallajökull magmatic gas emission is based on observations of H_2O-CO_2-SO_2-CO-(HCl) in the young plume of the summit eruption reported by Allard et al. (2011) who performed FTIR spectroscopy of volcanic gases in early May 2010, using hot rocks as an IR source. Note that the volcanic emission of HCl was replaced by Ar in our modeling that does include halogens. The emission scenarios for the model studies are summarized in **Table 2**.

A first simulation emissions scenario (Eyja CO) is based entirely on observations of Allard et al. (2011). This emission contains CO but no other reduced gases such as H_2 or H_2S, which typically cannot be resolved in this experimental set up. HF was also not reported, being below detection limits. The measurements by Allard et al. (2011) yield a CO/SO_2 molar ratio of 0.175 and CO/CO_2 = 0.0044. To evaluate how the presence of CO and SO_2 impact the high-temperature chemistry of the near-source plume, sensitivity studies were undertaken that excluded CO and SO_2 from the emission (Eyja no-CO no-SO2).

A further simulation (Eyja CO–H_2-H_2S) was undertaken that included estimates for H_2 and H_2S in the Eyjafjallajökull emission (based on thermodynamic equilibrium calculations) alongside CO and the other gases reported by Allard et al. (2011). It is assumed that the magmatic gases were in thermodynamic equilibrium and at magmatic temperature on emission. For the Eyjafjallajökull summit eruption a temperature of 1273 K is assumed (Keiding and Sigmarsson, 2012). The gases obey the equilibria $CO + 0.5\ O_2 = CO_2$, $H_2 + 0.5\ O_2 = H_2O$, $H_2S + 1.5\ O_2 = SO_2 + H_2O$ with corresponding thermodynamic equilibrium constants of 1.13×10^7, 1.92×10^7, and 1.54×10^{17} at 1273 K (constants obtained from HSC). For these conditions the CO/CO_2 molar ratio 0.0044 observed by Allard et al. (2011) corresponds to an oxygen fugacity of 4.0×10^{-10} bar (i.e., QFM+1.6 log units). The corresponding H_2O/H_2 molar ratio is 387 and SO_2/H_2S molar ratio is 1379. Combining these theoretical molar ratios with the mole fraction composition for H_2O and SO_2 in **Table 2** yields estimates for the mole fractions of $H_2 = 0.0024$ and $H_2S = 1.45 \times 10^{-6}$ in the Eyjafjallajökull emission. Thus, it is predicted that the eruption emitted a similar quantity (by mole) of H_2 compared to SO_2, but only a trace emission of H_2S.

Some volcanoes release a larger proportion of sulfur in reduced forms. To investigate the potential impact of H_2S on the high-temperature chemistry of near-source volcanic plumes, we undertook a sensitivity study using a composition based on measurements made at Mt Etna (passive degassing) whose emission composition is still relatively oxidized, but includes H_2S (Roberts et al., 2017 and references therein) and H_2 (Aiuppa et al., 2011; **Supplementary Table S4**). We emphasize that our combination of Eyjafjallajökull plume dynamics with Mt Etna emission composition for this sensitivity study is not representative of plume chemistry for Mt Etna passive degassing conditions. Rather it reflects a possible scenario for an ash-rich explosion from Mt Etna, assuming emission composition similar to that observed during passive degassing, and plume dynamics similar to Eyjafjallajökull. The Mt Etna composition used as input to our kinetics-model study is identical to the input used for a thermodynamic model study by Martin et al. (2011) [where the H_2 emission was calculated theoretically and is somewhat higher than that observed by Aiuppa et al. (2011)]. Notably, the SO_2 content of the Mt Etna emission composition (0.029 mole fraction) is more than an order of magnitude higher than the SO_2 content of Eyjafjallajökull emission (0.002 mole fraction). The H_2S content of the emission is also much higher for Mt Etna (also with a higher ratio to SO_2), whilst the H_2, H_2O, and CO_2 mole fractions are similar (although ratios to SO_2, X/SO_2, are lower). A sensitivity study was also performed without H_2S in the Etna emission (Etna no-H_2S).

Equilibrium Modeling: HSC Thermodynamic Model

Our study compares output from the chemical kinetics model outlined above to an equilibrium model (HSC) that has been previously applied to investigate volcanic plume chemistry (e.g., Martin et al., 2006). HSC model version 7.1 was used to calculate equilibrium compositions of mixtures of air with magmatic gases under the same temperature and VA:VM boundary conditions as for the chain-of-reactors model. The input composition was determined by mixing air (composed of 78% N_2, 21% O_2 and 1% Ar) with the Eyjafjallajökull magmatic gas composition (**Table 2**) for each VA:VM, whilst temperature was specified according to the PlumeRise boundary conditions. Pure magmatic gases are usually assumed to have compositions at chemical equilibrium when they are released from the volcano (and there is good evidence for this to first order for major C- and S-bearing species, e.g., Oppenheimer et al., 2018); however, some repartitioning of Eyjafjallajökull gases may be expected for thermodynamic equilibrium calculations even at VA:VM = 0:100 because the reported gas emission composition is incomplete and the initial PlumeRise temperature is slightly lower than magmatic temperature (see section "Magmatic Gas Emissions").

RESULTS

Model Diagnostics: Cooling and Mixing of Volcanic Gases With Air

Physical parameters from the PlumeRise model (temperature T, VA:VM, distance from the source, and plume cross-sectional area) used as boundary conditions for the chain-of-reactors model vary as a function of time, **Figures 2A,B**. Temperature is varied smoothly across the chain-of-reactors and decreases from 1000 K to 890 K (over the 30 PFRs) whereas VA:VM increases stepwise from 0 to 5.3 due to air-entrainment between each reactor. This T and VA:VM scenario is not representative of all volcanoes. Smaller volcanic emissions would likely disperse faster, particularly if ash-poor. The presence of ash in Eyjafjallajökull plume maintains high temperatures at higher VA:VM than would occur in an ash-poor emission (that for example for VA:VM > 3 would yield $T < 500$ K according to simple gas-phase mixing). This result is not surprising given 1D plume-rise models of explosive eruptions typically assume an emission containing volcanic gases at a few weight-percent, with the remainder as pyroclasts. We highlight that this "temperature buffering" effect of ash may significantly prolong the period in which volcanic gases undergo high-temperature chemistry as they mix with air.

As VA:VM increases, the abundance of air-dominated gases such as O_2 increases step-wise toward an asymptote of 21% (pure air) whilst major magmatic gases such as H_2O and CO_2 decrease step-wise due to dilution, **Figure 2C**. Plume chemistry can additionally cause gas abundances to rise or fall within each reactor. **Figure 2C** shows that there is negligible or only small impact of plume chemistry on O_2, H_2O, and CO_2 whose abundances are largely controlled by air entrainment/dilution. Also shown in **Figure 2C** is the product of the O_2 and H_2O mole fractions that reaches a maximum at around 0.5 s, of relevance to the high-temperature reactions discussed in Section "Discussion."

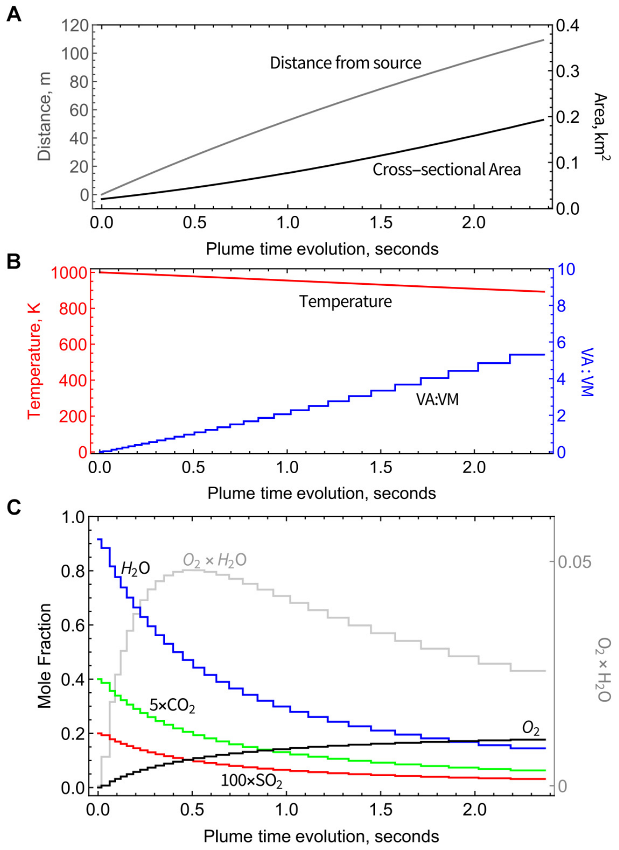

FIGURE 2 | Physical parameters used as boundary conditions for the chain-of-reactors model, from the PlumeRise model applied to Eyjafjallajökull 2010 eruption (Woodhouse et al., 2013). **(A)** Plume cross-sectional area and distance from source as a function of plume time evolution. **(B)** Decreasing temperature and increasing proportion of mixing between air and magmatic gases (VA:VM) as a function of time. **(C)** Output from the chain-of-reactors model as a function of time: mole fractions of major volcanic gases (H_2O, CO_2, and SO_2) decrease due to dilution and O_2 increases due to entrainment of background air. Also shown is the product of H_2O and O_2 exhibiting maximum around 0.5 s.

High-Temperature Production of Oxidants and Radicals

The chemical evolution of the Eyjafjallajökull near-source plume according to the high-temperature chain-of-reactors model is shown in **Figure 3A** (Eyja CO run) over a time-period of about 2.4 s, during which VA:VM increases from 0 to 5.3, and temperature decreases from 1000 K to 890 K. The slight declines in major gases H_2O, CO_2, and SO_2 mixing ratios show they are largely under the control of dilution whilst air is entrained, i.e., are largely conserved. The production of oxidant radicals such as OH, HO_2, and H_2O_2 increases rapidly with plume time evolution during the first 0.5 s, after which their absolute mixing ratios decrease. Formation of SO_3 follows a similar pattern. The volcanic gas CO decreases only slightly faster than the major gases, indicating that it is not substantially oxidized by the plume chemistry. The general pattern is similar for the Eyja CO–H_2–H_2S simulation, **Figure 3B**: a higher maximum abundance of oxidant radicals is reached (slightly earlier) and slightly more CO is oxidized, but still not completely depleted. In the Eyja CO–H_2–H_2S simulation both volcanic gases H_2 and H_2S become oxidized at around 0.5 s. To analyze the chemical kinetics model results in more detail and compare to field-observations and thermodynamic calculations, ratios are presented of the minor volcanic gases relative to the major (largely conserved) gases SO_2, CO_2, and H_2O.

Oxidation of CO Is Kinetics Limited in the Near-Source Plume

CO is only slightly oxidized by high-temperature chemistry, as shown by CO/SO_2 ratio, **Figure 4A** (as well as CO/CO_2, **Figure 4B**). At the end of the simulations (VA:VM = 5.3 after 2.4 s), CO/SO_2 has only declined by about 15% of the initial ratios for Eyja CO, and by 37% of the initial ratios for Eyja CO–H_2–H_2S. In contrast, HSC thermodynamic calculations predict near-complete oxidation of CO as soon as air is mixed with the

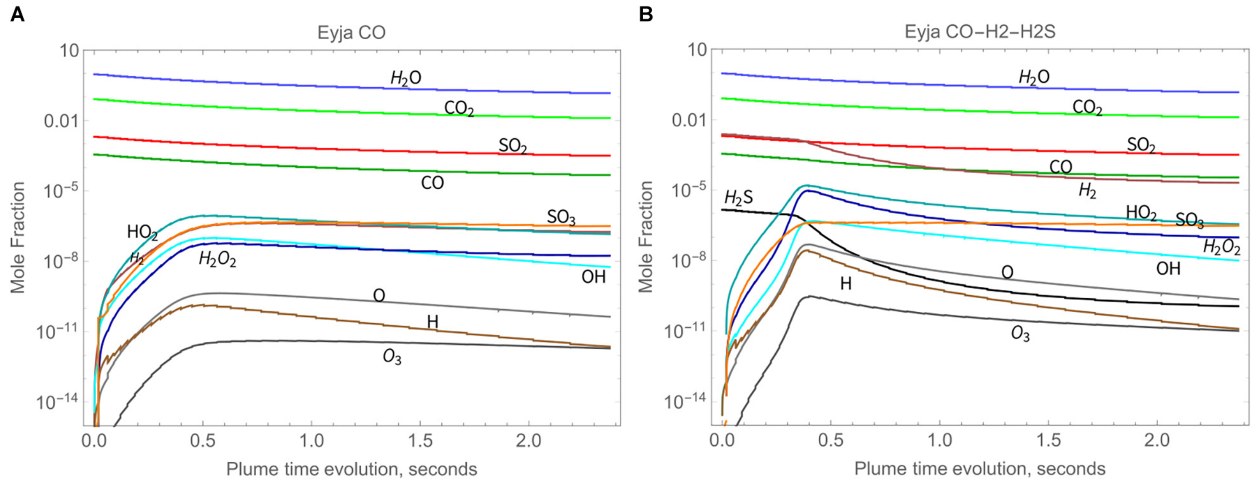

FIGURE 3 | High-temperature oxidant and radical production as a function of time in Eyjafjallajökull plume according to the chain-of-reactors model for two initial compositions, both of which include major volcanic gases H_2O, CO_2, and SO_2, as well as additional emitted gases as named: **(A)** Eyja CO and **(B)** Eyja CO-H_2-H_2S.

volcanic gases (VA:VM > 0), **Figure 4**. The kinetics model results are thus far more consistent with the presence of CO observed in the young Eyjafjallajökull plume by FTIR (Allard et al., 2011) and indeed in other volcanic gas emissions from more reduced magmas, e.g., at Mt Erebus (Oppenheimer and Kyle, 2008).

Additional observations of volcanic CO in the Eyjafjallajökull plume are reported by Schumann et al. (2011) who made instrumented aircraft measurements of the aged (10–100 h) plume over Europe during mid-April to mid-May. Both CO and SO_2 were observed above background levels. The molar ratio of excess CO and excess SO_2 (as averages) in transects of the aged plume is around ∼1, i.e., somewhat higher than the ratio reported by Allard et al. (2011) in the young plume. Reasons for this discrepancy are not clear. It is unlikely that CO was formed in the plume in an oxidizing atmosphere. Plume structure in the aircraft measurements as reported by Schumann et al. (2011) is smoother for SO_2 compared to CO. This may in part be due to the vastly different response times of the aircraft-based instruments for SO_2 (T95 response time to reach 95% signal is 80 s) and CO (response time < 2 s), which might cause a high bias in the derived CO/SO_2. There is some scatter in the CO and SO_2 measurements as well as variability in background CO. In addition, SO_2 could undergo atmospheric oxidation processes, resulting in an increase in the CO/SO_2 ratio in the downwind plume. Unusually, at Erebus volcano a rapid loss of SO_2 has been identified in the very young plume possibly aided by cloud processing (Oppenheimer et al., 2010). However, oxidation of SO_2 in volcanic plumes is typically slow (e.g., Galeazzo et al., 2018). The measurements of CO/SO_2 in the downwind Eyjafjallajökull plume do not show any clear dependency on plume age. In any case, the aircraft measurements of Schumann et al. (2011) detected volcanic plume CO alongside SO_2, confirming that CO was emitted during the 2010 Eyjafjallajökull eruption and that CO was not substantially oxidized by high-temperature near-source chemistry as is commonly predicted by thermodynamic modeling. Oxidation of CO was evidently kinetics-limited in the transient near-source plume. A summary of the model and observed CO/SO_2 is given in **Table 3**.

The Eyja CO–H_2–H_2S simulation that includes theoretical estimates for volcanic emission of H_2 and H_2S predicts near-complete oxidation of both gases, **Figure 4B**, as well as partial oxidation of CO. This is due to an oxidant enhancing feedback mechanism (see section "Discussion"). No specific observations of H_2 or H_2S are available for comparison in the Eyjafjallajökull near-source or far downwind plume. However, observations of H_2S in plumes from both passively degassing volcanoes (e.g., Roberts et al., 2017) and explosive eruption plumes (e.g., de Moor et al., 2016) indicate that H_2S is (largely) conserved, as for CO. Measurements of H_2 have been reported in plumes from some passively degassing volcanoes (e.g., Aiuppa et al., 2011; Moussallam et al., 2012). In general, observations of reduced gases in volcanic plumes (specifically CO/CO_2, H_2O/H_2, and SO_2/H_2S gas ratios) may be used to infer magmatic properties at emission such as oxygen fugacity (see section "Magmatic Gas Emissions"), on the condition that modification of the emitted composition by near-source plume chemistry is either negligible or well-constrained by plume chemistry models. Here the small decrease in CO/CO_2 predicted by the kinetics model (Eyja CO) is equivalent to a difference in oxygen fugacity of 1.5×10^{-10} bars or about 0.14 log unit QFM. We highlight two important areas of model uncertainty regarding the near-source oxidation of reduced gases. First, the reactions are temperature-dependent yet the temperature of the volcanic gas emission as well as subsequent plume physical evolution are both rather poorly known. Second, the kinetics of certain reactions, particularly for H_2S are poorly constrained by laboratory experiments. Thus, the presence of H_2 and H_2S observed in certain volcanic plumes may suggest either a lower emission temperature or faster cooling rate than the Eyjafjallajökull case presented here, or may reflect uncertainties in the model chemical schemes.

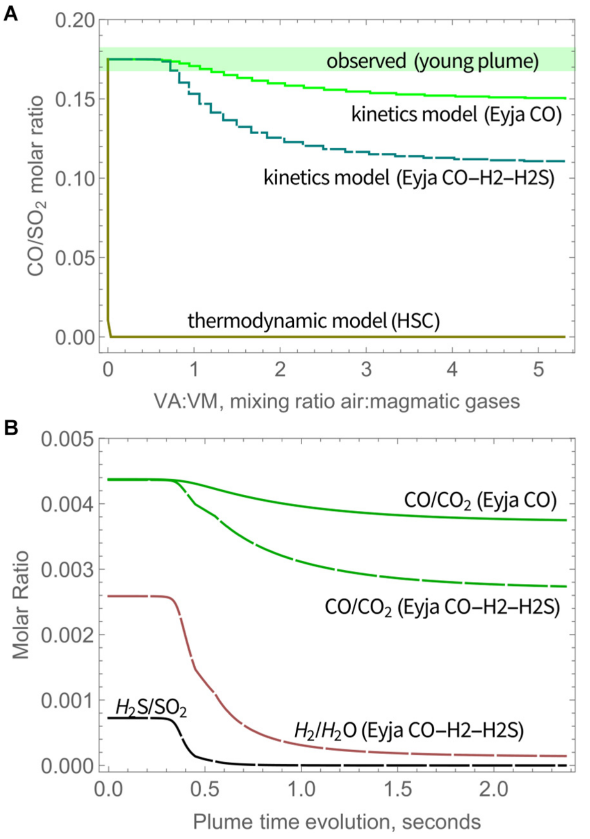

FIGURE 4 | (A) Molar ratio of CO/SO$_2$ in Eyjafjallajökull plume as a function of time according to the chain-of-reactors model for Eyja CO and Eyja CO-H$_2$-H$_2$S simulations, and the HSC thermodynamic model, compared to CO/SO$_2$ observed in the young plume by Allard et al. (2011), see also **Table 3**. Solid lines: Eyja CO simulation, Dashed lines: Eyja CO-H$_2$S-H$_2$ simulation. **(B)** Molar ratio of CO/CO$_2$ (Eyja CO and Eyja CO-H$_2$-H$_2$S simulations) as well as H$_2$S/SO$_2$ and H$_2$/H$_2$O (Eyja CO-H$_2$-H$_2$S simulation only) as a function of time according to the chain-of-reactors model. Solid lines: Eyja CO simulation, Dashed lines: Eyja CO-H$_2$S-H$_2$ simulation.

TABLE 3 | Molar CO/SO$_2$ ratio observed in Eyjafjallajokull eruption plume compared to model predictions.

Measurement/model	CO/SO$_2$ molar ratio
FTIR observations of the young plume on May 08, 2010 (Allard et al., 2011)	0.175
Aircraft measurements of the downwind plume on April 22, 2010 – May 18, 2010 (Schumann et al., 2011)	~1
Thermodynamic model HSC (at VA:VM = 5.3, T = 890 K)	10^{-10}
Kinetics model: Eyja CO (at t = 2.4 s, VA:VM = 5.3, T = 890 K)	0.15
Kinetics model: Eyja CO-H$_2$S-H$_2$ (at t = 2.4 s, VA:VM = 5.3, T = 890 K)	0.11

All models initialized with CO/SO$_2$ = 0.175.

High-Temperature Production of SO$_3$ as a Sulfate Aerosol Precursor

SO$_3$ abundance in magmatic gas is negligible but is predicted to form through high-temperature plume chemistry. SO$_3$ is a precursor to sulfate aerosol (as is well-known e.g., from studies of power station emissions). Upon further plume cooling, volcanic SO$_3$ will react readily with $H_2O_{(g)}$ to form $H_2SO_{4(g)}$ that is highly hygroscopic and will form sulfate particles. The widespread observation of near-source volcanic sulfate (see section "Introduction," **Table 1**), motivates our model investigation of high-temperature SO$_3$ as a possible sulfate source. The SO$_3$ abundance increases rapidly at around 0.5 s, **Figure 5A**. The SO$_3$/SO$_2$ molar ratio increases throughout the model simulations, indicating a continual production of SO$_3$ that is similar for Eyja CO and Eyja CO–H$_2$–H$_2$S. By the end of the simulations (2.4 s, VA:VM = 5.3, T = 890 K), the SO$_3$/SO$_2$ molar ratio reaches 10^{-3}. The fact that SO$_3$/SO$_2$ ratio is still increasing at the end of the model simulation indicates that additional high-temperature production of SO$_3$ is expected as the plume cools and dilutes further. Extrapolation of **Figure 5A** suggests SO$_3$/SO$_2$ may potentially reach up to ~2 × 10^{-3}. Whilst there are no reported sulfate/SO$_2$ measurements for the Eyjafjallajökull summit eruption for specific comparison, this modeled ratio of SO$_3$/SO$_2$ of around 10^{-3} lies within the range of observed near-source sulfate/SO$_2$ ratios, including the Eyjafjallajökull flank eruption (**Figure 5B** and **Table 1**). In contrast, calculations using the HSC thermodynamic equilibrium model at VA:VM = 5.3, T = 890 K predict SO$_3$/SO$_2$ of around 3.1, an order of magnitude above the highest ratio of sulfate/SO$_2$ in the field observations, and several orders of magnitude higher than the Eyjafjallajökull observations. We conclude that the chemistry producing SO$_3$ in the near-source volcanic plume is under kinetic rather than thermodynamic control.

High-Temperature Production of Oxidants HO$_2$, OH, and H$_2$O$_2$

High-temperature oxidants HO$_{xy}$ (HO$_2$, OH, and H$_2$O$_2$) are predicted to form in the Eyjafjallajökull plume through high-temperature plume chemistry, **Figures 6A,B** (absolute concentrations shown). Also shown for scale is the SO$_2$ concentration that decreases largely due to dilution. High-temperature HO$_{xy}$ reaches a maximum around 0.5 s. HO$_{xy}$ production is greater for Eyja CO–H$_2$–H$_2$S than for the Eyja CO simulation. In both cases HO$_x$ exists predominantly as HO$_2$. This contrasts with thermodynamic calculations that predict HO$_x$ to exit predominantly as OH (e.g., Gerlach, 2004). Another important feature of the chemical kinetics modeling is that H$_2$O$_2$ is predicted to form (at greatest abundance for Eyja CO–H$_2$–H$_2$S), whilst H$_2$O$_2$ is essentially not formed in HSC thermodynamic calculations (e.g., Martin et al., 2006).

High-temperature SO$_3$ was discussed above as a precursor to sulfate aerosols. The H$_2$O$_2$ formed by high-temperature chemistry may promote further sulfate formation upon plume cooling, due to its reaction with dissolved $SO_{2(aq)}$. If a condensed phase is formed already in the crater zone this could yield an additional source of "primary" or near-source sulfate. Alternatively, if plumes become condensed clouds further

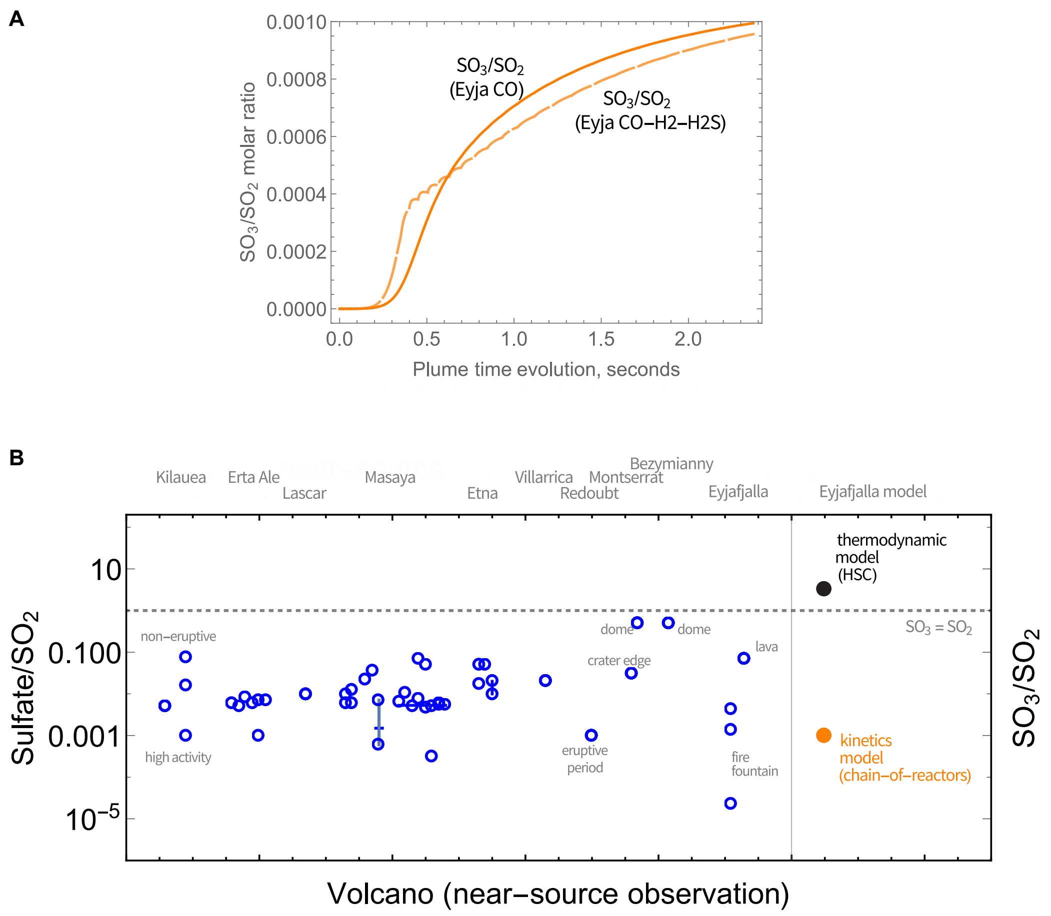

FIGURE 5 | (A) Evolution in the SO_3/SO_2 molar ratio in Eyjafjallajökull plume as a function of time, according to the chain-of-reactors model. Solid lines: Eyja CO simulation, Dashed lines: Eyja CO-H_2-H_2S simulation. **(B)** Observations of near- or at-source sulfate relative to SO_2 reported in volcanic plumes (**Table 1**) compared to the molar ratio of sulfate precursor SO_3 to SO_2 predicted by the chain-of-reactors model for Eyjafjallajökull eruption plume (time = 2.4 s, T = 890 K, VA:VM = 5.3) and HSC thermodynamic equilibrium calculations for the same plume conditions (T = 890 K, VA:VM = 5.3). The SO_3 = SO_2 is demarked by a dotted line.

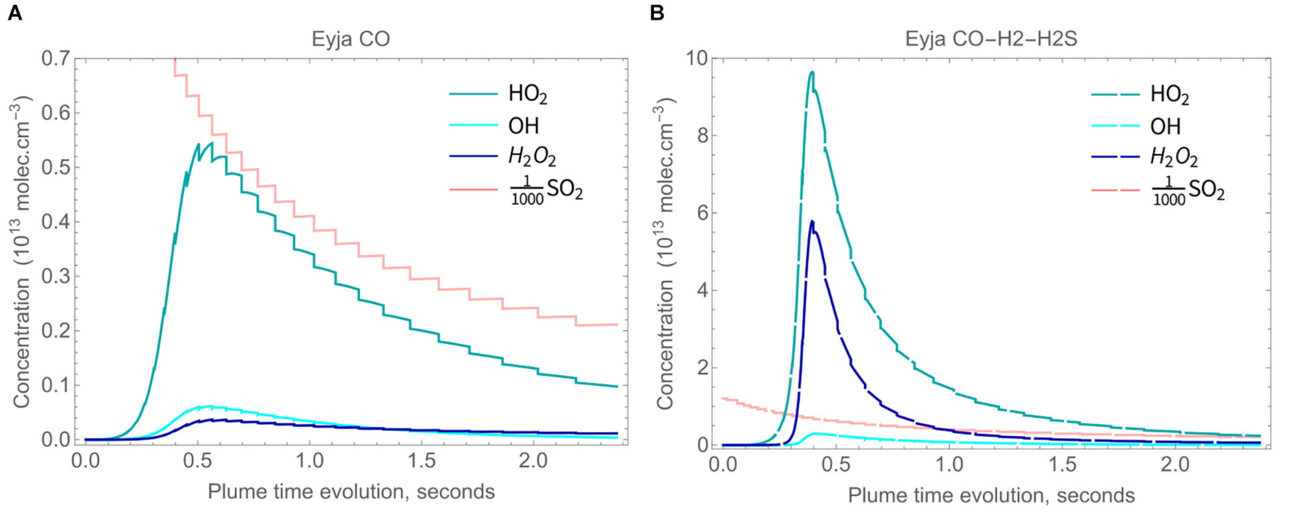

FIGURE 6 | Concentrations of HO_2 (blue), H_2O_2 (dark blue) and OH (cyan) in the plume, with SO_2 concentration also shown for scale, molec cm^{-3}. **(A)** solid lines: Eyja CO simulation and **(B)** dashed lines: Eyja CO-H_2-H_2S simulation.

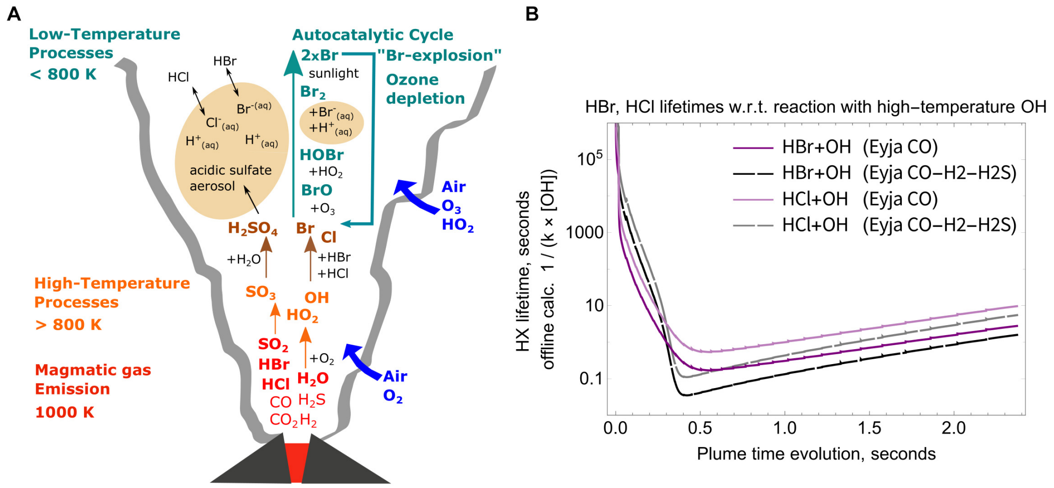

FIGURE 7 | (A) schematic of key high-to-low temperature processes in the volcanic plume, including high-temperature production of SO_3 as sulfate aerosol precursor, HOx oxidants and halogen radicals, and low-temperature multi-phase chemistry producing BrO. **(B)** Calculated lifetimes of HCl and HBr in the plume with respect to their reaction with high-temperature OH as a function of plume evolution time. Solid lines: Eyja CO simulation, Dashed lines: Eyja CO-H_2-H_2S simulation. Lifetime minima are <1 s, see **Table 4**.

downwind, the volcanic H_2O_2 may form secondary sulfates. In this respect, Carn et al. (2011) measured H_2O_2 in the plume emitted by Huila volcano (elevated above background by about 0.5 ppbv) that was rapidly titrated when the plume entered a cloudy phase. We are unaware of other observations of H_2O_2 in volcanic plumes.

We highlight two further potential impacts of volcanic H_2O_2. Studies have shown that iron on the surface of volcanic ash has the potential to generate substantial quantities of hydroxyl radicals that may affect the toxicity of inhaled ash particles (Horwell et al., 2003; Hillman et al., 2012). This occurs via the Fenton reaction involving H_2O_2. The elevated abundance of H_2O_2 in the volcanic plume predicted by our model study would likely enhance the production of OH radicals and their potential health hazard. Indeed, an observation that has puzzled the volcanology-atmospheric community to date is the presence of elevated OH (and HO_2) measured in the 2010 Mt Hekla eruption cloud in the stratosphere (Rose et al., 2006). This elevated OH is all the more surprising given the measurement was made during night-time and in the presence of major OH reactive sinks (e.g., HCl and SO_2). We propose the reaction of volcanic H_2O_2 on ash particles as a possible mechanism that could generate OH radicals in volcanic plumes even during night-time.

Potential for High-Temperature Formation of Halogen Radicals

High-temperature oxidants such as OH and radicals such as Br, Cl are believed to have an important role in accelerating the onset of low-temperature atmospheric chemistry "bromine explosion" cycles that form BrO and destroy ozone in the downwind plume (e.g., Bobrowski et al., 2007; Roberts et al., 2014; Surl et al., 2015; **Figure 7A**). The bromine explosion is autocatalytic so can be efficiently "kick-started" by a small quantity of high-temperature halogen radicals. Observations show that halogens were emitted during the eruption (young plume $HCl/SO_2 \approx 0.65$, Allard et al., 2011) and that reactive halogen chemistry was active in the plume (downwind plume $BrO/SO_2 \approx 1.3 \times 10^{-4}$, Heue et al., 2011). The Eyjafjallajökull volcanic halogen chemistry caused a depletion of tropospheric ozone (Vance et al., 2010; Schumann et al., 2011). Here offline calculations show the potential for formation of high-temperature halogen radicals to initiate this process.

The OH formed in the near-source volcanic plume is a powerful oxidant that can react with volcanic halogens (emitted as HCl and HBr) to produce halogen radicals (R1 and R2). The high-temperature chemical kinetics model scheme used in this study does not include halogen chemistry. Nevertheless, offline calculations of the lifetime of volcanic HCl, HBr emissions can be undertaken to estimate the potential for halogen radical formation, shown here for the Eyjafjallajökull simulations.

$$\text{R1} \quad HCl + OH \rightarrow Cl + H_2O$$

With bimolecular rate constant reported by Ravishankara et al. (1985) as $k = 4.5 \times 10^{-17} \times T^{1.65}\ \exp[112/T]$ cm^3 $molecule^{-1}$ s^{-1} (valid for 240–1055 K).

$$\text{R2} \quad HBr + OH \rightarrow Br + H_2O$$

With bimolecular rate constants estimated by Góger et al. (2018) as $k = (9.86 \pm 2.38) \times 10^{-16} \times T^{(1.23\,\pm\,0.03)} \times \exp[(5.93 \pm 0.33)\ kJ\ mol^{-1}/RT]$ cm^3 $molecule^{-1}$ s^{-1} (valid for 600–3200 K).

Lifetimes of HBr and HCl in the near-source plume are calculated by the inverse of the first-order rate constant, i.e., the product of the 2nd order rate constants for R1 and R2 with the OH concentration. The temperature dependence of the rate constants is only slight (variation of up to about 15%) over our studied temperature range 890–1000 K. Rather, **Figure 7B** shows that the calculated HCl and HBr lifetimes during the Eyja

TABLE 4 | Simulated maximum OH/SO_2 ratio and OH concentration in the high-temperature near-source plume according to the chain-of-reactors model, and minimum lifetime of HX (X = Br or Cl) with respect to reaction with OH by offline calculation (see section "Potential for High-Temperature Formation of Halogen Radicals" and **Figure 7B**).

Model run	Maximum OH/SO_2 (simulated) mol/mol	Maximum OH concentration (simulated) molec cm^{-3}	Minimum HBr lifetime (offline calculation) seconds	Minimum HCl lifetime (offline calculation) seconds
Eyja CO	1.06×10^{-4}	6.13×10^{11}	0.167	0.534
Eyja CO-H_2-H_2S	4.38×10^{-4}	2.93×10^{12}	0.035	0.110

For comparison, the observed Eyjafjallajökull plume HCl/SO_2 and BrO/SO_2 molar ratios are 0.6 and $\approx 1.3 \times 10^{-4}$, respectively, and the total time-duration of the high-temperature simulation is 2.4 s.

CO and Eyja CO–H_2–H_2S simulations are a strong function of OH concentration. The halogen halide lifetimes rapidly decrease as OH is formed in the near-source plume, and then increase as OH is consumed (and diluted). Lifetimes of HBr and HCl reach minima of <1 s in the plume, **Table 4**. Lifetimes are shortest for HBr that has the greater rate constant of reaction and for the Eyja CO–H_2–H_2S simulation that produces highest OH concentration. In all cases, the calculated HBr and HCl lifetime minima are shorter than the timescale of the plume simulation (2.4 s) indicating that significant halogen radical production will occur. Reactions R1 and R2 will likely cause a negative feedback on OH concentrations. Once formed the halogen radicals will react with CHOS and some may reform HBr or HCl. A more comprehensive understanding of the halogen interactions will require inclusion of halogen reactions explicitly in the high-temperature model chemical mechanism.

DISCUSSION

Chemical Reaction Mechanisms and Feedbacks

The chemical kinetics model identifies key reactions causing oxidation and oxidant production in the volcanic plume. In this study, the model simulations predict abundances of oxidants, and oxidized species increase rapidly around 0.5 s, at T = 980 K, corresponding to VA:VM around 1 according to the specific Eyjafjallajökull boundary conditions scenario used (different times or temperature conditions can be expected under other plume dyamics conditions). VA:VM = around 1 corresponds to the point where mixing of magmatic gases and air yields a maximum in the product of air-derived O_2 and magmatic-derived H_2O. Radical oxidants HO_x are produced from the reaction of H_2O with O_2 to form OH and HO_2, R3. This (two-way) reaction usually acts as a sink rather than source of radicals in combustion but OH and HO_2 formation in the near-source volcanic plume is driven by the unusually high H_2O content of the plume-air mixture at high temperatures. Production of HO_x is fastest at around 0.5 s or VA:VM = 1, coincident with the maximum in the product of H_2O and O_2 mole fractions.

$$\text{R3} \quad H_2O + O_2 \rightleftharpoons OH + HO_2$$

Formation of SO_3 occurs by the reaction R4 of SO_2 with HO_2.

$$\text{R4} \quad SO_2 + HO_2 \rightleftharpoons SO_3 + OH$$

When CO is present in the plume, some of it can react with OH to form CO_2 and H radicals, R5, which may further react with O_2 to form HO_2, R6.

$$\text{R5} \quad CO + OH \rightleftharpoons CO_2 + H$$

$$\text{R6} \quad H + O_2 + M \rightleftharpoons HO_2 + M$$

Once formed, HO_2 can react with itself, R7, to produce hydrogen peroxide, H_2O_2.

$$\text{R7} \quad HO_2 + HO_2 \rightleftharpoons H_2O_2 + O_2$$

Some H_2O_2 can also thermally decompose to form OH radicals, R8.

$$\text{R8} \quad H_2O_2 + M \rightleftharpoons OH + OH + M$$

In high-temperature chemistry (generally temperatures above 800–850 K), formation of H_2O_2 is usually considered as a sink of oxidant radicals. However, in the case of a near-source plume the removal of OH by CO (R5, followed by R6 and R7 leading to H_2O_2) drives the formation of more OH and HO_2 from the reaction of H_2O with O_2 (more specifically, the balance of this reaction, R3, with its reverse reaction). This feedback mechanism promotes the production of HO_{xy} in volcanic plumes containing CO, where only a fraction of the emitted CO needs to be oxidized to substantially enhance HO_{xy} abundances and promote the chain reaction. Similarly, the H_2 emission in the Eyja CO–H_2–H_2S simulation can also react with OH, R9 (followed by R6 and R7) to cause a similar positive feedback on HO_x production.

$$\text{R9} \quad H_2 + OH \rightleftharpoons H_2O + H$$

These feedbacks involving reduced gases may explain the greater production of oxidants in Eyja CO–H_2-H_2S than Eyja CO simulation. This hypothesis is supported by a sensitivity study without CO and SO_2 in the emission (Eyja no-CO no-SO_2, **Supplementary Figure S2**) that produces a lower OH abundance but where more OH accumulates more in the first hundreds of milliseconds, reflecting the balance of OH production and consumption.

We now consider the role of H_2S. The very low (theoretically estimated) H_2S emission from Eyjafjallajökull had a rather negligible impact on the near-source plume chemistry. The role of H_2S is investigated in a simulation of the high-temperature chemistry of Mt Etna emissions, that include H_2 and H_2S as well as SO_2, H_2O, and CO_2, see **Supplementary Table S4** (as well as a control run that excludes H_2S). The Etna simulation assumes an eruption with the same plume physics as for Eyjafjallajökull. A very rapid production of oxidants is predicted within the first 0.1 s of plume evolution, **Supplementary Figure S3**, coincident with a rapid decrease in H_2S (and a slower decrease in H_2). Abundances of oxidant radicals initially substantially exceed those predicted for Eyja CO and Eyja CO–H_2–H_2S, and later decline to lower levels. According to our model, the oxidation of emitted H_2S causes an extra production of O atoms (which is not observed in the case "without H_2S") with in the first milliseconds of the plume's mixing with air, following the sequence: $H_2S + H$ (or OH) = $SH + H_2$ (or H_2O), $2SH = H_2S + S$, $S + O_2 = SO + O$, and $SO + O_2 = SO_2 + O$. The production of sulfur atoms from H_2S and their subsequent reactions with O_2 are mostly responsible for this production of O, which, in turn, converts SO_2 into SO_3, resulting in the SO_3 peak observed at 0.1 s in the plume. Beyond this point, the conversion of SO_2 into SO_3 is mainly due to the abundance of HO_2 through $SO_2 + HO_2 = SO_3 + OH$. A significant part of SO_3 is then used to recycle SO_2 through the formation of $HOSO_2$ (SO_3+HO_2 = $HOSO_2$+O_2 and $HOSO_2$+M = SO_2+OH+M). Indeed, the formation of SO_3 in the Mt Etna scenario proceeds through two different mechanisms (with O, and then with HO_2) at different locations in the plume whereas in the Eyja CO and Eyja CO-H_2-H_2S or Etna no-H_2S scenarios, the formation of SO_3 is only linked to HO_2. It must be emphasized, however, that model predictions are limited by uncertainty in high-temperature H_2S chemistry.

This sulfur cycling regulates SO_3/SO_2 to reach around 10^{-3} after 2.4 s in all of the simulations (Eyja CO, Eyja CO-H_2-H_2S, Etna and Etna no-H_2S, **Figure 5A** and **Supplementary Figure S3**), despite their differences in CO-H_2-H_2S emissions that lead to vast differences in the production and abundances of HO_{xy}. Temperature and VA:VM evolution with time may be important controls on SO_3/SO_2, therefore production of near-source sulfate could vary for different physical conditions other than the Eyjafjallajökull case considered here.

Model Uncertainties and Future Directions

Our chain-of-reactors model provides a framework for quantitative studies into the high-temperature reactions occurring in the near-source plume to form oxidized products such as sulfate-precursors, OH, H_2O_2 that can impact subsequent physico-chemical processing in the cooled plume. We find that the high-temperature chemistry is under kinetic control; plume composition does not follow thermodynamic equilibrium (**Figures 4A**, **5B**, with example model output in **Supplementary Tables S5, S6**). Our exploratory study identifies several areas for further investigation.

Improved Model Chemistry at High-Temperatures and Link to Low-Temperature Plume Processes

Uncertainties in the high-temperature gas chemistry mechanism need to be addressed such as the chemical kinetics of sulfur species reactions, notably the oxidation of H_2S, that are poorly quantified from laboratory experiments. Future model developments should also incorporate the chemistry of halogens and nitrogen species coupled to CHOS. Simulations of longer duration should cover the whole regime where high-temperature chemical reactions may be important (e.g., down to 800/850 K). The gas-phase mechanism should be extended to consider photolysis reactions for plumes that are not too optically thick, and, especially, heterogeneous chemical reactions, for example reactions on ash surfaces (Delmelle et al., 2018), noting the oxidized products from high-temperature gas chemistry could act to modify ash properties. Models should ultimately be developed that encompass both high-temperature chemistry and also the transition to low-temperature plume chemistry as simulated by atmospheric models (e.g., Jourdain et al., 2016).

Influence of Emitted Magmatic Gas Composition on High-Temperature Chemistry

The composition of magmatic gases released is specific to each volcano and can vary with volcanic activity/unrest. The chemical feedback mechanisms identified by our model suggest that emissions of reduced gases can enhance the high-temperature production of oxidants. This might lead to a greater production of oxidant radicals in the near-source plume of volcanoes with a relatively reduced emissions composition, such as Mt Erebus, Antarctica, whose emissions are rich in CO and H_2. Few field-measurements exist to evaluate model predictions: the high-temperature region is difficult to access directly and few studies have quantified oxidized products in the cooled downwind plume, e.g., by instrumented aircraft. Another critical uncertainty is that the emission temperature of volcanic gases is poorly known. In some situations, according to the dynamics of the degassing, magmatic gas emissions at the surface may be neither in chemical nor thermodynamic equilibrium with the melt (Oppenheimer et al., 2018).

Influence of Plume Dynamics on High-Temperature Chemistry

The chemical kinetics model requires time-resolved boundary conditions in plume dynamics, notably temperature and VA:VM (degree of mixing of air with magmatic gases). This study used output from a 1D PlumeRise model for the Eyjafjallajökull 2010 eruption (Woodhouse et al., 2013) for this purpose. Variability in plume dynamics was not investigated but is expected to exert a strong influence on the near-source chemistry through the rate of entrainment of air and cooling. For example, smaller emission sources will typically disperse and cool faster in the troposphere. Ash-poor emissions will tend to cool more rapidly than ash-rich emissions where the solid pyroclasts buffer the temperature of the volcanic gas and air mixture. Large eruptions that inject gases and ash into the stratosphere should also be investigated. Spatial heterogeneity in the turbulent mixing of air into the plume might non-linearly impact the plume chemistry, potentially requiring the development of 3D model approaches to investigate the plume's high-temperature chemistry as a function of a more detailed turbulent mixing.

CONCLUSIONS

We present chemical kinetics model simulations of the high-temperature gas chemistry that occurs as magmatic gases mix with air and cool in the near-source volcanic plume. Volcanic gases released into the atmosphere undergo rapid processing including photochemistry, oxidation, and aerosol formation. Quantifying these processes in volcanic plumes is essential to assess atmospheric and environmental impacts of volcanic emissions. During the first few seconds after release, the hot magmatic gases mix with background air containing oxidants and undergo a high-temperature processing. The gas chemistry in this high-temperature region of the plume is poorly characterized, yet can critically modify the composition of the emission to produce oxidized products and radicals, such as near-source sulfates, HOxy, and halogen radicals. These high-temperature products influence the subsequent physico-chemical processing of the plume at low-temperatures as it disperses in the atmosphere. Studies to date have largely represented the chemical composition of the high-temperature region using thermal equilibrium calculations (e.g., Martin et al., 2006; Hoshyaripour et al., 2012). A source of uncertainty in thermodynamic modeling of the high-temperature chemistry of volcanic plumes is the assumption of equilibrium conditions, that may not always be valid for transient plumes (Martin et al., 2009).

The chain-of-reactors approach of this study is time-resolved and based on chemical kinetics thus differs markedly from thermodynamic equilibrium calculations used to date. We performed an exploratory study of the high-temperature chemistry in a near-source volcanic plume over the first 2.4 s, using as boundary conditions for the time-varying temperature and mixing of air output from 1D PlumeRise model simulations of Eyjafjallajökull plume (Woodhouse et al., 2013). The magmatic gas emission includes H_2O, CO_2, SO_2, and CO, based on observations of the young plume (Allard et al., 2011), with theoretical estimates for H_2S and H_2 gas emissions added in a sensitivity study and offline calculations performed for halogens.

A key finding is that the plume chemistry is under kinetic control and that thermodynamic equilibrium cannot be assumed. The simulation predicts that CO emission from Eyjafjallajökull is not fully oxidized (largely conserved) by high-temperature chemistry. This is consistent with field-observations of CO in the volcanic plume (Allard et al., 2011; Schumann et al., 2011) and contrasts to thermal equilibrium calculations of near-complete CO oxidation, **Table 3**. Instead, our study shows CO oxidation is under chemical kinetics control. The model predicts that sulfate-precursor SO_3 is formed at levels ($SO_3/SO_2 = 10^{-3}$) in general agreement to observations of near-source volcanic sulfate/SO_2 in volcanic plumes, **Table 1**. Conversely, thermodynamic calculations predict a much greater formation of SO_3 relative to SO_2 for the same plume dynamics conditions. The kinetics model predicts high-temperature formation of HO_2, OH, and H_2O_2. Formation of HO_{xy} is predicted to be enhanced when additional reduced gases (H_2S and H_2) besides CO are included in the emission.

Offline calculations demonstrate that volcanic halogens (HBr and HCl) will react rapidly with high-temperature OH, highlighting the potential for halogen radicals to form in the high-temperature plume. A key chemical mechanism is that HO_x oxidants are formed by the (reversible) reaction of H_2O with O_2 at high-temperatures to produce OH and HO_2. Chemical feedbacks occur when reduced gases in the volcanic emission (CO and H_2) react with OH to produce HO_2 that can self-react to form H_2O_2. Thus reduced gases in the volcanic emission act to promote formation of high-temperature HO_{xy}. Another chemical feedback occurs via the oxidation pathway for volcanic H_2S that rapidly generates additional oxidants in a chain-reaction. However, there is large uncertainty in some high-temperature reactions, particularly for sulfur species. Quantifying the chemical processes occurring at high-temperatures in the near-source plume is an essential step in understanding the reactivity and evolution of volcanic emissions and their impacts in the troposphere and stratosphere. Improved characterization of this high-temperature region of the plume will require the combination of model, field-observation and laboratory studies.

AUTHOR CONTRIBUTIONS

All authors contributed to the study design, analysis and interpretation of data, and manuscript writing.

ACKNOWLEDGMENTS

We are grateful to the reviewers for their comments on the original manuscript. TR acknowledges support from the ANR Projet de Recherche Collaborative VOLC-HAL-CLIM (Volcanic Halogens: from Deep Earth to Atmospheric Impacts), ANR-18-CE01-0018, and Labex Orléans Labex VOLTAIRE (VOLatils-Terre Atmosphère Interactions – Ressources et Environnement, ANR-10-LABX-100-0). GD and CO acknowledge support from the Orléans Labex Caprysses (convention ANR-11-LABX-0006-01) and the NERC Centre for Observation and Modelling of Earthquakes, Volcanoes, and Tectonics (COMET), respectively.

SUPPLEMENTARY MATERIAL

The Supplementary Material for this article can be found online at: https://www.frontiersin.org/articles/10.3389/feart.2019.00154/full#supplementary-material

REFERENCES

Aiuppa, A., Franco, A., von Glasow, R., Allen, A. G., D'Alessandro, W., Mather, T. A., et al. (2007). The tropospheric processing of acidic gases and hydrogen sulphide in volcanic gas plumes as inferred from field and model investigations. *Atmos. Chem. Phys.* 7, 1441–1450. doi: 10.5194/acp-7-1441-2007

Aiuppa, A., Inguaggiato, S., McGonigle, A. J. S., O'Dwyer, M., Oppenheimer, C., Padgett, M. J., et al. (2005). H2S fluxes from Mt. Etna, Stromboli, and

Vulcano (Italy) and implications for the sulfur budget at volcanoes. *Geochim. Cosmochim. Acta* 69, 1861–1871. doi: 10.1016/j.gca.2004.09.018

Aiuppa, A., Shinohara, H., Tamburello, G., Giudice, G., Liuzzo, M., and Moretti, R. (2011). Hydrogen in the gas plume of an open-vent volcano, Mount Etna, Italy. *J. Geophys. Res.* 116, B10204. doi: 10.1029/2011JB008461

Allard, P., Burton, M., Oskarsson, N., Michel, A., and Polacci, M. (2011). Magmatic gas composition and fluxes during the 2010 Eyjafjallajökull explosive eruption: implications for degassing magma volumes and volatile sources. *Geophys. Res. Abstracts* 13:EGU2011-12040-1.

Allen, A. G., Baxter, P. J., and Ottley, C. J. (2000). Ottley, Gas and particle emissions from Soufrière Hills Volcano, Montserrat, West Indies: characterization and health hazard assessment. *Bull. Volcanol.* 62, 8–19. doi: 10.1007/s004450050287

Allen, A. G., Oppenheiler, C., Ferm, M., Baxter, P. J., Horrocks, L. A., Galle, B., et al. (2002). Primary sulfate aerosol and associated emissions from Masaya, Volcano, Nicaragua. *J. Geophys. Res.* 107, ACH5-1–ACH5-8. doi: 10.1029/2002JD002120

Aubry, T. J., Carazzo, G., and Jellinek, A. M. (2017). Turbulent entrainment into volcanic plumes: new constraints from laboratory experiments on buoyant jets rising in a stratified crossflow. *Geophys. Res. Lett.* 44, 198–110. doi: 10.1002/2017GL075069

Bobrowski, N., von Glasow, R., Aiuppa, A., Inguaggiato, S., Louban, I., Ibrahim, O. W., et al. (2007). Reactive halogen chemistry in volcanic plumes. *J. Geophys. Res.* 112:D06311. doi: 10.1029/2006JD007206

Bobrowski, N., von Glasow, R., Giuffrida, G. B., Tedesco, D., Aiuppa, A., Yalire, M., et al. (2015). Gas emission strength and evolution of the molar ratio of BrO/SO2 in the plume of Nyiragongo in comparison to Etna. *J. Geophys. Res. Atmos.* 120, 277–291. doi: 10.1002/2013JD021069

Boichu, M., Menut, L., Khvorostyanov, D., Clarisse, L., Clerbaux, C., Turquety, S., et al. (2013). Inverting for volcanic SO2 flux at high temporal resolution using spaceborne plume imagery and chemistry-transport modelling: the 2010 Eyjafjallajökull eruption case study. *Atmos. Chem. Phys.* 13, 8569–8584. doi: 10.5194/acp-13-8569-2013

Boichu, M., Oppenheimer, C., Roberts, T. J., Tsanev, V., and Kyle, P. (2011). On bromine, nitrogen oxides and ozone depletion in the tropospheric plume of Erebus volcano (Antarctica). *Atmos. Environ.* 45, 3856–3866. doi: 10.1016/j.atmosenv.2011.03.027

Branan, Y. K., Harris, A., Watson, I. M., Phillips, J. C., Horton, K., Williams-Jones, G., et al. (2008). Investigation of at-vent dynamics and dilution using thermal infrared radiometers at Masaya volcano, Nicaragua. *J. Volcanol. Geothermal Res.* 169, 34–47. doi: 10.1016/j.jvolgeores.2007.07.021

Carn, S. A., Froyd, K. D., Anderson, B. E., Wennberg, P., Crounse, J., Spencer, K., et al. (2011). In situ measurements of tropospheric volcanic plumes in Ecuador and Colombia during TC4. *J. Geophys. Res.* 116:D00J24. doi: 10.1029/2010JD014718

de Moor, J. M., Aiuppa, A., Avard, G., Wehrmann, H., Dunbar, N., Muller, C., et al. (2016). Turmoil at Turrialba Volcano (Costa Rica): degassing and eruptive processes inferred from high-frequency gas monitoring. *J. Geophys. Res.*121, 5761–5775. doi: 10.1002/2016JB013150

de Moor, J. M., Fischer, T. P., Sharp, Z. D., King, P. L., Wilke, M., Botcharnikov, R. E., et al. (2013). Sulfur degassing at Erta Ale (Ethiopia) and Masaya (Nicaragua) volcanoes: implications for degassing processes and oxygen fugacity of basaltic systems. *Geochem. Geophys. Geosyst.* 14, 4076-4108. doi: 10.1002/ggge.20255

Delmelle, P., Wadsworth, F. B., Maters, E. C., and Ayris, P. M. (2018). High temperature reactions between gases and ash particles in volcanic eruption plumes. *Rev. Mineral. Geochem.* 84, 285–308. doi: 10.2138/rmg.2018.84.8

Donovan, A., Tsanev, V., Oppenheimer, C., and Edmonds, M. (2014). Reactive halogens (BrO and OClO) detected in the plume of Soufrière Hills Volcano during an eruption hiatus. *Geochem. Geophys. Geosyst.* 15, 3346–3363. doi: 10.1002/2014GC005419

Galeazzo, T., Bekki, S., Martin, E., Savarino, J., and Arnold, S. R. (2018). Photochemical box-modelling of volcanic SO2 oxidation: isotopic constraints. *Atmos. Chem. Phys. Discuss.* 18, 17909–17931. doi: 10.5194/acp-2018-381

Gerlach, T. M. (2004). Volcanic sources of tropospheric ozone-depleting trace gases. *Geochem. Geophys. Geosyst.* 5:Q09007. doi: 10.1029/2004GC000747

Glarborg, P., and Marshall, P. (2013). Oxidation of reduced sulfur species: carbonyl sulfide. *Int. J. Chem. Kinet.* 45, 429–439. doi: 10.1002/kin.20778

Góger, S., Szabó, P., Czakó, G., and Lendvay, G. (2018). Flame inhibition chemistry: rate coefficients of the reactions of HBr with CH3 and OH radicals at high temperatures determined by quasiclassical trajectory calculations. *Energy Fuels* 32, 10100–10105. doi: 10.1021/acs.energyfuels.8b00989

Guttmann, A., Bobrowski, N., Roberts, T. J., Rudiger, J., and Hoffman, T. (2018). Advances in bromine speciation in volcanic plumes. *Front. Earth Sci.* 6:213. doi: 10.3389/feart.2018.00213

Heue, K.-P., Brenninkmeijer, C. A. M., Baker, A. K., Rauthe-Schöch, A., Walter, D., Wagner, T., et al. (2011). SO2 and BrO observation in the plume of the Eyjafjallajökull volcano 2010: CARIBIC and GOME-2 retrievals. *Atmos. Chem. Phys.* 11, 2973–2989. doi: 10.5194/acp-11-2973-2011

Hillman, S. E., Horwell, C., Densmore, A. L., Damby, D. E., Fubini, B., Ishimine, Y., et al. (2012). Sakurajima volcano: a physico-chemical study of the health consequences of long-term exposure to volcanic ash. *Bull. Volcanol.* 74, 913–930. doi: 10.1007/s00445-012-0575-3

Hobbs, P. V., Radke, L. F., Lyons, J. H., Ferek, R. J., Coffman, D. J., and Casadevall, T. J. (1991). Casadevall, Airborne measurements of particle and gas emissions from the 1990 volcanic eruptions of Mount Redoubt. *J. Geophys. Res.* 96, 18735–18752.

Hörmann, C., Sihler, H., Bobrowski, N., Beirle, S., Penning de Vries, M., Platt, U., et al. (2013). Systematic investigation of bromine monoxide in volcanic plumes from space by using the GOME-2 instrument. *Atmos. Chem. Phys.* 13, 4749–4781. doi: 10.5194/acp-13-4749-2013

Horwell, C., Fenoglio, I., Ragnarsdottir, K. V., Sparks, R. S. J., and Fubini, B. (2003). Surface reactivity of volcanic ash from the eruption of Soufrière Hills volcano, Montserrat, West Indies with implications for health hazards. *Environ. Res.* 93, 202–215. doi: 10.1016/s0013-9351(03)00044-6

Hoshyaripour, G. A., Hort, M., and Langmann, B. (2012). How does the hot core of a volcanic plume control the sulfur speciation in volcanic emission? *Geochem. Geophys. Geosyst.* 13:Q07004. doi: 10.1029/2011GC004020

Hoshyaripour, G. A., Hort, M., and Langmann, B. (2015). Ash iron mobilization through physicochemical processing in volcanic eruption plumes: a numerical modeling approach. *Atmos. Chem. Phys.* 15, 9361–9379. doi: 10.5194/acp-15-9361-2015

Ilyinskaya, E., Martin, R., and Oppenheimer, C. (2012). Aerosol formation in basaltic lava fountaining: eyjafjallajökull volcano, Iceland. *J. Geophys. Res. Atmos.* 117:D00U27. doi: 10.1029/2011JD016811

Jourdain, L., Roberts, T. J., Pirre, M., and Josse, B. (2016). Modeling the reactive halogen plume from Ambrym volcano and its impact on the troposphere with the CCATT-BRAMS mesoscale model. *Atmos. Chem. Phys.* 16, 12099–12125. doi: 10.5194/acp-16-12099-2016

Kee, R. J., Rupley, F. M., Miller, J. A., Coltrin, M. E., Grcar, J. F., Meeks, E., et al. (2000). *CHEMKIN Collection, Release 3.6*. San Diego, CA: Reaction Design. Inc.

Keiding, J. K., and Sigmarsson, O. (2012). Geothermobarometry of the 2010 Eyjafjallajökull eruption: new constraints on Icelandic magma plumbing systems. *J. Geophys. Res.* 117:B00C09. doi: 10.1029/2011JB008829

Kern, C., and Lyons, J. J. (2018). Spatial distribution of halogen oxides in the plume of Mount Pagan Volcano, Mariana Islands. *Geophys. Res. Lett.* 45, 9588–9596. doi: 10.1029/2018GL079245

Kroll, J. H., Cross, E. S., Hunter, J. F., Pai, S., Wallace, L. M. M., Croteau, P. I., et al. (2015). Atmospheric evolution of sulfur emissions from Kilauea: reat-time measurements of oxidation, dilution, and neutralization within a volcanic plume. *Environ. Sci. Technol.* 49, 4129–4137. doi: 10.1021/es506119x

Martin, R. S., and Ilyinskaya, E. (2011). Volcanic lightning as a source of reactive radical species in eruption plumes. *Geochem. Geophys. Geosyst.* 12:Q03002. doi: 10.1029/2010GC003420

Martin, R. S., Ilyinskaya, E., and Oppenheimer, C. (2012). The enigma of reactive nitrogen in volcanic emissions. *Geochim. Cosmochim. Acta* 95, 93–105. doi: 10.1016/j.gca.2012.07.027

Martin, R. S., Mather, T. A., and Pyle, D. M. (2006). High-temperature mixtures of magmatic and atmospheric gases. *Geochem. Geophys. Geosyst.* 7:Q04006. doi: 10.1029/2005GC001186

Martin, R. S., Mather, T. A., and Pyle, D. M. (2007). Volcanic emissions and the early earth atmosphere. *Geochim. Cosmochim. Acta* 71, 3673–3685.

Martin, R. S., Mather, T. A., Pyle, D. M., Power, M., Allen, A. G., Aiuppa, A., et al. (2008). Composition-resolved size distributions of volcanic aerosols in the Mt. Etna plumes. *J. Geophys. Res.* 113:D17211. doi: 10.1029/2007JD009648

Martin, R. S., Robert, T. J., Mather, T. A., and Pyle, D. M. (2009). The implications of H2S and H2 kinetic stability in high-T mixtures of magmatic and atmospheric gases for the production of oxidized trace species (e.g., BrO and NOx). *Chem. Geol.* 263, 143–150. doi: 10.1016/j.chemgeo.2008.12.028

Martin, R. S., Sawyer, G. M., Spanpinato, L., Salerno, G. G., Ramirez, C., Ilyinskaya, E., et al. (2010). A total volatile inventory for Masaya Volcano, Nicaragua. *J. Geophys. Res.* 115:B09215. doi: 10.1029/2010JB007480

Martin, R. S., Witt, M. L. I., Pyle, D. M., Mather, T. A., Watt, S. F. L., Bagnato, E., et al. (2011). Rapid oxidation of mercury (Hg) at volcanic vents: insights from high temperature thermodynamic models of Mt Etna's emissions. *Chem. Geol.* 283, 279–286. doi: 10.1016/j.chemgeo.2011.01.027

Mastin, L. G. (2007). A user-friendly one-dimensional model for wet volcanic plumes. *Geochem. Geophys. Geosyst.* 8:Q03014. doi: 10.1029/2006GC001455

Mather, T. A., Allen, A. G., Davison, B. M., Pyle, D. M., Oppenheimer, C., and McGonigle, A. J. S. (2004a). Nitric acid from volcanoes. *Earth Planet. Sci. Lett.* 218, 17–30. doi: 10.1016/s0012-821x(03)00640-x

Mather, T. A., Allen, A. G., Oppenheimer, C., Pyle, D. M., and McGonigle, A. J. S. (2003). Size-resolved characterisation of soluble ions in the particles in the tropospheric plume of Masaya Volcano, Nicaragua: origins and plume processing. *J. Atmos. Chem.* 46, 207–237.

Mather, T. A., Tsanev, V. I., Pyle, D. M., McGonigle, A. J. S., Oppenheimer, C., and Allen, A. G. (2004b). Characterization and evolution of tropospheric plumes from Lascar and Villarrica volcanoes, Chile. *J. Geophys. Res. Atmos.* 109:D21303. doi: 10.1029/2004JD004934

Mathieu, O., Mulvihill, C., and Petersen, E. L. (2017). Shock-tube water time-histories and ignition delay time measurements for H2S near atmospheric pressure. *Proc. Combust. Inst.* 36, 4019–4027. doi: 10.1016/j.proci.2016.06.027

Moussallam, Y., Oppenheimer, C., Aiuppa, A., Gaetano, G., Moussallam, M., and Kype, P. (2012). Hydrogen emissions from Erebus volcano, Antarctica. *Bull. Volcanol.* 74, 2109–2120. doi: 10.1007/s00445-012-0649-2

Naughton, J. J., Lewis, V., Thomas, D., and Finlayson, J. B. (1975). Fume compositions found at various stages of activity at Kilauea Volcano, Hawaii, *J. Geophys. Res.* 80, 2963–2966. doi: 10.1029/JC080i021p02963

Oppenheimer, C., Fischer, T. P., and Scaillet, B. (2014). *Volcanic Degassing: Process and Impact. Treatise on Geochemistry*, 2nd Edn. Amsterdam: Elsevier, 111–179.

Oppenheimer, C., Keyp, P., Eisele, F., Crawford, J., Huey, G., Tanner, D., et al. (2010). Atmospheric chemistry of an Antarctic volcanic plume. *J. Geophys. Res.* 115:D04303. doi: 10.1029/2009JD011910

Oppenheimer, C., and Kyle, P. R. (2008). Probing the magma plumbing of Erebus volcano, Antarctica, by open-path FTIR spectroscopy of gas emissions. *J. Volcanol. Geotherm. Res.* 177, 743–754. doi: 10.1016/j.jvolgeores.2007.08.022

Oppenheimer, C., Scaillet, B., Woods, A., Sutton, J. A., Elias, T., and Moussallam, Y. (2018). Influence of eruptive style on volcanic gas emission chemistry and temperature. *Nat. Geosci.* 11, 678–681. doi: 10.1038/s41561-018-0194-5

Ravishankara, A. R., Wine, P. H., Wells, J. R., and Thompson, R. L. (1985). Kinetic study of the reaction of OH with HCl from 240–1055 K. *Int. J. Chem. Kinet.* 17, 1281–1297. doi: 10.1002/kin.550171206

Roberts, T. J., Braban, C. F., Martin, R. S., Oppenheimer, C., Adams, J. W., Cox, R. A., et al. (2009). Modelling reactive halogen formation and ozone depletion in volcanic plumes. *Chem. Geol.* 263, 151–163. doi: 10.1016/j.chemgeo.2008.11.012

Roberts, T. J., Braban, C. F., Oppenheimer, C., Martin, R. S., Freshwater, R. A., Dawson, D. H., et al. (2012). Electrochemical sensing of volcanic gases. *Chem. Geol.* 332-333, 74–91. doi: 10.1016/j.chemgeo.2012.08.027

Roberts, T. J., Lurton, T., Giudice, G., Liuzzo, M., Aiuppa, A., Coltelli, M., et al. (2017). Validation of a novel Multi-Gas sensor for volcanic HCl alongside H2S and SO2 at Mt. Etna. *Bull. Volcanol.* 79:36.

Roberts, T. J., Martin, R. S., and Jourdain, L. (2014). Reactive halogen chemistry in Mt Etna's volcanic plume: the influence of total Br, high temperature processing, aerosol loading and plume-air mixing (volcanic emissions flux). *Atmos. Chem. Phys.* 14, 11201–11219. doi: 10.5194/acp-14-11201-12014

Roberts, T. J., Vignelles, D., Liuzzo, M., Giudice, G., Aiuppa, A., Coltelli, M., et al. (2018). The primary volcanic aerosol emission from Mt Etna: size-resolved particles with SO2 and role in plume reactive halogen chemistry. *Geochim. Cosmochim. Acta* 222, 74–93. doi: 10.1016/j.gca.2017.09.040

Rose, W. I., Millard, G. A., Mather, T. A., Hunton, D. E., Anderson, B., Oppenheimer, C., et al. (2006). Atmospheric chemistry of a 33–34 hour old volcanic cloud from Hekla Volcano (Iceland): insights from direct sampling and the application of chemical box modeling. *J. Geophys. Res. Atmos.* 111:D20206. doi: 10.1029/2005JD006872

Sahyoun, M., Freney, E., Brito, J., Duplissy, J., Gouhier, M., Colomb, A., et al. (2019). Evidence of new particle formation within Etna and Stromboli volcanic plumes and its parameterization from airborne in-situ measurements. *J. Geophys. Res. Atmos.* 124, 5650–5668. doi: 10.1029/2018JD028882

Schumann, U., Weinzierl, B., Reitebuch, O., Schlager, H., Miniki, A., Forster, C., et al. (2011). Airborne observations of the Eyjafjalla volcano ash cloud over Europe during air space closure in April and May 2010. *Atmos. Chem. Phys.* 11, 2245–2279. doi: 10.5194/acp-11-2245-2011

Surl, L., Donohoue, D., Aiuppa, A., Bobrowski, N., and von Glasow, R. (2015). Quantification of the depletion of ozone in the plume of Mt Etna. *Atmos. Chem. Phys.* 15, 2613–2628. doi: 10.5194/acp-15-2613-2015

Vance, A., McGonigle, A. J. S., Aiuppa, A., Stith, J. L., Turnbull, K., and von Glasow, R. (2010). Ozone depletion in tropospheric volcanic plumes. *Geophys. Res. Lett.* 37:L22802. doi: 10.1029/2010GL044997

Voigt, C., Jessberge, P., Jurkat, T., Kaufmann, S., Baumann, R., Schlager, H., et al. (2014). Evolution of CO2, SO2, HCl and HNO3 in the volcanic plumes from Etna. *Geophys. Res. Lett.* 41, 2196–2203. doi: 10.1002/2013GL058974

von Glasow, R. (2010). Atmospheric chemistry in volcanic plumes. *Proc. Nat. Acad. Sci. U.S.A.* 107, 6594–6599. doi: 10.1073/pnas.0913164107

Woodhouse, M. J., Hogg, A. J., Philips, J. C., and Sparks, R. S. J. (2013). Interaction between volcanic plumes and wind during the 2010 Eyjafjallajökull eruption, Iceland. *J. Geophys. Res.* 118, 92–109. doi: 10.1029/2012JB009592

Zelenski, M., Taran, Y., and Galle, B. (2015). High emission rate of sulfuric acid from Bezymianny volcano, Kamchatka. *Geophys. Res. Lett.* 42, 7005–7013. doi: 10.1002/2015GL065340

Conflict of Interest Statement: The authors declare that the research was conducted in the absence of any commercial or financial relationships that could be construed as a potential conflict of interest.

The handling Editor declared a past co-authorship with one of the authors, TR.

frontiers
in Earth Science

ORIGINAL RESEARCH
published: 24 September 2019
doi: 10.3389/feart.2019.00249

Time Variation in the Chemical and Isotopic Composition of Fumarolic Gasses at Kusatsu-Shirane Volcano, Japan

Takeshi Ohba[1]*, Muga Yaguchi[2], Kana Nishino[1], Nozomi Numanami[1], Urumu Tsunogai[3], Masanori Ito[3] and Ryo Shingubara[3]

[1] Department of Chemistry, School of Science, Tokai University, Hiratsuka, Japan, [2] Meteorological Research Institute, Tsukuba, Japan, [3] Graduate School of Environmental Studies, Nagoya University, Nagoya, Japan

Minor seismicity may occur at volcanoes with hydrothermal system before a steam eruption. To forecast any steam eruption, it is indispensable to detect and understand the nature of this shallow seismicity. As the fumarolic gas resides in the hydrothermal system, it may provide insights for elucidating the nature of any seismicity and thus forecast steam eruptions. At Kusatsu-Shirane volcano Japan, intense seismic activity took place in 2014 and 2018. To investigate the relationship between the seismicity and gas chemistry, five fumarolic gas discharges have been repeatedly analyzed. Since July 2014 to November 2017 a monotonic decrease in CO_2/H_2O, He/H_2O and N_2/H_2O ratios was recorded in the fumarolic gasses located north of the summit of volcano, suggesting the decline of the magmatic component. On the contrary the CH_4/H_2O ratio significantly increased during the seismically quiet period, indicating that reduced conditions developed in the hydrothermal system, favoring the formation of CH_4. The high N_2/He ratio in the quiet period indicates the addition of N_2, likely deriving from the crustal rocks hosting hydrothermal reservoir. The N_2/He ratio in 2018 was significantly lower than those recorded in 2014, indicating the evolution of magma with the progress of degassing. The $\delta D(H_2O)$ and $\delta^{18}O(H_2O)$ values and the CO_2/H_2O ratios of fumarolic gas discharges were modeled with the following processes: generation of vapor phase after the mixing between magmatic gas and a cold groundwater with meteoric origin, addition of vapor phase with meteoric origin, and partial condensation of water vapor near surface. Only a single magmatic gas is necessary for the above modeling. These data suggest that at Kusatsu-Shirane volcano the activation of seismicity was synchronized with the increase of the magmatic component in the fumarolic gas. It is postulated that the injection of magmatic gas increased the fluid pressure in the reservoir, which triggered seismicity. The injection would have been triggered by a break of the sealing zone surrounding the degassing magma. The injection of magmatic gas can be detected by monitoring the composition of the fumarolic gas, thus giving the possibility to forecast any future seismicity.

Keywords: volcanic gas, seismic activity, hydrothermal system, magma, He

OPEN ACCESS

Edited by:
Franco Tassi,
University of Florence, Italy

Reviewed by:
Dmitri Rouwet,
National Institute of Geophysics and Volcanology (INGV), Italy
Orlando Vaselli,
University of Florence, Italy

***Correspondence:**
Takeshi Ohba
volcano.ohba@gmail.com;
takeshi_ohba@tokai-u.jp

Specialty section:
This article was submitted to Volcanology, a section of the journal Frontiers in Earth Science

Received: 02 October 2018
Accepted: 05 September 2019
Published: 24 September 2019

Citation:
Ohba T, Yaguchi M, Nishino K, Numanami N, Tsunogai U, Ito M and Shingubara R (2019) Time Variation in the Chemical and Isotopic Composition of Fumarolic Gasses at Kusatsu-Shirane Volcano, Japan. Front. Earth Sci. 7:249. doi: 10.3389/feart.2019.00249

INTRODUCTION

Minor seismicity episodically occurs at volcanoes with hydrothermal system. Such seismicity could be the precursor to a steam-driven explosive eruption (hereafter "Steam eruption"). The steam eruption is generally small in scale (Barberi et al., 1992), and difficult to forecast, due to the scarcity of precursors. Therefore, to forecast steam eruptions, it is indispensable to determine the cause of the seismicity occurring in the hydrothermal system. The fumarolic gas observed at volcanoes resides in the hydrothermal reservoir. Therefore, it may be useful for elucidating the occurrence and the nature of shallow seismicity.

Mt. Kusatsu-Shirane is an active volcano developed on the "volcanic front" (Sugimura, 1960) on Honshu Island, Japan and the summit consists of several pyroclastic cones and craters (**Figure 1**). One of the craters, Crater Yugama (Yg in **Figure 1**, the other acronyms used in the following text are listed in **Table 1**) has been filled with an acidic lake water. Mt. Kusatsu-Shirane has produced andesitic volcanic rocks with two age periods, which are hereafter termed the old and young eras. Eruptions of the old era terminated at 0.25 Ma (Kaneko et al., 1991). The recent active young era began approximately 14,000 years ago (Hayakawa and Yui, 1989). The pyroclastic cones occupying the summit area of Mt. Kusatsu-Shirane (**Figure 1**) formed 14,000 years ago. The lava flows extending from the summit area to the east slope of the volcano were developed 3,000 to 5,000 years ago (Hayakawa and Yui, 1989). The first historical eruption at Mt. Kusatsu-Shirane took place in 1882. Before the eruption, there was a long dormant period when the summit area was covered with groves (Ohashi, 1914), and fish lived in the lake within Crater Mizugama (Mi in **Figure 1**). The lake water within the Crater Yugama was acidic, although the temperature of the water was similar to ambient air temperature. From 1882 to the present day, Mt. Kusatsu-Shirane has undergone several active periods and intervening dormant periods. All of the historical eruptions were phreatic

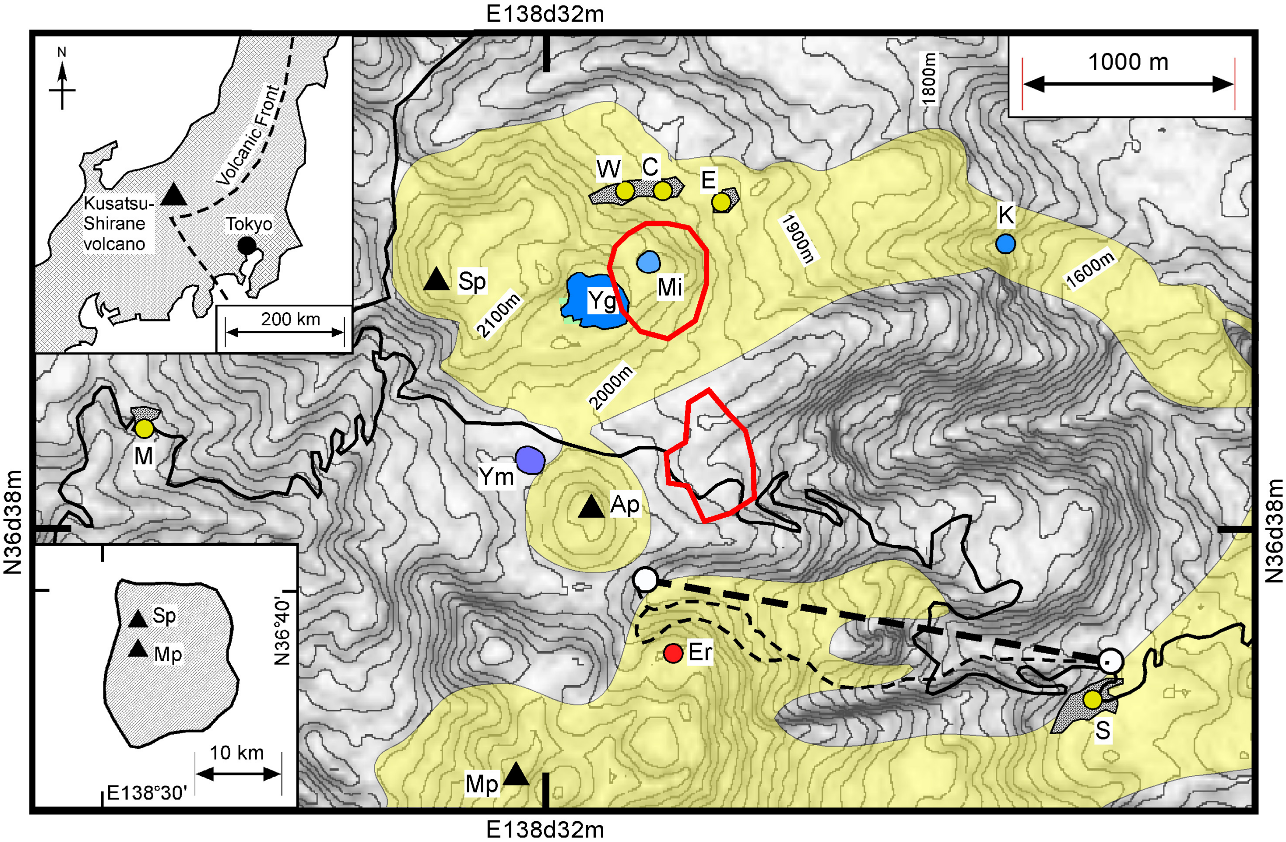

FIGURE 1 | Location of fumarolic gasses, W, C, E, S and M. The shaded regions overlapping the fumaroles indicate the region with geotherm. Yugama (Yg), Mizugama (Mi) and Yumiike (Ym) are craters with lake water. Sirane (Sp), Ainomine (Ap) and Motoshirane (Mp) are pyroclastic cones. The inserted figure on the upper left corner shows the location of Kusatsu-Shirane volcano on Island of Honshu, Japan with the volcanic front (Sugimura, 1960). The inserted figure on the lower left shows the distribution of lava and pyroclastic deposits emitted from Kusatsu-Shirane volcano, which are younger than 1,4000 years (Uto et al., 1983). The yellowish areas indicate the lava and pyroclastic deposit younger than 7,000 years (Hayakawa and Yui, 1989). The hypocenters of volcanic earthquake are distributed within the two bold red circles (HP of Japan Meteorological Agency (JMA), https://www.data.jma.go.jp). The hypocenters of the volcanic earthquakes cluster at a depth between sea level and up to 2000 m above sea level. A small steam explosion occurred at Er in January 2018. K is the position of hot spring water which contains high concentration of Cl$^-$. Ohba et al. (2000) suggested K represents the liquid phase of the hydrothermal system beneath Crater Yugama. The bold broken line shows the ropeway. Thin broken curves indicate the ski slopes. The altitude interval of the contour line is 20 m. The thin solid curve indicates the car road.

(Uto et al., 1983). Most of the historical eruptions occurred near Crater Yugama. Following the first historical eruption, several eruptions took place over the period 1897 to 1905, with an eruption in 1902 at Crater Yumiike (Ym in **Figure 1**). After an eruption in 1905 there was a dormant period lasting 20 years. The volcanic activity was maximized over the period 1925 to 1942. In 1932, Crater Yugama experienced the largest historical eruption, with 20 cm of volcanic ash deposition at 2 km east of Crater Yugama (Minakami et al., 1942). In 1976, a steam eruption took place within Crater Mizugama. One year prior to the eruption, an increase of the SO_2/H_2S ratio from the fumarolic gasses was observed (Ossaka et al., 1980). In 1982 and 1983, steam eruptions occurred at Crater Yugama (Ossaka et al., 1997). Lithics of 0.5–1 m in diameter were thrown over 500 m from the crater. Although the magnitude of the eruption was only 1 in the VEI scale (Global Volcanism Program, 2013), visitors would certainly have been at risks. Fortunately, the eruption occurred during winter when the access road was closed. In 1990, a large number of volcanic earthquakes occurred beneath Crater Yugama although no eruption took place. After the seismic activity started, the pH of lake water in Crater Yugama decreased, accompanying an increase of chloride concentration (Ohba et al., 1994, 2000). Ohba et al. (2008) estimated that the activity was caused by the break of sealing zone (Fournier, 1999) and subsequent "dry degassing" (Giggenbach, 1997). Based on the observation by Japan Meteorological Agency (JMA) two hypocenter clusters of volcanic seismicity have been recognized on the summit of volcano (**Figure 1**). One is a cluster beneath Crater Mizugama (Mi) and another cluster is located east of Ainomine peak (Ap). The hypocenters are distributed in the range of depth between sea level and the surface (up to 2000 m above sea level; **Figure 1**). In January 2018, a small steam eruption took place near Motoshirane peak (Er in **Figure 1**). This eruption occurred in an unexpected place far from Crater Yugama. In April 2018, a large number of volcanic earthquakes happened beneath Crater Mizugama (Mi) and the east side of Ainomine cone (Ap), although no eruption has yet occurred.

The unusual green–gray color of the lake water in Crater Yugama attracts sightseers who climb to a belvedere situated on the southern rim of the crater. The Crater Yugama is an important resource for the local economy. In order to reveal the relationship between the seismic activity and fumarolic gas composition, a periodical (2 or 3 times per year) sampling and analysis of five fumarolic gas discharges was carried out since July 2014 until August 2018. In this study we aim to investigate the processes affecting the magmatic-hydrothermal system beneath Crater Yugama on the basis of the chemical and isotopic composition of fumarolic gasses.

TABLE 1 | Acronyms used in the text.

Acronym	Meaning
Yg	Crater Yugama
Mi	Crater Mizugama
Ym	Crater Yumiike
Sp	Peak of the Shirane cone
Ap	Peak of the Ainomine cone
Mp	Peak of the Motoshirane cone
Er	Eruptive point in 2018 near Ap and Mp
JMA	Japan Meteorological Agency
W, C, E	Fumaroles located on the north of the Crater Yugama
M, S	Fumaroles located west and east slope of Kusatsu-Shirane volcano, respectively
AET1	Apparent equilibrium temperature defined for the reaction among H_2O, H_2S, SO_2 and H_2
AET2	Apparent equilibrium temperature defined for the isotope exchange reaction between H_2O and H_2
Mv	Magmatic gas derived from the degassing magma
Mc1	Components in the magmatic gas with high N_2/He ratio in the early stage (until October 2015)
Mc2	Components in the magmatic gas with low N_2/He ratio in the late stage (after April 2018)
Hc	Components generated in the hydrothermal reservoir, such as CH_4 and H_2S
Cc	Components extracted from the crustal rock hosting the hydrothermal reservoir
Lw	Local meteoric water
Vp	Vapor phase in the hydrothermal reservoir
Lp	Liquid phase in the hydrothermal reservoir
Lv	Water vapor generated from the local meteoric water with a conductive heating
Cd	Condensation of water vapor
En	Enthalpy used for the heating of groundwater

MATERIALS AND METHODS

Fumarolic gasses had been sampled since July 2014 until August 2018, with a frequency of a few times per year at the points W, C and E (**Figure 1**). The total number of samples was 10, 10 and 9 for the points W, C and E, respectively. Additionally fumarolic gasses were sampled at the points S and M (**Figure 1**). The total number of samples was 8 and 3 for the points S and M, respectively. Gas sampling was carried out with a titanium pipe that was inserted into the fumarolic orifice. One end of the titanium pipe was connected to a rubber tube. The end of the rubber tube was connected to a 120 ml Pyrex glass bottle with air tight stop cock (Giggenbach, 1975), in which a 5 molar 20 ml KOH solution was put. The head-space of the gas bottle was evacuated prior sampling. Water and acidic gasses were absorbed by the KOH solution. In the headspace, the residual gasses (hereafter R-gas) such as N_2, O_2, Ar, He, H_2 and CH_4 were collected. Components absorbed in the KOH solution, such as H_2O, CO_2, H_2S and SO_2 were analyzed according to the method by Ozawa (1968). The ratio of SO_2/H_2S in the fumarolic gas was determined using a KI-KIO_3 solution (Ozawa, 1968). The molar amount of R-gas was calculated by the gas state equation accounting the head space volume of bottle and the inner pressure in the head space at room temperature. Based on the molar amount of H_2O, CO_2, H_2S, SO_2 and R-gas, the relative concentration (%) of those components was calculated (**Table 2**).

The R-gas was analyzed using two different gas chromatographs with Ar and He as carrier gasses, hereafter

TABLE 2 | Chemical and isotopic composition of fumarolic gasses with the apparent equilibrium temperatures.

								R-gas										
Location	**Date**	**Temp** °C	**H_2O** %	**CO_2** %	**H_2S** %	**SO_2** %	**R-gas** %	**He** %	**H_2** %	**O_2** %	**N_2** %	**CH_4** %	**Ar** %	δD_{SMOW} ‰	$\delta^{18}O_{SMOW}$ ‰	$\delta D(H_2)_{SMOW}$ ‰	**AET1** °C	**AET2** °C
W	July 23, 2014	92.4	95.38	4.19	0.39	0.0050	0.0421	0.084	0.062	0.062	99.61	0.000	0.178	−65	−6.7	−562	166	161
W	May 15, 2015	93.5	96.43	3.11	0.43	0.0036	0.0321	0.071	0.141	0.000	99.56	0.025	0.205	−69	−7.8	−560	177	165
W	October 15, 2015	94.2	97.42	2.05	0.50	0.0010	0.0254	0.054	0.137	0.020	99.52	0.043	0.227	−67	−7.1	−555	156	169
W	April 22, 2016	93.5	97.52	1.93	0.52	0.0069	0.0294	0.033	0.147	0.047	99.38	0.184	0.210	−78	−8.2	−536	180	194
W	October 28, 2016	93.4	98.26	1.31	0.40	0.0049	0.0248	0.022	0.108	0.025	99.05	0.230	0.560	−66	−7.0	−510	165	215
W	April 25, 2017	93.3	98.12	1.42	0.44	0.0045	0.0190	0.026	0.170	0.056	99.17	0.309	0.268	−81	−10.1	−562	169	168
W	November 10, 2017	93.6	98.42	1.13	0.43	0.0027	0.0173	0.028	0.133	0.034	99.28	0.203	0.324	−75	−8.1	−556	155	171
W	May 18, 2018	94.3	97.86	1.72	0.40	0.0047	0.0187	0.086	0.120	0.015	99.49	0.044	0.242	−74	−7.8	−626	160	106
W	June 19, 2018	94.8	97.14	2.42	0.43	0.0016	0.0113	0.251	0.223	0.058	99.05	0.048	0.367	−70	−7.6	−568	153	158
W	August 06, 2018	94.6	97.70	1.89	0.40	0.0011	0.0097	0.209	0.229	0.045	99.21	0.057	0.251	−73	−8.0		147	
C	July 23, 2014	94.1	95.45	3.97	0.53	0.0072	0.0435	0.083	0.057	0.028	99.66	0.000	0.176	−77	−9.5	−538	165	191
C	May 15, 2015	93.4	96.80	2.76	0.41	0.0049	0.0298	0.074	0.080	0.015	99.66	0.008	0.167	−68	−7.2	−548	162	176
C	October 15, 2015	93.6	97.80	1.77	0.40	0.0021	0.0237	0.053	0.095	0.025	99.61	0.026	0.196	−70	−7.2	−533	153	193
C	April 22, 2016	97.2	97.80	1.75	0.42	0.0076	0.0258	0.034	0.087	0.052	99.47	0.145	0.209	−67	−5.4	−520	164	205
C	October 28, 2016	93.8	98.07	1.48	0.42	0.0050	0.0224	0.027	0.108	0.014	99.43	0.223	0.195	−66	−6.1	−482	162	247
C	April 25, 2017	93.6	98.21	1.34	0.42	0.0051	0.0194	0.025	0.112	0.035	99.36	0.233	0.231	−66	−6.3	−515	159	210
C	November 10, 2017	94.1	98.19	1.30	0.48	0.0038	0.0235	0.026	0.167	0.012	99.25	0.265	0.281	−75	−8.0	−546	172	182
C	May 18, 2018	94.3	97.86	1.73	0.40	0.0023	0.0183	0.089	0.089	0.020	99.51	0.055	0.238	−118	−16.3		145	
C	June 19, 2018	94.0	97.56	2.00	0.43	0.0005	0.0104	0.222	0.158	0.074	99.31	0.042	0.198	−109	−15.1	−553	133	192
C	August 6, 2018	94.5	97.80	1.78	0.41	0.0011	0.0114	0.165	0.165	0.034	99.22	0.042	0.375	−107	−14.6		142	
E	May 15, 2015	93.4	96.94	2.74	0.29	0.0035	0.0252	0.095	0.169	0.000	99.53	0.017	0.192	−88	−10.9	−529	179	206
E	October 15, 2015	93.3	97.75	1.93	0.30	0.0019	0.0212	0.069	0.238	0.015	99.44	0.025	0.214	−79	−8.8	−551	177	179
E	April 22, 2016	94.1	97.78	1.84	0.35	0.0060	0.0246	0.043	0.206	0.033	99.41	0.104	0.208	−88	−10.0	−549	187	186
E	October 28, 2016	93.6	98.62	1.09	0.27	0.0026	0.0174	0.029	0.328	0.023	99.23	0.150	0.235	−79	−8.5	−525	185	206
E	April 25, 2017	93.8	98.53	1.11	0.34	0.0024	0.0167	0.027	0.387	0.039	99.11	0.204	0.232	−96	−12.9	−510	185	233
E	November 10, 2017	93.0	98.89	0.84	0.26	0.0027	0.0147	0.029	0.326	0.010	99.19	0.170	0.278	−84	−9.6	−557	180	175
E	May 18, 2018	94.8	98.40	1.28	0.30	0.0018	0.0171	0.057	0.316	0.029	99.12	0.074	0.401	−84	−9.9	−560	178	172
E	June 19, 2018	94.0	98.06	1.63	0.30	0.0012	0.0111	0.154	0.495	0.056	98.94	0.076	0.277	−77	−8.4	−564	175	165
E	August 6, 2018	93.9	98.18	1.53	0.28	0.0023	0.0109	0.135	0.432	0.055	99.05	0.055	0.277	−77	−8.3		177	
S	July 22, 2014	94.5	95.17	3.42	1.34	0.0153	0.0500	0.031	0.065	0.000	96.79	1.65	1.46	−110	−18.5	−615	171	130
S	November 14, 2014	93.9	94.23	4.36	1.34	0.0077	0.0656	0.031	0.056	0.014	97.68	1.23	0.99				168	
S	April 25, 2017	94.1	94.71	3.44	1.77	0.0085	0.0731	0.023	0.225	0.010	96.69	1.66	1.39	−115	−19.1	−692	213	65
S	March 2, 2018	93.5	94.87	3.48	1.58	0.0124	0.0635	0.024	0.066	0.066	96.20	2.02	1.63	−115	−19.3	−626	174	122
S	April, 24, 2018	94.1	96.47	2.36	1.12	0.0064	0.0378	0.024	0.068	0.011	96.34	2.20	1.36	−113	−18.8	−655	157	96
S	May 18, 2018	94.8	96.62	2.20	1.13	0.0060	0.0385	0.022	0.072	0.005	96.33	2.22	1.35	−110	−18.3		159	
S	June 19, 2018	94.9	96.49	2.35	1.11	0.0040	0.0392	0.028	0.068	0.013	96.58	1.98	1.33	−106	−17.5	−634	154	111
S	August 6, 2018	94.7	96.42	2.41	1.13	0.0046	0.0359	0.036	0.074	0.022	96.56	2.03	1.28	−108	−18.0		155	
M	April 24, 2018	94.6	99.47	0.21	0.31	0.0010	0.0093	0.0083	1.16	0.042	95.73	1.57	1.49	−108	−17.6	−546	192	199
M	June 19, 2018	94.9	99.52	0.17	0.30	0.0024	0.0095	0.0063	1.19	0.090	95.65	1.63	1.43	−102	−16.7	−575	204	165
M	August 6, 2018	94.8	99.53	0.15	0.31	0.0017	0.0094	0.0078	1.16	0.105	95.80	1.60	1.32	−106	−17.2		199	

GC-Ar and CG-He, respectively. The GC-Ar was used to determine the concentration of He, H_2, O_2, N_2 and CH_4. In the GC-Ar, a 6m-long MS5A packed column and a TCD detector were installed. The temperature of the column and detector was kept at 50 and 100°C, respectively. The flow rate of Ar carrier gas was 30 ml/min. In general, He in volcanic gas is difficult to be analyzed due to the overlap of H_2 peaks if the amount of co-existing H_2 is high. In this study, the He peak of 17ppm STP was separated from the H_2 peak of 17% STP. All R-gas samples had a good separation between He and H_2 peaks on the chart of GC-Ar. By using a GC-He, the relative concentrations of N_2 and Ar were determined. In the GC-He a 6m-long Gaskuropack-54 column (GC Sciences Inc.) and a TCD detector were installed. The temperature of column and detector was kept at −70 and 50°C, respectively. With this condition, N_2, O_2 and Ar peaks in normal atmospheric air were separated. For all the R-gas

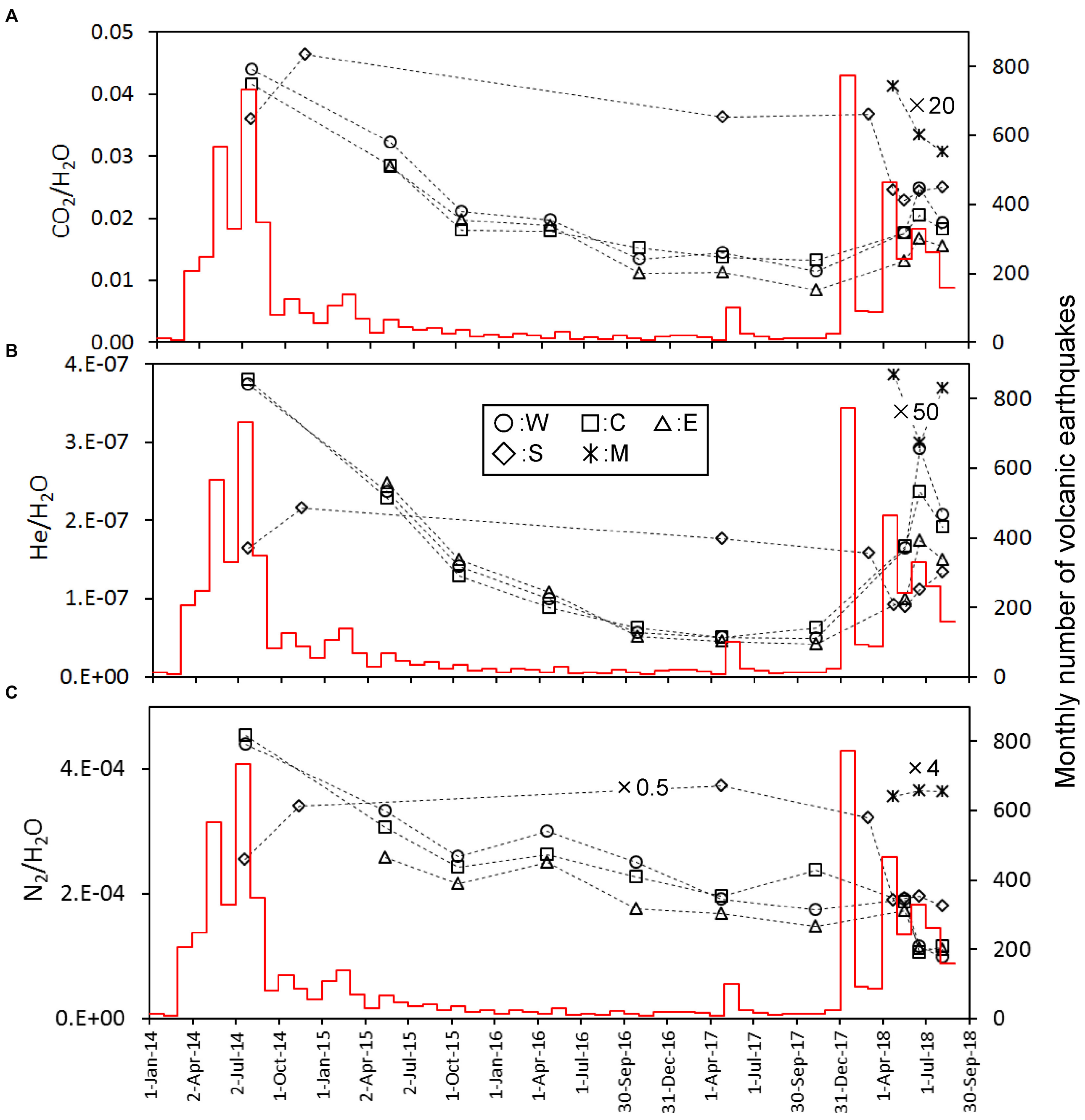

FIGURE 2 | Time variation of CO_2/H_2O **(A)**, He/H_2O **(B)**, and N_2/H_2O **(C)** molar ratios calibrated on the left *y*-axis. Some data were adjusted to the *y*-axis range by multiplying values indicated in figure. The red histogram calibrated on the right *y*-axis shows the monthly number of volcanic earthquakes observed by JMA.

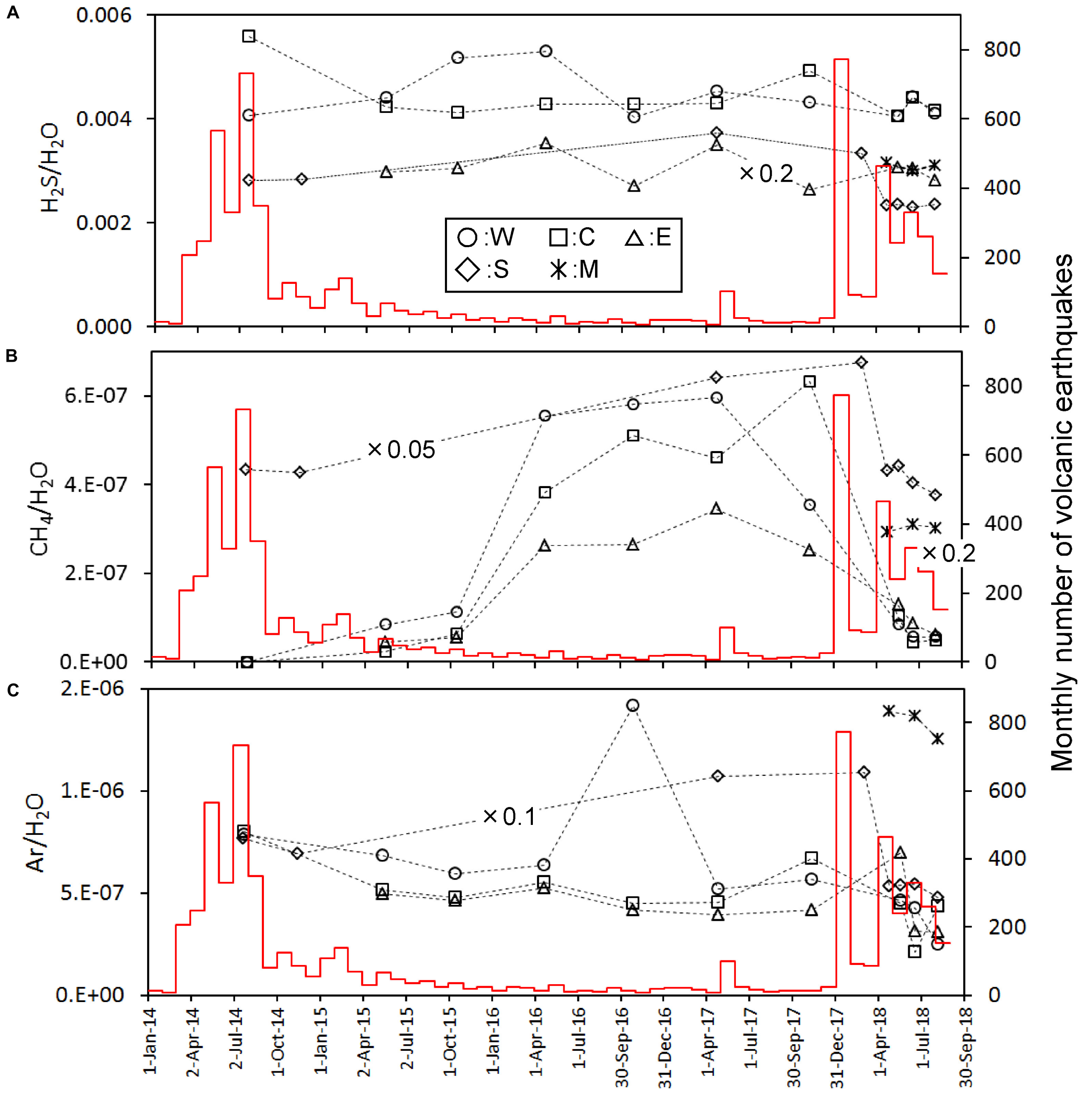

FIGURE 3 | Time variation of H_2S/H_2O **(A)**, CH_4/H_2O **(B)**, and Ar/H_2O **(C)** molar ratios calibrated on the left y-axis. Some data were adjusted to the y-axis range by multiplying values as indicated in figure. The red histogram calibrated on the right y-axis shows the monthly number of volcanic earthquakes observed by JMA.

samples a good separation among N_2, O_2 and Ar peaks was provided. The concentration of Ar in the R-gasses, X_{Ar} was calculated by,

$$X_{Ar} = \frac{X_{N2} R_{Ar}}{R_{N2}} \tag{1}$$

where R indicates the concentration of Ar or N_2 determined by GC-He. X_{N2} indicates the N_2 concentration determined by GC-Ar. The concentration of components in the R-gasses was normalized, so that the sum of X for He, H_2, O_2, N_2, CH_4 and Ar was 100% (**Table 2**). For the determination of the H_2O isotopic ratio, the fumarolic gas was cooled with a double tubes condenser made of Pyrex glass. The isotopic ratios of oxygen and hydrogen in the condensates were determined by an IR-laser cavity ring down analyzer (Picarro Inc., L2120-i). The isotopic ratio of the H_2 in R-gasses was determined by a continuous flow system combined with a mass spectrometer (Thermo Fischer Scientific Delta V) (Tsunogai et al., 2011).

RESULTS

The most abundant component in the fumarolic gasses was H_2O, up to 93–95% (**Table 2**). The content of other species was expressed as the molar ratio to H_2O in **Figure 2**. For the points W, C and E the CO_2/H_2O and He/H_2O ratios show a similar time variation; namely, they monotonically decreased since July 2014 until November 2017 and then increased in May 2018. The CO_2/H_2O and He/H_2O ratios of the point S were high in July 2014 until March 2018, and then dropped in April 2018 followed by an increase in He/H_2O and slight increase in CO_2/H_2O. The CO_2/H_2O and He/H_2O ratios of M were much lower than the values of other fumarolic gasses. The N_2/H_2O ratio of W, C and E slowly decreased since July 2014 until April 2017, followed by a stable period until May 2018 (**Figure 2**). After May 2018, the N_2/H_2O ratio of

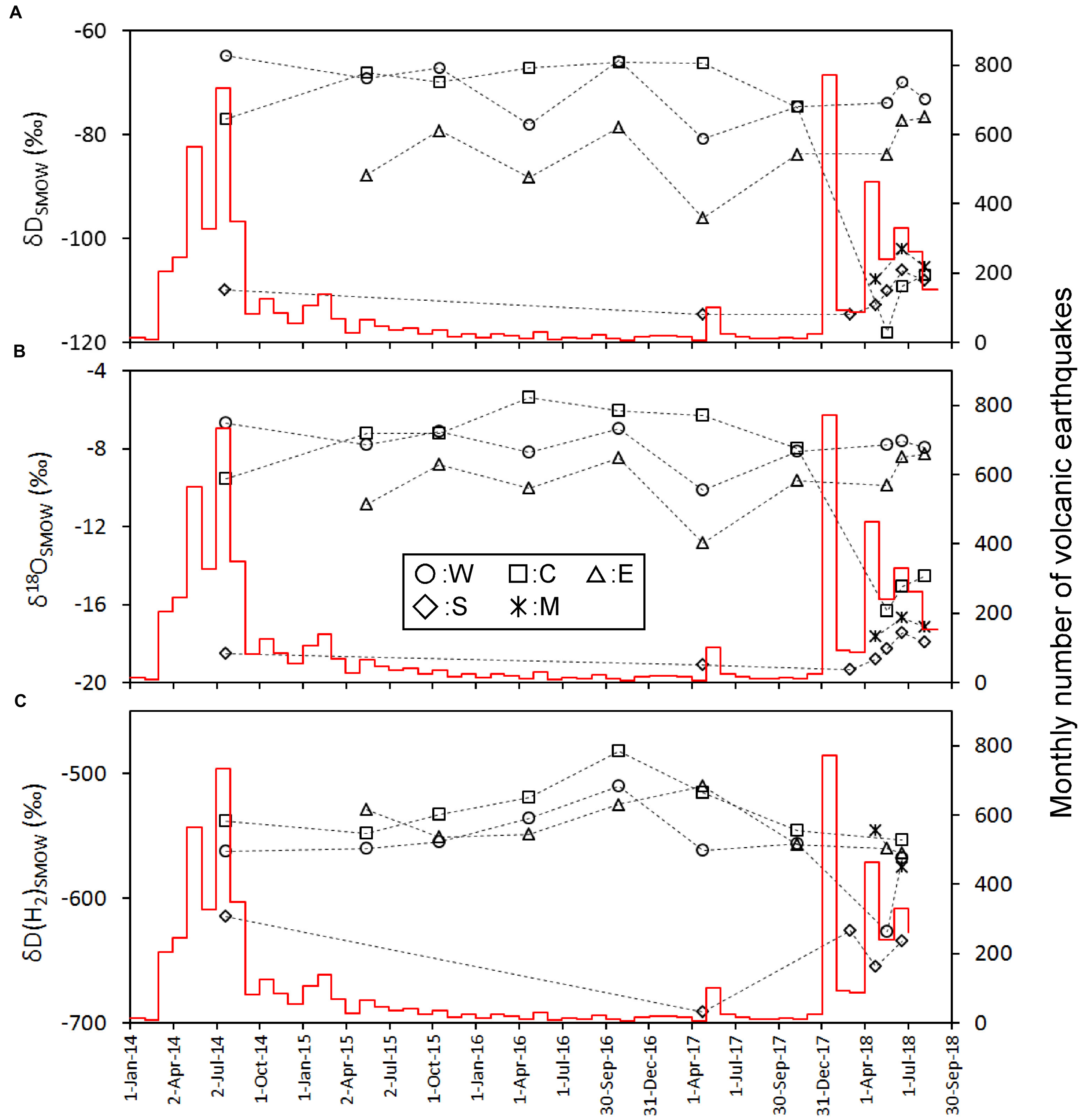

FIGURE 4 | Time variation of $\delta D(H_2O)$ **(A)**, $\delta^{18}O(H_2O)$ **(B)**, and $\delta D(H_2)$ **(C)** calibrated on the left *y*-axis. The red histogram calibrated on the right *y*-axis shows the monthly number of volcanic earthquakes observed by JMA.

W, C and E declined together in June 2018. The N_2/H_2O ratio of S was high until March 2018, and then it dropped after April 2018. The H_2S/H_2O ratio of W, C and E had no monotonic increase or decrease through the period of this study (**Figure 3A**). The stable H_2S/H_2O ratio of S until March 2018 declined significantly in May 2018. A similar decrease can be found in the CH_4/H_2O ratio of S (**Figure 3B**). The CH_4/H_2O ratio of W, C and E show a noticeable feature; namely, they were not detected in July 2014 when the seismic activity was high. They significantly increased in April 2016 until November 2017, followed a quick drop in May 2018. The Ar/H_2O ratio of S was almost higher than the ratios of W, E and C, except October 2016. The Ar/H_2O ratio of M was high relative to the ratios of W, E and C (**Figure 3C**). The δD and $\delta^{18}O$ of H_2O in fumarolic gas (**Figures 4A,B**) were almost stable beside a drop of C after May 2018. The δD and $\delta^{18}O$ of S were slightly increasing after April 2018. The $\delta D(H_2)$ in fumarolic gas (**Figure 4C**) of W, C, E was almost stable except the small rising in October 2016 and a drop of C in May 2018. The $\delta D(H_2)$ of S was lower than the $\delta D(H_2)$ of W, C, E over the whole period. The apparent equilibrium temperature (hereafter AET) was calculated assuming the equilibrium of the following reaction.

$$SO_2 + 3H_2 = H_2S + 2H_2O \tag{2}$$

AET is worth due to a potential measure for the temperature of gas source. The equilibrium of the above reaction depends on the total pressure of gas. The total pressure of gas was assumed to be the saturation pressure of H_2O at AET. For the calculation, the equation by Ohba et al. (2010) was used. The apparent equilibrium temperature (AET) was also calculated assuming the equilibrium of the following isotope exchange reaction.

$$HD + H_2O = H_2 + HDO \tag{3}$$

For the calculation, the fractionation factor given by Richet et al. (1977) was used. Hereafter, the AETs for the reactions (2) and (3) are designated to be ATE1 and AET2, respectively. As shown in **Figure 5**, AET1 of W, C, E was stable over the entire period. AET2 of W, C, E showed almost similar values each other. A weak rise of AET2 for W, C, E occurred in 2016.

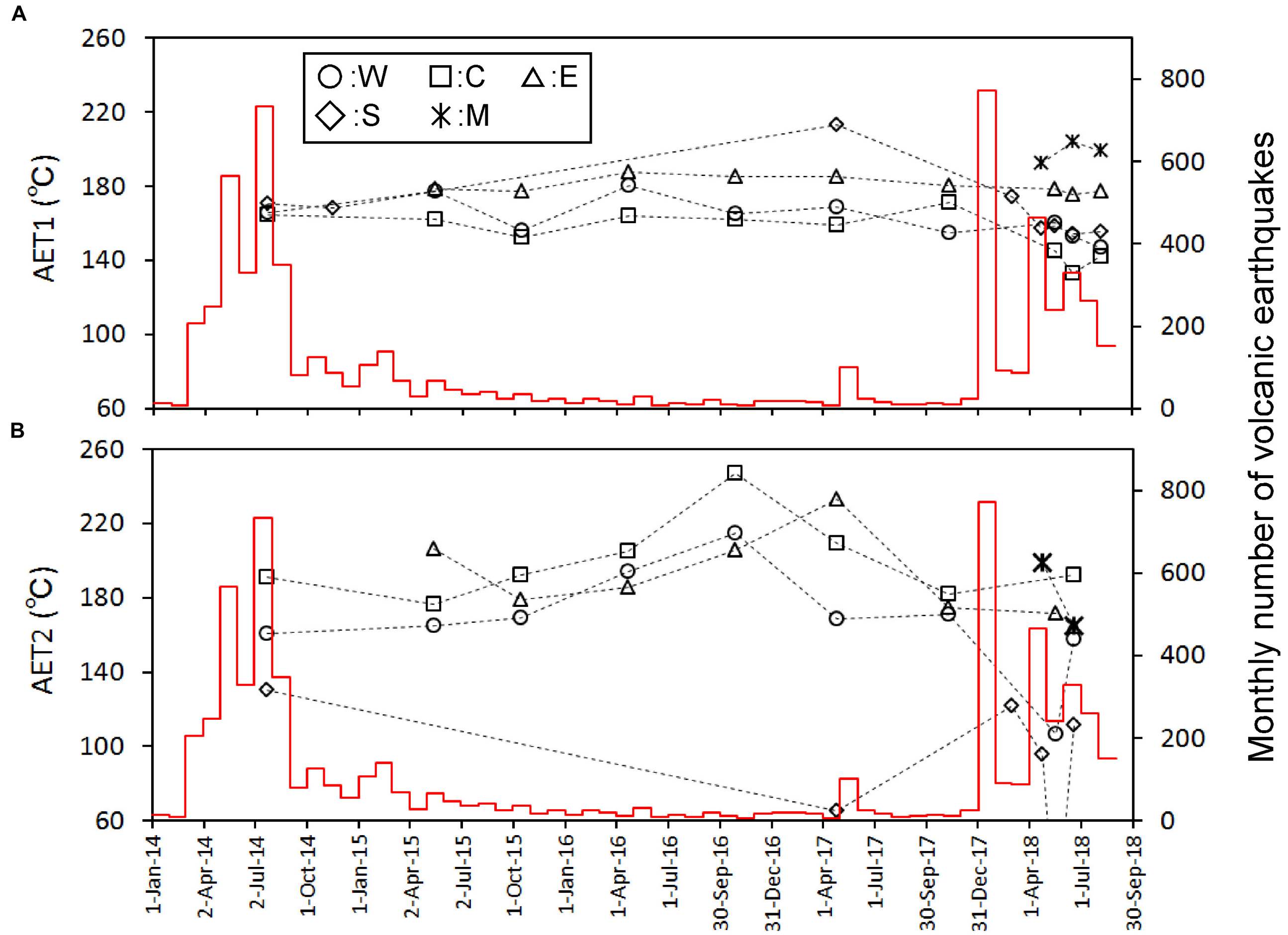

FIGURE 5 | Time variation of apparent equilibrium temperature [AET1 **(A)** and 2 **(B)** defined in the text] calibrated on the left *y*-axis. The red histogram calibrated on the right *y*-axis shows the monthly number of volcanic earthquakes observed by JMA.

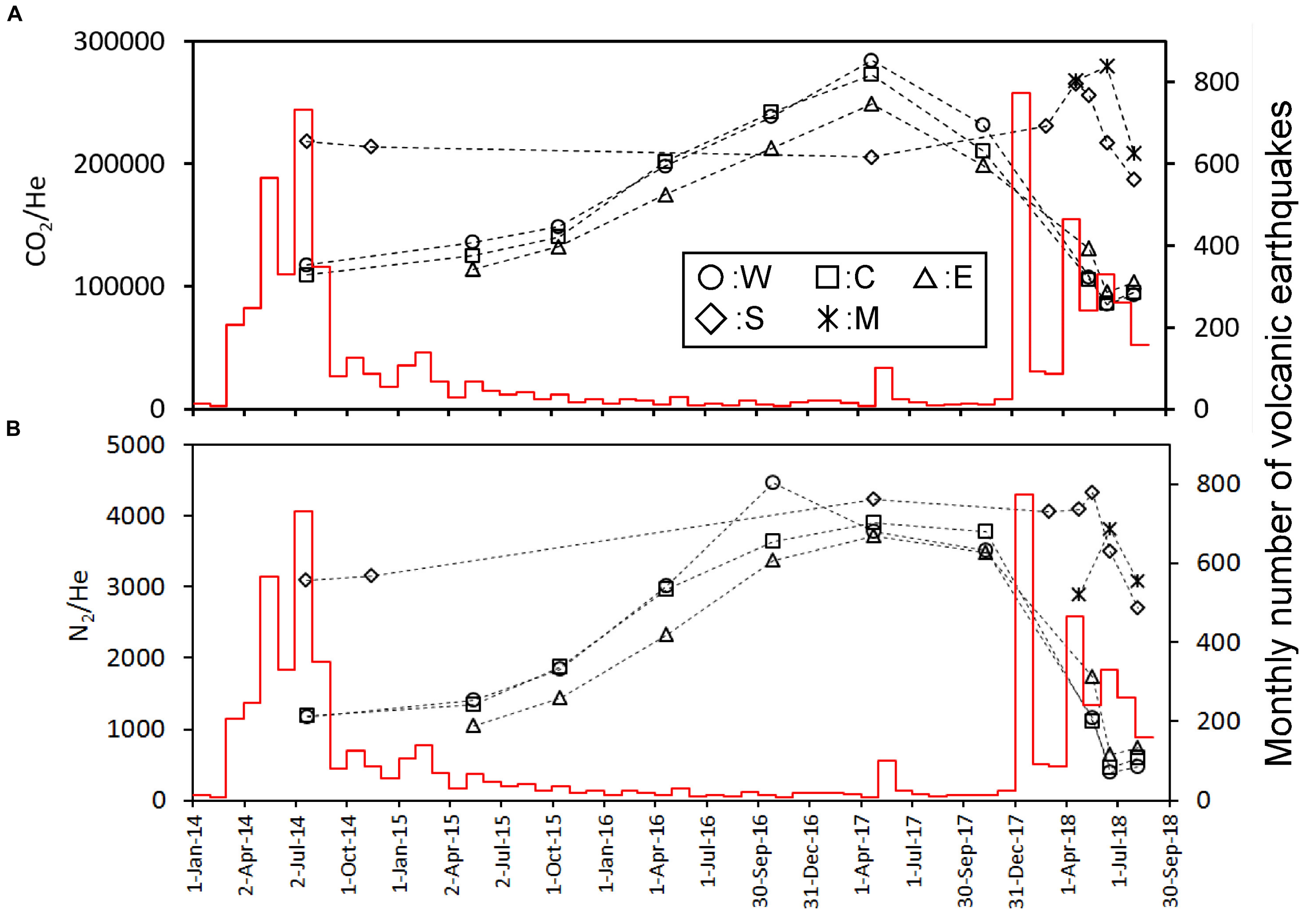

FIGURE 6 | Time variation of CO_2/He **(A)**, N_2/He **(B)** molar ratios calibrated on the left *y*-axis. The red histogram calibrated on the right *y*-axis shows the monthly number of volcanic earthquakes observed by JMA.

DISCUSSION

Multiple Components With Different Origins in the Fumarolic Gasses

For the source of He in fumarolic gas, two candidates are possible. One is He derived from a degassing magma. The other one is the He derived from the radioactive U and Th decay chain. According to Sano et al. (1994), the $^3He/^4He$ ratio in the fumarolic gas at Kusatsu-Shirane volcano was high as $8R_{atm}$, where R_{atm} is the atmospheric $^3He/^4He$ ratio, suggesting that the He in fumarolic gas originates in a degassing magma. Sano et al. (1994) recognized a negative correlation between $^3He/^4He$ ratio and $\delta^{13}C$ of CO_2 in fumarolic gas and bubble gas associated with hot spring discharges, suggesting an addition of CO_2 with high $\delta^{13}C$, likely derived from a limestone contained in the basement rock situated beneath Kusatsu-Shirane volcano (Uto et al., 1983). As shown in **Figure 2**, the variation pattern of He/H_2O, CO_2/H_2O and N_2/H_2O ratios resemble each other for W, C and E, namely, the ratios monotonically decreased since July 2014 until November 2017, suggesting that CO_2 and N_2 would also originate in a degassing magma. According to **Figure 6**, the CO_2/He and the N_2/He ratios of W, C and E are not constant throughout the study period, and cooperative fluctuations are observed. Namely, these ratios showed high values from April 2016 to November 2017. As a cause of this fluctuation, a) CO_2/He ratio and N_2/He ratio of magma component themselves fluctuated. Alternatively, b) CO_2 and N_2 other than magmatic component were contaminated during April 2016 to November 2017. At first we consider the possibility of a). As for the cause of the variation of the magmatic component, a change due to magma degassing is possible. Along with magma degassing, the He-N_2-CO_2 ternary composition will be governed by the solubility of each gas to magma. Namely, as degassing progresses, gasses with low solubility are selectively removed, and gas components with high solubility become gradually prominent. The solubilities of He, N_2 and CO_2 in magma are approximately 2.5×10^{-7} (mol g^{-1} bar^{-1}) (Carroll and Webster, 1994), 1.3×10^{-9} (mol g^{-1} bar^{-1}) (Humbert et al., 1998) and 1.3×10^{-8} (mol g^{-1} bar^{-1}) (Giggenbach, 1996), respectively. As the degassing progresses, the magmatic component is relatively rich in He having the highest solubility and is relatively deficient in N_2. Actually, as shown in **Figure 7**, from July 2014 (position-A) to November 2017 (position-B),

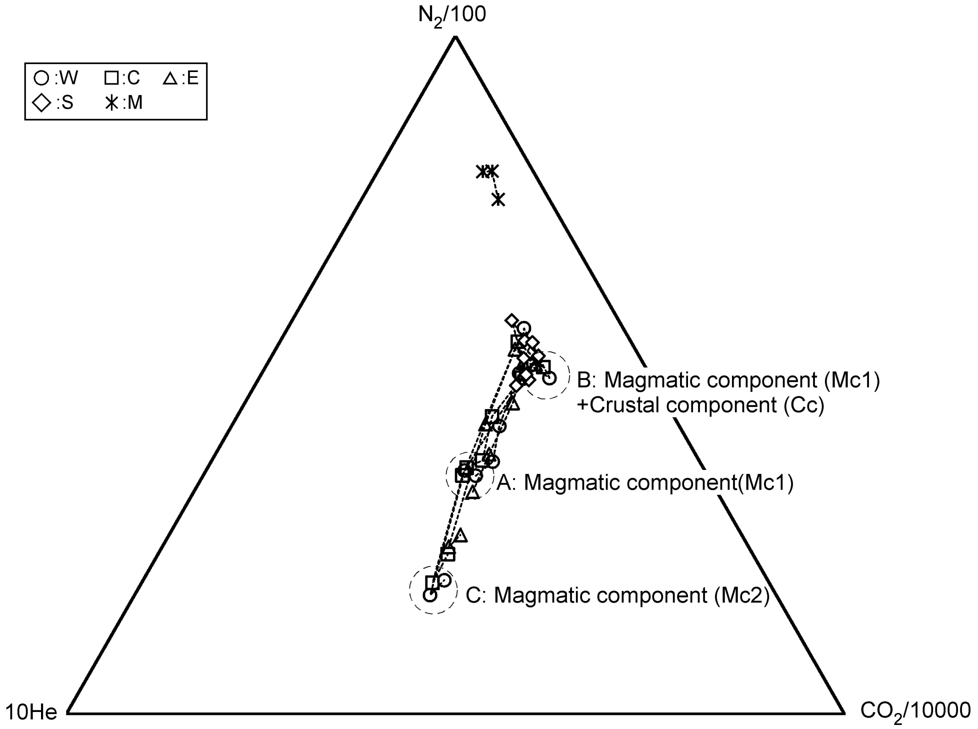

FIGURE 7 | He-N_2-CO_2 ternary molar composition of fumarolic gas. The position of A, B, and C indicate the composition in July 2014, November 2017 and August 2018, respectively.

N_2 temporally enriched, contradicting the prediction in the case of a). Therefore, the possibility of a) is low. Next, we consider the possibility of b). CH_4 is not a magmatic component, it is thought to be produced through the reduction of CO_2 by Fe^{2+} contained in the rocks (Giggenbach, 1997). Here, the component generated in the hydrothermal system is defined as hydrothermal component (Hc). CH_4 is a typical Hc. As other Hc, H_2S is also mentioned. H_2S can be generated by reduction of SO_2. The CO_2/He and N_2/He fluctuation of W, C and E (**Figure 6**) are similar to the variation pattern of CH_4/H_2O ratio (**Figure 3B**). This similarity suggests that CO_2 and N_2 other than magmatic component may have been added to W, C and E during April 2016 to November 2017. The trajectory of He-N_2-CH_4 ternary component fluctuation has an interesting pattern (**Figure 8**). In **Figure 8**, the composition of W, C, E was in the position of A in July 2014. Hereafter, the composition at the position-A is defined to be Mc1. The composition of W, C and E gradually moved to the direction of CH_4 corner and reached the position-B in November 2017. The trajectory from A to B depicts a convex upward curve. This indicates that at the beginning, the CH_4/N_2 ratio of the additional component to the composition of A was low and the CH_4/N_2 ratio of the additional component later increased. The composition in the position B changed toward another position C instead of returning to A. CH_4 and N_2 are likely to have different origins as components added in the process from A to B. Here, CO_2, N_2 derived from carbon and nitrogen contained in host rocks hosting hydrothermal reservoirs are defined as crustal component (Cc). As a source of N_2 as the additional component, it is highly likely Cc. In **Figure 7**, it is considered that the change of A to B, the CO_2/N_2 ratio of the additional component was constant. Therefore, CO_2 as an additional component is also regarded as crustal component (Cc). It is presumed that the CH_4/N_2 ratio of the additional component increased because the redox state of the hydrothermal reservoir became reduced. As a cause of the reduction, the decrease in the flow rate of magmatic gas enriched in SO_2 is possible.

According to the conventional theory (Kita et al., 1993), the He-N_2-Ar ternary composition of volcanic gasses is controlled by the tectonic environment where the target volcano is located. For example, in subduction zones volcanoes are strongly influenced by a subducting oceanic plate. Nitrogen supplied from the oceanic plate is taken into the magma and the N_2/He ratio of the volcanic gas is high (Sano et al., 2001). On the other hand, the volcanoes located in the back arc and hot spots have low N_2/He ratio because the influence of N supplied from the oceanic plate is small or negligible. **Figure 9** plots the He-N_2-Ar ternary composition of the fumarolic gas. Distribution of fumarolic gas on the figure is not consistent to the conventional theory. W, E and C were in the area specific to some Mediterranean volcanoes, such as Vulcano, Campli Flegrei and Milos (Giggenbach, 1997) around July 2014 (position-A), but moved to the position of Circum-Pacific Rim volcanoes by November 2017 (position-B). After that, again it moved to a region of the Mediterranean volcanoes (position-C), but with N_2/He ratios lower than the position-A in July 2014. The shift from A to B can be explained by the addition of N_2 as crustal component (Cc). Hereafter

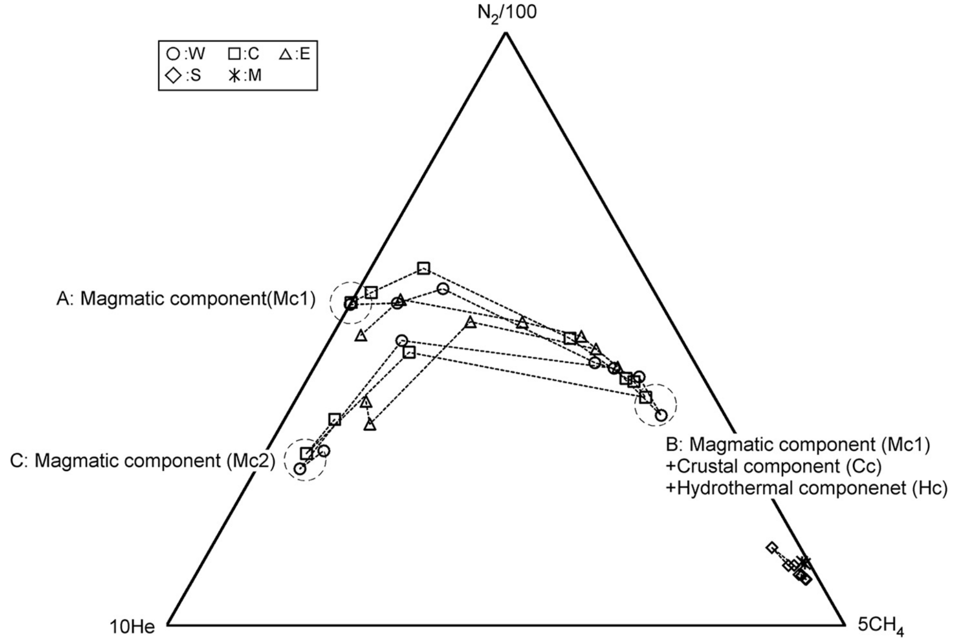

FIGURE 8 | He-N_2-CH_4 ternary molar composition of fumarolic gas. The position of A, B, and C indicate the composition in July 2014, November 2017 and August 2018, respectively.

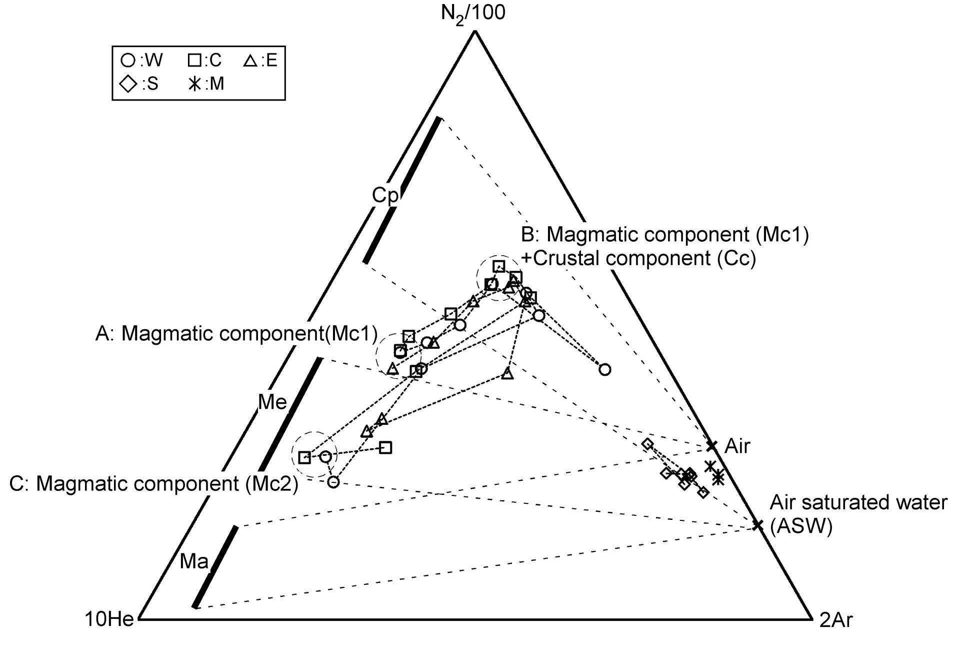

FIGURE 9 | He-N_2-Ar ternary molar composition of fumarolic gas. The position of A, B, and C indicate the composition in July 2014, November 2017 and August 2018, respectively. Cp, Me, Ma represent the typical endmember composition of gas from volcanoes on circum-Pacific volcanic belt, Mediterranean sea and hot spots with mantle origin, respectively (Giggenbach, 1997).

the component at C is defined as Mc2. The fumarolic gas at A and C contain little CH_4. Therefore, Mc1 and Mc2 are thought to represent the magmatic component. Mc2 is poor in N_2 relative to Mc1. This feature may have occurred with magma degassing, because N_2 is less soluble than He and CO_2. Based on the above discussion, the evolution of hydrothermal reservoir, which is the source of fumaroles W, C and E, is schematically shown in **Figure 10**. In Period I, magmatic gas is transported to hydrothermal reservoir passing through the sealing zone (Fournier, 1999). The composition of the magmatic

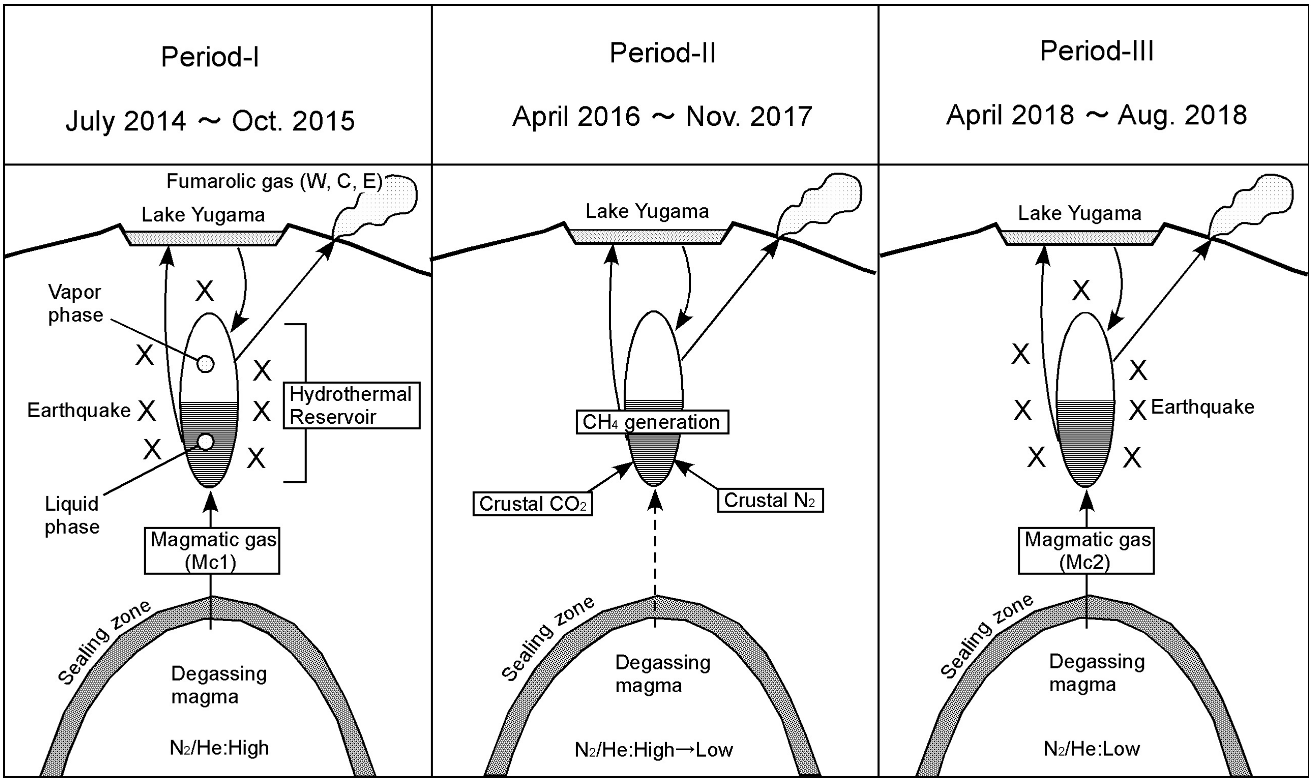

FIGURE 10 | Conceptual model for the evolution of magma hydrothermal system beneath Crater lake Yugama.

gas was Mc1. The fluid pressure in the reservoir was high, and earthquakes occurred frequently. Kusatsu-Shirane volcano experienced a seismic crisis in 1990 and 1991. Based on the temporal changes of the lake water in Crater Yugama, Ohba et al. (2008) modeled the magma-hydrothermal system. In 1990 and 1991, the chloride concentration of lake water increased quickly accompanying the decrease in pH of lake water, suggesting an input of HCl enrich magmatic gas to the hydrothermal reservoir beneath Crater Yugama through the sealing zone surrounding the degassing magma. In 2014, a chloride increase and pH drop, similar to those in 1990, were observed in the lake water (in preparation for publication). Considering the similarity between the activity in 1990 and 2014, an input of magmatic gas through the sealing zone was assumed in the Period-I. In period II, due to the regrowth of sealing zone, the release of magmatic gas was reduced. The hydraulic pressure in the reservoir decreased and the occurrence of the earthquake was suppressed. During this period, the flow rate of SO_2 supplied to the reservoir would decrease, the fluid in the reservoir gradually became reductive, and CH_4 was generated by the reductive reaction of CO_2. In addition, carbon and nitrogen contained in host rock of reservoir were extracted to the hydrothermal fluid as CO_2 or N_2. In Period III, magmatic gas whose composition is Mc2 again passed through the sealing zone. The fluid pressure in the reservoir again increased, causing frequent earthquakes. The N_2/He ratio of Mc2 decreased relative to the N_2/He ratio of Mc1, due to the progress of degassing.

Let us now examine the possibility that the compositional change of the fumarole occurred as a result of the earthquake. Such a situation can occur, for example, when a fluid is confined in a hydrothermal system, and the host rock is fractured by seismic activity and the fluid is released. The fluid should interact with the host rock. Generally, rocks are rich in Fe^{2+}, which acts as a reducing agent and converts CO_2 to CH_4 (Giggenbach, 1997). Therefore, the fluid confined in the space should contain CH_4. Moreover, CO_2 and N_2, which are crustal components contained in the host rock, will be extracted into the fluid. The fluid interacting with the host rock should be thus rich in hydrothermal components CH_4 and crustal components CO_2 and N_2. If such fluids are released by seismic activity, the CH_4/H_2O, CO_2/He, and N_2/He ratios will increase just after the seismic event. Since such changes are opposite to the actual observations, the possibility that seismic activity is responsible for the compositional change of fumarole is denied. Therefore, we postulate that the magmatic gas was injected into the hydrothermal system, triggering the seismicity.

Formation Process of Fumarolic Gas

The distribution of fumarolic gasses (W, C, and E) on the δD vs. $\delta^{18}O$ plane (**Figure 11**) coincides with the slope of the isotopic fractionation between water and steam at 100°C. A partial condensation of water vapor near the surface of the ground is presumed to produce the observed distribution. The isotope ratio of water vapor before condensation will be around

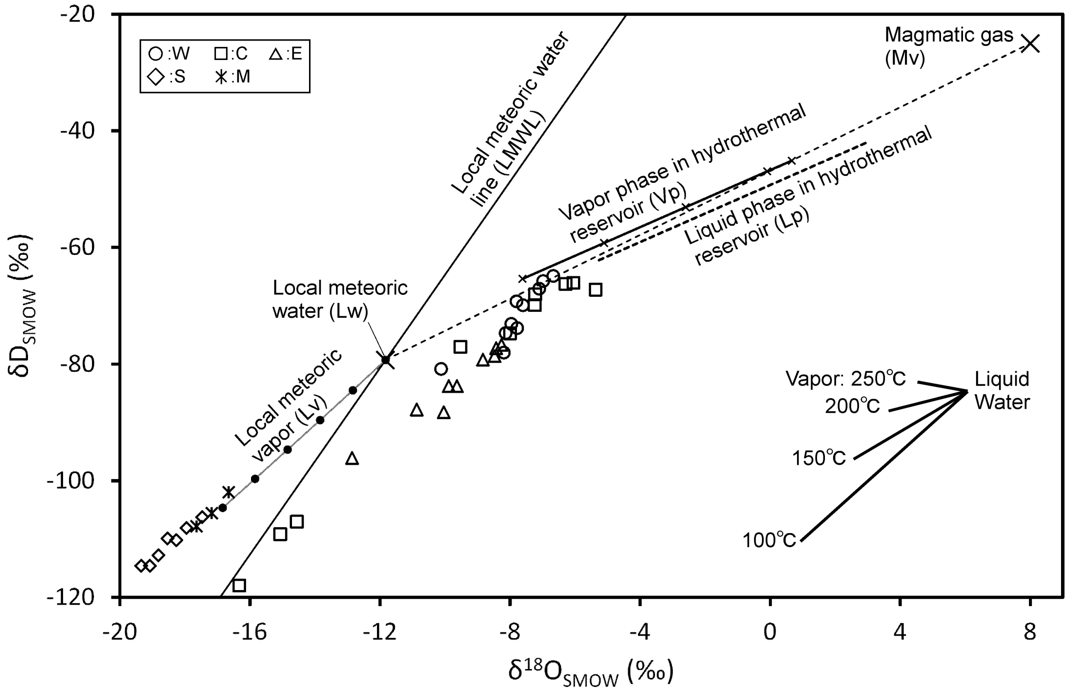

FIGURE 11 | δD and δ^{18}O of H_2O in fumarolic gas with the modeled vapor phase in hydrothermal reservoir. The isotopic fractionation between water and vapor with various temperatures is inserted.

the upper right of the distribution. As a model to generate water vapor for the explanation of isotopic ratios of W, C and E, we considered a mixing of high-temperature magmatic gas (Mv) and cold meteoric groundwater (Lw). Numerical values necessary for the model calculation are listed in **Table 3**. As a result of mixing of Mv and Lw, water vapor (Vp) and coexisting hot water (Lp) are generated. In the model calculation, the temperature of Vp and Lp is necessary. Considering the AET1 and 2 of W, C and E, 200°C was adopted as an appropriate and delimitating value for the temperature of Vp and Lp. In this model, CO_2/H_2O and stable isotopic ratios of Mv should be input and CO_2/H_2O and stable isotope ratios of Vp and Lp can be outputted. Equations necessary for calculation are, as follows:

$$H_{Mv}f + H_{Lw}(1-f) = H_{Vp}g + H_{Lp}(1-g) \tag{4}$$

$$\delta_{Mv}f + \delta_{Lw}(1-f) = \delta_{Vp}g + \delta_{Lp}(1-g) \tag{5}$$

$$C_{Mv}f + C_{Lw}(1-f) = C_{Vp}g + C_{Lp}(1-g) \tag{6}$$

$$\alpha = \frac{\delta_{Lp} + 1000}{\delta_{Vp} + 1000} \tag{7}$$

$$\beta = \frac{C_{Vp}}{C_{Lp}} \tag{8}$$

where H, δ, and C represent enthalpy, the δ-notated isotope ratio, and the CO_2/H_2O value, respectively. The phases are indicated by subscripts (Mv, Lw, Vp, and Lp). f and g denote the mixing fraction of Mv and the generating fraction of Vp, respectively. In general, g is not equal to f. The value of f and g is based on the amount of H_2O. Alpha (α) is the isotopic fractionation factor between liquid and vapor phase in terms of D/H and $^{18}O/^{16}O$ ratios (Horita and Wesolowski, 1994). Beta (β) is the

TABLE 3 | Parameters used for the model calculation generating Vp.

Term	Symbol	Value	Unit	References
Temperature of Mv		900	°C	
Temperature of Lw		15	°C	
Enthalpy of Mv	H_{Mv}	4391	kJ/kg	The Japan Society of Mechanical Engineers [JSME] (1999)
Enthalpy of Lw	H_{Lw}	64	kJ/kg	The Japan Society of Mechanical Engineers [JSME] (1999)
Enthalpy of Vp at 200°C	H_{Vp}	2790	kJ/kg	The Japan Society of Mechanical Engineers [JSME] (1999)
Enthalpy of Lp at 200°C	H_{Lp}	855	kJ/kg	The Japan Society of Mechanical Engineers [JSME] (1999)
δ^{18}O of Mv	δ_{Mv}	8	‰	
δ^{18}O of Lw	δ_{Lw}	−11.83	‰	Ohba et al. (2000)
δD of Mv	δ_{Mv}	−25	‰	
δD of Lw	δ_{Lw}	−79.3	‰	Ohba et al. (2000)
CO_2/H_2O molar ratio of Mv	C_{Mv}	0.008		
CO_2/H_2O ratio of Lw	C_{Lw}	0		
D/H and $^{18}O/^{16}O$ fractionation factor	α			Horita and Wesolowski (1994)
CO_2/H_2O distribution coefficient	β			Giggenbach (1980)

distribution coefficient between vapor and liquid phase in terms of CO_2/H_2O ratio (Giggenbach, 1980). Equations 4, 5, and 6 describe the conservation of enthalpy, isotopic ratio, and the amount of CO_2, respectively. Equations 7 and 8 describe the equilibrium distribution of stable isotope and CO_2, respectively, between Vp and Lp. Combing Eqs. 4 through 8, the isotopic ratio and CO_2/H_2O ratio for Vp can be calculated. As a result of the calculation, the isotopic ratio of Vp is represented by a line in **Figure 11**. Because the degree of freedom is left in the mixing ratio of Mv and Lw, Vp is expressed as the line. Comparing W, C, and E with the high isotopic ratios near the line of Vp, Vp that is the basis of W, C and E is considered to occur when the mixing ratio of Mv is 0.3–0.4. It seems that this mixing ratio was stable from 2014 to 2018.

The isotopic ratios of S and M are similar. The positions of S and M are clearly different from W, C and E. Although the similarity in isotopic ratios between S and M, they have quite different CO_2/H_2O ratios (**Figure 12**). By considering the CO_2/H_2O ratio in addition to the isotopic ratio, the formation mechanism of S and M is elucidated. In **Figure 12**, the scaled CO_2 fraction is taken on the horizontal axis. The scaled CO_2 fraction is defined by the following equation.

$$\mathrm{ScF}(CO_2) = \frac{50C}{50C+1} \qquad (9)$$

where C is the CO_2/H_2O molar ratio. In **Figures 12A,B**, the vertical axis shows δD and $\delta^{18}O$, respectively. First, the vapor (Vp) in reservoir condensed slightly, then mixed with

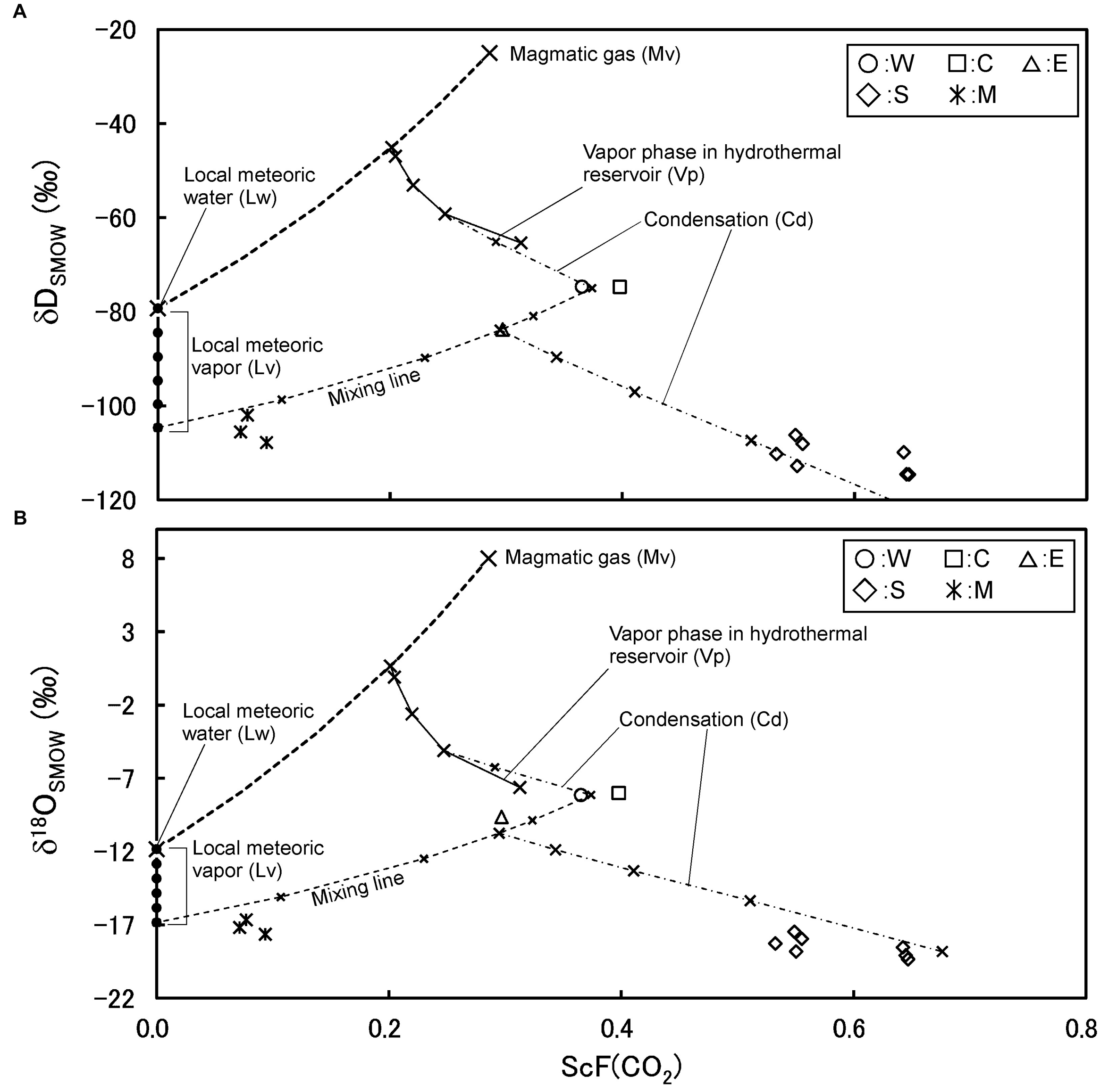

FIGURE 12 | Correlation between isotopic ratios and CO_2/H_2O molar ratio for fumarolic gasses and modeled vapor phase. $\mathrm{ScF}(CO_2)$ is the scaled CO_2 fraction in H_2O-CO_2 binary system.

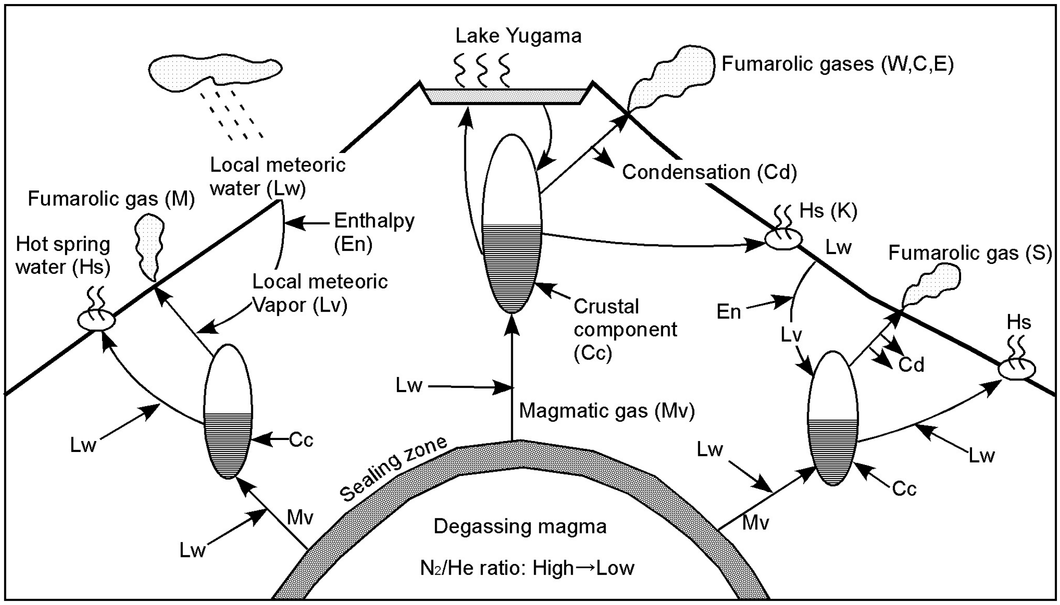

FIGURE 13 | Conceptual model for the magma hydrothermal system at Kusatsu-Shirane volcano.

a water vapor generated from the local meteoric water (Lv). A groundwater circulating in crust could be heated conductively. The groundwater gets enthalpy through the heating. The existence of Lv in Kusatsu Shirane volcano was demonstrated by Ohwada et al. (2003). The fumarolic gas S is considered to have formed from the mixture followed by a heavy condensation. The fumarolic gas M has the CO_2 concentration much lower than that of S. The low CO_2 concentration is due to the large mixing fraction of Lv. After the mixing little condensation took place. Some arbitrariness remains in the above model such as, the temperature of Vp and Lp, the exact isotopic ratio of Lv etc. However, this model successfully demonstrates the isotopic ratio and the CO_2/H_2O ratio of all the fumarolic gasses of Kusatsu Shirane volcano. In the model, a single magmatic gas (Mv) is required with the interaction of local meteoric water and the condensation of water vapor.

Magma Hydrothermal System Beneath Kusatsu Shirane Volcano

Figure 13 schematically shows the estimated magma hydrothermal system in Kusatsu-Shirane volcano. First, there is a single degassing magma emitting magmatic gasses (Mv) through the sealing zone. Mv mixes with the cold groundwater with meteoric origin (Lw), then vapor (Vp) and thermal water (Lp) are generated in hydrothermal reservoir. As shown in **Figures 7**, **9**, the fumarolic gas at the point M is significantly affected by atmospheric components relative to the fumarolic gas at the point W, C, E and S. As shown in **Figure 8**, the fumarolic gasses at the points M and S are enriched in CH_4 relative to the gasses at W, C and E. There is a compositional similarity among the gasses at W, C and E, suggesting the fumarolic gasses W, C and E are derived from a common hydrothermal reservoir. The compositional difference among the fumarolic gas at M, S and the group of W, C and E suggests the existence of individual hydrothermal reservoir for the gasses at S and M. In total, three reservoirs are necessary at Kusatsu-Shirane volcano. The vapor in hydrothermal reservoir beneath Crater Yugama discharges at surface as fumarolic gas after receiving a vapor condensation. The vapor in the reservoir beneath fumarole S is mixed with Lv and then appears on the ground surface after a heavy vapor condensation near the surface. The vapor in the reservoir beneath fumarole M undergoes mixing with a large fraction of Lv then appears on the surface as fumarolic gas. The fumarolic gas M is highly affected by the atmospheric N_2 and Ar (**Figures 7**, **9**), which were carried by the meteoric water vapor (Lv).

CONCLUSION

As a result of repeated collecting and analyzing fumarolic gas at Kusatsu Shirane volcano, a close relationship was found between the seismic activity and the chemical composition of fumarolic gas near the summit (W, C, and E). When seismic activity was active, He and CO_2 increased, and when seismic activity fell, CH_4 and N_2 increased. These components increase and decrease in response to the injection of magmatic gas to the hydrothermal reservoir. The N_2/He ratio of the fumarolic gas near the summit varies with two factors. When the crustal component is added to the hydrothermal reservoir, this ratio rises. As magma degassing progresses, this ratio decreases inversely. It is estimated that the fumarolic gasses of Kusatsu-Shirane volcano are generated by a single magmatic gas with the interaction of meteoric groundwater. The fumarolic gas (S) at the eastern slope has a relatively high CO_2 concentration due to considerable vapor condensation. The fumarolic gas (M) on the western slope contains CO_2 with low concentration due to the large contribution of water vapor generated from a meteoric groundwater, consistent to the high concentration of atmospheric N_2 and Ar. These data suggest that at Kusatsu-Shirane volcano the activation of seismicity was synchronized with the increase of magmatic components in fumarolic gas. It is postulated that the injection of magmatic gas increased the fluid pressure in the reservoir, which triggered the seismicity. The injection would be triggered by a break of the sealing zone surrounding the degassing magma. The injection of magmatic gas can be detected by monitoring the composition of the fumarolic gas, thus giving the possibility to forecast any future seismicity.

AUTHOR CONTRIBUTIONS

TO drafted the manuscript. TO, MY, KN, and NN sampled fumarolic gasses and analyzed them. UT, MI, and RS analyzed fumarolic gas samples. All authors read and approved the final manuscript.

FUNDING

This research was supported by the Japanese Ministry of Education, Culture, Sports, Science and Technology, under grant of the Integrated Program for Next Generation Volcano Research and Human Resource Development 2016 to 2018, also under its Earthquake and Volcano Hazards Observation and Research Program 2015 to 2018, the Japan Society for the Promotion of Science (JSPS) KAKENHI Grant Number 15K12485 in 2015 to 2017, the Earthquake Research Institute, The University of Tokyo Joint Usage/Research Program 2015 to 2018, and the General Research Institute of Tokai University 2016 to 2018.

ACKNOWLEDGMENTS

We sincerely thank the funders for their funding support for this research, the reviewers OV and DR for their efforts in reviewing and improving the quality of the manuscript, and the editor FT and Dr. Valerio Acocella for handling the editorial process.

REFERENCES

Barberi, F., Bertangnini, A., Landi, P., and Principe, C. (1992). A review on phreatic eruptions and their precursors. *J. Volcanol. Geotherm. Res.* 52, 231–246. doi: 10.1016/0377-0273(92)90046-g

Carroll, M. R., and Webster, J. D. (1994). Solubilities of sulfur, noble gases, nitrogen, chlorine, and fluorine in magmas. Volatiles in magmas, Mineralogical society of America. *Rev. Mineral.* 30, 231–278.

Fournier, R. O. (1999). Hydrothermal processes related to movement of fluid from plastic into brittle rock in the magmatic-epithermal environment. *Econ. Geol.* 94, 1193–1212.

Giggenbach, W. F. (1975). A simple method for the collection and analysis of volcanic gas samples. *Bull. Volcanol.* 39, 132–145. doi: 10.1007/bf02596953

Giggenbach, W. F. (1980). Geothermal gas equilibria. *Geochim. Cosmochim. Acta* 44, 2021–2032. doi: 10.1016/0016-7037(80)90200-8

Giggenbach, W. F. (1996). "Chemical composition of volcanic gases," in *Monitoring and Mitigation of Volcano Hazards*, eds R. Scarpa, and R. I. Tilling, (Berlin: Springer), 221–256. doi: 10.1007/978-3-642-80087-0_7

Giggenbach, W. F. (1997). "The origin and evolution of fluids in magmatic-hydrothermal systems," in *Geochemistry of Hydrothermal Ore Deposits*, ed. H. L. Barnes, (Hoboken, NJ: John Wiley & Sons), 737–796.

Global Volcanism Program (2013). *Smithonian Institution, National Museum of Natural History*. Available at: https://volcano.si.edu/

Hayakawa, Y., and Yui, M. (1989). Eruption history of the Kusatsu Shirane Volcano. *Quat. Res.* 28, 1–17. doi: 10.4116/jaqua.28.1

Horita, J., and Wesolowski, D. J. (1994). Liquid-vapor fractionation of oxygen and hydrogen isotopes of water from the freezing to the critical temperature. *Geochim. Cosmochim. Acta* 58, 3425–3437. doi: 10.1016/0016-7037(94)90096-5

Humbert, F., Libourel, G., Marty, B., and France-Lanord, C. (1998). "Nitrogen solubility in silicate melts as a function of oxygen fugacity and melt composition," in *Proceeding of the Goldschmidt Conference Toulouse*, Vandœuvre-lès-Nancy, 667–668. doi: 10.1180/minmag.1998.62a.2.18

Kaneko, T., Shimizu, S., and Itaya, T. (1991). K-Ar ages of the Quaternary volcanoes in the Shin-etsu highland area, central Japan, and their formation history. *Bull. Earthq. Res. Inst. Univ. Tokyo* 66, 299–332.

Kita, I., Nitta, K., Nagao, K., Taguchi, S., and Koga, A. (1993). Difference in N/Ar ratio of magmatic gases from northeast and southwest Japan: new evidence for different states of plate subduction. *Geology* 21, 391–394.

Minakami, T., Matsusita, K., and Utibori, S. (1942). Explosive activities of volcano Kusatsu-Shirane during 1938-1942. *(Part-II). Bull. Earthq. Res. Inst. Univ. Tokyo* 20, 505–526.

Ohashi, Y. (1914). The volcano Shirane, Prov. Kotsuke (IV). *J. Geol. Soc. Tokyo* 21, 359–368.

Ohba, T., Hirabayashi, J., and Nogami, K. (1994). Water, heat and chloride budgets of the crater lake, Yugama at Kusatsu-Shirane volcano, Japan. *Geochem. J.* 28, 217–231. doi: 10.2343/geochemj.28.217

Ohba, T., Hirabayashi, J., and Nogami, K. (2000). D/H and 18O/16O ratios of water in the crater lake at Kusatsu-Shirane volcano, Japan. *J. Volcanol. Geotherm. Res.* 97, 329–346. doi: 10.1016/s0377-0273(99)00169-9

Ohba, T., Hirabayashi, J., and Nogami, K. (2008). Temporal changes in the chemistry of lake water within Yugama crater, Kusatsu-Shirane volcano, Japan: implications for the evolution of the magmatic hydrothermal system. *J. Volcanol. Geotherm. Res* 178, 131–144. doi: 10.1016/j.jvolgeores.2008.06.015

Ohba, T., Sawa, T., Taira, N., Yang, T. F., Lee, H. F., Lan, T. F., et al. (2010). Magmatic fluids of Tatun volcanic group, Taiwan. *Appl. Geochem.* 25, 513–523. doi: 10.1016/j.apgeochem.2010.01.009

Ohwada, M., Ohba, T., Hirabayashi, J., Nogami, K., Nakamura, K., and Nagao, K. (2003). Interaction between magmatic fluid and meteoric water, inferred from 18O/16O and 36Ar/H2O ratios of fumarolic gases at the Kusatsu Shirane volcano, Japan. *Earth Planets Space* 55, 105–110. doi: 10.1186/bf03351737

Ossaka, J., Ossaka, T., Oi, T., Kikawada, K., Yamano, M., Hukuhara, H., et al. (1997). Volcanic activity of Kusatsu-Shirane volcano, Gunma, and secular change in water quality of crater lake, Yugama. *Chikyukagaku* 31, 119–128.

Ossaka, J., Ozawa, T., Nomura, T., Ossaka, T., Hirabayashi, J., Takaesu, A., et al. (1980). Variation of chemical compositions in volcanic gases and waters at Kusatsu-Shirane Volcano and its activity in 1976. *Bull. Volcanol.* 43, 207–216. doi: 10.1007/bf02597622

Ozawa, T. (1968). Chemical analysis of volcanic gases: I. Chemical analysis of volcanic gases containing water vapor, hydrogen chloride, sulfur dioxide, hydrogen sulfide, carbon dioxide, etc. *Geochem. Int.* 5, 939–947.

Richet, P., Bottinga, Y., and Javoy, M. (1977). A review of hydrogen, carbon, nitrogen, oxygen, sulphur, and chlorine stable isotope fractionation among gaseous molecules. *Ann. Rev. Earth Planet. Sci.* 5, 65–110. doi: 10.1146/annurev.ea.05.050177.000433

Sano, Y., Hirabayashi, J., Ohba, T., and Gamo, T. (1994). Carbon and helium isotopic ratios at Kusatsu Shirane Volcano, Japan. *Appl. Geochem.* 9, 371–377. doi: 10.1016/0883-2927(94)90059-0

Sano, Y., Takahata, N., Nishio, Y., Fischer, T. P., and Williams, S. N. (2001). Volcanic flux of nitrogen from the Earth. *Chem. Geol.* 171, 263–271. doi: 10.1016/s0009-2541(00)00252-7

Sugimura, A. (1960). Zonal arrangement of some geophysical and petrological features in Japan and its environs. *J. Fac. Sci., Univ. Tokyo Sec. II* 12, 133–153.

The Japan Society of Mechanical Engineers [JSME] (1999). *Steam Table, Japan Society of Mechanical Engineers*. Tokyo: JSME, 201.

Tsunogai, U., Kamimura, K., Anzai, S., Nakagawa, F., and Komatsu, D. (2011). Hydrogen isotopes in volcanic plumes: tracers for remote temperature sensing of fumaroles. *Geochim. Cosmochim. Acta* 75, 4531–4546. doi: 10.1016/j.gca.2011.05.023

Uto, K., Hayakawa, Y., Aramaki, S., and Ossaka, J. (1983). Geological map of Kusatsu-Shirane volcano. *Geol. Map Volcanoes* 3:10.

Conflict of Interest: The authors declare that the research was conducted in the absence of any commercial or financial relationships that could be construed as a potential conflict of interest.

Advantages of publishing in Frontiers

OPEN ACCESS
Articles are free to read
for greatest visibility
and readership

FAST PUBLICATION
Around 90 days
from submission
to decision

HIGH QUALITY PEER-REVIEW
Rigorous, collaborative,
and constructive
peer-review

TRANSPARENT PEER-REVIEW
Editors and reviewers
acknowledged by name
on published articles

Frontiers
Avenue du Tribunal-Fédéral 34
1005 Lausanne | Switzerland

Visit us: www.frontiersin.org
Contact us: info@frontiersin.org | +41 21 510 17 00

REPRODUCIBILITY OF RESEARCH
Support open data
and methods to enhance
research reproducibility

DIGITAL PUBLISHING
Articles designed
for optimal readership
across devices

FOLLOW US
@frontiersin

IMPACT METRICS
Advanced article metrics
track visibility across
digital media

EXTENSIVE PROMOTION
Marketing
and promotion
of impactful research

LOOP RESEARCH NETWORK
Our network
increases your
article's readership